SR-007
September 2007

Calibration of Particle Instruments in Space Physics

Editors

Martin Wüest
INFICON Ltd, Balzers, Principality of Liechtenstein

David S. Evans
Space Environment Center, NOAA, Boulder CO, USA

Rudolf von Steiger
International Space Science Institute, Bern, Switzerland

Cover: Example calibration data of the ASPERA-4/ELS sensor on the Venus Express mission of ESA (see p. 149).

The International Space Science Institute is a Foundation under Swiss law. It is funded by the European Space Agency, the Swiss Confederation, the Swiss National Science Foundation, and the University of Bern. For more information about ISSI see `www.issibern.ch`.

Published for:	The International Space Science Institute Hallerstrasse 6, CH-3012 Bern, Switzerland
by:	ESA Publications Division Keplerlaan 1, 2200 AG Noordwijk, The Netherlands
Publication Manager:	Karen Fletcher
Cover Design:	N.N.
Copyright:	©2007 ISSI/ESA
ISSN:	ZZZZ-YYYX
Price:	XX Euros

Contents

List of Figures

List of Tables

Preface

Those who do not learn the lessons of experience
will be forced to repeat them.

(after philosopher George Santayana)

Space physics deals with the properties and physical processes that occur in the near vacuum surrounding stars and planets. This volume of space is not empty but is permeated by electromagnetic fields and waves and by particles, both charged and neutral. Experimentally the science is largely pursued through in situ measurements by particles and fields instrumentation.

This instrumentation is designed to collect and return quantitative data that will enable scientists to validate or reject existing theories, formulate new questions, and broaden our understanding of the world, the solar system, and the universe around us. However, for this to happen effectively, it is essential that instrumentation be properly calibrated so that the measurements obtained are an accurate characterization of the environment. Without such an accurate calibration it is doubtful that the data obtained will be interpreted correctly.

Despite the importance of having accurate calibration, there are a number of reasons why calibration may be incomplete or inaccurate. The fundamental approach to calibrating an instrument, such as a particle sensor, is to determine the instrument's response to a particle beam having well-defined (known) properties in energy, angle, cross-sectional area, particle charge and particle mass. This is a time-consuming endeavor and it is clear that measurements can only be made for a discrete subset of the entire parameter space. Further, space research projects often have tight timelines for the development and deployment of instrument hardware. Although there are always good intentions to set aside sufficient time for a thorough calibration, experience has shown that unexpected delays accumulate, thus reducing the time available for calibration.

In addition, there are differences in the absolute calibration (easily by a factor two) between similar instruments calibrated at different institutions as well as between instruments of different design intended to measure the same physical parameters. The situation is further complicated because the parameters space physics instrumentation are intended to measure do not have a calibration standard available in space to provide an absolute calibration. This is in contrast to astronomy where standard candles are available in the form of stars that have been well characterized from the ground. Also remote sensing instruments have ground truth sites available to check on-board calibration. This underscores the need for better traceability and a calibration transfer standard for space physics instrumentation.

Even when an instrument has been adequately calibrated prior to launch, that instrument may degrade in the space environment and the initial calibration may no longer be valid. Degradations can occur due to contamination (e.g. outgassing), environmental effects (e.g. atomic oxygen, radiation), or aging. For example, bias voltages in open windowed electron multipliers, such as micro-channel plates, need to be increased periodically, as the gain of the device decreases with the amount of extracted charge. These issues become particularly important for in situ autonomous systems that are intended to provide valid measurements over long periods of time.

Another situation in which a single pre-flight calibration may prove inadequate is when the data returned from space indicate that phenomena are occurring that are outside the parameter space covered by the initial calibration. This can happen because many missions are unique in that they sample regions that have not been explored before (comet missions, solar polar orbit, interstellar space, Pluto) or regions that have not been explored in great detail (Mercury, outer planets). Once some data has been obtained from these regions, it may become clear that improving the instrument's calibration in certain areas of input space (e.g., for particular masses and energies) will become necessary to properly interpret data obtained in unanticipated physical situations. Re-calibration may be attempted using an engineering model as a surrogate for the flight instrument.

Multi-spacecraft missions involving a large number of identical instruments will place an even greater pressure on instrument calibration. First, calibration is time consuming and time at a calibration facility is limited. Calibrating at different facilities in parallel involves dealing with differences in absolute calibration and different capabilities of the facilities. Second, calibration in flight involves the difficulty of finding truly identical conditions in space. Third, the role of multi-point measurements is largely to determine gradients in physical parameters – which must be real and not artifacts of poor instrument calibrations if the science goals are to be met.

Today, most of the calibration knowledge and experience has been handed down within individual research groups. Some scattered reports exist on the calibration of space physics instruments, but generally calibration reports in this field are not published (in contrast to i.e. the Earth remote sensing community) since that task is often not considered science. There is no textbook that describes in one place the details and intricacies of the calibration of such instruments. However, thorough, exact and accurate calibration lays the foundation for the analysis and proper interpretation of space physics observations that are vital to progress in the field and, for that reason, should get the required attention. It is the goal of this monograph to provide the information necessary to lay this foundation.

Space physics addressing the particle environment must deal with many orders of magnitude dynamic range in particle energy range, flux, and density. In order to constrain the scope of the book, the material concentrates upon instruments for atomic and molecular particle measurements, both charged and neutral, with greater emphasis upon particle energies less than 100 keV. While material concerning neutral gas mass spectrometers designed for ionospheric and aeronomical research is included in this monograph, discussion of instruments dealing with typical planetary applications, such as lander instruments, laser ablation mass spectrometers or combination instruments such as gas chromatograph/mass spectrometers are not covered. However, many of the calibration methods that are discussed could be applied to those instruments with little modification.

The book is structured as follows:

Chapter 1 gives a brief background of the science questions important to the field of space physics and outlines the measurement requirements necessary to address those questions.

Chapter 2 describes the particle detectors that are currently employed and a subset of the many instrument designs incorporating such detectors that are used in experimental space physics research. Emphasis is given to instruments whose calibration and in-flight operation are discussed in more detail in subsequent chapters. Although the book focuses on particle instruments, a brief discussion of wave instruments is included because wave measurements provide independent information about certain aspects of the local charged

particle environment that are often used for in-flight cross calibration with particle measurements.

Chapter 3 describes the preflight calibration techniques. This material includes information about the proper design of the laboratory calibration facility but concentrates upon what aspects of an instrument warrant careful calibration and how to perform those tasks. The importance of determining in the laboratory the out-of-band or undesired responses on the part of an instrument is discussed because such responses are often significant in space operation.

Chapter 4 discusses techniques to assure proper calibration is verified and maintained once the instrument is in space and to identify and compensate for instrument degradation that will occur over time.

A brief summary and outlook chapter concludes the book and is followed by a number of appendices, which hopefully will be useful in the daily work.

The editors greatly appreciate the work of all working group participants as well as the external referees.

This book would not exist without the generous support provided by ISSI, who made resources available to support this project. We especially thank the ISSI staff for their warm hospitality that made this project possible and enjoyable.

Martin Wüest, David Evans and Rudolf von Steiger
Bern, August 2007

— 1 —

Introduction

MARTIN WÜEST[1], GÖTZ PASCHMANN[2], AND DAVID S. EVANS[3]
[1]*INFICON Ltd., Balzers, Liechtenstein*
[2]*International Space Science Institute, Bern, Switzerland*
[3]*Space Environment Center, NOAA, Boulder, CO, USA*

1.1 Particle Environments

This book is about calibration of particle instruments that are being flown on spacecraft to investigate the plasma and neutral gas environment of planetary upper atmospheres, ionospheres, magnetospheres, interplanetary space, and eventually, interstellar space. In these regions one finds particle populations that have very different energy ranges, directional characteristics, mass and charge composition, intensities, and time-variations. In this chapter we will introduce some typical characteristics of these environments and the implications they have on instrument design and calibration. We also briefly describe how basic measurements are converted to meaningful physical quantities used in scientific research.

To illustrate the range of intensities and energies that can be found in the various particle populations encountered in the heliosphere, Figure 1.1 shows the flux levels and energies of oxygen ions, which extend over 18 orders of magnitude in flux and 7 orders of magnitude in energy/nucleon.

As another example, Figure 1.2 shows the differential energy fluxes and the energy ranges encountered in various regions of Earth's magnetosphere and the adjacent solar wind. For ions, the fluxes have a dynamic range of 7 orders of magnitude. For electrons the dynamic range is less severe but still more than 4 orders of magnitude. The particles' energy ranges extend over nearly four orders of magnitude in either case.

Turning to neutral gas measurements, Figure 1.3 demonstrates, for the case of Earth's atmosphere, the large dynamic range in gas densities that instruments have to cope with.

1.2 Measurement Requirements

Depending on the particle characteristics - their energy range and directional characteristics, their mass and charge, their intensities, and time-variations - quite different measurement techniques and instrument designs must be employed. These are discussed in detail in Chapter 2. Here we only point out some general design considerations.

Fluxes, Energy Ranges, Time Resolution For the case of Earth's magnetosphere and its environs (cf. Figure 1.2), an ion instrument with a fixed total geometric factor would have to cover a dynamic range in count rates of 7 orders of magnitude, which is not presently feasible. Thus one either has to divide the task between different instruments, or provide a

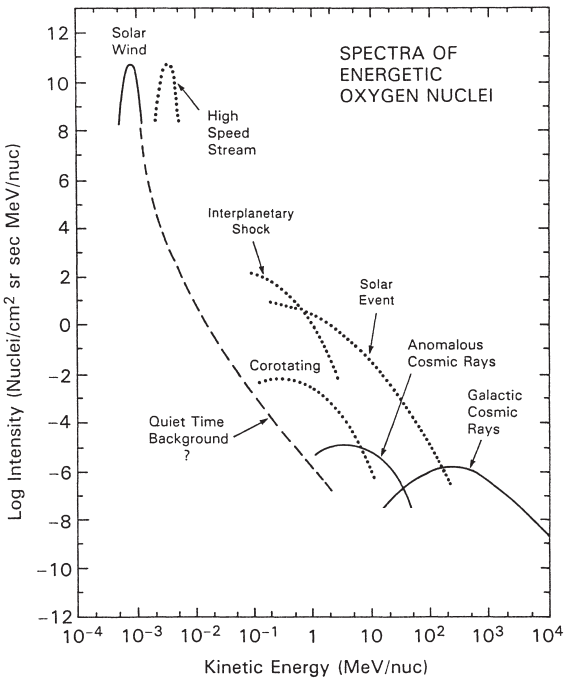

Figure 1.1: Typical oxygen spectra for different populations of particles in the heliosphere. Adapted from *von Rosenvinge et al.* [1995].

means to change geometric factors. For electrons the dynamic range is less severe but still more than 4 orders of magnitude. In either case, the instruments would have to cover an energy range of nearly four orders of magnitude.

Naturally, the particle environment and the science objectives also drive the time resolution with which the measurements need to be made. The highest demands arise from measurements of plasma discontinuities and their substructures in the solar wind or the magnetosphere that can pass over a spacecraft within less than a second; or the measurement of particles above narrow auroral arcs that low-altitude spacecraft cross within tens of milliseconds.

Angular Coverage A rough idea about the needed angular coverage can be obtained by considering three characteristic velocities: the thermal velocity of the particle distribution, V_{th}, their bulk velocity, V_b, and the spacecraft velocity, V_{sc}.

If V_b is much larger than V_{th}, as is the case for ions in the solar wind, particle velocities are constrained to a narrow range of directions and magnitudes, and an instrument therefore needs to cover only a limited range of directions and energies, but with high angle and energy resolution. In this case a three-axis stabilized spacecraft is adequate as long as one axis faces the sun.

If the opposite is true, i.e., V_b much smaller than V_{th}, particles will arrive from all directions and an instrument will therefore have to cover the complete 4π solid-angle sphere. This situation applies to solar wind electrons and to much of the plasma in Earth's

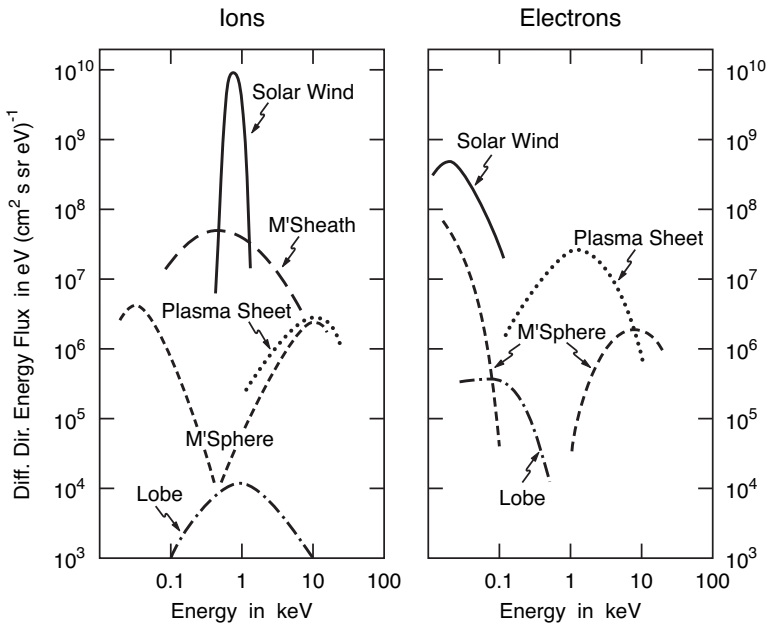

Figure 1.2: Differential directional energy fluxes of ions (left) and electrons (right) observed in various regions of Earth's magnetosphere and the adjacent solar wind. From plasma instrument proposal for Cluster, reproduced in *Baumjohann and Treumann* [1996].

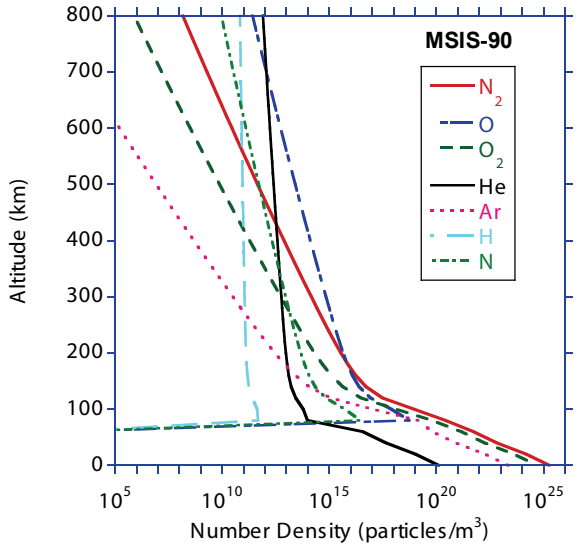

Figure 1.3: Density of major constituents of Earth's atmosphere [*Hedin*, 1991] for mean activities ($F_{10.7} = 140$, $A_p = 15$).

magnetosphere. The necessary 3-D coverage (energy, azimuth-, and elevation-angles) is easy to achieve on a spinning spacecraft. In this case a single instrument can sequentially sample all directions, but the time resolution will be limited to the spacecraft spin period.

The time resolution can be increased by placing a number of such detectors around the spacecraft circumference, at the expense of increased calibration requirements. Resource limitations not withstanding, one could deploy enough detectors so that their azimuth acceptance angles abut, and thus sample the full distribution instantaneously. The time resolution would then be limited only by the counting statistics. A more practical solution is to use fewer detectors, but equip them with electrically steerable azimuth acceptance angles to fill in the gaps that would otherwise remain. Multiple instruments, designed with this feature, may also provide for full angular coverage on non-spinning, three-axes stabilized spacecraft.

If in addition to $V_b \ll V_{th}$, the distributions are axially symmetric with respect to the magnetic field, then 2-D measurements (energy and pitch-angle) are adequate. This is the case for auroral electrons, for example.

A special situation arises if V_{sc} is much larger than V_{th}, and V_b is small as well (as is typical for low-altitude spacecraft). In this situation all particles will be incident on a forward facing detector aperture ("ram direction") at an energy determined by V_{sc} and particle mass.

Ion Composition Measurement of the ion mass- and charge-composition is important for two reasons. First, it provides information on the origin of the plasma. A good example is the distinction between solar wind and ionospheric origin of plasma in Earth's magnetosphere through the measurement of helium and oxygen ions and their charge state: He^{2+} ions indicate a solar wind origin, while O^+ ions indicate an ionospheric source.

The second reason is the effect of even small abundances of heavy ions for the plasma mass density. For example, the presence of only 6 % by number of oxygen ions will cause an almost 100 % increase in the mass density. The mass density, in turn, is what matters in many quantitative relations, such as momentum balance, or the Alfvén velocity.

Neutral Gas Composition In general, mission requirements dictate the gases desired to be measured while the pressure/flow regime and the speed of the gas relative to the spacecraft or probe dictate the type of gas inlet system. In the case of the orbiter or flyby instruments, atmospheric gas with no winds observed in the spacecraft frame of reference has an equivalent energy that depends on the mass of the gas and the spacecraft speed. The energy is $\frac{1}{2}MV_{sc}^2 = 5.182 \times 10^{-3} M V_{sc}^2$ eV where M stands for the species molecular weight in u (atomic mass units) and V_{sc} is the spacecraft speed in km s^{-1}. Room temperature gas at 300 K has 0.039 eV energy, independent of mass. The gas speed in the spacecraft reference frame ranges from 1 km/sec for the Rosetta comet Churyumov-Gerasimenko orbiter to as high as 68 km s^{-1} for comet Halley. This is an energy range of the order of electron volts to several thousand electron volts.

Another aspect of upper atmosphere sampling is the vehicle gas flow regime. The gas flow around the vehicle can be described by the Knudsen number, Kn, (equal to the ratio of the atmosphere mean free path to a typical vehicle dimension). It can range from continuum (viscous) flow ($Kn \ll 1$) to free-molecular flow ($Kn \gg 1$).

1.3 Conversion to Physical Quantities

To convert the raw measurements (i.e., counts collected as a function of energy, angle, particle species, etc.) into physical quantities, the instrument characteristics, i.e., the total geometric factor as function of direction, energy, mass, must be known (see Chapter 3 for details). Depending on the nature of the data and/or their intended use, different physical quantities are being used to characterize and quantify the properties of the particle populations.

1.3.1 Particle Fluxes

Particle intensities can be characterized in a number of ways (See also Table A.40). Some common choices are:

- *Number flux*. This term refers to the number of particles passing though a unit area per unit time, usually integrated over energy and angle. The units are particles $(\mathrm{cm}^2\ \mathrm{s})^{-1}$, which strictly speaking should be called number flux density. The unit area is usually understood to be oriented perpendicular to the particle's velocity vector.

- *Differential directional number flux*. This means particle flux per unit energy (commonly in units of eV) and solid angle (sr), usually measured over a range of energies and directions. Usually referred to as j, with units $(\mathrm{cm}^2\ \mathrm{s\ sr\ eV})^{-1}$.

- *Differential directional energy flux*. Often denoted (EJ). Units are $\mathrm{eV}(\mathrm{cm}^2\ \mathrm{s\ sr\ eV})^{-1}$. For a typical plasma instrument this quantity is directly proportional to its count rate. Some examples are given in Figure 1.2.

- *Total energy flux*. This denotes particle flux integrated over the energy range of an instrument at some fixed direction (or integrated over angle). Units are $\mathrm{eV}(\mathrm{cm}^2\ \mathrm{s})^{-1}$.

Conversion to flux sometimes requires making assumptions about the nature of the underlying distribution functions. For example, omnidirectional detectors have no intrinsic angular resolution. Thus the conversion to particle flux requires some assumption regarding the angular distribution of the incident particles.

1.3.2 Velocity Distribution Function

The velocity distribution function, $f(\boldsymbol{v})$, refers to the number of particles per phase space volume (denoted as phase space density), as a function of particle velocity. Units are $\mathrm{s}^3\ \mathrm{m}^{-6}$ or $\mathrm{s}^3\ \mathrm{cm}^{-6}$. Sometimes $\mathrm{s}^3\ \mathrm{cm}^{-3}\ \mathrm{km}^{-3}$ are used to indicate that densities are commonly in cm^{-3} while velocities are in $\mathrm{km\ s}^{-1}$.

Modern 3-D plasma instruments acquire thousands of samples per distribution. For example, an instrument that samples 30 energies E, 16 azimuth angles ϕ, and 8 polar angles θ, will collect a total of 3840 count rate samples, $C_{ijk} = C(E_i, \phi_j, \theta_k)$, per spacecraft spin. To transmit these distributions with full energy/angle resolution as often as they are measured usually far exceeds the telemetry allocation. Reduction of the number of energy/angle samples before transmission, application of efficient data compression

schemes, the reduction of the distribution function to a set of its moments (see below), or a combination of these measures, are possible solutions to this dilemma.

Full 3-D distributions are not measured instantaneously, but their sampling is typically spread over a spacecraft spin period. To construct the distributions one usually assumes that no time variations occur while the distribution is being accumulated.

To generate the velocity distribution function of a given particle species requires the conversion of the counts into phase space density as a function of velocity and direction. For an electrostatic analyzer, $f_{ijk} \propto C_{ijk}/v_{ijk}^4$, with a proportionality factor given by the detector total geometric factor.

Details on the measurements of the velocity distribution functions may be found in *Fazakerley et al.* [1998].

1.3.3 Moments

In many circumstances the quantitative analysis and interpretation of plasma measurements requires the knowledge of the moments of the distribution functions. The definition, computation and error sources of the moments, as well as their use are discussed in detail in *Paschmann et al.* [1998]. Here we repeat only some of the basics.

The moments of the velocity distribution function, $f(\boldsymbol{v})$, of a given particle species of mass m are defined as

$$M_j \equiv m \int f(\boldsymbol{v})\, \boldsymbol{v}^j \, \mathrm{d}^3 v \tag{1.1}$$

where $\boldsymbol{v}^j$ is a j-fold dyadic product, and $\mathrm{d}^3 v$ is the volume element in velocity space.

The moments commonly used are the zero-, first-, second-, and third-order moments, i.e., the mass density, ρ, the mass flux density vector, $\rho \boldsymbol{V}$, the momentum flux density tensor, Π, and the energy flux density vector, $\boldsymbol{Q}$, respectively:

$$\rho = m \int f(\boldsymbol{v})\, \mathrm{d}^3 v \tag{1.2}$$

$$\rho \boldsymbol{V} = m \int f(\boldsymbol{v}) \boldsymbol{v}\, \mathrm{d}^3 v \tag{1.3}$$

$$\Pi = m \int f(\boldsymbol{v}) \boldsymbol{v}\, \boldsymbol{v}\, \mathrm{d}^3 v \tag{1.4}$$

$$\boldsymbol{Q} = \frac{m}{2} \int f(\boldsymbol{v}) v^2 \boldsymbol{v}\, \mathrm{d}^3 v \tag{1.5}$$

Dividing ρ and $\rho \boldsymbol{V}$ by the particle mass m, one obtains the number density, n, and the number flux density vector, $n\boldsymbol{V}$, respectively.

From the zero- and first-order moments one can compute the average velocity, $\boldsymbol{V}$, of the particles, referred to as the bulk velocity:

$$\boldsymbol{V} = (\rho \boldsymbol{V})/\rho \tag{1.6}$$

Converting the momentum flux tensor and the energy flux vector to the frame where the average velocity is zero, one obtains the pressure tensor, P, and the heat flux vector, $\boldsymbol{H}$:

$$\mathsf{P} = \Pi - \rho\, \boldsymbol{V}\, \boldsymbol{V} \tag{1.7}$$

$$\boldsymbol{H} = \boldsymbol{Q} - \boldsymbol{V} \cdot \mathsf{P} - \frac{1}{2}\, \boldsymbol{V}\, \mathrm{Tr}\,(\mathsf{P}) - \frac{1}{2}\, \rho\, \boldsymbol{V} V^2 \tag{1.8}$$

Using the definition $\mathsf{P} \equiv n\, k_B\, \mathsf{T}$, where k_B is the Boltzmann constant (1.38×10^{-23} J K^{-1}), one can convert the pressure tensor into the corresponding temperature tensor. Scalar pressures and temperatures can be obtained from the trace of the associated tensors: $p = \mathrm{Tr}\,(\mathsf{P})\,/3$ and $T = \mathrm{Tr}\,(\mathsf{T})\,/3$.

From the measured count rates, the moments are computed according to the definitions given above. But because the distribution function is only sampled at discrete velocities, the integrations are replaced by summations, and usually the assumption is made that $f(\boldsymbol{v})$ is constant over the integration volume elements, $\mathrm{d}^3 v$. For details see *Paschmann et al.* [1998]. See also Appendix A.7.3 for a listing of moments.

1.3.4 Gas Densities

For thermal neutral gas spectrometers in a moving spacecraft, the detector output can be converted to the gas number density for several different geometries if the sensitivity of the instrument is known for the gases being measured (see Sections 3.1.2 and 3.1.3).

1.4 Required Accuracy

An important constraint on instrument design and calibration is imposed by the measurement accuracy required to answer a certain science question. This is illustrated below by considering two extreme cases. First, a monitoring mission, such as the NOAA satellites. Second, the four-spacecraft Cluster mission, where one of the goals is the determination of spatial derivatives of plasma and field properties.

POES The Polar Orbiting Environmental Satellites (POES) operated by the National Oceanic and Atmospheric Administration (NOAA) are in sun-synchronous, 98° inclination, low altitude (nominally 840 km) orbits. The instrument complement includes a Space Environment Monitor (SEM) designed to monitor the charged particle environment in the near-space environment.

The principal purpose of the SEM is to monitor routinely the intensity, location, and spatial extent of energetic charged particles at low altitudes over latitudes ranging from the equator to the polar regions. The intensities and spatial extents of these particle populations provide information about the levels of geophysical disturbance that affect, for example, trans-ionospheric radio propagation. The observations also provide information about the intensity and location of penetrating ionizing radiation for NASA's manned space flight program. On occasion the observations have assisted in the analysis and resolution of anomalies experienced by other spacecraft and by ground systems.

In order to appreciate the nature of the pre-flight calibration process and the post-launch performance verification and monitoring for the SEM instruments, it is important

to recognize the difference between the monitoring nature of the NOAA-POES mission and a scientific satellite program. The primary value of the monitoring function is perhaps best summarized by the term "situational awareness". This means, for example, providing information about the state of the space environment in terms of how "stressful" that environment is in comparison with its quiescent state. Because of the qualitative nature of "situational awareness", there is less incentive (albeit still desirable) to obtain the highest quality pre-flight calibration of the instruments than in the case for scientific satellite instrumentation.

Cluster Cluster is a science mission consisting of four identical spacecraft flying in close formation through Earth's magnetosphere and its environs. A prime goal of the mission is the determination of spatial derivatives of measured scalar or vector quantities. Taking differences between the magnetic field vectors measured at the four spacecraft positions, for example, allows to calculate $\nabla \times \boldsymbol{B}$, and thus to estimate the local electric current density directly from Ampère's law. Likewise, taking differences between the (scalar) plasma densities at the four spacecraft positions allows to construct the magnitude and direction of the density gradients.

To reliably measure such differences, particularly when the spacecraft are close together and the differences are therefore small, is an experimental challenge. Take the case of Earth's magnetopause, where gradient scale lengths are typically several hundred km. Using as an example a scale length of 300 km and spacecraft separated by 100 km along the magnetopause normal, measuring densities with 10 % accuracy, one can determine the density gradients with only 60 % accuracy. To increase this accuracy to 20 % would already require a 3 % measurement accuracy for the densities. This is a tight requirement for the calibration, albeit only required in a relative sense. Similarly, spacecraft at 100 km separation in the magnetopause current layer will record magnetic field differences of order 10 nT or less. To determine those with 10 % accuracy requires measurement accuracies of 1 nT or better.

Another goal of Cluster is to determine the orientation, speed and thickness of thin plasma boundaries, such as the Earth's bow shock, magnetopause, or the current sheet in the magnetotail, from the timing of their passage over the four spacecraft. This goal puts severe constraints on the necessary time resolution of the measurements, because these boundaries can move very fast and pass over the spacecraft within a few seconds.

1.5 Error Sources

Sources of errors or uncertainties in the measurements and the derived physical quantities are numerous. If the goal is to compute fluxes or distribution functions, then uncertainties arise from

- uncertainties in geometric factor,
- degradation of detector efficiency,
- degradation of analyzer voltages,
- out-of-band response,

- sensitivity to solar UV,
- dead-time effects at high count rates,
- poor counting statistics at low incident fluxes,
- aliasing caused by time variations in the incident particle population.

Some of these uncertainties are introduced by imperfections in design and/or calibration. Calibration concerns primarily the total geometric factor of an instrument, including detector efficiency, or the determination of the energy- and angle-passbands. Any degradation in detector efficiency after calibration introduces (unknown) uncertainties if such changes remain undetected or cannot be quantified. Similar uncertainties are introduced if the voltages applied to define the energy- and/or angle-passbands degrade in some unknown fashion. Any responses to solar UV, or to particles outside the primary energy-/angle-passbands can in principle be determined through extensive calibration, but complicate the conversion to meaningful quantities, and thus fall more into the category of design-driven uncertainties. Dead times in the detector or its associated electronics introduce losses in counts at high count rates that can be calibrated out in some limited sense only.

Low values of the counts accumulated per sampling interval introduce uncertainties that have nothing to do with calibration, but are a fundamental experimental limitation. Poisson statistics guarantees that their relative uncertainty decreases as one over the square-root of the counts. A design with increased geometric factor is not a solution for this problem if the detector would then be saturated in other, high intensity environments. Time variations in the incident particle distribution that occur within the accumulation time of the measurements are an obvious source of errors as well. Speeding up the sampling solves this problem only if the statistical error resulting from the reduced number of counts per sample remains adequate.

If the goal is to compute moments of the particle distribution function, then additional errors arise from

- limited energy range and/or energy resolution,
- incomplete angular coverage and/or resolution,
- spacecraft charging.

Obviously, if an important part of the incident distribution is not measured, because it falls outside the energy- and/or angle-range of the instrument, one cannot expect the moments, for example the particle number density, to correctly represent the incident population.

Spacecraft charging presents a special problem. If it is such that it attracts the particles of interest (negative in case of ions, positive in case of electrons), then it increases the energy of the incident particles. This energy increase can be corrected for if the value of the potential is known. However, if the sign of the potential is such that it retards the particles of interest, then there might be particles in the incident distribution that can no longer reach the detector, with obvious consequences that cannot be corrected for.

Bibliography

Baumjohann, W. and R.A. Treumann, *Basic Space Plasma Physics*, Imperial College Press, London, 1996.

Fazakerley A.N., S.J. Schwartz, and G. Paschmann, Measurement of plasma velocity distributions, in *Analysis Methods for Multispacecraft Data*, G. Paschmann and P.W. Daly, Eds., *ISSI Scientific Report*, **SR-001**, ESA Publications Division, Noordwijk, 91–124, 1998.

Hedin A.E., Extension of the MSIS thermosphere model into the middle and lower atmosphere, *J. Geophys. Res.*, **96**, 1159–1172, 1991.

Paschmann, G., A.N. Fazakerley, and S.J. Schwartz, Moments of plasma velocity distribution, in *Analysis Methods for Multispacecraft Data*, G. Paschmann and P.W. Daly, Eds., *ISSI Scientific Report*, **SR-001**, ESA Publications Division, Noordwijk, 125–158, 1998.

von Rosenvinge, T.T., L.M. Barbier, J. Karsch, R. Liberman, M.P. Madden, T. Nolan, D.V. Reames, L. Ryan, S. Singh, H. Trexel, G. Winkert, G.M. Mason, D.C. Hamilton, and P. Walpole, The Energetic Particles: Acceleration, Composition, and Transport (EPACT) investigation on the Wind spacecraft, *Space Sci. Rev.*, **71**, 155–206, 1995.

— 2 —

Review of Instruments

MARTIN WÜEST[1], DAVID S. EVANS[2], JAMES P. MCFADDEN[3],
WAYNE T. KASPRZAK[4], LARRY H. BRACE[5], BRONISLAW K. DICHTER[6],
WALTER R. HOEGY[7], ALAN J. LAZARUS[8], ARNAUD MASSON[9], AND
OLEG VAISBERG[10]

[1]*INFICON Ltd., Balzers, Liechtenstein*
[2]*Space Environment Center, NOAA, Boulder, CO, USA*
[3]*Space Sciences Laboratory, University of California, Berkeley, CA, USA*
[4]*Goddard Space Flight Center, NASA, Greenbelt, MD, USA*
[5]*Leelanau Research, Empire, MI, USA*
[6]*Air Force Research Laboratory, Hanscom Air Force Base, MA, USA*
[7]*Goddard Space Flight Center, NASA, Greenbelt, MD, USA*
[8]*Massachusetts Institute of Technology, Cambridge, MA, USA*
[9]*Research and Scientific Support Department, ESA/ESTEC, Noordwijk, The Netherlands*
[10]*Space Research Institute, Russian Academy of Sciences, Moscow, Russia*

2.1 Introduction

This book describes methods of laboratory calibration and in-flight performance verification for space particle instruments. To perform those tasks properly requires a good understanding of the instrument and its operating principle. This chapter describes the basic operating principles of common particle instrument designs whose laboratory calibration and post-launch operation are discussed in later chapters. This section is not meant to be an exhaustive review of all instruments and their variants. For in-depth understanding of the instruments, design guide lines or a particular instrument we refer to other review papers or books such as *Vasyliunas* [1971], *Wilken* [1984], *Benninghoven et al.* [1987], *Cruise et al.* [1998], *Wertz and Larson* [1999], *Pfaff et al.* [1998a], *Pfaff et al.* [1998b], *Balogh and Pedersen* [2008], and to specific instrument papers.

A typical space flight particle instrument consists of several elements (Figure 2.1). Which of the elements are present depends on the particular instrument technique and implementation. First, there invariably is a collimator or gas inlet structure. This structure essentially defines the field-of-view and shields the subsequent sections from unwanted stray particles, photons and penetrating radiation. Following this section, in neutral particle instruments only, there is an ionization element to convert the neutrals into ions that are amendable for further analysis by electromagnetic fields or, when appropriate, by time-of-flight techniques. After the collimator and ionization sections, there is an initial analyzer, such as a solid-state detector or an electrostatic analyzer, where the charged particles are filtered according to their energy per charge. This may be followed by a second analyzer section that performs ion mass discrimination. Finally, the particle encounters a detector

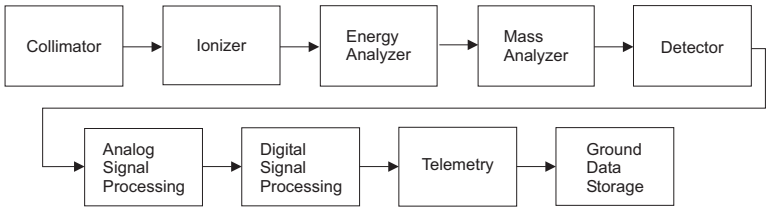

Figure 2.1: Major elements of a space flight particle instrument.

that that converts the arrival of the particle (and often its energy) into an electric signal that can be further processed in a signal processing section. The resulting digital data is passed to the spacecraft data handling system and relayed to the ground via regular spacecraft telemetry. On the ground the raw data is further processed to obtain physical parameters.

Mission design, spacecraft design, hardware design choices as well as software compression and binning schemes affect the performance of the instrument. Starting from what environment needs to be studied (density, species, characteristic velocity if any, characteristic Mach number if any, temperature ($T_\perp$, $T_\parallel$), pressure tensor, distribution function knowledge, intrinsic time of phenomenon, boundary types and characteristic lengths) measurement requirements are derived such as geometric factor, signal to noise, mass range, mass resolution, energy range, energy resolution, field-of-view, energy/angle resolution, time resolution of measurement, and analyzer type.

In spite of the fact that space particle instruments have been constructed in a wide variety of geometries and using many combinations of particle energy, charge state, particle mass, and species analysis, there are in fact only a few basic techniques that exist for selecting particles with specific properties. These are analysis solely by static electric fields, analysis solely by magnetic fields, analysis by combinations of electric and magnetic fields, analysis by time-varying electric fields (sometimes in combination with static magnetic fields), analysis by determining a particles time-of-flight over a fixed distance, and analysis by determining a particle's rate of energy loss through matter.

Contemporary space flight instruments almost always use either open window electron multipliers or silicon solid-state detectors to detect those particles that are passed by the various analyzer elements. Because determining the performance of such particle detectors is critical to the overall instrument laboratory calibration and because their post-launch stability is always an important factor, their operation is discussed in detail in this chapter. Since a Faraday cup is sometimes used as an integrating current detector in a few particle detector systems and often forms an important element in laboratory calibration facilities, the design and operation of a Faraday cup is also discussed.

The basic principle behind each of these analysis techniques is briefly described in this chapter. Each section on analysis principle usually contains a more detailed description of specific instruments in order to provide background for the material on the calibration and in-flight performance verification of those instruments that appears in subsequent chapters. Whenever a specific instrument involves a special feature, for example unusual collimator design or a process to convert a particle from a neutral to an ion, that feature is highlighted.

Not discussed in any detail in this chapter is the electronics section of an instrument. There are many excellent books on electronic design available such as *Horowitz and Hill* [1989]; *Tietze and Schenk* [2006]; *Cruise et al.* [1998]; or *Spieler* [2005].

This chapter also includes a brief discussion of plasma wave instruments because measurements of certain features in the plasma wave spectrum contain quantitative information about the local plasma number density. Independent knowledge of that density provides a powerful constraint for the in-flight performance verification of particle instrumentation as discussed in Chapter 4.

The chapter concludes with a brief discussion of some forms of on-board data compression that must be taken into account in calibration and with a short list of instrument problems and anomalies that laboratory calibration should be designed to expose.

2.1.1 Important Characteristics of Analyzers

When selecting an instrument for a particular mission or comparing different plasma instruments certain key parameters have proven to be very useful. These are: energy or velocity range, field of view, velocity space resolution ($\Delta v/v$, $\Delta\Omega$), and geometric factor that determines sensitivity and temporal resolution. Also to consider are the temporal resolution for a two-dimensional and for a three-dimensional cut of the velocity phase space. Equally important are resources that the instrument requires from the spacecraft such as mass, power, size and telemetry rate.

Charged particle optics makes many references to photon optics such as spectrograph, spectrometer, fringing fields, and aberration. For example a cylindrical ESA is a charged particle optics analog of the scanning spectrograph in photon optics. But there is an important difference between charged particle optics and photon optics: There is interaction between optical properties and dispersion in charged particle optics. Details on charged particle optics can be found e.g. in *Wollnik* [1987]; *Hawkes and Kasper* [1996] and others.

2.2 Detectors

There are relatively few detector types used in space physics to detect particles, either charged or neutral. These include Faraday cup devices to measure the current associated with charged particle distributions, windowless electron multipliers such as channel electron multipliers (Channeltrons) and microchannel plates that may be operated in either a pulse counting or an integrated current mode, and solid-state or scintillation detectors used for higher energy particles.

The succeeding sections discuss each of these particle detection technologies. We do that early in the chapter, because detectors are such a critical component of an instrument and later sections make often reference to a detector system.

2.2.1 Faraday Cups

Faraday cups are generally simple to construct and are fast, accurate, current collectors. These collectors are connected directly to current measuring devices, and current measurements as low as 10^{-15} A are possible with modern electrometers.

Measurement accuracy of a Faraday cup is affected by a series of secondary processes created by particles impacting onto a cup, such as emission of secondary electrons and secondary ions or reflection of charged particles, collection of electrons and ions produced near the cup (for example produced by ionization of the residual gas or produced at the

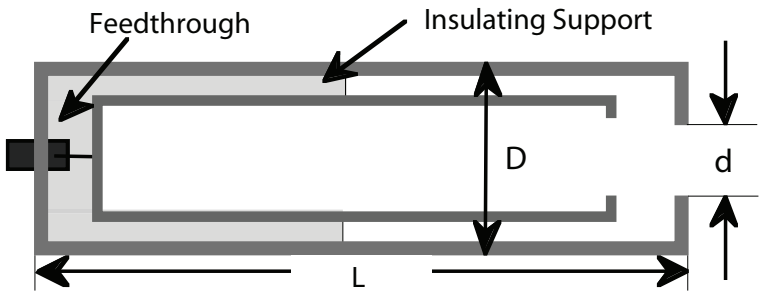

Figure 2.2: Schematic of Faraday cup as a particle detector.

aperture structure), current leakage to the ground, formation of galvanic elements due to the use of different materials and the penetration of particles through the cup structure.

Escaping secondary electrons are minimized by a suppressor grid biased to about −30 V placed directly in front of the collector plates or by biasing the cup together with the measuring electronics and by geometric design where the collector plates are mounted at the end of a long high aspect ratio tube such as a cylindrical tube (see Figure 2.2). To measure very low ion currents an additional shielding cylinder should be used to screen the Faraday cup from stray ions or electrons.

When taking the proper design precautions (see, e.g. *Gilmore and Seah* [1995]), Faraday cups are well suited for absolute current measurements because they are not affected by the same gain degradation as channel electron multipliers or multichannel electron multipliers.

A discussion of the implementation of Faraday cups for use in measuring space plasma properties is presented in Section 2.4. A Faraday cup detector in a plasma instrument is described for example in *Mel'nikov et al.* [1965].

The Rosetta/ROSINA double focusing mass spectrometer includes a Faraday cup in that instrument's detector system in addition to microchannel plates and Channeltrons. The long-term stability of the Faraday cup provides the absolute calibration for the other detectors that may suffer degradation with time, as well as providing measurements during times of exceptionally high fluxes [*Balsiger et al.*, 2007]. Faraday cups also serve the very important function of particle beam monitors in laboratory calibration facilities (see e.g. Section 3.3.2 or Appendix A.4.2, Figure A.23).

2.2.2 Discrete Electron Multiplier

Open windowed discrete dynode electron multipliers utilize the same electron multiplier technology as the conventional photomultiplier tube although without the protective glass envelope. The absence of a window permits entry of low energy particles to the cathode of these devices initiating a cascade of secondary electrons whose numbers increase from one dynode interaction to the next. The multiplication produces a detectable signal at the final dynode of the chain (see Figure 2.3). The fact that the dynode structure is not enclosed means that either the materials chosen must be stable on exposure to air or the device is enclosed under vacuum and exposed only when in space. These devices are also

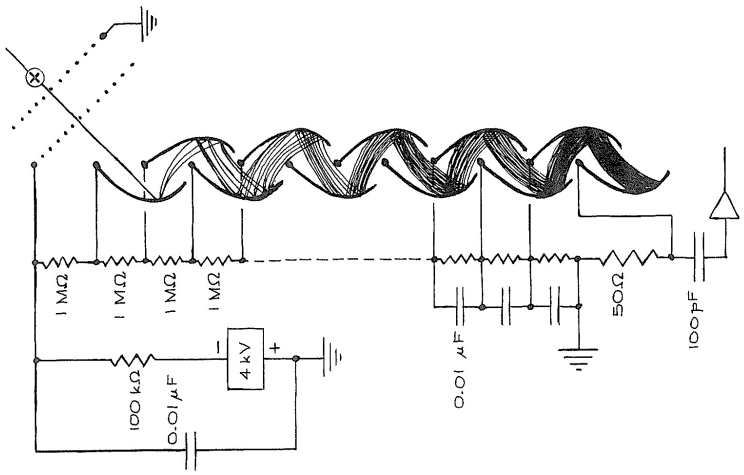

Figure 2.3: Open windowed discrete dynode multiplier with electrical connections to detect positive ions. Grids at the entrance of the multiplier prevent the escape of secondary electrons. From *Moore et al.* [1989].

rather bulky, although some compact versions (< 1.5 cm^3) are available, and have exposed high voltage surfaces that must be adequately shielded.

In spite of these disadvantages, open window discrete electron multiplier of photomultiplier design was used to detect low-energy charged particles on Injun 3 [*O'Brien et al.*, 1964] and in upper atmosphere research [*Balsiger et al.*, 1971]. A discrete dynode design electron multiplier was used in the ONMS instrument on the Pioneer Venus Orbiter [*Niemann et al.*, 1980] and a Johnston multiplier was used in the Ion Mass Spectrometer on ISEE-1 mission [*Shelley et al.*, 1978]. However, particle detection using discrete dynode electron multipliers has been almost totally replaced by much smaller channel electron multipliers of various designs.

2.2.3 Continuous Electron Multiplier

Processing procedures have been developed to produce high resistance surfaces on glass that have both a large secondary electron production ratio and are stable on exposure to air. These materials have formed the basis for electron multiplier devices of more compact design than the discrete dynode devices. Because the accelerating electric field, necessary to produce electron multiplication, can be distributed uniformly along the resistive surface by application of a voltage difference, these devices were originally known as continuous dynode electron multipliers in contrast to discrete dynodes.

The first devices using this technology that were suitable for use as particle detectors in space were channel electron multipliers (CEMs) [*Eschard and Manley*, 1971]. CEMs consist of small, $\sim$1 mm inside diameter and several cm long, capillary tubes. When several kilovolts potential is imposed from one end to the other, a single electron produced at the low potential end will be accelerated down the tube and, at every collision with the tube wall, will produce several secondary electrons that continue that process. Overall gains

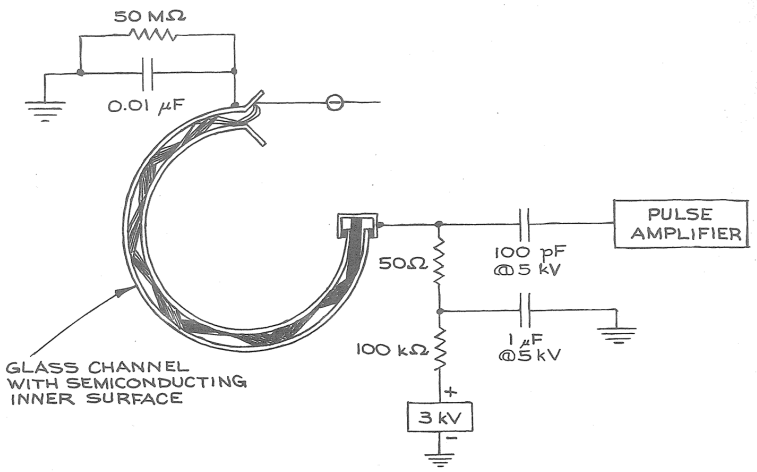

Figure 2.4: Continuous electron multiplier with electrical connections to detect electrons. From *Moore et al.* [1989].

of $> 10^8$ are possible. It was found that straight CEMs were unstable at gains of $> 10^4$ because of ion feedback. Ion feedback is caused by the cascading electrons that ionize residual gas inside the device toward the high potential end of the devices, the positive ions then being accelerated toward the low potential, input, where they may initiate a new cascade. To suppress ion feedback, CEMs are curved so that any ion that is created will strike the tube wall before gaining sufficient energy to reinitiate an electron cascade. CEMs can be fabricated in a variety of geometries including "C" shaped, spiral, and helical and with funnel-like entrance cones to increase particle collection area. One such configuration together with typical electrical connections is shown in Figure 2.4.

CEMs require a 2–4 kV bias voltage to achieve gains of 10^6 to $>10^8$ (Figure 2.5). For a fixed voltage, the gain depends on length to diameter ratio which sets the number of secondary electron multiplications. The gain and detection efficiency are weakly dependent on the incident particle mass and energy above some threshold energy (Figures 2.5–2.7). Incident electrons require several hundred eV and ions require several keV to obtain good detection efficiency. Uniform gain is observed for count rates whose pulse current is $<10\,\%$ of the nominal CEM bias current. Operating pressures $<10^{-5}$ mbar are recommended with background rates decreasing significantly as pressures drop below 10^{-6} mbar. For early work on CEM efficiencies see *Bennani et al.* [1973], which shows the range of variability of the energy dependent gain for a variety of devices.

CEMs are generally operated in pulse saturated counting mode with gains $\sim 10^7$–10^8. Detector thresholds can then be set to a small fraction of the nominal gain to eliminate dark current counts. One generally operates the CEM 50-100 V above the knee in the counting rate plateau (see Figure 2.5) to prevent loss of counts due to gain droop at high count rates. Higher bias voltages are not used to minimize background counts and to maintain CEM lifetime. Count rates $>10^6$ can be achieved in the linear regime with background rates $<0.5\ \mathrm{s}^{-1}$.

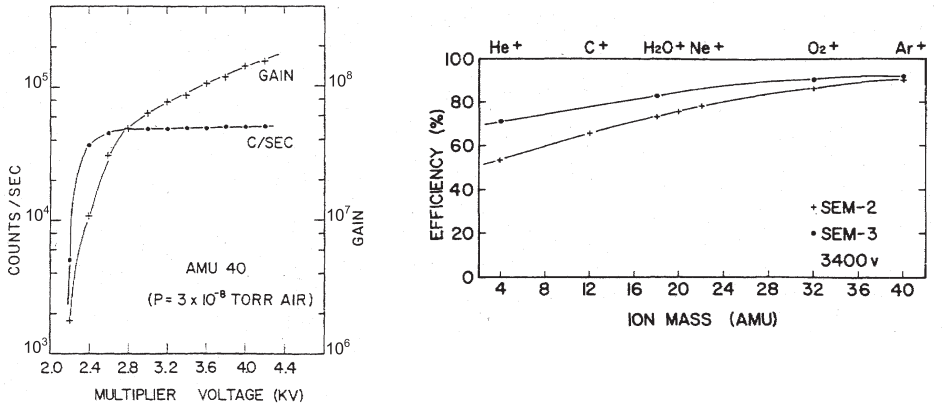

Figure 2.5: Left: Spiraltron (Bendix Model 4219) parameters as a function of the multiplier high voltage. *Right:* The percent efficiency as a function of the ion mass for two different Secondary Electron Multipliers (SEM). From *Potter and Maurersberger* [1972].

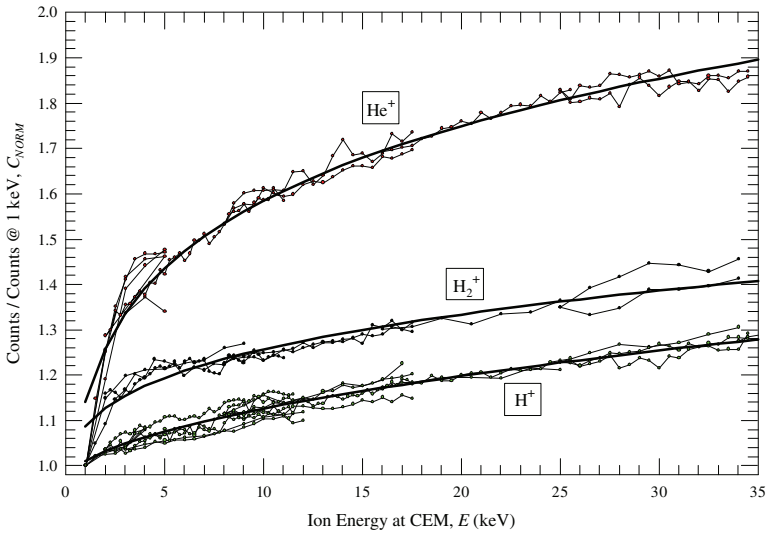

Figure 2.6: Comparison of relative channel electron multiplier detection efficiency of incident H^+, H_2^+, and He^+ as function of energy. The relative efficiency is determined by the ratio of the count rate at beam energy "E" to the count rate at a beam energy of "1 keV", where the beam flux is independent of energy. Above ∼2 keV, the CEM efficiency increases slowly with ion energy. Different ions manifest different energy dependent efficiencies. Figure courtesy of H. Funsten.

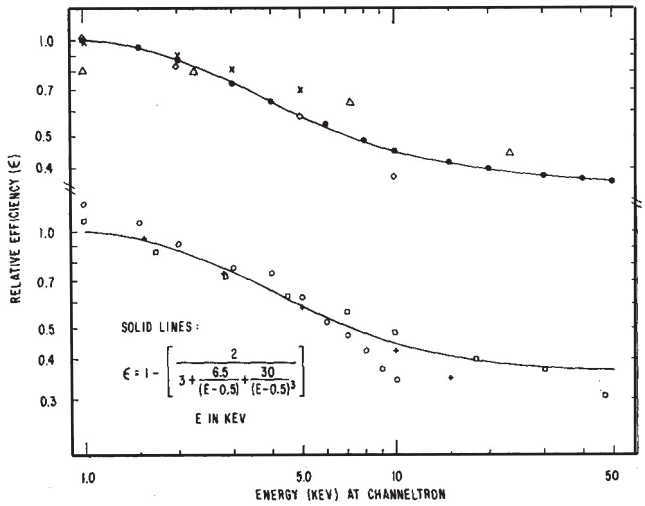

Figure 2.7: Comparison of relative detection efficiency channel electron multiplier for electrons. • – UCSD (ATS-E); × – UCSD (ATS-F); ◊ – Bosqued (calculated for glass (×1.35); △ – Arnoldy; + – Egidi; □ – Frank (×3.2); ◯ – Sharber (×2.0). From *Archuleta and DeForest* [1971].

CEMs can also be operated in analog mode where variations in the CEM current are used to measure the particle flux rather than counting individual events. Higher current CEMs are used to increase the dynamic range for analog mode. For a 40 μA bias current, a dark current of 1 pA, a gain of $\sim 6\times10^6$, and linear output up to $\sim$10 % of the bias current, a dynamic range of $\sim 4\times10^6$ can be achieved.

The multipliers are always baked at 250–280 °C in a vacuum after exposure to air to remove water vapor and other contaminants. An initial burn-in procedure is used which consists of gradually raising the high voltage while monitoring the outgassing pressure. The dark-current is characterized. After this period the multipliers are tested in an ion beam, where integrated pulse height distributions are taken and multiplier gains are calculated. If the multipliers are satisfactory they are then installed in the detector system.

For calibration purposes it is useful to test the detector signal chain. Most often the detector signal chain is tested with a pulser signal capacitively coupled into the detector signal line just after the anode. However, the CEM can be tested installed by using a built-in tungsten filament close to the CEM aperture to emit electrons that stimulate the CEM (see e.g. *Witte et al.* [1992]). Alternatively the CEM can be stimulated with a built-in UV lamp (see e.g. *Rosenbauer et al.* [1981]).

A review of CEM can be found in *Kurz* [1979].

2.2.4 Microchannel Plates

Microchannel plate (MCP) detectors began replacing channel electron multipliers (CEMs) as the detector of choice for low energy ion and electron detection in most plasma instruments beginning in the mid-1980s. As with CEMs, MCPs are electron multipliers

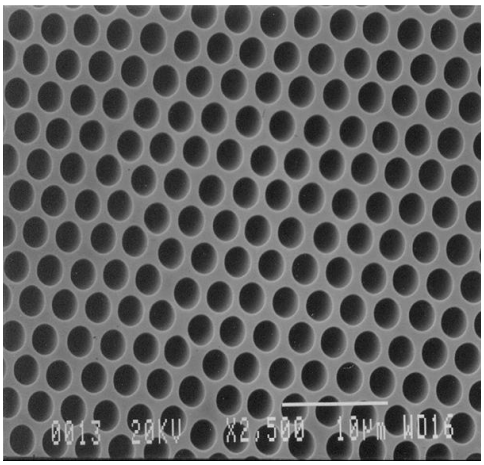

Figure 2.8: Photo of a microchannel plate surface. Figure courtesy of Burle Industries, Inc.

produced by voltage bias across a resistive glass tube that generates an electron cascade through secondary electron production [*Wiza*, 1979]. MCPs consist of an array of microscopic glass tubes (typically 12–25 μm spacing), hexagonally packed (Figure 2.8) and sliced as thin wafers (0.5 or 1.0 mm thick) with typical microchannel length to diameter (L:D) ratios between 40:1 and 80:1. The wafers are treated by high temperature (250–450 °C) reduction in a hydrogen atmosphere to produce a resistive coating along the microchannels, and the top and bottom surfaces are metallized (for a description of the manufacturing technique see *Lampton* [1981]). MCPs were developed for use in night vision equipment by the military, but have subsequently been replaced by CCD technology in most military applications. MCPs are still readily available and provide compact front-end particle or photon detection with a high signal to noise ratio allowing individual event counting. Background rates <1 cm^{-2}s^{-1} can be achieved with the limiting rate apparently due to beta decay of ^{40}K in the glass [*Siegmund et al.*, 1988]. As with CEMs, MCPs require operating pressures $<10^{-5}$ mbar. The microchannel plate (MCP) can also be used to obtain a spatial distribution of ions.

MCP wafers (typically 0.5 mm or 1.0 mm thick) are sliced at a small bias angle (typically 8–12°) relative to the microchannel axis. They are stacked in pairs (Chevron configuration) or in triplets (Z-stack), with adjacent wafers having opposite bias angles (Figure 2.9) to prevent ion feedback in order to suppress the ion feedback effect discussed in Section 2.2.3. Typical bias voltages are $\sim$1 kV per plate and typical gains are $\sim$1000 per plate. The bias voltage is generally chosen so the secondary electron production at the back of the MCP stack is near the microchannel saturation, resulting in a roughly fixed charge per microchannel firing (see Figure 2.10).

Chevron configurations produce charge pulses of $\sim 10^6$ e$^-$, which are readily detected with charge sensitive preamplifiers. Careful attention to the detection electronics design can result in electronic noise levels $<10^5$ e$^-$, allowing preamplifier thresholds well below the nominal gain. Pulse height distributions (PHDs) with a roughly Gaussian shape and a FWHM equivalent to $\sim$50–100 % of the peak height are typical, with the FWHM depending upon the MCP gain (Figure 2.11). These PHDs allow >95 % of the events to appear

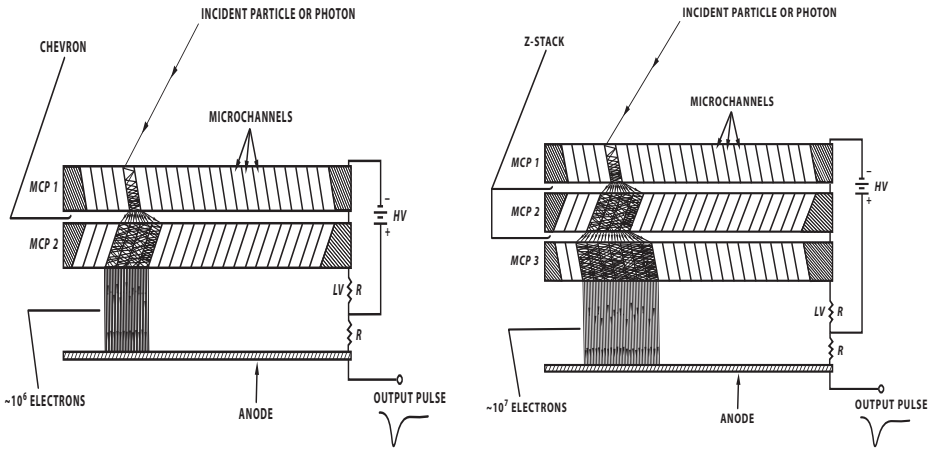

Figure 2.9: Schematic drawing of MCPs in chevron (left) and Z-stack (right) configuration. The LV next to the resistor between the back of MCP and anode is to indicate that the voltage drop across this resistor is small. Generally, the potential difference between anode and the back of the MCP is desired to be 50–100 V). The resistance is only about 2–4 % of the MCP resistance. Nearly all the MCP current flows through this resistor. The resistor from the anode to the HV carries only a tiny current from the charge pulses and has virtually no voltage drop. The anode resistor bleeds off the current since the preamplifier is generally capacitively coupled.

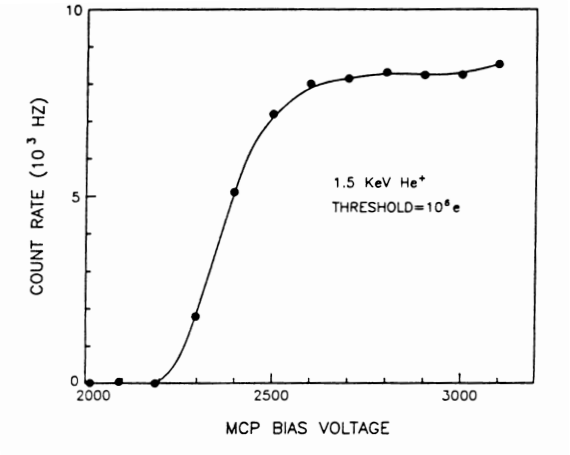

Figure 2.10: Akebono suprathermal ion mass spectrometer flight microchannel plate response as a function of MCP bias voltage. The nominal saturated gain was measured to be 10^7 and the threshold for the pulse height discrimination was set at 10^6. The count rate plateau for 1.5 keV He^+ beam is reached near 2600 V and the plateau is relatively flat up to 3000 V, where the MCP noise begins to make a significant contribution to the count rate. From *Whalen et al.* [1990].

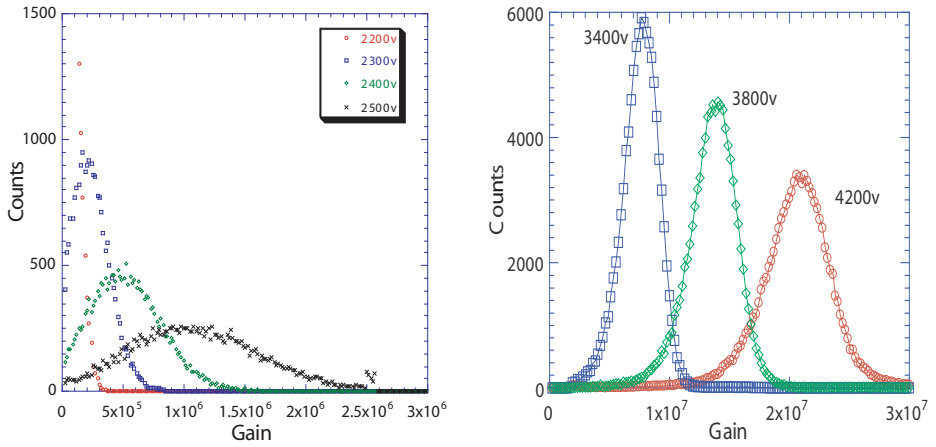

Figure 2.11: Pulse height distributions for Photonis 6 μm chevron pair (left) and Photonis 12 μm Z-stack (right). Figure courtesy of O. Siegmund.

above threshold. The voltage required for these gains depends upon the L:D ratio and the micropore diameter. The L:D ratio generally sets the number of electron multiplications for a fixed bias voltage. However, at high gains the micropores will saturate and the saturated gain will depend on pore diameter and the number of micropores that fire. A chevron pair of 80:1, 1 mm plates, will typically require several hundred volts more bias than 40:1, 1 mm plates. The need for higher voltage on 80:1 plates can also be compensated for by the use of a spacer between the plates, with $\sim$25 μm being typical. This results in more microchannels firing in the second plate, but tends to broaden the PHD.

For charge pulse imaging electronics [*Siegmund et al.*, 1995], whose position sensing accuracy requires much narrower PHDs, a Z-stack is often used. A Z-stack configuration can produce PHDs with a FWHM equivalent to $\sim$30 % of the peak height (see Figure 2.11). Since a Z-stack results in more microchannels in the back plate firing, it has a much higher gain with $\sim 5 \times 10^7$ e^- being typical.

Charge pulses from MCPs can be registered in several ways. See an early review on the different concepts by *Timothy* [1985]. Discrete anodes with separate preamplifiers allow for the highest counting rates but limit the position resolution for detecting counts. For better charge pulse position resolution, imaging systems utilize resistive anode [*Lampton and Carlson*, 1979; *Fraser and Mathieson*, 1981] (Figure 2.12), delay line anodes [*Lampton et al.*, 1987; *Siegmund et al.*, 1994] (Figure 2.13) or wedge and strip anodes [*Martin et al.*, 1981] (Figure 2.14) which offer extremely fine position sensing, approaching that of the microchannels. Another solution for position resolution are the Multi-Anode Microchannel Arrays (MAMA) detectors [*Timothy et al.*, 1981]. MAMA detectors are large arrays of pixels (e.g. 512$\times$512) of 25 μm size, which are placed behind a curved channel plate. These detectors have been developed for ground-based and space-borne instrumentation. Imaging systems generally require complex electronics that are sensitive to the MCP's PHD. Imaging systems typically allow count rates of 10^5–10^6 counts per second, depending upon the resolution desired. For high count rates, discrete anodes are preferred since

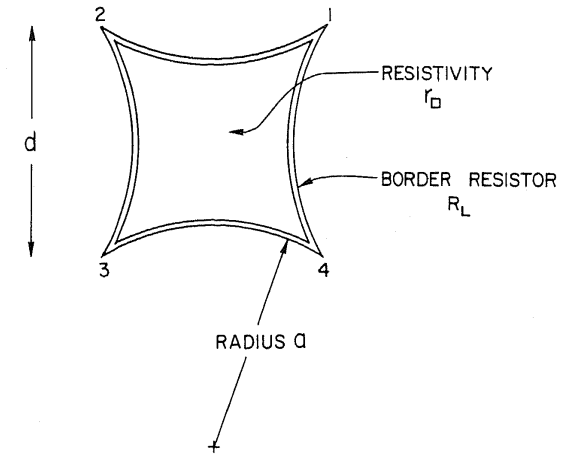

Figure 2.12: A circular arc terminated resistive anode. The anode is manufactured using thick-film resistor technique. Electrical connections are made at the four corners. The position of the detected event is computed from the ratio of charge pulse amplitudes. From *Lampton and Carlson* [1979].

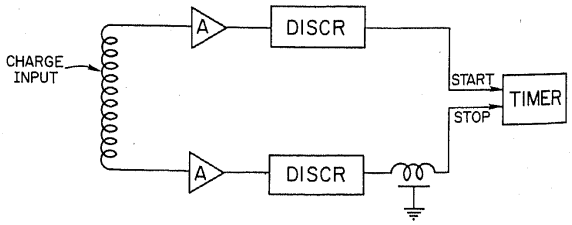

Figure 2.13: Schematic drawing of delay line position sensitive detector. A localized charge pulse collected by the delay line triggers START and STOP discriminators with a relative time delay that depends linearly on the centroid location of the event. From *Lampton et al.* [1987].

individual preamps are readily available that count at $\sim 10^7$ counts per second allowing total instrument rates of $\sim 10^8$ counts per second.

For discrete anodes care should be taken to characterize the response near anode boundaries. Depending upon the separation between anodes, the MCP to anode gap, the nominal MCP gain, and preamplifier threshold, double counting or missed counts may occur as the exiting charge is split between anodes. Similar non-uniform response can also arise from obstructions at the analyzer entrance or exit. Generally these non-uniformities will have little or no impact on the measurements unless the particle beam is extremely narrow in angle and falls on a small portion of the detector.

As part of the test and calibration procedures, it is important to characterize the instrument's response to high counting rate. In particular the instrument's lost counts at high counting rate may depend on both the preamplifier dead time (which may depend upon

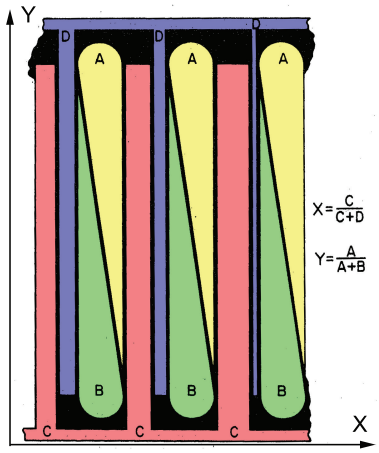

Figure 2.14: A portion of a four-electrode wedge and strip anode pattern. Black regions are insulators and white areas are conductors. All wedges marked "A" are connected together by a common conductor located beneath the anode plane; similarly the "B" wedges are connected to a second common conductor. The ratio of these two signals depends on the y coordinate of the event. Simultaneously the pairs of strips "C" and "D" are used to determine the x coordinate of the event, since the relative widths of these strips vary linearly with x. The coding is nearly distortionless if the size of the deposited charge footprint is somewhat larger than the distance between quartets. The formulae shown are coordinate recovery algorithms appropriate for this geometry. Adapted from *Martin et al.* [1981].

MCP gain) and upon the MCP PHD droop at high counting rates (which can result in loss of counts below threshold). Generally MCP droop is to be avoided since it does not allow for a simple dead-time correction algorithm. A general rule of thumb is to try to keep the average charge pulse current at the highest counting rates (using nominal gain) to less than 20 % of the MCP current. For high-count-rate environments, higher current MCPs should be used if possible. See also Chapter 4 for a more detailed discussion.

An important part of the calibration process is determining the MCP detection efficiency for particle counting, which is dependent upon the angle, energy and mass of the particles that strike the detector. Angle and energy efficiency variations have been characterized in numerous papers [*Goruganthu and Wilson*, 1984; *Gao et al.*, 1984; *Straub et al*, 1999; *Barat et al.*, 2000; *Stephen and Peko*, 2000]. Figures 2.15 through 2.18 show typical variations of these efficiencies with energy for neutrals, ions and electrons. In order to produce an instrument with a relatively uniform response to input particle flux, the front of the MCPs are voltage biased to accelerate incoming particles. Typically the full bias voltage (~ -2 kV) is applied to the front of ion detectors to assure adequate efficiency, and several hundred volts pre-acceleration is common for electron detectors.

To minimize angle efficiency variations, and especially to avoid particles striking the MCPs at angles aligned with the microchannels, instruments should be designed with knowledge of bias angle effects (see Figure 2.19). For the Wind 3D plasma analyzers [*Lin et al.*, 1995], two half-annulus (180°) MCP chevron pairs were used rather than full annulus MCPs to minimize bias angle effects. The half-annulus bias angle tip was chosen to be

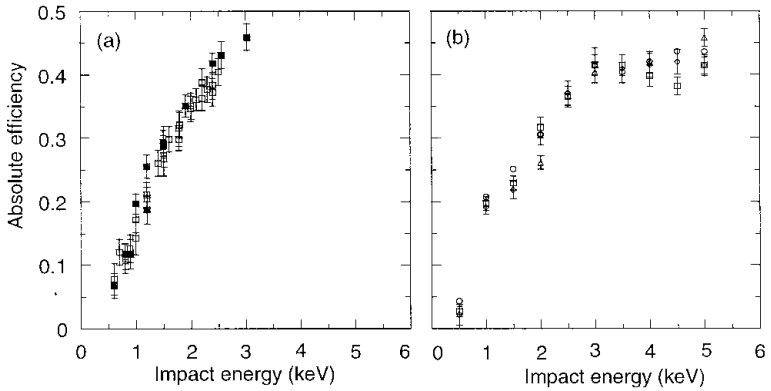

Figure 2.15: Absolute detection efficiency of MCP for neutral and ionic atoms as a function of impact energy. (a) Presents results for neutrals: open squares (Na), full squares (K). Error bars are calculated from the statistical uncertainties. (b) Measurements taken from *Brehm et al.* [1995]: open circles (H_2^+), open squares (D_2^+), open lozenges (HD^+), open triangles (Ar^+), measurements for H^+ and D^+ are not compared here due to their very large error bars. From *Barat et al.* [2000].

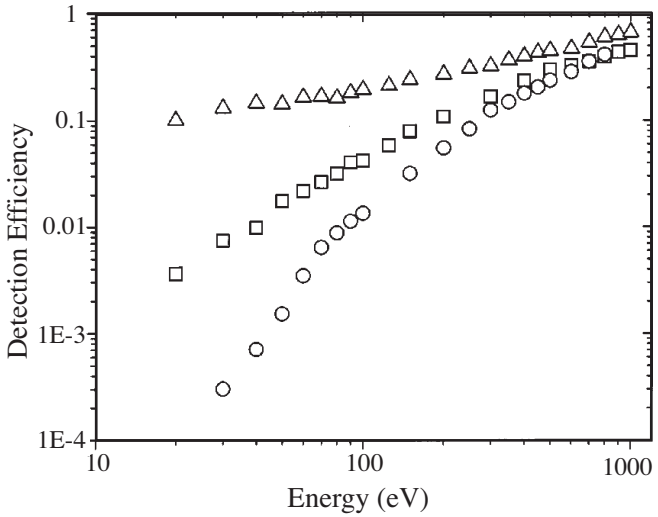

Figure 2.16: Absolute detection efficiencies, as a function of impact energy, for O^+ (○), O^- (△) and atomic oxygen (□). From *Stephen and Peko* [2000].

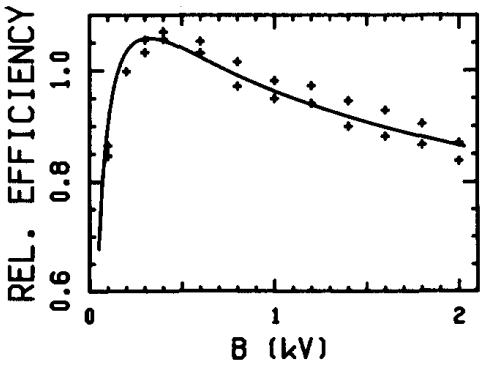

Figure 2.17: Variation of the relative detector efficiency $\epsilon(E, B)$ with the acceleration voltage B for electrons of energy 4 eV. The energy of the electron when it strikes the MCP surface will be $(4 + B)$ eV. Efficiency at 200 V is normalized to unity. The pluses are experimental points and the solid curve denotes the theoretical fit according to Bordoni. From *Goruganthu and Wilson* [1984]; *Bordoni* [1971].

radially aligned with the center of the half-annulus to minimize angle efficiency variations around the top-hat's 360° FOV. Computer simulations (particle ray tracing) were used to show that for this MCP bias angle selection, angle efficiency variations were minimal.

MCP efficiency variations also depend upon the electric field geometry at the front of the detector. Particles that strike the MCP front-face between microchannels do not generally produce a charge pulse. Therefore MCP have an inherent ∼50 % absolute efficiency, reflecting the ∼50 % microchannel pore area. However, if the front-end electric fields are arranged so that secondary electrons produced outside the microchannels are reflected back toward the MCP surface, this efficiency can be increased to ∼75 %, depending upon the field geometry [*Panitz et al.*, 1976; *Funsten et al.*, 1996]. Pre-acceleration of electrons to the front of the MCP naturally results in this increased efficiency. However, ion detecting MCPs require an additional biased grid in front of the detector to obtain this additional efficiency.

For ions, the number of secondary electrons produced by the initial particle depends on mass. For example, oxygen will typically produce several times the number of initial secondary electron as compared to protons. Therefore the pulse height distribution for oxygen is generally shifted to higher total charge over that of protons in MCPs that are not fully saturated. If the MCP bias voltage for an ion detector was selected using an oxygen beam, one could find the efficiency for proton detection was significantly degraded. Therefore it is important to test MCPs with different species in order to characterize the instrument. Since cross-talk between adjacent channels may also depend upon MCP gain, it is also important to test for cross-talk with higher mass species.

As is discussed later in Section 4.2.2, MCPs are sensitive to hydrocarbon contamination and have a gain that degrades with total charge through-put. Ultrasonic washing of newly acquired plates in a 50 %–50 % solution of isopropyl and methyl alcohol followed by baking at ∼100 °C for 30 minutes to remove volatiles is strongly advised [*Siegmund*, 1989]. Gain degradation, also known as scrubbing, is believed to result from contaminates (primarily H_2O) that evaporate from the surface as the plates are operated. Therefore, af-

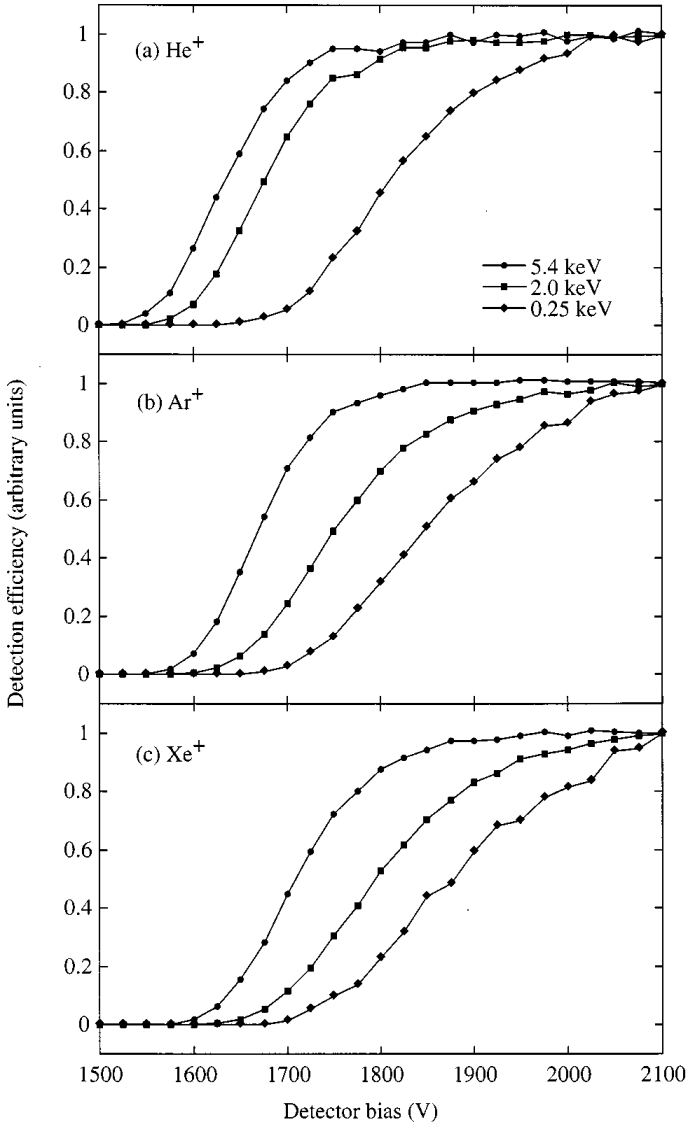

Figure 2.18: The relative detection efficiency as a function of detector bias for (a) He^+, (b) Ar^+, and (c) Xe^+ at impact energies of 0.25, 2, and 5.4 keV. Note that each of the nine curves has been normalized to unity at a detector bias of 2100 V. From *Straub et al* [1999].

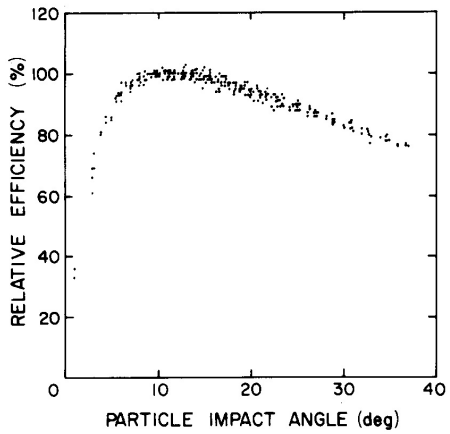

Figure 2.19: Relative detection efficiency as a function of the angle between the particle trajectory and the channel axis direction. The relative efficiency is found to be independent of particle species and energy. From *Gao et al.* [1984].

ter cleaning, MCPs should be stored in a dry nitrogen atmosphere or even better under vacuum. A new chevron stack will typically require several hundred volt increase in bias voltage to compensate for the scrubbing gain drop during the first several months or years of operation, depending upon counting rate. Scrubbing can also result in a narrowing of the PHD as microchannels become more uniformly saturated. If the instrument design can allow the MCPs to be maintained in a sealed environment prior to launch, then pre-flight scrubbing [*Siegmund*, 1989] will reduce the MCP gain maintenance requirements early in the mission.

A useful feature that should be implemented in instruments using CEMs and MCPs is the ability to capacitively couple artificial pulses of varying amplitude into the signal amplifier-discriminator chain to provide both a functional test of the signal processing electronics and a verification of threshold discriminator settings. We reiterate that both CEMs and MCPs are subject to gain degradation with use. For that reason the instrument design should include a method for periodically testing detector gains over the course of a mission. An effective technique is to step the pulse threshold discriminator level over a range of a factor of ten or more during times when particle fluxes are constant in time. A significant dependence of CEM or MCP response on the discriminator level indicates inadequate gain and the need for an increase in detector bias.

2.2.5 Solid-State Detectors

2.2.5.1 Energy Loss of Particles in Matter

The process of energy loss of particles in matter is important in trying to understand the response of sensors to high energy particles. Heavy charged particles, such as protons, interact with material they are traversing by a series of distant collision with the electrons in the material. Each interaction results in a small energy loss and almost no scattering. The result is that protons travel in nearly straight lines as they stop and the dispersion

in the energy loss or range, when traversing a material is small. Electrons, on the other hand, can lose a large fraction of their energy and undergo significant angular scattering in a single collision with a target material electron since both particles have the same mass. In addition, the electron direction of motion can also be changed, to the point of being reversed, by a collision with an atomic nucleus. Since the energy loss process is very different for heavy charged particles, (protons and other ions), and light particles (electrons), it is natural to consider them separately.

The stopping power, $\mathrm{d}E/\mathrm{d}x$, for heavy particles is given by the Bethe-Bloch formula

$$-\frac{\mathrm{d}E}{\mathrm{d}x} = \frac{4\pi N_A z^2 e^4}{m_e c^2 \beta^2} B \tag{2.1}$$

where

$$B = \frac{Z\rho}{A}\left[\ln\left\{\frac{2m_e c^2\beta^2}{I(1-\beta^2)}\right\} - \beta^2 - \frac{C}{Z} - \frac{\Delta}{2}\right] \tag{2.2}$$

where x is the path length, N_A is Avogadro's number, z is the effective charge of the incident ion (for protons it is unity for energies above 0.5 MeV), m_e is the electron rest mass, e is the electronic charge, β is v/c for the proton, Z, A and ρ are the atomic number, atomic weight and density of the stopping material, I is the adjusted ionization potential, C is the shell correction and Δ is the correction due to polarization of the stopping medium. A list of the relevant I, C and Δ parameters for all elements can be found in *Janni* [1982b]. For non-relativistic particles, $v \ll c$, only the first term in the expression for B is significant. Equation (2.1) is generally valid for ions with velocities greater than those of atomic electrons. Since the B term varies slowly with energy, the energy loss varies inversely with energy. For equal energy particles the stopping power varies approximately as z^2, thus the higher the charge of the incident ion, the greater the stopping power.

In case of thin absorbers, where incident particles energy loss is small compared to its initial energy, the energy loss in the material, ΔE, is given by

$$\Delta E = -\frac{\mathrm{d}E}{\mathrm{d}x}\, t \tag{2.3}$$

where t is the absorber thickness. For cases where the thin absorber approximation cannot be applied, the range energy table method must be used with the following recipe:

1. Let R_1 be the range of incident particle with energy E_0.
2. Subtract R_1 from the absorber thickness t to get a new range value, R_2.
3. Find the energy, E_1, that corresponds to R_2.
4. Energy Loss, $\Delta E = E_0 - E_1$.

Range-energy tables for elements and compounds can be found in *Janni* [1982a] and *Janni* [1982b].

Finally, if the energy loss and range must be computed for a compound, such as scintillator crystal or a Cherenkov radiator, the following approximations can be used:

$$\frac{1}{N_c}\left(\frac{\mathrm{d}E}{\mathrm{d}x}\right)_c = \sum_i W_i \frac{1}{N_i}\left(\frac{\mathrm{d}E}{\mathrm{d}x}\right)_i \tag{2.4}$$

where N is the atomic density, $\mathrm{d}E/\mathrm{d}x$ is the stopping power and W_i is the atom fraction of the $i\text{-}th$ element of compound.

The range in the compound R_c may be computed from Equation 2.5 where M_c is molecular weight of the compound and R_i, n_i and A_i are the range, number of atoms and atomic number of the $i\text{-}th$ element in the compound.

$$R_c = \frac{M_c}{\sum_i n_i (A_i/R_i)} \tag{2.5}$$

A final topic in thin absorber ion interactions is angular scattering, which alters the ion direction of motion while not significantly affecting its energy. Angular scattering may play an important role in instruments that use multi-element telescopes (see also Section 3.5). In this case angular scattering in the upstream detectors may prevent some particles from being detected. This will result in an underestimate of the true incident particle fluxes. The angular scattering for ions is given by

$$\left\langle \theta^2 \right\rangle = \frac{\pi N Z_1 (Z_1 + 1) Z_2^2 e^4}{E^2} \ln \left(\frac{4\pi N a_0^2}{Z_1^{2/3} + Z_2^{2/3}} \frac{Z_1 + 1}{Z_1} \right) \tag{2.6}$$

where θ is the scattering angle in radians, Z_2 is the nuclear charge of the incident ion, Z_1 is the nuclear charge of the target material atoms, N is the areal density of the target atoms, E is the incident particle energy, e is the electronic charge and a_0 is the Bohr radius. For ions with $Z_2 > 2$ an empirical factor of $(1.8)^2$ must be used to multiply the right side of Equation 2.6 [*Cline et al.*, 1969]. Equation 2.6 is valid for protons with energies above a few MeV (as long as the energy loss in the foil or detector is a small fraction of the total incident energy). For heavier ions the multiplicative factor of 1.8 is valid for energies from a few to a few tens of MeV/nucleon.

The process of energy loss by electrons is much more complex than for ions due to the electron's small rest mass. Electrons paths in material are typically full of sharp turns, some of them severe enough to cause the electron to be backscattered out of the material. The backscatter fraction depends on the Z of the material and rises from about 10–15 % for Al to about 40 % for NaI for electrons with energies below 1 MeV. Another factor in the electron stopping power is the emission of bremstrahlung or electromagnetic radiation. Bremsstrahlung is emitted whenever the electron is accelerated, such as when it is deflected through a large angle or undergoes a collision with a large energy loss. Nevertheless, range-energy tables for electrons have been developed [*Pages et al.*, 1972] and are used to compute model energy losses in a thin absorber cases and in determining the range of electrons to compute the amount of shielding needed for a particle detector or a radiation sensitive spacecraft component. Finally, angular distributions of scattered electrons have been studied and the published reports (see *Seltzer and Berger* [1974]) and references therein) can be used to statistically predict electron behavior in matter.

2.2.5.2 Silicon Solid-State Detectors

Silicon solid-state detectors (SSD) are built using ultra pure silicon crystals. They are manufactured in several types, depending on the dopants introduced to the crystal and the method by which they are introduced into the crystal lattice. However, the basic operation

of all the types of detectors is the same. As a charged particle traverses the crystal it interacts with the valence band electrons and promotes them to the conduction band. Once in the conduction band, electrons are free to move in response to an externally applied electric field. For each electron promoted, a hole is created in the valence band. The hole behaves as a positively charged particle and also moves in response to the electric field. Both electrons and holes are referred to as carriers. As the secondary (conduction band) electrons move through the crystal, they also interact with the valence electrons and create more electron-hole pairs. Approximately 3.6 eV are required to produce one electron-hole pair in silicon. Crystals have electrodes on both sides and operate as a reverse biased diode. The applied electric field attracts the carriers to their respective electrodes and prevents them from recombining. Total charge collected at the electrode is proportional to the energy lost in the crystal by the incident particle. If the incident particle is stopped in the crystal the collected charge is proportional to the particle energy.

A tube of high-density plasma (10^{15}–10^{17} cm^{-3}) is produced in the wake of the incident particle. The applied electric field must be sufficiently strong to drive the two types of carriers apart before they can recombine. In addition, the field must also result in a collection time much smaller than the carrier lifetime, limited by recombination and by trapping of carriers by impurities and defects in the silicon lattice. Under typical conditions, carrier collection times are of the order of 10^{-8}–10^{-7} s, which requires the detector carrier lifetimes to be about 10^{-5} s.

Defects and impurities in the silicon lattice result in the creation of trapping centers and recombination centers. The first center captures either electrons or holes, and due to the long trapping time, often of the order milliseconds, prevents them from being collected. The second type of center can capture both electrons and holes and cause them to recombine.

Two additional aspects of silicon solid-state detectors bear a brief discussion. The first is the effect of a dead layer, of order 100 nm thick, at the surface of the detector. The energy lost by incident particles transiting this layer to enter the active volume of the detector do not contribute to the creation of free charge in the detector proper and to the resultant signal. If the energy of the incident particle is to be recovered from the solid-state detector response, the energy lost in the dead layer (and any energy lost in passing through the electrode material) must be taken into account. This is particularly important when low energy particles are to be detected because those energy losses may be a significant portion of the original energy of the incident particle. The second effect is termed mass defect and occurs because a portion of the energy lost by an ion in the active volume of the detector does not result in the production of free charge that will contribute to the signal produced from the detector. That portion of the total energy loss of an ion that does not produce free charge in the SSD increases with the atomic weight of the incident ion. If the original energy of an incident ion is to be inferred from the SSD signal, especially if heavy ions are detected, the mass defect must be known so that the SSD signal can be corrected for this defect.

The current resulting from charge collection, usually taken from the anode (electron collection), is fed into a charge sensitive pre-amplifier that converts it into a voltage tail pulse (fast rise followed by a long decay). This pulse is fed, in turn, into a linear amplifier that shapes and amplifiers the signal to produce a short, peaked pulse with an amplitude proportional to the collected charge. Further processing can be carried out using standard pulse processing techniques.

A high energy heavy ion passing through the detector can produce a very large output signal that has been known to paralyze the charge sensitive pre-amplifier for a significant length of time, effectively introducing an abnormal dead time. The amplifier-discriminator electronics should be designed to avoid such paralysis.

A large number of low energy particles entering the detector within a short time compared to the charge sensitive pre-amplifier's integration time will mimic the signal from a higher energy particle (pulse pile-up). Because the pre-amplifier integration time cannot be made arbitrarily short, there is no electronic way of eliminating this problem. An instrument design that prevents access to the detector of particles having energies much lower than the desired threshold energy is the only way of mitigating pulse pile-up.

The advantages of SSD's are compact size, good energy resolution, fast timing resolution (coincidence timing is possible at sub nanosecond levels), and the ability to tailor the crystal thickness to match requirements. SSD disadvantages include: limitation to small thicknesses ($<$ 1 mm), susceptibility to damage by incident radiation (see also Section 4.2.4) and relatively high energy threshold (approximately 20 keV) for particle detection. The detection energy threshold is limited by detector thermal noise and can be significantly lowered by cooling the detector. However, this significantly increases the size, mass and power of the instrument and increases the complexity of the design.

The limitation on detector thickness means that protons with energies greater than about 14 MeV will not stop in the detector. One way of measuring energies of higher energy particles is to arrange two or more Si detectors, one after the other, in a co-axial configuration (detector telescope). The most common configuration has two detectors. The incident energy is set to be the sum of the energy depositions in the two detectors while the pattern of energy losses in the detectors can uniquely identify the incident particle type, proton, electron or heavy ion species. Occasionally a final detector element is placed behind the other detector elements in the telescope and operated in anti-coincidence to identify any particle that traversed through all detectors in the telescope and would otherwise have its energy and species misidentified.

Another possibility in the measurement of higher energy particles, is to use lithium-drifted silicon detectors, Si(Li). These detectors have the bulk silicon volume doped with lithium to mimic the response of a thick, high purity silicon slab. Thicknesses of up to one cm are possible. In detectors designed to measure low energy X-rays or γ-rays with excellent resolution ($<$ 200 eV), the design requires the storage and operation of Si(Li) detectors at cryogenic temperatures. Despite the obvious difficulties of operating such detectors aboard spacecraft, cryogenic Si(Li) instruments have been successfully flown. One example is the Atmospheric X-ray Imaging Spectrometer (PEM/AXIS) aboard the NASA Upper Atmosphere Research Satellite (UARS) [*Chennette et al.*, 1992]. When measuring charged particles, much coarser energy resolution is required ($\sim$30 keV) and room temperature Si(Li) detectors can be used. Some examples of these detectors are the Cosmic-Ray Isotope Spectrometer (CRIS) on the Advance Composition Explorer (ACE) [*Stone et al.*, 1998], Heavy Ion Counter on Galileo [*Garrard et al.*, 1992] and the Magnetic Electron Spectrometer on the Combined Release and Radiation Effects Satellite (CRRES) [*Vampola et al.*, 1992].

The discussion of SSD's in this section has been necessarily brief. Additional material describing silicon solid-state detectors can be found in *Knoll* [2000], *Kleinknecht* [1998], *Lutz* [1999] or *Spieler* [2005].

2.2.5.3 Scintillators and Cherenkov Radiators

Scintillators are materials that emit light when an incident charged particle traverses the material. The light output is, to a good approximation, linear with deposited energy. The density and stopping power of inorganic scintillators makes them highly useful for high energy particle spectroscopy for both protons and electrons. Key scintillator applications are those where SSD's are insufficiently thick to stop the high energy particle and a scintillator is used to complete the sensor.

Inorganic scintillator consists of an ionic crystal doped with activator atoms. Ionizing particles traversing the crystal produce free electrons and hole and electron-ion pairs (excitons). These travel through the crystal until they encounter activator atoms in their ground states and excite them. The subsequent decay of activator back to the ground state results in the emission of scintillation photons.

A second type of scintillator, organic plastics, is used only in limited roles on spacecraft. These materials are low density and so require greater amount of material to provide the same energy loss as a much smaller inorganic scintillator. Large detectors require extensive shielding and lead to large and massive detectors. One area where the plastics are useful is as veto counters or active shields. A shaped piece of plastic scintillator is placed nearly surrounding the sensors to be shielded. The signal from the plastic acts as a veto in a coincidence circuit with the detector signal, since the plastic signal indicated that an out-of-aperture particle must have struck the shielded sensors.

In a large class of organic scintillators, the effect of the incident particles is to produce a population of electrons in the first excited singlet state and its associated vibrational levels. These levels quickly decay, with no radiation emission, to the first excited state. This transition is followed by further decay to the various vibrational states associated with the ground state with a characteristic time of the order of a few ns (prompt fluorescence). In this case the fluorescent light is only weakly absorbed by the organic material making it suitable for use as a scintillator. Additional material on scintillators can be found in *Knoll* [2000] and *Kleinknecht* [1998].

An example of the use of SSD's and scintillators in a flight instrument (see *Redus et al.* [2002]) is shown in Figure 2.20. The instrument consists of four SSD's (D1–D4), two inorganic scintillators (S1 and S2) and plastic scintillator (S3). The SSD's are used to define the field-of-view of the instrument. The particle energies of interest are so high (up to 400 MeV) that no collimation or shielding is possible. The two inorganic scintillators are composed of a dense material, Gadolinium Silicate (GSO), and their function is to absorb as much energy as possible from the incident high energy particles. Finally, the S3 plastic scintillator is used as veto for out-of-aperture particles striking S1.

One advantage of inorganic scintillators is their high stopping power for spectroscopy of high energy particles. Organic scintillators have very short emission times, making them excellent choices for use as a veto in coincidence circuits. Finally both scintillator types can be physically shaped to meet design requirements. One disadvantage of scintillators is the relatively poor energy resolution relative to SSD's. This is due to 1) a much greater energy required to produce a scintillation photon (40–50 eV) than the energy required for production of electron-hole pair in silicon (3.6 eV) and 2) inefficiencies in transporting the photons to a light measuring device. Another disadvantage is that scintillator light is usually measured by photomultipliers. These are relatively large devices and this makes it difficult to design, package and shield the sensor. In the last few years, with the devel-

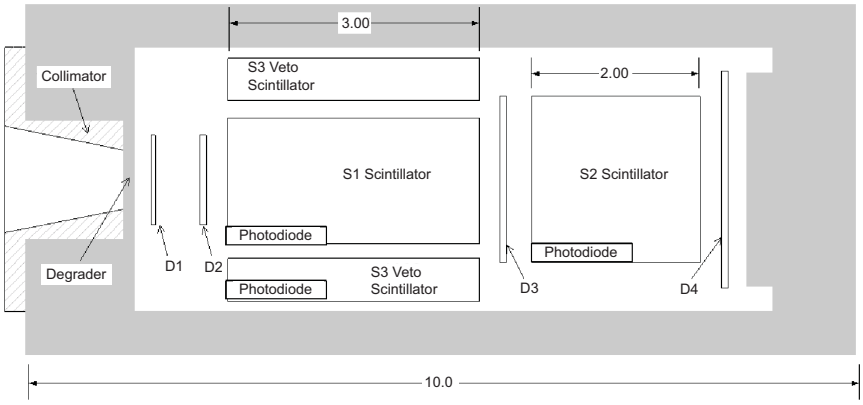

Figure 2.20: Cross-sectional diagram of a high energy scintillator instrument. This high energy proton spectrometer (HEPS) is scheduled to fly on the Air Force Demonstration and Science Experiment (DSX) mission scheduled for launch in 2009. Solid-state detectors (D1-D4) define the field-of-view, scintillators S1 and S2 measure the incident particle energy and veto scintillator S3 protects S1 from out of aperture protons. From *Redus et al.* [2002].

opment of fast, high light output scintillators it has become feasible in some cases to use photodiodes and avalanche photodiodes, which resolves the issues connected with photomultiplier size.

In very high energy applications, electrons with energies above a few MeV and protons above a few hundred MeV, a Cherenkov detector may be the sensor of choice. Cherenkov light is emitted when a particle travels through a medium at a velocity greater than that of light in that medium $v > c/n$ where c is the speed of light in vacuum and the n is the index of refraction of the medium. The emitted light is not isotropic but moves on the surface of a cone with the opening half-angle given by

$$\cos(\theta_c) = \frac{1}{n\beta} \tag{2.7}$$

where θ_c is the opening half-angle and $\beta = v/c$. The total number of emitted photons into a wavelength band λ_1 to λ_2 is given by

$$N = 2\pi\alpha \cos^2(\theta_c) L \int_{\lambda_1}^{\lambda_2} \frac{\mathrm{d}\lambda}{\lambda^2} \tag{2.8}$$

where L is length of the radiator, α is the atomic fine structure constant and λ_1 and λ_2 are wavelength of the upper and lower limits of the detection system sensitivity. In practice, most readout systems, such as photomultiplier tubes (PMTs) operate most efficiently in the visible region so setting λ_1 to 400 nm and λ_2 to 700 nm yields

$$N/L = 490 \sin^2(\theta_c) \text{ photons/cm} \tag{2.9}$$

This is a small amount of light and requires high gain amplification, such as a photomultiplier tube (PMT), to measure the signal. In space application, Cherenkov radiators fall into two groups, large n (Water 1.33, Plexiglass 1.48, Silica 1.5) and small n (Aerogels $1.01 \leq n \leq 1.05$). When designing a Cherenkov detector it is crucial to choose a material that does not emit any scintillation light since even weak scintillators can produce much more light than is produced by the Cherenkov process.

Cherenkov sensors are used in detecting energetic electrons in the presence of high energy protons [*Fillius and McIlwain*, 1974] since the latter will usually not have the required velocity to emit Cherenkov light. Another use of Cherenkov detectors is to detect high energy protons in an environment where high energy electrons are not present. An example of this type of sensor is the HEPAD instrument [*Rinehart*, 1978] that operated in geosynchronous orbit where energetic electrons were absent except during solar events, which produced both protons and electrons.

The discussion of scintillators and Cherenkov radiators in this section has been necessarily brief. Additional material describing scintillators can be found in *Knoll* [2000] and *Kleinknecht* [1998].

2.2.6 Avalanche Photo Diodes

Avalanche Photo Diodes (APDs) have been used recently for the detection of low-energy electrons, $E > 2$ keV, instead of SSDs [*Ogasawara et al.*, 2005, 2006]. An APD is also a reverse-biased diode where absorbed electrons (or photons) create electron-hole pairs. In the strong field of the avalanche, area charge carriers are accelerated high enough to create new carriers, the avalanche process, resulting in an internal amplification of the recorded signal by a factor of 30 [*Ogasawara et al.*, 2005]. In terms of characterization and calibration, the same rules and precautions as for SSDs have to be followed. One additional complication is that the amplification of APDs is a strong function of the bias voltage and of temperature. Thus, these dependencies have to be carefully calibrated in the laboratory and bias voltage and APD temperature have to be known when operated in flight. So far there is only one flight use of APDs for electron detection [*Ogasawara et al.*, 2006]. Since this application was very successful it is planned to be used on future Japanese space missions for medium energy (2–100 keV) electron measurements.

2.3 Langmuir Probes

Langmuir probes (LP) have been used extensively on rockets and satellites to measure ionospheric electron and ion densities, electron temperature, and spacecraft potential. This section discusses the design and implementation of LP measurements, with particular emphasis on cylindrical probes that have been used more extensively than any other type. The key lesson of more than three decades of LP use in space is that the accuracy of the measurements depends primarily on avoiding implementation errors. Experience with Langmuir probes since 1959, has shown that most measurement errors arise from: the type of collector surface material used, failure to avoid surface contamination, or failure to provide for inflight cleaning of the collector, failure to place the collector an adequate distance from the spacecraft and from various appendages that might interfere with its access to undisturbed plasma, failure to design the electronics to adequately resolve

those portions of the volt-ampere curves that contain the desired geophysical information, and failure to assure that the spacecraft is able to serve as a stable potential reference for the measurements. This section provides a short overview of LP instruments. For a more detailed discussion, the reader is referred to the review by *Brace* [1998] and references contained therein.

2.3.1 Overview of the Langmuir Probe Technique

The LP technique involves measuring the current to a probe as a function of an applied voltage. The current is the sum of the ion, I_i, and electron, I_e, currents collected by the probe. The voltage is applied to the probe with respect to the satellite reference potential. With careful spacecraft design, the applied potential is proportional to the voltage between the probe and the undisturbed plasma being analyzed. The resulting current-voltage characteristic, called the "volt-ampere curve" or "V-A curve" is a function of the plasma parameters, electron density, N_e, electron temperature, T_e, ion mass, m_i, and ion density, N_i, as well as the probe surface properties, and the probe geometry and orientation relative to the spacecraft velocity, magnetic field vector, and spacecraft body. Simple Langmuir probe theory [*Mott-Smith and Langmuir*, 1926] shows that the amplitude of the electron current, I_e, is proportional to N_e, and the amplitude of the ion current, I_i, is proportional to N_i. The current of retarded particles is proportional to the exponential of voltage, V, divided by temperature,

$$I_e \sim \exp \frac{eV}{kT_e} \tag{2.10}$$

Thus the logarithm of the retarded electron current is inversely proportional to the electron temperature, and the V-A curve is a strong function of temperature.

The operation of the Langmuir probe is illustrated in the theoretical V-A curve in Figure 2.21. A voltage generator varies the applied potential, V_a, of the LP relative to the spacecraft shown as the ground symbol, and an electrometer detects the current flowing between the probe and ground. The current, I, is the sum of ion and electron current flowing to the probe. A microprocessor controls the operation of the instrument: timing of the V-A curves, sensitivity of the electrometer, sweeping of V_a, and data processing. The V-A curve on the right illustrates the dependence of the current on the plasma parameters, N_e, N_i, and T_e. The plasma potential V_p is defined as the plasma to spacecraft potential, and V_s the spacecraft potential with reference to the plasma. Therefore, $V_p = -V_s$. At the special value of the plasma potential, where $V_a = V_s$, the probe to plasma voltage difference, $V_s + V_p$, is zero and electrons and ions experience no acceleration or retardation. For $V_a > V_s$, electrons are accelerated and ions retarded. This is called the electron saturation region, where the electron density can be determined from the amplitude of the current after first subtracting the ion current. V_s is a unique value of V_a when the probe is at the same potential as the plasma as determined by the inflection point in the V-A curve as illustrated in the figure. The V-A curve has a linear or square root dependence on voltage for spherical or cylindrical geometry respectively. Similarly, in the ion saturation region, the retarding voltage is sufficient to suppress the electron current thus the net current is dominated by ions and the ion density can be determined. Between the ion and electron saturation regions the V-A curve is exponential and the current is mainly dominated by retarded electrons allowing T_e to be determined directly.

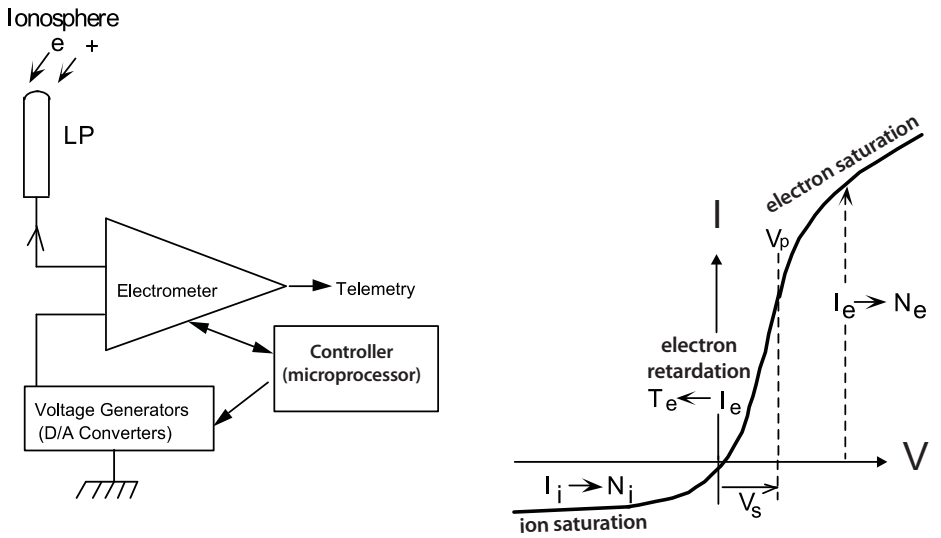

Figure 2.21: Block diagram of the Langmuir probe instrument and a theoretical V-A curve.

Of course the zero potential, or spacecraft ground in Figure 2.21, will also depend upon the plasma conditions. The spacecraft charges to whatever voltage is necessary so the current to the spacecraft is zero. For cold, dense, ionospheric plasmas, the primary currents are the plasma currents and the spacecraft generally charges a few T_e/e negative relative to the plasma. In more tenuous magnetospheric plasmas, or in interplanetary plasmas, the photoemission current can be large and the spacecraft will charge positive several volts to several tens of volts. Since the spacecraft potential can shift, it is important that the measurements are not sensitive to these shifts. Care must be taken to assure that Langmuir probe currents, or other experiment currents, are negligible and do not affect the spacecraft potential. The spacecraft should be uniformly conducting. If the photoemission is an important current, the spacecraft photoemission cross sectional area should be constant. If the magnetic field is large and electrons cold, then plasma currents may depend upon the spacecraft cross section parallel to B. In all cases measurements should be made much faster than the spacecraft spin and data that exhibit harmonics of the spin should be viewed with suspicion. This may be an indication of interference from changes in spacecraft currents, which change the spacecraft potential relative to the plasma.

2.3.2 Types of Probes Used in Ionosphere Measurements

Traditionally, Langmuir probes have been designed to operate under the condition of orbital-motion-limited or sheath-area-limited current collection [*Langmuir and Mott-Smith*, 1924; *Mott-Smith and Langmuir*, 1926]. These limiting cases permit simple asymptotic formulas to be used in the interpretation of the volt-ampere characteristics. To remain orbital-limited the probe radius must be small compared with the thickness of the sheath that surrounds it, while the radius of a sheath-area-limited probe must be large compared

to the sheath thickness. The equations for these limiting cases are simple enough to be incorporated easily into the data processing codes that are designed to process the tens of millions of volt-ampere curves that are recovered during a satellite mission. The "Dumbbell" probes used on early rockets by *Boggess et al.* [1959] and *Spencer et al.* [1965] are examples of sheath-area-limited probes. These probes were too large (radius ∼10 cm) for satellite use and would need to have been even larger to remain sheath-area-limited at the low densities of the upper F-region and plasmasphere. Therefore, Langmuir probes on satellites usually have been made small enough to remain orbital-motion-limited. The probe can be either spherical or cylindrical. Typically the cylindrical geometry is adopted because the probe radius can be made small enough to remain orbital-motion-limited at very high ionosphere densities, while its length can be made great enough to collect a measurable current at very low densities. See *Brace* [1998] for further details and references.

2.3.3 Measurement Accuracy

If the sources of error described later in the implementation Section 2.3.5 have been dealt with successfully, the absolute accuracy of the LP measurements should be better than 10 %, and perhaps better than 5 %, for T_e. The relative accuracy between density measurements (repeatability), however, can be much greater, depending on the number of bits employed in the telemetry words, the electrometer noise level, and interference from other spacecraft systems. Repeatability of better than 1 % is typical. One can assess the accuracy that has been achieved in a number of ways, including; (1) examining the internal consistency between LP theory and the shapes and amplitudes of the measured V-A curves, (2) comparing the measurements by different types of probes on the same rocket or satellite (discussed in Chapter 4), and (3) comparing the probe measurements with those made by incoherent radars during overflights (also discussed in Chapter 4). Details of this approach and the results of past assessments are outlined below.

2.3.4 Internal Consistency Checks

The simple exponential relationship between T_e and I_e, that is, $I_e \sim \exp(eV/kT_e)$ when eV is negative, provides a powerful test of the validity of the T_e measurements. If the retarding region is not actually exponential, that measurement can be assumed to be invalid. The quality of fit can be used to detect such instances, and they should be discarded. *Brace et al.* [1971] showed that the ISIS-1 probes exhibited retarding regions that were exponential over a range of 6 or 7 kT_e. Typical electronic resolution of the volt-ampere curves allows T_e to be measured with an accuracy of better than 5 %. Such accuracy may not be possible at very low density ($N_e < 10^2$ cm^{-3}) where electrometer sensitivity, subsystems electrical interference, and background currents due to photoemission may introduce errors. In darkness, where photoelectrons are largely absent, T_e can be measured to much lower densities than the above limit, depending largely on success in reducing these background electrical signals.

Surface contamination of the collector may also introduce T_e errors, as discussed in the implementation Section 2.3.5. The accuracy of the N_e and N_i measurements is typically of the order of 10 % after corrections of N_e for certain systematic errors. Errors can be detected and assessed most readily by comparing the N_e and N_i measurements from the

same V-A curve. N_e and N_i are independently measured because they come from different regions of the V-A curve. Since plasma neutrality requires N_e to equal N_i, one is free to use either as a measure of the density. The N_e measurements extend to lower densities because the electron saturation current is about a factor of 50 greater than the ion saturation current for the same density. The N_i measurements are more accurate, at least in the F-region, because the ion saturation current is almost exclusively due to the sweeping up of heavy ions by the known cross sectional area of the probe. At low densities ($N_i \ll 10^4$ cm^{-3}) photoelectrons emitted from a probe in sunlight introduces an error in the N_i measurements because those electrons add to the net I_i and produce an overestimate of N_i. The photoemission current in sunlight represents an effective I_i that is approximately equal to the true I_i for N_i densities of the order 1×10^4 cm^{-3} at the Earth-Sun distance. An empirically derived correction for the photo current can extend the N_i measurement down to densities of the order 1×10^3 cm^{-3}. Because the sources of N_e and N_i error differ, it is not surprising that they exhibit slight systematic differences where their dynamic ranges overlap, typically over the range 10^3–10^6 cm^{-3}. Such differences arise from deliberate compromises involving the best sensor length and diameter requirements for the T_e and N_e measurements as described in the implementation section. The lower limit on the N_e measurements is between 1 and 10 cm^{-3}, depending on the length of a boom (placing the probe outside of the spacecraft influence), whether the spacecraft is in sunlight, and where the probe is mounted relative to sunlit surfaces of the spacecraft.

2.3.5 Implementation Issues

A number of factors are critical for successful Langmuir probe measurements; (1) proper sensor placement, (2) reduction of collector work function patchiness, (3) reduction of collector surface contamination, (4) limitation of geomagnetically induced potentials in the collector, (5) adequate resolution and recovery of the V-A curves, and (6) attention to spacecraft design details. If these factors are not dealt with successfully, the full measurement accuracy that is possible will not be achieved. Inattention to some of these items can preclude measurements, especially for T_e.

2.3.5.1 Boom Mounting

The use of a boom is required to assure that the probe is placed in the undisturbed plasma; i.e., beyond the spacecraft sheath and outside the spacecraft wake. To achieve this goal a boom length of between 30 and 100 cm is usually adequate in the ionosphere. Longer booms may require hold-down devices to prevent damage during launch. Two independent sensors are usually required, particularly on a spinning satellite, to assure that at least one probe is in the undisturbed plasma at all times.

2.3.5.2 Collector Surfaces

Work function patchiness can be a significant source of error in the T_e measurements, especially in regions of very low temperature where the electrical patchiness of a normal (polycrystalline) collector approaches or exceeds the mean thermal energy of the electrons. Patchiness distorts the V-A curve in the vicinity of the plasma potential, thus it is important to avoid using the portion of the curve in that region. A polycrystalline probe can easily

have a built-in patchiness exceeding 100 mV, thus T_e of 50 mV (580 K) or less would be compromised. Such a probe would produce serious T_e errors at E-region temperatures ($\sim$300 K). The higher temperatures of the F-region ($\sim$2000 K) would be unaffected by this level of patchiness. The thin-wire probes used on the early satellites were made of stainless steel, so they undoubtedly had this problem to one degree or another. These satellites orbited at high altitudes, however, where T_e generally exceeded 1000 K. Enough of the retarding region remains at these temperatures to allow a good fit for T_e. Patchiness only slightly affects the N_e and N_i measurements (which are insensitive to voltage) by modifying the inflection point, used to determine the spacecraft potential. Patchiness makes V_s appear higher than the true value (see Figure 2.21) and thus the spacecraft potential is incorrectly identified as being more negative than the true value. This shift in plasma potential is less than the half-width of the patchiness voltage. Work function patchiness has been reduced in later applications by the use of either vitreous carbon probes [*Bujor*, 1973] or by using probes having highly oriented metal crystal surfaces [*Brace et al.*, 1973; *Brace*, 1998]. The latter solution was based on the work of *Weissman and Kinter* [1963] who employed a chemical vapor deposition process to produce cathodes having surface potentials that were uniform within 5 mV. This technology was first employed to make the cylindrical probes used on the AE missions, which were designed to dive deeply into the E-region where patchiness would have caused significant errors in the T_e measurements. Collectors of the same type were used later on the DE-2 and PVO spacecraft. This approach appears to have been very successful, since this type of probe was able to measure T_e down to temperatures of 300 K on the AE-C and PVO missions. DE-2 had a 300×1000 km orbit and so it did not experience regions of very low T_e.

2.3.5.3 Probe Contamination

Surface contamination can produce its own type of patchiness even when the potential of the probe surface is highly uniform. This issue is discussed in more detail in Chapter 4.

2.3.5.4 Magnetically Induced Potentials

When a cylindrical collector is moving at orbital velocity through the geomagnetic field a potential gradient of the order of 300 mV m^{-1} is induced along its length. This gradient will produce the same kind of energy smearing as surface contamination or patchiness. Thus one end of the collector could have a significantly different potential than the other end. The difference could be as high as 75 mV for the long probes used prior to AE-C ($\sim$23 cm), but only 16 mV for the shorter collectors ($\sim$5 cm) used from AE-C onward. These shorter collectors caused the induced voltage effect to remain negligible down to T_e values of 350 K or lower.

2.3.5.5 Adaptive Circuitry

There is a need for adaptive circuitry to permit measurements under a wide range of ionosphere conditions. T_e can vary by a factor of 20 or more around the orbit, so the amplitude of V_a must adapt to those changes to allow proper resolution of the V-A curves, given the limited telemetry rates that most spacecraft make available. A second benefit of this approach is that the resulting amplitudes of V_a provide an approximate value of T_e at

high sampling rates, while requiring much lower telemetry rates. Similarly, N_e may vary by 4 or 5 orders of magnitude around an orbit, thus the electrometer must have a wide dynamic range to follow the resulting amplitude variations of the V-A curves. Continuous curve-by-curve electrometer gain adjustments should be made to keep the V-A curve perfectly framed for telemetry. As a side benefit, the resulting gain settings provided measurements of N_i and N_e throughout the orbit without needing to telemeter or examining the individual V-A curves for processing on the ground [*Brace et al.*, 1973].

2.3.5.6 Spacecraft Design Factors

Since the LP sweep voltage is applied with respect to the spacecraft potential, V_p, the spacecraft design should be examined to see if it includes any features that might prevent V_p from remaining low and stable. Historically, the most common spacecraft potential problems are caused by; (1) exposed metal connecting tabs on the solar arrays, and (2) insufficient external conducting area to return the LP current to the ionosphere without causing excessive changes in V_p. Since the net current to the spacecraft-probe system must be zero, increases in I_e to the probes must be offset by identical reductions in I_e flowing to the spacecraft. The spacecraft design should support such I_e changes without significant changes in V_p. Such changes subtract from the voltage that actually reaches the probe and can interfere with measurements made by other instruments, which are referenced to V_p. The achievement of a stable V_p requires an external conducting area that is several hundred times larger than the combined probe and guard areas. The guard is placed next to the probe and driven at the same potential as the probe to insure a uniform cylindrical electric field geometry near the probe. This conducting area must not be in the wake of the satellite because ions and electrons do not have access to those surfaces [*Samir et al.*, 1979]. Although the total external area of the spacecraft is typically more than 10,000 times that of an LP, most of this area will be nonconducting. Bare metal surfaces tend to have absorptivity and emissivity coefficients that conflict with spacecraft thermal design requirements. This conflict can usually be resolved by painting some of the exposed spacecraft surfaces with a conductive thermal paint, or by adding grounded conductive surfaces elsewhere. Some spacecraft provide the required area ratio by employing conductive coatings over glass plates that cover the solar cells. When an adequate area ratio is not achievable in these ways, it may be necessary to accept a smaller area ratio. In this situation one might avoid using the LPs in the electron saturation regions where they collect the largest current. In this case, only T_e and N_i measurements would be possible. This approach was used in the AE missions to reduce possible interference with the retarding potential analyzers and the ion mass spectrometers. Several cases of unusually high V_p values have been observed. They all have been traced to the use of negative grounded solar arrays whose interconnecting metal tabs were exposed to the plasma. These tabs have voltages that range from 0 to about +40 volts with respect to the spacecraft and act as an array of small Langmuir probes that collectively attempt to draw a larger electron current from the ionosphere than the rest of the spacecraft is able to return. To maintain zero net current to the system, V_p shifts sufficiently negative to decrease the electron current to the solar array to sustainable levels. Such high negative potentials ($\sim$30–40 V) usually preclude the T_e and N_e measurements, since the available range of the applied voltage, V_a, is insufficient to drive the probe out of ion saturation. This problem is limited to the parts of the orbit where the spacecraft is sunlit. Two solutions to the solar array problem have been found successful. The first involves

grounding the positive end of the solar array thus exposing only negative potentials to the plasma. While the array draws an enhanced ion current, this current is easily balanced by a slight decrease in V_p to draw the required additional electron current to the spacecraft. The Explorer-22, AE and DE spacecraft used such negative arrays, and they experienced normal ranges of V_p. Alouette-2, ISIS-1, OGO-6, ISIS-2, and PVO had positive arrays. But high spacecraft potentials were avoided by painting the solar cell tabs with silicon rubber to prevent drawing electrons from the plasma. This was a simple, effective and low cost fix.

2.3.6 Summary of Langmuir Probe Operations in Dense Plasmas

The previous sections have discussed the Langmuir probe technique used on ionospheric missions and the various ways to improve measurement accuracy in that environment. Many years of experience indicate that the accuracy of the measurements depends on the details of the implementation. The factors most critical to success involve; (1) using a relatively short probe that has inherently low surface patchiness and that can be cleaned very early in the mission by electron bombardment, (2) mounting the probe on a boom that is long enough to place the collector in the undisturbed plasma that lies beyond the spacecraft ion sheath, (3) using adaptive circuitry in the electronics to resolve the V-A curves over a wide range of N_e and T_e values, (4) designing the spacecraft to have an adequate conducting area and a solar array that does not cause V_p to be excessively negative. The degree of success actually achieved can be determined by a series of internal consistency tests. First, the volt-ampere curves should exhibit the form indicated by the theory. The ion saturation regions should be approximately linear and have a slope that is consistent with the known mean ion mass in the region. The electron saturation region should exhibit the expected voltage dependence. The electron retarding region should be truly exponential over several kT_e. The N_e measurements should be consistent with the N_i measurements at densities where the two techniques overlap, recognizing that end effects (for short probes) will tend to cause N_e to be slightly higher than N_i. No hysteresis should be evident in the curves when the probe voltage is swept in opposite directions, and no time constants should be evident in I_i immediately following the sweep retrace. These criteria for internal consistency are very demanding and, if met, one can gain a high degree of confidence in the measurements. It can be concluded that Langmuir probes can provide accurate ionosphere measurements when several important implementation challenges are successfully addressed.

2.3.7 Langmuir Probe Measurements in Low Density Plasmas

In addition to using measurements of the Langmuir probe current-voltage relationships as a means of determining plasma densities, Langmuir probes are also used to measure geophysical electric fields and to measure the spacecraft potential relative to the plasma. The spacecraft potential can then be used to infer plasma density. This plasma density measurement technique is generally used in low density plasmas, such as the magnetosphere, where photoemission currents are large compared to plasma currents. In this case, a “bias current” is applied to the Langmuir probe that is a significant fraction of the photoemission current (typically 20–50 %). The Langmuir probe will float to within 1–2 volts

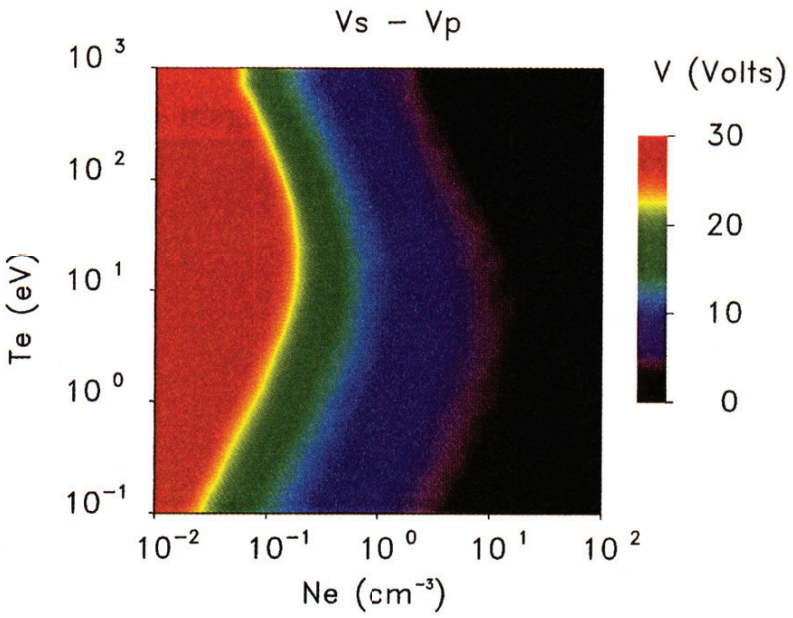

Figure 2.22: Modeled spacecraft potential with respect to the Langmuir probe ($V_s - V_p$) as function of electron number density and temperature. From *Escoubet et al.* [1997].

of the plasma potential, where the escaping photoelectron current balances the bias current. Since the bulk of the photoelectrons are <2 eV, the probe remains very close to the plasma potential. Since plasma currents are small, the probe-to-plasma potential is very insensitive to changes in plasma properties. With a probe providing a plasma potential reference, the spacecraft to plasma potential difference can then be measured. As with any object in space, the spacecraft will float to a voltage where the currents balance. In the spacecraft case, the primary currents are photoemission and plasma electron currents. Since the plasma electron current depends on density, spacecraft potential can be used to infer density as described below.

Starting with the assumption that we can ignore ion fluxes, the spacecraft potential in low density plasmas depends on a balance between the escaping photoelectron flux and the collection of plasma electrons, each integrated over their respective spectrum. The escaping photoelectrons have a sharp low energy cutoff at the plasma potential, which is easy to model. However, modeling the plasma electron flux is more complex. Plasma current collection depends, to first order, on both the density and thermal velocity. However, if the spacecraft potential is a substantial fraction of $T_e(eV)/e$, the spacecraft will focus plasma electrons, increasing the effective collection area. If the plasma electrons have energies the order of or greater than 100 eV, they will also produce secondary electrons, which can also affect the spacecraft potential. Since the spacecraft potential clearly depends on at least two parameters, namely electron density and temperature, accurately inferring density alone is not possible without a separate temperature measurement (see Figure 2.22). However, there are two compensating effects that combine to dramatically

reduce the dependence of the spacecraft potential upon temperature for typical magnetospheric and solar wind plasmas. For typical temperatures (5–100 eV) the focusing factor dependence on thermal velocity roughly cancels the natural velocity dependence of the plasma electron current to the spacecraft. That makes the spacecraft potential almost exclusively a function of density for this temperature range, the exact functional relationship being dependent upon the individual spacecraft characteristics. If an independent method can be found for obtaining density (i.e., by measuring the particle distribution or by measuring the plasma frequency) then the unique spacecraft potential versus density relation can be obtained. Once this relation is determined, spacecraft potential measurements can provide inferred density measurements at rates approaching $\sim$1 kHz. This is 2–4 orders of magnitude faster than other methods. For detailed studies of spacecraft potential dependence on density see *Escoubet et al.* [1997] or *Scudder et al.* [2000].

Before closing our discussion of this useful technique, we provide a few warnings about problems with absolute density inferences. As stated above, the spacecraft potential does have electron temperature dependence, can be affected by secondary electrons, and assumes the solar UV flux is constant. During solar flares, the UV flux can increase significantly, especially the higher energy photon flux, which can affect the density-potential relation. In the magnetosheath, the density can get high enough so the spacecraft potential drops to $<$+5 V. At these low potentials, secondary electrons can escape and therefore become part of the current balance. This can introduce factors of $\sim$2 errors in the inferred density if corrections for electron temperature are not included. In very low density regions, such as the Earth's magnetic lobes, the density can drop below 0.1 cm^{-3}. Under these circumstances, instrument currents may affect the density relation. For example, the bias currents to the Langmuir probes may be large enough to affect the spacecraft potential. The impact on spacecraft potential can be even larger if electron beam experiments, such as the Electron Drift Instrument on Cluster, emit a current comparable to the plasma collection current. This can drive the spacecraft potential to nearly the beam energy, which is typically about 1 keV. Care must be taken to avoid these potential problems.

2.4 Faraday Cups

2.4.1 Introduction

Faraday cups have a long history of use as a solar wind instrument. To this day, when used with modern electronics the Faraday cup remains an effective way to measure the properties of plasma, especially flowing plasma such as the solar wind. Important advantages are accuracy, simplicity and stability over tens of years.

To measure a flowing plasma, such as the solar wind, the particle's access to the cup is modulated by a voltage applied to a wire-mesh grid inside the cup. Modulated currents from the cup are AC-coupled to a "measurement chain" to be described below, and are detected in phase with the modulator. Logarithmic A-D conversion is performed directly by integrating charge on a capacitor and comparing the voltage across the capacitor to that of an RC discharging voltage. Counting clock pulses between the start of this operation and the time of voltage equality gives a number proportional to the logarithm of the current observed.

A Faraday cup does not employ particle multipliers, whose properties depend critically upon surfaces that change in time, but requires that the properties of electronic circuits remain stable. As shown below, that requirement is possible to achieve reasonably easily. One might suppose that such a sensor is bulky and weighty, but a 15 cm diameter cup has a mass < 1 kg, and the associated electronics can be much reduced by using custom integrated circuits, perhaps mounted on the back of the cup itself.

2.4.2 Instrument Description

In order to understand fully the calibration procedures of Faraday cups, we first describe the Faraday cup system, pointing out components that are susceptible to variation and that must therefore be calibrated. This description is based mainly on the two Faraday cups on the Wind spacecraft [*Ogilvie et al.*, 1995]. A functionally identical instrument was built for the Triana mission.

2.4.2.1 System Components

The Faraday cup (FC) system is composed of two major components: the sensor (which consists of the modulator assembly, the central limiting aperture, and the collector assembly) and the measurement chain, which converts measured currents into a digital output.

As illustrated in Figure 2.23, the sensor contains aperture stops, the "modulator section" which contains one or more grids to which the high-voltage modulator waveform is applied and its surrounding ground grids; a "suppressor" grid which prevents secondary emission of electrons due to ions striking the current-collecting "collector" plates, and the collector plates themselves. The use of a split collector plate (Figure 2.23 shows two halves of a circular collector plate) enables determination of flow angles in the plane of the figure through comparison of the currents collected by each collector segment. When the sensor is mounted on a spinning spacecraft and the split collector division line is mounted parallel to spacecraft spin plane, the relative currents from the two sections can be used to determine the flow angle relative to the spin plane. On non-spinning spacecraft, such as Triana, the relative currents from three, 120° segments of a circular collector plate would be used to determine the solar wind flow angle.

The operation of Faraday cups can be affected by photoelectron emission from the collector plates or grid structures if they are exposed directly to ultraviolet radiation. Suitable bias voltages on the collector and the various grids reduces the effect.

The Faraday cup sensor's phase-space acceptance for incoming ions has a geometrical as well as a velocity aspect. Figure 2.24 shows that the acceptance of the sensor is composed of a geometrical portion defined by aperture stops and an energy/charge portion that is determined by the upper and lower modulator voltages which form a particular energy/charge "window". There are three important geometrical constraints to particle trajectories in the FC: the entrance aperture; a central, limiting aperture just after the modulator grid section; and the collector plates. A voltage on the modulator grid only affects an ion's velocity component normal to the plane of the modulator grid. The unaltered component of an ion's velocity parallel to the modulator grid results in a refraction of a slowed ion's trajectory as it passes through the modulator assembly. When an ion arrives at the final grounded grid of the modulator section, its velocity is the same as it was when it

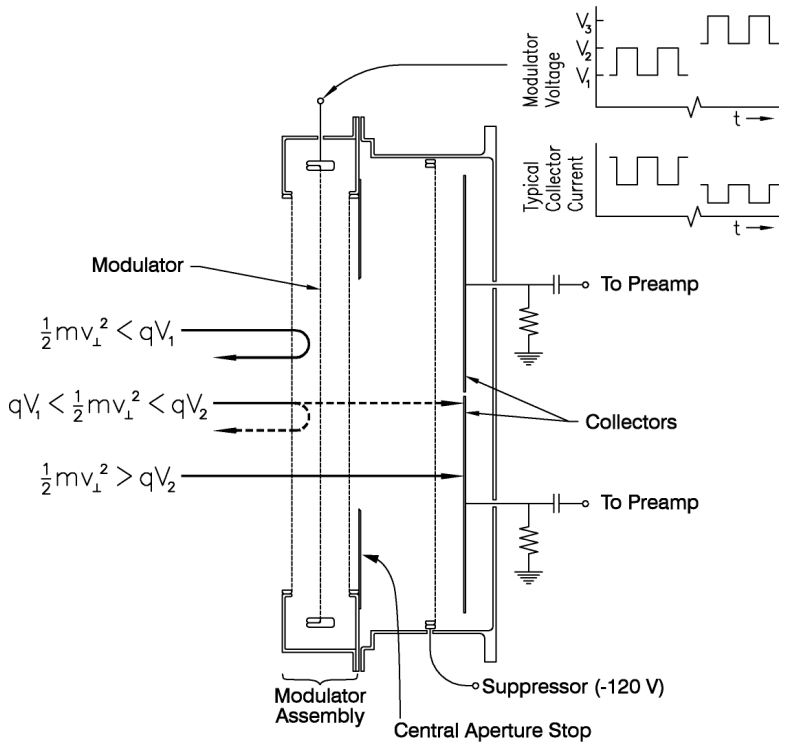

Figure 2.23: A schematic cross-section of the Wind FC instrument along its symmetry axis showing the entrance aperture, the modulator assembly, the limiting aperture, the suppressor grid, and the collector plate (oriented perpendicular to the page), which is split into two semicircular plates.

entered the cup. The limiting aperture that follows the modulator section then determines the accepted ion trajectories without further refraction (except for a negligible amount due to the suppressor grid), and the overall acceptance is a combination of the image of the entrance aperture as projected onto the central aperture and the subsequent projection of that image onto the collector plate. The limiting aperture is designed to be sufficiently smaller than the entrance aperture so that it is always uniformly illuminated by the incoming ions within the $\sim$45° half-angle acceptance of the FC, even in the presence of refraction.

Figure 2.24 illustrates the spatial as well as velocity space acceptance of a FC. As illustrated in Figure 2.23, the voltage applied to the modulator grid determines the component of velocity perpendicular to the modulator grid. Hence, the phase space acceptance of a FC is a disc with thickness determined by the voltages applied to the modulator grid; Figure 2.24 is a sketch of that acceptance. As the modulator voltage pairs are swept through their range in a series of steps, the FC measures the reduced distribution function of the ions in any given direction. As used on Wind, each current measurement requires $\sim$30 ms dur-

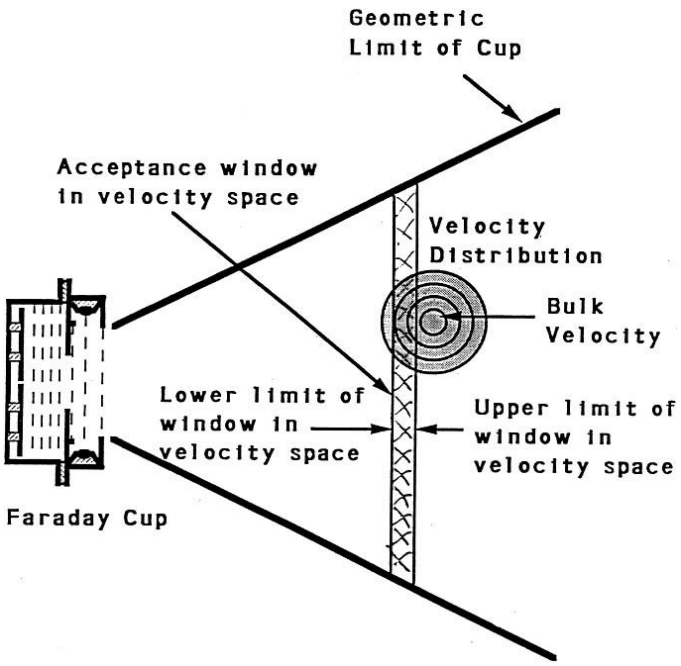

Figure 2.24: Schematic of the phase space acceptance of a Faraday cup. The cup itself is sketched at the origin of the coordinate system.

ing which time the spacecraft rotates ∼3.6°. The energy/charge window is held constant for the spacecraft 3 s spin period and is then moved to the next value for a given operating mode. Measurements of three-dimensional properties of ion distributions, such as heat fluxes and temperature anisotropies are determined by examining the reduced distribution function in multiple directions.

The description above assumes that the modulator grid is an ideal, conducting plane with a voltage, V_m applied to it. In fact, the potential of a grid surrounded by grounded grids (i.e., at zero voltage) is equal to V_m only at the grid wires themselves. In the mesh spaces, the potential is smaller because the electric field lines bend towards the wires. As a result, ions with energy/charge less than V_m are able to penetrate the spaces between the grid wires. That effect can be minimized by making the spacing between the grid wires small compared to the space between the ground grids and also by using two modulator grids in close proximity. Because of the reduction in potential of the grid, the cutoff voltage is not as sharp as it would be for conducting planes: normally-incident ions having energy/charge less than V_m can still pass through the modulator grid. (That effect is diminished for ions entering at an angle to the normal since they move sideways and tend to collide with the grid wires at very low speeds.) The energy window is somewhat blurred and slightly shifted. Modeling and detailed measurements using an ion beam demonstrate that current FC designs reduce the significance of these to the point where they play only a minor role in the derived ion parameters (see also Section 3.3.5.2).

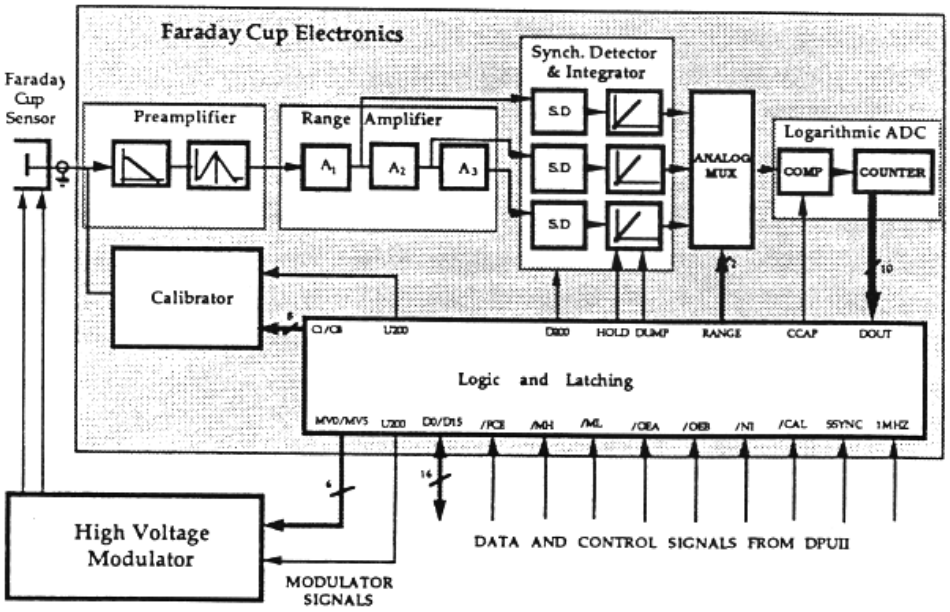

Figure 2.25: Schematic of the Faraday cup measurement chain.

2.4.2.2 Measurement Chain

The FC systems described here are designed to measure currents in the range from 10^{-13} to 10^{-8} A. Because the instrument's accuracy and long-term stability are dependent upon the determination of those currents, a detailed discussion of the measurement chain is warranted. As illustrated in Figure 2.23, a square wave voltage superposed on a DC level applied to the modulator grid affects incoming ions with the appropriate range of energy/charge; and their flux on the collector plates produces a current modulated at the frequency (200 Hz for Wind and Triana) of the square wave voltage. Those currents are brought to the measurement chain using low-noise coaxial cable and are AC-coupled to the input of the first operational-amplifier stage. A block diagram of the measurement chain is shown in Figure 2.25. Figure 2.26 shows details of the input stage of the measurement chain. The input stage performs a current-to-voltage conversion by providing a compensating current of opposite polarity through a 100 MΩ feedback resistor. An internal calibration circuit can also apply appropriately modulated currents to the same input point. (As shown in Figure 2.23, the collector plate itself is connected to ground through a large resistor in order to provide a DC-return path). The output from the first operational amplifier stage is then passed to two more op-amps in series. For very low currents, the output from the entire amplifier chain is used; as the input current increases, the amplifiers will progressively saturate, starting at the high-gain end. The outputs from each stage are individually synchronously detected using a phase-shifted signal obtained from the modulator driver. (The appropriate phase shift is a combination of several factors: the phase

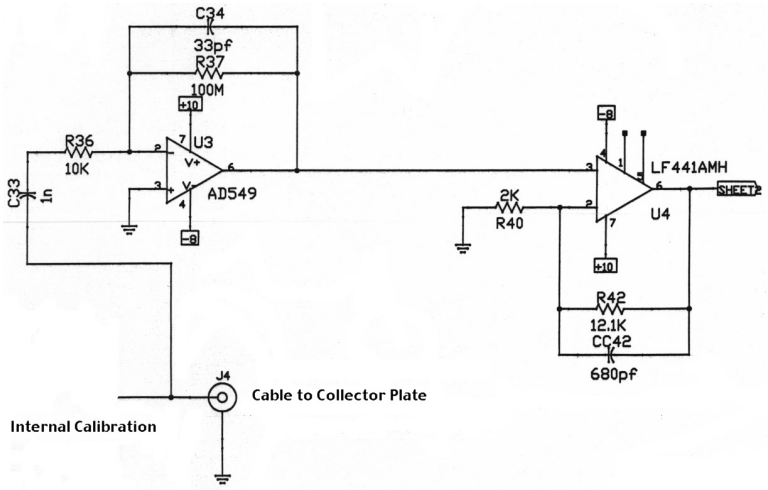

Figure 2.26: Electrical schematic of the preamplifier to the input stage of the analog measurement chain. Modulated currents from the internal calibrator and from the collector plate (via a low-noise coaxial cable) are capacitively coupled to a current-to-voltage converter. The thermal noise limiting currents are generated by the 100 MΩ feedback resistor shown in this figure and the DC return current resistor shown in Figure 2.23.

shift due to each operational amplifier and the phase shift due to the impedance between ground and the collector plate and its coaxial cable).

The output of each synchronous detector is a DC signal that is integrated on a capacitor for a selected "integration" period. At the end of the integration period, that voltage is held fixed and the voltage from the highest gain unsaturated amplifier stage is then compared to an exponentially decaying voltage from an RC circuit that had been started at a precise voltage. A 10-bit counter driven at a high frequency compared to the RC time constant records the time from the start of the comparison until the two voltages become equal. The resulting digital number on the counter represents a logarithmic conversion of the current integrated by the measurement chain. This number is transmitted to a central data processing unit together with a digital indication of which amplifier stage that signal came from. The logarithmic analog to digital conversion (hereafter log-ADC) results in an equal fractional uncertainty in the integrated current (0.4 % in the case of Wind) at all ranges from 10^{-13} to 10^{-8} A. One distinction between the FC and a "counting" instrument is that the uncertainty in any given current is not from $\sqrt{N}$ counting statistics. The lowest current of 10^{-13} A is equivalent to that produced by 6×10^5 charges incident on this collector (corresponding to $\sim 2 \times 10^4$ elementary charges per cm^2). Additionally, the minimum measurable current is determined by the values of the feedback resistor in the current-to-voltage conversion stage, the DC-return resistor, and the thermal noise generated therein.

The input to the current-to-voltage converter is also connected to an internal current source that can inject 12 currents spread evenly over the dynamic range of the measurement chain. The calibration currents are formed by a voltage divider that divides a precision square-wave voltage that oscillates at the modulator driven frequency. The modulator

square-wave is driven by a 200 Hz signal derived by counting down a basic 600 kHz signal. The phase of the calibration signal is set during pre-launch testing by digitally selecting the appropriate delay that maximizes the output of the amplifier chain.

By varying the injection current and the integration time, the internal calibration system can be used to generate signals over the entire range of the measurement chain and the log-ADC. As discussed in 3.3.5 and 4.3.6, the internal calibration system may be used to measure both gains and offsets and to identify variations in the FC response, both on the ground and in space.

2.5 Plasma Analyzers

2.5.1 Introduction

The science goal of many space missions requires the measurement of the properties of the local plasma environment. Among those properties are the energy distribution of both ions and electrons, the full three-dimensional velocity space distribution, the plasma bulk flow velocity, and both the spatial and temporal variations of these distributions. Moreover, these plasma properties must be determined over a wide range of particle energies and intensities, often with very high temporal resolution. Usually a given observation must be of only a small portion of the total plasma population entering the instrument. These measurements must often be made in the presence of high UV and energetic particle backgrounds. This places severe requirements on the rejection of unwanted responses in the instrument. Those problems and techniques to solve or correct for them are discussed in more detail in Chapters 3 and 4.

Both electric and magnetic fields can be used for analysis of charged particles. However, electrostatic analyzers are used in most space experiments due to the smaller mass of the analyzer providing similar performance.

Plasma analyzers for space studies evolve in order to improve the velocity space coverage and temporal resolution. The material in this section describes several different plasma analyzer designs that have been used in instruments for measuring the properties of space plasmas. The section concentrates on analyzer designs that utilize various, and ever more complex, electric field configurations to select charged particle energies and direction of particle arrival for detection. The electrostatic analyzer designs that are discussed in this section are often used to select particle energy and charge species that subsequently undergo further analysis to determine particle mass and charge state. The instrument designs that accomplish such further analysis are discussed later in this chapter. For completeness this section contains some brief descriptions of instruments not often used anymore such as magnetic spectrograph particle analyzers or simpler electrostatic analyzers.

Some, but not all, of the analyzer designs that are described also appear in subsequent chapters that discuss problems and solutions to the task of laboratory and in-flight calibration of instruments. However, the general approach to laboratory calibration, in-flight performance verification, the problems likely to be encountered and their solutions that are described in later chapters will apply to all forms and designs of electrostatic analyzers discussed here.

Young [1998] provides a good survey of various types of electrostatic analyzers in the introduction to the Geophysical Monograph: Measurement Techniques in Space Plasmas.

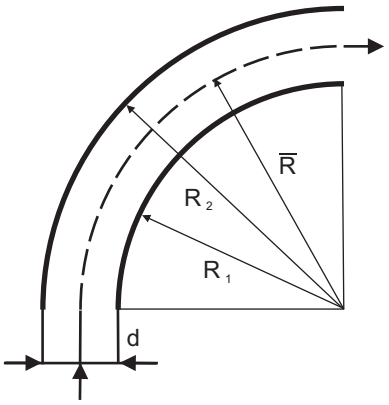

Figure 2.27: Cylindrical electrostatic analyzer.

The individual articles in that Monograph are also informative and many are cited in the chapter.

2.5.2 The Retarding Potential Analyzer

Perhaps the simplest form of energy analysis of a charged particle population by electrostatic means is the retarding potential analyzer. In this design charged particles are allowed to enter a cavity, usually through a field-of-view (FOV) limiting aperture structure. One or more grids within the cavity are biased at controllable voltages to present a potential barrier that prevents access of charged particles of insufficient energy to a particle detector or collection device. While offering large entrance apertures and high sensitivities, the analyzer provides basically an integral measurement of the particle flux above the energy determined by the bias voltage. There is also the further disadvantage that charged particles of an unwanted charge would be accelerated into the collector unless otherwise suppressed. Finally the particle energy range that can be analyzed is governed directly by the maximum bias voltages that create the potential barrier, which make this analyzer design unsuitable for measurements of plasma distributions that extend to energies much above several keV.

For these reasons the retarding potential analyzer is appropriate only for situations where the particle population is of lower energy and particles of unwanted charge sign can be excluded by suitable suppressor grids. An implementation of the retarding potential analyzer in a Faraday cup instrument has been described earlier in Section 2.4.

2.5.3 The Cylindrical Curved Plate Electrostatic Analyzer

The simplest form of electrostatic analyzer (ESA) that performs a differential selection in particle energy is the cylindrical analyzer first described by *Hughes and Rojansky* [1929]. This analyzer is composed of two plates that are sectors of concentric cylinders (Figure 2.27). Perhaps the first, and very notable, use of this analyzer configuration on a space mission was the Mariner-2 experiment that provided the first experimental con-

firmation of continuous solar wind and determined its basic characteristics [*Snyder and Neugebauer*, 1962].

The cylindrical curved plate analyzer has the virtue, in common with all electrostatic analyzers, of effectively rejecting incident particles of a charge sign opposite to that of the particles selected by the analyzer. However, the cylindrical geometry, unlike the spherical sector plate geometries discussed below, selects charged particles whose component of energy normal to the entrance plane is within the analyzer passband. This has the effect of broadening the energy passband because particles entering the analyzer at large angles from the normal can be selected even though their total energy may be significantly outside the desired energy passband.

The ion optics of cylindrical analyzers for space use has been described in *Theodoridis and Paolini* [1968] and others. Here we just give a few formulas without derivation, which might be useful in working with cylindrical analyzers.

The energy to which the cylindrical analyzer is tuned is related to the potentials on the plates and to the cylinder radii by

$$E = \frac{q(V_2 - V_1)}{2 \ln \frac{R_2}{R_1}} \tag{2.11}$$

where R_1 is the inner electrode radius, R_2 is the outer electrode radius and V_1, and V_2 are the potentials on the inner and outer electrodes, respectively, and q is the charge of the particle.

The analyzer constant K, sometimes also called deflection sensitivity, is the ratio between the energy, in eV, of the particle passed by the analyzer and the voltage V impressed between the analyzer plates over the gap $\Delta R = R_2 - R_1$. The analyzer constant K is generally much greater than 1.0 eV/V illustrating the advantage of electrostatic analyzers in selecting charged particle energies. Sometimes another definition for the analyzer constant k is used. The analyzer constant k is the mean radius $\bar{R} = (R_1 + R_2)/2$ divided by the gap distance ΔR. The analyzer constant k determines the energy resolution, energy-to-voltage ratio, and other properties of the analyzer.

The half-width of the energy band ΔE of particles that pass through a cylindrical ESA is

$$\Delta E \cong qV/2\Delta R \tag{2.12}$$

First-order focusing is obtained if the cylindrical electrodes subtend an angle of $\pi/\sqrt{2} = 127°$.

The cylindrical ESA has a narrow field of view, the width at half-maximum in the direction of dispersion (angle α) is

$$\Delta\alpha \quad \cong \quad \Delta R/\bar{R} \tag{2.13}$$

The field of view in the other direction is generally larger than $\Delta\alpha$ and is determined by the dimensions of collimating apertures and the particle detector.

An advantage of cylindrical ESA as well as many other ESA is that the use of a transverse electric field allows one to analyze relatively energetic particles, up to ~50 keV by relatively modest voltages. The upper limit of analyzed energies is determined by available spaceborne power supplies and by the danger of discharge between electrodes.

Another advantage of curved plate ESAs with deflecting electric fields is good UV rejection as light has to make several reflections on the walls of the ESA to pass from the entrance window to the detector. Special processing of the electrodes (such as blackening or serrating) for minimizing the scattering properties allows very strong UV rejection permitting measurements to be made even if the analyzer is viewing in the Sun's direction.

One of the disadvantages of electrostatic analyzers in general is chromatic aberration with displacement of the energy pass band along α. This energy dispersion is of the same order of magnitude as ΔE in Equation 2.12.

The narrow acceptance angle of cylindrical ESA has some merits and drawbacks. The merit is that for most velocity distributions the change of phase space density within $\Delta\alpha$ is relatively small giving the possibility to consider the measurement at a given energy and angle as a measure of local phase space density without complicated data analysis. The disadvantage is that the measurement of the energy spectrum with cylindrical ESA provides one-dimensional cut through the velocity distribution thus requiring multiple reorientation of the analyzer or use of multiple analyzers to obtain 3-D velocity distribution.

An example of cylindrical curved plate analyzers are the SSJ/4 sensors flown on the Defense Metrological Satellite Program (DMSP) missions F6, F7, F8 and F10 spacecraft [*Hardy et al.*, 1984]. These sensors measured the flux of electrons and ions in 20 energy channels in the range from 30 to 30000 eV. This was accomplished using a set of four cylindrical curved plate electrostatic analyzers arranged in two pairs. Each pair of analyzers consists of one set of cylindrical plates subtending an angular section of curvature of 60 ° and one set subtending 130°.

2.5.4 Spherical Sector Analyzers

A natural extension of the cylindrical plate analyzer to two-dimensions is to form the analyzer plates as sectors of spherical surfaces. A charged particle transiting this form of analyzer would very nearly follow a great circle path between the plates. These analyzers are categorized by the length of the great circle path from entrance to exit.

Focusing in both the deflection plane and the perpendicular plane can be obtained using any section of a sphere.

The basic theory of spherical sector analyzers and calculating charged particle trajectories through them has been discussed in *Purcell* [1938]; *Paolini and Theodoridis* [1967]; *Theodoridis and Paolini* [1969]; *Gosling et al.* [1978, 1984]; *DeSerio* [1989] among others. Figure 2.28 is a nomogram devised by [*Paolini and Theodoridis*, 1967] that allows estimates to be made of the energy-angle passband in a spherical analyzer.

In common with cylindrical plate analyzers, spherical analyzers require quite low electric potentials on the electrodes to select relatively energetic charged particles while still providing fairly high transmission and resolution. The main drawback of spherical analyzers is the difficulty of fabrication and mounting.

Spherical sector analyzers have been implemented in a variety of geometries of which two, the quadrispheric and hemispheric are discussed here.

Quadrispheric analyzers are concentric plates, each one-quarter section of a complete sphere, and so are bounded by two 180° annular rings. Particles that enter the analyzer through a collimating aperture centered along one annular ring will move through a 90° great circle and exit the analyzer at a point along the second annular ring that will map to

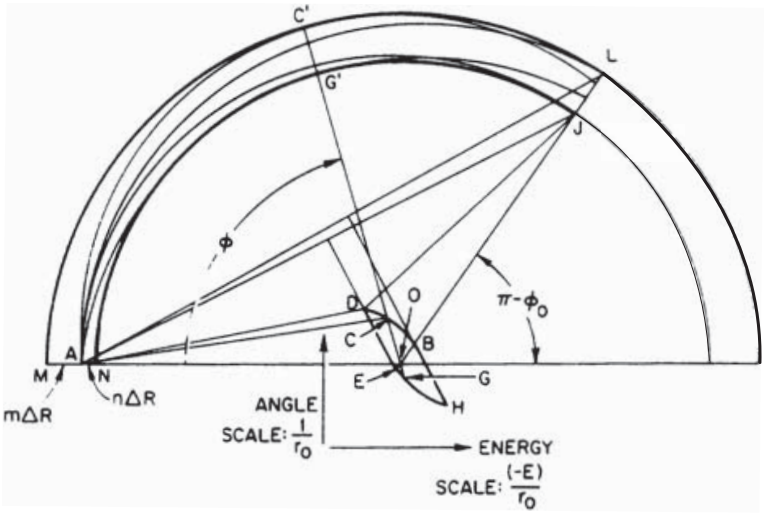

Figure 2.28: Locus of centers of transmitted particle trajectories in a spherical analyzer of arbitrary central angle ϕ_0 for an arbitrary point of incidence A. C′ and G′ are points of tangencies of trajectories with analyzer plates and J and L are points of intersection with the analyzer walls at the exit aperture defined by the angle ϕ_0. The locus is the total area within the curve DEGHBCD. The vertical displacement of any point within this area from AO is linearly proportional to the angle of incidence α of the particle whose trajectory center is that point. The horizontal displacement of that point from the normal to AO at O is linearly proportional to the energy deviation ΔE of the particle from the energy giving the unperturbed circular orbit. Scale factors are as given in the figure. From *Paolini and Theodoridis* [1967].

the particle's angle of incidence into the analyzer. Quadrispheric analyzers thus have fan-shaped fields of view enabling 2-dimensional cut in velocity space. The effective aperture area diminishes as the angle increases from the normal to the entrance aperture, and in combination with vignetting due to finite thickness of entrance diaphragm this effect limits fan expansion to 140°–160° instead of to the desired 180°. One particle detector can be used at the output of the analyzer thus providing an integral measurement over one phase space dimension. Using a position-sensitive detector or an array of detectors at the exit of analyzer provides a two dimensional cut in velocity space. Figure 2.29 shows examples of this form of analyzer that were used on Pioneer-6 [*Wolfe et al.*, 1966a] and IMP-1 [*Wolfe et al.*, 1966b]. This type of analyzer was also used in the Low Energy Particle (LEP) experiment on Geotail [*Mukai et al.*, 1994], together with arrays of CEMs and MCPs, to obtain the particle angular distributions that are discussed in detail in Chapter 4.

Bending angles are often varied so as to obtain good matching to subsequent analyzer sections or detectors. For example the Ulysses SWOOPS ion instrument uses a bending angle of 105° to give good resolution while allowing for slightly overlapping responses from the 16 CEMs arrayed behind the analyzer with 5° spacings [*Bame et al.*, 1992].

Analogous to the quadrispheric analyzer, the hemispheric analyzer utilizes two concentric hemispheric plates with the gap between the plates forming a full 360° annulus.

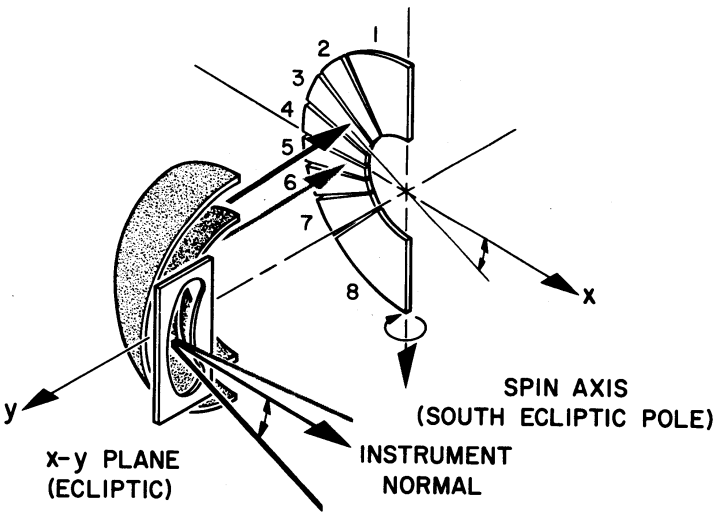

Figure 2.29: The Ames Research Center quadrispheric analyzer with sectored collector flown on the Pioneer-6 spacecraft. From *Scarf et al.* [1966].

Particles with the appropriate energy that enter the analyzer at one point on that annulus will move through 180° great circle paths to exit at a single point 180° displaced along the annulus. Collimating apertures are located along half of the annulus and individual CEMs or position sensitive MCPs placed along the other half to detect the energy selected particles. The field of view from each entrance aperture is fan shaped. Unlike the quadrispheric analyzer, the hemispheric analyzer does not disperse the particles according to their angle of incidence into the analyzer. A certain degree of angular separation is, however, provided by multiple collimators along the analyzer entrance, each mapping to a separate detector at the exit. Hemispherical analyzers are used because of the compact geometry that results from folding the beam back onto a line parallel to its original path.

Occasionally a hemispheric analyzer is coupled to a quadrispheric analyzer to gain both the energy resolving advantage of the hemispheric geometry and the angle resolving advantage of the quadrispheric geometry. Such an analyzer may be termed a 270° analyzer. This design was used, for example, in the low energy plasma analyzer (LEPA) for CRRES [*Hardy et al.*, 1993].

2.5.5 Top-Hat Analyzers

The top-hat electrostatic analyzer gets its name from a small analyzer section placed above the deflection plates (see Figure 2.30). This small section or top-hat and the hole in the curved analyzer plates underneath it define the entrance aperture. Originally the curved plates were spherical section analyzer plates, but toroidal variants have also been developed. Both versions are described in separate subsections below.

2.5.5.1 Spherical Top-Hat Analyzers

Modern top-hat instruments were described by [*Carlson et al.*, 1983], flown first on sounding rockets [*McFadden et al.*, 1986; *Moore et al.*, 1986] and then on the AMPTE [*Paschmann et al.*, 1985] and Giotto [*Rème et al.*, 1987] missions. The top-hat analyzer was a major advance in electrostatic analyzer design that has made possible simultaneous, angle resolved, measurement of a particle distribution function over a 360° field of view.

The Figure 2.30 shows in cross-section a spherical top-hat analyzer including the various design parameters. The analyzer section has the appearance of a full hemispherical analyzer described in Section 2.5.4 except that the particle access to the analyzer is at the pole. The analyzed particles thus transit 90° great circles through the analyzer to the exit aperture that encompasses a full annular ring. In practice the sensors are generally truncated at ∼70–75° so the particle focal point occurs at the detector.

The total FOV of the top-hat analyzer is disk-like covering a full 360° in azimuth but narrow in elevation. An array of detectors, or a position sensitive MCP, can be positioned along the exit annulus and each detector element will respond to particles originating from a limited sector of that disk as governed by the angle along the annulus subtended by that detector element. In this way measurements over a full 360° cut through the particle distribution function are obtained. On a spinning spacecraft 4π sr field-of-view can be obtained in half a spacecraft rotation, if the top-hat analyzer is mounted with its field-of-view along the meridional plane. This property made top-hat analyzers the workhorse in high time resolution space plasma research today.

The primary design parameters (see Figure 2.30) for a spherical top-hat analyzer are inner hemisphere radius, R_1, and the gap between hemispheres, $\Delta R = (R_2 - R_1)$. R_1 sets the physical size of the sensor and impacts the geometric factor, which scales as R_1^2. The gap is chosen to select energy resolution, but also impacts the geometric factor which scales as $\sim(\Delta R/R_1)^n$ where n varies from 3–4 depending upon details of the geometry. A first order planar angular response is obtained by choosing $(R_3 - R_1) = 2(R_2 - R_1)$. The top-hat opening angle Θ, and deflection truncation angle σ are the primary parameters that are varied to optimize the analyzer's angle imaging and planar response. Proper selection of σ and Θ can result in a near Gaussian out-of-plane response (see Figure 3.6) and imaging to a fraction of a degree. Figure 2.31 provides a summary of optimized analyzer parameters and the analyzer response as a function of $\Delta R/R_1$. Although the figure is useful for selecting Θ and σ, the parametrization does not include details of the entrance aperture and collimation. Therefore computer simulations are often used to optimize σ and Θ.

In addition to the 360° field-of-view other advantages are a lack of skewing in energy-polar-angle and good polar angle resolution. However, the focus in the polar angle direction occurs inside the spherical plates, resulting in a diverging beam from the exit, making the spherical top-hat less suitable for combination with a second, mass-resolving analyzer.

2.5.5.2 Toroidal Top-Hat Analyzers

Young et al. [1988] describe a modification to the top-hat design where the origin of the curvature for the analyzer plates is displaced from the axis of symmetry as shown in Figure 2.32. The resulting shape is toroidal and had the advantage of displacing the convergence

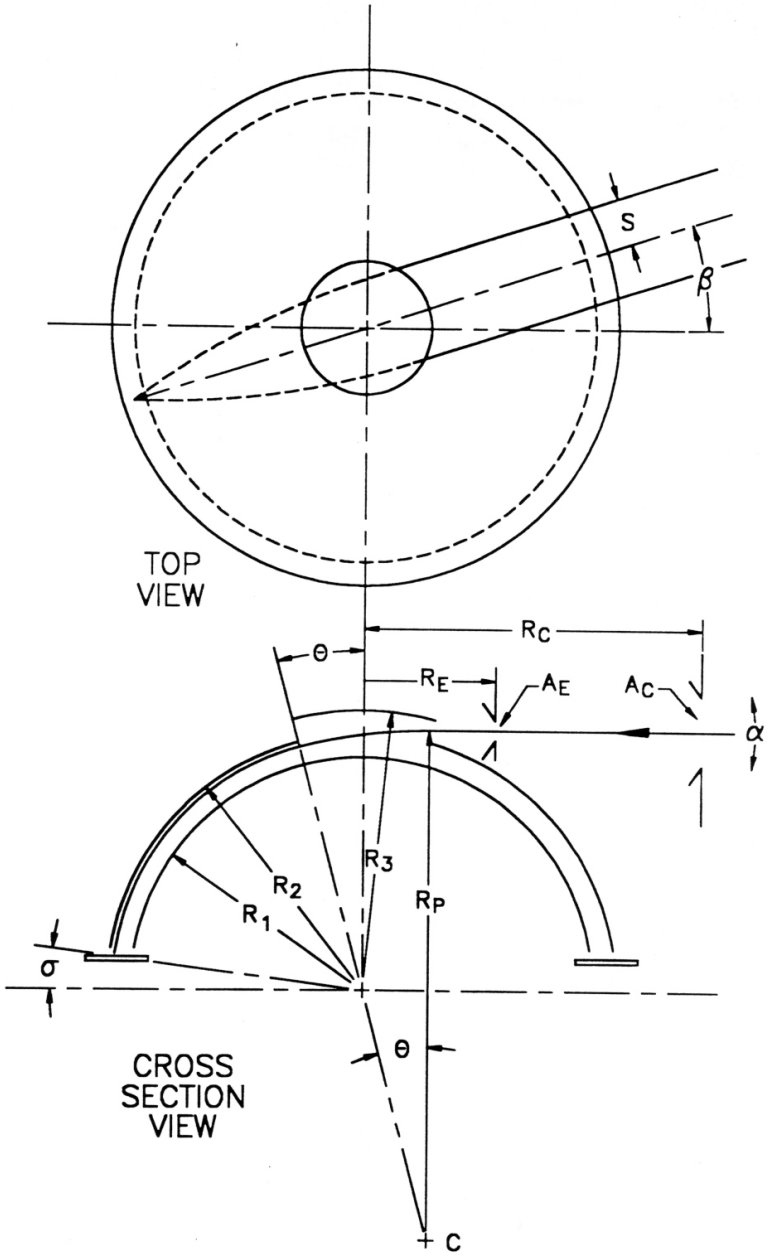

Figure 2.30: Top and cross-section views of spherical top-hat analyzer identifying principal parameters. A typical trajectory is shown. The particle's radius of curvature through the tophat region is approximately $2R_2$ with a center of curvature at C. From *Carlson and McFadden* [1998].

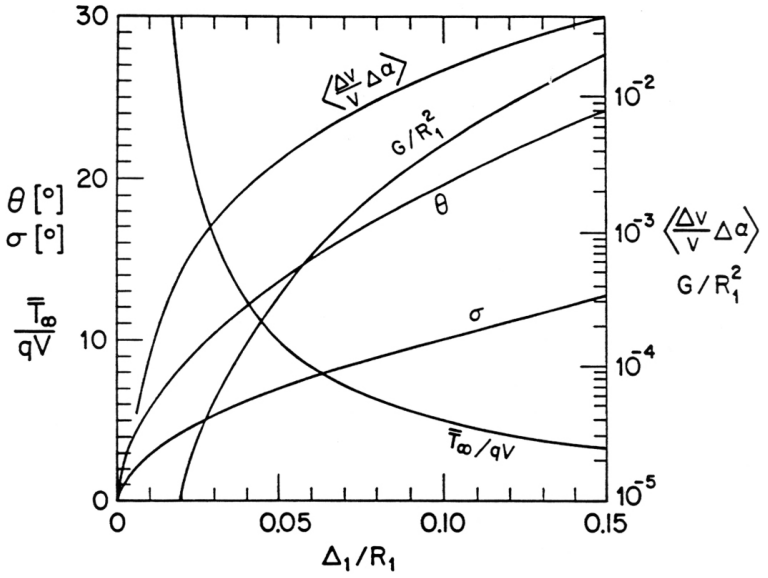

Figure 2.31: Summary of a spherical top-hat analyzer's performance parameter dependence on the ratio of the analyzer gap, $\Delta_1 = R_2 - R_1$, to the inner hemisphere radius, R_1. The indicated values for Θ and σ provide optimized angle imaging at the analyzer exit and zero average elevation angle "α" response at the analyzer entrance. Θ and $90° - \sigma$ are the entrance aperture opening and particle deflection angles, respectively, as defined in Figure 2.30. The other curves in the plot assume the optimal Θ and σ are used. T_∞/qV is the ratio of the average particle energy per charge far from the spacecraft to the applied inner hemisphere voltage, V, and is often referred to as the analyzer energy constant. For an analyzer with an acceptance area A and viewing a solid angle Ω, the normalized velocity geometric factor, $G/R_1^2 = G(v)/R_1^2 = A\Omega(\Delta v/v)/R_1^2$, and analyzer resolution, $(\Delta v/v)\Delta\alpha$, are illustrated in the remaining curves. Note that the more commonly used energy geometric factor, $G(E) = A\Omega(\Delta E/E)$, is equal to $2G(v)$ since $\Delta E/E = 2\Delta v/v$. These curves provide a useful starting point for selection of analyzer parameters (Δ_1, Θ, σ) to match the required sensitivity (G) and resolution ($\Delta v/v$, $\Delta\alpha$). From *Carlson and McFadden* [1998].

point for particles exiting the analyzer to greater than 90°. This allowed the analyzer optics to interface more effectively with the time-of-flight optics that followed the analyzer.

For toroidal analyzers, the shift of the R_1 curvature center away from the symmetry axis is used to move the angle-imaging focal point farther from the exit. In the limit of infinite displacement, the toroidal analyzer becomes cylindrical and the focal point moves to infinity. Computer simulation are necessary to optimize the design parameters for a particular application. For the Young design in Figure 2.32 that uses a flat-top for the analyzer entrance, design parameters include the toroidal radii R_1 and R_2, the gap ΔR, the top-hat gap Z_1, the deflection angle Θ_0, and the top-hat opening radius R_A. Two features of this design are the increased geometric factor due to the large aperture area and poorer angle-imaging optics compared to similar spherical sensors. The poorer optics is due to

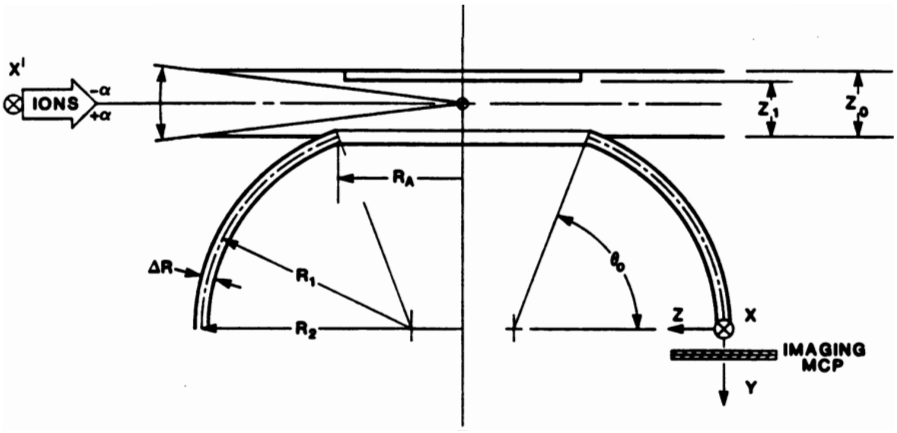

Figure 2.32: Schematic diagram of a toroidal top-hat analyzer. In this case the inner toroidal plate is truncated at $\theta = 75°$ by a flat surface. This lower surface is matched by an upper flat plate that forms part of a circular collimator and deflector. From *Young et al.* [1988].

over-focusing of particles that enter the analyzer away from the center line. Over-focused trajectories can be eliminated with collimation at the expense of geometric factor.

McFadden and Carlson [1998] describe a different toroidal parametrization scheme used for the Cluster/CODIF time-of-flight sensor. Figure 2.33 illustrates the curved surfaces R_3 and R_4 that are used for the analyzer top cap entrance. The radius R_4 is chosen to provide a continuous curved surface by matching slopes at the interface between different curvatures. As with spherical sensors, the top cap radius, R_3, is chosen to provide a first order planar response that requires $R_3 = R_4 + 2\Delta R(R_4/R_1)$. The analyzer entrance opening angle Θ is also tuned to provide planar response. Note that this design reduces to the spherical case as $R_0 \rightarrow 0$ and $R_4 \rightarrow R_1$. This design has additional benefits including reduction in the parameter space for analyzer optimization, reduction in particle and UV scattering from the curved entrance surfaces, and better imaging optics due to more uniform fringing fields at the edges of the analyzer entrance.

2.5.5.3 Electrostatic Deflection to Increase Field of View

A rather simple mechanism to increase a top-hat's field-of-view in the elevation direction is to include electrostatic deflection directly in front of the analyzer's entrance aperture. Figure 2.34 shows the entrance deflector modification to the Wind 3D Plasma top-hat analyzer, which allowed its field-of-view to be deflected into conical sections up to 45° from its nominal planar response. The largest deflections required a voltage about three times the inner hemisphere voltage, which limited the energy range where full deflections were possible. Large deflections caused significant distortion of the analyzer response with a much narrower out-of-cone angular response for upward deflection (see sample trajectory in Figure 2.34) and a much wider out-of-cone response for downward deflection. Since the deflectors were exposed to sunlight, only positive bias voltages were allowed in order to eliminate photoelectron emission. In addition, two grids were required at the

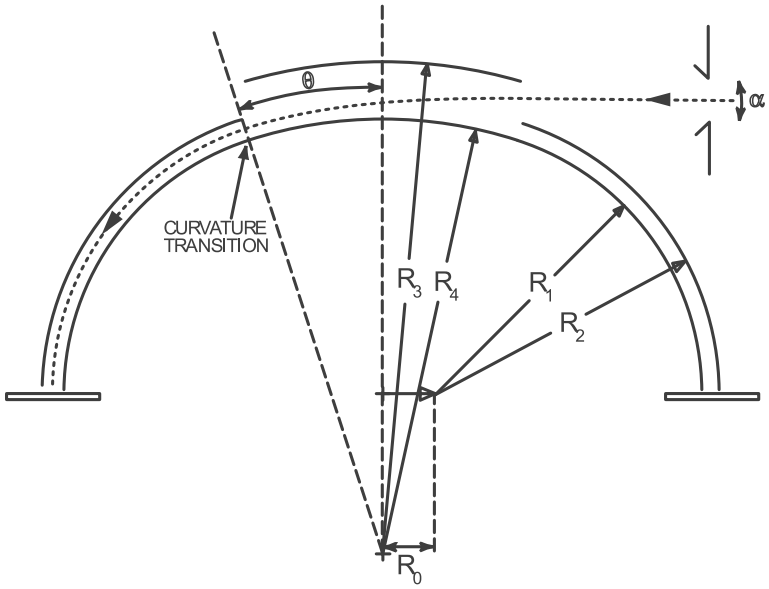

Figure 2.33: Schematic diagram of a toroidal top-hat analyzer with a spherical top-hat. The radius R_4 is chosen to provide a continuous curved surface by matching slopes at the interface between different curvatures. From *Carlson and McFadden* [1998].

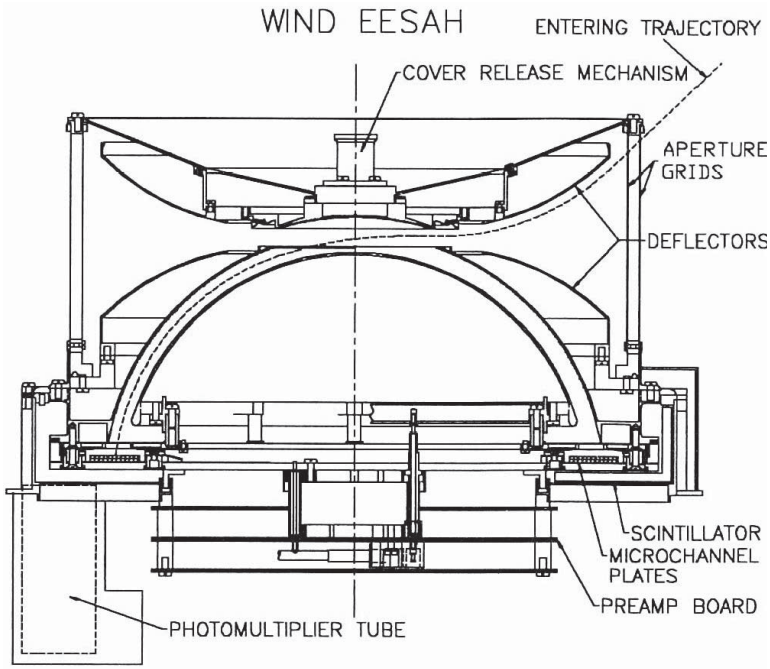

Figure 2.34: Top-hat analyzer EESAH on Wind spacecraft. From *Lin et al.* [1995].

outer surface of the instrument to minimize the effective potential of the outer grid due to leakage fields from the deflectors. The technique of steering charged particles into an analyzer aperture has been implemented in a wide variety of analyzer designs.

2.5.6 Magnetic Sector Analyzers

While the great majority of contemporary plasma instruments use electric fields or electrostatic potential barriers to select particle energies and species, the use of magnetic spectrographs for energy analysis of electrons offers some advantages. One of the more important is that magnetic spectrographs do not require either static or sweeping high voltages (except those required to operate the electron detectors, e.g. CEMs or MCPs). A second advantage is a larger accessible energy range for electrons compared to electrostatic analyzers. A third advantage is that there is a clear separation in the orbits of positive and negative charged particles so that species identification tends to be unambiguous. The disadvantages of magnetic spectrographs are, of course, their mass and the potential of magnetic field contamination upon other instruments on the spacecraft.

The general approach to pre-flight calibration and post-flight maintenance of electron instruments that utilize magnetic energy analysis are similar to those for the various forms of electrostatic analyzers. The particle detectors used in those systems are also the same (CEMs and MCPs). For those reasons magnetic spectrograph instruments are not treated in great detail here.

In a uniform magnetic field, the motion of a charged particle, with charge q, mass m and velocity v, moving perpendicular to the magnetic field B is given by

$$Bvq = mv^2/r_M \tag{2.14}$$

where r_M is the radius of the charged particle's path through the magnet. A magnetic sector analyzer is actually a momentum-to-charge analyzer.

The ion mass spectrometer IMS-HI on CRRES (see Figure 2.35 is an instrument based on momentum separation in a magnetic field . An entrance collimator consists of a series of rectangular baffles that define the field of view and a broom magnet to reject electrons with energy less than 1 MeV. After exiting the collimator ions enter a 0.7 T magnetic field where they are deflected (mv/qB) onto a set of six passively cooled silicon surface-barrier detectors. A seventh detector measures neutral particles and is positioned in line with the collimator. The ion energy range covered varies with ion species and is approximately 10–2000 keV q^2/m_i(u) [*Voss et al.*, 1992].

In the Medium Electron A (MEA) spectrometer on CRRES (Figure 2.36) a 180° magnetic electron spectrometer is used. In this kind of analyzer particles entering through the aperture encounter a uniform solenoidal magnetic field and travel a circular path in the plane transverse to the field. After being bent through approximately 180° the particle is detected by one of 18 detection areas in a linear array of planar reverse-biased P-N diodes. First order focusing occurs in the plane. Electrons with the same energy, although at different incident angles are focused on almost the same vertical line on the detection plane. There is no focusing in the vertical direction [*Vampola et al.*, 1992]. Clearly seen in Figure 2.36 are fins on the walls and ridges on the pole pieces (indicated by dashed lines) to suppress out-of-band response from scattering on the inside analyzer walls. The geometry insures that almost all off-angle electrons incident through the aperture are absorbed by a

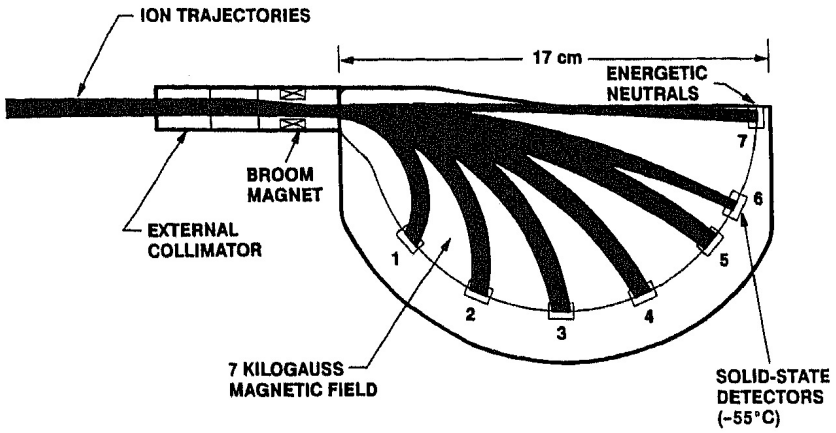

Figure 2.35: Principle of operation for IMS-HI is based on ion momentum, mass defect, and energy analysis using an array of cooled solid-state detectors. The magnet is shown in the lower portion of the figure and the ion optics in the upper portion. From *Voss et al.* [1992].

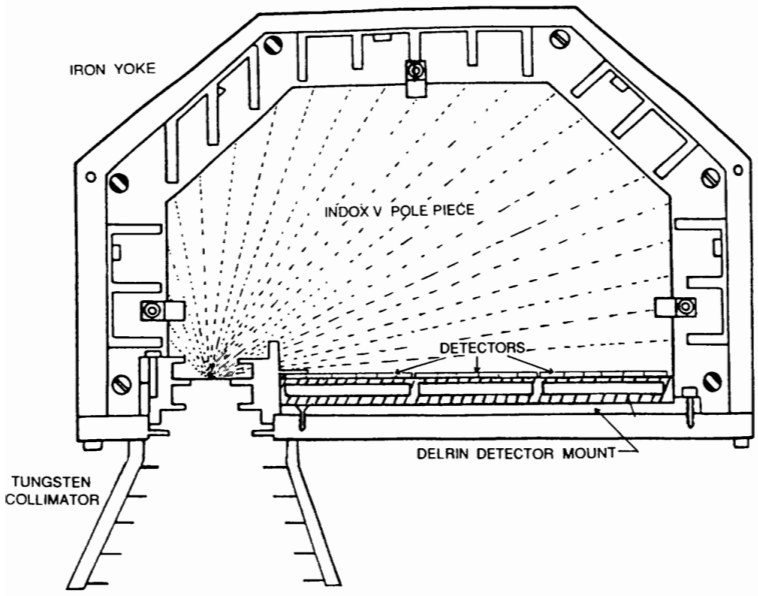

Figure 2.36: Schematic of the CRRES medium electron A (MEA) instrument. The disk-loaded collimator and the fins and ridges (indicated by dashed lines on the pole piece) in the housing structure ensure that an electron must undergo numerous scatterings in a low Z material in order to reach a detector unless its trajectory lies entirely within the collimator acceptance zone. From *Vampola et al.* [1992].

perpendicular wall rather than scattering forward off of a parallel wall. Aluminum is used for the fins and ridges to minimize bremsstrahlung generation. The fins and ridges were also anodized and coated with a black conductive paint to reduce light scattering to the detectors and to prevent charge buildup on the plates, which would cause unwanted, and uncontrolled, focusing in the vertical direction.

2.5.7 Plasma Analyzer Summary

The analyzer designs that have been described here are generally instruments whose laboratory calibration and in-flight performance verification are discussed in later chapters. Those instruments represent only a sub-set of the great variety of analyzer system designs that use combinations of electric and magnetic fields to guide incident particles through trajectories that select specific, well defined, elements of the full particle distribution. For details of other instrument designs, not described here, the reader may reference *O'Brien et al.* [1967], *Burke and Reasoner* [1972], *Heikkila et al.* [1970]; *Winningham et al.* [1975, 1981, 1993] and *Burch et al.* [1981], for descriptions of various parallel plate analyzer designs.

Descriptions of various forms of spherical and toroidal analyzer designs may be found in *Coon* [1966]; *Bame et al.* [1967, 1978, 1989, 1992]; *Montgomery et al.* [1973]; *Frank et al.* [1978]; *Wrenn et al.* [1981]; *Coates et al.* [1985]; *Johnstone et al.* [1987]; *Wollnik* [1987]; *Ghielmetti and Shelley* [1990]; *Yavor et al.* [1992]; *Vaisberg et al.* [1995, 1997].

Designs that involve various electrostatic mirror geometries may be found in [*Vaisberg et al.*, 1990; *James et al.*, 1998], [*Zurbuchen et al.*, 1998], *Koehn et al.* [2002], *Vaisberg et al.* [2001], and *Vaisberg* [2003].

As pointed out earlier, the general problems that need to be dealt with in laboratory calibration and in-flight calibration of plasma analyzers are common to all designs. The approaches to solving those problems are discussed in detail in subsequent chapters.

2.6 Mass Spectrometers

Mass spectrometers use the difference in the mass-to-charge ratio (m/q) of ionized atoms or molecules to separate them. The masses and relative abundances of the ions in a mass spectrum can be used to determine the structure and elemental composition of a molecule.

Mass spectrometry is one of the most sensitive analytical techniques available. The mass spectrum contains information on elemental composition (presence and number of certain elements), isotopic abundances (exact mass), and structure (fragmentation pattern or fingerprint).

Ion and neutral gas mass spectrometers have been used to determine the plasma and gas composition as well as density at all altitudes in the atmospheres, ionosphere and magnetosphere of the Earth, other planets and comets as well as the interplanetary space . They are particularly favored for exploratory missions because of their impartiality, sensitivity and large dynamic range.

The common methods to determine the mass in space instruments can be grouped in two classes. One relies on spatial separation, the other on temporal separation. The spatial

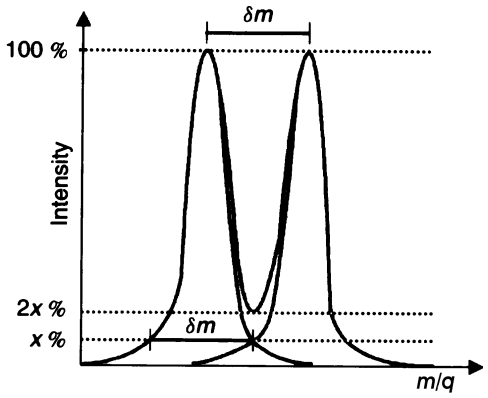

Figure 2.37: Definition of mass resolution. For two peaks of equal intensity, the mass resolution of the valley is twice the mass resolution of x % of the maximum of the isolated peak intensity. Adapted from *de Hoffmann and Stroobant* [2001].

separation occurs by the use of electro-magnetic fields. These include static magnetic field only, combination of magnetic and electric fields as well as radio frequency electric fields.

A general review of mass spectroscopy is given in *Duckworth et al.* [1986]; *McDowell* [1963]; *de Hoffmann and Stroobant* [2001] and *Gross* [2004]. A review of instrumentation used for neutral gas composition analysis on planetary missions has been given in *von Zahn* [1974], *Niemann and Kasprzak* [1983] and *Mahaffy* [1999] and for space physics instruments in *Young* [1989, 2002] and *Hilchenbach* [2002].

2.6.1 Performance Specifications

The three main characteristics of a mass analyzer are the upper mass limit, the transmission and the mass resolution . The mass limit determines the highest value of the m/q ratio that can be measured. The transmission is the ratio between the number of ions reaching the detector and the number of ions produced in the source or entering the analyzer.

The resolving power is the ability to yield distinct signals for two ions with a small mass difference. The definition of the mass resolution R is $R = m/\delta m$, where δm is the smallest mass difference for which two peaks with masses m and $m + \delta m$ are resolved (see Figure 2.37). Two peaks are considered to be resolved if the valley between the two peaks is equal to 10 % of the weaker peak intensity. Sometimes other definitions than the 10 % valley definition of resolution, $R_{10\,\%}$ are used, such as the full width at half maximum (FWHM) definition. For Gaussian peak shapes, the ratio of R_{FWHM} to $R_{10\,\%}$ is 1.8. Frequently two adjacent mass peaks differ in amplitude by several orders of magnitude. In order to adequately resolve ion masses in that situation, the shape of the peak, and in particular the amplitude and shape of the wings of the mass transmission curve have great importance.

The ability to independently characterize ion species as to mass and charge rather than m/q is an important distinguishing feature of different designs for mass spectrometers.

2.6.2 Introduction to Magnetic and Electric Analyzers

Magnetic and electric analyzers use the Lorentz force

$$\boldsymbol{F} = q\ (\boldsymbol{E} + \boldsymbol{v} \times \boldsymbol{B}) \tag{2.15}$$

on an ion, where $\boldsymbol{F}$ is the force on an ion, $\boldsymbol{E}$ is the electric field, $\boldsymbol{v}$ is the ion velocity, $\boldsymbol{B}$ the magnetic field, q the ionic charge (charge state $= 1e, 2e, \ldots$) and e the electronic charge.

There are a variety of ways to use the Lorentz force to build mass spectrometers and we will briefly describe some of the techniques that have been used in space flight.

2.6.2.1 Magnetic Mass Spectrometers

In a magnetic analyzer where the ion path is perpendicular to the magnetic field, the $\boldsymbol{v} \times \boldsymbol{B}$ force is balanced by the centripetal force and we obtain

$$qvB = \frac{mv^2}{r_M} \tag{2.16}$$

where r_M=path radius. Further rearrangement gives

$$\frac{m}{q}v = Br_M \tag{2.17}$$

and we see that the magnetic analyzer is a momentum analyzer rather than a direct mass analyzer.

If the ions entering the magnetic analyzer are accelerated by an electric field to a kinetic energy

$$E_{\text{kin}} = \frac{1}{2}mv^2 = qU \tag{2.18}$$

where U means the accelerating potential difference and m the species mass the ion speed becomes

$$v = \sqrt{\frac{2qU}{m}} \tag{2.19}$$

The addition of an electrostatic analyzer ahead of the magnetic field can be used to select ions of only a specific energy per charge range and together with equations 2.17 and 2.19 we obtain

$$\frac{m}{q} = \frac{B^2 r_M^2}{2U} \tag{2.20}$$

To obtain a mass spectrum the magnetic field can be scanned but for spaceflight the usual method is to scan the accelerating potential U with B constant (permanent magnet). The electrostatic analyzer follows the accelerating voltage and the m/q varies with the inverse of the accelerating potential. To first order there is no focusing in the plane perpendicular to the plane of deflection.

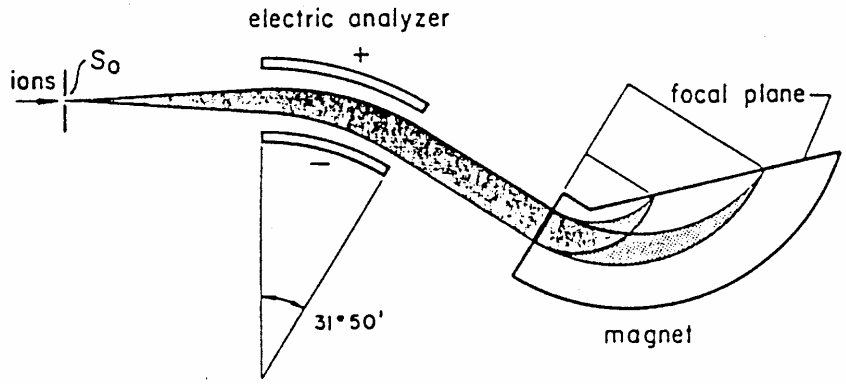

Figure 2.38: High-performance double focusing mass spectrometer of the Mattauch-Herzog design. From *Nier and Schuttler* [1985].

2.6.2.2 Double Focusing Magnetic Mass Spectrometers

In magnetic sector instruments a single m/q can be detected, or at best several, but by proper choice of the electric and magnetic field geometries the system can be made double focusing in both direction and energy [*Mattauch and Herzog*, 1934; *Duckworth and Ghoshal*, 1963; *Burgoyne and Hieftje*, 1996].

With the use of a Mattauch-Herzog geometry all masses along the focal plane can be detected simultaneously (true mass spectrum) on an MCP. A schematic of a Mattauch-Herzog geometry instrument used in spaceflight is shown in Figure 2.38. An example of a modern double focusing mass spectrometer used for the Rosetta mission is shown Figure 2.39.

The TIMAS (Toroidal Imaging Mass-Angle Spectrograph) flown on Polar is an example of an instrument (see Section 3.4.1, Figure 3.21, and *Shelley et al.* [1995]) where magnetic analysis is preceded by E/q analysis. This design utilizes a toroidal electrostatic analyzer with a 360° fan shaped field of view (see Section 2.5.5.2 on toroidal top-hat analyzers) to select ions of a given E/q. The selected ions, having been E/q selected and dispersed in entrance angle by the analyzer, were then passed through a magnetic field to disperse them according to their mass. A position sensitive MCP detected the angle and mass separated ions at the instrument's image plane. Further details, particularly regarding the calibration of this instrument, are in Chapter 3 Section 3.4.1.

2.6.2.3 $\boldsymbol{E} \times \boldsymbol{B}$ Instruments

Crossed electric and magnetic fields act as velocity filter and the type with linear $\boldsymbol{E} \times \boldsymbol{B}$ section is known as Wien filter [*Wien*, 1897]. The combination of a Wien filter and an electrostatic energy analyzer allows the determination of both the ion velocity and the energy per charge, and subsequently the mass per charge of ions.

$\boldsymbol{E} \times \boldsymbol{B}$ instruments have flown on solar wind [*Ogilvie et al.*, 1968] and the inner magnetosphere missions (e.g. *Shelley et al.* [1972]; *Balsiger et al.* [1976]; *Collin et al.* [1992]).

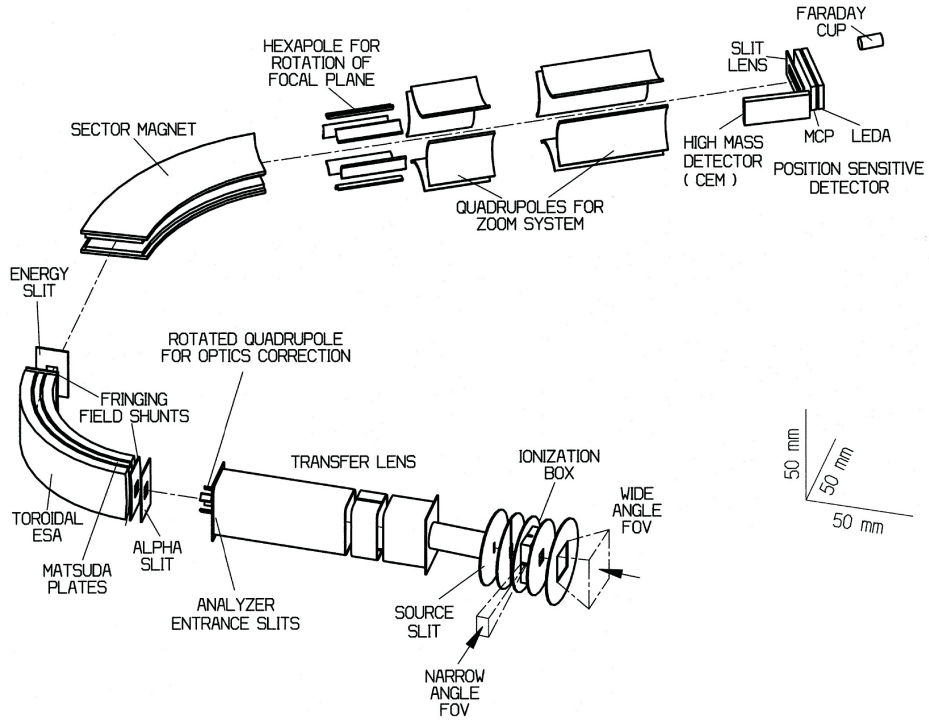

Figure 2.39: The double focusing mass spectrometer (DFMS) used in the Rosetta mission consisting of a magnetic and electric sector with hexapole and quadrupole lenses to rotate and "zoom" the final ion image. From *Balsiger et al.* [2007].

2.6.3 RF Mass Spectrometers

Several types of RF mass spectrometers used in space experiments are described in the following sections. An early review on RF mass spectrometers can be found in *Blauth* [1966], while more recent ones are published by *Dawson* [1986, 1995].

2.6.3.1 Quadrupole Analyzers

The radio frequency (RF) linear quadrupole mass spectrometer was developed by *Paul and Steinwedel* [1953] (see also *Farmer* [1963]). The mass to charge analyzer consists of four rod shaped electrodes with a hyperbolic cross section, arranged in a square (Figure 2.40), and spaced a distance of r_0 from the central axis. Rods with a circular cross section can also be used if the spacing is 1.16 r_0. Opposite pairs of electrodes are electrically connected and oppositely charged potentials are applied to each rod pair as a function of time t

$$V_x(t) = +(U + V_0 \cos \omega t) \tag{2.21}$$

$$V_y(t) = -(U + V_0 \cos \omega t) \tag{2.22}$$

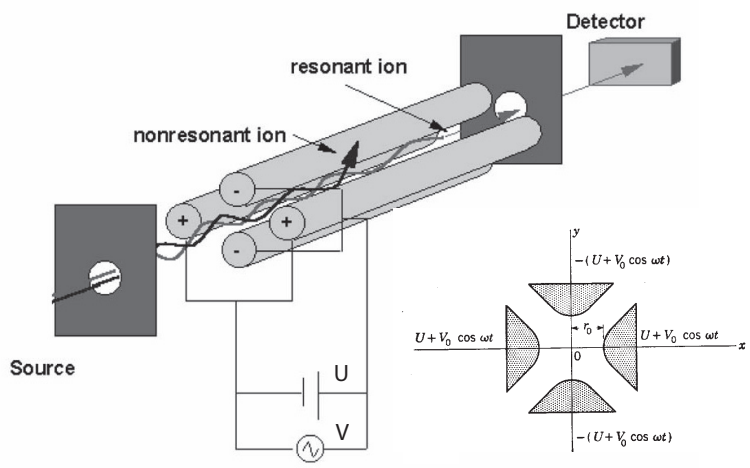

Figure 2.40: A schematic of a quadrupole mass spectrometer. Adapted from *Farmer* [1963] and `http://www.ivv.fhg.de/ms/ms-analyzers.html\#Quadrupole`.

where U is the DC voltage, V_0 is the RF voltage amplitude and $\omega = 2\pi f$ with f is the frequency. The potential distribution, ϕ, is

$$\phi = \frac{(U + V_0 \cos \omega t)\,(x^2 - y^2)}{r_0^2} \tag{2.23}$$

The equations of motion for a particle in this 2-D hyperbolic field are in the form of a Mathieu equation with the independent variable $\varepsilon = \pi f t = \omega t/2$

$$\frac{\mathrm{d}^2 x}{\mathrm{d}\varepsilon^2} + (A + 2Q\cos 2\varepsilon)\,x = 0 \tag{2.24}$$

$$\frac{\mathrm{d}^2 y}{\mathrm{d}\varepsilon^2} - (A + 2Q\cos 2\varepsilon)\,y = 0 \tag{2.25}$$

$$\frac{\mathrm{d}^2 z}{\mathrm{d}\varepsilon^2} = 0 \tag{2.26}$$

with two parameters

$$A = \frac{8eU}{mr_0^2\omega^2} \tag{2.27}$$

$$Q = \frac{4eV_0}{mr_0^2\omega^2} \tag{2.28}$$

These two parameters define regions of stable oscillation, where an ion can be transmitted through the rods along the z-direction and reach the detector, and unstable oscillation regions, where the ions are lost by lateral deflection from the beam and do not reach the detector (Figures 2.40, 2.41).

When ions are produced by electron impact from a stationary neutral gas or low energy ions (”thermal ions”) are being mass-to-charge analyzed, the DC voltage U is much larger

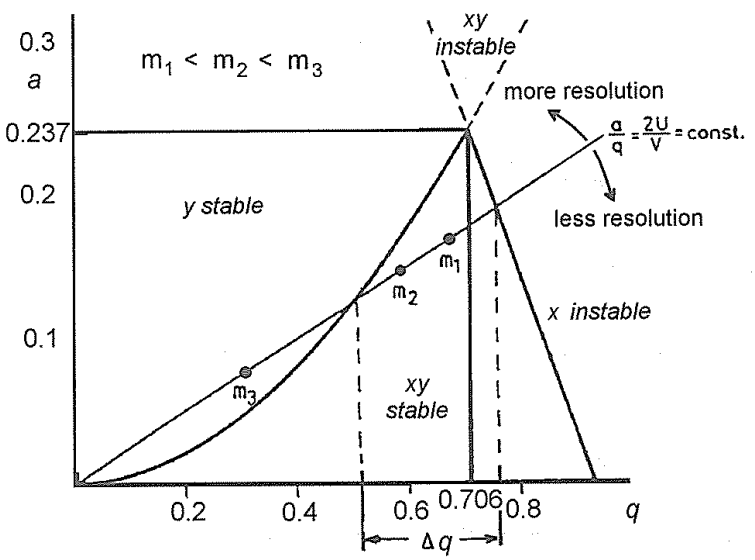

Figure 2.41: Stability diagram for a linear quadrupole analyzer. After *Paul* [1993].

than the ion energy. In the event that there is bulk motion of the gas or ions relative to the instrument, the mass resolution becomes degraded and the mass peaks become wider because the ion spends less time in the mass resolving RF electric field due to its forward motion. On solution to this problem is to add a retarding DC voltage to the rods that is a function of the ion energy as is done for the Cassini INMS instrument [*Waite et al.*, 2004].

The ratio A/Q determines the mass resolution and the range of masses transmitted in stable oscillation. Theoretically, the resolution becomes infinite (with the transmission becoming zero) when $A = 0.237$ and $Q = 0.706$. For this condition the mass of the ion, M_i, in u (atomic mass units) transmitted is

$$M_i = \frac{1.385 \times 10^7 \, V_0}{R_0^2 f^2} \tag{2.29}$$

with U and V_0 are related by

$$U = \frac{A}{2Q} V_0 = 0.168 \, V_0 \tag{2.30}$$

In practice, the analyzer is operated at an A/Q value less than this maximum value for which no ions would be transmitted. A mass spectrum is obtained by scanning U and V_0, keeping U/V_0 constant with a fixed frequency, f. Although it is possible to scan the frequency, keeping U and V_0 constant, in practice it is usually never done because of the difficulties in sweeping f over an extended mass range.

Examples of the use of a quadrupole mass analyzer include the Pioneer Venus ONMS [*Niemann et al.*, 1980], the S85-1 UACS [*Kayser et al.*, 1986], the Nozomi NMS [*Niemann et al.*, 1998], the CONTOUR NGIMS [*Mahaffy et al.*, 2002], and the Cassini INMS [*Waite et al.*, 2004] instruments.

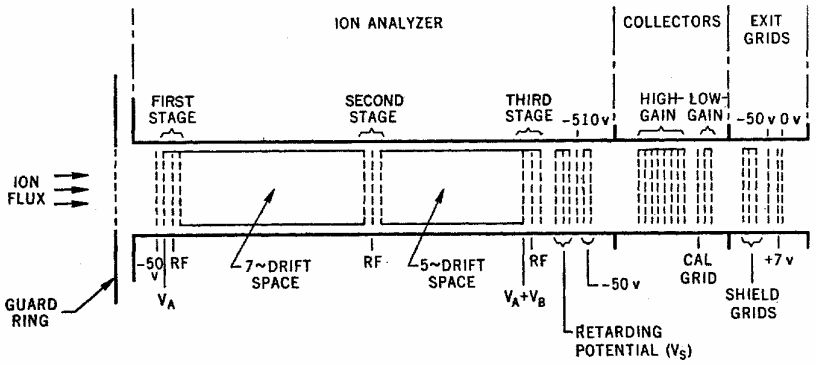

Figure 2.42: The Bennett Ion-Mass Spectrometer on Atmosphere Explorer C and E. From *Brinton* [1973].

2.6.3.2 Omegatrons

Mass separation is done using the cyclotron effect with a permanent magnetic field crossed by a radio frequency (RF) electric field. Ionization of neutral gas is by electron impact. If the cyclotron frequency of the ions is equal to that of the RF field, the ions are gradually accelerated in Archimedean spirals, gaining energy as they move outward. Resonant ions are measured by an appropriately placed collector whereas non-resonant ions do not gain enough energy to reach it [*Martel*, 1956]. Omegatrons were used to measure molecular nitrogen in a series of rocket probes [*Niemann and Kennedy*, 1966] into the Earth's upper atmosphere above 100 km.

2.6.3.3 Bennett Ion Mass Spectrometer

The Bennett spectrometer has been used for low energy ion measurements in the upper atmosphere of Earth [*Taylor et al.*, 1965, 1968; *Brinton*, 1973; *Iwamoto et al.*, 1975; *Grebowsky et al.*, 1987; *Grebowsky and Schaefer*, 1990; *Whalen et al.*, 1990; *Erlandson et al.*, 1994] as well as Venus [*Taylor et al.*, 1980]. The theory of its operation has been described by *Bennett* [1950], *Johnson* [1960] and *Farmer* [1963]. The Bennett instrument has primarily been used for ion detection rather than neutral gas measurements.

An instrument description for the AE satellite series is given in *Brinton* [1973] and a schematic representation is shown in Figure 2.42. This is a 3-stage analyzer with 7 to 5 RF cycle drift spaces. DC and RF potentials are applied to the intervening grids. Positive ions entering the instrument through a guard ring are accelerated by a slowly changing negative sweep potential (V_A). For a given ion mass there is a value of V_A that corresponds to the ion's resonant speed through the two drift spaces of the analyzer. The ions that transit the first stage in phase with an applied RF, gain energy from the three analyzer stages to penetrate the DC retarding field V_S, and are collected on grids. The ion mass, M, is given by

$$M = K \frac{|V_A| + |V_B| - \frac{1}{2}mv^2 + \phi_{SC}}{s^2 f^2} \tag{2.31}$$

where K is the analyzer constant, V_A the negative sweep potential, V_B the fixed DC potential, s the analyzer grid spacing, f the RF frequency, v the sum of spacecraft and ion speeds, $mv^2/2$ the ram energy term for each ion mass and ϕ_{SC} = spacecraft potential. Using an exponential waveform for V_A results in the mass peaks having approximately the same width. Changing the number of cycle drift spaces and the number of stages will alter the response characteristics.

Ions, which are harmonics of the fundamental frequency (e.g. 75 % and 260 % of the fundamental frequency for the MSX ion mass spectrometer parameters), can also reach the collector. While this harmonic feature can produce complexity in the data, it also allows a further check on the ion mass that enters the sensor.

The collected ion current, I_i, for species i at small angles of attack, small Debye length and an ion thermal speed less than the spacecraft speed is

$$I_i = nevA_{\text{eff}}\,\alpha_i\,\gamma_i \tag{2.32}$$

where n is the ambient number density, e the electronic charge, v the spacecraft speed, A_{eff} the spectrometer orifice area, α_i the efficiency and γ the mass discrimination factor. The efficiency factor is a function of the retarding potential V_S and can be evaluated in the laboratory or in-flight for a constant influx of ions. Mass discrimination is reduced for ions at low values of V_A and can be evaluated in the laboratory or in-flight by comparing the same mass at widely different V_A values. The V_S potential regulates the total ion flux, and the ratio of the ion harmonic and fundamental fluxes that are detected. V_S can also be used to compensate for spacecraft charge, which changes the ion input energy. The guard ring, which is normally at spacecraft ground, can compensate for positive spacecraft charging by setting it to a negative potential. Angle of attack corrections can be obtained from the flight data for non-zero angles of attack.

Another example of a Bennett instrument is the suprathermal mass spectrometer (SMS) on EXOS-D (Akebono) [*Whalen et al.*, 1990]. It is a three-stage, folded Bennett-type radio-frequency mass spectrometer designed to measure thermal (0.1–25 eV/q) and suprathermal ($<$ 4 keV/q) ions in the 0.9–67 u/q mass-per-charge range.

2.6.4 Time-of-Flight Analyzers

The time-of-flight (TOF) analyzer measures the time it takes a particle of known energy to traverse a given path length from a source to a detector to determine the particle's velocity and thus its mass [*Farmer*, 1963; *Wollnik*, 1993; *Wüest*, 1998].

A general review of time-of-flight analyzers, including those used for charged particles, is given in *Wollnik* [1993]. A review of TOF instruments for space flight can be found in *Wüest* [1998] and *Hilchenbach* [2002].

Time-of-flight (TOF) mass spectrometers for space research usually consist of a front-end and a mass resolving time-of-flight section. The front-end for ion instruments generally is some form of electrostatic analyzer as discussed in the previous Section 2.5. For neutral gas analysis the front-end consists of an ionization source such as those discussed in Section 2.7.3.

In recent years time-of-flight instruments have become extensively used in space research because of their high performance combined with excellent mass resolution and low weight. While the TOF sensor is quite simple and low mass, the associated electronics are

more complex compared to, for example, a magnetic mass spectrometer. An additional advantage of TOF sensors is the coincidence measurement inherent in the TOF measurement that reduces background of all sorts substantially.

TOF instruments can be sorted into two distinct classes of instruments. The first class uses secondary electrons emitted from a surface, such as a carbon foil, to generate a start signal. This class of instruments lets particles into the time-of-flight section on a continuous basis and, therefore, we label them as 'Continuous Operation TOFs'. The other class uses gated electric potentials to generate a start signal so that particles enter the time-of-flight section in a pulsed fashion. We call this class "Gated TOFs".

We will not be able to discuss all the variants of TOF instruments in this chapter. *Wüest* [1998] and the references therein provide more comprehensive descriptions of TOF systems.

2.6.4.1 Continuous Operation TOF

Continuous operation TOF instruments allow the arriving particles to enter the TOF section on a continuous basis.

A linear TOF refers to the fact that particles undergoing analysis move through the time-of-flight section in a straight line over a fixed distance s in time t. When coupled with electrostatic analyzers, the time-of-flight measurement allow the determination of ion mass per charge ratio (m/q) according to

$$\frac{m}{q} = 2\frac{(\frac{E}{q} + |V_a|) - \Delta E_f}{(s/t)^2} \tag{2.33}$$

where ΔE_f is the particle energy per unit charge lost to collisions in the foil in a foil based system, E the ion energy selected by the electrostatic analyzer, q the ion charge, and V_a is any post-acceleration voltage, if present.

When an ion passes through a thin foil secondary electrons are ejected from the foil. These secondary electrons from the foil are used to trigger a start signal. Ions continue to move on essentially straight paths through a basically field-free drift section of known length s. When the ions hit the detector a stop signal is generated. Linear TOF systems vary essentially in the way the timing system is designed. Typical foil based TOF systems are shown in Figures 2.43–2.45.

Figure 2.43 shows schematically the CODIF (COmposition and DIstribution Function) analyzer design *Rème et al.* [1997] that incorporated many of the features found in contemporary TOF instruments. A toroidal top-hat analyzer, with sections of different particle transmission, is used to select ions of a given E/q entering the analyzer over the 360° field of view. The selected ions then pass through a foil to generate secondary electrons that are detected by an MCP to produce a TOF start signal. After moving through the fixed distance TOF section, the ion is detected by the same MCP to produce the stop signal. A detailed discussion of the in-flight calibration of the CODIF instrument is given in Section 4.4.6, while the laboratory calibration of PLASTIC, a CODIF-like instrument, is described in Section 3.4.2.

The CODIF time-of-flight design used biased electrodes to steer the electrons from the foil to the MCP. Alternative designs have used electrostatic mirrors in the TOF drift section (see Figure 2.45) to steer secondary electrons created at both the start foil and at the stop

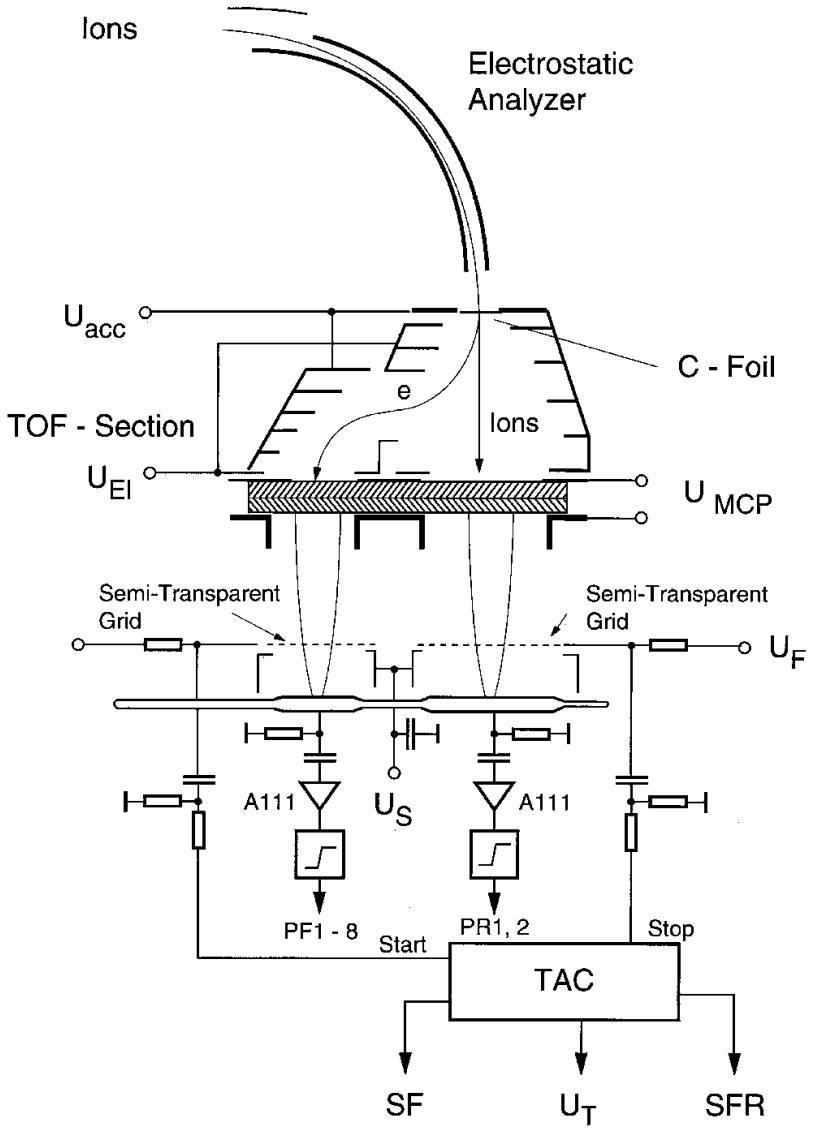

Figure 2.43: A schematic showing the Cluster CODIF TOF principle of operation. The top portion of the figure depicts the motion of an ion through an electrostatic analyzer and accelerated by the electrically biased carbon foil. The secondary electrons produced by the ion passing through the foil are steered by biased electrodes to the left hand side of the MCP to create the START signal while the ion continues on a linear path to the right hand side of the MCP to produce the STOP signal. The bottom portion of the figure shows the processing of the signals from each side of the MCP to the Time-to-Amplitude Converter (TAC) that provides the measure of the time-of-flight of the ion. From *Rème et al.* [1997].

foil or detector to the proper location on an MCP. The electrostatic mirror design offers the advantage of a physically compact TOF section and more precise TOF measurements because trajectories to the MCP detector for both the START and the STOP electrons can be made nearly isochronous. Position sensitive MCP/anode systems reduce the timing error to well below 0.5 ns, nearly independent of the particle energies. The disadvantages are that the grids of the electrostatic mirrors reduce transmission and increase background because of particle's scattering on the mirrors. Field distortions caused by the electrostatic mirrors, together with the scattering lead to peak broadening. Some of the disadvantages of the electrostatic mirror design can be eliminated by the grid-less design used in CODIF (see Figure 2.43). However, in the grid-less design the addition of electrostatic deflection plates to deflect the START and STOP electrons in the drift region can introduce variations in the path length traveled by the ions.

For cost and spacecraft resource reasons, the same MCP is sometimes used to detect both the START and STOP secondary electrons. However, since an MCP loses gain as a function of the extracted charge (see Chapter 4), and since there are many more START signals created than STOP signals, often the MCP bias voltage must be increased to maintain adequate gain for the START signal before that bias increase is necessary for the STOP signal. This results in an excessive bias voltage on that portion of the MCP devoted to detecting the STOP signal and potentially a higher noise background. The penalty paid for using a single MCP for both START and STOP functions is the inability to independently adjust the MCP gain for one or the other of those functions.

Sometimes, as was done in CODIF, a post-acceleration potential is introduced between the analyzer and the foil to reduce straggling in the foil and to improve the timing accuracy. Linear TOF sections are suitable for missions where high time resolution is required and no charge state information is needed.

Energy straggling and angular scattering of the incoming ion in the carbon foil that is used to create the START signal limit mass resolution in linear field-free time-of-flight systems. The spread in energy loss and in angle results in a significant time dispersion and thus to an uncertainty in m/q. The linear electric field (LEF) time-of-flight technique, also called isochronous TOF, overcomes these limitations.

In this TOF design the ion enters a region with an electric field $E = -kz$ that increases linearly with distance z from the entry point. The constant k is determined solely by the geometry of the device. A retarding electrostatic force $F = qE = -qkz$ acts on the particle. The equation of motion for an ion in the z direction is that of a simple harmonic oscillator in a harmonic potential. The time-of-flight of the particle is then given by

$$t = \pi \sqrt{\frac{m}{qk}} \tag{2.34}$$

The time-of-flight t is independent of both ion energy and angle of incidence into the electric field region and can be measured with a precision of a fraction of a nanosecond. In principle, mass resolution in a LEF-TOF is limited only by timing uncertainties, in practice, resolution is limited by nonlinearities of the field. A detailed analysis of these non-linearities has been presented in *Wurz et al.* [1998]. The LEF-TOF principle is incorporated in the high-resolution mass spectrometer (MASS) on Wind [*Gloeckler et al.*, 1995], SOHO/CELIAS [*Hovestadt et al.*, 1995] and ACE [*Gloeckler et al.*, 1998] instruments and in the IMS instruments [*McComas and Nordholt*, 1990] on Cassini [*Young et al.*, 2004] and Deep Space 1 [*Bolton et al.*, 1997; *Young et al.*, 2000, 2007].

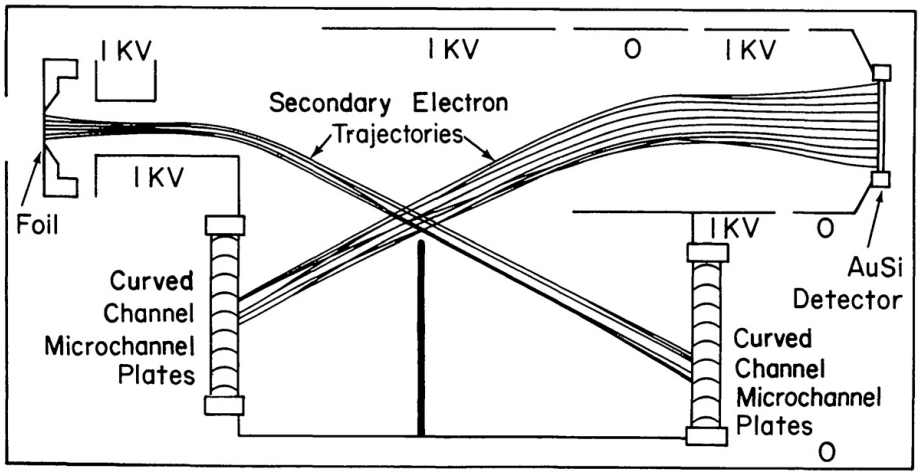

Figure 2.44: Schematic cross section of the Ulysses SWICS time-of-flight sensor showing computed trajectories of secondary electrons emitted from the carbon foil and the solid-state detector. The front surface of each of the two MCPs is biased slightly negatively with respect to the housing to repel low-energy (<100 eV) secondary electrons. A physical partition between the two MCPs prevents secondary electrons of one MCP triggering the other. From *Gloeckler et al.* [1992].

2.6.5 Linear Time-of-Flight Instruments with SSD

A solid-state detector can be introduced to replace an MCP as the STOP detector in a TOF system. Secondary electrons produced from the SSD surface serve as the STOP signal while the signal from the SSD is a measure of the total particle energy, E_{SSD}, lost in the detector. With knowledge of the particle's energy prior to encountering the START foil, E_{incident}, the particle mass can be calculated from

$$M = 2\frac{E_{\mathrm{incident}}}{(s/t)^2} \tag{2.35}$$

To obtain E_{incident} from the measurement of E_{SSD}, corrections must be made for the particle's energy loss in transiting the foil, E_{foilloss}, and SSD dead layer, $E_{\mathrm{deadlayerloss}}$, as well as for the pulse height defect α_1 in the solid-state detector.

$$E_{\mathrm{incident}} = \alpha_1 E_{\mathrm{SSD}} + E_{\mathrm{foilloss}} + E_{\mathrm{deadlayerloss}} \tag{2.36}$$

From Equations 2.33, 2.35 and 2.36 one can derive the charge state q and from the E/q value selected by the electrostatic analyzer setting one can obtain the incident particle energy E prior to any post-acceleration that might have been introduced.

The schematic of the Ulysses SWICS TOF instrument in Figure 2.44 illustrates the use of secondary electrons from a SSD to produce the STOP signal. A somewhat different implementation of a TOF instrument using a solid-state detector is shown in Figure 2.45. In this implementation electrostatic mirrors, as discussed earlier, have been used to steer

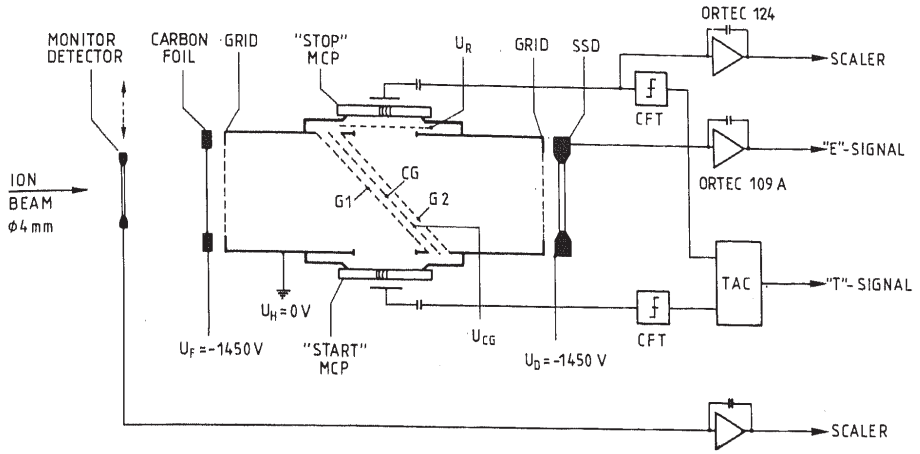

Figure 2.45: Schematic diagram of the time-of-flight system with electrostatic mirrors. A thin carbon foil and the surface of the solid-state detector serve as emitters of secondary electrons. Start and STOP electrons are deflected into opposite directions by the dual mirror system. START/STOP timing signals for the MCPs are generated by a constant fraction trigger (CFT). A time to amplitude converter (TAC) generates the time-of-flight signal. From *Wilken and Stüdemann* [1984].

START electrons from the foil and STOP electrons from the SSD to separate MCPs. In both these TOF designs the path lengths and transit times of electrons from their respective source to the appropriate MCP have been made nearly equal.

A very modern and capable TOF is the PLASTIC (Plasma and SupraThermal Ion Composition) instrument on the STEREO satellites (see Figure 3.24). This instrument uses the analyzer optics design of the CODIF instrument described earlier, but replaces the "STOP" MCP used in CODIF with a solid-state detector [*Blush et al.*, 2005]. In that way the instrument will simultaneously determine the E/q, velocity, and total energy of individual ions. A detailed description of the PLASTIC calibration program is given in Section 3.4.2.

Typical instruments for foil-based time-of-flight high energy instruments include e.g. the EPACT/STEP instrument on Wind [*von Rosenvinge et al.*, 1995] or the Cluster RAPID/SCENIC instrument [*Wilken et al.*, 1997]. Time-of-flight measurement taken directly from a START and STOP solid-state detector has also been demonstrated [*Williams et al.*, 1978].

The use of a SSD requires the addition of a post-acceleration potential to measure hot ions (<30 keV). This post-acceleration potential is needed so that the ions have sufficient energy to deposit an energy above the detector threshold of 20–30 keV.

The addition of a SSD also complicates the instrument design since the post-acceleration requires the detectors to be at high potential with respect to spacecraft electronics ground reference. The presence of high voltage potentials needs careful attention to instrument design to minimize the chances of electrical breakdown and arcing in the sensor.

Furthermore, the addition of a SSD reduces the temporal response of the TOF system, since the response time of the SSD is slower than that of an MCP. Therefore, these systems

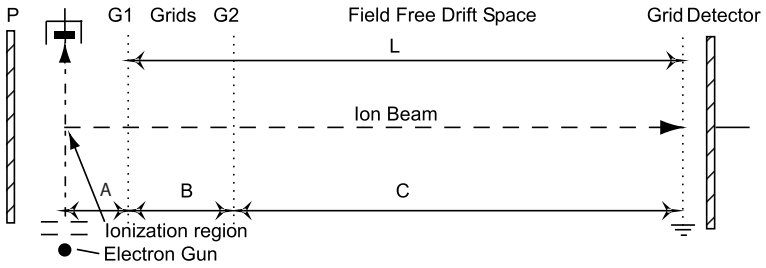

Figure 2.46: A schematic of the linear time-of-flight analyzer. After *Farmer* [1963].

are not well suited for high flux conditions. Consequently, these SSD based systems are typically used for the study of higher energy particle populations, where the particle flux is already reduced compared to the hot ion population in the magnetosphere or for solar wind composition studies.

Finally, high energy ions entering the detector from the front side can pass entirely through the detector and not deposit its total energy in the SSD. Conversely, high energy particles might penetrate the instrument housing and reach the SSD detector from the rear or the side to produce a spurious signal. To eliminate these spurious effects from further processing, a second solid-state detector can be added to the backside of the particle energy-determining detector and used as an anti-coincidence veto of an event.

2.6.5.1 Gated Time-of-Flight Analyzers

Gated TOF instruments let particles into the analyzer in a pulsed fashion providing for a very well defined starting time. Moreover gated time-of-flight analyzers are especially well suited for neutral gas mass spectrometers because neutrals can be ionized and concentrated during the period when the gate is closed.

In gated linear time-of-flight analyzers various types of electric switching are used as a gate to release in a very short time period the ions from the volume in front of the time-of-flight region (also called source or storage region) into the time-of-flight region. In neutral gas mass spectrometers a pulsed ionization method can also be used (e.g. pulsed electron beam or matrix-assisted laser desorption ionization (MALDI)).

In the simple neutral gas TOF shown in Figure 2.46, an electron beam is switched into the ionization region, by applying a voltage pulse to a control electrode, to create ions in a field free region. The electron beam is switched off and an electric field is applied across the ionization region by applying a voltage U to plate P with grid G1 and G2 at ground to accelerate the ions through G1. The extracted ions traverse the field-free drift path of length L. The kinetic energy of the ions, E_{kin}, is, neglecting thermal energy,

$$E_{\text{kin}} = qU = \frac{1}{2}mv^2 \tag{2.37}$$

the velocity is

$$v = \frac{L}{t} \tag{2.38}$$

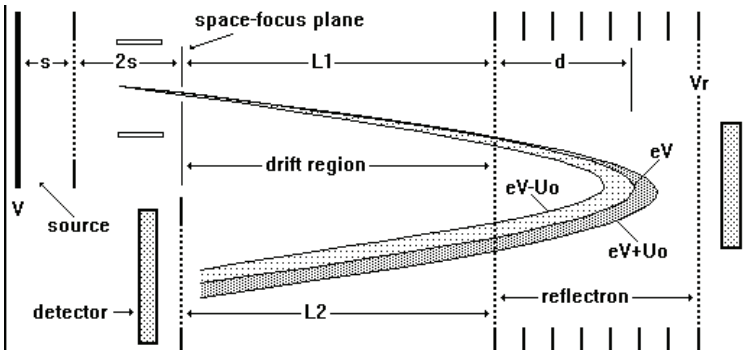

Figure 2.47: A schematic of a single stage reflectron time-of-flight analyzer in which the ions are turned around and energy focused by a constant electric field. From *Cotter* [1999].

where L = path length and t = flight time. The mass-to-charge ratio is

$$\frac{m}{q} = \frac{2Ut^2}{L^2} \tag{2.39}$$

When the ions leave the ion source there is a scatter in the starting locations and in initial kinetic energies which results in the ions not arriving at the detector at the same time. Various methods have been devised to compensate for these differences [*Cotter*, 1999] and two of those methods are described here.

The first is time-lag focusing that uses a dual stage source with two grids G1 and G2 plus the plate P. Various combinations of delayed voltage pulses are used to reduce the spatial and kinetic energy distributions in this two-stage extraction source. *Farmer* [1963] gives the relationship between the dimensions A, B, C and the ratio of the electric fields in region A and B needed to minimize the spread in ion flight times due to an initial spatial spread if the ions have zero kinetic energy. If the ions have an initial kinetic energy then it is still possible to specify the maximum mass for which a given adjacent-mass resolution can be obtained with the spatial focusing conditions previously mentioned.

The second technique for kinetic energy focusing is obtained with the reflectron. In the reflectron time-of-flight analyzer, the ions pass through a "mirror" (reflectron), consisting of one or more retarding fields after a drift region, and their direction of flight is reversed (Figure 2.47). In a one-stage linear potential reflectron, ions with greater kinetic energies penetrate deeper into the reflectron than those with lesser kinetic energies. Those that penetrate deeper take longer to return to the detector. The time-of-flight of the ions is proportional to the square root of the ion energy. The spread of the ion packet in time due to differences in initial kinetic energies is reduced thereby improving the time-resolution. The m/q value is approximately

$$\frac{m}{q} \approx \frac{2Ut^2}{(L_1 + L_2 + 4d)^2} \tag{2.40}$$

where L_1 and L_2 are the drift regions and d is the average penetration depth in the reflectron. *Managadze and Shutyaev* [1993] present a theoretical model of the potential distri-

bution inside a reflectron which makes the focusing independent of the initial energy over a given energy range.

Cotter et al. [1997] reviews several different reflectron constructions including a miniature coaxial curved field reflectron with an annular microchannel plate detector, suitable for use as a compact spaceflight sensor. A mini-TOF reflectron of the same configuration is described by *Brinkerhoff et al.* [2000] and by *Rohner et al.* [2003, 2004], all being part of a laser ablation mass spectrometer. *Cotter* [1999] also describes the use of an RF-only quadrupole for orthogonal ion injection for a time-of-flight analyzer that is relatively independent of initial conditions and which can accommodate almost any ion source type.

2.6.5.2 Foils

Carbon foils are used for measuring particles of lower and medium energy. The carbon foil should be of the appropriate thickness (0.5–5 μg cm^{-2}) . A too thin carbon foil would result in a significant reduction in the efficiency of secondary electron production for the START signal, while a too thick carbon foil does not increase the secondary electron emission significantly, but adds to the straggling [*Ritter*, 1985]. A recent review on carbon foils for mass spectrometers can be found in *McComas et al.* [2004].

For measuring particles of higher energies thicker foils and different foil material can be used (e.g. 10 μg cm^{-2} Lexan foil with aluminium coating). This protects the solid-state detector from the flux of lower energy particles, which contribute to radiation damage and higher background rates.

2.6.5.3 TOF Electronics

The complex electronics processing of sensor outputs from a TOF instrument is discussed in Section 2.11.2.

2.7 Upper Atmosphere Neutral Gas Mass Spectrometers

A basic neutral gas mass spectrometer consists of five parts: gas inlet, ion source (usually electron impact), mass-to-charge analyzer, detector and a signal processor (usually pulse counting). A review of instrumentation used for neutral gas composition analysis on planetary missions has been given in *von Zahn* [1974], *Niemann and Kasprzak* [1983] and *Mahaffy* [1999].

In this section we will focus on the gas inlet and the ion source of neutral gas mass spectrometers. The other three parts are similar to charged particle spectrometers and are described in other sections of this chapter.

Mission requirements dictate the gases desired to be measured while the pressure/flow regime and the speed of the gas relative to the spacecraft or probe dictate the type of gas inlet system. The instruments discussed will be confined to the upper atmosphere instruments where the Knudsen number $K_n \gg 1$ (equal to the ratio of the atmosphere mean free path to a typical vehicle dimension) and where the atmospheric pressure is low enough for direct electron impact ionization of the gas without first using pressure reduction (see Figure 2.48). This pressure is generally $< 10^{-2}$ mbar [*von Zahn and Mauersberger*, 1978]. In general, the gas flow around a spacecraft/probe can range from continuum flow ($K_n \ll 1$)

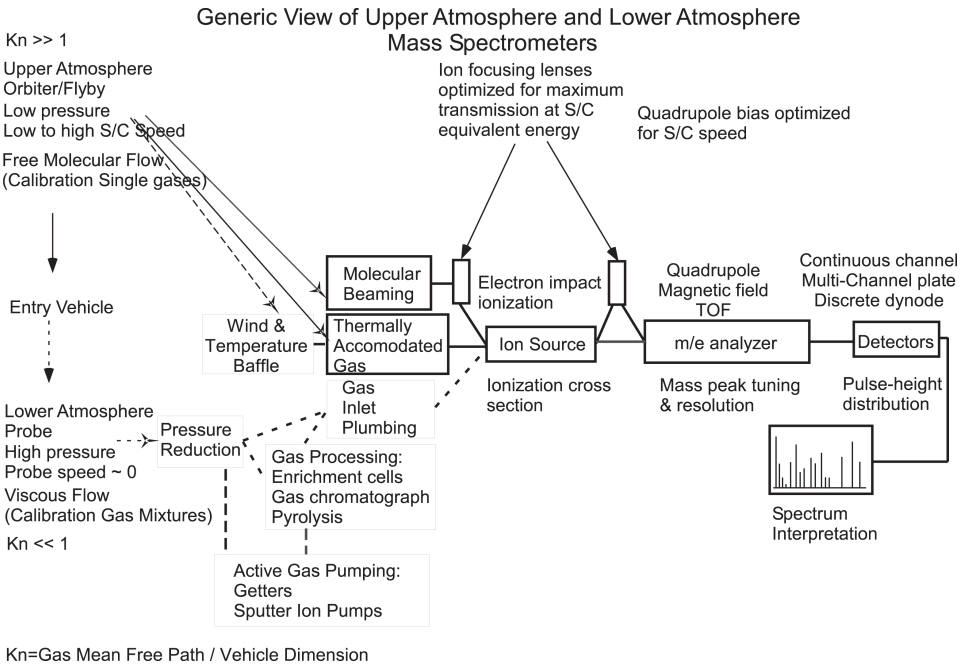

Figure 2.48: Overall view of the implementation of upper and lower atmosphere mass spectrometers. There is a major difference in spacecraft speed, ambient pressure, method of analysis and flow regime, although some items such as the gas sensitivity, mass analyzer tuning, secondary electron multiplier pulse height distribution and spectral interpretation are common to both.

to free-molecular flow ($K_n \gg 1$) [*Bird*, 1988]. Gas composition measurements representative of the ambient atmosphere are best made in the free-molecular flow range. For example, the San Marco 3 mass spectrometer, made measurements down to 137 km [*Newton et al.*, 1974] on Earth where the satellite $K_n \sim 26$. Small corrections [*McKinley et al.*, 1970] were already needed to the free molecular flow gas density calculations for heavy gas species. At lower altitudes, composition ratios change more and stagnation pressure calculations are no longer representative of the free-molecular results. The instrument described by *Hanson et al.* [1992] for measuring the pitch and yaw angles of the atmospheric wind, is limited by multiple gas collisions to about 125 km (slip flow regime).

2.7.1 Examples of Neutral Gas Mass Spectrometers

Planetary and cometary mass spectrometers include Cassini Ion and Neutral Mass Spectrometer (INMS) [*Waite et al.*, 2004; *Kasprzak et al.*, 1996], ROSINA Double Focusing (DFMS) and Time-of-Flight (RTOF) Mass Spectrometers, [*Balsiger et al.*, 1998, 2007], the Pioneer Venus Orbiter Neutral Mass Spectrometer (ONMS) [*Niemann et al.*, 1980], Nozomi Neutral Mass Spectrometer (NMS) [*Niemann et al.*, 1998], and the Comet Nucleus Tour (CONTOUR) Neutral Gas and Ion Mass Spectrometer (NGIMS) [*Mahaffy et al.*, 2002]. Earth orbiting mass spectrometers include magnetic double focusing instru-

ments [*Reber and Hall*, 1966; *Nier et al.*, 1973], Dynamics Explorer WATS (Wind and Temperature Spectrometer) [*Spencer et al.*, 1981], ESRO-4 mass spectrometer [*Trinks and von Zahn*, 1975], Atmosphere Explorer quasi-open mass spectrometer *Nier et al.* [1973] and the molecular nitrogen measuring Omegatrons [*Niemann and Kennedy*, 1966] on the Thermosphere Rocket Probes.

The orbiter instruments have not been restricted to measuring neutral gas composition only. The Neutral Atmosphere Temperature Experiment [*Spencer et al.*, 1973; *Spencer*, 1974a; *Spencer et al.*, 1974b] and the Dynamics Explorer Spectrometer mass spectrometer instruments [*Spencer et al.*, 1981; *Carignan et al.*, 1981] were equipped with moving mechanical baffles in front of the entrance aperture to infer *in situ* measurements of the gas kinetic temperature and two components of the neutral wind [*Brace et al.*, 1972]. Other groups have used different methods to measure one component of the wind [*Horowitz and La Gow*, 1957; *Knutson et al.*, 1977; *Kayser et al.*, 1979a, b; *Kayser*, 1988]. *Hanson et al.* [1992] describe an instrument for measuring the pitch and yaw angles of the atmospheric wind using two ion gauges in two chambers with orifices 90° apart. The COPS instrument [*Balsiger et al.*, 2007], which is part of the ROSINA package, also consists of two orthogonal ion gauges. The nude gauge, with a standard filament to supply ionization electrons, will measure the gas density. The ram gauge has a spherical antechamber that will measure the ram enhanced density which is a measure of the ram flux. The density inside the gauge is measured by an extractor gauge with the filament replaced by a micro-tip field-emitter. The two measurements together will provide a measure of ambient gas speed and temperature. Ion gauges measure the total ion current of all of the ionized species in a gas mixture and cannot be used for gas composition except under special conditions where the composition is known or at least its major component is known.

2.7.2 Gas Inlet

Upper atmosphere mass spectrometers operate in a pressure regime that is low enough for direct electron impact ionization of the gas without pressure reduction. Two different gas inlet configurations have been used: closed source and open source (or molecular beaming mode) (see Figures 2.49 and 2.50). In the closed source there is no direct line of sight from the ambient atmosphere to the electron beam, unlike an open source where particles travel unimpeded from the entrance aperture to the electron ionizing beam without a surface collision. The closed source inlet is designed so that the gas reaches a stagnation pressure, analogous to a Pitot tube [*Horowitz and La Gow*, 1957], before being ionized and measured. Particles in closed source impact the ion source antechamber walls multiple times, thermally accommodating to the wall temperature before being ionized. The value of the thermal accommodation coefficient is assumed to be 1 (complete thermal equilibrium); even if it is lower, but not extremely small, the many surface collisions will still assure thermal accommodation to the surface temperature. In some instruments, the antechamber is a sphere with a knife-edge orifice and an off axis tube that leads the thermally accommodated gas into the ionizing region [*Pelz et al.*, 1973; *Spencer et al.*, 1973]. Placing a baffle in the antechamber to block the open source view cone in Figure 2.50 (left) converts the source to a closed source [*Trinks and von Zahn*, 1975] (Figure 2.50, right). The source shown in Figure 2.50 (left) is sometimes referred to as a quasi-open source because both direct beaming and surface thermalized particles are present in the ionizing region and both gas particles are normally detected. In-line particle retarding or an en-

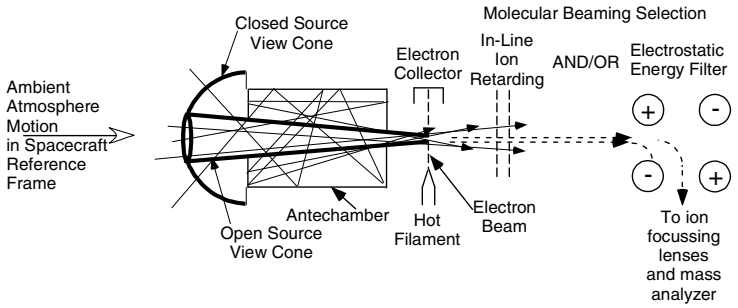

Figure 2.49: Simple schematic of an upper atmosphere mass spectrometer ion source with an antechamber. Open source particles have line of sight to electron beam. Closed source particles have one or more surface collisions with the antechamber walls, thermally accommodating to the wall temperature before reaching the electron beam. In-line particle retarding or an energy filter can be used to select the thermally accommodated or neutral beaming particles.

ergy filter can be used to select the thermally accommodated or neutral beaming particles. Another method, generally impractical for orbiter or flyby spacecraft, is to remove the thermally accommodated particles by cryopumping the surfaces [*Offermann and Trinks*, 1971]. The advantage of the open source operating in molecular beaming mode is that it can measure neutral radicals without surface interaction but there is no gain in sensitivity due to the velocity ram pressure enhancement as in the closed source (see Section 3.1.2).

While the quasi-open source has been used in the Pioneer Venus ONMS and Atmosphere Explorer OSS instruments, two separate ion sources, a separate quasi-open and a closed ion source are used in the Cassini INMS [*Waite et al.*, 2004] and CONTOUR NGIMS [*Mahaffy et al.*, 2002]. The basic gas inlet design had its origins in the Comet Rendezvous and Flyby (CRAF) mission [*Mahaffy et al.*, 1988]. The closed source permits the "classical" ram enhanced measurement of surface non-reactive species while the quasi-open source permits either molecular beaming measurements or ion mode measurements. In the NGIMS instrument, the standard circular aperture for the closed source antechamber is replaced by parallel set of tubes with a length-to-radius ratio of 20. Ions from either source are multiplexed into the quadrupole mass analyzer by means of a quadrupole switching lens [*Mahaffy and Lai*, 1990] based on a larger laboratory version by *Zeman* [1977]. The RTOF instrument also uses an orthogonal extraction ion source for its time-of-flight analyzer which will measure both neutral and ionized cometary gas [*Balsiger et al.*, 2007].

A quasi-open ion source can also measure ions if the ionizing electron beam is turned off and suitable potentials are put on the entrance electrodes.

2.7.3 Ionization Source

Several techniques exist to ionize a gas such as electron impact (EI), chemical ionization (CI), fast atom bombardment (FAB), field desorption (FD), electrospray ionization

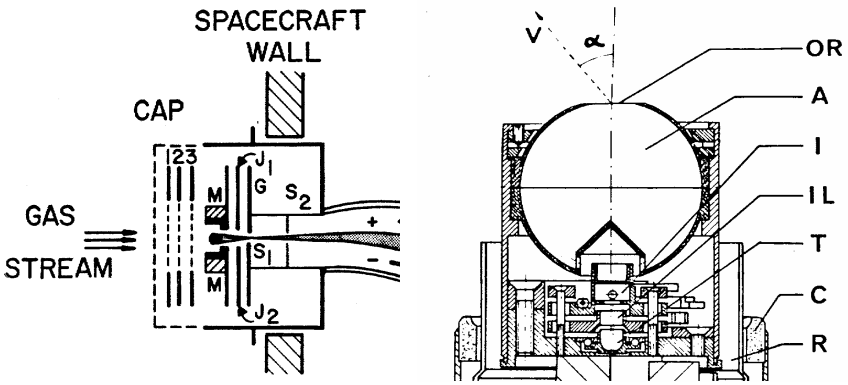

Figure 2.50: Left: A quasi-open ion source [*Nier et al.*, 1973] with a cap (dashed line) that is ejected in orbit. M is the electron beam source magnet, J's are plates, and the S's are slits. *Right:* The closed source of the ESRO-4 mass spectrometer [*Trinks and von Zahn*, 1975] where OR is the entrance orifice, A is the antechamber (diameter 40 mm), I the ionization region, IL and T are ion lenses. A conical baffle blocks direct beaming particles.

(ESI) and laser desorption (LD) (see for example *de Hoffmann and Stroobant* [2001]; *Gross* [2004].)

Most mass spectrometers designed for planetary atmosphere measurements use EI sources with a hot filament to supply electrons for ionization of neutral gas. The electron beam can be collimated with magnets (Bleakney-Nier type) or with electrostatic fields only.

In the case of the orbiter or flyby spacecraft, atmospheric gas measured in the spacecraft frame of reference has an equivalent energy that depends on the mass of the gas and the spacecraft speed which can range from 1 km s^{-1} [*Westermann et al.*, 2001] for the Rosetta comet Churyumov-Gerasimenko orbiter to as high as 68 km s^{-1} for the comet Halley flyby [*Krankowsky et al.*, 1986]. This is an energy range spanning from an electron volt to several thousand electron volts that must be accommodated by using the appropriate ion source and focusing potentials.

In many sensors several different electron energies are used to aid in the transposition of the spectrum to a gas composition since the mass spectral fragmentation pattern depends on the electron energy. For example, the Cassini Ion and Neutral Mass Spectrometer (INMS) [*Kasprzak et al.*, 1996; *Waite et al.*, 2004] uses 25 eV and 70 eV while the ROSINA Double Focusing Mass Spectrometer (DFMS) [*Balsiger et al.*, 1998, 2007] uses 10 eV and 90 eV. The INMS instrument uses electrostatic focusing of the electrons while the DFMS instrument uses a weak magnetic field to guide the electron beam. Magnetic fields have also been used in ion sources of Earth orbiting instruments [*Reber and Hall*, 1966; *Nier et al.*, 1973] and in the Galileo Probe mass spectrometer [*Niemann et al.*, 1992]. The presence of a magnetic field collimator narrows the electron beam width, increases the probability for ionization in a smaller volume and therefore reduces the energy spread of the ions that were being created. Measurements of ambient ions with such a source becomes more problematic because the source output is mass dependent.

Orbiter instruments can be configured to measure ions with a suitable change in focusing lens potentials and either turning the filament off or deflecting the electron beam out of the ionization region such as in the INMS, the Pioneer Venus Orbiter Neutral Mass Spectrometer (ONMS) [*Niemann et al.*, 1980], Dynamics Explorer WATS (Wind and Temperature Spectrometer) instrument [*Spencer et al.*, 1981], Nozomi Neutral Mass Spectrometer (NMS) [*Niemann et al.*, 1998], the Comet Nucleus Tour (CONTOUR) Neutral Gas and Ion Mass Spectrometer (NGIMS) [*Mahaffy et al.*, 2002], and the ROSINA DFMS and RTOF [*Balsiger et al.*, 1998, 2007].

The RTOF instrument uses an ionization source that is orthogonal to its mass-to-charge analyzer as do the Cassini INMS and CONTOUR NGIMS instruments, and both instruments can measure neutral gas as well as ions.

2.7.4 Cruise Conditions

Most neutral gas mass spectrometers are sealed off in a vacuum prior to final delivery and testing. These sensors can also be actively pumped by an ion pump or a getter material. At its destination, the sensor is opened to its environment. The purpose of sealing the sensor is to prevent contamination by other gases that could interfere with the species desired to be measured, especially low abundance species.

2.7.5 Spectra

The output of the mass spectrometer is a mass-to-charge ratio (m/z) or a series of mass-to-charge ratios. Using gases with known fragmentation masses determined by other instruments or methods, the voltage-to-mass scale or time-to-mass scale can be determined. Any chemical analysis of an atmosphere by a mass spectrometer assumes that the mass peaks in the spectrum of a gas mixture results from a linear addition of the contribution of each gas component. Known species fragmentation patterns and sensitivities can be used to unfold or deconvolute a mass spectrum that results from a gas mixture. An example of a deconvolved complex neutral gas mass spectrum of Titan's upper atmosphere is shown in Figure 2.51. For the interpretation of mass spectra individual single gas mass spectra from a library (calibration) are summed to form a net mass spectrum that is compared to the flight spectrum and the input composition ratios are adjusted. A similar problem exists when high speed neutral molecules pass through a foil, creating a shower of secondary ion fragments.

2.8 Neutral Atom Imagers

2.8.1 Introduction

Energetic neutral atoms (ENA) are ubiquitous in space. Energetic neutral atoms are produced when energetic ions in planetary magnetospheres charge exchange with the tenuous neutral gas that surrounds planets. Energetic neutral atoms also are present in the interstellar medium and can easily gain access to the inner heliosphere, and may even be observed at Earth's orbit, provided that those atoms are not photo-ionized by solar radiation or charge exchanged with solar wind ions in transit.

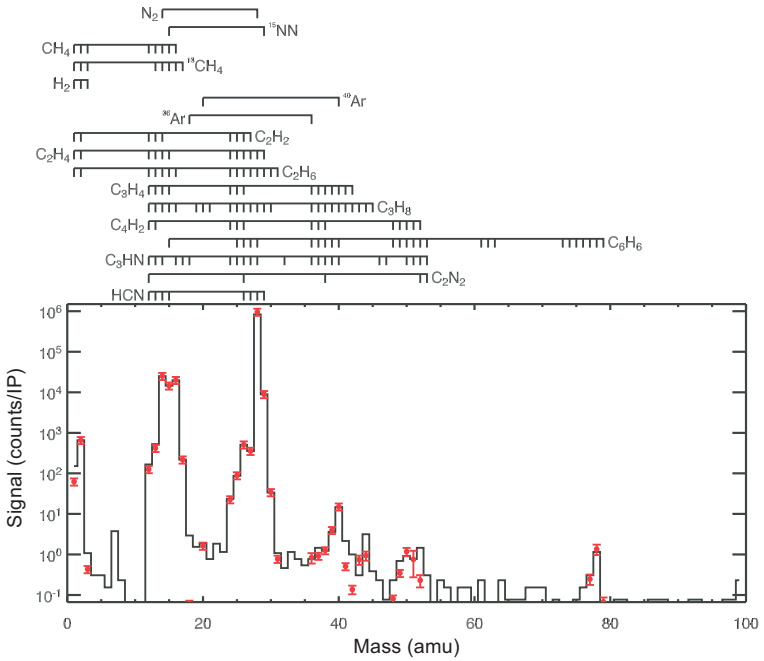

Figure 2.51: The average mass spectrum from 1 to 99 u measured by the Cassini INMS instrument on the first Titan fly-by pass between the altitudes of 1174 and 1230 km. The solid black line represents the measured, background-corrected spectrum and the symbols represent the reconstructed spectrum. From *Waite et al.* [2005].

Energetic neutral atoms move in ballistic paths and are not influenced by electric or magnetic fields in transit from their source regions. Observations of those atoms provide the opportunity to remotely sense the properties and spatial structure of the particle populations from which they originated.

2.8.2 Measurement Principles

The instruments that have been developed to observe energetic neutral atoms are, in most respects, similar or nearly identical to the instruments that measure energetic charged particles. There are, however, some important differences that are briefly described here.

2.8.3 Rejection of Other Signal Sources

The fluxes of neutral atoms are generally very much smaller than the fluxes of charged particles of the same energy, especially in and near the Earth's magnetosphere. Those charged particles must be eliminated from accessing the instrument devoted to measuring the neutral component of the particle population and that must be done with high efficiency because the neutral fluxes may be orders of magnitude less than the charged particle fluxes. In energetic neutral atom instruments this elimination is done in the entrance collimator

structure by imposing the combination of large electric fields and magnetic fields to direct charged particles into serrated plates that absorb those particles with a minimum of scattering. Large electric fields are needed in order to eliminate charged particles up to the highest energies of interest. For example, in a parallel plate condenser of length L and spaced a distance D apart, the minimum energy particle E_m that will pass between the plates, assuming no scattering, is given by

$$E_m = \left[1 + (L/4D)^2\right] eV_p \tag{2.41}$$

where V_p is the potential between the plates and e the electron charge. For reasonable L/D ratios ($>\sim$20) one expects rejection of particles with energies of several hundred keV for potentials of only a few kV between the plates. In order to achieve those large electric fields with reasonable voltages, the collimator structure often has multiple apertures with small plate separations but with large electric fields imposed. The degree of elimination of energetic charged particle access to the neutral atom detection section of the instrument is an important aspect of laboratory calibration. It is important to note that the elimination of charged particle access by the electric and magnetic fields does not eliminate access of UV and EUV photons to the instrument.

Light and especially ultraviolet light is unwanted inside an instrument because it can trigger the detectors and eject photo electrons from foils or other surfaces inside the instrument. It is therefore important to eliminate or reduce photon flux as far away as possible from the sensitive components. Several techniques have been used to separate photons from the particles. One such technique is the use of electric or magnetic fields perpendicular to the line-of-sight to guide charged particles on curved trajectories away from the photons. The instrument design should be such that UV light makes at least 3 to 4 specular reflections before it reaches the detector.

Another method at reducing the UV light is through the use of foils. The foils are made thick enough ($\sim$ 10–15 μg cm^{-2}) [*Funsten et al.*, 1998] to absorb or attenuate the photons while the energetic particles can penetrate through the foil. The thickness of the foil is given by balancing the conflicting needs for high UV attenuation and low particle stopping power. In neutral atom imagers any such foil must follow the charged particle filter since the particle transmission through the foil will also produce charged particles due to charge exchange.

Recently another technique has been employed in the form of UV diffraction grids. The grating's waveguide and polarization effect is used to efficiently damp the UV, while the open slits allow neutral atoms to pass. In this technique UV light is blocked without disturbing the incident neutral atom velocity, resulting in high image resolution and imaging over a broad energy range [*Funsten et al.*, 1998; *Pollock et al.*, 2000]. However, those gratings are optimized to suppress UV light from a particular wavelength region such as Lyman-α and still leak UV light at other wavelengths. The concept of UV rejection by grids has been further developed by staking several of them and move them laterally by ultrasonic motors. By proper selection of the frequencies, photons at the speed of light hit a grating, while the slower moving neutrals make it through the grid spacings. This concept is pursued for the BepiColombo SERENA/ELENA instrument [*di Lellis et al.*, 2004; *Mura et al.*, 2006].

Further, coincidence techniques could be used to discriminate between UV photons and charged particles. In time-of-flight systems such as shown in Figure 2.52 outputs from

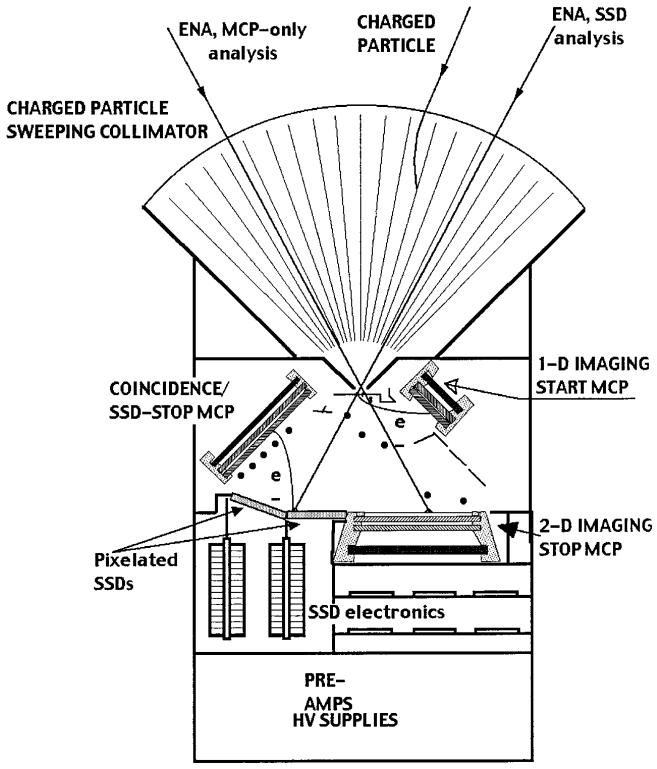

Figure 2.52: Schematic drawing of the HENA sensor on the IMAGE spacecraft. HENA is a wide slit camera. Electrically-biased and serrated collimator plates provide the electric field to sweep charged particles out of the entrance slit. Those ENAs penetrating the front foil that covers the entrance slit, produce secondary electrons from the foil to trigger the 1-D imaging start MCP. The same ENAs travel to either the SSD or the back foil and the 2-D imaging MCP immediately behind it. Secondary electrons produced by the arriving ENAs at either the SSD or the front of the back foil are steered to trigger the coincidence/SSD-stop MCP. The dots indicate the locations of the wire electrodes for steering the secondary electrons to their respective MCPs. The spacecraft spin vector is perpendicular to plane of the figure. From *Mitchell et al.* [2000].

the START and STOP detectors are required to trigger a particle event, while a single EUV photon will produce a response in only one of the MCPs.

2.8.4 ENA Measurement Techniques

Measurements of neutral atoms of energies greater than about 20 to 30 keV are done using conventional time-of-flight techniques similar to those described in Sections 2.6.4 and 2.6.5. The High Energy Neutral Atom (HENA) detector on the IMAGE satellite [*Mitchell et al.*, 2000], shown in Figure 2.52, is one such example. Neutral atoms enter the TOF section through the fan-like collimator structure that sweeps out charged par-

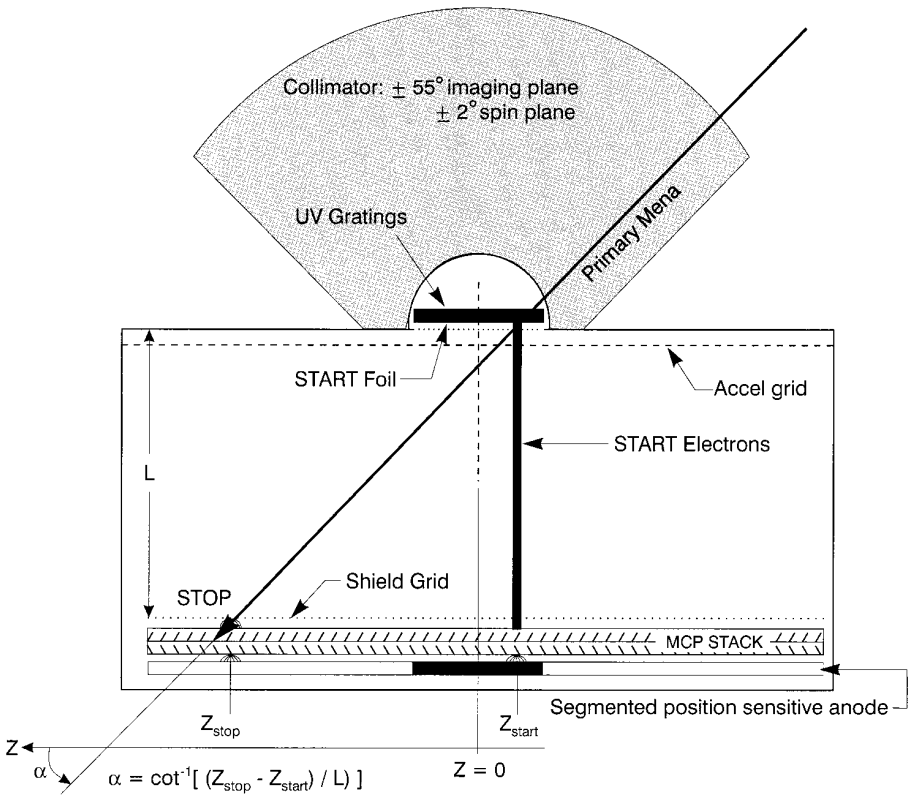

Figure 2.53: Schematic view of an IMAGE MENA sensor. A neutral atom passes through the START foil, producing secondary electrons. Secondary electrons are accelerated towards the START segment of the detector, whereas the ENA will impact the detector STOP segment. Particles incident on the START and STOP segment of the detector will provide TOF timing signals, which together with their respective pulse height and impact location on the detector provide the required information for polar incidence angle, energy and species determination of the ENA. From *Pollock et al.* [2000].

ticles. The atoms are passed through a thin foil that both suppresses EUV photons and produces secondary electrons that form the start signal for the time-of-flight measurement. The particles continue through the TOF section to strike either a thin foil above an MCP or directly on a solid-state detector depending on their angle of incidence through the collimator. In either case secondary electrons are created to form the stop signal for the TOF. Both the solid-state detector and the MCP are position sensitive designs so that the atom's angle of incidence into the instrument is determined providing a degree of imaging capability. The particle's energy loss in the solid-state detector, together with the time-of-flight measurement, provides the atomic species identification. A similar, albeit cruder, species identification is provided by the MCP output that is larger for heavy atoms than for hydrogen.

Measurements of neutral atoms of energies below some 10's of keV are somewhat more challenging because solid-state detectors are insensitive to those energies and low energy atoms scatter and suffer significant energy loss in transiting thin foils. Very thin foils are also less effective in suppressing EUV photons. An early such instrument for these lower energies used electric and magnetic fields across the entrance collimator to eliminate charged particles followed by a thin foil where the neutral atom had a $\sim$10 % probability of being stripped to become an ion that was then passed into a conventional curved plate electrostatic analyzer to determine its energy [*Wax and Bernstein*, 1967]. The low probability of stripping in the foil and the scattering of the atom/ion in passing through the foil reduced the overall instrument sensitivity and were disadvantages to the technique. The Medium Energy Neutral Atom detector for IMAGE [*Pollock et al.*, 2000] is a contemporary and improved technique for observations in the few to 30 keV energy range (see Figure 2.53). In common with neutral atom instruments, strong electric and magnetic fields in the collimator structure eliminate charged particles. The neutral atom that passes the collimator impinges a thin foil, creating secondary electrons that form the start signal for conventional time-of-flight analysis. The secondary electrons, initially with eV energies, are accelerated though 1000 V to a position sensitive MCP, a technique that determines the location on the start foil the atom passed. A unique feature of the MENA instrument is an optical transmission grating that is integrated with the start foil assembly to suppress EUV photons from entering the TOF section. The particle continues through the time-of-flight section to a position sensitive MCP that forms the stop signal and, knowing the path length, the particle's velocity is determined. The location of the stop pulse on the MCP, coupled with the collimator design, provide a measure of the atom's source direction and an imaging capability to the instrument. The pulse amplitude from the stop MCP section provides a first order measure of the atomic species, the pulse being larger for heavy atoms.

The detection and analysis of neutral atoms with energies less than 1 or 2 keV represents a very significant challenge. Such low energy atoms suffer large angular scattering and significant energy loss in passing through even the thinnest foil that ordinarily would be used to provide the start signal in a TOF analysis of particle velocity, making that an ineffective technique to use. Instead instruments designed for low energy neutral atoms make use of the interaction between an atom encountering a surface at near grazing angle of incidence.

The Neutral Particle Detector in the ASPERA-3 experiment on the Mars Express Mission is one such example [*Barabash et al.*, 2004]. In this instrument neutral atoms (after charged particles have been removed in the collimator) impinge on a highly polished surface at near grazing angles where they reflect in a near specular fashion producing in the process secondary electrons that are steered to an MCP to form a start signal for a TOF analysis. The surface material was specially chosen to maximize secondary electron production and efficiency for reflecting atoms while maximizing the absorption of UV photons which otherwise would contaminate the TOF analysis. The reflected atom (often an ion having either lost or picked up an electron in the interaction) having lost perhaps 20 % in energy continues on a path through the TOF section to a stopping surface. The secondary electrons produced at the stop surface are directed to an MCP to form the stop signal thus determining the atom's velocity. Because the number of secondary electrons produced at the stop surface increases with the atom mass, the amplitude of the signal from the stop MCP is a rough measure of the atom's mass. A somewhat different approach is

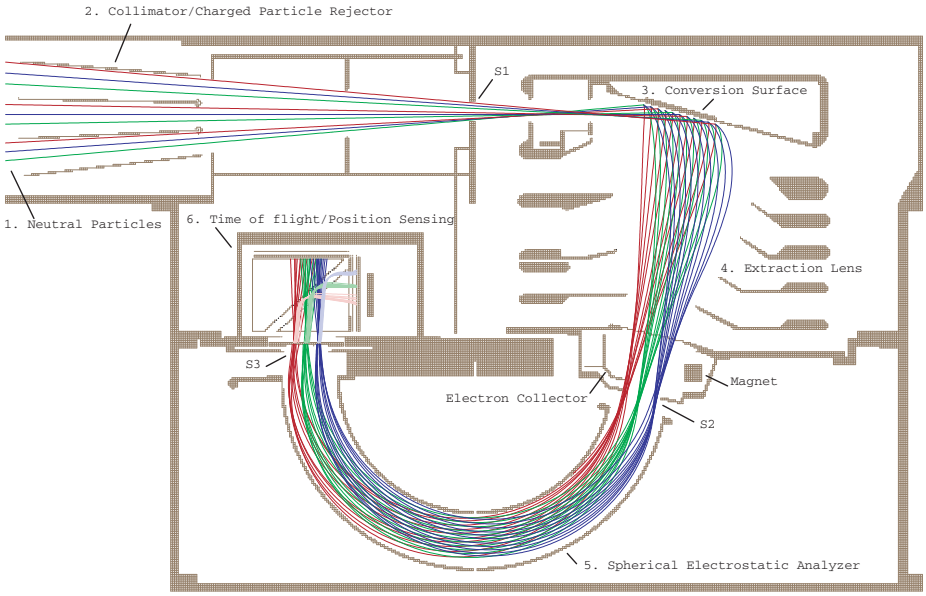

Figure 2.54: End-to-end simulation of the ion optics of LENA, also showing the TOF optics in a 2-D section through the symmetry axis of the instrument. From *Moore et al.* [2000].

used in the Low Energy Neutral Atom (LENA) instrument flown on the IMAGE satellite [*Moore et al.*, 2000] and designed to measure neutrals from 10s of eV to about 1000 eV. In this very complex instrument (Figure 2.54) neutral atoms, after charged particles have been excluded by electric fields in the entrance aperture structure, are allowed to impinge upon a specially prepared tungsten surface at near grazing angles. A small fraction of those atoms (about 1 %) pick up an electron in the course of being reflected off the surface, termed a charge conversion surface, to become negative ions. Some 5 % to 20 %, of the initial energy of the atom, depending upon species, is lost in this charge conversion.

The charge conversion surface is biased up to -20 kV and so any negative ions formed are accelerated away from the surface as well as secondary electrons that are created in the interaction. As the negatively charged particles are accelerated away they are passed through an elaborate electrostatic lens system that steers those particles to an entrance slit (labeled S2 in Figure 2.54). The energized secondary electrons are removed from the population in transit by a broom magnet while the lens system focuses the negative ions at positions along slit S2 according to their residue energy after reflection from the charge conversion system. The ions that pass through S2 enter a curved plate electrostatic analyzer.

The purpose of the analyzer is not to determine the ion energy per unit charge for after all the negative ions have nearly identical energies determined by the residue energy after reflection and the accelerating potential. Instead, the analyzer is designed to pass the ions through about 180° to exit slit S3 in Figure 2.54 while maintaining the spatial separation

in initial energy that was imposed by the lens system. The analyzer also greatly reduces spurious response from UV photons that require three bounces to transit the analyzer.

The ions, having 20 keV energies, are suitable for the conventional TOF techniques and upon exiting the electrostatic analyzer pass through a foil to produce the start signal for TOF analysis. Secondary electrons originating from a specific point on the foil are directed by an electrostatic mirror to a specific location on a position sensitive MCP so that the location of the ion impact on the start foil is determined, which is a measure of the ion's residue energy at the point of charge conversion. The ion's impact on the stop MCP completes the TOF analysis. In this way LENA determines neutral atom composition (from determining velocity at the fixed energy) and, in a cruder manner, the original energy of the incident neutral atom.

Many further details on neutral atom detection techniques and various alternative instrument designs are given in the reviews by *Gruntman* [1997] and *Wurz* [2000].

2.9 Solid-State Detector Instruments

Solid-state detectors are used for electrons and ion with energies above about 20 keV. Among these are simple solid-state detectors located under an energy degrader or absorber, multiple element solid-state detector systems capable of identifying both particle energy and mass. Cherenkov detector systems for detecting very high-energy particles and scintillation detector systems. A combination of detector techniques may be used in the same instrument to suppress background.

2.9.1 Overview

Solid-state instruments are used above 20 keV energy. This threshold energy is determined by the thermal detector noise of the solid-state detectors (SSD).

Details about the solid-state detectors proper can be found in Section 2.2.5. Here we briefly describe their use in high-energy particle instruments. There are basically two types of such SSD instruments, the SSD telescopes based on the energy loss in matter and the time-of-flight technique.

2.9.2 Solid-State Detector Telescopes

Solid-State detector (SSD) telescopes are based on the specific energy loss in matter (see Section 2.2.5.1). The SSD telescopes consist of a stack of two or more solid-state detectors. If the thickness ΔX of the front element is small compared to the range of the incident particle, then the energy loss ΔE is approximately equal to $(\mathrm{d}E/\mathrm{d}x)\Delta X$. The last detector must be thick enough to absorb the entire residual energy of the particle to be measured. The ΔE and E signal provided by the detectors can be used to determine the incident particle energy. Expanding the concept to telescopes consisting of several SSD detectors can lead to the determination of the incident ion mass, even at isotopic resolution.

An example of such an isotope telescope is given in Figure 2.55 and described in [*von Rosenvinge et al.*, 1995]. Here, particles enter through a collimator. This is followed by two foils. The purpose of the foils is to protect the following SSD from sunlight and from radiation damage from high counting rates due to particles at energies just below the

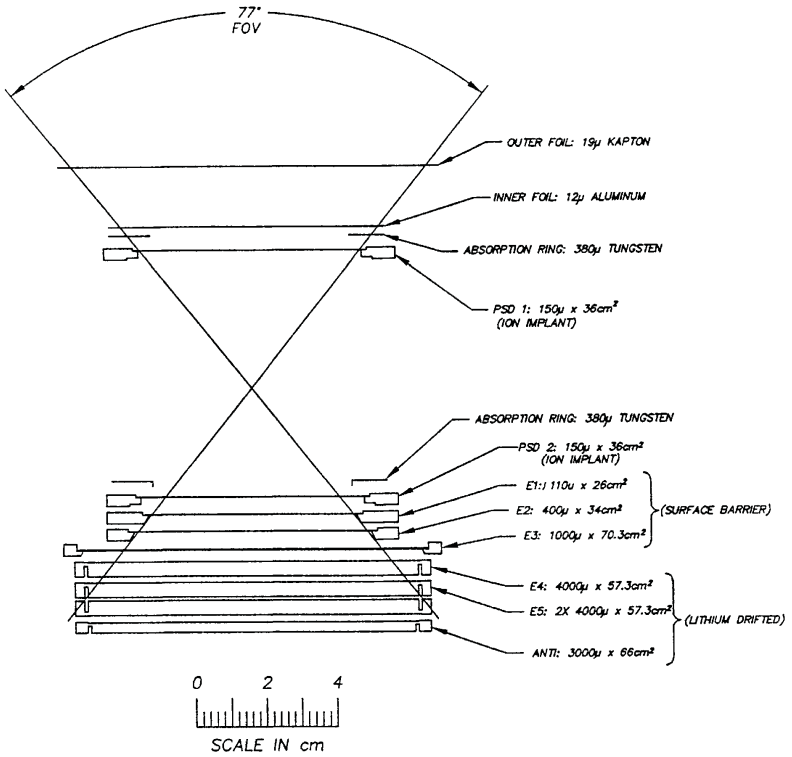

Figure 2.55: Cross section of the EPACT isotope telescope on Wind. The first two detectors are two-dimensional position sensitive strip detectors (PSD1, PSD2). They are required so that path-length corrections may be made for the angle of incidence and for non-uniformities in detector thickness. Tungsten rings are used to mask off circular areas for each PSD. There are 6 solid-state detectors increasing in thickness with depth in the stack in order to minimize Landau fluctuations. From *von Rosenvinge et al.* [1995].

energy range of the instrument. Double foils provide better protection than a single foil against sunlight coming through pinholes, especially when using vacuum deposited aluminum foils. The particles then pass through two position sensitive detectors. The purpose is to make path-length corrections due to angle of incidence and due to non-uniformities in detector thickness. This is followed by 5 increasingly thicker SSDs followed by an anticoincidence detector. The detector thickness increases systematically with depth in the stack in order to minimize statistical fluctuations in the average energy loss, also called Landau fluctuations [*Bichsel*, 1988]. Figure 2.58 depicts the electronic block diagram to operate the instrument. The detectors are biased up to about 500 V. Each detector is connected to a charge amplifier. The resulting signal is further pulse shaped and amplified in a shaping amplifier and pulse height analyzed before digitized and further processed to data products in the data processing unit.

Other SSD telescopes are discussed in Section 3.5.

2.10 Plasma Wave Instruments

Great advantage has been taken of observations of plasma wave spectra to obtain an independent, and usually very accurate, measure of local electron density to which the density moment obtained from particle measurements can be compared. As described in Chapter 4 this comparison has proved invaluable for in-flight verification of plasma measurements and developing necessary corrections to the particle observations.

The technique makes use of the dependence of the electron plasma frequency f_p on local electron density N_e.

$$\omega_p = 2\pi f_p = \left(\frac{N_e e^2}{m_e \epsilon_0}\right)^{\frac{1}{2}} \tag{2.42}$$

where e is the elementary charge, m_e is the electron mass and ϵ_0 is the permittivity of free space.

Langmuir waves are often present in the solar wind, magnetosheath, and magnetosphere where generally $f_p \gg f_{ce}$, with f_{ce} being the local electron gyro frequency. In this situation the Langmuir wave frequency spectrum is located at the plasma frequency and broadened by the thermal motion of the local electron population.

$$f = \left(f_p + k_{v_{\text{th}}}/2\right)^{\frac{1}{2}} \tag{2.43}$$

The Langmuir wave frequency spectrum is often very narrow and a measurement of the frequency can provide an accurate measure of f_p and the local electron density.

Other features in the plasma wave spectrum can provide indirect measures of the local electron density, although with less confidence. If electromagnetic waves are present, the low frequency cutoff in that spectrum can be used as a proxy for f_p because EM waves do not propagate at frequencies lower than f_p. Similarly, if electrostatic waves are present and $f_{ce} > f_p$, the high frequency cutoff in that spectrum occurs at f_p and can be used as a proxy for density. Finally, if upper hybrid waves can be identified in a plasma wave spectrum, and the local f_{ce} is known from magnetic field measurements, the electron plasma frequency can also be obtained.

The plasma wave instruments that provide these measurements must have adequate sensitivity, operate over the appropriate frequency range, and have the frequency resolution to identify those features in the frequency spectrum with sufficient precision to provide accurate local plasma densities.

Three types of plasma wave instruments are typically employed for these measurements. The first is a passive plasma wave receiver, usually with a long dipole antenna, that is sensitive to the AC electric fields occurring naturally in the local environment. This type of instrument has been used on numerous space missions and details of various instrument designs and operation may be found in *Knoll et al.* [1978], *Häusler et al.* [1985], *Paschmann et al.* [1985], *Bougeret et al.* [1995], *Matsumoto et al.* [1998], and *Gurnett et al.* [2004]. Figure 2.56 shows a frequency spectrogram obtained in the solar wind by the Unified Radio and Plasma wave (URAP) passive plasma wave receiver on Ulysses [*Stone et al.*, 1992]. The narrow band emission near 20 kHz is from Langmuir wave emissions that, as shown above, are a measure of the local electron plasma frequency.

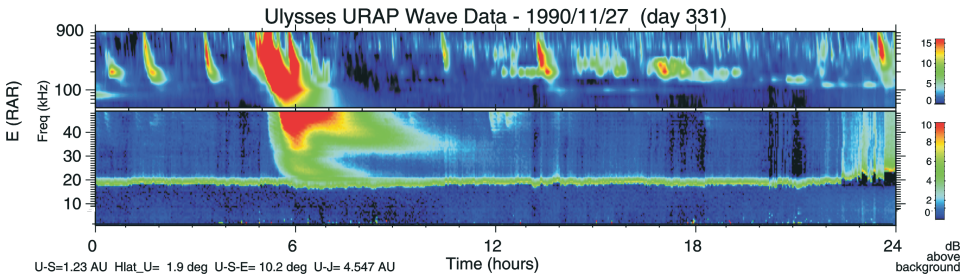

Figure 2.56: Radio astronomy receiver spectrogram of the URAP instrument on the Ulysses spacecraft measured on November 27, 1990. Linear frequency scale is used from 1 to 50 kHz, and then non-linear scale applies up to 940 kHz. The electrostatic Langmuir waves emissions are seen around 20 kHz. The impact of a type III radio burst is clearly seen around 6 UT.

The second form of plasma wave instrument includes a passive plasma wave receiver with the addition of a device to actively inject waves of varying frequency into the local plasma to stimulate and enhance the natural emissions from the medium. This instrument is also called sounder. Unlike naturally occurring waves near f_p that may be electromagnetic and therefore above the plasma frequency or Langmuir waves with finite k that may also be above the plasma frequency, active simulation can accurately identify the electron plasma resonance. In this way the sensitivity of the instrument to identifying the local electron density is much improved. While providing information on f_p in a manner identical to the passive receiver, these instruments can provide information on non-Maxwellian plasmas by the detection and careful analysis of natural resonances excited by a sounder. This kind of plasma wave instrument has been flown on many space missions including GEOS [*Jones*, 1978], ISEE-1 [*Harvey et al.*, 1978], Viking [*Décréau et al.*, 1987], IMAGE [*Reinisch et al.*, 2000], Cluster [*Décréau et al.*, 1997], Ulysses [*Stone et al.*, 1992], and on the Cassini spacecraft [*Gurnett et al.*, 2004].

Figure 2.57 shows an example of frequency spectrograms obtained by the WHISPER (Waves of High Frequency and Sounder for Probing of Density by Relaxation, *Décréau et al.* [1997], *Gustafsson et al.* [1997]) instrument on one of the Cluster spacecraft during intervals when the instrument was actively exciting plasma oscillations (denoted by the orange bars.) The plasma wave intensities at a variety of resonances are clearly enhanced by the excitation signal and, through analysis of that frequency spectrum, f_p can be extracted.

The third type of plasma wave experiment of interest is the mutual impedance instrument (also called a quadrupolar probe.) This instrument employs a low power, swept frequency transmitter feeding a dipole antenna. A second antenna and receiver placed on the same spacecraft detects that radiated signal. Measurements of the amplitude and phase of the received signal relative to the transmitted yields information about the properties of the plasma in the medium between the two. Details of the design and operation of a mutual impedance instrument may be found in *Décréau et al.* [1978a, b] and *Trotignon et al.* [1999].

While plasma wave observations can provide highly accurate determinations of local electron densities, there are problems and some care should be exercised in the selection of specific data for this purpose. For example, the plasma wave receiver may exhibit interfer-

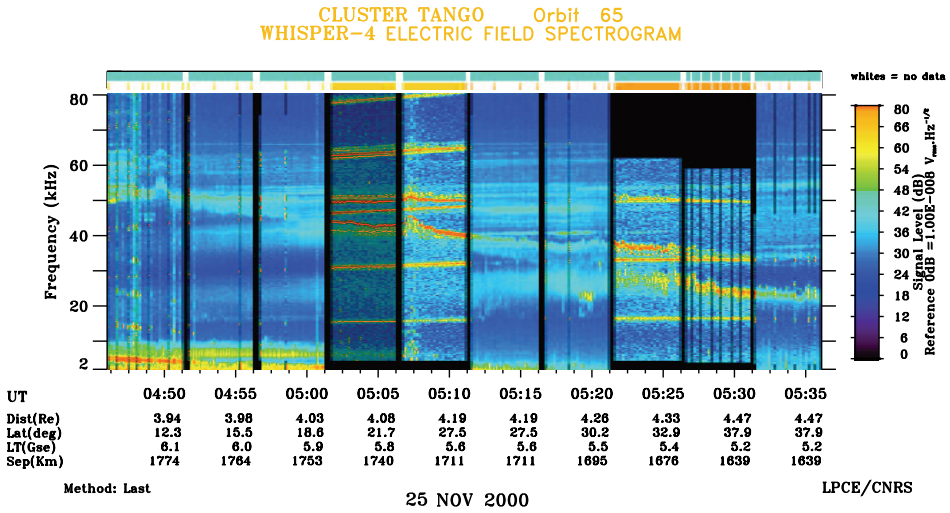

Figure 2.57: Electric field spectrogram measured by the WHISPER relaxation sounder onboard the Tango satellite of the Cluster spacefleet on the 25th of November 2000, from 04:45 till 05:35. During this time period, Whisper was partially in active mode (orange overline) with a higher sampling rate than the standard Whisper sounding time resolution (every 28 s). Natural resonances are significantly enhanced. The plasma frequency f_p is deduced from the pattern of resonances excited at a given time. From *Canu et al.* [2001].

ence or spurious signals originating from other systems on the spacecraft. The frequency range or the sensitivity of the plasma instrument may not be appropriate for the geophysical conditions that exist at a given location or time. Careful choice of the physical situations, locations and time intervals that are selected for using plasma wave observations to provide the plasma density standard for comparison with particle observations will mitigate these problems.

2.11 Electronics

Electronics is an integral part of an instrument. In the electronics the detector signal is shaped and converted into digital data. That processing can be very complex as shown in Figure 2.58. We will not discuss the design and construction of instrumentation electronics for space use as that subject is covered in a number of text books such as *Horowitz and Hill* [1989]; *Tietze and Schenk* [2006]; *Cruise et al.* [1998]; *Spieler* [2005]; *Leo* [1987]. It is appropriate to point out here some of the effects that impact electronics and influence instrument operation that should be addressed by laboratory calibration procedures.

2.11.1 Amplifier and Discriminator Operation

The signals provided by the commonly employed space physics detectors are quite small. For example a single charged particle amplified in an MCP with a gain of 10^5 gives a charge of 1.6×10^{-14} C. The charge provided by a typical high-energy detector is

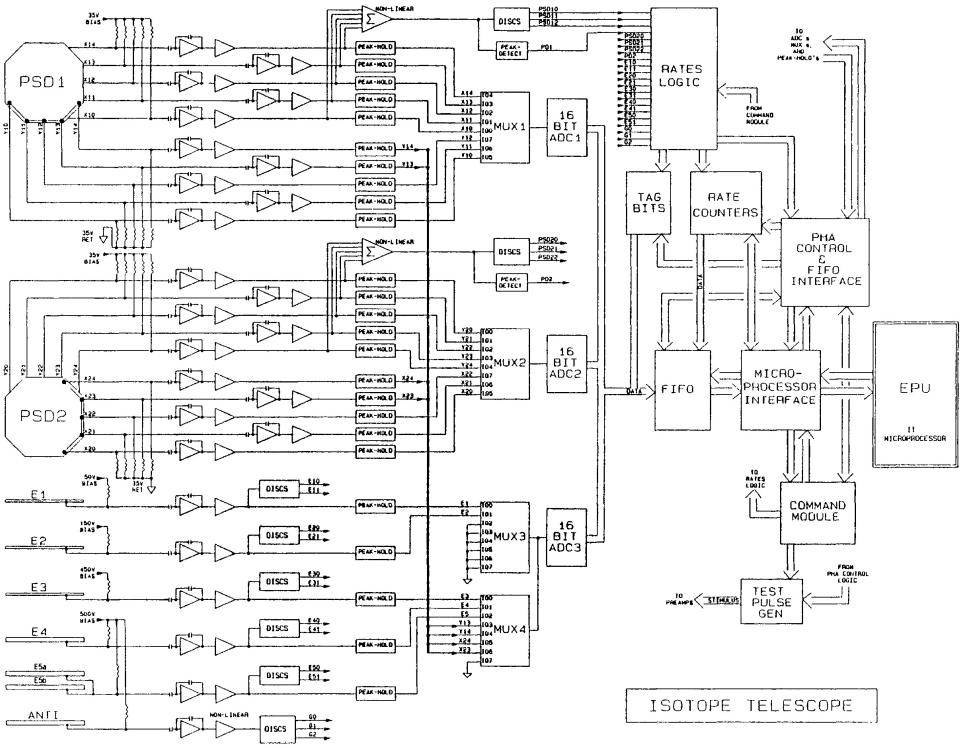

Figure 2.58: Block diagram of the signal acquisition electronics for the EPACT Isotope Telescope. It shows the many pre-amplifiers and pulse-shaping amplifiers used and which affect the signal-to-noise ratio. The count rate for each discriminator setting should be calibrated. From *von Rosenvinge et al.* [1995].

about 4×10^{-15} C. The sensor signal must be amplified for further processing (see also Figure 2.58). Statistical fluctuations of the sensor output signal and electronic noise further smear the signal. The sensor and the preamplifier must therefore be designed carefully to minimize electronic noise. The primary function of a pulse shaper, if employed, is to improve the signal-to-noise ratio. This is done by taking advantage of the fact that the frequency content of the noise and the signal differ. Changing the frequency response by reducing the bandwidth to favor the signal while attenuating the noise changes the time response of the signal to a longer pulse. The optimum must be found between reducing noise and increasing speed. Further, the optimum peak shape from a signal-to-noise point of view may be too short for an analog-to-digital converter to process. Since discriminator levels will need to be changed in flight, it is important to properly calibrate the effects of the different threshold levels on count rate.

Further, temperature can affect electronics operation, such as amplifier gains or threshold discriminator settings. Those effects should be calibrated in the laboratory so that corrections can be made to data received after launch.

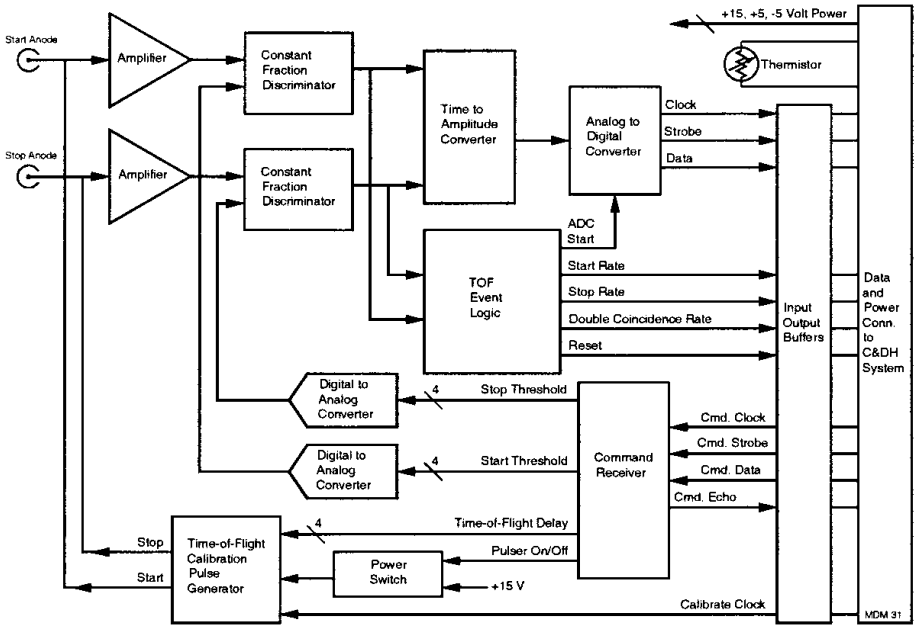

Figure 2.59: Time-of-flight electronics block diagram of the IMAGE LENA instrument. From *Moore et al.* [2000].

2.11.2 TOF Electronics

An essential part of a TOF instrument is its electronics. Time-of-flight electronics are especially complex and need careful attention in the calibration procedures. Examples of TOF electronics are given in Figures 2.43, 2.45, and 2.59.

Typically the front face of the MCP is biased to a positive potential to collect secondary electrons from the dead area of the MCP into the multiplier. A high positive potential is applied to the rear face of the MCP to multiply the electrons in the MCP channels. A position sensitive anode near ground potential collects the electron cloud output of the MCP. The resulting charge pulse is capacitively coupled to a high gain, linear charge sensitive amplifier.

From the resulting preamplifier signal there are a few different ways the signal is processed in a time-of-flight electronics. One technique uses the time-to-amplitude converter. The other methods use a form of time-to-digital converters or fast analog-to-digital converters.

The time-to-amplitude converter (TAC) technique relates the time interval between two events to the quantity of charge discharged by a capacitor during this period. A START signal begins a constant discharge of a capacitor. The discharge is cutoff when the STOP signal arrives. The total charge collected forms an output signal whose height is proportional to the time difference between the START and STOP signals. The output signal can then be pulse height analyzed or digitized using an analog to digital converter (ADC). Dead time of the TAC/ADC combination is influenced by the conversion speed of the

ADC. However, fast ADC quickly become power-prohibitive in space flight applications. The Cluster CODIF instrument is an example where a TAC is used.

The time-to-digital converter (TDC) directly converts the timing signal into a digital signal. The basic principle is to use the START signal to gate on a scaler which counts a constant frequency oscillator (or clock). At the arrival of a second STOP signal, this scaler is gated off to yield a number proportional to the time interval between the pulses. The resolution of the counting TDC depends on the clock frequency used. TDC offer high sampling rates and low dead times.

Another digital counting method is the vernier technique. Here two oscillators of slightly different frequencies, f_1 and f_2, are used. The arrival of a START signal gates the first clock while the second remains off. The moment the STOP signal arrives, the second clock is gated on and continues oscillating along with the first clock until the two are in phase. At this point both clocks are stopped. The time interval can be calculated from the number of pulses counted n_1, n_2 by

$$\delta t = \frac{n_1}{f_1} - \frac{n_2}{f_2} \tag{2.44}$$

The Cassini ion mass spectrometer *Young et al.* [2004] is an instrument that uses a form of delay line vernier TDC.

More details about timing methods and calibrating timing systems can be found in *Spieler* [2005], *Leo* [1987] or *Porat* [1973].

In addition to determining the time-of-flight, the electronics generates logical output signals for each START and STOP pulse. The conditions for valid events are established by the event-selection logic. For example, a valid STOP signal must arrive within a certain time window after the START signal. This feature reduces the dead time effect. An event may be rejected if a second START signal occurs before a STOP signal is detected (pulse pile-up rejection), a feature that serves to eliminate events that might be misidentified because of very high START rates during times of high fluxes. Such START/STOP coincidence requirements for a valid TOF determination lead to high immunity of the TOF technique to background signals compared to a non-coincidence system. Sources of background in TOF systems are chance coincidence counts due to penetrating radiation or high particle fluxes, dark counts, internally scattered ions and electrons, secondary ions from the exit area of the ESA and single STARTS or single STOPS due to low MCP detection efficiencies stemming from insufficient MCP gain. Further, several instrument event rates may be accumulated in electronic scalers. These include individual START and STOP rates as well as total count rates of TOF coincidences. These rates as well as other housekeeping values provided by the electronics, such as all voltages (deflection, post-acceleration, MCP bias etc.) and threshold levels as well as temperatures of the detector and electronics have to be monitored during calibration and in-flight to properly evaluate the data.

2.11.3 Other

Electronic noise created by noisy detector power supplies, RF pickup, stray capacitances or electromagnetic interference causes signal spread into adjacent digital bins or reduces signal-to-noise. As discussed earlier, radiation damage can affect both detector and electronics operation, for example increasing noise, changing overall sensitivity, and in extreme cases leading to failure. Testing under extreme radiation conditions should be

Table 2.1: Background problems (after D.T. Young, personal communication)

Cause	Remedy
External Sources	
Penetrating radiation	Shield parts with high-Z material
- Radiation belt	Shield instrument with low-Z material
- Solar proton events	
UV	Collimation and baffling
- Solar UV,	Anti-scattering surface treatments
- H-corona UV	
Plasma	Collimation, baffling
- Outside of pass band	Anti-scattering surface treatment
- Spacecraft charging	Conducting S/C surface
- Cross-talk in pass band	Fringe field control
Internal sources	
Detector dark current	Detector selection, surface treatment
- Thermionic emission,	
- Field emission	
- Radioactivity in detector	
Electronic noise	Electrical isolation, grounding concept, filtering
- Competing detector signals (electronic cross talk)	EMI/EMC control program
- Digital signals	
- Power supplies	Power line filtering
- Other spacecraft electronics	
Magnetic field	μ-metal shielding, proper magnet/yoke/shims
- image distortion	design

done prior to flight to insure the instrument can operate properly in the expected radiation environment.

2.12 Common Instrument Problems

Table 2.1 lists some of the problems commonly encountered in implementing many of the analyzer designs described in this chapter together with suggestions for their mitigation. A careful and thorough laboratory calibration procedure should in large part be designed to expose design and implementation problems of this sort. It is only through early recognition that a problem exists, that there can be a rectification and a quality instrument put into space.

2.13 Data Handling

While the most critical elements in assuring the success of an energetic particle or plasma experiment in space are the laboratory calibration and in-flight performance verification techniques that are the focus of this book, there are some other factors that warrant mention. Instrument data from the spacecraft in space needs to be brought back to Earth to be stored in a mission data archive. The data handling from the instrument to the ground is complex. The end user of the data needs to be aware that the instrument data he gets on the ground may be degraded due to data compression or corrupt or lost telemetry packets. As it is easy to introduce software bugs, the end user needs also to be aware that the data analysis software might contain sometimes subtle bugs.

2.13.1 Data Compression

Today's particle instrument produce a far larger data stream than can be transmitted to the ground by the allocated telemetry rate. On-board data prioritization may be used to select the most important data to be transmitted with information of lesser importance transmitted when possible if at all. Further, data compression is used to bring as much information to the ground as possible. Depending on the data compression method used additional uncertainties in the data can be introduced. Those errors can impact, to one extent or another, the results of the laboratory calibration of an instrument and the ability to conduct a quantitative in-flight verification task.

Historically, approaches to data compression schemes have centered around techniques such as on-board averaging of data and pseudo-logarithmic or square root compression of sensor counts to reduce the volume of raw data transmitted. Examples of such approaches may be found in [*Rice and Plaunt*, 1971; *Niemann et al.*, 1980, 1997; *Rice et al.*, 1993; *Shelley et al.*, 1995; *CCSDS*, 1997a, b], and [*Gowen et al.*, 2003]. More details on data compression techniques can be found e.g. in [*Sayood*, 2000].

Depending on the data compression technique used, the errors introduced can be greater than the accuracy that is needed for quantitative in-flight verification of instrument performance. For example, the pseudo-logarithmic compression of accumulated sensor counts that is used in the data processing unit for particle detectors in the Space Environment Monitor on the POES satellites has a 5 % increment from one compressed value to the next for accumulated counts of order 5×10^5. This uncertainty is much greater than the statistical uncertainty for that number of counts and might compromise the value of a comparison of those particle data with an independent measure of local plasma density that might be accurate to 1 %.

Some data compression schemes depend upon transmitting for a given block of data only the difference in data value from one sample to the next. This approach is vulnerable, however, to random bit errors that will not only corrupt that single data value but all subsequent data values within that data block.

The advent of powerful microcomputers has allowed the on-board computation of moments of the particle distribution directly from the instrument observations, a task that had earlier been performed by ground processing of raw sensor data. Onboard moment computation was pioneered on the AMPTE mission [*Paschmann et al.*, 1985]. Even more recent missions are reducing the electrical power requirements for calculations of moments by shifting the computations from the microprocessor to a dedicated piece of hardware. The

THEMIS mission uses a Field-Programmable Gate Array (FPGA) to perform moment computation for four instruments (electron and ion plasma and solid-state sensors) with a three second cadence.

It is important that on-board calculations of particle moments take into account spacecraft potentials. The THEMIS mission is the first to include spacecraft potential corrections to the onboard moments (see also Subsection 3.2.6).

The scientific data also has to be suitable for moment calculations. E.g. for non-thermal distributions, the moment calculations will not work that well.

It is also important that whenever data compression using on-board computation of moments is adopted as the primary means of recovering data it is supplemented by periods when the raw particle data is transmitted with high accuracy to verify the calculations.

While on-board processing of particle observations is a very effective method of reducing telemetry requirements, the value of the technique is critically dependent on knowledge of instrument calibration and in-flight performance. This is additional motivation for conducting the best possible pre-flight instrument calibration and post-launch instrument performance verification.

2.13.2 Transmission and Ground Processing

Once the instrument has made its measurements in space and those data processed by any on-board data processing system, the resulting data set must be sent via telemetry to the ground where data are further processed. The telemetry chain can be very complex (see e.g. *CCSDS* [1997a]) and it is not surprising that individual data bits can be lost or corrupted in the process. Identifying and handling those situations can greatly complicate ground processing.

The telemetry downlink may occasionally have noisy data due to low signal strength and such instances must be identified in ground processing to maintain data integrity. The spacecraft data handling system and telemetry downlink may introduce differences between the time given a specific telemetry packet and the actual time interval that the instrument acquired data and those timing differences may be affected by changes in telemetry modes on the spacecraft. Merging of particle and plasma data with data from other instruments on the spacecraft may also involve corrections for timing between various data acquisition periods. These factors, and others, must be taken into account. For this reason it is suggested that the laboratory calibration of instruments be done in conjunction with a spacecraft simulator and planned ground data processing procedures so that the entire data chain from instrument sensor head to final data analysis is exercised.

Even after exercising the data chain on the ground, in-flight data still may hold surprises. For example, on Ulysses the experiment data records (EDRs) obtained from the spacecraft telemetry were of less than optimum quality during the first few months of the mission. The Ulysses SWICS team then used a 6-bit number available within each individual data frame, indicating the position of the data frame within the 13-minute long instrument cycle of the Ulysses SWICS [*Gloeckler et al.*, 1992] experiment data, to help the Ulysses data management team generate well-formed, time-ordered experiment data records (EDRs). This is an example of how success depends upon understanding of the entire experiment chain from sensor head to the numbers received on the ground.

Recognizing that misunderstandings, misinterpretations, and just plain errors occur frequently, especially if an instrument uses novel techniques or explores new regions in

space, and despite the fact that each team member works as best as possible, the Ulysses SWICS team developed flight data analysis software at two different sites independently. The SWICS team frequently met to compare and exchange their results. This redundant software development allowed it to catch many errors well before much time was lost or even science "results" were obtained that were mere phantoms of an erroneous data interpretation. In 1998 a major effort was made to compare the results of the data analysis software used by the Bern and the Michigan branches of the SWICS team. Differences and even errors were still found in both codes, eight years after launch, but none of them were critical enough to deteriorate the quality of the published results of either group. The result of this intercomparison led to a publication that summarizes the Ulysses SWICS data analysis procedures now adopted by the whole team [*von Steiger et al.*, 2000].

2.14 Conclusion

This chapter has described, sometimes briefly, the very broad spectrum of particle detector systems that either have been flown or will be flown on space missions. The intent was to provide the reader with a sense of the diversity in designs with some idea of their advantages and disadvantages. No matter what instrument design is chosen for a space experiment, it is very important that detailed numerical modeling be performed to determine the expected instrument performance in terms of system field of view, particle energy, and particle species. If possible, this modeling should be extended to provide an estimate of the instrument's ability to reject sources of unwanted response be that due to UV photons, particle scattering within the instrument, or penetrating radiation. Such modeling will provide the indispensable basis to which the results of the laboratory calibration and instrument performance verification procedures described in the next chapter must be compared.

Acknowledgements

The authors would like to thank the following colleagues for their contributions to this chapter: Joseph M. Grebowsky, NASA/GSFC, Justin C. Kasper, MIT/CSR, Keith W. Ogilvie, NASA/GSFC, Dennis J. Chornay, NASA/GSFC, John T. Steinberg, LANL and M. Vosbury, UNH.

Bibliography

Archuleta, R.J. and S.E. DeForest, Efficiency of channel electron multipliers for electrons of 1–50 keV, *Rev. Sci. Instrum.*, **42**, 89–91, 1971.

Balogh, A., Space physics instrumentation and missions, in *Payload and Mission Definition in Space Sciences*, V. Mártínez Pillet, A. Aparicio, F. Sánchez, Eds., Cambridge University Press, Cambridge, 233–322, 2005.

Balogh, A. and A. Pedersen, Space Instruments, *ISSI Scientific Report*, **SR-008**, ESA Publications Division, Noordwijk, 2008.

Balsiger, H., P. Eberhardt, J. Geiss, and E. Kopp, A mass spectrometer for the simultaneous measurement of the neutral and the ion composition of the upper atmosphere, *Rev. Sci. Instrum.*, **42**, 475–476, 1971.

Balsiger, H., P. Eberhardt, J. Geiss, A. Ghielmetti, H.P. Walker, D.T. Young, H. Loidl, and H. Rosenbauer, A satellite-borne ion mass spectrometer for the energy range 0 to 16 keV, *Space Sci. Instrum.*, **2**, 499–521, 1976.

Balsiger, H., K. Altwegg, E. Arijs, J.-L. Bertaux, J.-J. Berthelier, B. Block, P. Bochsler, G.R. Carignan, L. Duvet, P. Eberhardt, B. Fiethe, J. Fischer, L.A. Fisk, S.A. Fuselier, A.G. Ghielmetti, F. Gliem, T.I. Gombosi, M. Illiano, T. Koch, E. Kopp, A. Korth, K. Lange, H. Lauche, S. Livi, A. Loose, T. Magoncelli, C. Mazelle, M. Mildner, E. Neefs, D. Nevejans, H. Rème, J.A. Sauvaud, S. Scherer, A. Schoenemann, E.G. Shelley, J.H. Waite, C. Westermann, B. Wilken, J. Woch, H. Wollnik, P. Wurz, and D.T. Young, Rosetta Orbiter Spectrometer for Ion and Neutral Analysis-ROSINA, *Adv. Space Res.*, **21**, 1527–1535, 1998.

Balsiger, H., K. Altwegg, P. Bochsler, P. Eberhardt, J. Fischer, S. Graf, A. Jäckel, E. Kopp, U. Langer, M. Mildner, J. Müller, T. Riesen, M. Rubin, S. Scherer, P. Wurz, S. Wüthrich, E. Arijs, S. Delanoye, J. De Keyser, E. Neefs, D. Nevejans, H. Rème, C. Aoustin, C. Mazelle, J.-L. Médale, J. A. Sauvaud, J.-J. Berthelier, J.-L. Bertaux, L. Duvet, J.-M. Illiano, S.A. Fuselier, A.G. Ghielmetti, T. Magoncelli, E.G. Shelley, A. Korth, K. Heerlein, H. Lauche, S. Livi, A. Loose, U. Mall, B. Wilken, F. Gliem, B. Fiethe, T.I. Gombosi, B. Block, G.R. Carignan, L.A. Fisk, J.H. Waite, D.T. Young, and H. Wollnik, Rosetta Orbiter Spectrometer for Ion and Neutral Analysis ROSINA, *Space Sci. Rev.*, **128**, 745–801, doi:10.1007/s11214-006-8335-3, 2007.

Bame, S.J., J.R. Asbridge, H.E. Felthauser, E.W. Hones, and I.B. Strong, Characteristics of the plasma sheet in the Earth's magnetotail, *J. Geophys. Res.*, **72**, 113–129, 1967.

Bame, S.J., J.R. Asbridge, H.E. Felthauser, J.P. Glore, H.L. Hawk, and J. Chavez, ISEE-C solar wind plasma experiment, *IEEE Trans. Geosci. Electr.*, **GE-16**, 160–162, 1978.

Bame, S.J., R.H. Martin, D.J. McComas, J.L. Burch, J.A. Marshall, and D.T. Young, Three-dimensional plasma measurements from three-axis stabilized spacecraft, in *Solar System Plasma Physics*, J.H. Waite, Jr., J.L. Burch and R.L. Moore, Eds., Geophys. Monogr. Ser., **54**, American Geophysical Union, Washington, D.C., 441–452, 1989.

Bame, S.J., D.J. McComas, B.L. Barraclough, J.L. Phillips, K.J. Sofaly, J.C. Chavez, B.E. Goldstein, and R.K. Sakurai, The Ulysses solar wind experiment, *Astron. Astrophys. Suppl. Ser.*, **92**, 237–265, 1992.

Barabash, S., R. Lundin, H. Andersson, J. Gimholt, M. Holmström, O. Norberg, M. Yamauchi, K. Asamura, A.J. Coates, D.R. Linder, D.O. Kataria, C.C. Curtis, K.C. Hsieh, B.R. Sandel, A. Fedorov, A. Grigoriev, E. Budnik, M. Grande, M. Carter, D.H. Reading, H. Koskinen, E. Kallio, P. Riihela, T. Säles, J. Kozyra, N. Krupp, S. Livi, J. Woch, J. Luhmann, S. McKenna-Lawlor, S. Orsini, R. Cerulli-Irelli, M. Maggi, A. Morbidini, A. Mura, A. Milillo, E. Roelof, D. Williams, J.-A. Sauvaud, J.-J. Thocaven, T. Moreau, D. Winningham, R. Frahm, J. Scherrer, J. Sharber, P. Wurz, and P. Bochsler, ASPERA-3: Analyser of Space Plasmas and Energetic Ions for Mars Express, *ESA Special Publication*, **SP-1240**, ESA Publications Division, Noordwijk, 121–139, 2004.

Barat, M., J.C. Brenot, J.A. Fayeton, and Y.J. Picard, Absolute detection efficiency of a microchannel plate detector for neutral atoms, *Rev. Sci. Instrum.*, **71**, 2050–2052, 2000.

Bennani, A.L., J. Pebay, and B. Nguyen, Measurement of the absolute detection efficiency of a channel multiplier (channeltron), *J. Phys. E.: Sci Instrum.*, **6**, 1077–1079, 1973.

Bennett, W.H., Radio-frequency mass spectrometer, *J. Appl. Phys.*, **21**, 143–149, 1950.

Benninghoven, A., F.G. Rüdenauer, and H.W. Werner, *Secondary Ion Mass Spectrometry: Basic Concepts, Instrumental Aspects, Applications and Trends (Chemical Analysis)*,

Wiley-Interscience, London, 1987.

Bichsel, H., Straggling in thin silicon detectors, *Rev. Mod. Phys.*, **60**, 663–699, 1988.

Bird, G.A., Aerodynamic effects on atmospheric composition measurements for rocket vehicles in the thermosphere, *Planet. Space Sci.*, **36**, 921–926, 1988.

Blauth, E.W., *Dynamic Mass Spectrometers*, Elsevier, Amsterdam, 1966.

Blush, L.M., F. Allegrini, P. Bochsler, H. Daoudi, A. Galvin, R. Karrer, L. Kistler, B. Klecker, E. Möbius, A. Opitz, M. Popecki, B. Thompson, R.F. Wimmer-Schweingruber, and P. Wurz, Development and calibration of major components for the STEREO/PLASTIC (plasma and suprathermal ion composition) instrument, *Adv. Space Res.*, **36**, 1544–1556, 2005.

Boggess, R.L., L.H. Brace, and N.W. Spencer, Langmuir probe measurements in the ionosphere, *J. Geophys. Res.*, **64**, 1627–1630, 1959.

Bolton, S.J., D.T. Young, J.L. Burch, N. Eaker, J.E. Nordholt, H.O. Funsten, and D.J. McComas, Plasma Experiment for Planetary Exploration (PEPE), in *Space Technology and Applications*, *AIP Conf. Proc.*, **387**, 241–244, 1997.

Bordoni, F., Channel electron multiplier efficiency for 10–1000 eV electrons, *Nucl. Instrum. Methods*, **97**, 405–408, 1971.

Bougeret, J. L., M.L. Kaiser, P.J. Kellogg, R. Manning, K. Goetz, S.J. Monson, N. Monge, L. Friel, C.A. Meetre, C. Perche, L. Sitruk, and S. Hoang, WAVES: The radio and plasma wave investigation on the Wind spacecraft, *Space Sci. Rev.*, **71**, 231–263, 1995.

Brace, L.H., Langmuir probe measurements in the ionosphere, in *Measurement Techniques for Space Plasmas: Particles*, R. Pfaff, J. Borovsky, and D.T. Young, Eds., Geophys. Monogr. Ser., **103**, American Geophysical Union, Washington, D.C., 23–35, 1998.

Brace, L.H., G.R. Carignan, and J.A. Findlay, Evaluation of ionospheric electron temperature measurements by cylindrical probes, *Space Res.*, **11**, 1079–1105, 1971.

Brace, L.H., W.R. Hoegy, R.F. Theis, and L.E. Wharton, Neutral-particle wake method for measuring the atmospheric temperature from a satellite, *J. Geophys. Res.*, **77**, 1885–1895, 1972.

Brace, L.H., R.F. Theis, and A. Dalgarno, The cylindrical electrostatic probes for Atmosphere Explorer-C, -D and -E, *Radio Sci.*, **8**, 341–348, 1973.

Brehm, B., J. Grosser, T. Ruscheinski, and M. Zinner, Absolute detection efficiencies of a microchannel plate detector for ions, *Meas. Sci. Technol.*, **6**, 953–958, doi:10.1088/0957-0233/6/7/015, 1995.

Brinkerhoff, W.B., G.G. Managadze, R.W. McEntire, A.F. Cheng, and W.J. Green, Laser time-of-flight mass spectrometry for space, *Rev. Sci. Instrum.*, **71**, 536–545, 2000.

Brinton, H.C., L.R. Scott, M.W. Pharo, and J.T. Coulson, The Bennett ion-mass spectrometer on Atmosphere Explorer-C and E, *Radio Sci.*, **8**, 323–332, 1973.

Bujor, M., Work function variation across the surface of tungsten and vitreous carbon, in *Photon and Particle Interactions with Surfaces in Space*, R.J.L. Grard, Ed., *Proc. 6^{th} ESLAB Symposium, Astrophysics and Space Science Library*, **37**, Reidel, Dordrecht, 323–330, 1973.

Burch, J.L., J.D. Winningham, V.A. Blevins, N. Eaker, W.C. Gibson, and R.A. Hoffman High-altitude plasma instrument for Dynamics Explorer-A, *Space Sci. Instrum.*, **5**, 455–463, 1981.

Burgoyne, T.W. and G.M. Hieftje, An introduction to ion optics for the mass spectrograph, *Mass Spectr. Rev.*, **15**, 241–259, 1996.

Burke, W.J. and D.L. Reasoner, Absence of the plasma sheet at lunar distance during geomagnetically quiet times, *Planet. and Space Sci.*, **20**, 429–436, 1972.

Canu, P., P.M.E. Décréau, J.G. Trotignon, J.L. Rauch, H.C. Seran, P. Fergeau, M. Lévêque, Ph. Martin, F.X. Sené, E. Le Guirriec, H. Alleyne, and K. Yearby, Identification of natural plasma emissions observed close to the plasmapause by the Cluster-Whisper relaxation sounder, *Ann. Geophys.*, **19**, 1697–1709, 2001.

Carignan, G.R., B.P. Block, J.C. Maurer, A.E. Hedin, C.A. Reber, and N.W. Spencer, The neutral mass spectrometer on Dynamics Explorer B, *Space Sci. Instrum.*, **5**, 429–441, 1981.

Carlson, C.W., D.W. Curtis, G. Paschmann, and W. Michael, An instrument for rapidly measuring plasma distribution functions with high resolution, *Adv. Space Res.*, **2**, 67–70, 1983.

Carlson, C.W. and J.P. McFadden, Design and application of imaging plasma instruments, in *Measurement Techniques in Space Plasmas: Particles*, R. Pfaff, J. Borovsky, and D.T. Young, Eds., Geophys. Monogr. Ser., **102**, American Geophysical Union, Washington, D.C., 123–140, 1998.

CCSDS Report Concerning Lossless Data Compression, Green Book, Consultative Committee for Space Data Systems, **CCSDS121.0-G-1**, 1997a.

CCSDS Recommendation for Lossless Data Compression, Blue Book, Consultative Committee for Space Data Systems, **CCSDS121.0-B-1**, 1997b.

Chennette, D.L., D.W. Datlowe, W.L. Imhof, T.L. Schumaker, and J.D. Tobin, Global spectroscopy and imaging of atmospheric X-ray bremstrahlung. Instrumentation and initial results from the PEM/AXIS instrument aboard the Upper Atmosphere Research Satellite, in *Instrumentation and Terrestrial Atmospheric Remote Sensing*, S. Chakrabarti and A.B. Christensen, Eds., *Proc. SPIE*, **1745**, 16–25 (1992).

Cline C.K., T.E. Pierce, K.H. Purser, and M. Blann, Small-angle scattering of S^{32} and O^{16} beams in thin foils, *Phys. Rev.*, **180**, 450–455, 1969.

Coates, A.J., J.A. Bowles, R.A. Gowen, B.K. Hancock, A.D. Johnstone, and S.J. Kellock The AMPTE UKS three-dimensional ion experiment, *IEEE Trans. Geosci. Remote Sens.*, **23**, 287–292, 1985.

Collin, H.H., J.M. Quinn, G.R. Smith, E. Hertzberg, S. Roselle, and S.J. Battel, Low-energy ion mass spectrometer on CRRES, *J. Spacecraft and Rockets*, **29**, 617–620, 1992.

Coon, J., Vela satellite measurements of particles in the solar wind and the distant geomagnetosphere, in *Radiation Trapped in the Earth's Magnetic Field*, B.M. McCormac, Ed., Astrophysics and Space Science Library, **5**, 231–255, Reidel, Dordrecht, 1966.

Cotter, R.J., The new time-of-flight mass spectrometry, *Analytical Chemistry, News and Features*, **71**, 445A-451A, July 1, 1999.

Cotter, R.J., T.J. Cornish, and W. Bryden, Time-of-flight mass spectrometry new technology for biological and environmental analyses, Cyber Congress on Analytical Biosciences, in *Trends in Analytical Life Sciences*, **1**, mini-review paper 15, Elsevier Science, Amsterdam, 1997.

Cruise, A.M., J.A. Bowles, T.J. Patrick, and C.V. Goodall, *Principles of Space Instrument Design*, Cambridge University Press, Cambridge, 1998.

Dahl, D.A., *SIMION 3D Version 7.0 User's Manual*, Idaho National Engineering and Environmental Laboratory, **INEEL-95/0403**, 2000.

Dawson, P.H., Quadrupole mass analyzers: Performance, design and some recent applications, *Mass Spectrom. Rev.*, **5**, 1–37, 1986.

Dawson, P.H., *Quadrupole Mass Spectrometry and its Applications*, AVS Classics in Vacuum Science and Technology, Springer, Heidelberg, 1995.

Décréau, P.M.E., C. Béghin, and M. Parrot, Electron density and temperature as measured by the mutual impedance experiment on board GEOS 1, *Space Sci. Rev.*, **22**, 581–594, 1978a.

Décréau, P.M.E., J. Etcheto, K. Knott, A. Pedersen, G.L. Wrenn, and D.T. Young, Multiexperiment determination of plasma density and temperature, *Space Sci. Rev.*, **22**, 633–645, 1978b.

Décréau, P.M.E., M. Hamelin, R. Massif, H. De Feraudy, E. Pawela, S. Perraut, R. Potelette, and A. Bahnsen, Plasma probing by active experiments on the Viking satellite, *Ann. Geophys., Ser. A*, **5**, 181–186, 1987.

Décréau, P.M.E., P. Fergeau, V. Krasnosels'kikh, M. Lévêque, P. Martin, O. Randriamboarison, F.X. Sené, J.G. Trotignon, P. Canu, and P.B. Mögensen, Whisper, A resonance sounder and wave analyzer: Performances and perspectives for the Cluster mission, *Space Sci. Rev.*, **79**, 157–193, 1997.

de Hoffmann, E. and V. Stroobant, *Mass Spectrometry*, 2^{nd} Ed., Wiley, Chichester, 2001.

DeSerio, R., Spherical sector electrostatic analyzers for measurements of energy and angular distributions, *Rev. Sci. Instrum.*, **60**, 381–388, 1989.

Di Lellis, A.M., S. Orsini, S. Livi, P. Wurz, and A. Milillo, The neutral atoms detector technologies developed for the SERENA package in view of ESA BepiColombo planetary orbiter, in *Proc. 37th ESLAB Symposium, Tools and Technologies for Future Planetary Exploration*, *ESA Special Publication*, **SP-543**, ESA Publications Division, Noordwijk, 2004.

Duckworth, H.E. and S.N. Ghoshal, High-resolution mass spectroscopes, in *Mass Spectrometry*, C.A. McDowell, Ed., McGraw-Hill, New York, 201–274, 1963.

Duckworth, H.E., R.C. Barber, and V.S. Venkatasubramanian, *Mass Spectroscopy*, 2^{nd} Ed. Cambridge University Press, 1986.

Erlandson, R.E., M.T. Bois, O.M. Uy, J.M. Grebowsky, and J.T. Coulson, The MSX ion mass spectrometer: Measurement of contaminant and ambient ions, *Proc. SPIE*, **2261**, 181–187, 1994.

Eschard, G. and B.W. Manley, Principle and characteristics of channel electron multipliers, *Acta Electronica*, **14**, 19–39, 1971.

Escoubet, C.P., A. Pedersen, R. Schmidt, and P.-A. Lindqvist, Density in the magnetosphere inferred from the ISEE-1 spacecraft potential, *J. Geophys. Res.*, **102**, 17595–17609, 1997.

Farmer, J.B., Types of mass spectrometers, in *Mass Spectrometry*, C.A. McDowell, Ed., McGraw-Hill, New York, 7–44, 1963.

Fillius R.W. and C.E. McIlwain, Measurements of the Jovian radiation belts, *J. Geophys. Res.*, **79**, 3589–3599, 1974.

Findlay, J.A. and L.H. Brace, Cylindrical electrostatic probes employed on Alouette II and Explorer 31 satellites, *Proc. IEEE*, **57**, 1054–1056, 1969.

Frank, L.A., D.M. Yeager, H.D. Owens, K.L. Ackerson, and M.R. English Quadrispherical LEPEDEAS for ISEE's-1 and -2 plasma measurements, *IEEE Trans. Geosci. Electr.*, **16**, 221–225, 1978.

Fraser, G.W. and E. Mathieson, Signal location by uniform resistive anodes, (A) Square anodes in the DC limit, *Nucl. Instrum. Methods*, **179**, 591–604, 1981.

Funsten, H.O., D.M. Suszcynsky, R.W. Harper, J.E. Nordholt, and B.L. Barraclough, Effect of local electric fields on microchannel plate detection of incident 20 keV protons, *Rev. Sci. Instrum.*, **67**, 145–154, 1996.

Funsten, H.O., D.J. McComas, and M.A. Gruntman, Neutral atom imaging: UV rejection techniques, in *Measurement Techniques in Space Plasmas: Fields*, R. Pfaff, J. Borovsky, and D.T. Young, Eds., Geophys. Monogr. Ser., **103**, American Geophysical Union, Washington, D.C., 251–256, 1998.

Gao, R.S., P.S. Gibner, J.H. Newman, K.A. Smith, and R.F. Stebbings, Absolute and angular efficiencies of a microchannel-plate position-sensitive detector, *Rev. Sci. Instrum.*, **55**, 1756–1759, 1984.

Garrard, T.L., N. Gehrels, and E. Stone, The Galileo heavy element monitor, *Space Sci. Rev.*, **60**, 305–315, 1992.

Geiswiller, J., Application de la méthode des distributions surfaciques de charges discrètes à la modélisation d'antennes électriques en milieu plasma, Ph.D. thesis, Université d'Orléans, p. 252, 2001.

Ghielmetti, A. and E. Shelley, Angle, energy, and time-of-flight focusing with poloidal toroid electrostatic analyzers, *Nucl. Instrum. Methods A*, **298**, 181–188, 1990.

Gilmore, I.S. and M.P. Seah, Fluence, flux current and current density measurement in Faraday cups for surface analysis, *Surface and Interface Analysis*, **23**, 248–258, 1995.

Gloeckler, G., J. Geiss, H. Balsiger, P. Bedini, J.C. Cain, J. Fisher, L. A. Fisk, A. B. Galvin, F. Gliem, and D.C. Hamilton, The Solar Wind Ion Composition Spectrometer, *Astron. Astrophys. Suppl. Ser.*, **92**, 267–289, 1992.

Gloeckler, G., H. Balsiger, A. Bürgi, P. Bochsler, L.A. Fisk, A.B. Galvin, J. Geiss, F. Gliem, D.C. Hamilton, T.E. Holzer, D. Hovestadt, F.M. Ipavich, E. Kirsch, R.A. Lundgren, K.W. Ogilvie, R.B. Sheldon, and B. Wilken, The solar wind and suprathermal ion composition investigation on the Wind spacecraft, *Space Sci. Rev.*, **71**, 79–124 1995.

Gloeckler, G., J. Cain, F.M. Ipavich, E.O. Tums, P. Bedini, L.A. Fisk, T.H. Zurbuchen, P. Bochsler, J. Fischer, R.F. Wimmer-Schweingruber, J. Geiss, and R. Kallenbach, Investigation of the composition of solar and interstellar matter using solar wind and pickup ion measurements with SWICS and SWIMS on the ACE spacecraft, *Space Sci. Rev.*, **86**, 497–539, 1998.

Goruganthu, R.R. and W.G. Wilson, Relative electron detection efficiency of microchannel plates from 0–3 keV, *Rev. Sci. Instrum.* **55**, 2030–2033, 1984.

Gosling, J.T., J.R. Asbridge, S.J. Bame, and W.C. Feldman, Effects of a long entrance aperture upon the azimuthal response of spherical section electrostatic analyzers, *Rev. Sci. Instrum.*, **49**, 1260–1268, 1978.

Gosling, J.T., M.F. Thomsen, and R.C. Anderson, A Cookbook for Determining Essential Transmission Characteristics of Spherical Section Electrostatic Analyzers, Los Alamos Report, **LA-10147-M**, 1984.

Gowen, R.A. and A. Smith, Square root data compression, *Rev. Sci. Instrum.*, **74**, 3853–3861, 2003.

Grebowsky, J.M., H.A. Taylor, M.W. Pharo III, and N. Reese, Thermal ion perturbation observed in the vicinity of the Space Shuttle, *Planet. Space Sci.*, **35**, 501–513, 1987.

Grebowsky, J.M. and A. Schaefer, Ion mass spectrometer measurements from the Space Shuttle, *Indian J. Radio Space Phys.*, **19**, 49–61, 1990.

Gross, J.H., *Mass Spectrometry*, Springer-Verlag, Berlin, 2004.

Gruntman, M., Energetic neutral atom imaging of space plasmas, *Rev. Sci. Instrum.*, **68**, 3617–3656, 1997.

Gurnett, D.A., W.S. Kurth, D.L. Kirchner, G.B. Hospodarsky, T.F. Averkamp, P. Zarka, A. Lecacheux, R. Manning, A. Roux, P. Canu, N. Cornilleau-Wehrlin, P. Galopeau, A. Meyer, R. Boström, G. Gustafsson, J.-E. Wahlund, L. Åhlén, H.O. Rucker, H.P. Ladreiter, W. Macher, L.J.C. Woolliscroft, H. Alleyne, M.L. Kaiser, M.D. Desch, W.M. Farnell, C.C. Harvey, P. Louarn, P.J. Kellogg, K. Goetz, and A. Pedersen, The Cassini radio and plasma wave investigation, *Space Sci. Rev.*, **114**, 395–463, 2004.

Gustafsson, G., R. Bostrom, G. Holmgren, A. Lundgren, K. Stasiewicz, L. Ahlen, F.S. Mozer, D. Pankow, P. Harvey, P. Berg, R. Ulrich, A. Pedersen, R. Schmidt, A. Butler, A. Fransen, D. Klinge, C.-G. Falthammar, P.-A. Lindqvist, S. Christenson, J. Holtet, B. Lybekk, T.A. Sten, P. Tanskanen, K. Lappalainen, and J. Wygant, The electric field experiment for the Cluster mission, *Space Sci. Rev.*, **79**, 137–156, 1997.

Hamilton, D.C., G. Gloeckler, F.M. Ipavich, R.A. Lundgren, R.B. Sheldon, and D. Hovestadt New high-resolution electrostatic ion mass analyzer using time of flight, *Rev. Sci. Instrum.*, **61**, 3104–3106, 1990.

Hanson, W.B., U. Ponzi, C. Arduini, and M. Di Ruscio, A satellite anemometer, *J. Astronaut. Sci.*, **40**, 429–438, 1992.

Hardy, D.A., L.K. Schmitt, M.S. Gussenhoven, F.J. Marshall, H.C. Yeh, T.L. Schumaker, A. Huber, and J. Pantazis, Precipitating electron and ion detectors (SSJ/4) for the block 5D/flights 6-10 DMSP satellites: calibration and data presentation, Environmental Research Papers No. **AFGL-TR-84-0317-902**, Air Force Geophysics Laboratory, Hanscom AFB, 1984.

Hardy, D.A., D.M. Walton, A.D. Johnstone, M.F. Smith, M.P. Gough, A. Huber, J. Pantazis, and R. Burkhardt, Low energy plasma analyzer, *IEEE Trans. Nucl. Sci.*, **40**, 246–251, 1993.

Harvey, C.C., R. Manning, J. Etcheto, Y. de Javel, and M. Petit, The ISEE electron density experiment, *IEEE Trans. Geosci. Electr.*, **GE-16**, 231–238, 1978.

Häusler, B., R.R. Anderson, D.A. Gurnett, H.C. Koons, R.H. Holzworth, O.H. Bauer, R. Treumann, K. Gnaiger, D. Odem, W.B. Harbridge, and F. Eberl, The plasma wave Instrument on board the AMPTE IRM Satellite, *IEEE Trans. Geosci. Remote Sens.*, **GE-23**, 267–273, 1985.

Hawkes, P.W. and E. Kasper, *Principles of Electron Optics*, Academic Press, London, 1996.

Heikkila, W.J., J.B. Smith, J. Tarstrup, and J.D. Winningham, The soft particle spectrometer on the ISIS-1 satellite, *Rev. Sci. Instrum.*, **41**, 1393–1402, 1970.

Hilchenbach, M., Space-borne mass spectrometer instrumentation, *Int. J. of Mass Spectrometry*, **215**, 113–129, 2002.

Horowitz, R. and H.E. La Gow, Upper air pressure and density measurements from 90-220 kilometers with the Viking 7 rocket, *J. Geophys. Res.*, **62**, 57–78, 1957.

Horowitz, P. and W. Hill, *The Art of Electronics*, 2^{nd} Ed., Cambridge University Press, Cambridge, 1989.

Hovestadt, D., M. Hilchenbach, A. Bürgi, B. Klecker, P. Laeverenz, M. Scholer, H. Grunwaldt, W.I. Axford, S. Livi, E. Marsch, B. Wilken, H.P. Winterhoff, F.M. Ipavich, P. Be-

dini, M.A. Coplan, A.B. Galvin, G. Gloeckler, P. Bochsler, H. Balsiger, J. Fischer, J. Geiss, R. Kallenbach, P. Wurz, K.-U. Reiche, F. Gliem, D.L. Judge, H.S. Ogawa, K.C. Hsieh, E. Möbius, M.A. Lee, G.G. Managadze, M.I. Verigin, and M. Neugebauer, CELIAS - Charge, Element and Isotope Analysis System for SOHO, *Solar Phys.*, **162**, 441–481, 1995.

Hughes, A.L. and V. Rojansky, On the analysis of electronic velocities by electrostatic means, *Phys. Rev.*, **34**, 284–295, 1929.

Iwamoto, I., T. Suitz, and N. Fugono, The Benett ion mass spectrometer aboard "TAIYO" (CPI), *J. Geomag. Geoelectr.*, **27**, 303–320, 1975.

James, A.M., A.D. Johnstone, D.M. Walton, O.L. Vaisberg, and A.O. Fedorov, A fast omni-directional ion detector for the study of space plasmas, in: *Measurement Techniques in Space Plasmas: Particles*, R.F. Pfaff, J. E. Borovsky, D.T. Young, Eds., Geophys. Monogr. Ser., **102**, American Geophysical Union, Washington, D.C., 281–285, 1998.

Janni J.F., Proton range-energy tables, 1 keV – 10GeV: Part 1 compounds, *Atomic Data and Nuclear Data Tables*, **27**, 147–339, 1982a.

Janni J.F., Proton range-energy tables, 1 keV – 10GeV: Part 2 elements, *Atomic Data and Nuclear Data Tables*, **27**, 341–529, 1982b.

Johnson, C.Y., Bennett radio frequency spectrometer, in *The Encyclopedia of Spectroscopy*, G.L. Clarke, Ed., Rheinhold, New York, 587–598, 1960.

Johnstone, A.D., A.J. Coates, B. Wilken, W. Stüdemann, and W. Weiss, The Giotto three-dimensional positive ion analyser, *J. Phys.E: Sci. Instrum.*, **20**, 795–802, 1987.

Jones, D., Introduction to the S-300 wave experiment onboard GEOS, *Space Sci. Rev.*, **22**, 327–332, 1978.

Kasprzak, W.T, H. Niemann, D. Harpold, J. Richards, H. Manning, E. Patrick, and P. Mahaffy, Cassini orbiter ion and neutral mass spectrometer instrument, *Proc. SPIE*, **2803**, 129–140, 1996.

Kayser, D.C., L.H. Johnson, W.E. Potter, and A.O. Nier, Theory of the fly-through mode for neutral mass spectrometers, *Space Sci. Instrum.*, **4**, 339–350, 1979a.

Kayser, D.C., A.O. Nier, E.L. Breig, R.A. Power, and W.B. Hanson, Direct *in situ* measurements of the thermospheric temperature, *J. Geophys. Res.*, **84**, 4321–4327, 1979b.

Kayser, D.C., W.T. Chater, C.K. Howey, and J.B. Pranke, The upper atmosphere composition spectrometer, *J. Spacecraft and Rockets*, **23**, 336–341, 1986.

Kayser, D.C., Measurements of the thermospheric meriodonal wind from the S85-1 spacecraft, *J. Geophys. Res.*, **93**, 9979–9986, 1988.

Kleinknecht, K., *Detectors for Particle Radiation*, Cambridge University Press, Cambridge, 1998.

Klobuchar, R.L., J.J. Ahumada, J.V. Michael, and P.J. Karol, Details of dead time losses in scaling and multiscaling, *Rev. Sci. Instrum.*,**45**, 1073–1076, 1974.

Knoll, G.F., *Radiation Detection and Measurement*, John Wiley & Sons, New York, 2000.

Knoll, R., G. Epstein, S. Hoang, G. Huntzinger, J.L. Steinberg, J. Fainberg, F. Grena, R.G. Stone, and S.R. Mosier, The 3-dimensional radio mapping experiment on ISEE-C, *IEEE Trans. Geosci. Electr.*, **GE-16**, 199–204, 1978.

Knutson, J.R., D.C. Kayser, and W.E. Potter, Mass spectrometric measurement of the thermospheric wind, *J. Geophys. Res.*, **82**, 5253–5256, 1977.

Koehn, P.L., T.H. Zurbuchen, G. Gloeckler, R.A. Lundgren, and L.A. Fisk, Measuring the plasma environment at Mercury: The fast imaging plasma spectrometer, *Meteoritics and*

Planetary Sci., **37**, 1173–1191, 2002.

Krankowsky, D., P. Lammerzahl, I. Herrwerth, J. Woweries, P. Eberhardt, U. Dolder, U. Herrmann, W. Schulte, J.J. Bertherier, J.M. Illiano, R.R. Hodges, and J.H. Hoffman, *In-situ* gas and ion measurements at comet Halley, *Nature*, **321**, 326–329, 1986.

Kurz, E.A., Channel electron multipliers, *American Laboratory*, **11**, 67–82, 1979a.

Laakso, H., T. Aggson, and R.F. Pfaff, Jr., Plasma gradient effects on double probe measurements in the magnetosphere, *Ann. Geophys.*, **13**, 130–146, 1995.

Lampton, M., The microchannel image intensifier, *Sci. American*, **245**, 62–71, 1981.

Lampton, M. and C.W. Carlson, Low-distortion resistive anodes for two-dimensional position sensitive MCP systems, *Rev. Sci. Instrum.*, **50**, 1093–1097, 1979.

Lampton, M., O. Siegmund, and R. Raffanti, Delay line anodes for microchannel-plate spectrometers, *Rev. Sci. Instrum.*, **58**, 2298–2305, 1987.

Langmuir, I. and H. Mott-Smith, Jr., Studies of electric discharges in gas at low pressures, *Gen. Elec. Rev.*, **27**, 616, 1924.

Leo, W.R., *Techniques for Nuclear and Particle Physics Experiments*, Springer, Berlin, 1987.

Lin. R.P., K.A. Anderson, S. Ashford, C. Carlson, D. Curtis, R. Ergun, D. Larson, J. McFadden, M. McCarthy, G.K. Parks, H. Rème, J.M. Bosqued, J. Coutelier, F. Cotin, C. d'Uston, K.-P. Wenzel, T.R. Anderson, J. Henrion, and G. Paschmann, A three-dimensional plasma and energetic particle investigation for the Wind spacecraft, *Space Sci. Rev.*, **71**, 125–153, 1995.

Lutz, G., *Semiconductor Radiation Detectors, Device Physics*, Springer-Verlag, New York, 1999.

Mahaffy, P., Mass spectrometers developed for planetary missions, in *Laboratory Astrophysics and Space Research*, P. Ehrenfreund, K. Krafft, H. Kochan, and V. Pirronello, Eds., Astrophysics and Space Science Library, **236**, Kluwer Acad. Publ., Dordrecht, 355–376, 1999.

Mahaffy, P.R., D. Harpold, and H.B. Niemann, SIMS on the Comet Rendezvous Asteroid Flyby Mission (CRAF) in *Secondary Ion Mass Spectrometry, SIMS VI*, A. Benninghoven et al., Eds., Wiley, New York, 957–960, 1988.

Mahaffy, P.R. and K. Lai, An electrostatic quadrupole deflector for mass spectrometer applications, *J. Vac. Sci. Technol. A*, **8**, 3244–3246, 1990.

Mahaffy, P.R., W.T. Kasprzak, D. Harpold, H.B. Niemann, R. Bitzel, B. Block, J. Demick, S. Feng, C. Gunderson, S. Leake, J. Maurer, R. Miller, T. Owen, E. Patrick, M. Paulkovich, E. Raaen, J. Richards, F. Tan, S. Schwinger, S. Way, and J. Winchester, The neutral gas and ion mass spectrometer for the CONTOUR mission, prepared for *Space Sci. Rev.*, 2002.

Managadze, G.G. and I. Yu Shutyaev, Exotic instruments and applications of laser ionization mass spectrometry in space research, in *Laser Ionization Mass Analysis*, A. Vertes, R. Gijbels, and F. Adams, Eds., Chemical Analysis Series, **124**, John Wiley & Sons, Inc., 505–549, 1993.

Martel, H.C., An Investigation of the Omegatron Type Mass Spectrometer, Ph.D. thesis (http://resolver.caltech.edu/CaltechETD:etd-06072004-153528), California Institute of Technology, Pasadena, CA, 1956.

Martin, C., P. Jelinsky, M. Lampton, R.F. Malina, and H.O. Anger, Wedge-and-strip anodes for centroid-finding position-sensitive photon and particle detectors, *Rev. Sci. Instrum.*, **52**, 1067–1074, 1981.

Mattauch, J. and R. Herzog, Über einen neuen Massenspektrographen, *Z. Phys*, **89**, 786–795, 1934.

Matsumoto, H., T. Okada, K. Hashimoto, I. Nagano, S. Yagitani, M. Tsutsui, Y. Kasaba, K. Tsuruda, H. Hayakawa, A. Matsuoka, S. Watanabe, H. Ueda, Y. Kasahara, Y. Omura, K. Ishisaka, T. Imachi, and Y. Tateno, Low Frequency plasma wave Analyzer (LFA) onboard the PLANET-B spacecraft, *Earth Planets Space*, **50**, 223–228, 1998.

McComas, D.J. and J.E. Nordholt, New approach to 3-D, high sensitivity, high mass resolution space plasma composition measurements, *Rev. Sci. Instrum.*, **61**, 3095–3097, 1990.

McComas, D.J., F. Allegrini, C.J. Pollock, H.O. Funsten, S. Ritzau, and G. Gloeckler, Ultrathin ($\sim$ 10 nm) carbon foils in space instrumentation, *Rev. Sci. Instrum.*, **75**, 4863–4870, 2004.

McDowell, C.A., *Mass Spectrometry*, McGraw-Hill, New York, 1963.

McFadden, J.P., C.W. Carlson, and M.H. Boehm, Field-aligned electron precipitation at the edge of an arc, *J. Geophys. Res.*, **91**, 1723–1730, 1986.

McFadden, J.P. and C.W. Carlson, Computer simulation in designing electrostatic optics for space plasma experiments, in *Measurement Techniques in Space Plasmas: Particles*, R. Pfaff, J. Borovsky, and D.T. Young, Eds., Geophys. Monogr. Ser., **102**, American Geophysical Union, Washington, D.C., 249–256, 1998.

McKinley, R.R., G.K. Bienkkowski, and S.M. Siskind, Final report for a low altitude satellite interaction study (neutral gases), contract NAS5-11241, *NASA Contract. Rep. 111136*, **AC N71-10611**, 1970.

Mel'nikov, V.V., I.A. Savenko, B.I. Savin, and P.I. Shavrin, Experiment in the use of an electrostatic analyzer on the Cosmos-12 satellite, *Geomagn. Aeron.*, **5**, 107–112, 1965.

Mitchell, D.G., S.E. Jaskulek, C.E. Schlemm, E.P. Keath, R.E. Thompson, B.E. Tossman, J.D. Boldt, J.R. Hayes, G.B. Andrews, N. Paschalidis, D.C. Hamilton, R.A. Lundgren, E.O. Tums, P. Wilson IV, H.D. Voss, D. Prentice, K.C. Hsieh, C.C. Curtis, and F.R. Powell, High Energy Neutral Atom (HENA) imager for the IMAGE mission, *Space Sci. Rev.*, **91**, 67–112, 2000.

Montgomery, M.D., J.R. Asbridge, S.J. Bame, and E.W. Hones, Low-energy electron measurements and spacecraft potential: Vela 5 and Vela 6, in *Photon and Particle Interactions with Surfaces in Space*, R.J.L. Grard, Ed., Reidel, Dordrecht, 1973.

Moore, J.H., C.C. Davis, and M.A. Coplan, *Building Scientific Apparatus, a Practical Guide to Design and Construction*, 2^{nd} Ed., Addison-Wesley, Redwood City, 1989.

Moore, T.E., C.J. Pollock, R.L. Arnoldy, and P.M. Kintner, Preferential O^+ heating in the topside ionosphere, *Geophys. Res. Lett.*, **13**, 901–904, 1986.

Moore, T.E., D.J. Chornay, M.R. Collier, F.A. Herrero, J. Johnson, M.A. Johnson, J.W. Keller, J.F. Laudadio, J.F. Lobell, K.W. Ogilvie, P. Rozmarynowski, S.A. Fuselier, A.G. Ghielmetti, E. Hertzberg, D.C. Hamilton, R. Lundgren, P. Wilson, P. Walpole, T.M. Stephen, B.L. Peko, B. Van Zyl, P. Wurz, J.M. Quinn, and G.R. Wilson, The low-energy neutral atom imager for IMAGE, *Space Sci. Rev.*, **91**, 155–195, 2000.

Mott-Smith, J.M. and I. Langmuir, The theory of collectors in gaseous discharges, *Phys. Rev.*, **28**, 727–763, 1926.

Mukai, T., S. Machida, Y. Saito, M. Hirahara, T. Teresawa, N. Kaya, T. Obara, M. Ejiri, and A. Nishida, The Low Energy Particle (LEP) experiment onboard the GEOTAIL satellite, *J. Geomag. Geoelectr.*, **46**, 669–692, 1994.

Mura, A., S. Orsini, A. Milillo, A.M. Di Lellis, and E. De Angelis, Neutral atom imaging at Mercury, *Planet. and Space Sci.*, **54**, 144–152, 2006.

Newton, G.P., W.T. Kasprzak, and D.T. Pelz, Equatorial composition in the 137- to 225-km region from the San Marco 3 mass spectrometer, *J. Geophys. Res.*, **79**, 1929–1941, 1974.

Niemann, H.B. and B.C. Kennedy, Omegatron mass spectrometer for partial pressure measurements in upper atmosphere, *Rev. Sci. Instrum.*, **37**, 722–728, doi:10.1063/1.1720304, 1966.

Niemann, H.B. and W.T. Kasprzak, Comparative neutral composition instrumentation and new results, *Adv. Space Res.*, **2**, 261–270, 1983.

Niemann, H.B., J.R. Booth, J.E. Cooley, R.E. Hartle, W.T. Kasprzak, N.W. Spencer, S.H. Way, D.M. Hunten, and G.R. Carignan, Pioneer Venus Orbiter neutral gas mass spectrometer experiment, *IEEE Trans. Geosci. Electr. Remote Sens.*, **GE-18**, 60–65, 1980.

Niemann, H.B., D.N. Harpold, S.K. Atreya, G.R. Carignan, D.M. Hunten, and T.C. Owen, The Galileo Probe neutral mass spectrometer, *Space Sci. Rev.*, **60**, 111–142, 1992.

Niemann, H.B., S. Atreya, S.J. Bauer, K. Biemann, B. Block, G. Carignan, T. Donahue, L. Frost, D. Gautier, D. Harpold, D. Hunten, G. Israel, J. Luhnine, K. Mauersberger, T. Owen, F. Raulin, J. Richards, and S. Way, The gas chromatograph mass spectrometer aboard Huygens, *ESA Special Publication*, **SP-1177**, ESA Publications Division, Noordwijk, 85–107, 1997.

Niemann, H.B., D.N. Harpold, S. Feng, W.T. Kasprzak, S.H. Way, S.K. Atreya, B. Block, G.R. Carignan, T.M. Donahue, A.F. Nagy, S.W. Bougher, D.M. Hunten, T.C. Owen, S.J. Bauer, H.J. Hayakawa, T. Mukai, Y.N. Miura, and N. Sugiura, The Planet-B neutral gas mass spectrometer, *Earth Planets Space*, **50**, 785–792, 1998.

Nier, A.O., W.E. Potter, D.R. Hickman, and K. Mauersberger, The open-source neutral-mass spectrometer on Atmosphere Explorer-C, -D, and -E, *Radio Sci.*, **8**, 271–276, 1973.

Nier, A.O. and D.J. Schuttler, High-performance double focusing mass spectrometer, *Rev. Sci. Instrum.*, **56**, 214–219, 1985.

NIST02 Mass Spectral Library, U.S. Department of Commerce, Technology Administration, National Institute of Standards and Technology, Standards Reference Data Program, Gaithersburg, MD 20899, 2002.

O'Brien, B.J., C.D. Laughlin, and D.A. Gurnett, High-latitude geophysical studies with satellite Injun 3, 1. Description of the satellite, *J. Geophys. Res.*, **69**, 1–12, 1964.

O'Brien, B.J., F. Abney, J. Burch, R. Harrison, R. LaQuey, and T. Winiecki, SPECS, a versatile space-qualified detector of charged particles, *Rev. Sci. Instrum.*, **38**, 1058–1067, 1967.

Offermann, D. and H. Trinks, A rocket-borne mass spectrometer with helium-cooled ion-source, *Rev. Sci. Instrum.*, **42**, 1836–1843, 1971.

Ogilvie, K.W., T. McIlrath, and T.D. Wilkerson, A mass energy spectrometer for space plasmas, *Rev. Sci. Instrum.*, **39**, 441–451, 1968.

Ogilvie, K.W., D.J. Chornay, R.J. Fritzenreiter, F. Hunsaker, J. Keller, J. Lobell, G. Miller, J.D. Scudder, E.C. Sittler, Jr., R.B. Torbert, D. Bodet, G. Needell, A.J. Lazarus, J. T. Steinberg, J.H. Tappan, A. Mavretic, and E. Gergin, SWE, A comprehensive plasma instrument for the wind spacecraft, *Space Sci. Rev.*, **71**, 55–77, 1995.

Ogasawara, V., K. Asamura, T. Mukai, and Y. Saito, Avalanche photo diode for measurement of low-energy electrons, *Nucl. Instrum. Methods A*, **545**, 744–752, 2005.

Ogasawara, K., K. Asamura, T. Takashima, Y. Saito, and T. Mukai, Rocket observation of energetic electrons in the low-altitude auroral ionosphere during the DELTA campaign, *Earth Plan. Sci.*, **58**, 1155–1164, 2006.

Pages L., E. Bertel, H. Joffre, and L. Sklavenitis, Energy loss,range and bremsstrahlung, yield for 10 keV to 100 MeV electrons in various elements and chemical compounds *Atomic Data* **4**, 1–127, 1972.

Panitz, J.A., and J.A. Foesch, Areal detection efficiency of channel electron multiplier arrays, *Rev. Sci Instrum.*, **47**, 44–49, 1976.

Paolini, F.R. and G.C. Theodoridis, Charged particle transmission through spherical plate electrostatic analyzers, *Rev. Sci. Instrum.*, **38**, 579–588, 1967.

Paschmann, G., H. Loidl, P. Obermayer, M. Ertl, R. Laborenz, N. Sckopke, W. Baumjohann, C.W. Carlson, and D.W. Curtis, The plasma instrument for AMPTE IRM, *IEEE Trans. Geosci. Remote Sens.*, **GE-23**, 262–266, 1985.

Paul, W., Electromagnetic traps for charged and neutral particles, in *Nobel Prize Lectures in Physics 1981–1990*, World Scientific Publishing, Singapore, 601–622, 1993.

Paul, W. and H.S. Steinwedel, A new mass spectrometer without a magnetic field, *Z. Naturforsch.*, **8A**, 448–450, 1953.

Pelz, D.T., C.A. Reber, A.E. Hedin, and G.R. Carignan, A neutral-atmosphere composition experiment for the Atmosphere Explorer-C, -D, and -E, *Radio Sci.*, **8**, 277–285, 1973.

Pfaff, R.F, J.E. Borovsky, and D.T. Young, Eds., *Measurement Techniques in Space Plasmas: Particles*, Geophys. Monogr. Ser., **102**, American Geophysical Union, Washington, D.C., 1998a.

Pfaff, R.F, J.E. Borovsky, and D.T. Young, Eds., *Measurement Techniques in Space Plasmas: Fields*, Geophys. Monogr. Ser., **103**, American Geophysical Union, Washington, D.C., 1998b.

Pollock, C.J., K. Asamura, J. Baldonado, M.M. Balkey, P. Barker, J.L. Burch, E.J. Korpela, J. Cravens, G. Dirks, M.-C. Fok, H.O. Funsten, M. Grande, M. Gruntman, J. Hanley, J.-M. Jahn, M. Jenkins, M. Lampton, M. Marckwordt, D.J. McComas, T. Mukai, G. Penegor, S. Pope, S. Ritzau, M.L. Schattenburg, E. Scime, R. Skoug, W. Spurgeon, T. Stecklein S. Storms, C. Urdiales, P. Valek, J.T.M van Beek, S.E. Weidner, M. Wüest, M.K. Young, and C. Zinsmeyer, Medium Energy Neutral Atom (MENA) imager for the IMAGE mission, *Space Sci. Rev.*, **91**, 113–154, 2000.

Porat, D.I., Review of sub-nanosecond time-interval measurements, *IEEE Trans. Nucl. Sci.*, **NS-20**, 36–51, 1973.

Potter, W. and K. Maurersberger, Spiral electron multiplier operation characteristics using positive ions, *Rev. Sci. Instrum.*, **43**, 1327–1330, 1972.

Purcell, E.M., The focusing of charged particles by a spherical condenser, *Phys. Rev.*, **54**, 818–826, 1938.

Reber, C.A. and L.G. Hall, A double focusing magnetic mass spectrometer for satellite use, NASA Technical Note, **TN D-3211**, National Aeronautics and Space Administration, Washington, D.C., 1966.

Redus R.H., B.K. Dichter, M.R. Oberhardt, J.O. McGarity, J. Dalcomo, S. Woolf, A.C. Huber, and J.A. Pantazis, Design, development and calibration of a high energy proton telescope for space radiation studies, *Nucl. Instrum. Methods A*, **482**, 281–296, 2002.

Reinisch, B.W., D.M. Haines, K. Bibl, G. Cheney, I.A. Galkin, X. Huang, S.H. Myers, G.S. Sales, R.F. Benson, S.F. Fung, J.L. Green, S. Boardsen, W.W.L. Taylor, J.-L. Bougeret, R. Manning, N. Meyer-Vernet, M. Moncuquet, D.L. Carpenter, D.L. Gallagher, and P. Reiff, The radio plasma imager investigation on the IMAGE spacecraft, *Space Sci. Rev.*, **91**, 319–359, 2000.

Rème, H., F. Cotin, A. Cros, J.L. Médale, J.A. Sauvaud, C. D'Uston, K.A. Anderson, C.W. Carlson, D.W. Curtis, R.P. Lin, A. Korth, A.K. Richer, A. Loidl, and D.A. Mendis, The Giotto electron plasma experiment, *J. Phys. E*, **20**, 721–731, 1987.

Rème, H., J.M. Bosqued, J.A. Sauvaud, A. Cros, J. Dandouras, C. Aoustin, J. Bouyssour, Th. Camus, J. Cuvilo, C. Martz, J.L. Medale, H. Perrier, D. Romefort, J. Rouzaud, C. d'Uston, E. Möbius, K. Crocker, M. Granoff, L.M. Kistler, M. Popecki, D. Hovestadt, B. Klecker, G. Paschmann, M. Scholer, C.W. Carlson, D.W. Curtis, R.P. Lin, J.P. McFadden, V. Formisano, E. Amata, M.B. Bavassano-Cattaneo, P. Baldetti, G. Belluci, R. Bruno, G. Chionchio, A. Di Lellis, E.G. Shelley, A.G. Ghielmetti, W. Lennartsson, A. Korth, H. Rosenbauer, R. Lundin, S. Olsen, G.K. Parks, M. McCarthy, and H. Balsiger, The Cluster Ion Spectrometry (CIS) experiment, *Space Sci. Rev.*, **79**, 303–350, 1997.

Rice, R.F. and J.R. Plaunt. Adaptive variable-length coding for efficient compression of spacecraft television data. *IEEE Trans. Comm.*, **19**, 889–897, 1971.

Rice, R.F., P.-S. Yeh, and W.H. Miller, Algorithms for high speed universal noiseless coding, in *Proc. AIAA Computing in Aerospace 9 Conference*, Paper **AIAA-93-4541** American Institute of Aeronautics and Astronautics, Washington, D.C., 499–506, 1993.

Rinehart M.C., Cerenkov counter for spacecraft application, *Nucl. Instrum. Methods*, **154**, 303–316, 1978.

Ritter, H., Sekundärelektronenemission von Kohlenstoffolien beim Durchgang von Ionen im Energiebereich von 40 bis 500 keV, MPE Report, **190**, 1985.

Rohner, U., J.A. Whitby, and P. Wurz, A miniature laser ablation time-of-flight mass spectrometer for *in situ* planetary exploration, *Meas. Sci. Technol.*, **14**, 2159–2164, 2003.

Rohner, U., J.A. Whitby, P. Wurz, and S. Barabash, Highly miniaturized laser ablation time-of-flight mass spectrometer for a planetary rover, *Rev. Sci. Instrum.*, **75**, 1314–1322, 2004.

Rosenbauer, H., R. Schwenn, H. Miggenrieder, B. Meyer, H. Grünwaldt, K.-H. Mühlhäuser, H. Pellkofer, and J.H. Wolfe, Die Instrumente des Plasma Experiments auf den HELIOS-Sonnensonden, BMFT-FB-W **81-015**, Max-Planck-Institut für Aeronomie, Katlenburg-Lindau, 1981.

Samir, U., L.H. Brace, and H.C. Brinton, About the influence of electron temperature and relative ion composition on the ion depletion in the wake of the AE-C satellite, *Geophys. Res. Lett.*, **6**, 101–104, 1979.

Sayood, K., *Introduction to Data Compression*, Morgan Kauffmann, San Francisco, 2000.

Scarf, F.L., J.H. Wolfe, and R.W. Silva, A plasma instability in the solar wind, Space Science Laboratory TRW Systems Report **06500-6001-R000**, Redondo Beach, 1966.

Scudder, J.D., X. Cao, and F. Mozer, Photoemission current-spacecraft voltage relation: Key to routine quantitative low energy plasma measurements, *J. Geophys. Res.*, **105**, 21281–21294, 2000.

Seltzer S.M. and M.J. Berger, Transmission and reflection of electrons by foils, *Nucl. Instrum. Methods* **119**, 157–179, 1974.

Shelley, E.G., R.G. Johnson, and R.D. Sharp, Satellite observations of energetic heavy ions during a geomagnetic storm, *J. Geophys. Res.*, **77**, 6104–6110, 1972.

Shelley, E.G., R.D. Sharp, R.G. Johnson, J. Geiss, P. Eberhardt, H. Balsiger, G. Haerendel, and H. Rosenbauer, Plasma composition experiment on ISEE-A, *IEEE Trans. Geosci. Electr.*, **GE-16**, 266–270, 1978.

Shelley, E.G., A.G. Ghielmetti, H. Balsiger, R.K. Black, J.A. Bowles, R.P. Bowman, O. Bratschi, J.L. Burch, C.W. Carlson, A.J. Coker, J.F. Drake, J. Fischer, J. Geiss, A. Johnstone, D.L. Kloza, O.W. Lennartsson, A.L. Magoncelli, G. Paschmann, W.K. Peterson, H. Rosenbauer, T.C. Sanders, M. Steinacher, D.M. Walton, B.A. Whalen, and D.T. Young, The Toroidal Imaging Mass-Angle Spectrograph (TIMAS) for the Polar mission, *Space Sci. Rev.*, **71**, 497–530, 1995.

Siegmund, O.H.W., Preconditioning of microchannel plate stacks, in *Proc. SPIE*, **1072**, 111–118, 1989.

Siegmund, O.H.W., J. Vallerga, and B. Wargelin, Background events in microchannel plates, *IEEE Trans. Nucl. Sci.*, **NS-35**, 524–528, 1988.

Siegmund, O.H.W., J.M. Stock, D.R. Marsh, M.A. Gummin, R. Raffanti, J. Hull, G.A. Gaines, B.Y. Welsh, B. Donakowski, P.N. Jelinsky, T. Sasseen, J.L. Tom, B. Higgins, T. Magoncelli, J.W. Hamilton, S.J. Battel, A.I. Poland, M.D. Jhabvala, K. Sizemore, and J. Shannon, Delay-line detectors for the UVCS and SUMER instruments on the SOHO Satellite, *Proc. SPIE*, **2280**, 89–100, 1994.

Siegmund, O.H., M.A. Gummin, T. Sasseen, P.N. Jelinsky, G.A. Gaines, J. Hull, J.M. Stock, M.L. Edgar, B.Y. Welsh, S.R. Jelinsky, and J.V. Vallerga, Microchannel plates for the UVCS and SUMER instruments on the SOHO satellite, in *The International Society for Optical Engineering, EUV, X-Ray, and Gamma-Ray Instrumentation for Astronomy VI*, O.H. Siegmund and J.V. Vallerga, Eds., *Proc. SPIE*, **2518**, 344–355, 1995.

Snyder, C.W. and M. Neugebauer, The mission for Mariner II: Preliminary observations, solar plasma experiment, *Science*, **138**, 1095–1100, 1962.

Sommer, H., H.A. Thomas, and J.A. Hipple, The measurement of e/m by cyclotron resonance, *Phys. Rev.*, **82**, 697–702, 1951.

Spencer, N.W., L.H. Brace, G.R. Carignan, D.R. Taeusch, and H. Niemann, Electron and molecular nitrogen temperature and density in the thermosphere, *J. Geophys. Res.*, **70**, 2665–2698, 1965.

Spencer, N.W., H.B. Niemann, and G.R. Carignan, The neutral-atmosphere temperature instrument, *Radio Sci.*, **8**, 287–296, 1973.

Spencer N.W., Neutral atmosphere temperature, San Marco 4, NSSDC ID **1974-009A**, 1974a.

Spencer, N.W., D.T. Pelz, H.B. Niemann, G.R. Carignan, and J.R. Caldwell, The neutral atmosphere temperature experiment, *J. Geophys. Res.*, **40**, 613–624, 1974b.

Spencer, N.W., L.E. Wharton, H.B. Niemann, A.E. Hedin, G.R. Carignan, and J.C. Maurer, The Dynamics Explorer wind and temperature spectrometer, *Space Sci. Instrum.*, **5**, 417–428, 1981.

Spieler, H., *Semiconductor Detector Systems*, Oxford University Press, Oxford, 2005.

Stephen, T.M. and B.L. Peko, Absolute calibration of a multichannel plate detector for low energy O, O^-, O^+, *Rev. Sci. Instrum.*, **71**, 1355–1359, 2000.

Stone, R.G., J.L. Bougeret, J. Caldwell, P. Canu, Y. de Conchy, N. Cornilleau-Wehrlin, M.D. Desch, J. Fainberg, K. Goetz, M.L. Goldstein, C.C. Harvey, S. Hoang, R. Howard,

M.L. Kaiser, P.J. Kellog, B. Klein, R. Knoll, A. Lecacheux, D. Lengyel-Frey, R.J. MacDowall, R. Manning, C.A. Meetre, A. Meyer, N. Monge, S. Monson, G. Nicol, M.J. Reiner, J.L. Steinberg, E. Torrès, C. de Villedary, F. Wouters, and P. Zarka, The unified radio and plasma wave investigation, *Astron. Astrophys. Suppl. Ser.* **92**, 291–316, 1992.

Stone E.C., C.M.S. Cohen, W.R. Cook, A.C. Cummings, B. Gauld, B. Kecman, R.D. Leske, R.A. Mewaldt, M.R. Thayer, B.L. Dougherty, R.L. Grum, B.D. Milliken, R.G. Radocinski, M.E. Wiedenbeck, E.R. Christian, S. Shuman, H. Trexel, T.T. von Rosenvinge, W.R. Binns, D.J. Carary, P. Dowkont, J. Epstein, P.L. Link, J. Klarmann, M. Lijowski, and M.A. Olevitch, The cosmic-ray isotope spectrometer for the Advanced Composition Explorer, *Space Sci. Rev.*, **86**, 285–356, 1998.

Straub, H.C., M.A. Mangan, B.G. Lindsay, K.A. Smith, and R.F. Stebbings, Absolute detection efficiency of a microchannel plate detector for kilo-electron volt energy ions, *Rev. Sci. Instrum.*, **70**, 4238–4240, 1999.

Taylor, H.A., Jr., H.C. Brinton, and C.R. Smith, Positive ion composition in the magnetosphere obtained from the OGO-A satellite, *J. Geophys. Res.*, **70**, 5769–5781, 1965.

Taylor, H.A., Jr., H.C. Brinton, M.W. Pharo, III, and N.K. Rahman, Thermal ions in the exosphere. Evidence of solar and geomagnetic control, *J. Geophys. Res.*, **73**, 5521–5533, 1968.

Taylor, H.A., H.C. Brinton, T.C.G. Wagner, B.H. Blackwell, and G.R. Cordier, Bennett ion mass spectrometers on the Pioneer Venus Bus and Orbiter, *IEEE Trans. Geosci. Remote Sens.*, **GE-18**, 44–49, 1980.

Theodoridis, G.C. and F.R. Paolini, Charged particle transmission through cylindrical plate electrostatic analyzers, *Rev. Sci. Instrum.*, **39**, 326–330, 1968.

Theodoridis, G.C. and F.R. Paolini, The angular response of spherical plate electrostatic analyzers, *Rev. Sci. Instrum.*, **40**, 621–631, 1969.

Tietze, U. and C. Schenk, *Electronic Circuits, Handbook for Design and Application*, 2^{nd} Ed., Springer, New York, 2006.

Timothy, J.G., G.H. Mount, and R.L. Bybee, Multi-anode microchannel arrays, *IEEE Trans. Nucl. Sci.*, **NS-28**, 689–697, 1981.

Timothy, J.G., Electronic readout systems for microchannel plates, *IEEE Trans. Nucl. Sci.*, **NS-32**, 427–432, 1985.

Trinks, H. and U. von Zahn, The ESRO 4 gas analyzer, *Rev. Sci. Instrum.*, **46**, 213–217, 1975.

Trotignon J.G., R. Boström, J.L. Burch, K.-H. Glassmeier, R. Lundin, O. Norberg, A. Balogh, K. Szegö, G. Musmann, A. Coates, L. Åhlen, C. Carr, A. Erksson, W. Gibson, F. Kuhnke, K. Lundin, J.L. Michau, and S. Szalai, The Rosetta plasma consortium: Technical realization and scientific aims, *Adv. Space Res.*, **24**, 1149–1158, 1999.

Trotignon, J.G., P.M.E. Décréau, J.L. Rauch, O. Randriamboarison, V. Krasnosels'kikh, P. Canu, K. Yearby, E. Le Guirriec, H.C. Seran, F.X. Sené, Ph. Martin, M. Lévêque, and P. Fergeau, How to determine the thermal electron density and the magnetic field strength from the Cluster/Whisper observations around the Earth, *Ann. Geophys.*, **19**, 1711–1720, 2001.

Vaisberg, O.L., A.O. Fedorov, A. Johnstone, E.I. Kolesnikova, A.I. Kozhukhovsky, and V.M. Balebanov, The possibility of making fast measurements of ion distribution function, in *Proc. Int. Workshop on Space Plasma Physics Investigations by Cluster and Regatta*, Graz, *ESA Special Publication*, **SP-306**, ESA Publications Division, Noord-

wijk, 143–148, 1990.

Vaisberg, O.L., A.W. Leybov, L.A. Avanov, V.N. Smirnov, E.B. Ivanova, A.A. Klimashev, B.I. Khazanov, I.I. Cherkashin, M.V. Iovlev, A.Yu. Safronov, and V.H. Lichtenstein, Complex plasma analyzer SCA-1, in *Interball Mission and Payload*, RKA-IKI-CNES, 170–177, 1995.

Vaisberg, O.L., L.A. Avanov, V.N. Smirnov, J.L. Burch, A.W. Leibov, E.B. Ivanova, J.H. Waite, Jr., A.A. Klimashev, B.I. Khazanov, I.I. Cherkashin, M.V. Iovlev, A.Yu. Safronov, A.I. Kozhukhovsky, C. Gurgiolo, and V.H. Lichtenstein, Initial observations of fine plasma structures at the flank magnetopause with the complex plasma analyzer SCA-1 onboard the Interball Tail Probe, *Ann. Geophys.*, **15**, 570–586, 1997.

Vaisberg, O., B. Goldstein, D. Chornay, J. Keller, L. Avanov, V. Smirnov, D. Brinza, D. Croley, E. Sittler, T. Moore, P. Rozmarynowski, S. Fuselier, and A. Ghielmetti, Ultra fast plasma analyzer - all-sky camera for charged particles, in *Solar Encounter: The First Solar Orbiter Workshop*, *ESA Special Publication*, **SP-493**, ESA Publications Division, Noordwijk, 451–454, 2001.

Vaisberg, O.L., Advanced method for exploration of plasma velocity distribution functions: All-sky camera for very fast plasma measurements, *Adv. Space Res.*, **32**, 385–388, 2003.

Vampola, A.L., J.V. Osborn, and B.M. Johnson, CRRES magnetic electron spectrometer AFGL-701-5A (MEA), *J. Spacecraft and Rockets*, **29**, 592–595, 1992.

Vasyliunas, V.M., Deep space measurements, in *Plasma Physics, Part B*, R.H. Lovberg and H.R. Griem, Eds., Academic Press, New York, 1971.

von Rosenvinge, T.T., L.M. Barbier, J. Karsch, R. Liberman, M.P. Madden, T. Nolan, D.V. Reames, L. Ryan, S. Singh, H. Trexel, G. Winkert, G.M. Mason, D.C. Hamilton, and P. Walpole, The Energetic Particles: Acceleration, Composition, and Transport (EPACT) investigation on the Wind spacecraft, *Space Sci. Rev.*, **71**, 155–206, 1995.

von Steiger, R., N.A. Schwadron, L.A. Fisk, J. Geiss, G. Gloeckler, S. Hefti, B. Wilken, R.F. Wimmer-Schweingruber, and T.H. Zurbuchen, Composition of quasi-stationary solar wind flows from Ulysses/Solar Wind Ion Composition Spectrometer, *J. of Geophys. Res.*, **105**, 27217–27238, 2000.

von Zahn, U., Composition studies in the thermosphere by means of mass spectrometers, in *Structure and Dynamics of the Upper Atmosphere*, F. Veriani, Ed., Developments in Atmospheric Science, Elsevier, Publishing Co, Amsterdam, **1**, 389–434, 1974.

von Zahn, U. and K. Mauersberger, Small mass spectrometer with extended measurement capabilities at high pressures, *Rev. Sci. Instrum.*, **49**, 1539–1542, 1978.

Voss, H.D., E. Hertzberg, A.G. Ghielmetti, S.J. Battel, K.L. Appert, B.R. Higgins, D.O. Murray, and R.R. Vondrak, Medium energy ion mass and neutral atom spectrometer, *J. Spacecraft and Rockets*, **29**, 566–569, 1992.

Waite, J.H., W.S. Lewis, W.T. Kasprzak, V.G. Anicich, B.P. Block, T.C. Cravens, G.G. Fletcher, W.-H. Ip, J.G. Luhmann, R.L. McNutt, H.B. Niemann, J.K. Parejko, J.E. Richards, R.L. Thorpe, E.M. Walter, and R.V. Yelle, The Cassini Ion and Neutral Mass Spectrometer (INMS) investigation, *Space Sci. Rev.*, **114**, 113–231, 2004.

Waite, J.H., H.B. Niemann, R.V. Yelle, W.T. Kasprzak, T.E. Cravens, J.G. Luhmann, R.L. McNutt, W.-H. Ip, D. Gell, V. De La Haye, I. Mueller-Wodarg, B. Magee, N. Borggren, S.A. Ledvina, G. Fletcher, E. Walter, R. Miller, S. Scherer, R. Thorpe, J. Xu, B. Block, and K. Arnett, Ion neutral mass spectrometer results from the first flyby of Titan, *Science*, **308**, 982–985, 2005.

Wax, R.L. and W. Bernstein, Energy-independent detector for total hydrogen fluxes in the range 1–10 keV for space and laboratory applications, *Rev. Sci. Instrum.*, **38**, 1612–1615, 1967.

Weissman, I. and M.L. Kinter, Improved thermionic emitter using uniaxial oriented tungsten, *J. Appl. Phys.*, **34**, 3187–3194, 1963.

Wertz, J.R. and W.J. Larson, *Space Mission Analysis and Design*, 3^{rd} Ed., Space Technology Library, Vol. 8, Springer, New York, 1999.

Westermann, C.B., W. Luithardt, E. Kopp, T. Koch, R. Liniger, H. Hofsetter, J. Fischer, K. Altwegg, and H. Balsiger, A high precision calibration system for the simulation of cometary gas environments, *Meas. Sci. Technol.*, **12**, 1594–1603, 2001.

Whalen, B.A., J.R. Burrows, A.W. Yau, E.E. Budzinski, A.M. Pilon, I. Iwamoto, K. Marubashi, S. Watanabe, H. Mori, and E. Sagawa, The Suprathermal ion Mass Spectrometer (SMS) onboard the Akebono (Exos-D) satellite, *J. Geomag. Geoelectr.*, **42**, 511–536, 1990.

Wien, W., Die electrostatischen Eigenschaften der Kathodenstrahlen, *Verhandl. Phys. Ges. zu Berlin*, A. König, Ed., Verlag v. Johann Ambrosius Barth, Leipzig, **16**, 165–172, 1897.

Wilken, B., Identification techniques for nuclear particles in space plasma research and selected experimental results, *Rep. Prog. Phys.*, **47**, 767–853, 1984.

Wilken, B. and W. Stüdemann, A compact time-of-flight mass-spectrometer with electrostatic mirrors, *Nucl. Instrum. Methods in Phys. Res.*, **222**, 587–660, 1984.

Wilken, B., W.I. Axford, I. Daglis, P. Daly, W. Guttler, W.H. Ip, A. Korth, G. Kremser, S. Livi, V.M. Vasyliunas, J. Woch, D. Baker, R.D. Belian, J.B. Blake, J.F. Fennell, L.R. Lyons, H. Borg, T.A. Fritz, F. Gliem, R. Rathje, M. Grande, D. Hall, K. Kecsuemety, S. McKenna-Lawlor, K. Mursula, P. Tanskanen, Z. Pu, I. Sandahl, E.T. Sarris, M. Scholer, M. Schulz, F. Søraas, and S. Ullaland, RAPID - The imaging energetic particle spectrometer on Cluster, *Space Sci. Rev.*, **79**, 399–473, 1997.

Williams, D.J., E. Keppler, T.A. Fritz, B. Wilken, and G. Wibberenz, The ISEE 1 and 2 medium energy particles experiment, *IEEE Trans. Geosci. Electr.*, **GE-16**, 270–280, 1978.

Winningham, J.D., W.J. Heikkila, F. Yasuhara, and S.-I. Akasofu The latitudinal morphology of 10-eV to 10-keV electron fluxes during magnetically quiet and disturbed times in the 2100-0300 MLT sector, *J. Geophys. Res.*, **80**, 3148–3171, 1975.

Winningham, J.D., J.L. Burch, N. Eaker, V.A. Blevins, and R.A. Hoffman The Low Altitude Plasma Instrument (LAPI), *Space Sci. Instrum.*, **5**, 465–475, 1981.

Winningham, J.D., J.R. Sharber, R.A. Frahm, J.L. Burch, N. Eaker, R.K. Black, V.A. Blevins, J.P. Andrews, J. Rudzki, and M.J. Sablik, The UARS particle environment monitor, *J. of Geophys. Res.*, **98**, 10649–10666, 1993.

Witte, M., H. Rosenbauer, E. Kepler, H. Fahr, P. Hemmerich, H. Lauche, A. Loidl, and R. Zwick, The interstellar neutral-gas experiment on Ulysses, *Astron. Astrophys. Suppl. Ser.*, **92**, 333–348, 1992.

Wiza, J.L., Microchannel plate detectors, *Nucl. Instrum. Methods*, **162**, 587–601, 1979.

Wolfe, J.H., R.W. Silva, D.D. McKibbin, and R.H. Mason, The compositional, anisotropic, and nonradial flow characteristics of the solar wind, *J.Geophys. Res.*, **71**, 3329–3335, 1966a.

Wolfe, J.H, R.W. Silva, and M.A. Myers, Observations of the solar wind during the flight of IMP 1, *J. Geophys. Res.*, **71**, 1319–1339, 1966b.

Wollnik, H., *Optics of Charged Particles*, Academic Press, San Diego, 1987.

Wollnik, H., Time-of-flight mass analyzers, *Mass Spec. Rev.*, **12**, 89–114, 1993.

Wrenn, G.L., J.F.E. Johnson, and J.J. Sojka, The supra-thermal plasma analyzers on the ESA GEOS satellites, *Space Sci. Instrum.*, **5**, 271–293, 1981.

Wüest, M., Time-of-flight ion composition measurement techniques for space plasmas, in *Measurement Techniques in Space Plasmas: Particles*, R. Pfaff, J. Borovsky, and D.T. Young, Eds., Geophys. Monogr. Ser., **102**, American Geophysical Union, Washington, D.C., 141–155, 1998.

Wurz, P., L. Gubler, P. Bochsler, and E. Möbius, Isochronous mass spectrometer for space plasma applications, in *Measurement Techniques in Space Plasma: Particles*, R.F. Pfaff, J.E. Borovsky, and D.T. Young, Eds., Geophys. Monogr. Ser., **102**, American Geophysical Union, Washington, D.C., 229–235, 1998.

Wurz, P., Detection of energetic neutral atoms, in *The Outer Heliosphere: Beyond the Planets*, K. Scherer, H. Fichtner, and E. Marsch, Eds., Copernicus Gesellschaft, Katlenburg-Lindau, 2000.

Yavor, M.I., H. Wollnik, M. Nappi, and B. Hartmann, Image aberrations of poloidal toroid electrostatic analyzers, *Nucl. Instrum. Methods A*, **311**, 448–452, 1992.

Young, D.T., Space plasma mass spectroscopy below 60 keV, in *Solar System Plasma Physics*, J.H. Waite, Jr., J.L. Burch and R.L. Moore, Eds., Geophys. Monogr. Ser., **54**, American Geophysical Union, Washington, D.C., 143–157, 1989.

Young, D.T., Space plasma particle instrumentation and the new paradigm: Faster, cheaper, better, in *Measurement Techniques in Space Plasmas: Particles*, R. Pfaff, J. Borovsky, and D.T. Young, Eds., Geophys. Monogr. Ser., **102**, American Geophysical Union, Washington, D.C., 1–16, 1998.

Young, D.T., Mass spectrometry for planetary science, in *Atmospheres in the Solar System: Comparative Aeronomy*, M. Mendillo, A. Nagy, and J.H. Waite, Eds., Geophys. Monogr. Ser., **130**, American Geophysical Union, Washington, D.C., 353–365, 2002.

Young, D.T., S.J. Bame, M.F. Thomsen, R.H. Martin, J.L. Burch, J.A. Marshall, and B. Reinhard, 2π-radian field-of-view toroidal electrostatic analyzer, *Rev. Sci. Instrum.*, **59**, 743–751, 1988.

Young, D.T., J.E. Nordholt, and J.J. Hanley, Plasma Experiment for Planetary Exploration (PEPE), in *Deep Space 1 Technology Validation Reports*, JPL Publication, **00-10 No. 7**, Jet Propulsion Laboratory, Pasadena, CA, October 2000.

Young, D.T., J.J. Berthelier, M. Blanc, J.L. Burch, A.J. Coates, R. Goldstein, M. Grande, T.W. Hill, R.E. Johnson, V. Kelha, D.J. McComas, E.C. Sittler, K.R. Svenes, K. Szegö, P. Tanskanen, K. Ahola, D. Anderson, S. Bakshi, R.A. Baragiola, B.L. Barraclough, R.K. Black, S. Bolton, T. Booker, R. Bowman, P. Casey, F.J. Crary, D. Delapp, G. Dirks, N. Eaker, H. Funsten, J.D. Furman, J.T. Gosling, H. Hannula, C. Holmlund, H. Huomo, J.M. Illiano, P. Jensen, M.A. Johnson, D.R. Linder, T. Luntama, S. Maurice, K.P. Mccabe, K. Mursula, B.T. Narheim, J.E. Nordholt, A. Preece, J. Rudzki, A. Ruitberg, K. Smith, S. Szalai, M.F. Thomsen, K. Viherkanto, J. Vilppola, T. Vollmer, T.E. Wahl, M. Wüest, T. Ylikorpi, and C. Zinsmeyer, Cassini plasma spectrometer investigation, *Space Sci. Rev.*, **114**, 1–112, 2004.

Young, D.T., J.E. Nordholt, J.L. Burch, D.J. McComas, R.P. Bowman, R.A. Abeyta, J. Alexander, J. Baldonado, P. Barker, R.K. Black, T.L. Booker, P.J. Casey, L. Cope, F.J. Crary, J.P. Cravens, H.O. Funsten, R. Goldstein, D.R. Guerrero, S.F. Hahn, J.J. Hanley, B.P. Henneke, E.F. Horton, D.J. Lawrence, K.P. McCabe, D. Reisenfeld, R.P. Salazar,

M. Shappirio, S.A. Storms, C. Urdiales und J.H. Waite, Plasma experiment for planetary exploration (PEPE), *Space Sci. Rev.*, doi:10.1007/s11214-007-9177-3, 2007.

Zeman, H.D., Deflection of an ion beam in the two-dimensional electrostatic quadrupole field, *Rev. Sci. Instrum.*, **48**, 1079–1085, 1977.

Zurbuchen, T.H., G. Gloeckler, J.C. Cain, S.E. Lasley, and W. Shanks, A low-weight plasma instrument to be used in the inner heliosphere, in *Missions to the Sun II*, C. M. Korendyke, Ed., *Proc. SPIE*, **3442**, 217–224, 1998.

— 3 —

Calibration Techniques

PETER WURZ[1], ANDRE BALOGH[2], VICTORIA COFFEY[3], BRONISLAW K. DICHTER[4], WAYNE T. KASPRZAK[5], ALAN J. LAZARUS[6], WALTER LENNARTSSON[7], AND JAMES P. MCFADDEN[8]

[1]*Physikalisches Institut, University of Bern, Bern, Switzerland*
[2]*Imperial College of Science and Technology, London, UK*
[3]*NASA Marshall Space Flight Center, Huntsville, AL, USA*
[4]*Air Force Research Laboratory, Hanscom Air Force Base, MA, USA*
[5]*Goddard Space Flight Center, NASA, Greenbelt, MD, USA*
[6]*Massachusetts Institute of Technology, Cambridge, MA, USA*
[7]*Lockheed Martin Missiles and Space, Palo Alto, CA, USA*
[8]*Space Sciences Laboratory, University of California, Berkeley, CA, USA*

3.1 Introduction to Calibration

Calibration and characterization of particle instruments with supporting flight electronics is necessary for the correct interpretation of the returned data. Generally speaking, the instrument will always return a measurement value (typically in form of a digital number), for example a count rate, for the measurement of an external quantity, which could be an ambient neutral gas density, an ion composition (species measured and amount), or electron density. The returned values are used then to derive parameters associated with the distribution such as temperature, bulk flow speed, differential energy flux and others. With the calibration of the instrument the direct relationship between the external quantity and the returned measurement value has to be established so that the data recorded during flight can be correctly interpreted. While calibration and characterization of an instrument are usually done in ground-based laboratories prior to integration of the instrument in the spacecraft, it can also be done in space (see Chapter 4).

Ideally, the instrument should be calibrated before flight with particle sources replicating the conditions in space as closely as possible. See Chapter 1 for a survey of the range of values the measured quantities can have in the space environment. Fortunately, most instruments are simply detectors of particle beams rather than plasma detectors (e.g. a Langmuir probe) and they can be calibrated with standard technology. There is no need to reproduce the actual plasma the instrument is intended to measure, with the only exception at low ion energies where spacecraft charging and local plasma effects play an important role in the way particles reach the instrument entrance [e.g. *Berthelier and Roussel*, 2004]. The situation is also somewhat different for thermal neutral gas instruments and is discussed in a separate section below.

Some special precautions should, in any case, be observed. The particle fluxes encountered by the instrument in flight are assumed to be uniform over that portion of the

entrance aperture that corresponds to a single detector pixel. Hence the calibration must be performed with effectively uniform illumination of the entrance aperture that images to a single detector pixel, either directly with a wide, uniform beam or by scanning a narrow beam across the aperture. The spread of the beam in energy and angle must be small compared with the width of the transmission function of the instrument, typically the energy spread should be less than 1 % and the angular spread less than 1°. Both of these requirements are easy to achieve with modern equipment. Moreover, the particle beam needs to be sufficiently stable in intensity and spatial distribution during the periods of measurements to meet calibration accuracy requirements. Unidentified temporal fluctuations in the primary particle beam may appear like deviations from the nominal response of the instrument [*Vilppola et al.*, 2001]. Sometimes it is desired to completely fill the energy passband of the instrument, which is usually achieved by an energy wobble of the electron or ion beam within a precise energy range. The particle beam of the calibration system is monitored by a beam monitoring system.

There are many different types of ion sources, which can be used for the calibration of ion instruments. There are several books, mostly very recent, covering different types of ion sources, ion beam transport, and ion source operation [e.g. *Vályi*, 1977; *Alton*, 1993; *Wolf*, 1995; *Zhang*, 1999; *Brown*, 2004]. During recent years, the electron-cyclotron-resonance ion source [*Geller*, 1996] became a popular ion source type for calibration work because of its capability to easily generate stable ion beams of almost any gas and even from solids. The generation of highly charged ions is covered in [*Shirkov and Zschornack*, 1996], and aspects of ion beam transport can be found in [*Humphries*, 1990]. Common ion sources in calibration facilities are electron impact ion sources, Colutron ion sources, and duo-plasmatron ion sources (see Appendix A.4 for a list of existing calibration facilities). Some ten years ago, these ion sources typically were home made, tailored to the demands of the ion calibration needs. Nowadays there are many commercial suppliers and one can buy almost any ion source from a specialized company. Electron sources suitable for calibration work are discussed together with the calibration of electron instruments in Section 3.2.1. For high-energy particle calibration one usually has to go to an accelerator facility that provides the particles of interest in the desired energy range, which is discussed in Section 3.5.

It is obvious that the instrument calibration can only be as good as the knowledge of the particle source of the calibration facility. Therefore, a reference is needed in the calibration facility. For example, for electron or ion beams, the beam current can be measured with a Faraday cup and an accurate electrometer. However, space plasma instruments are usually built for electron or ion fluxes typically being much lower than can be handled by a current measurement, thus a suitable secondary standard based on the primary standard (the Faraday cup with an electrometer), has to be established. This secondary standard often is a channeltron with a pulse counter. Microchannel plate (MCP) detectors with appropriate read-out electronics are another possibility to directly measure the beam flux, and may have the additional possibility to provide a spatial profile of the particle beam. Unfortunately, channeltrons and MCPs have detection efficiencies that vary with vacuum conditions and usage (see Sections 2.2.3 and 2.2.4) and thus have to be calibrated every time before they are used as a reference for the actual instrument calibration. For high energy particles there are three basic component sensor types that can be used as a reference: silicon solid-state sensors, scintillators and Cherenkov radiators, which are discussed in detail in *Knoll* [2000]. The aspects of references will be discussed in some cases at the

individual sections of this chapter. Depending on the accuracy required for the calibration of a particular instrument some modules of the calibration system have to be recalibrated themselves before calibration of the flight instrument (e.g. the voltmeters measuring the beam energy, the positioning accuracy of the turntable, or the absolute gas pressure).

Using a reference detector to measure the particle beam flux means that this detector has to be moved into the ion beam for this measurement and the instrument to be calibrated will not be in the particle beam, thus the two measurements are done sequentially. This requires the particle beam to be sufficiently stable with time, e.g. no significant short- and long-term drifts, which is satisfied by modern calibration facilities but, nevertheless, should be verified regularly during a calibration campaign. With good monitoring, slow long-term drifts can be corrected for. Often it is practical to continuously monitor the beam during calibration by placing the monitor outside the instrument's field of view. An alternative to the sequential measurement would be non-invasive current measuring devices, like the parametric current transducer (PCT) or the superconductor cryogenic current comparator (CCC). A PCT measures the ion current passing through a specially designed toroidal transformer [*Unser*, 1981]. A CCC is a device for precisely measuring the ratio of two currents, e.g. the ion beam and a reference current, using a SQUID [*Harvey*, 1972; *Grohmann et al.*, 1977]. A high temperature superconductor CCC is reported in [*Hao et al.*, 2002]. Using a PCT or a CCC the ion beam is not touched and thus it can be used for calibrating the instrument at the same time. PCTs measure the ion current with absolute accuracies of up to 0.05 %, CCC have the potential to measure current even more precisely. Unfortunately, the present current range from μA and higher handled by the PCTs [*Bergoz*, 2004] or nA and higher handled by CCCs [*Peters et al.*, 1999; *Hao et al.*, 2002; *Vodel et al.*, 2005] does not allow a direct application for calibration purposes.

Calibration is an end-to-end test of the sensor and its flight electronics as an integrated unit, which we refer to as the *instrument*, that is usually carried out shortly before integration of the instrument on the spacecraft. It is important to have the instrument available in its final configuration (including the collimator, the deflection system, detectors, amplifiers, electronics, data processing, etc.), since the interplay between different components may significantly influence its performance. Often, however, a calibration campaign actually starts with testing the instrument to verify its proper functioning and to learn to operate the instrument. The calibration serves to establish not only a precise relationship between the returned value and the measured external quantity, but also verifies that the instrument discriminates against sources that are outside the intended response band. For example, in case of an instrument with energy analysis one wants to check that the returned value is indeed acceptably low (i.e. close to zero) if the particle energy is outside the energy band, even if the energy is far outside the energy band.

The amount of data recorded by the instrument typically exceeds the data volume that can be transmitted back to Earth by a large factor (one or more orders of magnitude). Therefore, data selection, data compression and binning of data are frequently employed in the instrument data handling system. These data compression routines have to be tested and calibrated before launch as well. Often in data compression routines the parameter values necessary for flight operation are established during calibration. Sometimes larger sets of calibration data are needed onboard during flight in the form of look-up tables.

During thermal qualification tests instruments, by themselves and after integration into spacecraft, are typically subjected to thermal cycling to expose infantile component failures and workmanship problems. While these tests are necessary, they are not designed to

reveal detailed temperature dependencies in instrument performance that may compromise observations in space. Thermal qualification tests can reveal temperature dependencies of voltages, through monitors, and some timing issues. It is one of the objectives of pre-flight calibrations to expose and characterize such dependencies within the temperature range given by the mission profile so that appropriate corrections can be applied to the on-orbit observations. For example, Sections 3.2.4 and 3.2.5 detail the need to establish the temperature dependence of electrostatic analyzer electrode voltage, especially at voltages necessary to select low charged particle energies where a small variation in absolute voltage can convert to a large relative variation in the particle energy passed by the analyzer. Section 3.3.5 illustrates the need for a temperature calibration of the RC time constant that is critical in the circuit that measures the current collected by the Faraday cup in the Wind and Triana solar wind instruments. The bias voltage supplies for detectors, especially if the detector gain is critical and dependent on bias voltage (for example, photomultiplier tubes in scintillation counters), should be characterized as a function of temperature. Linear circuits, for example charge sensitive amplifiers used in solid-state detector systems where amplifier gain is directly related to the correct identification of particle energy, should be characterized for temperature dependence. The discrimination level in threshold discrimination circuits must also be calibrated as a function of temperature for the same reason. Of course, the circuits used to monitor those critical temperatures within an instrument that are needed for corrections to flight data must be positioned at appropriate locations within the instrument and be calibrated carefully in the laboratory.

Particle instruments cover a wide range of scientific objectives, thus we have to divide our discussion on their calibration to classes of instruments with similar requirements. First, it is necessary to distinguish between neutral particles and charged particles (electrons and ions). Within each of these categories the discussion of instrument calibration will be divided into three energy ranges, which are somewhat arbitrary and which may overlap. The distinction in energy range arises partly from the different instrumentation needed for different energies, and partly from the different scientific objectives. Low energy ion calibration, see in Section 3.3, comprises ions with thermal energies up to a few hundred eV[1]. In this energy range spacecraft charging, instrument charging, and the local plasma environment around the spacecraft play a non-negligible role. Going to higher energies we discuss ion instrumentation for medium energies in Section 3.4 ($\sim$100 eV to a few 100 keV). This is the range for most of the magnetospheric plasma. If ions (particles) have energies that allow them to penetrate matter, we classify them as high energy particles. Their measurement requires a different kind of instrument, and a different calibration, which is discussed in Section 3.5.

For neutral particles we have also distinctions in separate energy ranges. At the lowest energies there are the instruments for thermal gas, e.g. pressure sensors and partial pressure analyzers, measuring the local particle density. Thermal gas calibrations are described in Section 3.6. In case of a modest relative speed of the instrument with respect to the gas (for example planetary flybys, planetary or cometary outflows) the instrument will measure a directed flux of suprathermal particles, which has to be reproduced in calibration and is discussed in Section 3.7. At even higher particle energies, in the range of about 10 eV to 1 MeV, one speaks of Energetic Neutral Atoms (ENAs), which again have different requirements for calibration and are discussed in Section 3.8. ENAs mostly arise from

[1] 1 eV = 1.602176462(63) $\times 10^{-19}$ J

the interaction of an energized plasma with a neutral gas [*Wurz*, 2000]. The distinction in energy range is somewhat arbitrary and arises partly from the different instrumentation needed for different energies, and partly from the different scientific objectives.

The basic parameters that define the generic performance of a charged particle measuring instrument and its calibration are discussed in Section 3.1.1. The generic mass spectrometer response, which characterizes instruments measuring neutral gas species, are discussed in Section 3.1.2. Dead time and pulse pile-up effects in detector counting systems, which are a common problem for many of these instruments, are discussed in Section 3.1.3.

3.1.1 The Geometric Factor of Particle Instruments

A typical particle instrument consists of an entrance system accepting ions, electrons, or neutral particles, an ionizing source for neutral particles, an energy analyzer (i.e., energy per charge filter), and a mass analyzer (i.e., mass per charge filter) and a detector (see also Figure 2.1 in Section 2.1). In this section we will discuss the case of a directed particle flux the instrument has to measure. The case of a density measurement (no bulk flow velocity) will be discussed in Section 3.6 below. Therefore, the transmission, T, will be not only a function of direction of the particle flow with respect to the orientation of the entrance area, but will also depend on the particle's energy, charge, and the species. As mentioned above, we assume that the appropriate segment of the entrance area is filled completely by the particle beam used for calibration.

For a phase space density[2] f of particles of species i with a velocity $\boldsymbol{v}$ one gets a certain number of counts C depending on the transmission of the instrument and its detection efficiencies, T_i. In differential form this is expressed as [*Vasyliunas*, 1971]

$$\mathrm{d}C_i = \boldsymbol{v}\, f_i(\boldsymbol{v})\; T_i(\boldsymbol{v})\; \mathrm{d}\boldsymbol{v}\; \hat{\boldsymbol{v}} \cdot \mathrm{d}\boldsymbol{A}\; \mathrm{d}t \tag{3.1}$$

with the aperture area $\mathrm{d}\boldsymbol{A}$, the various efficiencies and transmissions summarized in T_i, the particle velocity $\boldsymbol{v}$, and $\hat{\boldsymbol{v}} \cdot \mathrm{d}\boldsymbol{A}$ giving the projection of the aperture area toward the direction $\hat{\boldsymbol{v}}$ of the particle flux. When calibrating the instrument it is exposed to a defined particle flux, $\boldsymbol{F}$, of simple form

$$\boldsymbol{F}(v, \theta, \varphi) = \int \boldsymbol{v}\, f_i(v, \theta, \varphi)\; \mathrm{d}\boldsymbol{v} = n_s \boldsymbol{v} \delta(v - v_0) \tag{3.2}$$

with v_0 the nominal speed of the particles and n_s the particle density in the beam, which allows the determination of the instrument characteristics. Equation 3.1 can be written as

$$\mathrm{d}C_i(v, \theta, \varphi) = v f_i(v, \theta, \varphi)\; T_i(v, \theta, \varphi)\; v^2 \mathrm{d}v\; \cos\theta_v \cos\varphi_v \mathrm{d}A\; \sin\theta\; \mathrm{d}\theta\; \mathrm{d}\varphi\; \mathrm{d}t \tag{3.3}$$

using $\mathrm{d}\boldsymbol{v} = v^2 \mathrm{d}v \mathrm{d}\Omega$, with $\mathrm{d}\Omega$ the acceptance solid angle, and $\mathrm{d}\Omega = \sin\theta\; \mathrm{d}\theta\; \mathrm{d}\varphi$ with the polar angle θ and azimuth angle φ in some instrument centered coordinate system[3], and

[2] The phase space density gives the number of particles contained in a volume element $\mathrm{d}\boldsymbol{r}\mathrm{d}\boldsymbol{v}$, where $\mathrm{d}\boldsymbol{r}$ is the volume element in configuration space and $\mathrm{d}\boldsymbol{v}$ is the volume element in velocity space. See also Chapter 1 for a definition of the phase space density.

[3] Often the elevation angle is used in space research instead of the polar angle, as is done here for the instrument centered coordinate system. The elevation angle is measured with respect to the equatorial plane. Thus, the term $\cos\theta_v$ is used in Equation 3.3, which would be $\sin\theta_v$ in a polar coordinate system.

$\hat{\boldsymbol{v}} \cdot \mathrm{d}\boldsymbol{A} = \cos\theta_v \cos\varphi_v \, \mathrm{d}A$ the entrance area as seen by the incoming flux moving in the direction $\hat{\boldsymbol{v}}$ assuming a planar aperture. This term can take different shapes depending on the aperture geometry. For example, annular apertures spanning a field-of-view of 180° or even 360° are quite common for space plasma physics instrumentation.

A plasma instrument typically records a number of counts in a specific time interval, e.g. a count rate R_i for species i, in response to a flux of incoming particles. Thus, we rewrite Equation 3.3 and obtain

$$\mathrm{d}R_i(v,\theta,\varphi) = v f_i(v,\theta,\varphi)\; T_i(v,\theta,\varphi)\; v^2 \mathrm{d}v\; \cos\theta_v \cos\varphi_v \mathrm{d}A\; \sin\theta\; \mathrm{d}\theta\; \mathrm{d}\varphi \tag{3.4}$$

Usually the instrument dependent terms are combined in the geometric factor of the instrument. In differential form the geometric factor is written as

$$\mathrm{d}G_i(v,\theta,\varphi) = T_i(v,\theta,\varphi)\; \mathrm{d}A\; \sin\theta\; \mathrm{d}\theta\; \mathrm{d}\varphi \tag{3.5}$$

One can integrate Equation 3.5 over the angular coordinates and the entrance surface area to derive an integral geometric factor

$$G_i(v) = \iiint T_i(v,\theta,\varphi)\; \mathrm{d}A\; \sin\theta\; \mathrm{d}\theta\; \mathrm{d}\varphi \tag{3.6}$$

Note that the geometric factor given in Equation 3.6 is not strictly a geometric quantity, but also contains instrument efficiencies, thus it may be energy and species dependent. For this reason it is sometimes preferred to keep the instrument efficiencies $T_i(v,\theta,\varphi)$ separate from a purely geometric factor $\widetilde{G}$, which is given by the integral

$$\widetilde{G} = \iiint \mathrm{d}A\; \sin\theta\; \mathrm{d}\theta\; \mathrm{d}\varphi \tag{3.7}$$

The knowledge of the geometric factor G allows to easily compare different instruments and to estimate if a candidate instrument possibly fulfills its scientific goal prior to selection for a mission.

If the incoming flux is completely inside the angular acceptance of the instrument and if there is no dependence of the differential geometric factor on direction then one can write

$$\begin{aligned} R_i &= \int G_i(v) \iint \cos\theta_v \cos\varphi_v v f_i(v,\theta,\varphi)\; \sin\theta\; \mathrm{d}\theta\; \mathrm{d}\varphi\; v^2 \mathrm{d}v \\ &= \int G_i(v)\; v\; f_i(v) v^2 \mathrm{d}v \end{aligned} \tag{3.8}$$

Equation 3.8 can easily be inverted and the flux $f_i(v)$ can be derived once the integral geometric factor has been established and θ_v and φ_v are known. A typical example for such an integral measurement is the solar wind measurement with a Faraday cup (see also Section 3.3.5). Such an instrument has a wide angular acceptance, much wider than the solar wind angular spread. The solar wind flows away from the Sun in radial direction within a few degrees, plus the aberration because of the spacecraft motion, thus its direction is known reasonably accurately. Even modern solar wind composition instruments are designed to integrate over the solar wind angular distribution [e.g. *Hovestadt et al.*, 1995]. If the incoming flux is not completely inside the angular acceptance of the instrument or

θ_v and φ_v are not known, then one has to infer the missing information from modeling the particle distribution function to obtain the particle flux from the measured count rate and inversion of Equation 3.4.

With modern instrumentation one aims to measure complete particle distribution functions, that is one measures differential count rates depending on all variables (v, θ, φ) with a certain resolution $(\Delta v, \Delta\theta, \Delta\varphi)$ given by the instrument. Thus, the count rate in one resolution element is (see Equation 3.4)

$$R_{i,jkl} = \int_{\varphi_l-\Delta\varphi/2}^{\varphi_l+\Delta\varphi/2} \int_{\theta_k-\Delta\theta_k/2}^{\theta_k+\Delta\theta_k/2} \int_A \int_{v_j-\Delta v/2}^{v_j+\Delta v/2} v f_i(v,\theta,\varphi)\, T_i(v,\theta,\varphi) \times v^2 \mathrm{d}v\, \cos\theta_v \cos\varphi_v \mathrm{d}A\, \sin\theta\, \mathrm{d}\theta\, \mathrm{d}\varphi \tag{3.9}$$

which often is approximated as

$$R_{i,jkl} = v_j\ f_{i,jkl}\ T_{i,jkl}\ v_j^2 \Delta v\ \cos\theta_k \cos\varphi_l A_{\mathrm{eff}}\ \sin\theta\ \Delta\theta\ \Delta\varphi \tag{3.10}$$

with $T_{i,jkl}$ the transmission for species i for velocity step j, polar angle step k, and azimuth angle step l, and A_{eff} is the effective entrance area, e.g. the size of the smallest aperture along the particle trajectory inside the instrument. $f_{i,jkl}$ is the incoming particle flux and is assumed to be constant over $\Delta\Omega\Delta E$. $R_{i,jkl}$ is the count rate in these discrete instrument coordinates. In modern plasma instruments energy analysis is performed most of the time (e.g. by using an electrostatic analyzer) and therefore it is convenient to write

$$R_{i,jkl} = f_{i,jkl}\ \widetilde{T}_{i,jkl}\ \frac{2E_j^2}{m_i^2} \left(\frac{\Delta E}{E}\right)_j \cos\theta_k \cos\varphi_l A_{\mathrm{eff}}\ \sin\theta\ \Delta\theta\ \Delta\varphi \tag{3.11}$$

where $(\Delta E/E)_j$ is the energy resolution at step j, and the substitution

$$v^2 \Delta v = \frac{\sqrt{2}E^{3/2}}{m^{3/2}} \frac{\Delta E}{E} \tag{3.12}$$

was used. Note that the transmission in Equation 3.10 changed from $T_{i,jkl}$ to $\widetilde{T}_{i,jkl}$ in Equation 3.11 because of the variable change. In analogy to Equation 3.5 we can combine the instrument related terms in Equation 3.11 to the geometric factor $G_{i,jkl}$ for a resolution element as

$$G_{i,jkl} = \widetilde{T}_{i,jkl}\ \frac{2E_j^2}{m_i^2} \left(\frac{\Delta E}{E}\right)_j\ A_{\mathrm{eff}}\ \sin\theta\ \Delta\theta\ \Delta\varphi \tag{3.13}$$

If $\Delta\theta$ and $\Delta\varphi$ are constant over the measured parameter space, which is often the case, we can write

$$R_{i,jkl} = G_{i,j}\ f_{i,jkl}\ \cos\theta_k \cos\varphi_l \tag{3.14}$$

and if even $(\Delta E/E)_j$ is constant we can write

$$R_{i,jkl} = G_i\ f_{i,jkl}\ \cos\theta_k \cos\varphi_l \tag{3.15}$$

The ultimate aim of any calibration campaign is the determination of the full set of $G_{i,jkl}$ for all discrete values of E_j, θ_k, φ_l, which are covered by the instrument, and for

all species of interest. The step size in these variables has to be commensurate with the resolution and the complexity of the instrument. With the discrete measurements for the geometric factors for each resolution element the integral in Equation 3.6 for the total geometric factor transforms into a sum. For an energy E_j we get for the total geometric factor

$$G_{i,j} = \sum_k \sum_l \widetilde{T}_{i,jkl} \frac{2E_j^2}{m_i^2} \left(\frac{\Delta E}{E} \right)_j (A_{\text{eff}})_{k,l} \, \Delta\varphi \, \Delta\theta \tag{3.16}$$

with $(A_{\text{eff}})_{k,l}$ the measured active area at φ_l and θ_k. For plasma instruments the energy resolution often is independent of the energy which simplifies Equation 3.16 to

$$G_{i,j} = \left(\frac{\Delta E}{E} \right) \sum_k \sum_l \widetilde{T}_{i,jkl} \frac{2E_j^2}{m_i^2} (A_{\text{eff}})_{k,l} \, \Delta\varphi \, \Delta\theta \tag{3.17}$$

whereas the energy dependence of $\widetilde{T}_{i,jkl}$ usually remains.

Ideally, when calibrating the instrument, the explored range of these parameters spans the full parameter range of the instrument with a grid size small enough to safely interpolate for the conditions to be encountered when performing measurements in space. Having a parameter space spanned by three external variables and probably a few instrument variables in addition, one easily sees that a thorough instrument calibration takes a considerable time, which often is not available in the time after completion of the instrument and before delivery for integration into the spacecraft. If possible, an analytic form of the differential geometric factor will be derived from the discrete measurements, combining the theoretical model of the instrument with the instrument calibration. The theoretical model can either be a truly theoretical derivation of the instrument response, or be the result of an ion-optical simulation, or, most commonly, be the combination of both [e.g. *Wurz*, 1999]. Of course it is very beneficial to have a good analytical (theoretical) description of the instrument, which can place a limit on the number of individual data points needed to be measured during the calibration campaign. Comparison between the predictions of the theoretical model and the calibration data will allow verification of the proper build and functioning of the instrument and identify spurious sensor responses, for example from particles scattering through the analyzer structure. Often subtle problems in the real instrument are identified by comparing the calibration data with the simulated instrument response. By changing the simulation to represent the non-ideal instrument the understanding of the instrument is improved and the calibration itself may be better as well [e.g. *McCarthy and McFadden*, 1998; *Vilppola et al.*, 2001]. Furthermore, with sufficient confidence in the theoretical model one may extrapolate the calibration results to parameter ranges, for example to higher energies, that could not be covered by calibration measurements. Moreover, having an analytical model will make the data analysis easier and also be useful in forward modeling.

See Section 3.4 for the geometric factor determination for medium energy ion instrumentation, which gives an example where the complete particle distribution function is measured. Section 3.5.2 gives details on the geometric factor determination of high energy telescopes, which is an example of an integral measurement.

Often the number of counts per measurement step is not transmitted to Earth directly, but some data interpretation is done by onboard processing, e.g. calculation of the density,

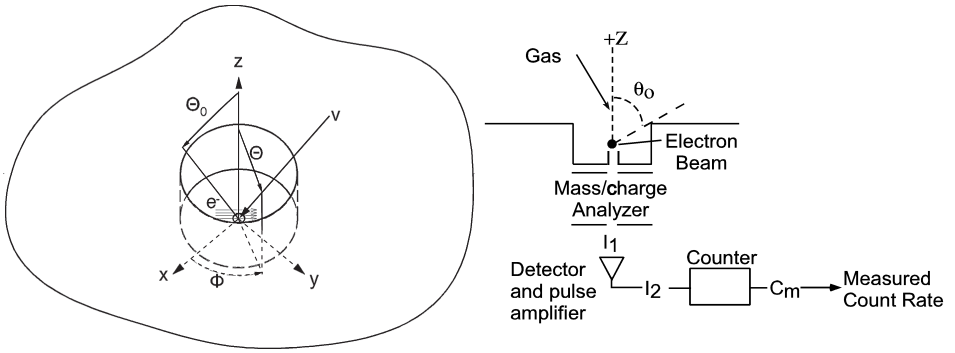

Figure 3.1: Left: Coordinate system for the ion source, which is represented as a hole in the spacecraft skin, and a particle stream of velocity $\boldsymbol{v}$ arriving at the source. *Right:* A schematic representation of the overall mass spectrometer response. After *Kayser et al.* [1979].

bulk velocity, phase space density and others, which is referred to as moment calculations. This was done first on the IRM instrument on the AMPTE mission [*Curtis et al.*, 1989] and is quite standard for modern instrumentation for magnetospheric research, such as the ion and electron instruments on the Cluster and Equator-S missions. For a detailed discussion of moments see Section 1.3.3 above or *Paschmann et al.* [1998]. Obviously, if such calculations are performed by the instrument their verification has to be part of the calibration of the instrument.

In conclusion of this section the reader is advised to look up the exact definition and the precise units when a geometric factor is reported for an instrument. The term geometric factor, although used widely, is a generic term and the meaning and definition changes from author to author, in part influenced by the specifics of a class of instruments or the scientific scope of an investigation.

3.1.2 The Generic Mass Spectrometer Response

In the following we will derive mathematical formulas for the response of a generic mass spectrometer that is located on a spacecraft and therefore moves with a certain velocity with respect to the neutral gas to be investigated. A generic neutral gas mass spectrometer system is shown in Figure 3.1. In the open source or neutral beaming mode, gas comes into the ion source at an angle (θ, φ) and is ionized by an electron beam (in most applications). In the closed source mode, some of the incoming gas particles collide with the ion source walls, becoming thermally accommodated to the wall temperature after several collisions and are then ionized. The combination of the two modes, as illustrated in Figure 3.1, is called a quasi-open source. The ion current produced for the ionization fragment f of a species m at time t

$$I_0(m, f, t) = \sigma(m, f)\, n_s(m, t - t_0)\, L_e\, A_e\, j_e\, \varepsilon(f) \tag{3.18}$$

where $I_0(m, f, t)$ is the ion current at exit slit of the ion source, $\sigma(m, f)$ is the ionization cross-section for producing fragment f from species m, $n_s(m, t)$ is the number density

of species m at time t in the electron beam (i.e., inside the ion source), A_e is the cross-sectional area of the electron beam, j_e is the electron beam current density (and the electron current for ionization is $I_e = A_e j_e$), L_e is the path length of electron beam, $\varepsilon(f)$ is the extraction efficiency and t_0 is the instrumental time offset for time constants and other delays. The equation assumes that the ionization probability depends on the electron speed alone (i.e., the electron speed is much higher than the gas speed) and is constant for a given electron energy.

$$I_0 = \frac{\Delta Q}{\Delta t} = q_0 \frac{\Delta N_I}{\Delta t} \tag{3.19}$$

with ΔN_I the number of created ions per time interval Δt and q_0 is the elementary charge. Using an ionization probability, P_I, and the number of neutral species, N_N, in the ionization region one can rewrite Equation 3.19 as

$$I_0 = \frac{\Delta Q}{\Delta t} = q_0 \frac{P_I \; N_N}{\Delta t} \tag{3.20}$$

The number of neutral species in the ionization region is $N_N = n_s V_I$, with V_I the ionization volume, which is $V_I = L_e \; A_e$. Thus we get for Equation 3.19

$$I_0 = \frac{\Delta Q}{\Delta t} = q_0 \frac{P_I \; n_s \; L_e \; A_e}{\Delta t} \tag{3.21}$$

The probability for ionization (e.g. detecting fragment f of species m) is derived using Equations 3.18 and 3.21 as

$$P_I(m, f) = \sigma(m, f) \; \frac{j_e}{q_0} \; \varepsilon(f) \; \Delta t = \sigma(m, f) \; \frac{j_e}{q_0} \; \varepsilon(f) \; \frac{\Delta x}{v_m} \tag{3.22}$$

where Δx is the geometrical dimension of the electron beam along the trajectory of the neutral gas molecule and v_m is average speed of the species m of the neutral gas.

For surface non-reactive gases and for small inlet chamber volumes with negligible time constants $t_0 = 0$. The ion current into the detector is

$$I_1 = I_0 \; \tau \; (1 - \alpha n) \equiv S \; n_s \; (1 - \alpha n) \tag{3.23}$$

where τ is the transmission efficiency for fragment f from species m, n is the average particle density in the ionization region and α is the attenuation factor due to pressure-induced scattering in the sensor. Usually the interior pressure in the sensor is low enough so that the last pressure attenuation factor can be ignored ($\alpha = 0$). Combining all source parameters into the "sensitivity" factor S for gas m and fragment f gives

$$I_1 = I_0 \; \tau = S(m, f) \; n_s \tag{3.24}$$

with

$$S(m, f) = \sigma(m, f) \; L_e \; A_e \; j_e \; \varepsilon(f) \; \tau \tag{3.25}$$

Often the sensitivity, defined in Equation 3.24, is referred to the pressure (via $p_s = n_s k_B T_a$) rather than the density assuming the ambient gas temperature, T_a, is known

$$I_1 = \tilde{S}(m, f) \; p_s = \frac{S(m, f)}{k_B \; T_a} \; p_s \tag{3.26}$$

with the typical unit of $\tilde{S}(m, f)$ being A/mbar or in older publications A/Torr. In some cases the sensitivity is defined without the electron current

$$I_1 = \hat{S}(m, f)\, I_e\, p_s \tag{3.27}$$

where

$$\hat{S}(m, f) = \sigma(m, f)\, L_e\, \varepsilon(f)\, \tau \tag{3.28}$$

with the typical unit of $\hat{S}(m, f)$ being mbar^{-1} or in older publications Torr^{-1}. This definition is particularly useful for instruments with variable electron emission, I_e.

The output of the detector, I_1, will be amplified to I_2 and may be subject to dead time and pulse pile-up effects (see Section 3.1.3 below). The output of the counter over an integration period, δt, is then

$$C_{m,f} = \int_t^{t+\delta t} I_2 \, \mathrm{d}t \tag{3.29}$$

The differential number density $\mathrm{d}n_s$ at speed, v, due to the spacecraft motion is [*Kayser et al.*, 1979]

$$\mathrm{d}n_s = n_a(m, t)\, vf(v, u)\, \frac{q(v, \theta, \varphi)}{v}\, v^2\, \cos\theta\, \mathrm{d}\theta\, \mathrm{d}\varphi\, \mathrm{d}v \tag{3.30}$$

where f is the distribution function, θ the elevation angle of v, φ the azimuthal angle of v, $n_a(m, t)$ the ambient density of species m, $q(v, \theta, \varphi)$ the source acceptance function. Equation 3.30 is almost identical to Equation 3.3, with the only difference being that instead of the instrument transmission we use the source acceptance function for an open source $q(v, \theta, \varphi)/v$. The division by v is because the probability for ionization is proportional to the time the gas molecule spent in the electron beam (see Equation 3.25).

In the spacecraft reference frame, the apparent bulk motion of the atmosphere is

$$\boldsymbol{u} = \boldsymbol{w} - \boldsymbol{v}_{sc} \tag{3.31}$$

where $\boldsymbol{w}$ is the atmospheric wind vector, $\boldsymbol{v}_{sc}$ is the spacecraft velocity vector, and $\boldsymbol{u}$ is the net velocity vector observed in the spacecraft. In the ionizing region of the open source, where molecules travel unimpeded into the electron beam, the number density, $n_{s,1}$, is

$$n_{s,1} = \int_0^{\theta_0} \int_0^{2\pi} \int_{v_0}^{\infty} n_a q(v, \theta, \varphi)_1\, f(v, u)\, v^2\, \cos\theta\, \mathrm{d}\theta\, \mathrm{d}\varphi\, \mathrm{d}v \tag{3.32}$$

where $v_0 = v_{z,0}/(\cos\theta \cos\varphi)$, $v_{z,0}$ is the lower limit on velocities due to a retarding potential, and n_a is the ambient density. The distribution function is

$$f(\boldsymbol{v}, \boldsymbol{u})\, \mathrm{d}\boldsymbol{v} = (\beta/\pi)^{3/2}\, e^{-\beta(\boldsymbol{v}-\boldsymbol{u})^2}\, \mathrm{d}\boldsymbol{v} \tag{3.33}$$

where $\beta = m/2k_BT$, m is the species mass, k_B is the Boltzmann's constant, and T is the absolute temperature (K) for a Maxwell-Boltzmann distribution. The resulting ion current, I_1, is proportional to the number density, n_{s1}.

For example, the approximation of the angular transmission $q(\theta, \varphi)$ by a Gaussian in $\sin\theta$ and $\sin\varphi$ gives a good representation for some instruments

$$q(\theta, \varphi) = \frac{1}{\pi \sin\phi_0 \ \sin\theta_0} \exp\left(-\frac{\sin^2(\theta)}{\sin^2(\theta_0)} - \frac{\sin^2(\varphi)}{\sin^2(\varphi_0)}\right) \tag{3.34}$$

Solutions using this source acceptance function have been given by *Kayser et al.* [1979] along with an example of the solution to the integral for q as a delta function (high speed case) (see also *Kasprzak et al.* [1987]). The angular coefficients can be determined in flight on a spinning spacecraft or from laboratory data.

The analytic solution for the quasi-open source, which can be derived only for a sphere with an ionization source at its center, has been given in *Hedin et al.* [1964]. Assuming the m and t dependence is implicit in the densities, adopting their notation for the open source cone half-angle as

$$\omega = \theta_0 \tag{3.35}$$

and assuming no dependence on φ, i.e., a symmetric source, then the total number density in the ionization region is

$$n_s = n_{s,1} + n_{s,2} \tag{3.36}$$

where $n_{s,1}$ is the 'open source' contribution to the number density and $n_{s,2}$ is the 'closed source' contribution to the number density. The closed source contribution is

$$n_{s,2} = n_a \sqrt{\frac{T_a}{T_s}} \ \frac{F(S)\, k_2 \ \sin^2(\omega/2) \ \cos^2(\omega/2)}{1 - k_2 \cos^2(\omega/2)} \tag{3.37}$$

where ω is the cone half-angle of the open source as viewed from the electron beam, k_2 is the probability of a molecule being re-emitted after colliding with the surface, n_a is the ambient gas density, T_a is the ambient gas temperature, and T_s is the ion source temperature, and

$$F(S) = e^{-S^2} + \pi^{\frac{1}{2}} \ S \ (1 + \mathrm{erf}(S)) \tag{3.38}$$

with the speed ratio along the source normal direction

$$S = v_{sc} \cos\chi \sqrt{\frac{m}{2k_B T_a}} \tag{3.39}$$

where v_{sc} is the spacecraft speed, χ the angle between the normal to the entrance aperture and the spacecraft velocity vector, m is the mass of the gas, and k_B is the Boltzmann constant. The open source contribution is

$$n_{s,1} = \frac{n_a}{2}\left(1 + \mathrm{erf}(S) - M_0\, e^{-S^2} - H(S, S_p, \omega)\right) \tag{3.40}$$

with the total speed ratio

$$S_T = v_{sc} \sqrt{\frac{m}{2k_B T_a}} \tag{3.41}$$

and the speed ratio in the plane of the orifice (or beam perpendicular speed, v_p)

$$S_p = \sqrt{S_T^2 - S^2} = S_T \ \sin\chi \tag{3.42}$$

The remaining functions are

$$H(S, S_p, \omega) = e^{-S^2 - S_p^2} \sum_{l=1}^{\infty} \frac{(S_p^2)^l}{l!} \ \sum_{k=1}^{l} \Big(\sin^2(\omega)\Big)^k \ M_k \tag{3.43}$$

with

$$M_0 = \Big(1 + \mathrm{erf}\big(S\cos\omega\big)\Big) \cos\omega \, e^{S^2\cos^2(\omega)} \tag{3.44}$$

$$M_1 = \left(\frac{1}{2} + S^2\cos^2(\omega)\right) M_0 + (S/\pi)^{\frac{1}{2}} \cos^2(\omega) \tag{3.45}$$

and for $k > 1$

$$M_k = \left\{\left(S^2\cos^2(\omega) + \frac{4k-3}{2}\right) M_{k-1} - \frac{2k-3}{2} \ M_{k-2}\right\} \frac{1}{k} \tag{3.46}$$

In the laboratory with $S = 0$ and no wall absorption ($k_2 = 1$) using a thermally accommodated gas, the number density in the ion source is

$$n_{s,\mathrm{lab}} = n_{\mathrm{lab}} \ \left(\sqrt{\frac{T_{\mathrm{lab}}}{T_s}}\cos^2(\omega/2) + \sin^2(\omega/2)\right). \tag{3.47}$$

The gas sensitivity $K(m)$, which is the prime quantity describing the performance of the instrument, can be obtained from the calibration

$$C_{s,\mathrm{lab}}(m, f) = K(m, f) \ n_{s,\mathrm{lab}}(m) + C_{bkg,\mathrm{lab}}(m, f) \tag{3.48}$$

where $C_{s,\mathrm{lab}}$(m, f) and $C_{bkg,\mathrm{lab}}$ are the recorded counts for a gas density $n_{s,\mathrm{lab}}$ and the background, respectively. Thus, we get for the sensitivity

$$K(m, f) = \frac{C_{\mathrm{lab}}(m, f) - C_{bkg,\mathrm{lab}}(m, f)}{n_{s,lab}(m)} \tag{3.49}$$

or

$$K(m, f) = \frac{\kappa(m, f)}{\sqrt{T_{\mathrm{lab}}/T_s} \ \cos^2(\omega/2) + \sin^2(\omega/2)} \tag{3.50}$$

with

$$\kappa(m, f) = \frac{C_{\mathrm{lab}}(m, f) - C_{bkg,\mathrm{lab}}(m, f)}{n_{\mathrm{lab}}(m)} \tag{3.51}$$

where $C_{bkg,\mathrm{lab}}$ is the count rate arising from the background gas in the calibration facility and $\kappa(m, f)$ is the usual definition of the gas sensitivity.

During flight, the number density inside the ion source for species m is derived from

$$n_s(m) = \frac{C_{s,\text{flight}}(m,\, f) - C_{bkg,\text{flight}}(m,\, f)}{K(m,\, f)} \tag{3.52}$$

where $C_{s,\text{flight}}(m,\, f)$ are the recorded counts. $C_{bkg,\text{flight}}(m,\, f)$ is the signal contributed by background processes (outgassing, multiplier dark noise etc.) and K(m, f) is the calibration factor for gas m and mass fragment f previously determined in the laboratory.

If $\omega = 0$, Equation 3.52 predicts the response of the ideal closed source. In such a source the entrance aperture area is small compared to the antechamber surface area and gas molecules thermally accommodate to the chamber walls before escaping, making the system act like a hohlraum[4], independent of the internal structure. The equation was originally derived by applying the continuity equation and balancing the incoming and outgoing particle flux assuming no surface loss or transformation [*Tsein*, 1946; *Schultz et al.*, 1948; *Horowitz and La Gow*, 1957]. The ion source density is related to the ambient density by

$$n_s(m) = n_a(m)\sqrt{\frac{T_a}{T_{\text{lab}}}}F(S) \tag{3.53}$$

The ion source temperature is no longer present because of the balance of flux into and out of the ion source region from the antechamber. It is assumed that the ion source temperature is dominated by the filament temperature and is the same for flight conditions as well as laboratory calibration conditions. For $S\cos\chi \geq 1.2$, $F(S\cos\chi) \sim 2\pi^{\frac{1}{2}} S\cos\chi$ within 1 % and is independent of the ambient gas temperature T_a.

Note that the open source measurement is a population counting mode while closed source measurement is a flux measuring mode.

For the Ion-Neutral Mass Spectrometer (INMS) on Cassini, the number density enhancement in the closed source at a 6 km s^{-1} spacecraft speed is about a factor of 50 above that of the ambient density for N_2 [*Kasprzak et al.*, 1996; *Waite et al.*, 2004]. For the Double Focusing Mass Spectrometer (DFMS) of the ROSINA instrument [*Balsiger et al.*, 2007] on the Rosetta spacecraft a factor of about 4 enhancement for Neon was found for a speed of 800 m s^{-1}. Monte Carlo techniques are frequently used to provide a better estimate of the transmission probability for non-ideal closed source geometries [e.g. *Hughes*, 1965; *Hedin and Nier*, 1966; *Kasprzak et al.*, 1968; *Cohen*, 1968].

It has been pointed out by *von Zahn* [1974] that even for the most open quasi-open ion source, which is just a flat plate moving with the spacecraft speed and with ionization by an electron beam above the plate, the ratio of the reflected particles, N_{out}, to those coming in toward the plate, N_{in},

$$N_{\text{out}}/N_{\text{in}} = \frac{F(S)}{\big(1 + \text{erf}(S)\big)}\sqrt{\frac{T_a}{T_s}} \tag{3.54}$$

where T_s is the source temperature, is still much larger than 1. This is because the speed of the reflected particles after thermal accommodation is very low and the total number density above the plate is mainly determined by the reflected particles. So a quasi-open

[4] After the German word for cavity

source behaves more like a closed source than an open source if both types of particles are detected. In order to separate out the faster moving open source particles from the thermally accommodated particles, a retarding potential [*Nier et al.*, 1973; *Niemann et al.*, 1980a, 1998] or an energy range selection using an energy filter [*Zeman*, 1977; *Mahaffy and Lai*, 1990; *Kasprzak et al.*, 1996; *Waite et al.*, 2004; *Mahaffy*, 2004] have been employed.

For a quasi-open source the equation could be

$$C_{s,\text{flight}}(m, f) = (1 - \psi)\, K(m, f)\, N_{\text{closed}}(S, \omega) + \psi\, K_b(m, f, v, v_p)\, N_{\text{open}}(S, S_p, \omega) \tag{3.55}$$

where N_{closed} is the closed source contribution and N_{open} is the open source contribution, which both are functions of the open source cone half-angle ω. $K(m, f)$ and $K_b(m, f, v, v_p)$ are calibration values and ψ is a method of distinguishing the two ion populations.

The above analysis assumes a single gas or a gas mixture whose mass peak fragments f do not interfere with each other. When this is not the case, the resulting mass spectrum of overlapping fragment peaks must be deconvolved to determine the count rates for the individual species before applying Equation 3.52.

3.1.3 Dead Time Corrections in Pulse Counting Systems

Ion and electron signal detectors are varied: direct current detection using a Faraday cup or a high transmission grid with an electrometer; discrete or continuous channel multipliers (channeltrons) operating in pulse counting mode or current mode; and microchannel plates operating in either current or pulse counting mode. For example, the ROSINA Double Focusing Mass Spectrometer (DFMS), the most complex such particle instrument today, uses all three detector types: Faraday cup, channel electron multiplier (CEM) and microchannel plate (MCP) detectors [*Balsiger et al.*, 2007].

In nearly all pulse-counting detector systems, there will be a minimum amount of time separating successive events in order that they be recorded as two separate pulses. In some cases the limiting time may be set by the processes in the detector itself, and in other cases the limit may arise in the associated electronics. Every type of pulse processing circuit has an electronic dead time associated with it. Events that occur during the dead time of the system are lost and are not analyzed. Therefore, the system will undercount the number of incident particles. Because of the random nature of particle detection there is always some probability that a true event will be lost because it occurs too quickly following a preceding event.

There are two extreme types of a detector response to an event, a non-paralyzable and a paralyzable response [*Knoll*, 2000]. In a non-paralyzable response, any event that occurs during the electronic event processing time does not influence the length of dead time of the first event. In a paralyzable response an event occurring during a dead time starts another dead time interval. Each electronic pulse processing circuit must be examined to determine its dead time characteristics. Most circuits used in spacecraft applications are non-paralyzable at lower count rates, but as the rates go up the dead time characteris-

tics may become paralyzable. The counting rate correction factors for the two different responses are

$$m = \frac{n}{1 + n\ \tau} \qquad \text{(non-paralyzable)} \tag{3.56}$$

and

$$m = n\ \exp(-n\ \tau) \qquad \text{(paralyzable)} \tag{3.57}$$

where n is the true event rate, m is the measured event rate and τ is the per event dead time. When the rates are low the two models give virtually the same result, only at high rates the behavior becomes markedly different. Knowing τ one can calculate the true event rate from the measured event rate. However, Equation 3.57 cannot be solved analytically for n but must be solved numerically. Note, that for both Equations 3.56 and 3.57 there are maximum measured rates: in the non-paralyzable case $m_{\max} = 1/\tau$ for $n \gg 1/\tau$ and in the paralyzable case $m_{\max} = 1/(\tau\ e)$ at $n = 1/\tau$, where $e = 2.718281828\ldots$. For the paralyzable case m will become smaller for larger n beyond the maximum. Equation 3.57 is double valued and one will not be able to deduce the true event rate when operating the sensor at input event rates exceeding $m_{\max}$. It is recommended that sensor operation is in a range of $m/n > 0.6$ where inversion of Equations 3.56 and 3.57 can be performed safely (see Figure 3.2).

There are three ways of handling the dead time undercount: with hardware, with software and/or with direct calibration. The software correction does not require any additional circuitry but uses the actual measured count rate of analyzed events and the Equations 3.56 or 3.57, as appropriate, to compute the dead time corrected rates. The advantages of this method are that it does not require any additional hardware, and it generally performs very well as long as the count rates are not too high (computed dead time below 30–40 % of the measurement time). The disadvantage is that the simple formulas may not represent the complex behavior of the pulse analysis circuit.

In the widely used carbon-foil time-of-flight (TOF) instruments the dead time usually occurs in the time-to-amplitude converters (TAC) used for the TOF measurement. The start pulse of the time measurement system triggers a time window during which the electronics waits for an associated stop pulse. This is a typical case for a non-paralyzable system where the true event rate can be calculated from the measured rate. In addition, with individual counters for the start and the stop rates, which are much faster and are useful also for other purposes, one gets additional information to correct for the counting loss resulting from the dead time. In a sensor for energetic particles, the largest components of dead time usually occur in the pulse shaping and amplification chain (a few μs) or in analog-to-digital converters (up to tens of μs for very slow converters). Again, an instrument can be equipped with additional counting circuits that normally operate much faster than the pulse processing circuits so that a counter in parallel can provide the total number of the incident particles and that number can be used to correct the analyzing system's dead time losses. The advantage of this approach is that it provides a direct measurement of the dead time. The disadvantage is that it requires additional circuitry, power and telemetry.

The calibration method requires a particle source of suitable energy and flux, in the best case replicating the situation expected in space. If fluxes can be varied sufficiently, one can explore the full range of dead time effects, as they are described by Equations 3.56

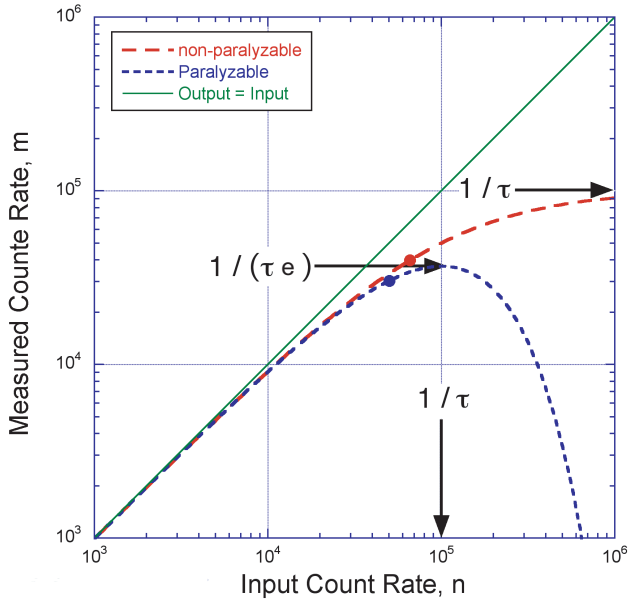

Figure 3.2: Measured count rate versus input count rate for a non-paralyzable and a paralyzable system, Equations 3.56 and 3.57, using a dead time $\tau = 10^{-5}$ s. The two filled circle symbols indicate the points where $m/n = 0.6$, for the paralyzable (short dashes) and non-paralyzable case (long dashes), respectively.

and 3.57, and one can derive a value for τ. Such a calibration can also be performed using an electronic random pulser, a device producing pulses with a fixed average rate but random spacing in time. The pulser must be connected to the pre-amplifier input and then the system count rate monitored as a function of the pulse rate, as set on the dial. The advantage of this method is that, under certain circumstances, it provides a measure of dead time corrections for the electronics. The disadvantages are 1) it is cumbersome to use, 2) the pulser produces uniform amplitude pulses so that the true response of the system to a variety of pulse amplitudes cannot be tested, 3) the particle detector is not evaluated.

For a neutral gas mass spectrometer there is another method for determining the dead time correction parameters in the laboratory and in flight. The fractionation ratio for a gas species that is thermally accommodated with the surface should be constant as function of gas pressure as long as the pressure is below about 10^{-4} mbar. For example, for N_2 gas, the 14 u/q peak due to N^+ and N_2^{2+} is a small fraction of the 28 u/q due to the N_2^+ ion. By tracking the apparent change in the 14/28 ratio due to pulse counting dead time in the major intensity 28 u/q peak, but not the minor intensity 14 u/q peak, as a function of pressure and assuming that the real ratio should be constant, the dead time parameters can be deduced. In the Cassini INMS instrument there are two pulse counting multipliers that differ in gain and are used to cover the dynamic range [*Waite et al.*, 2004]. Tracking the ratio of the two signal outputs simultaneously enables the lower count rate output to

be used when the higher count rate detector has a signal that is large enough to have a significant pulse-pile-up correction.

3.2 Low and Medium Energy Electron Calibration

Electrons in the energy range from a few eV to about 30 keV generally contain most of the electron number density in the near Earth environment (the magnetosphere and the solar wind), with the exception of the lower ionosphere. These particles play a leading role in much of the plasma physics both as current carriers and in determining many of the various wave modes in the plasma. Along with spacecraft emitted photoelectrons, they play a primary role in determining the spacecraft potential. Their energy spectra are varied, see for example the summary by *Lin et al.* [1995] or Figure 1.2 and the discussion in Section 3.4.1.2. Ionospheric photoelectrons are observed from ~0 to ~60 eV, plasmasheet electrons vary in temperature from about 100 eV to several keV, and magnetosheath electrons have temperatures in the range of 30–100 eV. In the auroral regions, plasmasheet and magnetosheath electrons can be accelerated along the magnetic field to tens of keV. Solar wind electrons are generally cool ($T_e \approx$ 5–10 eV), however a suprathermal tail often extends beyond 1 keV [*McComas et al.*, 1992] and solar flares cause even more energetic electrons as discussed in Section 3.5. In addition, cold ionospheric electrons (T_e <1 eV) are also present throughout the Earth's magnetosphere and can often be measured by standard electron plasma instruments since spacecraft charging generally increases electron energies above the instrument's lower energy threshold.

We define electron plasma instruments as those measuring electrons at energies from near 0 eV to about 30 keV. They generally consist of electrostatic analyzers (ESAs) combined with microchannel plate (MCP) or channel electron multiplier (CEM) detectors. Electron plasma instruments are usually considerably simpler than ion plasma instruments and mass spectrometers, since the mass of the registered particle does not need to be measured, but they still present several challenges to the calibration effort. These challenges include the development of electron sources suitable for calibrations over a large energy range, maintaining beam stability on the time scales of the measurements, and correcting beam deflections associated with the Earth's magnetic field.

This section begins with a discussion of several electron sources (Section 3.2.1). Various difficulties with electron beams, such as scattering and finite gyro radius, are pointed out. We include a discussion of test equipment considerations (Section 3.2.2), followed by a description of the ideal analyzer response (Section 3.2.3) determined from computer simulations. We continue with a discussion of the primary sources of non-ideal instrument behavior (Section 3.2.4) to set the stage for calibration procedures (Section 3.2.5). This last section describes several calibration procedures that should provide adequate information about an instrument's response to verify its proper operation. We also include suggestions and warnings regarding problems that can arise during calibrations. We conclude (Section 3.2.6) with a discussion about how calibrations, both pre-flight and in-flight, will be used to transfer the collected data into physical parameters, both on the ground and on the spacecraft.

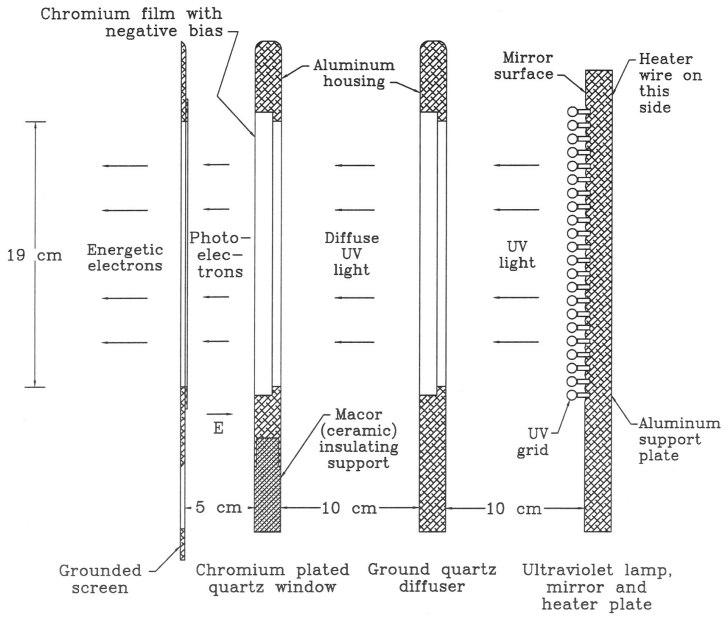

Figure 3.3: Schematic of an electron calibration source. UV photons emitted from a mercury arc lamp are passed through a ground quartz diffuser and strike a thin chromium film. The film is biased at a negative voltage and placed near a grounded screen so that photoelectrons emitted from the film are accelerated to the desired energy. From *Lessard et al.* [1998].

3.2.1 Electron Sources for Instrument Calibrations

3.2.1.1 Ultraviolet Photocathode Electron Sources

Since calibrations generally require a wide, uniform electron beam, an ultraviolet (UV) photocathode electron source is a good choice [*Burch et al.*, 1981; *Lessard et al.*, 1998]. Figure 3.3 shows a schematic drawing of such an electron calibration source. An UV photocathode electron source was first introduced to measure the detection efficiency of channeltrons for electrons [*Østgaard*, 1979] and has been used for calibration purposes since then [e.g. *Winningham et al.*, 1981; *Johnstone et al.*, 1997]. The photocathode consists of a thin (350 Å) layer of pure chromium deposited on a quartz window. The cathode is biased at a negative voltage and a grounded acceleration grid is placed a few cm in front of the cathode to provide a uniform accelerating field. The cathode metalization thickness is chosen so that most of the UV is transmitted to maximize the photoelectron emission. A ground or frosted quartz window is placed between the UV lamp and photocathode to diffuse the UV light and create a more uniform illumination. A mercury-arc lamp, typically temperature controlled, gives almost pure (99 %) flux of 2537 Å UV photons, corresponding to a photon energy of 4.9 eV, which is just slightly higher than the work function of chromium. Also, a commercial EPROM eraser lamp can be used as UV source [*Lessard et al.*, 1998]. With a good choice of the UV lamp and a stable high voltage (HV) power supply the produced electron flux can be very nearly mono-energetic.

If the UV source is powered by an AC power supply, it will flicker at the double of the mains frequency and produce time aliasing in the calibration for short sample times. The alternative is to use a DC current source and a ballast resistor or to use an AC supply whose frequency is much higher than the instrument sampling time. *Lessard et al.* [1998] reports that the stability of the UV lamp can also be increased by heating the lamp to about 75 °C.

Although an UV photocathode electron source is the first choice, several problems have been observed with these electron sources. Since the UV photons are transmitted through the photocathode, these sources are not suitable for component testing of the MCP or CEM detectors. This is because the UV light can scatter down the microchannels before producing secondary electrons. This creates an unsaturated, exponential pulse height distribution superimposed on the distribution produced directly by the cathode electrons. For testing of a complete instrument, UV attenuation in the analyzer should be sufficient to reduce UV at the detector to undetectable levels.

In one photocathode source system, a large decrease in electron flux was observed after several years of proper operation. It was initially thought that the chromium had evaporated (perhaps due to ion bombardment) and a new coating was applied. However, it was later determined that the flux reduction was due to poor electrical contact to the photocathode. A second problem was identified as due to improper acceleration grid construction. If the acceleration grid is not rigid and stretched tightly onto the grid mounting ring, the electric field will cause the grid to bow toward the photocathode. This will cause the accelerated electrons to focus into a narrower beam rather than remaining a broad uniform beam. The amount of bowing depends on the accelerating field strength, so the focusing will be energy dependent. In addition, the grid itself will cause shadowing and micro-lensing so that the beam at the detector will not be completely uniform. Some of the lensing problems can be minimized by using a fine grid attached to the photocathode side of a more rigid coarse grid. Also, electron scattering and secondary electron production are likely to occur at the accelerating grid but should be minimal for high transmission grids.

Unfortunately, the UV photocathode electron sources are also a source of negative ions because of neutral particles from the residual gas that become negative ions near the photocathode via electron attachment. If substantial numbers of negative ions are created and they are accelerated to energies >30 keV they can cause significant damage to the dead layer of SSDs resulting in an increased leakage current, a loss of energy resolution, and a reduced pulse height [*Knoll*, 2000]. Although subject to specifics of the detector and the radiation, serious changes appear for fluences of 10^{12} to 10^{13} protons cm^{-2}, for fluences of 10^{11} alpha particles cm^{-2}, and for fluences of 3×10^{8} heavy ions cm^{-2}. Note that at much higher ion energies noticeable damage to a SSD will occur already at much lower ion fluxes [*Simons et al.*, 1997]. Typical SSD configurations for electron detection will use a thin foil in front of the SSD to eliminate ions. However, if electron calibrations are performed without foils, the SSDs will be susceptible to damage from the ions. SSD configurations for ion detection do not have foils and may be damaged if they are exposed to fluxes of energetic negative ions. Broom magnets that keep out the electrons will not eliminate the negative ions from ion SSDs. If the instrument has electron and ion SSDs mounted in pairs and looking in the same direction, the ion detector will get a dose of negative ions that may damage its dead layer during an electron calibration. Generally, small negative ion fluxes are not a problem. However, if the vacuum is poor the negative ion flux will be significant and may even be comparable to the electron flux. Thus, monitoring the flux on the electron

SSD will not tell much about the ion detector's dose. Monitoring the ion detector during the electron detector calibration will help. However, the big problem happens if the electron source arcs, which produces a huge flux of negative ions that can damage the ion SSD. Since this ion flux will saturate the ion SSD, there is no way of monitoring the dose in such an event. The best solution is to not expose bare SSDs to an electron source during calibrations. Foils should always be in place for electron SSDs and ion SSDs should be covered.

3.2.1.2 Hot Filament Electron Sources

Filament sources are a common electron source, having the advantage of being relatively inexpensive and compact. They produce a fairly mono-energetic electron beam, depending on the quality of the power supplies. For low energy measurements, power supplies capable of 1–2 A filament current can often be floated to several hundred volts and used to power a hot filament electron source. Sources operated at higher accelerating potentials require more complicated power supplies with the filament powered by an AC voltage that introduces a current ripple that floats on the high voltage. In this case the filament source will often incorporate a rectifier filter at the filament to reduce the current ripple. Because of the strong temperature dependence of the electron emission from hot filaments

$$J_e \propto T^2 \exp(-\Phi/k_B T), \tag{3.58}$$

where Φ and T are the filament work function and temperature, and k_B is Boltzmann's constant (Richardson's law), the electron flux is a strong function of the filament current. Small current variations may remain leading to fluctuations in electron flux at the AC driving frequency. In this case the source will introduce variations in the measured counts that may be greater than statistical fluctuations. In addition, because of the exponential temperature dependence, small drifts in the filament current may result in significant changes in flux over longer time scales. A further drawback of hot filament sources is that the electron source is relatively small and therefore the electron beam will either be physically small or will have angle-position non-uniformities within a spreading beam. For these reasons filament sources are generally not as useful for most electron calibrations. However, filament sources can be essential for some tests. For example, filament sources smaller than a cubic centimeter can be mounted directly in front of an instrument providing a compact, low electron energy, test system for thermal vacuum testing. This arrangement allows thermal drift testing of the analyzer energy sweep, in particular for low energy offset drifts.

3.2.1.3 Radioactive Electron Sources

^{63}Ni provides a third useful source of electrons for both calibration and general testing. ^{63}Ni is radioactive and decays into ^{63}Cu via beta decay with a half-life of 100.1 years. Stainless steel strips with ^{63}Ni deposits of about 10 mCi and sized comparable to detector apertures provide adequate counts for most electron plasma instruments. These sources provide a virtually constant flux of electrons with a broad angle range that can uniformly fill the analyzer field-of-view (FOV). The energy range of the ^{63}Ni source is broad so it is useful for relative sensitivity calibrations of the instrument over nearly the entire energy range. The theoretical end-point energy of the beta decay is 66.85 keV. Figure 3.4 shows an

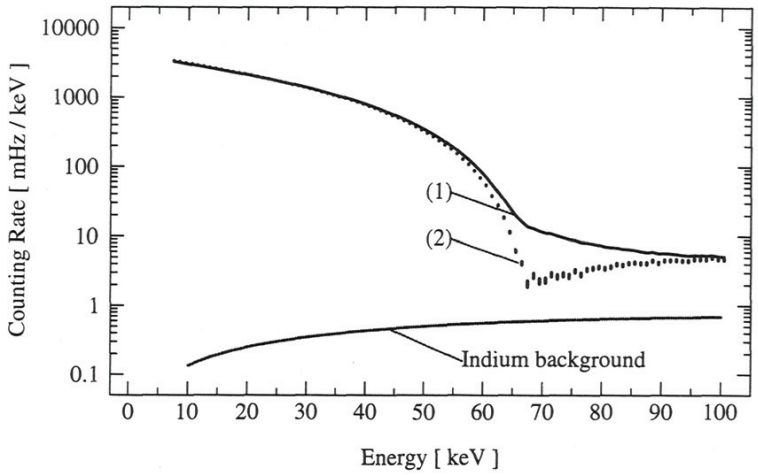

Figure 3.4: Beta decay spectrum from ^{63}Ni. Curve (1) is the measured spectrum including pulse pile-up and background. Curve (2) results from deconvolving pile-up response function. The calculated background from beta decay of ^{115}In is also shown. From *Gaitskell et al.* [1996].

electron energy spectrum for a ^{63}Ni source using a cryogenic particle detector [*Gaitskell et al.*, 1996].

^{63}Ni electron sources are also useful for thermal vacuum testing since they provide a simple stimulus for the instrument over a broad energy range, with completely stable flux. The primary drawback to these sources, other than proper care in handling radioactive materials, is their relatively low electron flux. Accumulation times of several seconds may be required for statistically significant counts.

Alternatively, a tritium (^{3}H) source has been used for calibration for the PEACE instruments [*Johnstone et al.*, 1997]. Tritium emits electrons with a range of energies up to a maximum energy of 18.6 keV and its half-life is 12.33 years.

3.2.2 Test Equipment Considerations

Electron plasma instruments using MCP or CEM detectors require clean, high vacuum chambers. System pressures lower than 5×10^{-6} mbar are recommended for proper operation of such instruments. If the MCPs are buried inside the instrument, or being used for the first time, it is recommended that the instrument be in high vacuum for more than 24 hours, preferably at an elevated temperature, before applying any high voltage. Operation at higher pressures can result in higher noise levels due to ion generation in the microchannels, may shorten the detector's lifetime, or may result in high voltage discharge that could damage the detector.

For low energy (< 1 keV) electron calibrations, Helmholtz coils are essential for proper testing. The Earth's magnetic field can cause significant deflections of electrons from the nominal source direction even at keV energies. A 1 keV electron has a gyro radius of about 2 m and is typically deflected by several degrees over beam paths of about 50 cm,

Figure 3.5: Electron beam calibration facility of the University of Calgary, Canada. View of vacuum system from inside the cleanroom with the Helmholtz coil system. For details see Appendix A.4.

depending upon the orientation of the source axis relative to the local magnetic field. To perform low energy ($\approx$10 – 1000 eV) electron calibrations, Helmholtz coils should be constructed to null out the bulk of the Earth magnetic field. We point out that for most buildings, structural steel will cause significant distortions in the Earth's field so magnetic field measurements in the vacuum chamber prior to construction of the Helmholtz coils are recommended. A single pair of coils will often suffice if the physical orientation of the coils can be controlled. The design should also consider the coils physical impact on access to the chamber. At the University of California at Berkeley a rather simple, about 1.2 m diameter single-axis coil system was constructed for the calibration of the Wind 3D Plasma instrument [*Lin et al.*, 1995]. The coils had 80 turns per coil of ϕ = 0.64 mm wire (22 Gauge wire), requiring about 250 mA for operation. These coils could be easily attached to or removed from an 80 cm (30 inch) diameter vacuum chamber and provided adequate magnetic field reduction to allow testing down to about 20 eV from a photocathode electron source. A much larger two-axis Helmholtz coil system is shown Figure 3.5.

An important part of the calibration process is the development of automated test equipment and testing procedures. The test equipment includes the electron source, the beam monitoring system, the manipulator table that will orient the instrument in the electron beam, and the instrument specific ground support equipment (GSE) that interfaces to the instrument. Since calibration facilities will likely be used by several missions, it may be convenient to develop a stand-alone computer system that commands the source and the manipulator. The GSE can then be designed to command the computer controlling the electron source and the manipulator to synchronize the test equipment with the instrument settings and data collection, i.e., the GSE is the master controlling the activi-

ties. The GSE should create calibration files that contain information about the source and manipulator settings, the instrument settings, and the sensor response. To facilitate data collection, the GSE generally operates the instrument in a calibration mode during most procedures, where the sensor parameters, such as the energy sweep voltage, are changed slowly. However, it is important to perform calibration procedures using all flight modes to confirm proper instrument operation.

One question that often arises during the calibration of electron plasma instruments is whether to vary the electron energy or the ESA voltage in order to determine the analyzer's energy response. In principle this should not matter since simulation data can be compared in either form. In practice, the choice depends upon the resolution or accuracy that the electron accelerator and analyzer electrode voltages can be controlled. If there are concerns about source drift, varying the ESA voltages is the obvious choice. If the ESA sweep voltage has limited programmability, perhaps due to limited DAC control, varying the source energy may be necessary.

A second consideration during calibrations is the beam intensity. Higher beam intensities will generally speed up the calibration process. However, intense beams can introduce both dead time errors, which should be characterized in the calibration campaign (as discussed in Section 3.1.3 above) and MCP gain problems, which should be avoided in the instrument operation. *Kataria et al.* [2003] show an example for the latter problem encountered during flight from the PEACE instrument on Cluster. Top-hat designed ESAs generally have very good spatial focusing of a parallel beam to a spot on the detector plane. Beam intensities that are well below the electronic dead-time limit may be focused onto such a small portion of the MCP that the microchannels do not have time to recover. If the gain drops significantly, counts will be lost. This will generally affect the core portion of the instrument response rather than the low sensitivity wings leading to a distorted measurement of the response.

A third consideration is the mounting location on the manipulator. It is important to make sure that the rotation axis of the manipulator is centered on the instrument aperture. This will avoid introducing any unwanted beam asymmetries into the calibrations.

A beam monitor is a useful addition to the calibration facilities. Having a detector that can be moved into the beam's field of view at the beginning and end of a test provides an additional measurement of beam stability. Alternatively, the instrument itself can provide this measurement by beginning and ending the test in an identical high-count-rate configuration. However, a separate beam monitor provides a long-term stability measurement of the beam that is useful for multi-instrument calibrations or for detecting degradation of the source. An MCP or CEM can be used to monitor an electron beam, however, since the properties of these detectors (such as gain) can change as they are exposed to large fluxes or to air, caution must be used. Generally these monitors must also be evaluated periodically for their proper operation. Alternatively a current monitor (Faraday cup) could be used to monitor the electron flux. However, for the low flux sources typically required for high sensitivity electron analyzers, a direct current measurement is generally not suitable and a channeltron (CEM) typically serves as flux reference. Of course, the CEM detection efficiency itself has to be calibrated, which can be done by comparing to a reference CEM [*Bordoni*, 1971] or using an adjustable photoelectron source [*Østgaard*, 1979].

Although it is convenient to have comprehensive displays for initial instrument turn-on and testing, GSE displays for calibrations can be kept quite simple as long as the collected data is readily available after each test for plotting using standard software. It is critical

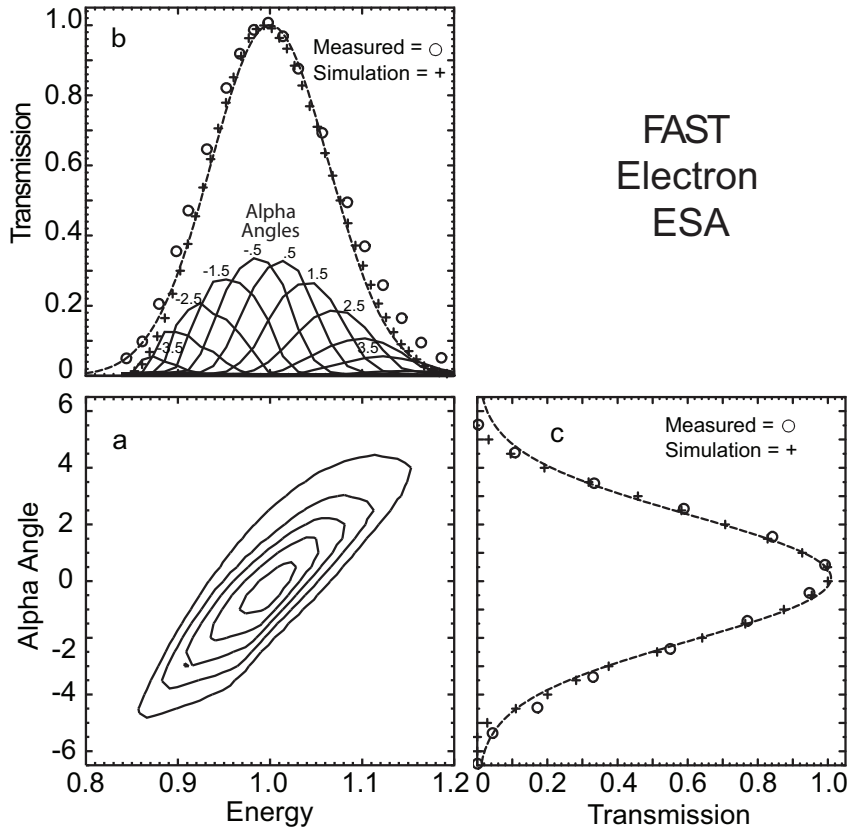

Figure 3.6: The input energy and angle response of the FAST electron ESA are compared to numerical simulations and a Gaussian fit. Adapted from *Carlson and McFadden* [1998].

that calibration data be analyzed within a short time (minutes) after data collection. This is important not only to assure that the instrument continues to function properly, but also to prevent loss of time due to equipment failure. If an obvious anomaly in the instrument response is identified that requires an adjustment of the instrument, there may be no reason to continue the collection of calibration data until the problem is resolved.

3.2.3 Instrument Simulations

Computer simulations of the instrument response are an essential part also of the calibration procedures. Not only do they provide a benchmark for comparison of calibration data, but also provide insight into the instrument response and therefore can be used to tailor the calibration procedures. Simulations generally supply the differential response of the analyzer as a function of look direction. For top-hat electrostatic analyzers that have azimuthal symmetry [*Carlson et al.*, 1983], a single set of energy-angle curves characterizes the analyzer response as shown in Figure 3.6. For instruments without azimuthal symmetry, a family of energy-angle curves must be calculated.

Simulations are most useful in the design phase since they allow quick calculations of instrument response, including the geometric factor, that accompany design changes often implemented for mechanical considerations. Simulations can also provide insight into subtle features of the analyzer response that are not always obvious from the instrument design or from integrated response curves. For example, at some beam energies and input angles, the angle imaging in spherical top-hat analyzers can produce two spatially separated response peaks at the detector plane. This dual peak response to a mono-energetic planar beam is even more apparent in toroidal top-hat analyzers (see also Section 3.4.2). When an unexpected feature like this appears in the calibration data, one can quickly refer to simulation data to confirm this is the normal response. (Although dual peaks at the detector plane can occur for some input beam parameters, the response of properly designed top-hat analyzers, averaged over all input beam parameters should give a single peak at the detector plane.)

In comparing simulated and measured instrument response, the experimenter should be aware of possible limitations in the calibration setup. Calibration sources have a finite beam width in both angle and energy. If the analyzer being calibrated has a narrow energy or angle response, comparison with simulations may require a convolution of the simulated ideal response with the actual beam parameters. For identical analyzer Gaussian-width response and beam Gaussian-width, the convolution results in a broadening of the measured beam width by a factor of $\sqrt{2}$. For ESA designs typical for electron plasma measurements with an analyzer FWHM response of about 6° and $\Delta E/E \approx 15\,\%$, the electron source should have negligible impact on measured response. A more difficult problem is the precise beam alignment relative to the instrument orientation. Alignment to better than 1° may be difficult to reproduce, especially at low energies where magnetic deflection of the electron beam may occur or on systems where the manipulator alignment can change during analyzer installation. Small variations in the analyzer's center angle response can often be attributed to misalignment. Lastly we note that simulations should be used to identify non-ideal instrument response. For example, internal electron scattering is difficult to simulate, but can be identified by comparing the simulated response with the measured out-of-band response.

Agreement between the simulated and the measured analyzer energy constant is important in verifying proper analyzer construction. The analyzer energy constant is defined as the ratio of particle energy, averaged over beam energy-angle, to the applied analyzer electrode voltage. In comparing the simulated analyzer energy constant with the measured constant, care must be taken in both calculation and measurement to compensate for surface irregularities. Since the analyzer hemispheres are generally serrated and blackened, the average gap between hemispheres is affected by this surface treatment. In addition, the numerical simulation will often have a finite grid resolution, which can also introduce artificial variations in analyzer gap along the particle flight path. Especially for small analyzer gaps, these variations can be significant and should be estimated and corrected before the measured and simulated analyzer constants are compared. If after all corrections have been made, there remains a significant disagreement between measured and simulated analyzer constants, improper analyzer construction is indicated. Although most analyzer problems, such as improper deflector electrode dimensions, should be detected during component testing, more subtle problems may only show up at instrument level testing.

Agreement between the simulated and measured analyzer response in both angle and energy provide confidence that the sensor is properly constructed. The simulations also

provide an accurate estimate of the analyzer's geometric factor. Since the absolute beam flux may not be calibrated, simulations generally provide the most accurate value of analyzer geometric factor. For overall instrument sensitivity, non-ideal features of the instrument such as grid transmission and MCP-preamplifier-discriminator counting efficiency must also be included. Since the overall system efficiency can vary with age, absolute instrument calibration must be left for in-flight calibrations (see Chapter 4).

3.2.4 Sources of Non-Ideal Response

Before proceeding with a discussion of calibration procedures, it is important to understand the sources of non-ideal instrument response that requires these procedures. An ideal electrostatic analyzer would have a uniform response with look direction and an energy dependent sensitivity that only depends upon the analyzer geometry. The sensitivity of this instrument could be summarized in a single number, the geometric factor as discussed in Section 3.1.1, which characterizes the geometric properties of the instrument. Most contemporary electron plasma instruments rely on ESAs and MCPs (or CEMs). ESAs can introduce variations in response with look direction either by design [e.g. *Gosling et al.*, 1978; *McGarity et al.*, 1992; *Johnstone et al.*, 1997], or, in the case of azimuthally symmetric designs, from machining tolerances [*Vilppola et al.*, 1993, 1996, 2001]. The high voltage electronics that powers the ESA energy sweep is also non-ideal. MCP and CEM detectors vary in efficiency with both incident particle direction and energy. In addition, since the particle detection efficiency also depends upon electron multiplier gain relative to an electronic threshold, detector calibrations are as important as the analyzer calibrations. Since the MCP and CEM gain vary with accumulated flux, which in turn can vary with time and location on the detector, the relative efficiency may vary with time. All these variations combine to produce departures from the ideal instrument response that must also be determined from in-flight data (see Chapter 4). Pre-flight calibrations should be used to identify and minimize any variations from the ideal response, and to provide a baseline to which future in-flight calibrations can be compared. Below we describe in more detail the sources of non-ideal response. For the following discussion we will assume top-hat ESAs and MCP detectors since they are currently the analyzers and detectors of choice. However, most of the discussion will also apply to asymmetric ESAs and to CEMs.

Non-concentric electrostatic analyzer hemispheres can introduce variations in both energy response and sensitivity with look direction. A comparison of the calibration data from two "identical" electrostatic analyzer instruments, one of nominal build and one with non-concentric hemispheres is shown in Figures 3.7 and 3.8. In Figure 3.7, the energy responses for the 16 azimuthal sectors are shown, where the variable response of the non-ideal analyzer (right panel) is clearly seen as compared to the "constant" response of the nominal analyzer. The small variations in energy response of the nominal analyzer are ascribed to the limitations in the turning table. More detailed information on the performance of the instrument is contained in the spectrogram data, where the two-dimensional instrument response for the elevation angle versus ESA voltage are plotted. These data are shown in Figure 3.8, again for the two "identical" electrostatic analyzer instruments. For the nominal-built instrument (Figure 3.8, top panel) the response ellipses in the spectrogram are all the same within the measurement uncertainty. For the instrument with non-concentric hemispheres (Figure 3.8, bottom panel) the energy response are considerably more asymmetric both in elevation angle as well as in ESA voltage, because of the me-

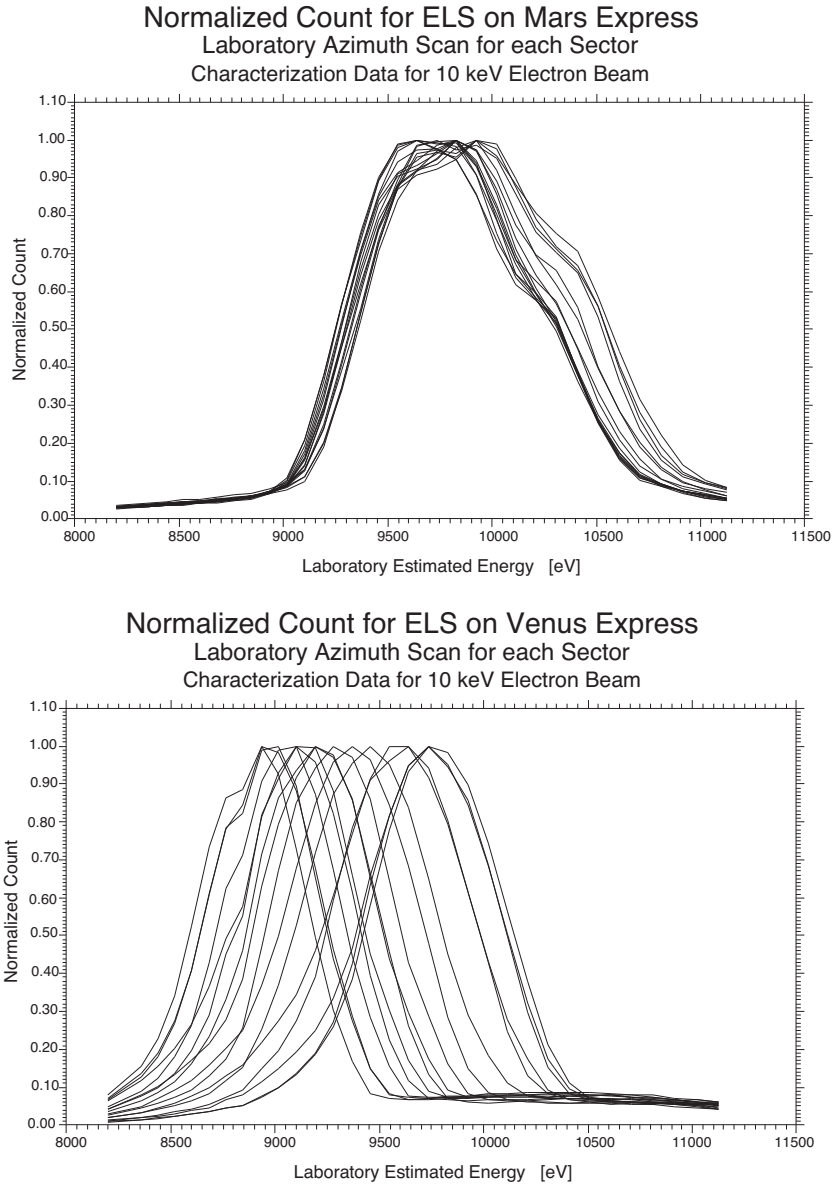

Figure 3.7: Normalized counts of energy scans for the 16 azimuthal sectors of the ASPERA-3/ELS sensor (top), and the ASPERA-4/ELS sensor (bottom), for the European Mars Express and Venus Express missions, respectively. From *Frahm* [2005].

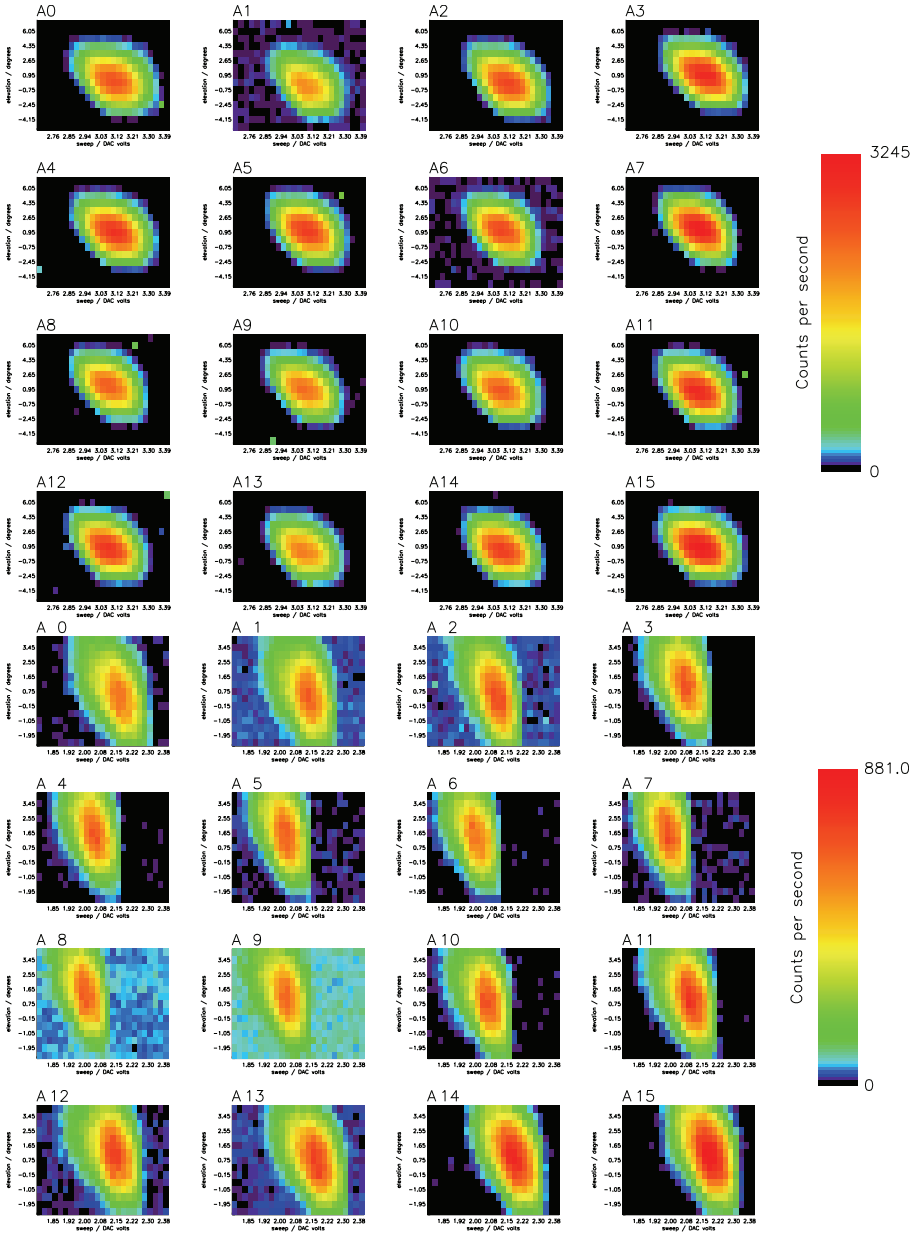

Figure 3.8: Spectrograms (elevation angle versus ESA voltage) for the 16 azimuthal sectors (A0 to A15) of the ASPERA-3/ELS sensor (top), and the ASPERA-4/ELS sensor (bottom), for the Mars Express and Venus Express missions, respectively, of ESA. The 100 eV electron beam is incident such that the particles are focused to the center of the anode sectors. From *Kataria* [2005].

chanical imperfections. Additionally, the peak of the response has a large variation, giving a difference of more than 10 % across the azimuth range.

Unfortunately, the way from measuring a non-ideal response to identifying the actual reason of the non-ideal behavior is often not as direct and additional measurements might be necessary. In any case, these variations should be determined and minimized during normal ground testing, but their effects will eventually mix with other sources of instrument response. For normal machining tolerances (typically 0.05 mm), variations in energy of a few percent with look direction might be observed for top-hat style analyzers with $R \approx 4$ cm and $\Delta R/R \approx 0.75$ (see Figure 3.7, top). For steeply falling energy spectra, these variations may be noticeable in the data. Since the geometric factor of these analyzers varies roughly as $(\Delta R/R)^3$ this can introduce about 10–20 % variations in sensitivity. Large deviations from concentricity might necessitate the manufacture of new parts. Some designs allow for minor trimming of the analyzer hemispheres to maximize their concentricity.

Another difficult problem associated with the ESA concerns small offsets in the sweep voltage. A typical high voltage supply will sweep from 0–4 kV, corresponding to an ESA energy range of 0–30 keV. The low energy portion of the sweep must be accurate to about 0.1 mV, or the control voltage must be accurate to about 0.2 mV, to achieve about 1 eV accuracy in the measured electron energy. Thermal drifts of resistors and offset drifts in operational amplifiers may impact these measurements. If the low energy measurements are important to the mission requirements, then care must be taken on the ground to determine these offsets as a function of temperature, and the instrument temperature may have to be monitored to correct for thermal drifts during the mission. Operational amplifier offsets may also change with radiation dose necessitating in-flight determination of the offset. This can be determined if the sweep voltage can be swept through zero to negative values and the zero-energy electron cutoff is accurately measured.

The efficiency of MCPs (or CEMs) may vary across the detector. The magnitude of these variations generally depends upon details of the pulse height distribution and the preamplifier discriminator threshold, and may also depend upon accumulated flux. In addition, MCP detection efficiency is also dependent upon the angle between the particle velocity and MCP pore bias angle [*Gao et al.*, 1984]. For example, the top-hat analyzer RPA-1 on the Giotto spacecraft utilized a 360° annulus MCP chevron pair for detection [*Rème et al.*, 1987]. Because the electrons exited from the analyzer at an angle not perpendicular to the MCP plane, there was an azimuthal dependence of the average electron velocity relative to the individual microchannels. This problem was reduced on later missions (Wind, Mars Surveyor, FAST, Cluster) by splitting the MCPs into 180°, half-annulus, C-shaped segments, with the bias angle direction centered on the C. Simulations and ground testing showed this was effective in eliminating the majority of MCP bias angle skewing. Even with this arrangement, pre-acceleration between the analyzer exit and the detectors may introduce additional small efficiency variations due to changes in angle between particle velocity and pore bias. It is important that these variations in efficiency are measured in the flight configuration with a broad angular source rather than with a single parallel beam. Rather than requiring the calibration source be extremely stable on time scales to scan all look directions and energies, a simpler alternative is to use a ^{63}Ni radioactive source that can fill the detector FOV in a single azimuthal direction. A single azimuthal rotation can then be used to perform this relative calibration.

The energy dependence of the MCP efficiency is also a part of the calibrations. These variations in response are difficult to determine since they require a very stable particle beam over a broad energy range. As discussed in Section 2.2.4, an MCP detector operated with the front surface biased several kV negative to accelerate positive ions will have a detection efficiency for ions that varies by only about 20 % over an energy range up to 30 keV. The variation in detection efficiency for electrons with a typical front surface bias voltage of several hundred volts is much greater, about 60 % over the same energy range. It is not clear that this dependence, once measured, will remain constant through the mission. To the authors' best knowledge, no one has determined whether this energy dependence varies with accumulated dose. Therefore for a mission requiring accurate, long-term measurement of spectral shape over a broad energy range, ground testing of this energy dependence as a function of accumulated dose on the MCP should be made. An alternative would be to use an in-flight cross-calibration between the electron analyzer and a solid-state detector (SSD) at about 20–30 keV where their energy coverage overlaps. This form of cross-calibration to determine MCP and CEM efficiency decrease at higher particle energies is more effective than, for example, using the in-flight comparisons between local plasma densities estimated from plasma wave frequency observations (Section 4.4.2.1) and plasma densities estimated directly from particle measurements. This is because the determination of the local density from the particle measurements tends to emphasize the data taken at the lower energies rather than at the higher particle energies where detector efficiency loss with energy is most important. It should be noted that the success of the suggested in-flight approach to determining the energy dependence of detector efficiency requires that the SSD has experienced little or no degradation from radiation damage (Section 4.3.3).

Another source of non-ideal response can be caused by the discrete nature of the anodes that collect the charge from the MCP. Charge pulses that exit near the border between anodes will not be fully collected by a single anode. This can lead to double counting of particles at the boundaries and to lower pulse height distributions (PHDs, see Section 2.2.4). Double counting can be eliminated by adding a non-anode conducting strip between anodes, but this approach may introduce its own problems by creating gaps in the response between anodes. Lower PHDs are only a problem if a significant fraction of the charge pulses are split between anodes. These problems can generally be minimized by reducing the gap between the MCP and anodes and by avoiding conducting strips between anodes. Anode to MCP spacing of about 0.2 mm are easily achieved with current printed circuit board techniques. In general this non-ideal response would only be noticed for extremely narrow beams as in up-going electron beams observed in the auroral zones [*Carlson et al.*, 1998].

In addition to the above sources of non-ideal response, electron plasma analyzers also have several sources of out-of-band response. Electrons have a high probability of forward scattering in ESAs and measurements of the scattering wings from a mono-energetic beam are important to determine the limits to which steep energy spectra can be resolved. Solar UV is another source of background, especially for electron sensors. UV photons can scatter into the detector producing background counts, can produce photoelectrons near the analyzer exit, which can then be accelerated into the detector by a pre-acceleration voltage, or can generate photoelectrons near the analyzer entrance, which can then be detected at the lowest analyzer energies. Problems with both UV and scattered electrons can be minimized by designing the analyzer to be at least a two bounce system, by using

a serrated (or scalloped) outer analyzer electrode, and by incorporating blacking on the hemispheres.

A final source of non-ideal response is due to a little understood process called "after-emission". When MCPs (or CEMs) are exposed to an intense particle flux that is abruptly turned off, residual counts occur that decay with varying time constants after the exposure. Pre-flight measurement of the phenomenon, including the pulse height distribution of the after-emission, may help in the data analysis if intense fluxes will be encountered. Additional details on this anomalous response can be found in Section 4.2.9.

3.2.5 Test and Calibration Procedures

The testing and calibration of electron instruments can be divided into four categories:

- Component testing,
- Calibration runs to determine deviations from ideal response,
- Determination of out-of-band response,
- Testing using nominal operating modes.

Component testing includes mechanical fit checks, electrical contact tests including grounding, electronics tests, software tests, and detector tests. Once the individual components are verified as constructed and functioning properly, the instrument can be assembled and prepared for calibration runs. The calibration runs are primarily functional tests to determine that the instrument operates in a manner close to the ideal. The calibration response is compared to simulations that have the ideal analyzer response. Tests of out-of-band response are also important, especially for electron analyzers. These tests include determination of internal scattering of electrons, which smear the analyzer energy response, and the impact of UV contamination both from production of internally produced photoelectrons and direct scattering of UV into the detector. Finally, it is critical that the instrument is operated in its nominal modes, rather than in the test modes generally used for most calibration procedures, and that end-to-end testing of the instrument validate its operation.

In this section we will assume that the electron instruments are symmetric electrostatic analyzers of the top-hat design, and have chevron configuration microchannel plate detectors. The calibration procedures described will be directly applicable to these designs. However, there are other low and medium energy electron instruments still in use (asymmetric ESAs, retarding potential analyzers, magnetic electron spectrographs) that would require similar, but perhaps more extensive procedures. For the calibration descriptions, the term "azimuthal" is used to describe rotation about the analyzer's symmetry axis and "elevation" to describe rotation out of the analyzer's planar FOV.

3.2.5.1 Component Testing

Before instrument calibrations can be started, component testing of the subassemblies is strongly advised. Components that experience high voltage should be tested for proper operation, especially for the absence of arcing or discharge in vacuum. Partial discharge tests should be performed at a test voltage significantly exceeding the nominal maximal operational values for accelerated life-time tests. The effect of the electric field strength on

the voltage life, L, is very large and typically expressed by $L = c/E^k$, with E the electric field strength and c a constant [*Krueger*, 1989]. The exponent k may vary between 5 and 20 depending on type of material and quality. For polyethylene, for example, $k = 9$. Using this relationship, one finds that for testing for an operational life of 5 years one has to apply 1.9 times the nominal voltage if accelerating the life-time test to a week. MCP HV supplies should be checked for voltage ripple under proper load since the MCP gain is a strong function of voltage. A 2 % voltage ripple could produce significant MCP gain shifts. Understanding the operation of the energy sweep HV supply is also critical. The slew rate of the supply must be measured under proper load at both high and low voltages, and in all the various operating modes. These supplies will typically perform a rapid charge up, followed by a slow exponential decay. Any signs of retrace bounce, or oscillations, at the highest energy steps should be minimized or the energy sweep designed to allow settling before proceeding with the next measurement step. Any thermal drift of the low energy steps should also be measured over the entire expected temperature range.

The most important subassembly testing is the matching and testing of detectors, including final tests with detectors mounted in the flight fixtures. MCPs purchased from the same fabrication run will vary in both resistance and gain. They must first be matched for similar resistance so that similar voltage differences are observed across each MCP in the chevron pair. After cleaning (see Section 2.2.4), MCPs can be mounted and tested for noise and uniformity of gain. If the MCPs are not flat or are not tightly clamped, variations in the small spacing between the MCPs can dramatically affect both the peak and FWHM of the pulse height distribution. Uniformity of gain across the MCP is important to minimize efficiency differences between anodes. If the MCP bias voltage is increased to minimize the detector losses below the discriminator threshold in a low gain portion of the MCP, it is likely that higher noise levels will be present in the high gain portions. CEMs may also require some selection and matching since normally a single high voltage supply will power an array of CEMs.

Once MCP matching is complete, the optimal bias voltage must be determined. This is done by recording pulse height distributions, PHDs (see Chapter 2 and Section 2.2.4), for the full range of MCP bias voltages. The interesting quantities of a PHD are the peak location (the modal gain), the peak width (which typically is of Gaussian shape), and the noise level. Often, electronics for recording PHDs are not part of the flight electronics and laboratory equipment has to be used for this purpose. For well matched chevron-pair MCPs, the PHD of output charge pulses will have a FWHM that is roughly half the distribution peak. Selecting a peak in the PHD that is five times the electronic threshold results in detection of about 98 % of the pulses, assuming the PHD is exactly Gaussian. However, partial charge collection near the edge of anodes results in poorer PHDs so the efficiency is generally lower. The key consideration is to make the peak in the PHD large enough so that most pulses are detected without introducing significant background counts. The bias voltage selection is generally a compromise that maximizes signal to noise. Once an operating voltage is selected, it should be used for all further testing so as not to distort the calibration results. However, if the instrument calibration will involve significant charge extraction (about 0.1 C cm^{-2}), it may be necessary to adjust the MCP bias voltage during calibrations to compensate for MCP scrubbing (see Section 2.2.4).

Noisy MCPs are relatively common and often the problems are associated with the edge of the MCP being too near a charge collection anode. MCP edges should be at least 2 mm from anode boundaries. In addition, if the edge of the anode is not clamped and in-

sulators are present behind the MCP, the insulator may charge up and electron clouds from the noisy edge may be deflected toward a nearby anode. For a properly designed MCP mounting fixture, noise from MCP edges may be due to misaligned MCPs and can be eliminated by realigning the MCPs. For noisy channels in the middle of a chevron pair, cleaning the MCPs or reversing the front and back MCP can often remove the noise. MCP noise has also been observed to decrease with MCP scrubbing, and therefore may be reduced with adequate pre-flight operation. Background rates of approximately 1 count cm^{-2} s^{-1} can generally be obtained.

There have been instances where MCPs mounted in flight fixtures were originally not noisy, but became noisy when mounted with the flight analyzer. This noise was typically near the edge of the MCP active area, and appeared to be associated with field emission. Mounting the analyzer introduced a grounded surface that could reflect electrons back toward the active MCP area. To identify this problem prior to final assembly, we suggest performing the MCP-anode component testing with a grounded surface placed in front of the detector that mimics the flight configuration.

Lastly, background counts are often observed in the final flight configuration when the analyzer sweep voltage is near its highest value. This has been observed on both electron and ion instruments. Field emission, originating from internal dust can be the culprit and therefore cleaning may remove the noise. However, at higher sweep voltages one would expect that field emission would primarily result in attraction of field-emitted electrons to the inner hemisphere and not in additional electrons reaching the MCP. Scattering of field-emitted electrons off the inner hemisphere may explain some of this background, but similar background is also observed in ion instruments. Another possible background source is discharging of the high voltage between the ESA hemispheres, perhaps associated with field emission from dust. Analyzer discharge noise was observed in FAST ESAs during ground testing after an anomalous high voltage turn-on in low vacuum. Prior to the anomaly the sensors were quiet, but following the high voltage discharge the background was found to increase with sweep voltage and decrease with lower pressure. A discharge path was identified on the insulator that supported the inner hemisphere and cleaning of the insulator removed the problem.

3.2.5.2 Calibration Runs

Energy-Angle Calibration: For azimuthally symmetric top-hat style electrostatic analyzers, the ideal analyzer is characterized by a single set of energy-angle curves and an analyzer energy constant that defines the ratio of average transmitted particle energy to analyzer voltage. The energy-angle calibration involves stepping the source energy and elevation angle (beam angle out of the detector planar field of view) through about 30 discrete steps surrounding the analyzer response peak. Equivalently, the analyzer voltage can be varied instead of the source energy. Since the mechanical settling of the manipulator elevation angle may be less reproducible than the electronic setting of the source or analyzer energy, it is advised to minimize the number of angle increments. Therefore, the elevation angle is fixed while the beam energy is incremented, then the angle is incremented and the beam energy steps repeated. Figure 3.6 shows an example of this set of curves for an electron ESA of the FAST spacecraft. It is advised that this energy-angle response is measured at two energies, one above and one below the detector pre-acceleration energy, to demonstrate that the acceleration of electrons into the detector has no significant impact on the

overall response. This response should also be measured at several azimuthal angles in order to identify any non-concentricity of analyzer hemispheres. 90° spacing between azimuthal locations should be adequate and non-concentricity will be indicated by a change in the analyzer energy constant. These calibration runs can also identify if there is any skewing in the analyzer-manipulator mounting. If the analyzer is not mounted symmetrically about the azimuthal rotation axis, the energy-angle response curves will be identical except for a shift in the center elevation angle. It is also important that this calibration is not run at an azimuthal angle where the analyzer images the beam near a detector or anode boundary, or near an exit aperture obstruction, otherwise coupling between elevation and imaging will distort the response. For count rates of about 10 kHz, 1 s accumulations, 1 s settling times, and a 30 by 30 energy-angle array, each calibration run can be completed in approximately half an hour.

Analyzer Symmetry Test: The analyzer symmetry test can be used to quickly identify higher order asymmetries in the analyzer energy response once analyzer concentricity has been established. For example non-concentric top-hat analyzer hemispheres introduce a distortion in energy response with an azimuthal period of 360°, whereas a hemisphere that had been dropped and deformed away from a spherical shape might show energy distortion with a 180° or higher period. For the analyzer symmetry test, the electron beam is fixed at the peak in elevation response and the analyzer is rotated azimuthally through about 10° steps. At each azimuthal step, the source energy (or analyzer voltage) is varied over the energy range to identify the peak in the analyzer energy response. Variations in concentricity, analyzer-manipulator asymmetric mounting, or higher order skewing should be readily apparent from shifts in the peak response with azimuthal angle as can be seen in Figure 3.7. If the energy-angle calibration showed significant skewing in the analyzer's energy response, then the symmetry test may not as useful in identifying higher order skewing and the analyzer should be corrected before proceeding with this test. We point out that the analyzer symmetry test could be replaced by large number of energy-angle calibration runs at equivalent azimuthal locations. However, since a set of energy-angle calibration runs would require about 30 times the calibration data collection time, the symmetry test is an attractive alternative and can be performed in about 30 minutes.

Entrance Deflector Testing: Some top-hat ESA designs, for example the EESA sensor on the Wind spacecraft [*Lin et al.*, 1995], include additional deflector electrodes at the analyzer entrance that skew the analyzer FOV from planar to conical (see Figure 2.34). These entrance deflectors were extremely useful during the FAST mission allowing the ESA's 2-D spin-plane FOV to be deflected to continuously measure field aligned electrons when the magnetic field varied by small angles from the spin plane [*Carlson et al.*, 2001]. On the spin-stabilized STEREO spacecraft, the Solar Wind Electron Analyzer (SWEA) has deflectors capable of $\pm 65°$ conical deflections from the planar FOV. Energy-angle calibration runs, as describe above, are required for several deflector setting to assure proper operation. For small angle deflections the energy-angle response curves remain nearly the same with only a change in the center elevation angle. For large deflections ($> 20°$), distortion can become significant with narrowing or broadening of the energy-angle curves depending on the sense of deflection. Comparison of the energy-angle response with simulations is essential to assure proper analyzer construction. Azimuthal symmetry of the

deflectors should also be evaluated with a test similar to the analyzer symmetry test discussed above. For systems with multiple deflection electrodes, azimuthal asymmetries are more difficult to control since there are more mechanical interfaces, each with its own tolerance. However, since the deflection asymmetry is proportional to differences in the deflection gap, the large gap between entrance deflectors generally introduces a negligible azimuthal asymmetry.

Relative Efficiency Calibration Test: The determination of relative efficiency between different look directions in a single analyzer is essential for the accurate determination of the odd moments of a plasma distribution function, where differences between look directions are of prime importance. Differences in relative efficiency can be caused by overall instrument variations (analyzer asymmetries or detector efficiency changes with MCP bias angle), as well as small variations caused by entrance/exit aperture blockage, grids, anode size variations, etc. Although this test can be performed using a set of energy-angle curves at appropriate azimuthal intervals ($\sim 1°$), for a 360° analyzer and 30 minutes per energy-angle test, more than a week of calibration run time would be required. A much simpler test can be performed using a radioactive ^{63}Ni source that fills the analyzer FOV in elevation angle. Since these sources produce a broad energy and angle spectrum, a single azimuthal scan at approximately 10 keV can be performed in about 30 minutes with a 10 mCi source providing adequate statistics. If care is taken so the angle spacing during an azimuthal scan is a fixed fraction of the anode spacing, the relative efficiency table is proportional to the total counts in each anode.

Energy Dependent Efficiency Test: MCPs have an energy dependent efficiency that is governed by the secondary electron production caused by the analyzed particle striking the detector. For electrons the detection efficiency peaks around 200 eV and has a slow decrease with increasing energy, which at 30 keV is about 40 % of peak efficiency (Section 2.2.4). Measurement of this functional dependence requires an electron source whose flux is independent of energy. The photocathode source is the most suitable source, provided the accelerating grid is rigid enough so that grid deformation is negligible. The beam should be centered on the analyzer planar FOV and the source energy stepped through its entire energy range. Since electron detectors involve pre-acceleration to several hundred eV, it is not necessary to test down to the lowest energies. To compensate for any small beam deflections due to residual magnetic fields, the analyzer voltage should be stepped through a range to find the maximum count rate peak at each electron beam energy. This test should be performed for each detector anode since the angle between particles and MCP pore bias is often a function of MCP location and energy, and since MCP efficiency depends on this angle.

Absolute Calibration Test: An absolute calibration test provides the overall scale factor for the measurements to correctly convert measured counts to physical units. Along with the analyzer energy constant, relative efficiency constants, and energy efficiency curve, this scale factor is required for accurate flux and moment determinations. An absolute calibration test is generally the most difficult test since it requires a stable electron source and cross comparison with a known reference detector that is used to characterize the electron beam. Since all electron detectors (MCPs, CEMs) in this energy range suffer from similar

changes with age, an absolute detector standard is difficult to maintain. In addition, since the absolute calibration of the instrument will change during the mission due to detector aging, this calibration procedure is often neglected in favor of in-flight absolute calibrations using other measurements as described in Chapter 4. The primary reason to perform this test on the ground is to provide assurance that the sensor has the correct sensitivity and therefore no significant detector problems. If a stable, energy-independent electron source is unavailable, an alternative is to maintain a test setup using ^{63}Ni sources to determine the energy dependent efficiency. Figure 3.4 shows the ^{63}Ni spectrum, which can be convolved with the analyzer response to determine the ideal instrument spectrum. Comparison of the measured spectra with the ideal spectra determines the energy independent efficiency. Since ^{63}Ni sources have a half-life of 100 years, comparisons made over long periods can provide assurance that the sensors have the correct sensitivity prior to launch. Radioactive sources eventually lose integrity and must be retired, therefore, maintaining a set of sources and performing cross-calibrations can assure long term stability for absolute ground calibration setups.

Out-of-Band Response Tests: The primary out-of-band response tests are for scattered UV, scattered electrons, and secondary electron production. Electron scattering tests are performed by increasing the electron beam energy range in the energy-angle tests, while also increasing the beam flux or the accumulation time. Single bounce wings should be identified and their extent in energy measured since they may impact the detector's ability to resolve steep energy spectra. Low-energy secondary electrons produced in the aperture by a higher energy beam are another source of background. For spectra peaked at high energies, as found in the Earth's auroral acceleration region, these secondary electrons may be a significant background. Measuring the detector system's low energy count rate as a function of the energetic beam energy and elevation angle should be performed. UV rejection tests are performed with a Lyman-α source, with the UV intensity calibrated with a photocathode. UV tests are required over a wide set of analyzer elevation angles relative to source direction. Figure 3.9 illustrates UV background counts for an electron ESA for a set of inner hemisphere voltages. The curves show that UV produced photoelectrons contribute significantly to the background at low electron energies.

Testing Using Nominal Operating Modes: Once the above calibration tests are complete, it is essential that testing is performed using flight operation modes. Critical tests include confirming that count binning during analyzer energy sweeps are properly time tagged and ordered in the data packets for correct decommutation on the ground. Beam intensity should be varied for each anode to check for proper operation to cover a wide dynamic range of count rates. In-flight modes for testing the MCPs for proper voltage bias should be exercised and compared with earlier MCP tests. Thermal vacuum testing should include a low-energy electron source to test for low-voltage offset drifts of the analyzer energy sweep as a function of temperature. Any onboard moment calculations or data averaging, should be compared with ground based computations of the same type. Finally, all housekeeping data should be crossed checked with the operational mode to confirm that the instrument monitoring can corroborate instrument operation.

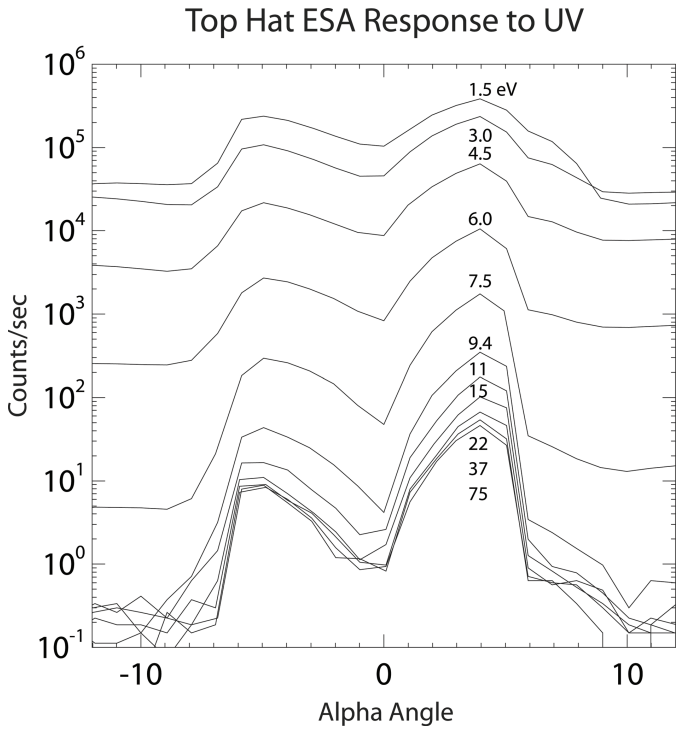

Figure 3.9: Angle response of a top-hat ESA to a Lyman-α photon source. Curves are labeled for values of the analyzer pass energy between 1.5 and 75 eV. The response for energy settings higher than 10 eV is mainly due to scattered photons reaching the MCP. At lower energy settings, photoelectrons produced inside the analyzer dominate over scattered photons. From *Carlson and McFadden* [1998].

3.2.6 How to use the Calibrations for Post-Launch Data Processing

In addition to certifying proper construction and operation of the instrument, the calibration effort produces a small number of instrument specific calibration parameters that are used in post launch data analysis. These are:

- Analyzer Energy Constant,
- Energy and Elevation Angle Widths,
- Entrance Deflector Angle-Voltage Table,
- Relative Anode Efficiency,
- Energy Dependent Efficiency,
- Absolute Calibration Constant.

For a symmetric top-hat analyzer, the Analyzer Energy Constant, or ratio of average transmitted particle energy to applied analyzer voltage, should be independent of the anode

or look direction. Asymmetric analyzers, either by design or due to fabrication tolerance problems, may require separate energy constants for each anode. The analyzer energy constant provides the conversion from analyzer voltage to the electron's "entrance energy" into the analyzer. This entrance energy must be used to convert from counts to physical units such as distribution function. The presence of external fields, such as those due to spacecraft charging, do not change the analyzer's internal response, and the conversion of counts to physical units at the instrument entrance depends on this internal response.

Once the spacecraft becomes positively charged it will attract negatively charged particles. Negatively charged particles, electrons, will accelerate towards the spacecraft and gain additional kinetic energy, $e\phi$, equal to the spacecraft potential ϕ. Assuming the spacecraft is in sunlight, i.e., the spacecraft is charged positively, the spacecraft induced energy gain varies from about 5 eV at high plasma densities (≈ 100 cm^{-3}) to about 40 eV for low plasma densities (about 0.1 cm^{-3}). Since these energy shifts are comparable to most space plasma electron temperatures, spacecraft potential corrections are essential for data analysis of electrons. The effects on the details of the measured electron distribution function, however, are more complicated since the trajectories of electrons entering the instrument will be distorted by the spacecraft potential such that ambient electrons are focused to the instrument. In case of a negatively charged spacecraft the electrons will be defocused.

The analyzer's Energy Width and Elevation Angle Width are often unused in data analysis since most geophysical or solar wind electron distributions are much broader than the typical analyzer's response. Care must be made to include any additional energy width broadening due to analyzer voltage changes during a counter accumulation. For electron energy distributions several times the analyzer energy passband, there is no need to correct for analyzer broadening and a delta function response approximation is adequate. If the spectra have regions with steep slopes, proper analysis may require a deconvolution using the detailed analyzer response width. For spectral features with gradients in pitch angle or energy of the same order as the analyzer's response, an approximation of Gaussian response may be adequate and simplify the deconvolution. However, for extremely steep spectra or narrow beams, as might be found in the auroral acceleration regions, the analyzer response wings, including the out-of-band response, may affect the measurement. In this case, a full deconvolution of the analyzer response may be required to extract subtle features in the distribution.

When the analyzer includes entrance angle deflectors, the analyzer's angle response will have to be corrected depending upon the deflection voltage. For small angle deflections, the conical deflection generally scales linearly with the deflection voltage and simple corrections to the response can be implemented. Large deflections may require a deflection table to convert from deflection voltage to conical deflection angle. In addition, spacecraft charging can result in similar angle deflections that may require angle corrections at low energies. This is especially true if the analyzer has look directions that are tangent to a spacecraft surface.

One of the primary calibration results is the Relative Anode Efficiency table. Although this could be folded into a calibration array along with the energy dependent efficiency table and absolute calibration constant, these tables and the calibration constant are easier to treat separately. The relative anode efficiency table is a set of near unity values that reflect the small differences in sensitivity from detector anode to anode. Since most of these differences are geometric (variation in anode size, FOV obstructions, etc.), this table

can be treated as independent of energy. In this case any sensitivity dependence on energy-anode coupling may be merged into the energy-dependent efficiency table.

The Energy Dependent Efficiency table is a near unity table that records the variation in detector efficiency as a function of both incident electron energy and anode. Factor of two variations in efficiency for electrons are expected over the energy range of interest (0.2–30 keV). Variations between anodes should be small and are likely the result of differences between the average particle velocity at the front of the MCP and the MCP pore bias direction. If these differences are small enough, the table can be reduced to a one-dimensional table that depends only on energy. For significant anode variations, it is important to renormalize the energy-dependent efficiencies to unity at the same energy that was used to define the relative anode efficiency.

The Absolute Calibration Constant is a final single number, obtained after small multiplicative corrections, of order unity, are made to the relative and energy-dependent efficiency tables, that are used to convert counts to physical units. Although separating these two tables from this constant is somewhat artificial, it is typically this constant that is varied during the mission as part of the in-flight calibration effort. As pointed out above, this constant is difficult to accurately determine during pre-launch calibrations and will change during the mission as the detectors age. If in-flight calibrations will allow accurate determination of this constant, it may be easier to forgo its pre-flight measurement and instead estimate its value. This constant can be approximated from the analyzer geometric factor determined from numerical simulation, combined with corrections for finite obstructions, such as grids, and an estimate of MCP average detection efficiency.

If onboard data processing, such as moment calculation, is to be performed accurately, it is essential to include the calibration tables in the computation. Assuming the particle data is a complete 3-D measurement, incorporation of the calibration tables in the moment computation tables requires very few additional resources. However, since the spacecraft potential has a strong impact on the calculated moments of the electron distribution function, onboard correction for the spacecraft potential is essential. This requires adjusting the moment computation tables as the spacecraft potential changes. To the authors' knowledge, no onboard spacecraft potential corrections have been performed before the launch of THEMIS. The first mission to attempt these corrections is THEMIS using electric field measurements of the spacecraft potential [*Angelopolous et al.*, 2006].

If an independent spacecraft potential measurement is unavailable, then the moment algorithm will become even more complex because features in the measured energy spectra must then be used to estimate the spacecraft potential [*Johnstone et al.*, 1997]. An alternative would be to use the moments determined from the immediate previous measurement, together with a table uploaded from the ground that would convert those moments to spacecraft potential in order to estimate the potential to be applied to the current measurement. The algorithm would require additional correction should the moments change significantly from measurement to measurement. If the spacecraft charges up positively, which is rather typical, plasma electrons will be accelerated to the instrument by the positive potential, and below the energy corresponding to the spacecraft potential only the spacecraft generated photoelectrons are registered. Details for onboard spacecraft potential corrections are discussed in Sections 4.4.2.2.

It is also important to understand how uncertainties in the determination of the calibration tables and constants will affect the measurements. This applies to both onboard computations and ground computations. An error in the absolute calibration constant re-

sults in a simple scale error for all moments and is easily corrected by comparison with alternate measurements of plasma density as described in Chapter 4.

An error in the analyzer constant of the ESA will result in moment errors that scale as (velocity)$^{n-1}$, where $n = 0$ for the density moment, $n = 1$ for the velocity moment, etc. The "1" stems from the integral that has dv to the third power and the phase space density $f \sim$ (counts $\times$ energy^{-2}) $\sim$ velocity^{-4}. A cross-calibration between electron and ion velocity in a high flux region such as the solar wind is the best way to identify any problems with the analyzer constant of the ESA (see also discussion in Chapter 4). Since the analyzer constant of the ESA is the easiest calibration parameter to measure on the ground, it is generally the most reliable. Changes during the mission should only be a result of a failure of the ESA high voltage sweep.

Errors in the energy-dependent efficiency are generally noticed in the even moments (density, pressure). For multi-spacecraft missions where density or pressure gradients are important, the use of the same functional efficiency dependence on energy, and cross-calibration of the sensors on different spacecraft, reduces the chance that errors in this dependence will introduce significant errors in the gradients. Errors are most easily detected by comparing with overlapping energy spectra from solid-state detectors (SSD) once the absolute calibration constant has been determined from density comparisons. Since the electron density is largely determined from low energy measurements, where there is little dependence of the detection efficiency upon electron energy, comparison at high energies with SSD measurements will identify problems in the functional dependence of the energy-dependent efficiency.

Errors in relative anode efficiency will primarily impact the odd moments (velocity, heat flux). Since much of the physics is tied to particle or energy flows, determination of the relative efficiency with look direction is critical. The relative anode efficiency can be checked post-launch by comparing sensor count rates during times of isotropic particle distributions, or at similar pitch angles at times when the distributions are anisotropic. If convective flows are present, care must be taken to transform the distribution into the frame of the flowing plasma before pitch angle comparisons are made. Since the transformation to the proper reference frame will often depend upon the uncalibrated data, it is best to minimize these transformations in order to avoid any feedback in the process. Spacecraft charging must also be properly accounted for, especially if the potentials are large enough to significantly affect particle trajectories. Problems introduced by both flows and spacecraft charging favor confining these in-flight calibrations to the more energetic portion of the particle population.

3.3 Low Energy Ion Calibration

Continuous research showing the contribution of steady, low-energy ions outflowing from the ionosphere and its mass loading of the magnetosphere has brought an enhanced appreciation for low-energy plasma measurements. Previously these populations were excluded from observations by positive floating potentials on the spacecraft exposed to sunlight or low-density plasma. With the advent of aperture biasing techniques and plasma source instruments placed on spacecraft, this problem has been minimized thereby allowing the measurement of this core population or the maximum of the velocity distribution. These populations can now be observed within a large and dynamic range of

particle fluxes and have been shown to have non-thermal features that cannot be fully described by simple velocity moment calculations of density, flow velocity, and temperature. Therefore, the instrumentation developed to observe this plasma requires full-sky coverage and may measure particle energies ranging from 0.1 – 500 eV, plasma densities ranging from 0.1–10^6 cm^{-3}, and a dynamic flux range from 10^2–10^{12} cm^{-2} s^{-1}. Typically, an energy-per-charge measurement is made that is converted to velocity if the mass-per-charge is known. Mass discrimination, therefore, is important if simple assumptions cannot be made to constrain the data [*Moore et al.*, 1998]. Mass analysis can be done by radio frequency, magnetic deflection, or time-of-flight techniques. The important ions observed at the ionosphere-magnetosphere interface are H^+, He^+, O^{2+}, O^+, N^+, and, to a lesser extent, N_2^+, NO^+, and O_2^+.

The discussion of determining the geometric factor of ion instruments provided in the introduction, Section 3.1.1 above, and for the medium energy range, Section 3.4 below, applies also for low energy ion instrumentation. The equations in these two sections, Equations 3.1 through 3.15 and Equations 3.68 through 3.70 provide the same basis for making low energy plasma calibrations. Since electrostatic analyzers are typically used, we can use Equation 3.16, which includes the $(\Delta E/E)_j$ factor within the combined instrument related terms for the differential geometric factor. For an energy E_j the geometric factor is

$$G_{i,j} = \sum_k \sum_l T_{i,jkl}\,(\Delta E/E)_j\,(A_{\text{eff}})_{kl}\,\Delta\theta\,\Delta\varphi \tag{3.59}$$

where i and j denote species and energy step, respectively, and $(A_{\text{eff}})_{kl}$ is the measured active area for an ion beam arriving from the direction θ_l and φ_k. Each of the $T_{i,jkl}$ components is determined during calibration.

The physics of low energy (e.g. cold) ion plasmas and the employed plasma instrumentation have been reviewed recently by *Moore et al.* [1998]. Modern instruments perform energy-, mass-, and directional analysis of the local plasma environment. The Thermal Ion Dynamics Experiment (TIDE) on the Polar satellite is an example of an instrument developed for three-dimensional (3-D) plasma composition measurements capable of tracking the circulation of low-energy (0–500 eV) plasma through the polar magnetosphere [*Moore et al.*, 1995]. It has a unique design to measure the large dynamic range of low energy ion fluxes observed during its orbit at low and high altitudes. In concert with TIDE the operation of the Plasma Source Instrument (PSI) reduces the spacecraft potential to allow these measurements [*Moore et al.*, 1995]. Another recent example is the CIS instrument on Cluster where a separate entrance for low energy ions was added to cover a large dynamic range [*Rème et al.*, 1997]. Details of the design and the calibration of this low-energy ion channel are given by *McCarthy and McFadden* [1998].

TIDE has a unique method of obtaining a varying geometric factor that was designed for its satellite orbit. It is also used to help protect the MCP's from high count rates. It has a mirror-RPA system that provides differential energy analysis by a two-stage selection process. Ions that are too energetic pass through the quasi-parabolic electrostatic mirror and subsequently are lost, while those of insufficient energy are reflected by the RPA and excluded from admittance to the TOF analyzer. Adjustment of the energy response width is used to control overall instrument sensitivity. The mirror voltage, V_{m}, is referenced to the output of the RPA voltage, V_{rpa}, and in this way, the mirror and the RPA are commanded together by the ratio, $R_{\text{m}} = V_{\text{m}}/V_{\text{rpa}}$. This ratio controls TIDE sensitivity because the energy passband (as well as the effective area and solid angle) is directly related to this

ratio. Thus, ideally, a boxcar-shaped energy pass band is provided, which is adjusted in width and center energy by selection of R_m. The actual energy response is asymmetric with a sharp cutoff on the low-energy side (due to the the RPA), and a more gradual cutoff on the high-energy end (due to the mirror). The practical range over which TIDE's sensitivity can be varied is approximately three orders of magnitude. The electrostatic mirror plays an important role in the achievement of this large geometric factor and is discussed further in *Moore et al.* [1995].

As mentioned above, spacecraft and sensor charging modifies the ion energy and leads to erroneous energy and angle estimates or excludes the ions from the instrument altogether [*Knudsen et al.*, 1998; *Moore et al.*, 1998]. These problems that are encountered in flight are not too different from those found in the laboratory. It is the purpose of this section to focus on the testing and calibration at ion energies of less than 1 eV to above 100 eV, the lowest of our energy ranges for ions. Sources of noise or diagnostic errors within the vacuum chamber, laboratory devices, and the instrument are all to be considered and minimized to obtain precise factors for Equation 3.16 so that the resulting geometric factor and finally the particle fluxes measured in space are accurately determined. In this section we discuss the optimization of the instrument through numerical raytracing, the special attention required of certain laboratory devices, some reminders needed during testing and calibration, and then describe a few facilities developed for calibrating these analyzers.

3.3.1 Numerical Raytracing

An essential task before the developing and testing of an analyzer is the numerical raytracing or simulation of its various ion-optical systems using computer simulation programs. Raytracing offers an efficient and cost-effective means of iterating an instrument design while learning its characteristics, optimizing its particle throughput, determining a geometric factor, and assisting in the interpretation of the calibration data. The requirements for the ion source for simulation are the same as for ground calibration: a monoenergetic and monodirectional ion beam with a cross-sectional area sufficient to completely illuminate the aperture. With these criteria, each component of the geometric factor can be simulated: the energy bandpass, the azimuthal response, the elevation angle response, and the effective area. Although simulation results often do not take into account grid losses, edge-effect losses, or detection efficiencies, each of these products can be determined and adjusted for optimization before fabrication begins. In addition, with specular reflection codes, these same ion-optical sections can be analyzed and adjusted for UV photon rejection. The iterative opportunities that simulations provide are particularly helpful for today's complex analyzer designs and low energy analyzers.

Before evaluating the components of the geometric factor, simulations of each ion-optical section can be evaluated and optimized for particle throughput before starting any fabrication. Non-uniform and fringing electric fields can be minimized or eliminated. One method of doing this is to modify or add grids such that the particle trajectories pass through flat potential contours at the entrance and exit of ion-optical sections. Specifically, potential contours affecting low-energy incident trajectories can be "straightened" by redesigning the insulators between mounting grid rings so that all incident trajectories are normal to an entrance grid. This allows the low energy trajectories to enter into the section of the instrument as intended by the ion-optical design [*Coffey et al.*, 1998]. Changing focal lengths can increase or decrease particle throughput as needed. During all simulations

runs, the energy conservation should be monitored for accuracy. A more detailed discussion and some results obtained from the numerical optimization of several low energy analyzers are discussed in Section A.1.

Another important application of ray tracing is when the measurement conditions in space cannot be duplicated in the laboratory, or only with great difficulty. This is the case when spacecraft charging, caused by release of photoelectrons and the interaction of the spacecraft with the surrounding plasma raises the potential of the spacecraft to values larger than the ion energy of the plasma. In the absence of any device to eliminate at least in part the spacecraft's positive charge, the spacecraft with its instruments generally float at positive potentials of several tens of volts which has to be compared with the typical energy of thermal ions of the order of eV and less (e.g. in the ionosphere or cometary plasmas). With biased apertures ions can be guided into the aperture of the instrument. However, the electric field of the spacecraft together with the instrument in such a plasma situation has ion-optical properties that cannot easily be duplicated in the laboratory and have to be simulated numerically. Such a simulation includes the calculation of the spacecraft potential when it is immersed in the plasma and illuminated by the Sun [e.g. *Roussel and Berthelier*, 2004]. Once the spacecraft potential and the potential distribution around the spacecraft are known, ion trajectories can be calculated numerically to assess the ion-optical transmission for ions starting far away from the spacecraft (at a location unperturbed by the spacecraft) until their arrival at the instrument aperture. The result of such a calculations performed for the Rosetta mission is shown in Figure 3.10 [*Nyffenegger et al.*, 2001]. Obviously, this is not a simple ion-optical system and the aperture bias (see Figure 3.10) of the instrument has to be suitably set with regard to the prevailing plasma conditions and spacecraft potential. Probably the best way to deal with ray tracing problems when a spacecraft is immersed in a plasma and under the influence of the Sun is the PicUp3D software library available under the GPL license[5], which is a project of the European Space Agency.

3.3.2 Laboratory Equipment

There are several concerns and devices in the laboratory that must be given special attention for accurate testing and calibration of the instrumentation. Here, we discuss some specifics that might be especially relevant to this energy range.

Before each test, careful attention should be paid to the electrical grounding plan of the laboratory, instruments racks, and sensors to obtain a well-designed signal common. Heavy copper bars, braid, or welding cable should be used between the vacuum chamber, instrument racks and experimental apparatus according to this grounding plan. There should also be no introduction of ground loops in this ground scheme that may allow the pickup of stray magnetic fields. Proper cable shielding, signal conditioning, and proper connections between devices whether it be single-ended or differential is important. This discussion is out of the scope of this book but there are several references for designing a high-quality ground system and establishing good sensor signals [*Morrison*, 1986; *Grunn*, 1987; *Johnson*, 1994].

Low-energy ion instruments have inherent sources of error due to stray electric fields, magnetic fields, non-uniform response of the detector, etc. While it is not possible to accurately predict these errors, they can be quantified by determining the response of the detec-

[5]The PicUp3D web page: `http://dev.spis.org/projects/spine/home/picup/`

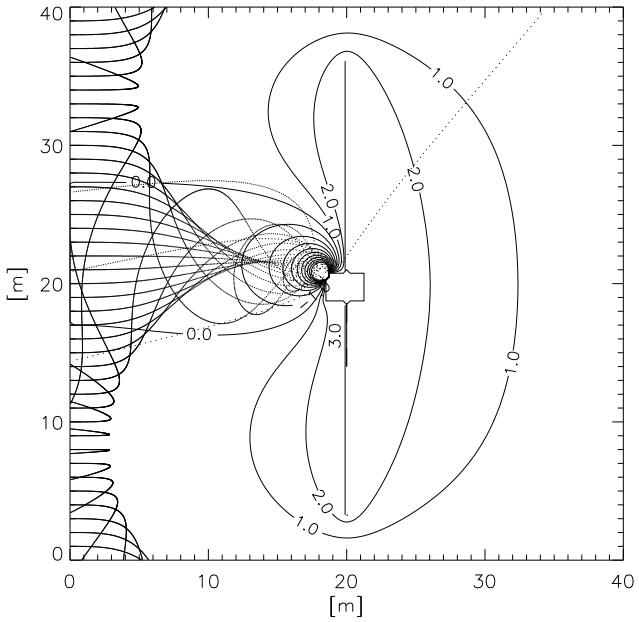

Figure 3.10: View onto the Rosetta spacecraft with ion trajectories of H_2O^+ molecules. The Rosetta spacecraft is at +3 V potential and located in the wake of the comet. The attraction grid (aperture bias) of the ROSINA/RTOF sensor is at −50 V. Incoming ions have a bulk velocity of 1000 m s^{-1}, which corresponds to an energy of about 0.1 eV. From *Nyffenegger et al.* [2001].

tor to a known source [*Lessard et al.*, 1998]. As mentioned in the introduction, Section 3.1, the instrument calibration can only be as good as the knowledge of the particle source of the calibration facility. Therefore, the ion source should be well known in its characteristics. Such a source should deliver an ion beam with an angular and energy width that is much narrower than the response of the instrument and a beam that is spatially uniform and large enough to flood the entire aperture of the instrument. The beam energy and intensity must also be tunable to accommodate the instrument energy range and the expected plasma densities [*Lessard et al.*, 1998]. The source can then be used to quantify various components of the instrument geometric factor. In calibrations at very low ion energies, a source of error from electron-impact ionization ion sources with a hot filament is that the temperature of the ion beam, i.e., the ion energy spread, is too large a fraction of the ion energy. RF ion sources can eliminate this problem for higher energies but cannot achieve the low particle energies due to plasma instability. *Lessard et al.* [1998] have minimized this problem for an electron source.

For calibrations at the low ion energies, the Earth's magnetic field becomes a concern for the accurate characterization of the instrument's response. For example, the radius of curvature for a 10 eV proton is about 15 m. A minimum magnetic field environment (10^{-3} of the Earth's intrinsic field) is critical for accurate characterization of the particle

detector response for very low energy of a few eV's (< 10 eV) charged particles, and for evaluation of instrument performance in deep space and planetary missions [*Knudsen*, 2004]. There are a few ways to minimize this problem. Coaxial coils of wire, referred to as Helmholtz coils, can be used around the chamber to cancel or minimize the Earth's ambient magnetic field. Calculations of the field along the axis of a Helmholtz coil pair is discussed by *Moore et al.* [1983]. This coil pair can be controlled by a 12-bit magnetometer in a feedback loop. High-permeability magnetic material, e.g. μ-metal, can be used to shield the Earth's magnetic field. The proper design of μ-metal shields is difficult though and is discussed in [*Wadley*, 1956]. It is also important not to use μ-metal shields (and other hardware) in close proximity of the instrument's aperture so that the ion beam is not scattered into the aperture. With the aid of μ-metal and Helmholtz coils the residual magnetic field can be below 100 nT [*Moore et al.*, 1983]. One way to see the effect of the Earth's field on the particle beam is by allowing the test fixture to rotate in the north-south plane. At different angles of rotation, the instrument's "nominal direction" will change as a function of particle energy. This angle knowledge can be used and subtracted from the data for non-critical tests.

The Faraday cup is used in the laboratory as a reference detector and also in space for plasma measurements (see also Section 3.3.5 below for calibration of Faraday cups for space flight). The typical difficulty in performing an accurate absolute calibration is in knowing the calibration beam flux and the Faraday cup can be reliable in terms of this measurement. It can serve as both a current or a charge measurement device. The simplest design consists of two, electrically isolated concentric cups. With the addition of grids and a current-collector plate, it will provide additional energy analysis of the particle source and can be referred to also as a planar retarding potential analyzer (RPA). The Faraday cup and the calibration of it is discussed in Sections 3.3.5 below, in Sections 2.2.1 and 2.4, as well as in the literature [*Knudsen*, 1966; *Donley*, 1969; *Moss and Hyman*, 1968; *Patterson*, 1969; *Troy and Maier*, 1975]. Several design aspects of the Faraday cup should be examined for the accurate measurement of very low energy ion beams. The levels of measured current with electrostatic analyzers in space is typically small, in the pico-ampere range, and currents of lower energy ion beams are even lower. For a positive-ion collector, the loss of a secondary electron appears to the current measuring instrument as an additional ion. To prevent the escape of secondary electrons, the depth of a Faraday cup should be at least five times its diameter. A "suppressor" grid biased to -30 V or more in front of the collector plate effectively prevents the escape of most secondary electrons. A grounded grid in front of the suppressor grid prevents field penetration from the suppressor in the direction of the incident current source [*Moore et al.*, 1983]. In addition, the cables coming from the Faraday cup to the electrometer or other electronic circuitry should be low-noise cables with the addition of graphite shielding. These cables should be tied down and not allowed to move during measurements to prevent current spikes. Low noise cables and documentation on low current measurements and sources of error can be obtained from *Keithley Instruments* [2005]. With care, current measurements made with an electrometer can reliably achieve 0.01 pA.

RPAs are typically used to analyze the particle beam energy using the beam current as a function of the varying voltage on the retarding grid. To resolve the lower ion energies, the retarding grid voltage range may be divided into multiple decades with a 12 or 16 bit analog resolution for each decade. For extremely low energies, it is important for this grid to be computer controlled with a high bit resolution to accurately determine the particle

energy. The ion source anode voltage range can also be treated the same way for proper measurement.

Often for the analysis of the plasma or particle beam in the laboratory, a standard RPA fitting curve is applied to the experimental data points comprising the collected current, I, versus the retarding voltage, V, curve. The formula to fit this I-V curve is given by *Troy and Maier* [1975]. The current registered by an RPA is the sum of the contributions of the individual ion species

$$I = \sum_i I_i \tag{3.60}$$

which for a RPA with n grids are given by

$$I_i = A \cos\theta \, \tau^n e N_i v_{sc} \, \frac{1}{2} \left(1 + \mathrm{erf}(S - U) + \frac{e^{-(S-U)^2}}{S\sqrt{\pi}} \right) \tag{3.61}$$

with

$$S = v_{sc} \cos\theta \sqrt{\frac{m_i}{2k_B T_+}} \tag{3.62}$$

with a transparency of each grid of

$$\tau(\theta, \varphi) = \left(1 - \frac{b}{a} \sqrt{1 + \tan^2\theta \cos^2\varphi} \right) \left(1 - \frac{b}{a} \sqrt{1 + \tan^2\theta \sin^2\varphi} \right) \tag{3.63}$$

where a is the wire spacing, b is the wire diameter, θ is the angle between the normal to the entrance aperture, A, and the spacecraft velocity vector (the elevation angle), and φ is the azimuth angle, and

$$U = \begin{cases} \sqrt{e(V + \phi_s)/k_B T_+} & \text{for } V + \phi_s \geq 0 \\ 0 & \text{for } V + \phi_s < 0 \end{cases} \tag{3.64}$$

where v_{sc} is the satellite velocity, k_B is the Boltzmann's constant, T_+ is the ion temperature, m_i is the mass of ith ion species, e is the electron charge, V is the potential of retarding grid relative to satellite, N_i is the ion density of ith ion species, and ϕ_s is the satellite potential. All ion species are assumed to have the same temperature T_+. A sample multispecies ion curve with theoretical fit and results is shown in Figure 2 in the paper by *Troy and Maier* [1975].

Computer programs have been developed that can deduce the density, energy, and temperature from these data using the standard RPA fitting curve [*Moss and Hyman*, 1968; *Patterson*, 1969]. There are several assumptions made when analyzing this standard RPA curve [*Troy and Maier*, 1975]. These assumptions are particularly important if working with ion beams of low current or low energy particles. These assumptions are:

1. The ambient ion velocity distribution is Maxwell-Boltzmann and this distribution is unchanged at the RPA aperture except for a uniform translation due to the spacecraft potential.

2. Each grid in the RPA represents an equipotential plane according to the voltage applied to that grid and only ions with energy greater than the applied grid potential can reach the collector. Potential depressions occur between the grid wires so that ions with energy less than the applied retarding potential do penetrate the grid openings.
3. The fraction of ions passing through each grid is equal to the optical transparency of that grid taken at normal incidence.
4. Grids and the collector are infinite in extent, so that any ion entering the aperture is either collected by the collector, collected by a grid, or rejected by the retarding electric field.
5. The measured current is due only to ions.

In order to obtain accurate particle beam parameters using a standard RPA, it is important to calculate the errors and correct for them, or to show that these assumptions produce negligible errors. Several papers have been written on different aspects of the assumptions listed above. *Parker and Whipple* [1970] examined the first assumption of translating the ion distribution at the RPA. The second assumption, the effects of assuming an equipotential plane, have been explored by *Knudsen* [1966], *Hanson et al.* [1972], *Goldan et al.* [1973], and *Read et al.* [1998]. *Chao and Su* [1999] studied the third assumption and found that for the same theoretical optical transparency, different mesh alignments will affect the fluxes at the RPA collector. They conducted computer simulations and provided many insights of RPA detection characteristics; one being that the ion transparency cannot be represented by only the physical grid sizes of the detector. The physical alignment of the meshed grids at the dual aperture planes, the dual retarding planes, the suppressor plane, and the shield plane will affect the ion transparency. They also noticed electron contamination in the collector plate if the mesh sizes were larger than the electron Debye length[6]. *Whipple et al.* [1968] investigated the last three assumptions but only for high energy, isotropic, particle data. *Troy and Maier* [1975] looked into the effects of grid transparency and finite collector size on the values of thermal ion density and temperature.

Typically there are three types of beam monitors that can be used in the chamber during testing and calibration. These include the Faraday cup or RPA, a large area MCP-based imager similar to the Quantar Technology imaging-detector system to measure spatial uniformity, and or a channel electron multiplier similar to the Amptektron^{TM} MD501 detector system. The Amptektron^{TM} is a channeltron placed behind a small pinhole. Each of these monitors has virtues and drawbacks. The Faraday cup is most reliable in terms of an absolute ion flux measurement. It can be used at currents of 0.01 pA cm^{-2} as long as there is careful attention paid to noise reduction. The MCP-based imager provides a spatial beam profile but has a poorly known absolute efficiency and will saturate at lower current levels than the Faraday cup can operate at. The Amptektron^{TM} performs a local measurement, operating near $\sim$ 0.1 pA cm^{-2} and can also be used for angular profiling.

3.3.3 Testing and Calibration

In our efforts to achieve the most accurate values for each of the terms of the geometric factor defined in Equation 3.16, there are several things that can be done during testing to

[6]The Debye length is the shielding length of the electrostatic potential of an isolated particle in the plasma: $\lambda_D = (\varepsilon_0 k_B T/(n e^2))^{1/2}$.

minimize error and the influence of noise. A few reminders are briefly listed here. To reduce emission noise, shield the ion gauges within the chamber. If this is not possible and if there are multiple ion gauges, turn off the electronics to any ion gauge that can be turned off, at least the ones that are close to the analyzer. Verify the voltage settings that power the position and angle readout devices so that accurate readings are obtained. If the translation or rotation motion is computer automated, turn off the power to the motor windings before reading any signals that will pickup this source of noise.

Each time a filament current is varied for an electron-impact ionization ion source and the tuning of other beam parameters have been completed, wait approximately 30 minutes or more for the ion current to stabilize. This is especially true for low-energy beams that are typically low in ion current and less stable. A closed feedback system can be used during the procedure to monitor and vary the filament current based on the readout. This need can sometimes be eliminated if there is enough time to stabilize the current before starting the testing procedure. Even if the current is stabilized, make regular and frequent checks of the beam current during the testing procedure.

There are variations in detector efficiencies due to differences in MCP gains, but also there are variations for different species and for different ion energies (see also Section 2.2.4). Therefore, it is important to test the instrument's overall effective area at low energies for different masses. *Stephen and Peko* [2000], studied absolute detection efficiencies in commercial microchannel plate detectors for O, O^+, and O^- in the energy range of 30–1000 eV (see Figure 2.16). These measurements were performed without electrical bias at the front surface of the MCP to avoid acceleration or deceleration of ions. They found the efficiencies to be strongly dependent on energy and varied for each charge state. Of the three species in that study, the strongest energy dependence was found for O^+ where the detection efficiency varied by three orders of magnitude over the energy range studied. Therefore, test all possible parameters and document all chamber and ion source settings that go with the current instrument state.

3.3.4 Low-Energy Ion Calibration Facilities

There are a few laboratories that can offer the full calibration of ion particle instruments at low ion energies. We will briefly describe a few facilities in this section. Facilities of all types are described in tabular form in the Appendix A.4.

The Low Energy Electron and Ion Facility (LEEIF) at the NASA Marshall Space Flight Center in Huntsville, Alabama, USA, offers ion beams from less than 1 eV up to 3000 eV. Within each decade the ion energy can be set with 12-bit resolution. This ion source is now being modified to accommodate higher energies. The laboratory was designed to calibrate single and multiple instruments over their range of particle energy, mass, flux, and angular acceptance and has been used for several satellite and sounding rocket instruments. It has a 3-axis turntable, a translation system, a Faraday cup to measure absolute beam intensities, a Quantar Technology imaging-detector system to measure spatial uniformity, and the Amptektron^{TM} MD-501 for local angular beam profiling. Various gases such as H_2, He, N_2, Ne, and O_2 can aid in mass calibration. The laboratory devices are automated using National Instruments LabVIEW software and data acquisition cards. For documentation, long calibration sequences are automated with all of the chamber parameters combined and time tagged with the parameter states from the instrument's ground support equip-

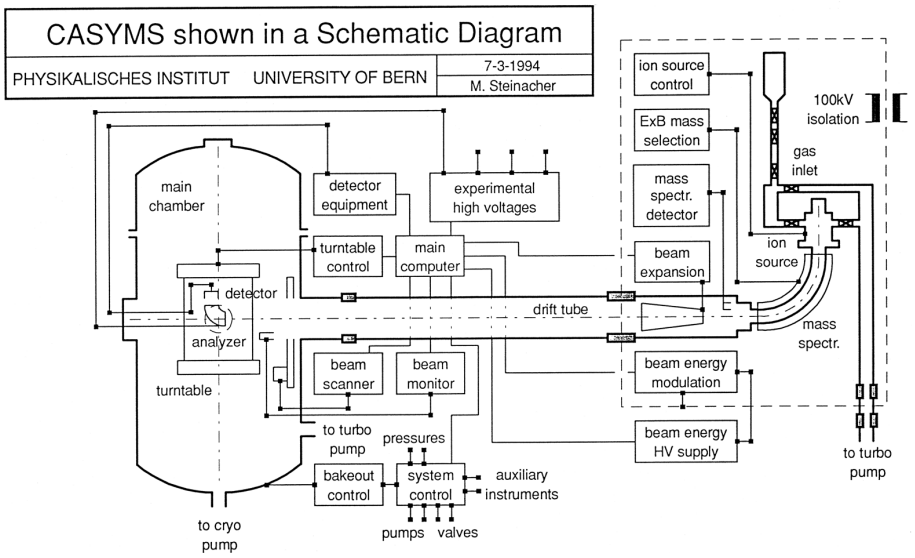

Figure 3.11: Schematic diagram of the CASYMS facility showing the ion source with the mass spectrometer and the beam expander on the right-hand side, the drift tube in the middle, and the main chamber with the beam diagnostics and the turntable with a sample instrument on the left-hand side. From *Steinacher et al.* [1995].

ment (GSE). *Biddle and Reynolds* [1986] give a detailed description of the ion source and its characteristics.

The CASYMS (calibration system for mass spectrometers) in Bern, Switzerland, has been used to calibrate many spacecraft instruments. The ion source in this facility delivers a mass-selected ion beam at 3 keV, and with a deceleration and acceleration system, lower and higher energies ranging from ∼5 eV/q – 100 keV/q can be used for calibration, respectively. It has a 4-axis turntable, is fully computer controlled, has a fixed beam monitor used to continuously survey the beam intensity, and a movable beam scanner to record beam profiles and measure absolute beam intensities. A full description of the ion source and the facility is provided in [*Ghielmetti et al.*, 1983] and [*Steinacher et al.*, 1995]. Figure 3.11 shows the elements of this calibration system.

Another low energy charged particle calibration facility is described by [*Knudsen*, 2004] and supports the testing and evaluation of thermal and suprathermal ion and electron flight instruments. It contains a one-meter high vacuum chamber, a horizontal laminar flow bench, and a Helmholtz coil to minimize the Earth's ambient magnetic field. The vacuum chamber is equipped with a low energy ion source (5 eV $< E_i <$ 10 keV), a low energy electron source (10 eV $< E_e <$ 1 keV), a high-energy ion source (200 eV $< E_i <$ 150 keV), and a high-resolution positioning table. A supersonic neutral particle beam source will be added in the near future.

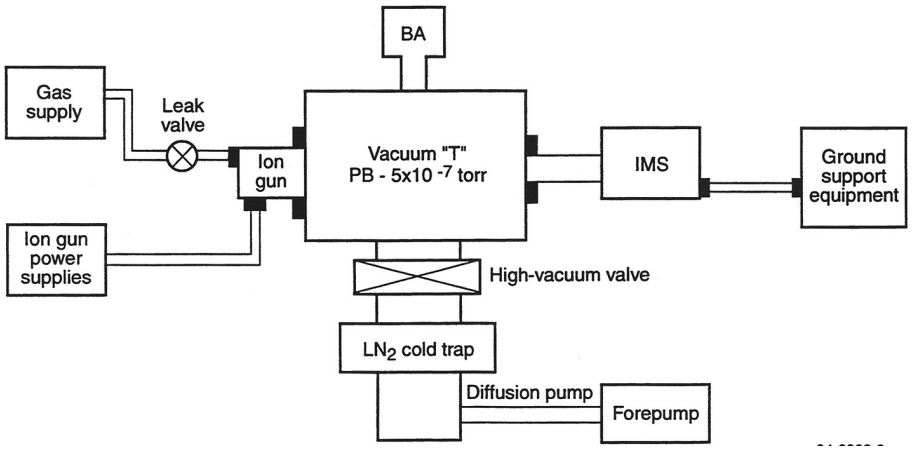

Figure 3.12: Schematic diagram of the Bennett Ion Mass Spectrometer calibration facility. From *Erlandson et al.* [1994].

3.3.4.1 Bennett Ion Mass Spectrometer Calibration

Erlandson et al. [1994] describe a calibration system that has been used to calibrate the Bennett spectrometers [*Bennett*, 1950] used for low-energy ion measurements in the upper atmosphere of the Earth and Venus. The ion energy range of the calibration system is from a few eV to about 50 eV. The Bennett spectrometer is explained in Section 2.6.3.3, and has been used for low-energy ion measurements in the upper atmospheres of Earth (MSX, Atmosphere Explorer, OGO, Space Shuttle) and Venus (Pioneer Venus Orbiter and Bus) [*Taylor et al*, 1965; *Taylor et al.*, 1968; *Brinton et al.*, 1973; *Taylor et al.*, 1980; *Grebowsky et al.*, 1987; *Grebowsky and Schaefer*, 1990]. The calibration system is different than the facilities described in Section 3.3.4 and therefore is briefly described here and shown in Figure 3.12. An ion gun and the Ion Mass Spectrometer (IMS) instrument are mounted on opposite ports of the vacuum system. The instrument electronics are mounted outside the vacuum chamber. Note that the instrument is located outside of the vacuum chamber and attached via an interface. The Retarding Potential Analyzer (RPA) of the calibration facility is mounted in front of the IMS and is used to determine the ion beam energy and the total ion flux entering the IMS. Figure 3.13 shows a schematic of the ion gun and of the RPA systems.

The ion collection efficiency of the Bennett instrument, ε, is a function of the ion species, i. Therefore calibrations were performed with several gases H_2, He, H_2O, N_2, O_2, Ar and CO_2. The efficiency, ε_i, for each ion species i is

$$\varepsilon_i = \kappa_i \, \varepsilon_r \, (V_s + \Delta V_{s,i}) \tag{3.65}$$

where ε_r is the reference efficiency, V_s is the retarding potential, and $\Delta V_{s,i}$ is the stopping potential for each species. The reference ε_r is based on He^+ for light ions and Ar^+ for heavy ions. The laboratory determined correction factor κ_i (for each species), and ε_r together with the $\Delta V_{s,i}$ and V_s from flight telemetry are used to determine the efficiency for post-flight analysis. The effective ion collection area, A_{eff}, is the actual sensor area of

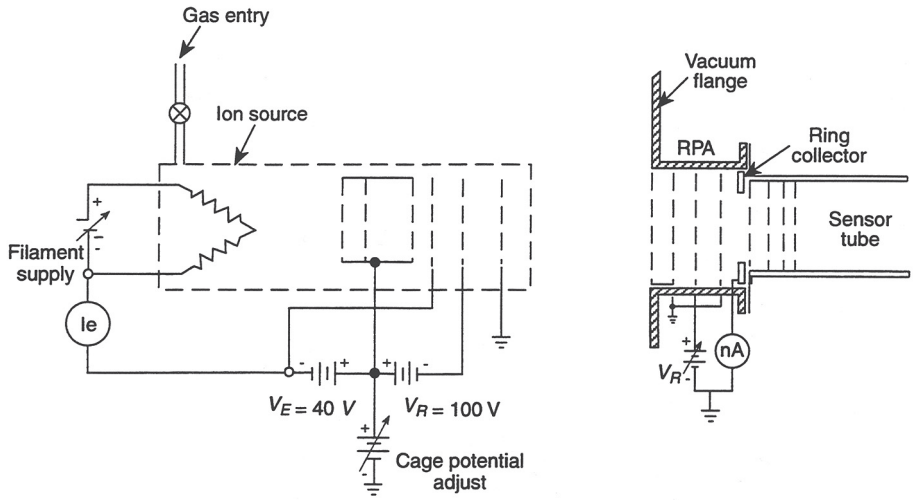

Figure 3.13: Left: The ion source of the calibration facility. *Right:* The retarding potential analyzer (RPA) of the calibration facility is directly mounted onto the Bennett mass spectrometer. From *Erlandson et al.* [1994].

the IMS if there is a spacecraft ground plane surrounding the aperture. However, surrounding the instrument opening with a guard ring set at a negative potential can increase the effective ion collection area for positive ions. The number density for species i is then

$$n_i = \frac{I_c}{v^* q_0} \frac{g(\hat{\boldsymbol{v}} \cdot \hat{\boldsymbol{A}}_{\text{eff}})}{\varepsilon_i} \tag{3.66}$$

where I_c is the measured current for species i arriving with a velocity of v^*, and $g(\hat{\boldsymbol{v}} \cdot \hat{\boldsymbol{A}}_{\text{eff}})$ is the angle of incidence correction that can be determined from flight data for a spinning spacecraft in a region of constant ion density within a certain angle range by observing the IMS collected current as its angle of attack changes.

An example of the angular response is given for the Cassini Ion and Neutral Mass Spectrometer (INMS) instrument open source, which can measure either ions or neutral gas coming in at the spacecraft speed [*Kasprzak et al.*, 1996; *Waite et al.*, 2004]. For calibration, INMS is mounted on a bellows outside of the vacuum system of a neutral beam facility. In-line with the sensor was an ion gun that could be rotated out of the way when using a neutral beam. A measurement of the angular response of the open source is shown in Figure 3.14 for a low energy ion beam in two different orthogonal directions. The INMS open source is at right angles to the quadrupole mass analyzer with the ions being deflected by quadrupole "switching" lens. The Y angle refers to angles in the plane of the open source, switching lens and mass analyzer while the Z angle is in the orthogonal direction. For the ion test, data from the flight unit (FU) instrument and the engineering unit (EU) instrument are shown to be comparable. The open source ion mode response has also been studied by numerical simulation using the Sarnoff BEAM 3-D software [*Swaminathan et al.*, 1996] to model the lens system from the entrance aperture to the

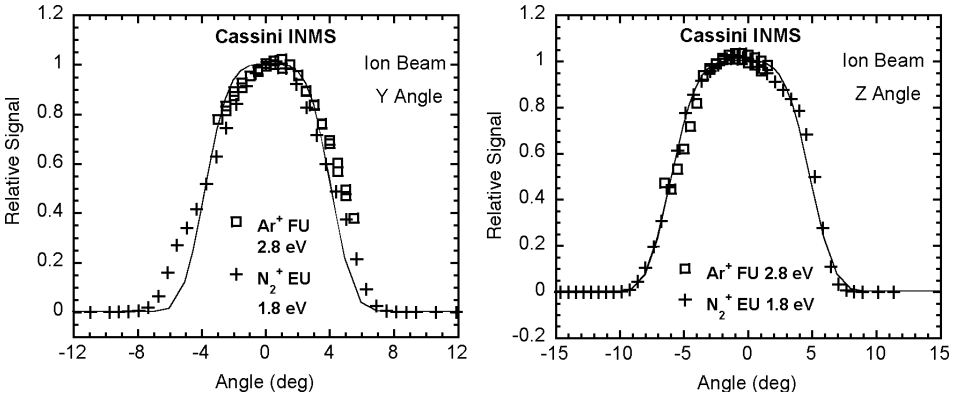

Figure 3.14: The angular response of Cassini INMS flight unit (FU) and engineering unit (EU) to a low energy ion beam in the Y angle (left) and in the Z angle (right).

entrance of the quadrupole mass analyzer. Results of that simulation are also shown in Figure 3.15 together with calibration data. Although the conditions of the simulation and the laboratory data are not exactly identical, both sets of data show a similar decrease of transmission with increasing angle of incidence.

3.3.4.2 Calibration in a Real Plasma Environment

Sometimes performing the calibration with an ion or an electron beam is not sufficient to characterize the performance of the instrument. This is the case when the Debye length of the plasma is small, that is if λ_D is similar or smaller than typical spacecraft dimensions, which is the case for low-energy plasmas such as ionospheric or cometary plasmas. Then the calibration has to be performed in a plasma environment duplicating the space environment as well as possible. The JONAS facility in Toulouse, France, is a typical simulation chamber for low-energy plasmas [*Roussel et al.*, 1997]. Also, the interaction of the plasma with the spacecraft will influence the measurements of a low-energy ion or electron instrument. Spacecraft charging resulting from photoelectron emission and a cold photoelectron population in the plasma moving with the spacecraft complicate the situation even more. For a complete understanding of the instrument performance, for example the effectiveness of a biased aperture, the measurements need to be done in a real plasma environment with a suitable spacecraft mock-up [*Berthelier and Roussel*, 2004]. Since the spacecraft mock-up is typically a scaled version of the real spacecraft and the plasma parameters have to be scaled as well, such measurements are accompanied by simulations to project to the real situation in space [*Roussel and Berthelier*, 2004].

3.3.5 Calibration of Faraday Cup Instruments

This section discusses pre-flight calibration techniques for characterizing Faraday cup (FC) instruments. These measurements are conducted either on a laboratory bench or in a vacuum chamber using an ion beam. Basis for the following discussion are the calibrations

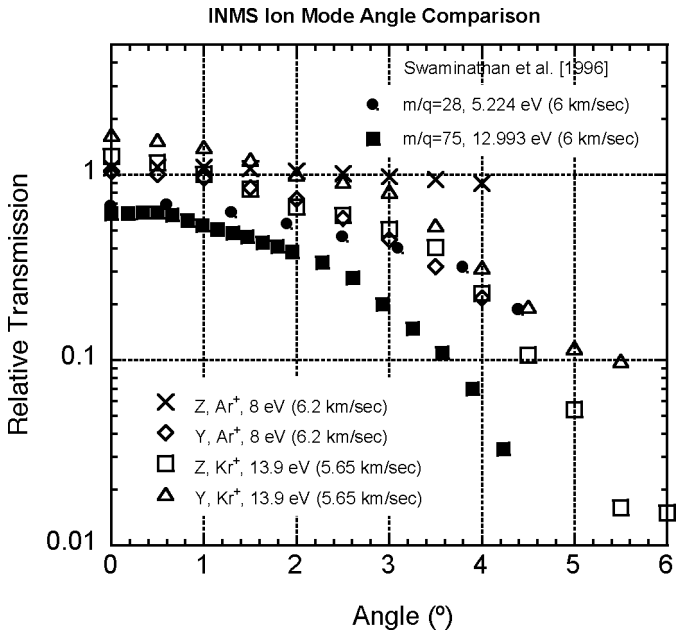

Figure 3.15: Laboratory data showing the relative transmission of the Cassini INMS instrument in the open source ion mode for Kr^+ and Ar^+ corresponding to a spacecraft velocity of 6 km s^{-1} (open symbols and X). The INMS Y and Z correspond to rotations about the spacecraft Y and Z axes, respectively (outward INMS source normal is $-$X). These laboratory data are compared with similar data from a numerical study by *Swaminathan et al.* [1996] (solid symbols).

of the PlasMag Faraday cup built for the Triana mission [*Aellig et al.*, 2001]. The launch of the Triana mission has been postponed because of the Space Shuttle accident in February 2003.

3.3.5.1 Bench Testing

The internal calibration system described in Section 2.4.2.2 is used in pre-flight bench testing to determine characteristics of the measurement chain such as the transition points between amplifier stages and the individual gains of the amplifiers. Such measurements are used to determine the stability of the sensor properties, to identify properties such as temperature dependencies of the instrument response, and to provide a pre-flight baseline for in-flight calibration of the instrument. First the bench measurements of the response time (RC time) of the Triana log-ADC are discussed. Then the temperature dependence of the FC response is demonstrated.

RC Circuit Decay Times Variation of the RC time, τ_{RC}, of the log-ADC circuit in the measurement chain affects the digital number returned for a given integrated current. Knowledge of τ_{RC} and the gains of the amplification stages are essential to convert correctly the digital number back into a current.

The internal calibrations of the measurement chain for the Faraday cup for the Triana spacecraft were carried out over the course of a year of pre-flight testing. These calibrations were performed in clean rooms and vacuum chambers, before and after vibration and thermal testing, and after the instrument had been moved to various laboratories. As will be seen, the values for the τ_{RC} times were nearly identical at room temperature in every case.

The procedure for determining τ_{RC} is as follows. A particular injection current from the internal calibrator is selected and applied to the measurement chain. The current is integrated on a measurement chain capacitor and then held. It is converted to a channel number by comparing that voltage to a decaying exponential obtained from the discharge of the log-ADC capacitor, which had been initially charged to a stable voltage. The channel number is given by

$$\text{ADC channel} = 1024 - \frac{A_0}{\tau_{\mathrm{DPU}}} \ln \frac{V_{\mathrm{RC}}}{A_1(I\,\Delta t) + A_2} \tag{3.67}$$

where 1024 is the maximum channel number, A_0 is the RC time of the discharge circuit, τ_{DPU} is the DPU clock period, V_{RC} is the voltage to which the RC circuit is charged, $I\,\Delta t$ is the product of the current and the integration time, A_1 is the conversion of integrated charge to voltage, and A_2 is a small offset voltage. The channel number returned from the log-ADC is recorded as the integration time of the measurement varies from 40 ms to 400 ms. This procedure is repeated several times and the average and standard deviation of the channel number are calculated. The dependence of the channel number upon the integration time is given by a simple three-parameter equation. Figure 3.16 demonstrates the results. The average channel number is plotted as a function of integration time as symbols, and the solid line is the best fit of the model equation. The first free parameter in the equation, A [0], is τ_{RC}.

A strength of this procedure is that the determination of τ_{RC} does not depend on the actual value of the injection current. This is demonstrated in the upper panel of Figure 3.17, which shows the values of τ_{RC} measured in 64 calibration runs spread over the course of a year using different injection currents. The lower panel of Figure 3.17 is a histogram of the individual measurements, which have a Gaussian distribution and are centered at 0.398 ms. The uncertainty in the mean for these measurements is 0.001 ms.

Temperature Dependence of Results The Triana instrument was placed in a thermal chamber and the internal calibration system was run over the full range of possible injection currents and integration times. The observed output channel numbers over the temperature range $-25\,^{\circ}\mathrm{C}$ to $60\,^{\circ}\mathrm{C}$ were compared with the standard values at room temperature. The variation of output channel number for each combination of current and integration time was a linear function of the temperature. Figure 3.18 shows a plot of the dependence of output channel number on the temperature as a function of the nominal channel number at room temperature. The different symbols represent the dependence of output from the same measurement chain but in the three different gain ranges. Note that the temperature dependence is a linear function of the nominal output channel number and is the same in all three gain stages. These features are distinct signatures of the effect of a temperature-dependent variation in the RC time of the log-ADC circuit.

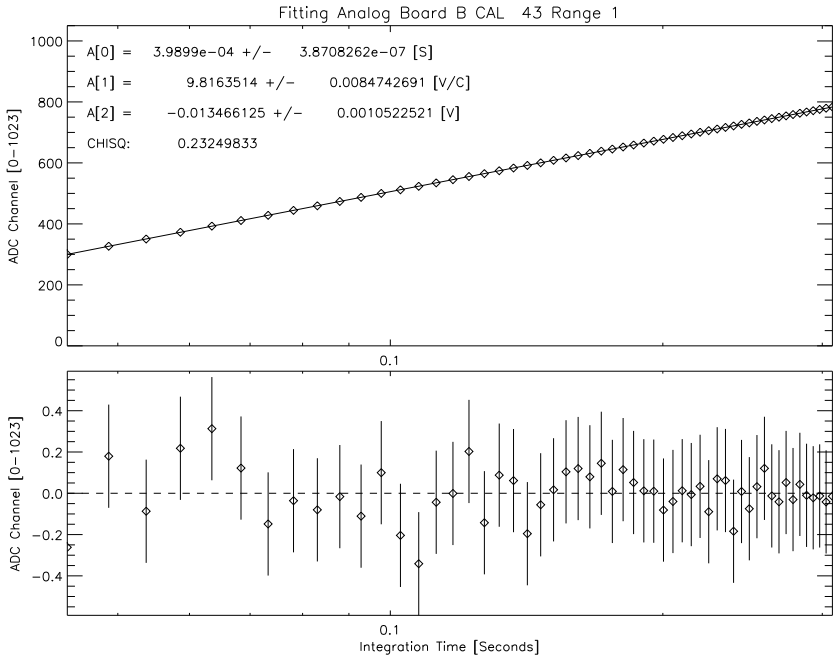

Figure 3.16: Measuring the RC time of the log-ADC using the internal calibration system of the Faraday cup. For this figure a single injection current was supplied to the measurement chain and the integration time was varied from 40 ms to 400 ms. The upper panel is a plot of the digital number returned from the log-ADC as a function of the integration time. The solid line is the best-fit of a three-parameter equation that models the response of the measurement chain. The first parameter, A [0], is the RC time, see Equation 3.67. The lower panel is a plot of the residual to the fit in output channel numbers.

3.3.5.2 Beam Testing

An ion beam was used to calibrate the geometric acceptances and to measure the energy-per-charge window cutoffs. The cup was mounted on rotating platform with the rotation axis in the plane of the central, limiting aperture. The modulator grid voltage was set to zero, and a DC-current was measured with a calibrated electrometer as the cup was rotated relative to the beam direction. The geometrical cutoffs due to the apertures were as expected, and the cup was also translated perpendicular to the beam axis to verify the area calculations. The beam diameter was determined to be approximately 7 mm, large enough to avoid domination by a single grid wire but small compared to the central aperture.

Grid Transparencies For the Wind FC, indicated in the cross-section in Section 2.4 Figure 2.23, there are seven wire grids inside the sensor [*Ogilvie et al.*, 1995]. Each of these grids blocks a small portion ($\sim 5\,\%$) of the ions entering the instrument from reaching the collector plates. The overall transparency of these grids must be known to correctly relate the incident flux of solar wind ions to the currents produced at the collector plates. The

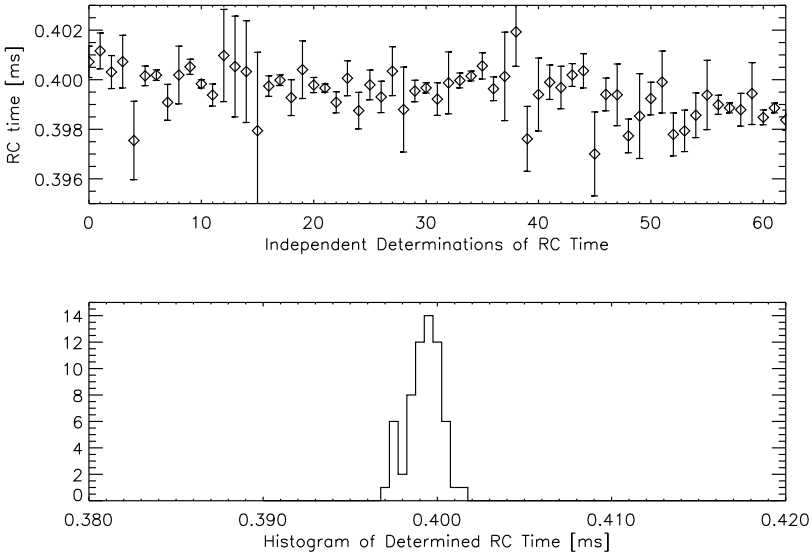

Figure 3.17: Stability of determinations of τ_{RC} using the internal calibration system. The upper panel is a plot of the values of τ_{RC} determined during 64 different calibration runs. The lower panel is a histogram of the the measurements given in the upper panel. The histogram is Gaussian with a width consistent with the uncertainties in the individual fits to determine τ_{RC}. From these measurements we determined that $\tau_{RC} = 0.398$ ms with an uncertainty in the mean of ± 0.001 ms.

grids were constructed of knitted, 25 μm diameter, tungsten wires. The resulting mesh was approximately rectangular with a 1 mm spacing between the wires.

The transparency of the grids is independent of ion properties such as charge, mass, and energy. The angular dependence of the transparency is a geometrical function of the thickness and spacing of the tungsten wires which make up the grids. Both the angular dependence and the transparency at normal incidence can be calculated analytically (see Equation 3.63), but it is useful to measure the transparency at normal incidence to verify these predictions.

A stack of five flight spare grids was suspended from a motor which traveled along a rail mounted in the vacuum chamber. As was done in the flight cup, the grids were angularly displaced to avoid Moiré effects. A beam was normally directed into the FC and the stack of grids was moved into and out of the beam path. The grid transparency at normal incidence was then determined by comparing the currents measured with and without the stack in place.

Assuming a uniform square distribution of the tungsten wires and the separation and thickness listed above, each grid theoretically blocks approximately 5 % of the particles at normal incidence. The opacity of a single grid inferred from the beam chamber measurement is 3.9 %.

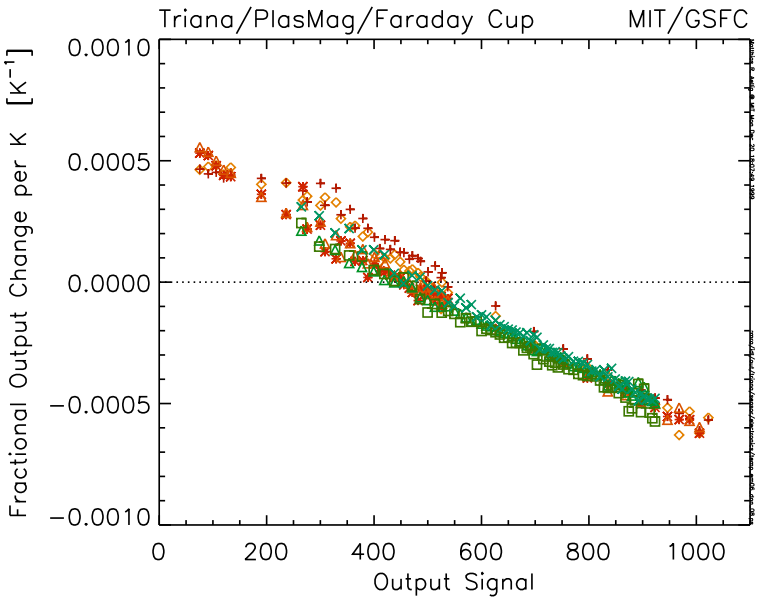

Figure 3.18: Temperature sensitivity of the Triana FC measurement chain as determined by testing in a thermal chamber. The different symbols correspond to measurements in different gain stages and temperature ranges. The fractional change in the output current per degree Kelvin is plotted as a function of the nominal output current for that calibration signal at room temperature.

Properties of Energy Windows The measured voltages produced by the high voltage modulator were compared with the observed boundaries of the energy windows by sweeping the FC through a series of energy windows while exposing the instrument to a narrow beam of ions in a vacuum chamber. The energy distribution of ions in the beam (1 to 2 eV) was small compared to the width of the energy windows. The energy of the ion beam was raised at a slow rate compared with the frequency of the FC measurements in the energy windows. The observed currents were then plotted as a function of beam energy. The transitions when the current decreased in one energy window and increased in the next window were identified. There is a finite width to this transition, which is a convolution of the energy of the beam and the sharpness of the windows produced by the modulator grids.

Figure 3.19 shows the measured cutoff efficiency of the modulator grid. The beam energy was varied from 800 to 1200 V and the corresponding measured current was recorded. For each window, the width of the transition on each edge and the width of the window were determined by examining the measured currents. This procedure was repeated for several energy/charge windows spread from 500 to 5000 V. Figure 3.20 is a plot of the measured transition width as a function of the modulator voltage. The measured transition widths are well-fit by a line with a slope of 1.3 % and an offset of 1.1 V. The offset voltage is consistent with the dispersion of ion energies in the beam.

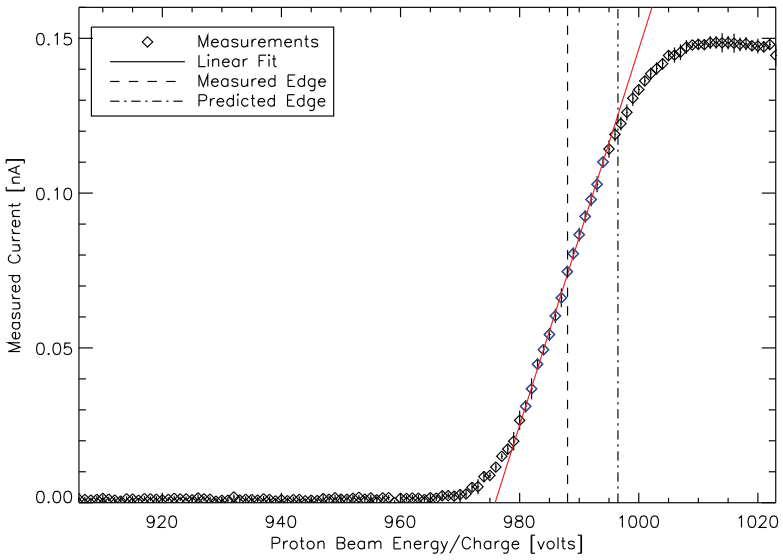

Figure 3.19: The measured cutoff efficiency of the modulator grid. The beam energy was varied from 800 to 1200 V and the corresponding currents measured in a series of energy windows was recorded. This figure shows the current (diamonds) seen in an energy/charge window in the range from 905 to 1025 V with an expected edge at 996 volts (indicated by the dot-dashed line). The "Predicted Edge" was determined by measurements of the modulator voltage waveform. The "Measured Edge" is at 988 V (halfway between the maximum and minimum measured currents) and differs by 0.8 % from the predicted value. The finite width of the edge is due in part to the velocity dispersion of ions in the accelerator beam and to the non-ideal potential of the grids (see text).

3.3.5.3 Absolute Calibration with an Ion Beam

The final step in determining the absolute calibration of a Faraday cup was to measure the output channel number from the log-ADC for a known ion beam current. The transparency of the grids, the efficiency of the collector plates, and the characteristics of the amplifier and log-ADC are not functions of ion properties such as mass, charge, or energy. A single ion beam with a known current is sufficient to determine the absolute response of the instrument.

In this section we describe the absolute calibration of the Triana Faraday cup, which uses three 120° wedge-shaped sectors of a circular collector plate. The multiple collector plates make the absolute calibration procedure straightforward.

An ion beam was formed and sharply focused with electrostatic lenses so that its profile was much smaller than any of the individual collector plates. The spatial profile of the beam was determined by slowly translating the Faraday cup so the beam was gradually moved from one collector plate to another. This procedure established that the beam was sufficiently small to illuminate only one collector plate at a time.

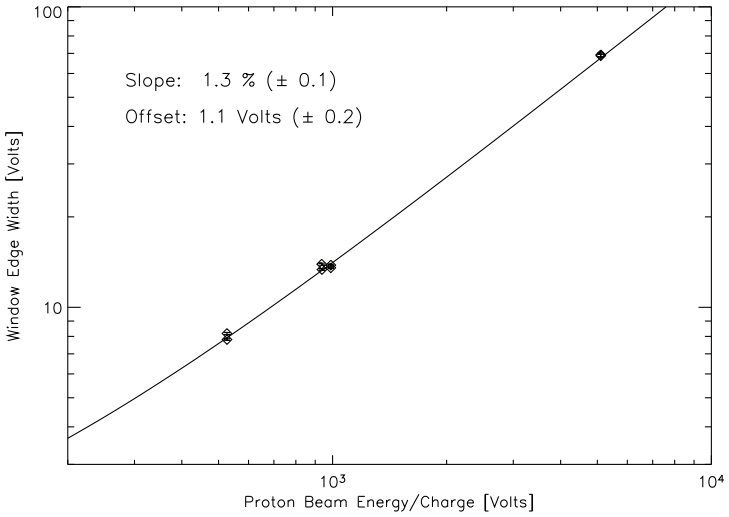

Figure 3.20: Measuring the properties of the energy windows with a narrow ion beam. The fact that there is a finite width in the transition of the measured current as the beam energy is increased and moved through the energy/charge window is due to the energy dispersion of the beam and to the non-ideal potential of the grids.

The beam was then placed successively on each of the collector plates, and the relative response of the individual measurement chains to the same input current was determined. That procedure established the relative calibration of the measurement chains.

The absolute calibration was then established by disconnecting one of the collectors from its corresponding measurement chain and running a low-noise cable from that collector plate through the side wall of the vacuum chamber to a calibrated sensitive, DC electrometer. We then directly compared the data numbers from the collectors with measurement chains to the output of the electrometer. For the Triana FC, the absolute calibration measured in the vacuum chamber with an ion beam was within 0.5 % of the predicted values based on the instrument components.

3.4 Medium Energy Ion Calibration

The range of medium energy ions mainly covers the fields of solar wind instrumentation and magnetospheric instrumentation. The solar wind is a flow directed approximately radially away from the Sun with a Mach number between 6 and 20 and velocities of about 300 to 800 km s^{-1}, corresponding to energies of about 400 eV/u to 4 keV/u. For solar wind research all elements from hydrogen up to iron are of interest, with ion charge states up to 10 and more. In magnetospheric research one is mostly interested in hydrogen, helium, and oxygen in form of single or perhaps doubly ionized state. However, the particle distribution functions can be wide (hot plasma) and the energy range spans basically from

eV to hundreds of keV, see for example summaries by *Lin et al.* [1995] and *Rème et al.* [1997]. More information on the different plasma populations in space has been given in Chapter 1. The typical reference detector for calibrations in this energy range is the channeltron with a pulse counting system that has been calibrated against a Faraday cup with a precise current measurement.

The required number of calibration constants is arguably greatest with charged particle instrumentation for magnetospheric research in the energy range from a few eV to tens of keV. This is because such particles are chiefly responsible for the electromagnetic processes in Earth's magnetosphere and that the study of these processes requires detailed measurements of the particles' three-dimensional velocity distribution, as well as their density and ion mass composition. For that reason the following description is laid out with a recent generation ion mass spectrometer as the tangible model, specifically the Toroidal Imaging Mass-Angle Spectrograph (TIMAS) for the Polar mission [*Shelley et al.*, 1995].

However, TIMAS is a rather untypical instrument for medium-energy plasma measurements since it still uses magnetic deflection for the mass analysis and, for a magnetic instrument, has a large field-of-view. More than two decades ago the time-of-flight (TOF) technique using carbon foils, which then was already an established technique in particle physics, was introduced to space physics [*Gloeckler and Hsieh*, 1979; *Wilken and Stüdemann*, 1984]. In such a TOF spectrometer an incoming particle is identified by having it pass through a thin start-foil (a carbon foil of typically 100 Å thickness) to produce a start signal and then by measuring the time until the particle hits a stop detector at a given distance. This measurement gives the velocity of the particle, and if the stop detector is a solid-state detector the particle's energy is also measured. Together with the E/q measurement of an electrostatic analyzer the particles energy, mass, and charge can be determined. TOF instruments were flown first on the AMPTE mission [*Gloeckler et al.*, 1985; *McEntire et al.*, 1985; *Möbius et al.*, 1985], and thereafter on many magnetospheric missions [e.g. *Möbius et al.*, 1998], and on solar wind missions [e.g. *Hovestadt et al.*, 1995; *Gloeckler et al.*, 1998]. As a state-of-the-art instrument of this kind we will discuss the PLASTIC instrument for the STEREO mission. PLASTIC uses electrostatic deflection with a toroidal analyzer for energy-per-charge analysis and a TOF spectrometer for mass analysis, which is a concept common to many instruments used in this energy range, both in solar wind and magnetospheric research.

3.4.1 The Toroidal Imaging Mass-Angle Spectrograph

The Toroidal Imaging Mass-Angle Spectrograph (TIMAS) is a first-order double focusing (angle and energy), imaging spectrograph that simultaneously measures all mass per charge components from 1 u/e to greater than 32 u/e over a nearly 360° by 10° field-of-view [*Shelley et al.*, 1995]. An engineering drawing of TIMAS is shown in Figure 3.21. Mass per charge is dispersed radially on an annular microchannel plate detector and the azimuth position on the detector is a map of the instantaneous 360° field-of-view. With the rotation of the spacecraft, the TIMAS instrument sweeps out very nearly a 4π solid angle image in a half-spin period. The energy per charge range from 15 eV/e to 32 keV/e is covered in 28 non-contiguous steps spaced approximately logarithmically with adjacent steps separated by about 30 %. In addition, the 360° field-of-view fan is divided in 32 11.25°-wide angular sectors. Four sectors of these 32 angular sectors are used for detector

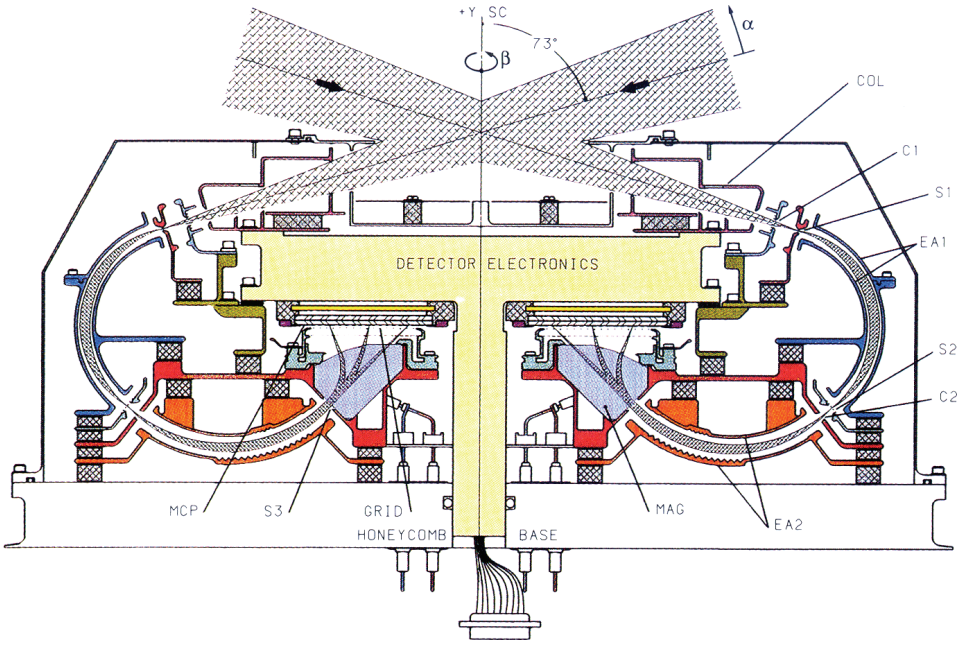

Figure 3.21: Schematic cross section of the TIMAS ion optics. Elements include the collimator, COL, ion repeller, C1, object slit, S1, first toroidal electrostatic analyzer, EA1, image slit for EA1, S2, first field terminator for EA2, C2, second toroidal electrostatic analyzer, EA2, second field terminator for EA2, S3, sector magnets, MAG, grid assembly, GRID, microchannel plate detector, MCP, and detector electronics. The entire assembly is rotationally symmetric about the vertical center line. From *Shelley et al.* [1995].

mounting. This leaves 28 sensitive angular sectors on the MCP anode. Therefore, there are 28 geometric factors for each energy channel (for each ion species). This angular dimension is referred to by the symbol β below. The orthogonal ("elevation") angle is denoted by α (the field-of-view is 10° wide in α at FWHM). The angles α and β are part of the internal coordinate system of the instrument (see Figure 3.23).

3.4.1.1 Extraction of Calibration Constants From Calibration Measurements

The principal calibration constants needed for measurements of particle velocity distributions are the so called geometric factors, a separate set of which is needed for each of several major ion species in the case of a mass spectrometer. Although the geometric factor was described in its most general form in Section 3.1.1 above, this section applies these considerations to a concrete example.

Given a single particle species, whether ions or electrons, the corresponding geometric factors can be identified starting from Equation 3.1, in the differential form, where the counts resulting from particles passing through a small surface area d$\boldsymbol{A}$ during a short time interval dt are given by

$$\mathrm{d}C = vf(\boldsymbol{v})\, v^2\, \mathrm{d}v\, \mathrm{d}\Omega\, \mathrm{d}A\, \mathrm{d}t \tag{3.68}$$

where $f(\boldsymbol{v})$ is the phase space density, $\boldsymbol{v}$ is the velocity vector and is assumed parallel to the surface normal (thus $\hat{\boldsymbol{v}} \cdot \mathrm{d}\boldsymbol{A} = \mathrm{d}A$), $\mathrm{d}\boldsymbol{v} = v^2 \mathrm{d}\Omega \mathrm{d}v$ is a differential velocity volume, and $\mathrm{d}\Omega$ is a differential solid angle. Note that in Equation 3.68 the detection efficiency, $T(\boldsymbol{v})$, is not considered explicitly anymore. Since the instrument measures the energy, or the energy per charge, of an ion, it is useful to substitute the velocity by the particle's energy

$$\mathrm{d}C = f(\boldsymbol{v}) \frac{2E}{m^2} \, \mathrm{d}E \, \mathrm{d}\Omega \, \mathrm{d}A \, \mathrm{d}t \tag{3.69}$$

where E is the particle energy $(mv^2)/2$, m is the particle mass. The first two factors are the number flux

$$J(\boldsymbol{v}) = \frac{\mathrm{d}C}{\mathrm{d}t} \frac{1}{\mathrm{d}E \, \mathrm{d}\Omega \, \mathrm{d}A} = \frac{2E}{m^2} f(\boldsymbol{v}) \tag{3.70}$$

J usually is measured in units of $(\mathrm{cm}^2 \text{ s sr eV})^{-1}$, or $(\mathrm{cm}^2 \text{ s sr keV})^{-1}$ or $(\mathrm{cm}^2 \text{ s sr keV/q})^{-1}$, if the particle species is ions with a charge of Q units.

Equation 3.69 can be approximated for finite resolution elements of the instrument and a finite time interval and we obtain for the number of particle counts

$$C = J \, A \, \Delta\Omega \, \Delta E \, \Delta t \tag{3.71}$$

with the "Δ"s indicate the finite resolution of the instrument for that variable and ΔE is a narrow energy passband, A is the active area, and $\Delta\Omega$ is the solid angle.

The, purely, geometric factor, G, is here identified as

$$G = A \, \Delta\Omega \tag{3.72}$$

in the normal units of cm^2 sr. In terms of the simple form of Equation 3.69, it represents the instantaneous angular acceptance onto the area A at given particle energy, a property that is defined by the instrument optical design. However, since the counts C are to be inferred from the instrument output, the geometric factor G is not strictly geometric in practice. Rather it is used as a proportionality factor that also includes transmission and detection efficiencies as discussed above.

Common practice with electrostatic energy discrimination is to not derive geometric factor G by itself (i.e., calculated using Equation 3.72) but rather as a combined factor $A \, \Delta\Omega \, \Delta E$. Here the energy passband ΔE refers to external particle energy E and is often proportional to that energy with ordinary electrostatic particle analyzers for protons and heavier ions. With internal pre-acceleration required for proper mass discrimination, ΔE is not simply proportional to the external particle energy with the TIMAS instrument, although it is a function of that energy.

Given a known differential calibration flux J_C of a single particle species, the compound factors $G\Delta E$ can thus be determined one by one from inverting Equation 3.71

$$G\Delta E = \frac{C}{J_C \, \Delta t} \tag{3.73}$$

where C is the number of counts obtained during time Δt, and Δt is chosen long enough to ensure good counting statistics (typically longer than the dwell time to be used during

cycling of onboard power supplies). Note that the geometric factor derived from Equation 3.73 implicitly contains the instrument efficiencies and transmissions, thus it will be species dependent, as well as vary with instrument settings.

It is essential that the calibration particle beam has a cross section that is at least as large as the instrument aperture and that the flux fills the (typically small) angle-energy phase space $\Delta\Omega\Delta E$ uniformly. In terms of the energy passband ΔE of the instrument, this is accomplished by using either (1) multiple and closely spaced discrete beam energies, (2) a linear ramp, or (3) energy wobble. In either case the beam energy width needs to be well defined. Rather than spreading the flux of the calibration beam in angle, it may be more practical to turn the instrument itself, ensuring that each part of $\Delta\Omega$ of the instrument is exposed equally long while averaging the counts. Again, the input range needs to be well defined and broad enough to ensure complete coverage of instrument window. Knowing the calibration flux means continually reading a beam monitor placed in the vicinity of the instrument and scanning the beam cross section at regular intervals.

While this procedure typically allows a great deal of automatic data recording and yields the most essential instrument constants with the minimum manual effort, it is also prudent to make detailed measurements of the angle-energy response on a finer scale in representative cases to verify instrument design. Examples of such measurements for the TIMAS instrument are shown in Figure 3.22. These were made at the University of Bern ion beam calibration facility (See Figure 3.11) [*Ghielmetti et al.*, 1983; *Steinacher et al.*, 1995].

With a mass spectrometer it is also necessary to verify the shape and location of mass peaks in appropriate coordinates. In the TIMAS case (not shown), different ions are separated by geometric dispersion in a magnetic field produced by 32 wedge-shaped magnets arranged in a spoke-like pattern. The mass-spectral part of the calibration thus amounted to mapping the radial impact position of ions with known momentum, that is with known rigidity $(M/Q \cdot E/Q)^{1/2}$, on an annular position-sensitive detector (MCP), sector by sector. The resulting map, using 64 discrete radial steps for the output coordinate, was subsequently stored in the onboard processor as a lookup table for automatic sorting of the detector's counts by ion species into various energy-angle data arrays. This sorting allows for four species at a time, and those four can be selected by command from the ground. In addition, some data arrays contain complete mass spectra at selected energies and angles. The time available for ground calibration only allowed for a relatively limited set of representative combinations of ion species and energies. Other combinations were inferred by interpolation in terms of rigidity.

A mass spectrometer like TIMAS, with magnetic mass dispersion, can be made very sensitive, but without a coincidence measurement of the individual ion, it also necessitates separate monitoring of counts from penetrating radiation (e.g. bremsstrahlung emitted by MeV electrons) to obtain a measure on the background count rate. This is accomplished in flight by setting the analyzer electrode voltages at frequent intervals to such values that no ions can reach the detector. In the TIMAS case the associated background counts are sorted into a separate data array that has position information but uses a coarser radial resolution than the regular mass spectra. The approximate background to be subtracted from each ion signal at given energy is determined during ground data processing from the known radial position and width of the corresponding mass peak, the width being defined by whatever number of radial mass steps is used by the instrument processor to represent the ion.

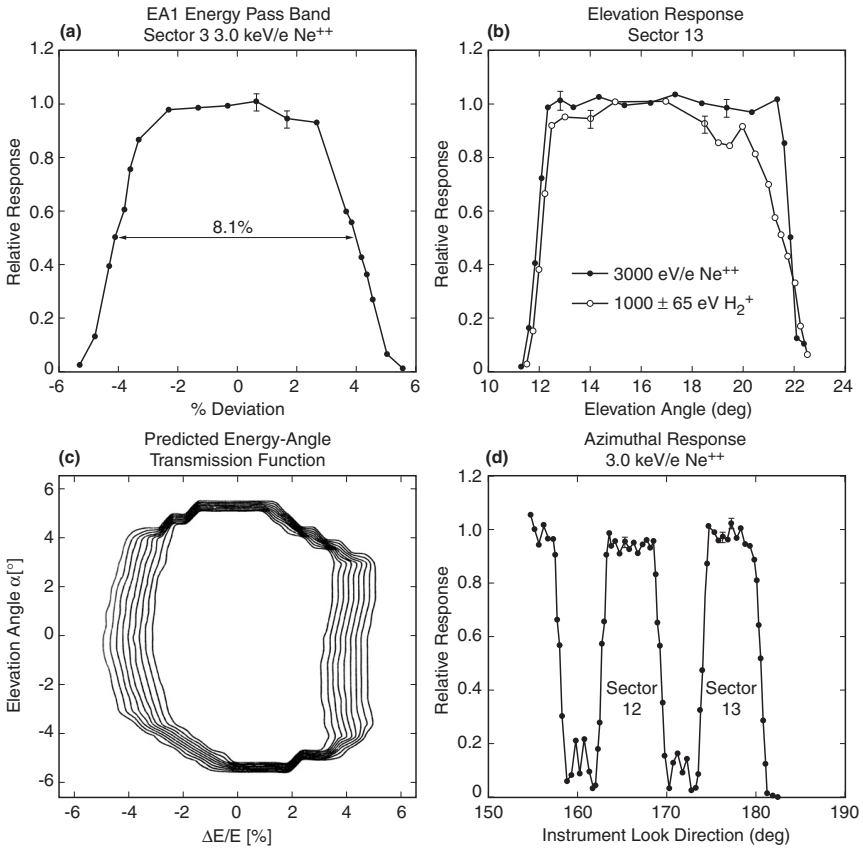

Figure 3.22: Sample results from calibration of an electrostatic ion energy analyzer with multi-sectored field-of-view (error bars indicate 1 σ counting statistics). (a) Energy passband inferred with a large-area monoenergetic ion beam by varying electrode voltages. (b) Elevation angle response (angle α) with ion energy centered in given passband (centered at 3000 eV/q; solid symbols) and with energy spread across given passband (about 1000 eV/q; open symbols). (c) Ray tracing prediction of the slightly different elevation response with and without energy spread in panel b. (d) Azimuthal response (angle β) to monoenergetic (3.0 keV/q) ion beam (gaps between sectors contain magnets for mass analysis). Adapted from *Shelley et al.* [1995].

3.4.1.2 From Count Rates to Physical Quantities

An essential first step in converting in-flight count rates to particle parameters in physical units is to translate the internal instrument angles α and β to external look angles, for example to elevation and azimuthal angles θ and φ, respectively, in a de-spun spacecraft-oriented coordinate system, one that has its z-axis along the spin axis. This is illustrated in Figure 3.23, which assumes that the field-of-view (FOV) has its symmetry axis perpendicular to the spin axis. This is the orientation of the TIMAS instrument on the Polar satellite and is the one that provides the maximum angular coverage by a single instrument over

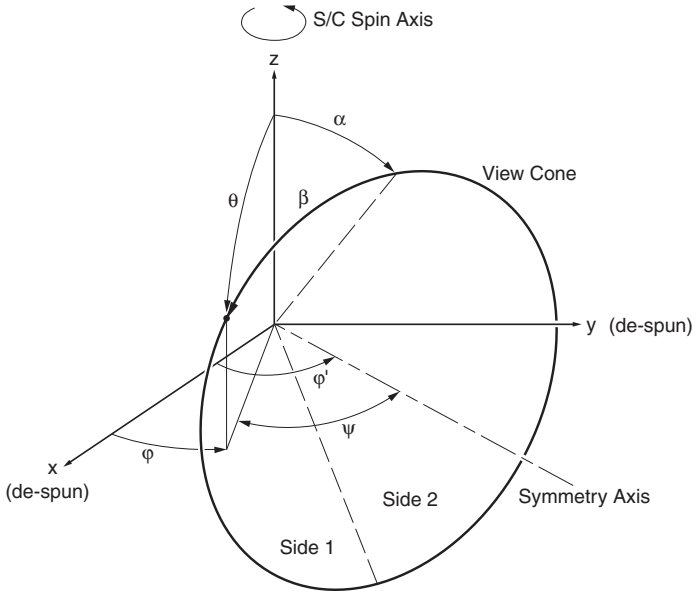

Figure 3.23: Relating internal instrument look angles α and β to external de-spun angles θ and φ. Elevation angle α is measured from a plane that contains the spin axis (see text for details).

the course of a spin cycle. A plane through both axes divides the FOV into leading and trailing halves, called Side 2 and Side 1, respectively, which are associated with separate azimuthal angles φ_2 and φ_1. The internal angle β is measured left or right from the upper boundary between the two halves. With α being the elevation, φ' the azimuth of the symmetry axis and ψ the angle between this axis and the projection in the x-y-plane of a line of sight, the relationships between internal and external angles are

$$\theta = \arccos(\cos\alpha \cos\beta) \tag{3.74}$$

$$\varphi_1 = \varphi' - \psi \qquad \text{and} \qquad \varphi_2 = \varphi' + \psi \tag{3.75}$$

$$\psi = \arccos\left(\sin\alpha \left(\sin^2\alpha + \cos^2\alpha \, \sin^2\beta\right)^{-1/2}\right) \tag{3.76}$$

For instruments with a true top-hat field of view [e.g. *Rème et al.*, 1997] the angle α is centered on 0°, and these formulas are strongly simplified with respect to the FOV center, but they are still needed for exact treatment of the FOV edges. With the TIMAS instrument it proved impractical to have zero elevation angle, because the ideal focusing properties require that ions enter the first analyzer with an angle α of about 17° at the center (Figure 3.22b). This offset could be compensated for by external electrostatic deflection, in principle, but having a deflector reducing the external elevation uniformly over the full energy range would have added significant complexity as well as weight. One beneficial aspect of the TIMAS FOV is that it made possible a very nearly flush mounting of the instrument aperture on the satellite surface. Another benefit is that it reduces possible perturbations from booms and antennas. With the actual α range being $17° \pm 5°$ the solid

angle swept by the FOV during a complete spin cycle is nevertheless very close to 4π (98 %, the FOV gaps in Figure 3.22d are offset from the 0°–180° symmetry line in order to provide complementary θ coverage by sides 1 and 2). The Equations 3.74–3.76 are applied during ground data processing.

The next step is to divide each accumulated count number $C(E, \theta, \varphi)$ by the associated $G(E, \theta)\Delta E$ and by the accumulation time t (presumed to be a fixed constant-voltage dwell time) to infer the differential number flux J and/or the phase space density f:

$$J(E, \theta, \varphi) = \frac{2}{m^2} f(E, \theta, \varphi)E = \frac{C(E, \theta, \varphi)}{G(E, \theta)\ \Delta E\ t} \tag{3.77}$$

Although C depends on physical processes that are not necessarily random in nature, it tends to display a random scatter of Poisson type. Therefore, it is customary to use its square root $\sigma = C^{1/2}$ as a measure of the uncertainty in each sampling interval, that is its "sigma", a measure that is to be propagated through all subsequent weighting and summing of multiple count numbers (via their variances σ^2), as will be outlined below.

Because count rates in space plasmas vary by several orders of magnitude, while available telemetry rates are strictly limited, it is necessary to bin large numbers onboard and only telemeter a fixed number of bits, representing for instance a mantissa and an exponent, or simply the position in a lookup table. This is further justified by the fact that the ground calibration can only be made with some modest precision, typically by a few percent at best. In the TIMAS case count rates are telemetered with 8 bits, using a lookup table with numbers in the range 0 through 255, where 0 through 41 are equal to the raw counts and higher numbers represent groups of raw counts to within better than 2 %. By comparison, the instrument counts with 16 bits, thus in principle allowing raw counts as high as 65535. As an aside, it is strongly recommended to let unexpectedly high counts saturate rather than roll over. To further reduce the telemetry load, the TIMAS onboard processor also employs a lossless compression scheme to suppress zeroes [*Rice and Lee*, 1983], which are restored during ground data processing.

For dead-time correction (see Section 3.1.3 above) the TIMAS processor monitors two reference counts, a "fast event count", FEC, and a "processed event count", PEC, both of which are sums of all counts of a certain kind during a single dwell time t. The FEC is recorded under virtually non-paralyzable conditions but without position information, while PEC is a sum of all counts by the position-sensitive and paralyzable counter. Assuming that the FEC dead time (160 ns) is negligible, which is usually a fair assumption with magnetospheric count rates, the PEC/FEC ratio is a measure of the dead-time induced degradation of the mass analyzer counts, and the inverse of this ratio is multiplied with each position labeled count before that number is telemetered. The FEC and the PEC are also telemetered, so the position labeled counts can be further corrected for FEC dead time during ground data processing, if deemed necessary, by applying Equation 3.56.

For plotting purposes, spectral information is usually conveyed by the differential number flux J, or by the differential energy flux $J \cdot E$, rather than by the phase space density f. The latter, however, is usually what one refers to when deriving macroscopic physical parameters, such as number density n, flow density $n\boldsymbol{v}$, etc. In practice f will not be measured in a uniform subset of velocity space, even if energy channels are contiguous or overlapping, since those channels cannot all be monitored simultaneously with existing instrument designs. It is thus (presently) necessary to treat the measurements as samplings within some suitable three-dimensional grid and ascribe each measurement to a finite box,

one of a set of boxes that together fill velocity space uniformly between minimum and maximum velocities.

Measurements from a spinning satellite lend themselves naturally to a spherical coordinate system, where the radius is a measure of speed v, derived from the external center energy E of a given energy channel, and the polar and azimuthal angles are the θ and φ used in Figure 3.23. Assuming that the energy sweeps are synchronized with the satellite spin cycle, that is assuming there are an integer number of complete sweeps per spin (or an integer number of spins per sweep), and assuming also that spacecraft charging effects are negligible (see below), the various integer orders η of velocity moments may thus be approximated by the following triple sums:

$$\iiint f(\boldsymbol{v})\boldsymbol{v}^{\eta}\mathrm{d}^3v \approx \frac{2^{(\eta+1)/2}}{m^{(\eta+3)/2}}\left(\sum_E\sum_\theta\sum_\varphi f(E,\theta,\varphi)\boldsymbol{u}^{\eta}E^{(\eta+1)/2}\Delta\Omega\,\Delta E\right) \quad (3.78)$$

where the unit vector $\boldsymbol{u} = (\sin\theta\cos\varphi, \sin\theta\sin\varphi, \cos\theta)$, the η-fold multiplication of $\boldsymbol{u}$ (and $\boldsymbol{v}$) is carried out in such a manner as to produce a 3^{η}-dimensional array (with numerous identical elements), and the factors $\Delta\Omega$ and ΔE refer to the spherical grid steps, independently of the instrumental $\Delta\Omega$ and ΔE. The mass m is assumed measured in kg here and the energy E in eV, that is in units of 1.602×10^{-19} J, taking into account multiple charge states of ions. For maximum accuracy it may be worth choosing the E, θ and φ coordinates of each box to be at the center of gravity of the box, since its shape varies with E and θ. The order η is generally limited to ≤ 3, and only part of the $3 \times 3 \times 3$ array is widely used (the part corresponding to energy flux). For a more detailed discussion of velocity moments and their physical meaning, see for instance *Paschmann et al.* [1998]. See also Section 1.3 or Appendix A.7.2.

By combining Equations 3.70, 3.77 and 3.78 it follows that any arbitrary component v_{mom} of the various velocity moments has the general structure of

$$v_{\mathrm{mom}} \approx \sum_E\sum_\theta\sum_\varphi K(E,\theta,\varphi)\,C(E,\theta,\varphi) \quad (3.79)$$

where each $C(E,\theta,\varphi)$ is the measured particle counts and each $K(E,\theta,\varphi)$ a combination of pre-determined multipliers, including physical constants and instrumental parameters, which may be either positive or negative. The same multipliers are to be used for the propagated statistical uncertainty of the moment as well, but only positive values come into play with the linear kind of summation in Equation 3.79. Specifically, if each $C(E,\theta,\varphi)$ is a single sample (from single accumulation time t), its Poisson variance $[\sigma(E,\theta,\varphi)]^2 = C(E,\theta,\varphi)$, and the standard deviation of the moment, σ_{mom}, becomes

$$\sigma_{\mathrm{mom}} \approx \left(\sum_E\sum_\theta\sum_\varphi (K(E,\theta,\varphi))^2\,C(E,\theta,\varphi)\right)^{1/2} \quad (3.80)$$

The reasons for the squared multipliers in Equation 3.80 are that (1) the terms in Equation 3.79 are statistically independent, (2) the statistical uncertainty in each term is proportional to the standard deviation of the count number, rather than its variance, that is equal to $K(E,\theta,\varphi)\,(C(E,\theta,\varphi))^{1/2}$, and (3) independent (orthogonal) statistical uncertainties add in quadratic fashion. If each count number is itself an average $\langle C\rangle$ of N samplings

within the same $E-\theta-\varphi$ box, then C in Equation 3.80 is to be replaced by $N^{-1}\langle C\rangle$ (one N^{-1} is already part of the averaged counts).

With moments normalized by number density n, such as mean velocity, mean energy and "temperature", deriving the statistical uncertainty is more cumbersome, because both numerator and denominator contain the same set of samples (counts). In this case multipliers will appear with both positive and negative values. For a rigorous discussion of this subject the reader is referred to textbooks on statistical error analysis, for example *Taylor* [1997] or *Bevington and Robinson* [2003]. However, it may be mentioned that the basic approach is to take the partial derivative with respect to each $C(E,\theta,\varphi)$, square the derivative, multiply it with $C(E,\theta,\varphi)$, sum all such terms to obtain a total variance and take its square root for the final sigma.

The moment calculations are less straightforward if the energy sweeps are not synchronized with the spin (e.g. by accident), but if they are being performed during ground data processing it is possible to make corrections, provided the rate of drift of the sweeps with respect to the spacecraft spin period is known. In particular, if the drift is slow, it is mainly a matter of recalculating the sines and cosines of the drifting φ angle once per spin cycle. Another complication arises from spacecraft charging, especially at energies below 100 eV/q, and the effects depend on the sign of the charging and are different for electrons and positive ions.

As a complement to Equation 3.70, it is often helpful to have an approximate conversion formula between differential number flux J and the more tangible quantity of partial number density Δn, measured in cm^{-3}, for instance. Thus, if m_p is the proton mass, $m = M\,m_p$ (i.e., $M \approx 1/1836$ for electrons[7]), Q is the particle charge state (set to +1 for electrons), E is the average energy within the interval ΔE, both measured in keV/Q, J is the average flux within ΔE, measured in the standard units of $(\mathrm{cm}^2\ \mathrm{s\ sr\ keV/q})^{-1}$, then

$$\Delta n \approx 2.3\times 10^{-8}(M\,Q)^{1/2}E^{-1/2}\Delta E\ \Delta\Omega\ J \qquad (\mathrm{cm}^{-3}) \tag{3.81}$$

where $\Delta\Omega$ is any solid angle ($\leq 4\pi$) within which J may be considered isotropic. The equivalent formula with differential energy flux has the factor $E^{-1/2}$ replaced by $E^{-3/2}$.

3.4.2 The Plasma and SupraThermal Ion Composition Instrument

The PLasma And SupraThermal Ion Composition (PLASTIC) instrument is a state-of-the-art carbon-foil TOF instrument for the angle-, energy-, and mass-resolved measurement of solar wind plasma and suprathermal ions [*Galvin et al.*, 2006]. PLASTIC is flown on the STEREO mission, launched in October 2006. An engineering drawing of PLASTIC is given in Figure 3.24. PLASTIC simultaneously measures mass from 1 u to greater than 56 u, charges up to 20 (depending on element), and arrival angle within the full ecliptic plane (azimuth angle from 0 to 360°). The azimuth angle information is derived from the particle's position on the start detector of the TOF sensor, which is of annular shape. The energy-per-charge is measured with an electrostatic analyzer covering a range from 0.2 to 100 keV/e in 128 contiguous steps spaced logarithmically with a constant step size of 5 %. The resolution of the energy analyzer is $\Delta E/E = 6\,\%$. Since STEREO is a three-axis stabilized spacecraft always pointing at the Sun additional electrodes for ion deflection at the instrument entrance were necessary, the so-called duck bills, to access ion arrival angles

[7] $m_e = 5.4857990945(24)\times 10^{-4}$ u

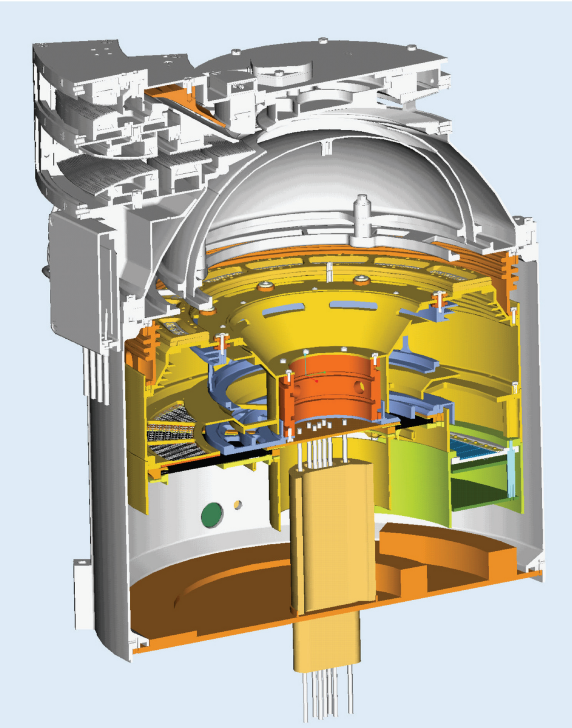

Figure 3.24: Cross sectional diagram of the PLASTIC instrument for the STEREO mission [*Galvin et al.*, 2006]. From top to bottom: Entrance system, toroidal electrostatic analyzer, carbon-foil time-of-flight mass spectrometer, MCP and SSD detectors. The electrostatic entrance system, the energy analyzer, and the TOF MS are rotationally symmetric about the vertical center axis (aside from the different geometric factor in solar wind direction pointing to the left).

out of the ecliptic plane (elevation angle), which sweep from +20° to −20° during each energy-per-charge step.

Because the PLASTIC instrument orientation is always fixed with respect to the Sun direction the sector pointing toward the Sun has been optimized for detailed distribution function measurements of solar wind ions, with a field-of-view of $\pm 22.5° \times \pm 20°$, in azimuth and elevation angle, with the elevation angle being scanned, with respect to the spacecraft-Sun line. The remaining sector of the 360° ecliptic plane is the Wide-Angle-Partition, which has an instantaneous field-of-view of $315° \times \pm 7°$ without the possibility for a scan in elevation angle.

The high dynamic range of the solar wind necessitates a variable geometric factor to cover all species ranging from protons to iron ions. In the PLASTIC instrument this is accomplished by switching between two separate entrance channels, the main-channel and the so-called S-channel, with the latter having a geometric factor that is about a factor of 1000 smaller than in the main-channel [*Blush et al.*, 2005]. The concept of alternative geometric factors has been used already earlier, e.g. in the CIS experiment on Cluster

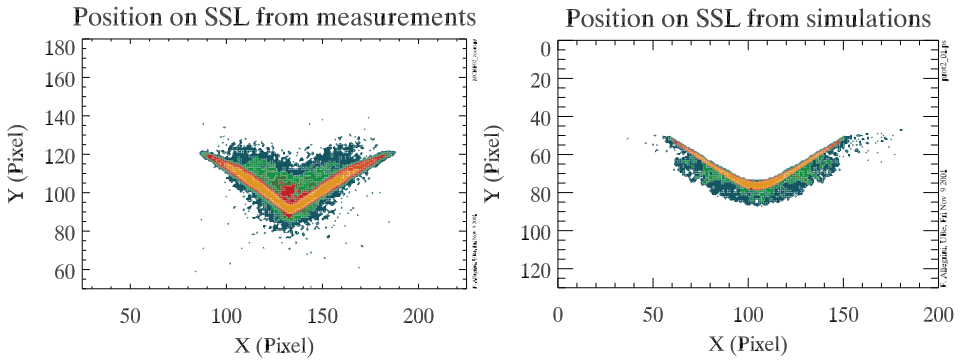

Figure 3.25: Comparison of the measured (left) and calculated (right) ion-optical image (using an imaging particle detector, SSL) at the exit of the toroidal energy analyzer. X and Y give the Cartesian coordinates at the analyzer exit, where a pixel corresponds to 0.16 mm. From *Allegrini* [2002].

[*Rème et al.*, 1997; *McCarthy and McFadden*, 1998] where a factor of about 100 was realized.

The PLASTIC instrument consists of several subsystems, similar to many instruments for medium energy plasma measurements, namely the entrance system (comprising the duck bills and the toroidal electrostatic analyzer), the carbon-foil time-of-flight mass spectrometer, the MCP and SSD detectors, the sensor electronics (analog and digital), and the digital processing unit (see Figure 3.24). All these subsystems contribute to the over-all performance of the instrument. It is helpful to test and calibrate the individual subsystems before the fully integrated instrument is being calibrated. This substantially increases the understanding and knowledge of the instrument, which helps for resolving instrument problems but also to establish a good theoretical instrument description necessary for data analysis. In the following we will take STEREO/PLASTIC as an example.

Before such an instrument is being built extensive ion-optical calculations are performed to optimize the performance of the instrument with respect to the scientific scope of the foreseen measurements. Moreover, issues of technical realization often modify the design, and their effect on the performance is assessed with the help of the ion-optical simulations as well. Finally, these simulations are very helpful in the testing and calibration at the subsystem level because they show the signal to be expected. An example is the toroidal energy analyzer of the PLASTIC instrument of STEREO, where the actual V-shape of the ion-optical image at the analyzer exit of a parallel ion beam entering the analyzer is at first glance counter-intuitive, but correct. Figure 3.25 shows a comparison of an ion-optical calculation and the actual measurement performed on the prototype instrument [*Allegrini*, 2002]. Although the agreement is good there are differences that are attributed to the non-ideally parallel ion beam, the imperfect mechanical build of the analyzer, and limitations in the resolution of the ion-optical simulations.

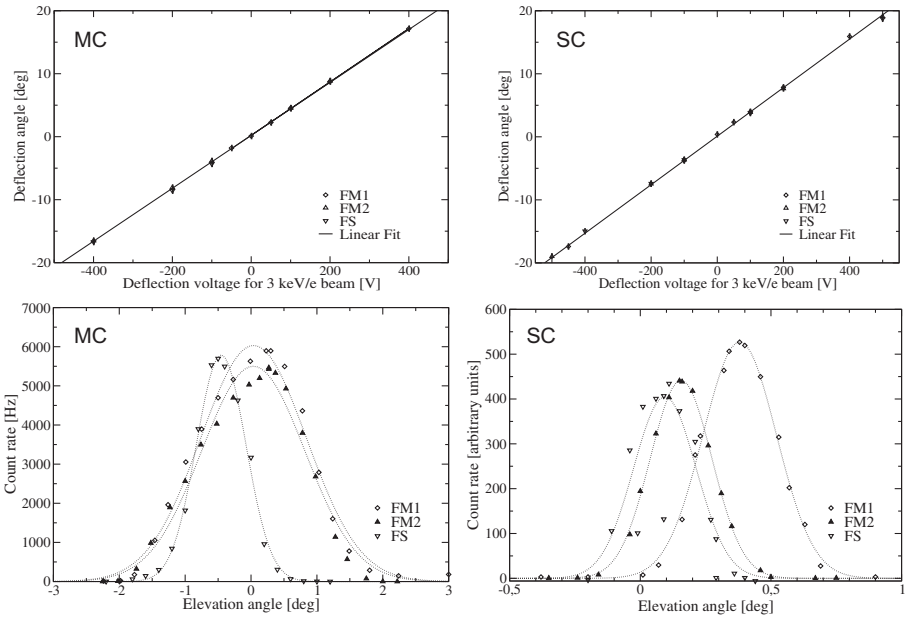

Figure 3.26: Calibration data for the duck bills of the main-channel (MC) and the S-channel (SC) of the STEREO/PLASTIC instrument. Data from the two flight models (FM1 and FM2) and from the flight spare model (FS) are shown. Error bars are smaller than the symbol size. The solid lines are fits through the data. From *Karrer* [2006].

3.4.2.1 Calibration of the Entrance System

The entrance system of the PLASTIC instrument serves several purposes: i) defines the geometrical factor, ii) selects elevation angle, iii) selects E/Q, iv) suppresses UV radiation to better than 10^8, v) suppresses scattered ions (e.g. ions outside the E/Q pass band), and vi) eliminates solar wind electrons. All these functions have to be verified and calibrated during the calibration of the instrument.

Following a plasma ion on its way through the instrument, we start at the duck bills, which select the elevation angle. Their calibration data are shown in Figure 3.26, where the relationship between the applied voltages and the selected elevation angle, and the angular response in elevation angle are shown for the main- and the S-channel. The former data are needed to understand from which direction the recorded ions are arriving, the latter information is needed for the geometric factor determination. The data in Figure 3.26 are shown for the two flight models (FM1 and FM2) and the flight spare model (FS).

After passing the duck bills, the plasma ions have to pass through the S-channel electrodes and the toroidal energy analyzer (S-channel) or they enter directly in the toroidal energy analyzer (main-channel). Calibration data for these sections are shown in Figure 3.27, again for the FM1, FM2, and FS units, which agree well with the theoretical calculation for these parameters. The two panels in Figure 3.27 show the relationship between applied ESA voltage and the E/Q of the ions passing through (i.e., the analyzer constant of the energy analyzer, which is the slope of the linear fit in Figure 3.27) for the main- and the

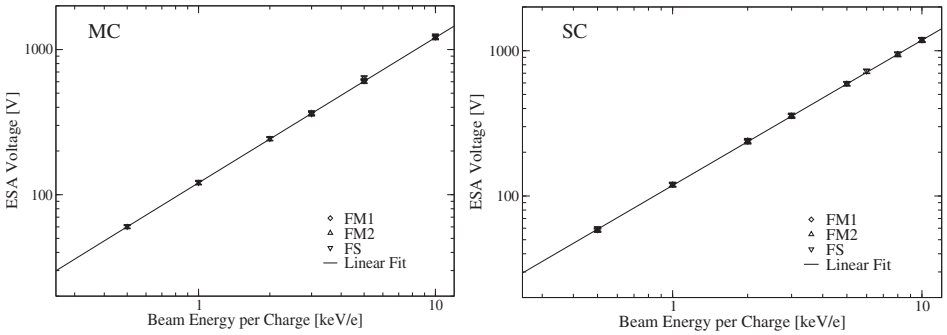

Figure 3.27: Measurement of the analyzer constant for the main-channel (MC) and the S-channel (SC) of the STEREO/PLASTIC instrument. Data from the two flight models (FM1 and FM2) and from the flight spare model (FS) are shown. Error bars are smaller than the symbol size. From *Karrer* [2006].

S-channel. The data points for the individual units fall on top of each other indicating a reliable and reproducible mechanical design and construction. The analyzer constant is needed to infer the ion's E/Q from the applied analyzer voltage.

The four panels in Figure 3.28 show the ion optical transmission of the main-channel as a function of the elevation angle and the E/Q. The data for the engineering qualification model (EQM), the FM1, FM2, and FS units agree well, as expected, with the small differences being attributed to the limitations of what can be built. Note the correlation of the E/Q center with the elevation angle, which is typical for electrostatic analyzers of this kind, and has to be considered in the data analysis. The data of Figure 3.28 are needed to calculate the geometric factor of the main-channel.

The three panels in Figure 3.29 show the ion optical transmission of the S-channel as a function of the elevation angle and the E/Q. Note the correlation of the E/Q center with the elevation angle, which was seen for the main-channel, is not observed here because there is a collimator in elevation angle between the duck bills and the S-channel electrodes geometrically defining an elevation angle acceptance in the S-channel much smaller than the angular acceptance of the S-channel ion optics, which is very narrow as can be seen also in Figure 3.26. In this respect, the analysis of data recorded with the S-channel is easier than for the main-channel, since the correlation between elevation angle and E/Q is absent. The data shown in Figure 3.29 are needed to calculate the geometric factor of the S-channel.

The angular acceptance in azimuth-elevation coordinates of the S-channel is shown in Figure 3.30. Similar data have been recorded for the main-channel but are not shown here. In azimuth direction the 45° field-of-view in the solar wind direction can be seen, and in elevation direction the S-channel has a very narrow field-of-view of only 0.5°. As mentioned above, in elevation direction the field-of-view can be shifted up or down using the duck bills. In flight the azimuth angle of the incoming plasma ion will be measured by the position resolving MCP detectors but in the calibration this angle is set externally, and thus known more precisely, by the orientation of the instrument with respect to the ion beam. Since the field-of-view is very narrow in the elevation direction small mechanical imperfections show up readily. For example the center of the field-of-view in elevation

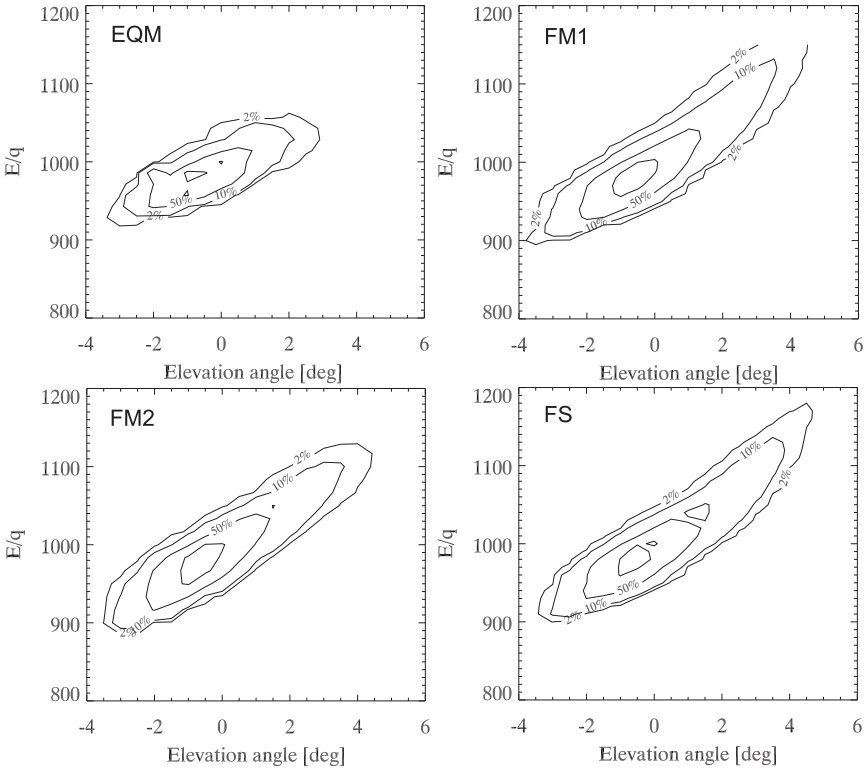

Figure 3.28: Ion optical transmission of the main-channel as a function of the elevation angle and the E/Q of the STEREO/PLASTIC instrument, for the engineering qualification model (EQM), the flight models (FM1 and FM2) and the flight spare model (FS). From *Karrer* [2006].

direction is not exactly centered at 0° elevation, or the collimating slit is not perfectly aligned with the S-channel toroidal electrodes in the FM1 unit (see also Figure 3.26). Such imperfections are not a problem for the analysis of data recorded with this instrument if their effects on the instrument performance have been established in the calibration in sufficient detail.

3.4.2.2 Calibration of the Solid-State Detectors

The kinetic energy of the plasma ion is measured with a solid-state detector, SSD [see e.g. *Knoll*, 2000]. Since for the given energy range of the PLASTIC instrument of 0.2 to 100 keV/e many ions would fall below the energy threshold of a SSD (about a few 10 keV for ions), ions leaving the entrance system are post-accelerated by a potential of up to 26 kV before entering the TOF section. Post-acceleration of ions after energy selection is a common technique in instruments in this energy range. Despite the considerable energy gain in the post-acceleration section, the ion energies for many species will be on the lower end of the detection range of a SSD and a detailed calibration of the SSD energy response

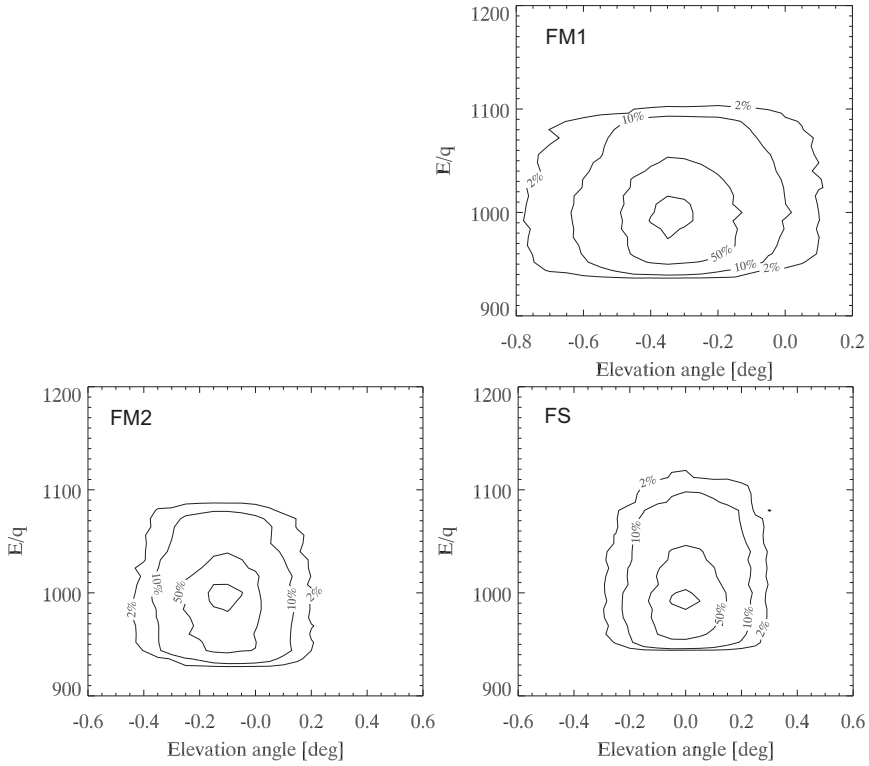

Figure 3.29: Ion optical transmission of the S-channel as a function of the elevation angle and the E/Q of the STEREO/PLASTIC instrument, for the flight models (FM1 and FM2) and the flight spare model (FS). From *Karrer* [2006].

is necessary for interpreting the energy measurements. The main problems of SSDs for the energy measurement in medium energy ion instruments are the energy loss in the dead layer of the SSD and the fraction of the ion energy that goes into nuclear stopping, since only the particle energy that goes into electronic stopping gives the energy signal.

Calibration data for one of the SSDs of the PLASTIC instrument are shown in Figure 3.31. Gamma-ray sources of suitable energy are used to establish the conversion from energy deposited in the SSD, the incident energy, and the channel number of the measured energy provided by the read-out electronics (see also the discussion in Section 3.5.2.3). A ^{133}Ba source has been used for the measurements presented in Figure 3.31, an ^{155}Eu source was used for the RAPID instrument on Cluster [*Wilken et al.*, 1997]. The relationship between these two quantities should be a straight line, the calibration of the energy conversion, which can be seen in Figure 3.31. Even though this is only a subsystem calibration, it is important to use the flight version of the SSD read-out electronics for these measurements. Since the capacitance of the SSD and the input capacitance of the first amplifier stage affect the overall signal gain of the system it is necessary not to interchange amplifiers or SSD units. Energy calibration of SSDs is discussed in more detail in Section 3.5.1.2).

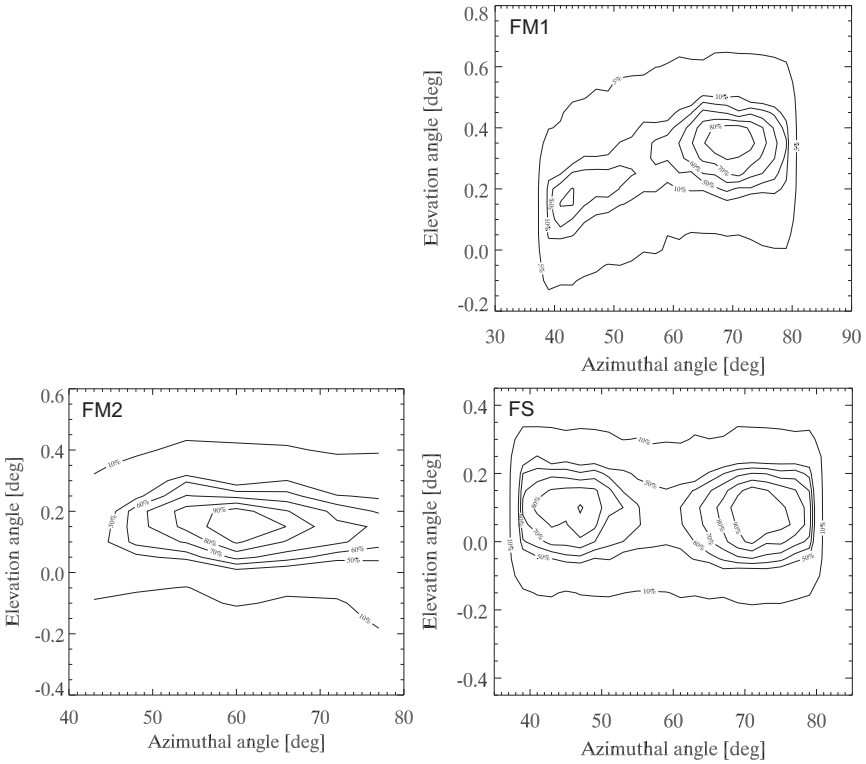

Figure 3.30: Angular acceptance of the S-channel as a function of the azimuth and elevation angle of the STEREO/PLASTIC instrument, for the flight models (FM1 and FM2) and the flight spare model (FS). Data for the FM2 model have been taken with lower resolution. From *Karrer* [2006].

Once the energy conversion of the SSD is established, one can proceed with the ion measurements. The energy losses, e.g. the fraction of the ion energy that does not contribute to the measured signal provided by the SSD, are species dependent. Therefore, all species of interest have to be measured over the respective energy range, e.g. the energies after post-acceleration. Since solar wind ions can have charge states of about +10 e and more, quite high ion energies inside the instrument will be attained and the SSDs have to be calibrated at these energies. Data from ion measurements at the MEFISTO calibration facility are shown in Figure 3.31 as well. One can clearly see that the measured energy for the different ions falls short of the incident energy (measurements are below the straight line of the energy calibration) because of the various energy losses. For the same ion energy, these losses increase with increasing mass of the ion. The relationship between measured energy and incident energy is clearly non-linear for ions in this energy range. Once the detailed relationship between measured energy and incident energy is established, by fitting a suitable mathematical function to the data and inverting the function, one can deduce the incident energy of an ion from its measured energy (the measured channel number). Knowing the energy of the measured plasma ion from the SSD detector and its E/Q value

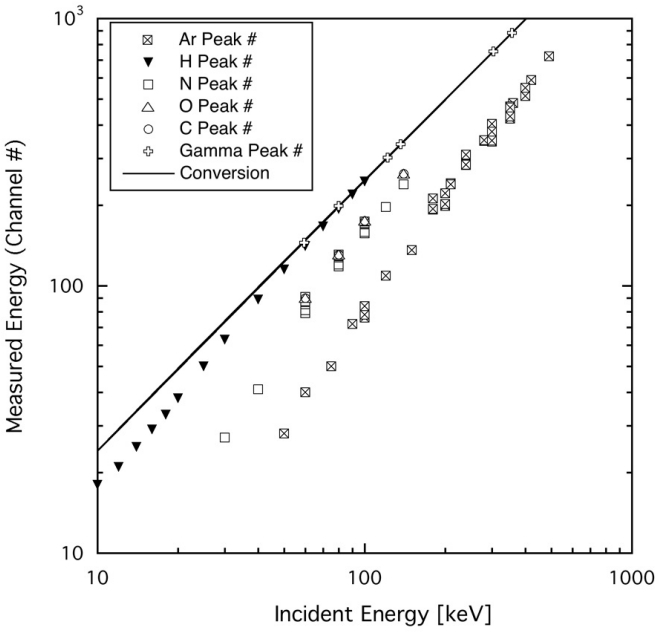

Figure 3.31: Energy calibration of a SSD of the STEREO/ PLASTIC instrument, using γ-rays and energetic ions. Data from *Daoudi* [2005].

from the electrostatic analyzer one can deduce the charge of the recorded ion, which will be discussed below.

3.4.2.3 Calibration of the Microchannel Plate Detectors

In the PLASTIC instrument, MCPs are mounted in a circular configuration with chevron-paired MCPs in each quadrant (see Figure 3.24). Since two of the four quadrants accommodate two SSD detectors, mounted concentrically with the MCPs, two sizes of MCPs are required. The geometry of each MCP is a 90° circular arc. Each PLASTIC flight model utilizes two pairs of small MCPs and two pairs of large MCPs. The main aim of the MCP calibrations was to grade the MCPs for flight selection as well as to understand the response of these particular MCPs. Tests were carried out on individual MCP pairs, previously matched to same resistance by the manufacturer. The characterizations focused on the MCP modal gain and background noise level response for various MCP bias voltages. MCPs chosen for flight should exhibit high gain at moderate bias voltages. This allows for a low initial bias voltage while attaining maximum detection efficiency of single charge pulses. Additionally, the background signal level of the MCP in the absence of a direct particle source should be at a minimum.

To characterize the detectors, an MCP pair and an anode assembly were mounted in the MCP test facility of the University of Bern facing a ^{63}Ni beta decay source (see page 141) [*Blush et al.*, 2005]. Under vacuum the electron source could be shielded to allow for background measurements to compare with electron irradiation measurements. The MCP

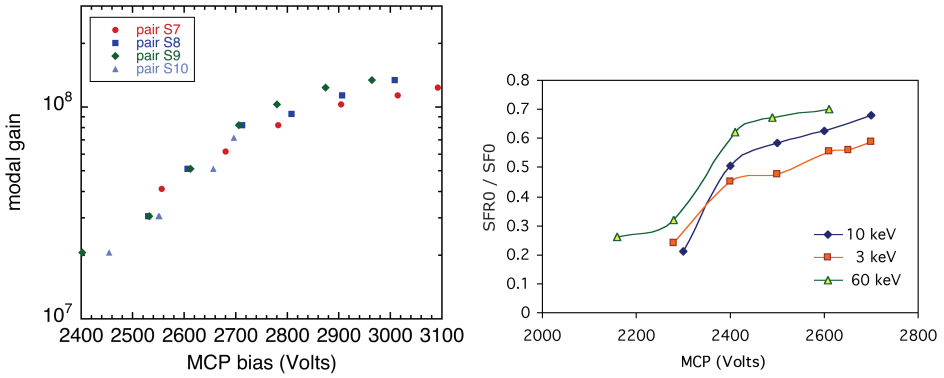

Figure 3.32: Left: Modal gains for the small MCP pairs number S7 – S10 using a ^{63}Ni electron source. *Right:* Stop efficiency (MCP efficiency) for 3, 10, and 60 keV protons. All data are from the STEREO/PLASTIC instrument. From *Blush et al.* [2005].

bias voltage was varied and for each voltage step a pulse height distribution (PHD) was measured yielding the gain response, where the peak of the signal distribution gives the modal gain. From the comparison of signal to background a measure of noisiness of the MCP pairs is derived. These tests were repeated for all MCP detectors of PLASTIC. All MCPs have been graded and selected MCP pairs have been integrated in the TOF section of the PLASTIC flight instruments.

Figure 3.32, left, shows a plot of the modal gain (in number of electrons per incident particle) versus MCP bias voltage for various pairs of the small MCPs. Small MCP gains are typically in the range of 2×10^7–1×10^8 for measurements with bias voltages of 2400–3000 V (about 1200–1500 V per MCP). The plots indicate high gain for moderate bias voltages. Similar results were attained for the large MCP, although they exhibited slightly lower gains of 6×10^6–5×10^7 in the test range of 2500–3100 V (about 1250–1550 V per MCP). Figure 3.32, right, shows MCP detection efficiency for protons at energies of 3, 10, and 60 keV, the "stop efficiency", measured in the PLASTIC EQM unit. Note that in the investigated sector, the solar wind sector of the PLASTIC instrument, the incident ions do not hit the MCP stop detector but the SSD detector, where the impinging ion releases secondary electrons that are registered on the stop detector. Therefore, the initial MCP tests with the ^{63}Ni electron source were performed.

3.4.2.4 TOF Section Calibration

Mass spectrometric analysis is done with a TOF measurement, where the flight time, t, of an ion along a known path of given length, L, is measured. The ion starts the time measurement by passing through a thin carbon foil where it releases electrons, which are registered on a start detector that triggers the time measurement. The time measurement is stopped when the ion hits a stop detector. The stop detector can either be an MCP detector or a SSD, where with the latter the secondary electrons released at ion impact are recorded with an MCP detector. From the TOF the ion velocity, $v = L/t$, is derived. With the

additional measurement of the kinetic energy of the ion by the SSD, E_{SSD}, the ion mass can be calculated

$$m = \frac{2E_{SSD}}{v^2} = 2E_{SSD}\frac{t^2}{L^2} \tag{3.82}$$

where E_{SSD} is the ion energy considering the correction for energy defect in the SSD. E_{SSD} is given by

$$E_{SSD} = \widetilde{E}_{SSD}/\varepsilon_{SSD} \tag{3.83}$$

where $\widetilde{E}_{SSD}$ is the actual energy measured by the SSD and ε_{SSD} is the factor accounting for the fraction of deposited energy in the SSD that does not contribute to the energy signal (see page 194 and Figure 3.31). The ion energy at the entrance of the carbon foil is

$$E_{SSD} + E_{foil} = \left(\frac{E}{Q}\right) Q + U_{acc}\, Q \tag{3.84}$$

where (E/Q) is set by the energy analyzer, Q is the charge of the ion (in units of e), U_{acc} is the post-acceleration potential, and E_{foil} is the energy loss in the carbon foil. E_{foil} depends on species and energy and can be measured in calibration because it is the only unknown in Equation 3.84 after the SSD has been calibrated. There are also formulas to calculate E_{foil} [*Betz and Wien*, 1994].

In flight, the charge of the registered ion can then be calculated from

$$Q = \frac{E_{SSD} + E_{foil}}{(E/Q) + U_{acc}} \tag{3.85}$$

using the calibration data from E_{foil}. Finally, the energy of the incoming ion, E, is derived from

$$E = \left(\frac{E}{Q}\right) Q \tag{3.86}$$

In the instrument calibration the variables E_{SSD}, t, and E_{foil} have to be calibrated for all species and for the energy range of ions after post-acceleration to fully characterize the TOF-E mass spectrometer. The calibration of the (E/Q) measurement is part of the entrance system calibration, and U_{acc} is part of the high voltage power supply calibration.

For the full characterization of an ion in a TOF-E mass spectrometer it has to trigger three signals, a start signal, a stop signal, and a SSD signal (the energy measurement). These are described by the single efficiencies η_{Start}, η_{Stop}, and η_{SSD}. The start-efficiency combines the probability of secondary electron emission when the ion passes through the carbon foil and the electron detection efficiency of the start detector. The stop-efficiency combines the probability of secondary electron emission when the ion hits the SSD detector and the electron detection efficiency of the stop detector. In addition, there are efficiencies associated with the coincident (within a short time interval) triggering of two signals (often referred to as double-coincidence), and efficiencies associated with the coincident (within a short time interval) triggering of all three signals (often referred to as triple-coincidence). For the double-coincidence there are the efficiency η_{TOF} for a successful TOF measurement, and the efficiency η_{Energy} if an energy measurement was made

for an incoming ion triggering the start detector. For the triple-coincidence, there is the efficiency η_{TC} when all three signals are triggered. Typically, count rates corresponding to these efficiencies are recorded in a TOF-E instrument, which are

$$R_{Start} = \widetilde{R}_{Start} - B_{Start} = I_0 \eta_{Start} \tag{3.87}$$

$$R_{Stop} = \widetilde{R}_{Stop} - B_{Stop} = I_0 \eta_{Stop} \tag{3.88}$$

$$R_{SSD} = \widetilde{R}_{SSD} - B_{SSD} = I_0 \eta_{SSD} \tag{3.89}$$

$$R_{TOF} = \widetilde{R}_{TOF} - B_{TOF} = I_0 \eta_{TOF} = I_0 \eta_{Start} \eta_{Stop} \tag{3.90}$$

$$R_{Energy} = \widetilde{R}_{Energy} - B_{Energy} = I_0 \eta_{Energy} = I_0 \eta_{Start} \eta_{SSD} \tag{3.91}$$

$$R_{TC} = \widetilde{R}_{TC} - B_{TC} = I_0 \eta_{TC} = I_0 \eta_{Start} \eta_{Stop} \eta_{SSD} \tag{3.92}$$

where I_0 is the flux of ions entering the TOF-E mass spectrometer. For each rate R_{xxx} in Equations 3.87–3.92 the corresponding background rate (B_{xxx}) has to be measured without the ion beam entering the instrument and subtracted from the rates $\widetilde{R}_{xxx}$ measured with ion beam. Note that the background rates may vary with instrument settings and also with time, and should be measured shortly before or shortly after the actual rate measurement. Suitable dead time corrections, as explained in Section 3.1.3, may have to be applied to the measured rates. From the rates R_{xxx} one can easily calculate all the single efficiencies and one double efficiency, even in the absence of the knowledge of I_0, by

$$\eta_{Start} = \frac{R_{TOF}}{R_{Stop}} \tag{3.93}$$

$$\eta_{Stop} = \frac{R_{TOF}}{R_{Start}} \tag{3.94}$$

$$\eta_{SSD} = \frac{R_{Energy}}{R_{Start}} \tag{3.95}$$

$$\eta_{Mass} = \frac{R_{TC}}{R_{Start}} \tag{3.96}$$

Any losses of particles between the start and stop detectors are absorbed in η_{Stop} or η_{SSD}. In principle the start efficiency could be calculated also from the ratio R_{Energy}/R_{SSD}, but because R_{SSD} goes to very low values at smaller ion energies this is not very practical.

From the singles efficiencies one can calculate the efficiencies for double- and triple-coincidence using Equations 3.87–3.92. If these rates are also transmitted to ground during flight, these TOF efficiencies can be established during data acquisition in space and time varying MCP efficiencies, for example, will not be a problem. Figure 3.33 from *von Steiger* [1994] shows an example of the various efficiencies of the TOF-E unit from the SWICS instrument on the Ulysses spacecraft [*Gloeckler et al.*, 1992], where DCR/FSR is η_{Stop}, MSS/FSR is η_{SSD}, and TCR/FSR is η_{Mass}.

Often the amount of data to downlink from an instrument in space is limited and the resolution with which E_{SSD} and t are transmitted is less than is actually available inside the instrument. Moreover, binning of data is often used onboard, or even processing of data using Equations 3.82, 3.85, and 3.86 to obtain m, Q, and E. All the on-board data processing and data reduction steps have to be verified during calibration.

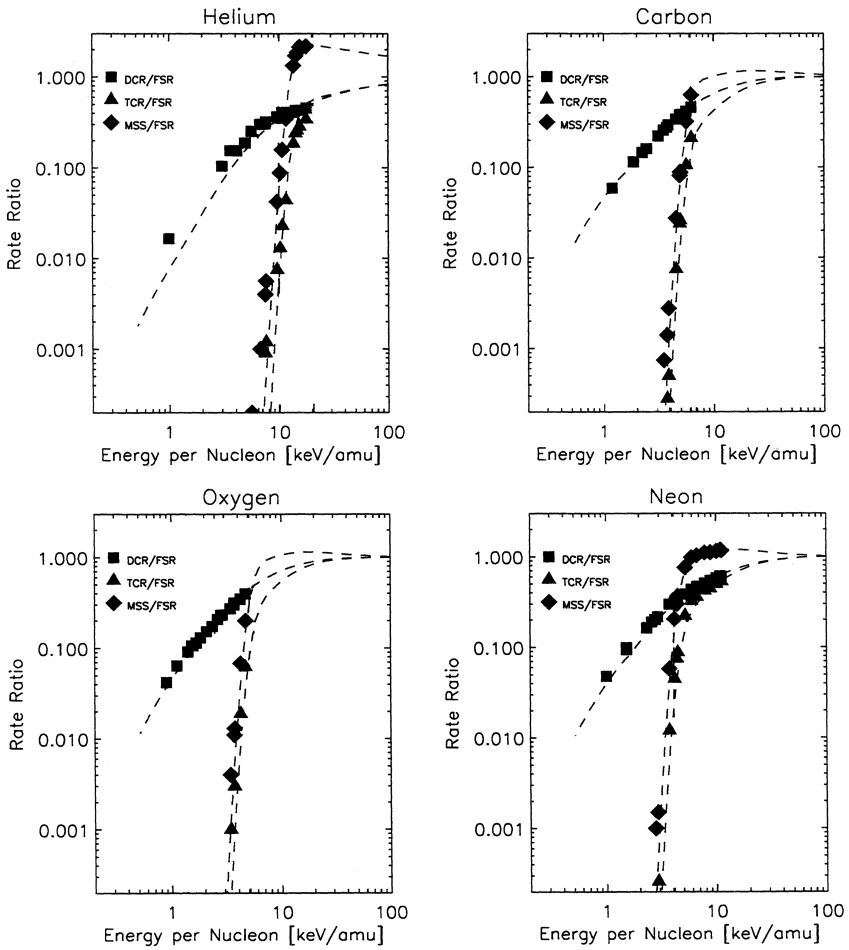

Figure 3.33: TOF-E mass spectrometer detection efficiencies depending on the energy of the ion entering the TOF mass spectrometer for the Ulysses/SWICS instrument. FSR is the start rate, DCR is the TOF rate, MSS is the energy rate, and TCR is the triple-coincidence rate. Adapted from *von Steiger* [1994].

3.5 High Energy Particle Calibration

In addition to thermal and suprathermal plasma, the Earth's magnetosphere, planetary magnetospheres, and the heliosphere include a range of high energy particles of interest to space science. The interest is both scientific, because of the role these particles play in the flow of energy throughout the magnetosphere, and engineering, because of the damage these particles can inflict on instruments and spacecraft systems. High energy particles pose very challenging problems to instrument designers and calibrators. For example, due to the great penetrating power of high energy particles, it is usually impossible to shield the sensor from rear entry and side entry particles, thus complicating the usual meaning of apertures, collimators and shielding.

High energy particle populations near Earth can be divided into trapped and un-trapped. The trapped particles include the Inner Belt protons with energies up a few hundred MeV and electrons mostly in the Outer Belt, with energies of up to several MeV [*Spjeldvik and Rothwell*, 1985]. The untrapped particles from the Sun reach the Earth as a result of Solar proton and electron events and can be detected in the Polar regions and at geosynchronous altitude. Their energies are similar in their range to the trapped particles but their intensity, during solar events can be orders of magnitude greater [*Reames*, 1999]. Finally, the last population is galactic cosmic rays, ultra relativistic protons and other atomic nuclei that can penetrate to geosynchronous altitudes [see recent review by *McDonald and Ptuskin*, 2001].

Although a great variety of high energy particle instruments have been built, most of them are composed of a small number of basic component sensor types: silicon solid-state sensors, scintillators and Cherenkov radiators [*Knoll*, 2000].

- A solid-state detector (SSD) is a disk of high purity silicon with electrodes coated on both sides and configured to be reverse biased so that no current flows between the electrodes. When a particle impacts the disk, electron-hole pairs are generated and a charge proportional to the deposited energy flows between the electrodes. An electronic circuit can then read out the charge pulse to determine the deposited energy.

- A scintillator is a transparent material that emits light when a particle traverses it. Since the conversion efficiency between deposited energy and the light output is very low, a light amplification device such as a photomultiplier tube (PMT) must be used.

- A Cherenkov detector makes use of the fact that if a particle travels through a medium at a velocity greater than the velocity of light in that medium, it will emit a small amount of light. That light can be collected, amplified and measured by one or more PMT's.

For a more complete discussion of these detectors see Sections 2.2.5 and 2.9.

3.5.1 Calibration of Dosimeters

The function of a radiation dosimeter is to determine radiation dose in some material. On Earth and on manned space missions, the material of interest is usually the human body. In spacecraft systems that material is silicon, since it is the predominant component of electronic systems. Virtually all space-borne electronics are built from Si and since electronic performance degrades with radiation dose, measuring that dose is clearly of great importance.

Radiation dose is the measure of energy deposited in a given amount of material. The most commonly used unit is the rad (1 rad = 100 erg/g), while the SI unit[8] is the Gray (1 Gy = 1 J/kg = 100 rad). The definition of dose requires that the material that absorbed the energy be specified. For example, if the material of interest is silicon, then the dose is written as rad(Si).

[8] SI: Système International d'unités, International System of Units. See also Appendix A.8.

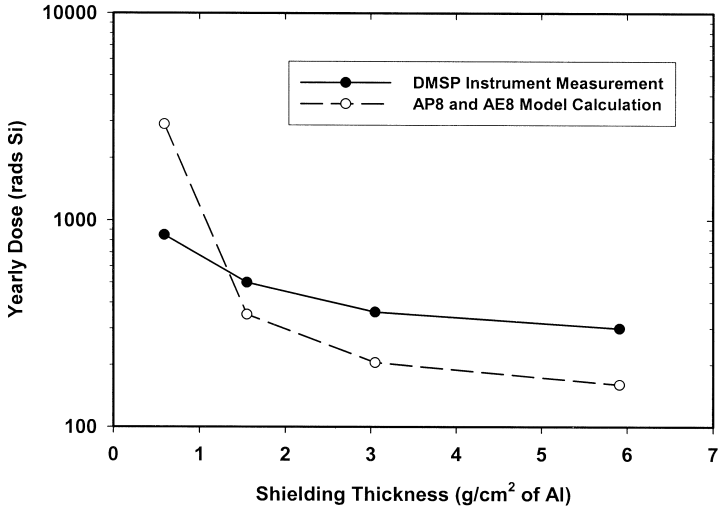

Figure 3.34: Dose-depth curve, for the DMSP spacecraft in polar 840 km orbit at solar minimum. From *Gussenhoven et al.* [1997].

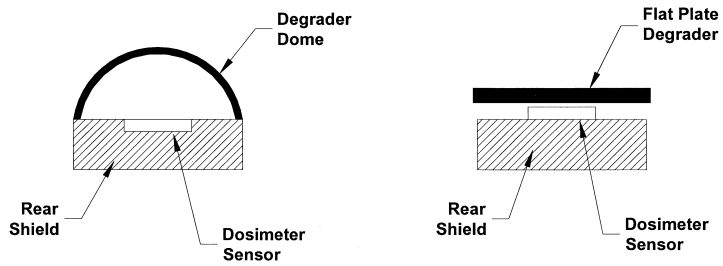

Figure 3.35: Sketch of two common dosimeter configurations.

Space borne dosimetry has the advantage that the material of interest, Si, is the same as the material used in dosimeter sensors. Thus, in principle, we can measure the radiation dose in a Si solid-state detector and then transfer it to electronic components. The transfer process uses the measured doses behind various thicknesses of shielding material (degrader) to create a dose-depth curve. The curve and the amount of shielding for a given component are then used to determine the component radiation dose. Although it is possible to use radiation belt models to calculate the dose-depth curve, this process is not as accurate as a direct measurement. Variability due to solar events and the solar cycle, together with inaccuracy of the models, introduces errors into the calculations of factors of two or three. A typical dose-depth curve, for a polar orbiting spacecraft is shown in Figure 3.34 [*Gussenhoven et al.*, 1997], with both calculated and measured values. For a more complete review of space radiation dosimetry see *Hanser and Dichter* [1993].

Dosimeters come in a variety of shapes and sizes. Two typical dosimeter configurations are shown in Figure 3.35. The first dosimeter type, Figure 3.35 left panel, has a hemispherical dome and a thick tungsten shield at its back. The shield prevents all but

the highest energy particles from penetrating from that direction. The advantage of this type of dosimeter is that the particles incident from the upper hemisphere traverse the same amount of dome material regardless of the angle of incidence. This design has a uniform response in the upper hemisphere and is better for extracting particle fluxes from dosimeter count rates. The disadvantage of this design type is that it is relatively large and massive. The next type, Fig 3.35 right panel, uses a flat degrader plate on top and a small shield underneath. An advantage of this design is that, due to geometry, the detector can be placed very close to the degrader plate, thus resulting in a compact, light weight design. A second advantage of this design is that the sensor-plate geometry is similar to that of electronic components mounted in aluminum boxes. Both of these dosimeters work in the same way. A particle strikes the top degrader and, if its energy is high enough, reaches the detector behind the dome/flat plate and deposits energy. Electronic circuitry separately counts the number of incident particles and the dose due to those particles. Operationally, the measured dose, D, is defined as

$$D = \sum_{i=1}^{N} \Delta E_i \tag{3.97}$$

where ΔE_i is the energy deposited in the dosimeter sensor by the i^{th} of the N particles that struck the sensor.

A third type of instrument is based on a transistor using metal-oxide technology, the radiation-sensitive metal-oxide-silicon field-effect transistor (RADFET). The device is very small, and contains a metal-oxide transistor sensitive to radiation damage [*Adams and Holmes-Siedle*, 1978; *August et al.*, 1983], and has been launched in space and used in the laboratory to measure the doses from a variety of sources [*Holmes-Siedle and Adams*, 1986]. Recently, 130 RADFET dosimeters have been installed in the BaBar experiment at the PEP-II accelerator at the Stanford Linear Accelerator Center (SLAC) [*Camanzi et al.*, 2001]. In addition to the name RADFET, these devices have been called "MOS Dosimeters", "Mosimeters" and "Space Charge (SC) Transducers". As the radiation damage to the chip increases, the voltage required to turn the transistor on, the threshold voltage, increases giving a measure of the accumulated dose. The sensor electronics monitor the threshold voltage, typically once per day. The advantages of the RADFET dosimeters are their very small size, power and telemetry requirements. The disadvantages are the slow rate of threshold voltage change and a difficulty in calibration. Since the RADFET transistor is radiation sensitive, it is not possible to calibrate the actual flight unit. Normally, a few transistors from the same manufacturer's lot are calibrated using radiation sources and the calibration is transferred by similarity to the flight units. This dosimeter type will not be further discussed.

Although dosimeters are simple sensors, their calibration contains subtleties that makes cross-calibration difficult. There are three aspects to dosimeter calibration: active volume determination, energy response and flux response. The first two are key to an accurate dose measurement and will be described in the next sections. The complexity of the dosimeter flux response is beyond the scope of this book. For a detailed discussion of this topic see *Gussenhoven et al.* [1986].

3.5.1.1 Active Volume Determination

The definition of the dose includes the sensitive mass of the detector. Since the material density is known, the volume of the material in the detector must be determined. The sensitive area of a Si solid-state detector is normally well known from the manufacturer's specifications, this is especially true for photodiodes. Their manufacturers provide active area values with typical uncertainties better than 1 %. It should be noted that some manufacturers provide sensors with active areas greater than the specified value, relying on the use of collimation by the user to reduce the sensitive area. Since the use of collimation in dosimetry is not appropriate, these detectors should not be used in dosimeters. In general, failure to fully understand the active area of the dosimeter detector can lead to large calibration errors.

The final component needed to determine the active volume is the depletion depth. This is a distance, perpendicular to the detector faces that, together with the active area, defines the sensitive volume of the detector. The electron-hole pairs generated in this volume are collected and analyzed; those outside of the region are not. In fully depleted detectors, the depletion depth is the same as the Si wafer thickness, normally provided by the manufacturer, and known to few percent. Even so, an independent check of this parameter can be useful. It must be noted that full depletion of this type of detector depends on the applied bias voltage. If the detector bias voltage decreases during the life of the mission due to radiation damage, it may drop below the threshold needed for full depletion, thus changing the active volume.

Partially depleted detectors have depletion depths that may be a small fraction of the wafer thickness and may not be accurately specified by the manufacturer. It is normally necessary to independently measure depletion depths of these detectors. The measurement can be at an accelerator facility or with a radiation source in the laboratory.

Accelerator Calibration The calibration described in this section provides most accurate results when the bare dosimeter detector is irradiated by an energetic proton beam in vacuum. An alternate possibility is to use a high energy beam to irradiate the sensor in air, minimizing the amount of matter between the beam exit port and the dosimeter. Electron beams can also be used but due to electron scattering will require much more analysis, and lead to larger uncertainties than working with proton beams. The sequence of actions needed to perform an accelerator measurement of a depletion depth is as follows:

1. The detector under test should be calibrated for its energy response before the beam test begins (see page 208).

2. Place the dosimeter sensor in the beam and as close to perpendicular to it as possible. The energy deposition will vary as $1/\cos\theta$ where θ is the angle of deviation between the beam and a line perpendicular to the sensor. For example a deviation of 5° will result in a 0.4 % energy deposition error.

3. Determine the beam energy, E_{out}, as it exits the accelerator.

4. Note all material, dimensions and composition, including air, if needed.

5. Using energy loss table (see Section 2.2.5), compute the energy loss between the accelerator exit port and the sensor under test, ΔE_L, and subtract it from E_{out} to

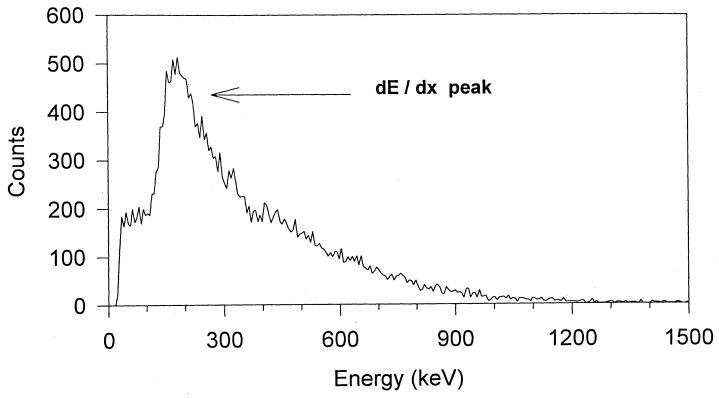

Figure 3.36: Energy deposition spectrum from ^{90}Sr/^{90}Y γ-ray source in a 500 μm depletion depth sensor.

obtain the incident beam energy at the sensor, $E_{\text{sen}} = E_{\text{out}} - \Delta E_L$. The beam energy E_{out} should be high enough so that the range of particles with energy E_{sen} is much larger than the sensor wafer thickness. Otherwise, the computation of the depletion depth will be difficult.

6. Measure the calibrated energy loss in the sensor, ΔE_{sen}.

7. Using energy loss tables, compute the rate of energy loss of a particle with energy E_{sen} traversing though the material of the sensor, $(\mathrm{d}E/\mathrm{d}x)$.

8. The depletion depth, t, is now given by $t = \Delta E_{\text{sen}} / (\mathrm{d}E/\mathrm{d}x)$.

Note that the dosimeter energy calibration is critical to this calibration procedure as it is needed to get ΔE_{sen}. Without the energy calibration, we have one measurement (energy loss in the detector in arbitrary units) and two unknowns (energy calibration and depletion depth). It is straightforward, in the case the depletion depth is known, to use a slightly modified version of this procedure to determine the energy calibration.

Source Calibration The advantage of the accelerator method, described above, is that it is extremely accurate. The disadvantage is that is very expensive and presents logistical difficulties. An alternate technique, using radiation sources, is not as accurate but is significantly cheaper and more convenient than the accelerator technique as it can be done in the sensor development laboratory.

This method works best with electron, β, sources that produce high energy electrons. For depletion depths of the order 400–600 μm, effective sources are ^{90}Sr/^{90}Y (electron energy endpoint 2.27 MeV) and ^{137}Cs (line source: 624 and 656 keV). These sources are available from commercial manufacturers. The ^{90}Sr/^{90}Y source is always sold as a β source, coated by a thin Mylar foil that does not significantly degrade the energy of the emitted electrons. The ^{137}Cs source is sold both as β source or as a plastic-sealed γ-ray source. Care should be taken to order the source in its β version. The procedure for β-source depletion depth measurement is as follows:

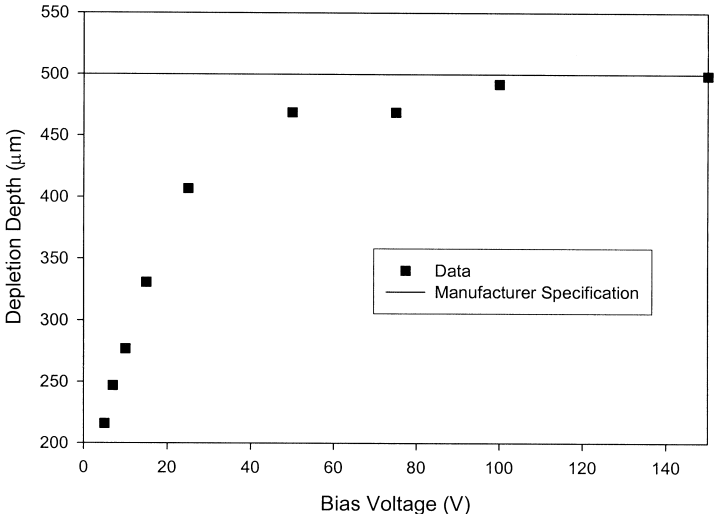

Figure 3.37: Detector depletion depth measured using a ^{90}Sr/^{90}Y γ-ray source, plotted as function of voltage applied to the detector.

1. The detector under test should be calibrated for its energy response before the source test begins (see below).

2. Place the β source close to the sensor to minimize electron energy losses in air. Collimate as needed to allow the electrons to strike the sensor under test at near normal incidence.

3. Collect the energy deposition spectrum. Spectrum of deposited energy for ^{90}Sr/^{90}Y electron spectrum incident on a 500 μm depletion depth sensor is shown in Figure 3.36.

4. The shape of the spectrum is dominated by a peak superimposed on a background. The peak arises from the fast electrons from the source that traveled on nearly normal trajectories through the sensor. The shape of the background, which is due to highly scattered electrons, depends strongly on the detector geometry, but the location of the peak does not.

5. From the center of the peak in the spectrum, using the sensor energy calibration, compute the energy deposited by the electrons, ΔE_{peak}.

6. Energy loss rate of fast electrons, $\mathrm{d}E/\mathrm{d}x$, is only weakly dependent on energy for energies above 500 keV. For Si the energy loss rate is about 3.7 MeV cm^{-1}.

7. Compute the depletion depth, t, using $t = \Delta E_{\text{peak}}/(\mathrm{d}E/\mathrm{d}x)$.

An example of the results of this method is shown in Figure 3.37. The plot shows the depletion depth as a function of applied bias voltage. The data demonstrate both the dependence of the depletion depth on the applied bias voltage, and the accuracy of the

procedure. Comparing the manufacturer specified depletion depth (for bias voltages above 100 V) with the data, shows agreement to better than 5 %.

A technique that uses X-ray attenuation methods can also be used to determine detector thickness, with a precision of about 1 %, for transmission mounted, fully depleted, detectors [see *Hanser and Sellers*, 1974]. This accuracy is not generally needed in dosimetry; however, it can be useful in calibrating particle telescope detectors (Section 3.5.2). This technique is only sensitive to the total wafer thickness so that it can only provide a depletion depth measurement for fully depleted detectors.

3.5.1.2 Energy Calibration

Energy calibration of the dosimeter sensor is required to provide the dose in physical units such as rads or Grays. In general, the simplest and most direct method of calibrating a sensor is to use γ-ray radiation sources. The energies of γ-ray have been determined to a great precision. If the dosimeter sensor could absorb the full energy of a captured γ-ray, the calibration would be very straightforward and very accurate. Unfortunately, the detectors normally used in dosimeters are too small to efficiently capture the full γ-ray energy. There are two key processes that take place when a γ-ray interacts with a dosimeter.

Absorption: γ-ray is absorbed by an electron in the target material, creating a high-energy electron. The primary electron scatters producing secondary electrons. For γ-ray energies below about 300 keV most of the energy of the incident photon remains in the detector, producing a full energy peak. For higher photon energies, many of the electrons leave the sensor, taking some of the γ-ray's energy with them. For these high energy photons: 1) an absorption event is unlikely in a sensor the size of a typical dosimeter, and 2) much of the γ-ray energy leaves the sensor. In this case the "full energy" peak in the sensor will be small and sometimes may be missing altogether.

Compton Scattering: In this process, the incident γ-ray scatters off an electron. The γ-ray exits the sensor leaving the electron to deposit its energy. As in the absorption process, some of the energy will be lost. The major difference between Compton scattering and absorption is that the primary electrons have many different energies. The maximum energy any electron may have, $E_{\max}$, is

$$E_{\max} = E_\gamma - \frac{m_e c^2 E_\gamma}{m_e c^2 + 2E_\gamma} \tag{3.98}$$

where E_γ is the initial γ-ray energy, m_e is the mass of the electron and c is the speed of light. The effect of Compton scattering is to produce a continuum of measured energies from almost zero up to the value given by Equation 3.98. Note that the energies above $E_{\max}$ are not allowed. The edge of the Compton continuum (Compton edge) can also be used to calibrate sensors. Some of the key radioisotopes, together with the energies of their full energy peaks and Compton edges are listed in Table 3.1. Experimentally (see Figure 3.38), the Compton edge is taken as the "half-max" point on the fast rising, high energy portion of the Compton continuum.

The energy calibration is a straightforward process.

1. The dosimeter is turned on with its nominal bias voltage.
2. Place a γ-ray source on or next to the dosimeter and collect the resulting spectrum using a multichannel analyzer (MCA). The calibration using γ-ray sources does not

Table 3.1: Some key radioisotopes used for γ-ray calibration of high energy telescopes.

Isotope	Event Type	E [keV]
^{133}Ba	Total Absorption	81
^{155}Eu	Total Absorption	87
^{155}Eu	Total Absorption	105
^{57}Co	Total Absorption	122
^{57}Co	Total Absorption	136
^{133}Ba	Compton Edge	207
^{22}Na	Compton Edge	341
^{133}Ba	Total Absorption	356
^{137}Cs	Compton Edge	478
^{22}Na	Total Absorption	511
^{137}Cs	Total Absorption	662

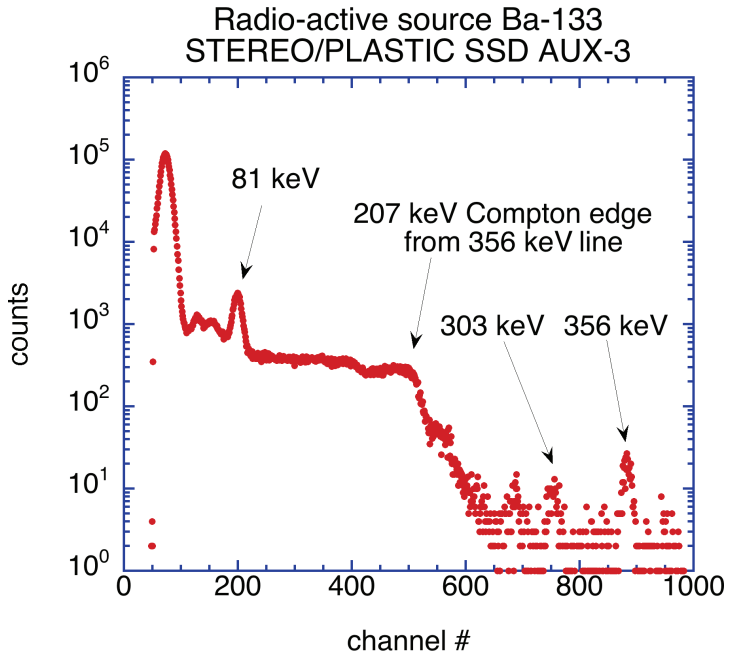

Figure 3.38: Absorbed energy spectrum from a ^{133}Ba γ-ray source for a 500 μm thick SSD detector from the PLASTIC instrument on STEREO. Measured energy is plotted along the x-axis with increasing channel numbers for increasing energies (see also Figure 3.31). From *Blush* [2004].

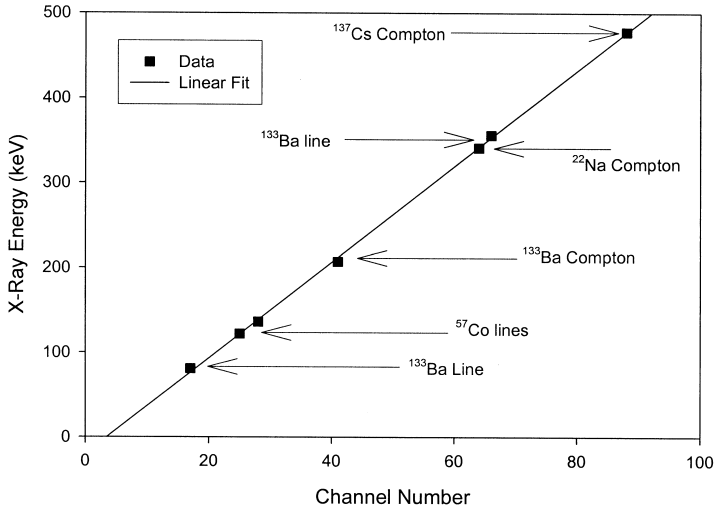

Figure 3.39: Energy calibration plot for a solid-state detector. Data points corresponding to each γ-ray absorption and Compton edge are labeled.

depend on source location. Bringing the source close to the sensor simply reduces the time needed for the test.

3. Repeat step 2 with other sources as needed.

4. Perform energy-pulse height calibration, plotting peak energies and Compton edges against the pulse heights associated with these structures.

An example for a 9×9 mm^2 area, 500 μm depletion depth photodiode (Hamamatsu S-3590-05) energy calibration spectrum is shown in Figure 3.39 with each data point identified by the radioactive source used to measure that energy [*Redus*, 2002]. In all four γ-ray sources were used ^{57}Co, ^{133}Ba, ^{137}Cs, and ^{22}Na. The energy calibration is highly linear and can be extrapolated to lower and higher energies. As always, care must be taken when extrapolating. When extrapolating to much higher energies than provided by sources in the calibration, use of a precision pulser is recommended. The pulser should be connected to the system between the sensor and the pre-amplifier. As the pulser amplitude is varied over its large dynamic range, sensor response can be mapped over a range much greater than the radioactive source allow. Pulser output may be checked for linearity using traceably calibrated oscilloscopes.

In addition to γ-ray sources, β- and α-ray sources may also be used for detector calibration. In case of β-rays, they can be used as they were in the depletion depth calibration. High energy line sources and sources that have high energy endpoints provide fast electrons to strike the sensor. The measured shape of the spectrum is dominated by a peak located on top of a background (see Figure 3.36). The peak is due to the fast electrons from the source that traveled on near normal trajectories through the sensor. The shape of the background, which is due to highly scattered electrons, depends strongly on the detector geometry, but the location of the peak does not. If the depletion depth is known, then

the rate of energy loss, as obtained from the Range-Energy tables [*Pages*, 1972], allows a computation of the energy lost in the detector. The disadvantage of this technique is that the rate of energy loss varies very slowly with energy for electrons above 500 keV so that its very difficult to obtain more than one calibration point.

α-particle sources offer the advantage of higher energies, in excess of 5 MeV, that are well above those that any practical γ-ray and β-ray source can deliver. These sources have three disadvantage: 1) the α-particle loses energy rapidly in air so that accurate calibrations need to be performed under vacuum, 2) the particle stops within microns after entering the detector, only testing the energy response of a small portion of the sensor, and 3) due to pulse height defect the measured energy is less than the deposited energy [*Knoll*, 2000].

Finally, if the depletion depth of the sensor is known, then the energy calibration can be performed using high energy protons from accelerators. The procedure is similar to that described above but in this case the depletion depth is known and the deposited energy is the variable. The beam energy can be varied to provide a wide range of calibration energies. This procedure has the drawback of high cost and logistical difficulties.

3.5.2 Calibration of Telescopes

Telescopes made up of solid-state detectors are frequently used on space missions to measure both ions and electrons. A telescope consists of two or more solid-state detectors mounted coaxially one behind the other (see also Section 2.9). With a typical proton operating energy range of 1 to 15 MeV, these instruments are unmatched in measuring directional particle fluxes. They are capable of measuring the energies of incident particles and, using the pattern of energy deposition in the detectors, distinguishing protons from other ions and from electrons.

To identify heavier nuclei multi-element arrays of solid-state detectors are used. Multi-sensor telescopes can be calibrated to identify heavy ions and to measure their energies over a wide range in cosmic ray studies in a similar way as the simpler electron and proton telescopes discussed here. Calibration of these instruments is discussed in Section 3.5.3 below. The interested reader is also directed to the papers by *von Rosenvinge et al.* [1995], *Müller-Mellin et al.* [1995], *Torsti et al.* [1995] and *Stone et al.* [1998a] for recent high-energy solar particle instruments on the SOHO and ACE missions, and by *Stone et al.* [1998b] for a recent cosmic-ray instrument.

A typical proton telescope configuration, shown in Figure 3.40, demonstrates key features of the instrument. The front part is the collimator. It consists of two shielding collimators as well as sweeping magnets and baffles to remove electrons[9]. In electron telescopes a light-tight foil is used to protect the instrument from the Sun and to prevent low energy protons from reaching the detectors as they are a significant radiation damage hazard (see Section 4.2.4). The back part of the instrument contains the detector stack, the electronics and back shielding for the detectors. Typically, but not always, the detector stack includes a veto detector, which will identify high energy protons or electrons that penetrate through the telescope's other detectors.

The low end of the proton and electron range is limited by the thickness of the light-tight foil that protects the front detector. A typical foil used for this purpose is a 10 μm

[9]Note that in many cases the use of a magnet to discriminate against electrons is not possible due to magnetic cleanliness requirements or size and mass limits.

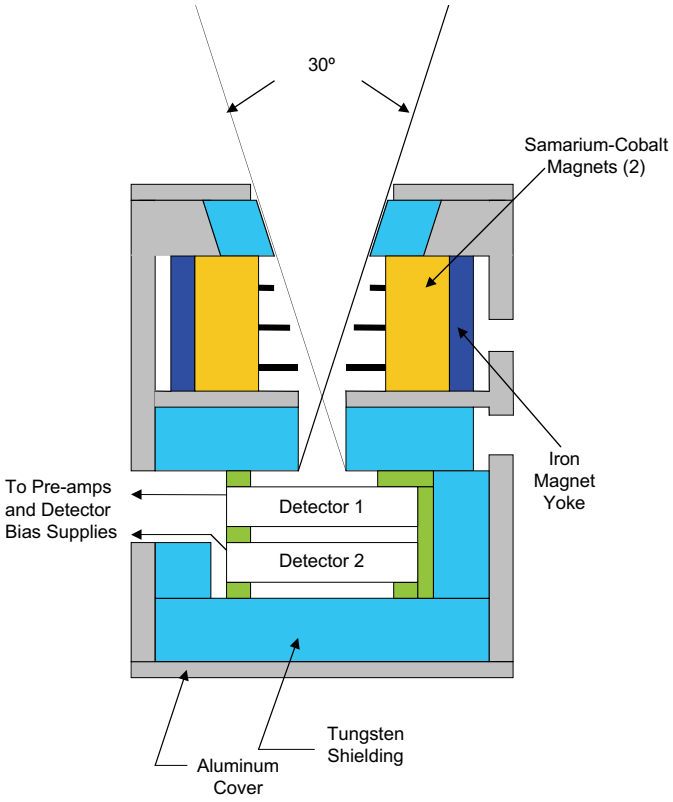

Figure 3.40: Cross-sectional diagram of a proton telescope flying aboard the Polar Orbiting Environmental Satellite. From *Evans and Greer* [2000].

of Al resulting in lower range of about 50 keV for electrons and 800 keV for protons. It is possible to deposit a thin light-tight coating on the front of the first solid-state detector (SSD) so that the foil is no longer necessary. This changes the lower limit to a few tens of keV for protons. Care must be used with this technique, as the foil has a second purpose, absorbing the intense low energy proton and electron fluxes that can interfere with the measurement or damage the detector. The upper energy limit for protons is limited by the total depletion depth in the telescope stack. For a typical amount of 1300 μm, it corresponds to 14 MeV.

3.5.2.1 Geometric Factor Calculation

In instruments where the collimator thickness is small compared to the aperture size the geometric factor, G, can be simply written as

$$G = \iint A_0 \cos\theta \sin\theta \, \mathrm{d}\theta \, \mathrm{d}\varphi \tag{3.99}$$

where A_0 is the entrance aperture area, θ the polar angle, and φ the azimuth angle (see also Section 3.1.1). Since the response of high energy telescopes is independent of the azimuth angle, i.e., rotationally symmetric, we can simplify Equation 3.99 to

$$G = 2\pi \int A_0 \cos\theta \sin\theta \, \mathrm{d}\theta \tag{3.100}$$

which evaluates to

$$G = \pi A_0 \left(1 - \cos^2\theta_0\right) \tag{3.101}$$

with θ_0 the polar field-of-view of the telescope (half-width).

In many high energy instruments Equation 3.100 does not hold. There are several reasons for this, the use of two collimators to define the solid angle, the thickness (length perpendicular to aperture area) of the collimator may be larger relative to the aperture radius and the field of view may be determined by two telescope detectors. The two-aperture formula works in these cases. The two aperture geometric factor is given by

$$G = 2\pi \int A(\theta) \sin\theta \, \mathrm{d}\theta \tag{3.102}$$

with $A(\theta)$ the angle dependent area. $A(\theta)$ is given by [*Sullivan*, 1971]

$$A(\theta) = \begin{cases} \pi r_s^2 \cos\theta & \text{if } 0 \leq \theta \leq \theta_c \\ \left[\frac{1}{2} r_1^2 \left(2\psi_1 + \sin(2\psi_1)\right) + \right. & \\ \left. \frac{1}{2} r_2^2 \left(2\psi_2 + \sin(2\psi_2)\right)\right] \cos\theta & \text{if } \theta_c < \theta \leq \theta_M \\ 0 & \text{if } \theta > \theta_M \end{cases} \tag{3.103}$$

where r_1 and r_2 are the two aperture radii, r_s is the smaller of (r_1, r_2), and D is the distance between the apertures. The limit angles are defined as

$$\theta_C = \arctan\left(\frac{|r_1 - r_2|}{D}\right) \quad \text{and} \quad \theta_M = \arctan\left(\frac{r_1 + r_2}{D}\right) \tag{3.104}$$

and the ψ functions are given by

$$\psi_1 = \arccos\left(\frac{r_1^2 + D^2 \tan^2\theta - r_2^2}{2D\, r_1 \tan\theta}\right) \tag{3.105}$$

and

$$\psi_2 = \arccos\left(\frac{r_2^2 + D^2 \tan^2\theta - r_1^2}{2D\, r_2 \tan\theta}\right). \tag{3.106}$$

Although the geometric factor is ultimately determined by experimentation, it is important to do early computations as part of the design process and also to provide independent quality checks when reviewing calibration data. A comparison of a two-aperture calculation and measured data is shown in Figure 3.41 for 1 MeV protons and 300–700 keV

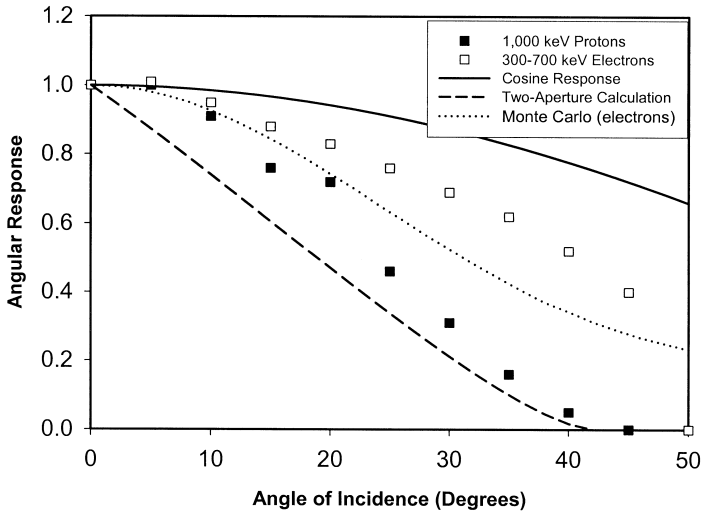

Figure 3.41: Comparison of measured (symbols) and calculated (lines) angular telescope response.

electrons incident on a 9 μm Al foil and then passing through an aperture of a collimator with large length to diameter ratio. Even though the foil causes scattering at the upstream side of the collimator, broadening the angular distributions, the agreement between proton data and calculation, Equation 3.103, is good. For electrons, which undergo severe angular scattering in the foil, the response is intermediate between the two-aperture formula, Equation 3.103, and cosθ, Equation 3.100. This illustrates the need to understand the interaction of all particle types with the entrance aperture elements. In cases when more complex collimator-detector geometry is in use, an analytical computation becomes unfeasible and a approach becomes the preferred method [*Sullivan*, 1971], especially if scattering of particles inside the telescope and penetrating radiation through side walls are considered for the telescope response as well [*Tuszewski et al.*, 2002].

3.5.2.2 Geometric Factor Measurement

Typically, a telescope instrument will be designed to subdivide its full proton energy range into a number of narrow energy channels (for a discussion of electron energy channels see discussion on page 218 below). Each channel will have its own geometric factor and energy range. The instrument geometric factor and range are simply the sum of the corresponding channel quantities. This energy dependence motivates the development of an energy dependent channel geometric factor, $G_i(E)$, which is defined as

$$G_i(E) = 2\pi \int A_i(\theta, E) \sin(\theta)\, \mathrm{d}\theta = 2\pi\, R_i(E) \int H_i(\theta) \sin\theta\, \mathrm{d}\theta \tag{3.107}$$

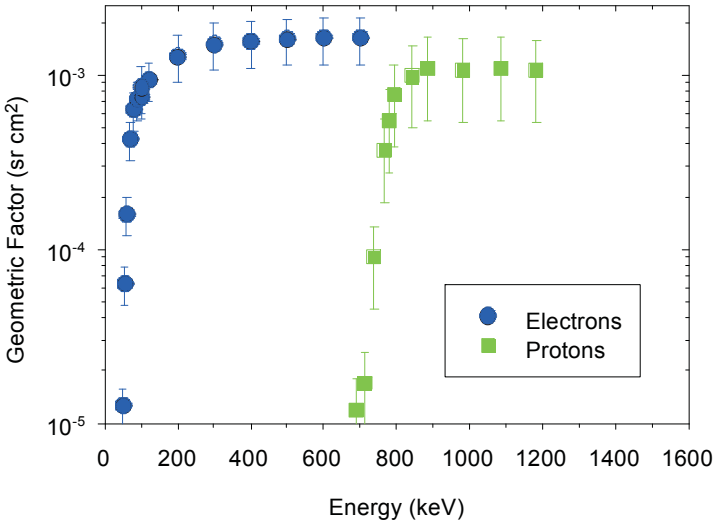

Figure 3.42: Example of an energy dependent geometric factor of a telescope detector. Due to a 9 μm aluminum entrance foil, the low energy threshold is 50 keV for electrons and 800 keV for protons. From *Dichter et al.* [1998].

where the energy dependence $R_i(E)$ and the angular dependence $H_i(\theta)$ have been separated. The total instrument geometric factor G is

$$G = \sum_{i=1}^{N} G_i(E) \tag{3.108}$$

where i is the given energy channel and N is the number of energy channels. The separability of the energy dependence and the angular dependence, $A(E,\theta) = R(E)H(\theta)$, is a good working assumption in most energy ranges. For electrons, where angular scattering is very strong at all energies the assumption is valid under almost all circumstances. An example, where the separability assumption is not accurate is for particles with energies near the threshold energy because their angular distributions may be broader than those at higher energies.

An accurate knowledge of $R(E)$ from threshold to where it reaches its maximum value is important. Particles with energies well above the detection threshold have a nearly unity probability of being detected. However, as the particle energy decreases, the probability of detection gradually decreases until it reaches zero for energies at the threshold. This behavior is illustrated in Figure 3.42 where the total instrument energy dependent response to electrons and protons is plotted for a detector with a 9 μm Al foil in its entrance aperture. The total instrument count rate will be proportional to the product $J(E)R(E)$ where J is the flux of incident particles. Since $J(E)$ rapidly increases with decreasing energy, the near threshold instrument response may have a significant effect on instrument geometric factor. Therefore, the number of data points taken at low energies must be high enough to accurately reconstruct $R(E)$ in the region where it changes most quickly. This behavior further motivates the development of an energy dependent geometric factor.

Due to the telescope proton energy range of 1 – 15 MeV these devices are most often calibrated in tandem Van de Graaff accelerators. These machines are extremely suitable to calibrations and feature DC beams that can be run at very low intensity and with extremely good energy resolution, about 1 part in 10^4. There is very little, if any, contamination from other ions and almost no background from protons at other energies. The electron energy range of typical telescopes, about 50 keV to a few MeV, leads to the use of single ended Van de Graaff accelerators, with much lower maximum accelerating voltages. The one significant source of background for these machines is dark current; electrons that are produced by neutral atom collisions with the acceleration column and scattered into the instrument. This current can be measured by detecting instrument counts with the electron source turned off and the results used to correct the calibration data.

The key parameter in calibrating a sensor is the absolute beam flux. This quantity must be determined or estimated during the entire calibration procedure. Several beam monitor detectors are needed in order to perform this task. The absolute flux monitor, M_{AF}, is a bare, collimated Si detector that can be moved into a location so that its collimated area is exactly where the telescope aperture is during the test (telescope must be temporarily moved out of the way). This is referred to as aperture substitution. The stationary monitor, M_{ST}, is always in the same location relative to the telescope and transfers the absolute calibration from M_{AF} to the telescope. The beam-mapping monitor, M_{BM}, serves to measure the physical spread of the beam at the telescope location. M_{BM} may be physically the same detector as M_{AF}.

In principle, the M_{AF} aperture should be the same as the telescope aperture. However, due to inevitable imperfections in registration, the M_{AF} aperture should be made larger to ensure that it overlaps the location of the telescope aperture. If the physical setup does not permit a true aperture substitution, M_{AF} may be located slightly upstream of the telescope location. This arrangement will give satisfactory results if the distance from the M_{AF} location to the telescope is small compared with the distance between M_{AF} and the last beam focus. The focal point location will be provided to the experimenter by the accelerator operators as part of beam tuning parameters. If the beam focal point is close to the detector locations, then the beam is diverging from that point and the relative beam intensities at the detectors may be estimated by assuming a $1/r^2$ divergence from the focal point.

The M_{BM} must be mounted on a mobile stage so that it can traverse perpendicularly to the beam. Measurements made by this monitor are used to obtain the beam profile, with the intent of placing the telescope and, if possible, M_{ST} in an area where the beam varies little spatially. Although the measurement is only made in one axis, Van de Graaff ion optics and collimation systems are nearly rotationally symmetric. Thus even a one-dimensional measurement of a flat beam profile gives a strong likelihood that there is no significant spacial variability, in any direction, at the telescope location. If this monitor is available, it is strongly recommended to run it at least once for every beam energy.

If in a given setup M_{AF} has an aperture with an area A_{AF} and data collection interval τ_{AF} and the total counts during this interval are C_{AF} then the absolute beam flux, f_B, and its statistical error, Δf_B, are given by

$$f_B = \frac{C_{\mathrm{AF}}}{A_{\mathrm{AF}}\,\tau_{\mathrm{AF}}} \qquad \text{and} \qquad \frac{\Delta f_B}{f_B} = \frac{1}{\sqrt{C_{\mathrm{AF}}}} \tag{3.109}$$

The magnitude of Δf_B depends on the counting statistics only. Systematic errors due to imperfect knowledge of the collimator areas and spatial and temporal variations of the

beam have to be separately determined. The measurement made by M_{ST}, either at the same time as M_{AF} or nearly at the same time can be written as:

$$f_B = K\frac{C_{ST}}{A_{ST}\ \tau_{ST}} \qquad \text{and} \qquad \frac{\Delta f_B}{f_B} = \frac{1}{\sqrt{C_{ST}}} \tag{3.110}$$

where K is the correction factor that accounts for the fact that M_{ST} is not in the same location as M_{AF} and is sampling a different region of the beam. Setting Equations (3.109) and (3.110) equal to each other provides for a formula for the correction factor K.

$$K = \frac{C_{AF}}{A_{AF}\ \tau_{AF}}\frac{A_{ST}\ \tau_{ST}}{C_{ST}} \qquad \frac{\Delta K}{K} = \sqrt{\frac{1}{C_{AF}} + \frac{1}{C_{ST}}} \tag{3.111}$$

Once K is computed, it may be used to determine the absolute beam flux, f_B, using just M_{ST} count rates. Note that the statistical errors in determining the beam flux are quite small since thousands of counts can usually be obtained. The uncertainty in determining f_B is dominated by systematic error. The most important systematic effects are variation of beam uniformity with time and location. Frequent beam scans and M_{AF} measurements can be performed to obtain estimates of the beam spatial and temporal variability. The value of K should be re-computed as often as practical because of the possibility of beam profile variations with time. A typical sequence of calibration steps is as follows:

1. Perform beam scan using the beam-mapping monitor, M_{BM}.
2. Move the absolute flux monitor into beam and measure the respective count rates on the absolute flux monitor and the stationary monitor (C_{AF} and C_{ST}).
3. Compute the correction factor K.
4. Move telescope into beam at 0° and measure the count rates $C_{TEL}(0)$ and $C_{ST}(0)$.
5. Use value of K to get absolute telescope response.
6. Move the absolute flux monitor into beam and measure the count rates C_{AF} and C_{ST}.
7. Compute the correction factor K.
8. Move telescope into beam at angle θ and measure the count rates C_{TEL} and C_{ST}.
9. Use the correction factor K to get absolute telescope response.
10. Repeat steps 6 to 9 until the response at all desired angles has been measured.
11. Perform beam scan using beam-mapping monitor M_{BM}.

Once the correction factor K is determined, the value of $R(E)$, in dimensions of area, can be determined from a beam run at normal incidence ($\theta = 0$ and $H(\theta) = 1$) as

$$R_i(E) = \frac{A_{ST}\ \tau_{ST}}{K\ C_{ST}(0)\ \tau_{TEL}}\ C^i_{TEL}(0) \tag{3.112}$$

where C^i_{TEL} is the count rate in the i^{th} energy channel of the telescope. With $R(E)$ known, the angular response, the dimensionless function $H(\theta)$, can be similarly determined with detector counts taken at a variety of angles and $R(E)$ from the $\theta = 0°$ run.

$$H_i(\theta) = \frac{A_{\mathrm{ST}}\ \tau_{\mathrm{ST}}}{K\ C_{\mathrm{ST}}(\theta)\ \tau_{\mathrm{TEL}}}\ \frac{C^i_{\mathrm{TEL}}(\theta)}{R_i(E)} \tag{3.113}$$

The experimentally determined quantities R_i and H_i can then be substituted into Equation 3.107 to obtain the channel geometric factor. This can either be done by interpolating between measured values and fitting R_i(E) and $H_i(\theta)$ with continuous functions and then numerically computing the resulting integral or by performing a discrete sum as an approximation to the integral

$$G_i(E) = 2\pi\, R_i(E) \sum_j H_i(\theta_j) \sin\theta_j\ \Delta\theta_j \tag{3.114}$$

The accuracy of either procedure depends strongly on beam systematic effects such as beam variations in time and space and beam angular dispersion (non-parallel beam). The calibration team should work with the accelerator operators to understand the beam and take frequent beam monitoring measurements to verify beam parameters.

Each detector has to be checked to verify that the sensor responses were insignificant for particles entering the aperture at angles beyond the normal field-of-view of the instruments. Moreover, for a proton telescope detector it has to be verified that the magnetic field imposed across the telescope collimator structure, if sweeping magnets are used to eliminate electrons, is sufficient to reduce any sensor response to energetic electrons to a negligible level.

3.5.2.3 Electron Detection

When compared with protons, electrons scatter more intensely when traversing absorber and detector materials. As a result, the measurement of electron energies is more difficult than proton energies. In addition, measurement of incident fluxes is subject to greater uncertainties.

The proton calibration beam normalization relies on the use of a bare Si detector. All incident protons that enter the sensor either stop in it or pass through it. In either case, due to their nearly straight path and a large rate of energy loss, nearly all of them will be detected and counted. However, a significant fraction of electrons, 5–15 % will simply be reflected back from beam monitor and likely not be counted at all [*Berger et al.*, 1969; *Seltzer and Berger*, 1974; *Carrington et al.*, 1986]. Thus, the measurement of absolute response will have an uncertainty of up to 15 % before any of the other effects are added in.

A second effect on electron measurement is due to severe multiple scattering which strongly affects energy deposition. Electron paths inside a detector are convoluted and result in a complex pattern of energy loss. Data displayed in Figure 3.43 show the electron energy deposition in a two detector telescope from a beam calibration experiment. The front detector was 150 μm and the back one 700 μm. The telescope response to electrons is shown in Figure 3.43 in four energy deposition bands. Band 1 requires no energy loss in the back detector and any non-zero energy loss in the front detector. Bands 2, 3 and 4

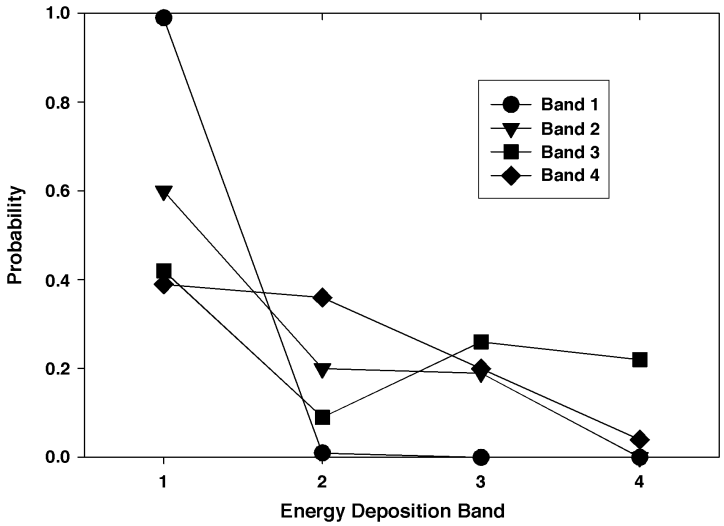

Figure 3.43: Energy deposition by electrons in a two detector telescope. See description in the text.

require a non-zero energy loss in the front detector and energy losses of 30–60, 60–120 and 120–350 keV, respectively, in the back detector. A review of Figure 3.43 reveals that the energy deposition process is complex. Even though the incident electron energy is well defined, the sensor response is spread among several channels. Furthermore, electrons with different energies have similar energy deposition patterns. The similarity and overlap of high energy distributions make it difficult to associate unique incident energies to a particular energy loss channel. It is still possible to form combinations of channels that will result in broad differential channels as well as integral channels. Extensive calibrations with electron beams and computer simulations of the instrument response (see Appendix A.1) are needed to accurately describe the on-orbit performance of the instrument.

The electron energy loss patterns provide a convenient method for differentiating electrons and protons in telescope and dosimeter data. In general, electrons do not deposit more than a few hundred keV in telescope detectors. This is true for higher energy (E > 1400 keV) electrons, which lose even less energy, on the average, in the detectors. It is straightforward, adapting to the thickness of the detectors, to choose energy boundaries to separate the electrons and protons. Particles that deposit more than a certain energy are protons while those that deposit less are most likely electrons. In the telescope, for which data are shown in Fig 3.43, that energy boundary was 820 keV for both detectors.

3.5.2.4 Conversion to Physical Units

The physical quantity that high energy telescopes are designed to measure is the incident particle flux as a function of energy and angle, $J(E, \Psi)$, where the angle Ψ is measured with respect to the local magnetic field line (pitch angle). The relationship be-

tween the observed count rate in the i^{th} energy channel, CR_i, and the differential particle flux is given by

$$\mathrm{CR}_i = 2\pi \int_{E_i-\Delta E_i/2}^{E_i+\Delta E_i/2} \mathrm{d}E\ R_i(E) \int_0^{\theta_{\max}} J(E, \Psi(\theta))\ H_i(\theta)\ \sin\theta\ \mathrm{d}\theta \tag{3.115}$$

where θ_{max} is the angle beyond which $H(\theta) = 0$, E_i is the channel center energy and ΔE_i is the energy channel width. For telescope instruments with narrow angular fields-of-view and with narrow energy channels, Equation 3.115 can be simplified by assuming that the quantities R and H are nearly constant in any given differential channel. In that case, Equation 3.115 can be rewritten as

$$J(E_i, \Psi) = \frac{\mathrm{CR}_i}{G_i(E_i)\ \Delta E_i} \tag{3.116}$$

where G is the channel geometric factor defined in Equation 3.114. In cases where the simplification cannot be made, for example for electron measurement, Equation 3.115 must be solved by trying different forms of the function J to reproduce the observed count rates. For example, the energy dependence of particles in the magnetosphere can often be represented by $J(E) = kE^{-n}$. This form can be used in solving Equation 3.115 for all the channel count rates and varying the parameters k and n until the optimal fit was found. If the pitch angle distribution varies across the entrance angle or the instrument is on a spinning spacecraft and the spin rate is high relative to the data acquisition interval then, in most cases, unless an approximate form of the distribution is known, only an averaged value can be extracted.

3.5.3 Calibration of Mass-Resolving Telescopes

An important objective for a large class of energetic particle telescopes goes beyond the detection of electrons and protons and the determination of their energy in the sensitivity range of the telescope. Instruments with more limited capability have been described earlier in Section 2.9. A wider objective is the determination of the elemental and even isotopic composition of high energy particles from several hundred keV/nucleon to tens and even hundreds of MeV/nucleon. Such particles are found in populations accelerated near the Sun and in the heliosphere, as well as in the radiation belts of planetary magnetospheres. The telescopes that detect the highest energies also measure cosmic rays that reach the inner heliosphere and the vicinity of the Earth from the boundary of the heliosphere (the anomalous cosmic rays) or from beyond it.

This section outlines those aspects of the high-energy, species- and isotope-resolving particle telescopes that affect their calibration and presents representative results of typical, currently used instruments. Particles in this energy range are usually measured with instruments using the ΔE versus E technique, where the energy loss of the registered particle is measured in two or more consecutive solid-state detectors along the particle path in the instrument. For particle velocities where $\beta\gamma$ is above about 0.3, where $\beta = v/c$ and the Lorentz factor $\gamma = 1/\sqrt{1 - v^2/c^2}$, the energy loss is given by the Bethe-Bloch formula with high accuracy [*Eidelman et al.*, 2004]

$$-\frac{\mathrm{d}E}{\mathrm{d}x} = \frac{Z_1^2 Z_2 e^4}{4\pi\varepsilon_0^2 m_2 m_e v^2}\left(\frac{1}{2}\ln\left(\frac{2m_e v^2\gamma^2 T_{\max}}{I^2}\right) - \frac{v^2}{c^2} - \frac{\delta}{2}\right) \tag{3.117}$$

where Z_1 and Z_2 are the nuclear charges of the particle and the target atoms, i.e. the detector atoms (in units of e, the elementary charge), m_2 is the mass of the target atom, ε_0 is the permittivity of free space, m_e is the electron mass, v is the particle velocity, $T_{\max}$ is the maximum kinetic energy which can be imparted to a free electron, I is the mean excitation energy, and δ is the density effect correction to the ionization energy loss. Below kinetic energies of the incoming particle of $E \approx m_1 c^2$ Equation 3.117 can be simplified largely and the rate of energy loss of a particle in a solid-state detector can be approximated as

$$-\frac{\mathrm{d}E}{\mathrm{d}x} \approx K\frac{Z_1^2}{v^2} = K\frac{m_1 Z_1^2}{2E} \tag{3.118}$$

for the energies of interest here. The energy loss rate is measured usually in keV/μm or keV/mg of silicon, the usual material for solid-state detectors used in telescopes. Equation 3.118 describes to a generally sufficient accuracy the relationship between the energy loss rate and measured total energy of the particles. The "constant" K in fact depends weakly on the particle type and its velocity (below relativistic velocities), and is a parameter that is directly or indirectly determined during calibration of a particle telescope. Equation 3.118 requires additional terms at relativistic energies. However, in all energetic particle telescopes, the accurate measurement of the particle energy loss rate and the total energy leads to the determination of the particle species and even of isotopes, given that at these high energies all particle species are in fact fully ionized.

The key objective of the calibration of high-energy particle telescopes is the determination of the energy loss rate versus incident energy, for the range of particle species and energies of interest, of the specific detector stack used in a given telescope. While, in principle, the dependence of energy loss rate on incident energy and particle species can be calculated, given both experimentally determined and theoretically calculated tables, these do not provide, in general, a sufficient accuracy for a specific instrument. Calibration with representative particle species, at energies within the range of interest to the telescope, is therefore necessary.

The energy loss of a particle that traverses a detector or detector stack depends on its path length and therefore on its angle of incidence. Particles incident at an angle θ with respect to the normal have a path length $\Delta d(\theta) = d/\cos\theta$, where d is the detector thickness, assuming a straight-line trajectory across the detector. Particle telescopes usually have relatively wide opening angles ($\sim 30°$ half-cone acceptance angle is typical); in order to increase the geometric factor of telescopes. This means that the energy loss of a particle of given energy, in a planar detector, varies by about $\pm$ 15 %, as a function of its angle of incidence. Correction for non-normal incidence can be made either by assuming an isotropic flux over the telescope opening and using the theoretically determined angular sensitivity of the telescope, or by directly determining the path of each incident particle as discussed below.

A typical energetic particle telescope, the Low Energy Telescope (LET) of the COSPIN group of instruments on the Ulysses mission is shown schematically in Figure 3.44 [*Simpson et al.*, 1992]. LET measures the flux, energy spectra and elemental composition of solar energetic particles and cosmic rays from about 1 MeV/nucleon to 75 MeV/nucleon. The telescope contains four solid-state detectors (D1 to D4) and is surrounded by a scintillator used as an active anti-coincidence shield (D5). The calibration of the telescope using energetic protons was carried out using the Philips variable energy AVF cyclotron of the

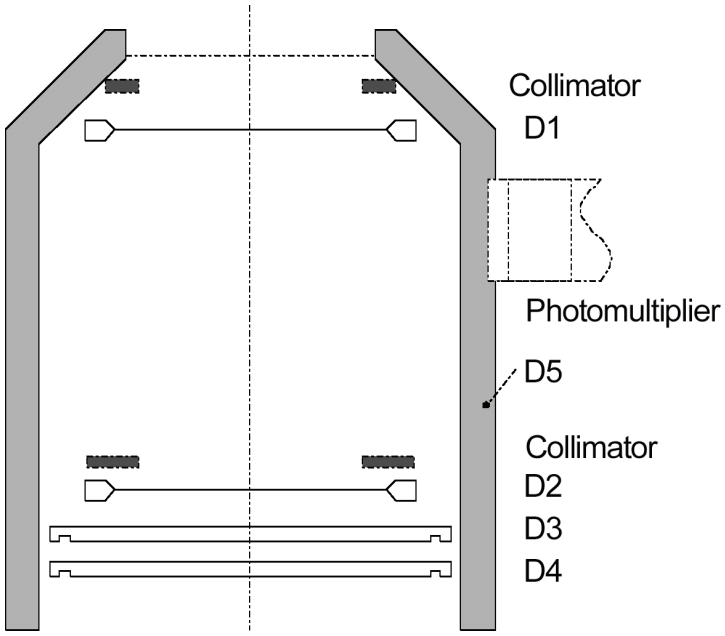

Figure 3.44: Schematic cross section of the Low Energy Telescope (LET) on the Ulysses mission. This instrument measures energetic solar particles and cosmic rays in the energy range 1 MeV/nucleon (^{1}H) to 75 MeV/nucleon (^{56}Fe), with a charge resolution extending to $Z = 26$.

Free University, Amsterdam, The Netherlands [*Marsden et al.*, 1984]. The primary beam from the cyclotron has the disadvantage that changing its energy requires time-consuming tuning and it also has a beam current that is too high for a particle-counting instrument. The calibration was therefore performed using inelastically scattered protons and other reaction products (deuterons and alpha particles) from a thick carbon (and, alternatively, nickel) target. The primary beam of protons incident on the target had an energy of 25 MeV. The energy of the secondary particles from the target was determined using a magnetic spectrograph. The energy spectra of the scattered secondary particles was determined independently. The directional properties of the incident particle beam and protection of the particle telescope from unwanted products (neutrons, scattered electrons) was achieved using collimators and sweep magnets near the telescope entrance. The experimental setup for the calibration used is illustrated schematically in Figure 3.45.

A typical result of the calibration runs is shown in Figure 3.46 in the form of a pulse height matrix of energies measured in detector D1 (the front detector), representing the energy loss of the particles $\Delta E(\mathrm{D1})$ versus the residual energy $E(\mathrm{D2})$ measured in detector D2. (These particles do not penetrate to detector D3.) As can be seen in Figure 3.46, the LET telescope can identify clearly protons, deuterons and alpha particles in the energy range of interest.

The calibration of the LET for particles of higher atomic number was carried out at the VICKSI accelerator of the Hahn-Meitner Institut in Berlin, Germany [*Kamermans et*

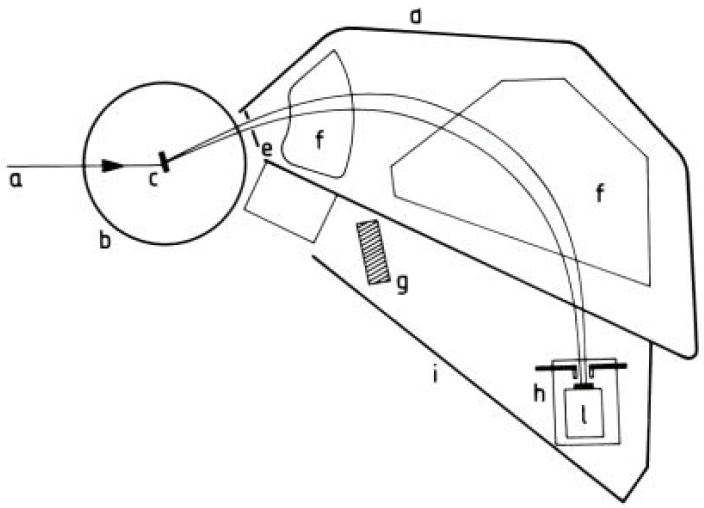

Figure 3.45: Experimental setup for the calibration of the LET instrument. This figure shows schematically (a) the incoming proton beam, (b) the scattering chamber, (c) the target, (d) the magnet chamber, (e) the entrance slit, (f) the magnet pole pieces, (g) paraffin blocks, (h) the LET mounting platform and collimator, (i) the detector chamber, and (l) the LET instrument. From *Marsden et al.* [1984].

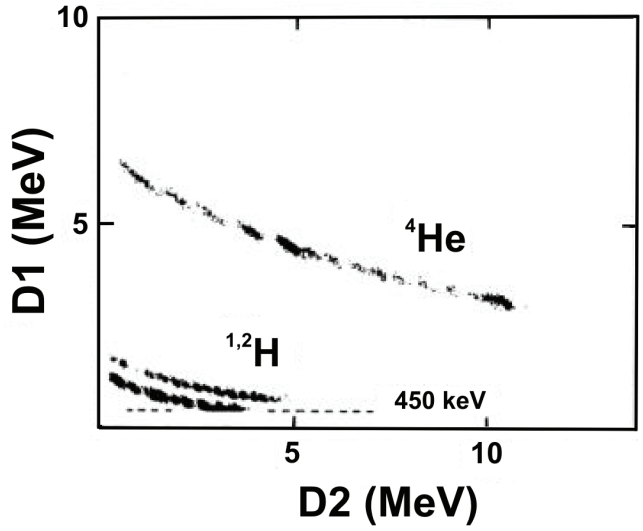

Figure 3.46: Energy loss measured in the front detector of the Ulysses/LET versus the residual energy measured in the second detector, showing the characteristically distinct tracks for protons, deuterons and alpha particles. From *Marsden et al.* [1984].

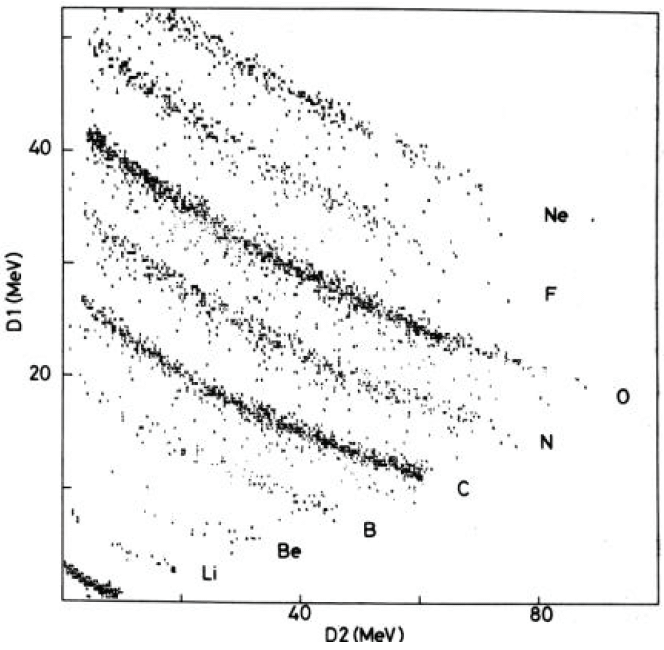

Figure 3.47: Energy loss measured in the front detector of the LET versus the residual energy measured in the second detector, when calibrating the instrument using the ion fragments produced by a 147 MeV ^{20}Ne primary beam impacting a ^{12}C target. The light elements produced in this calibration run produce clearly resolved tracks up to the primary ion in the accelerator beam. From *Kamermans et al.* [1980].

al., 1980][10]. The primary beam used consisted of ^{20}Ne of energy 147 MeV; this impacted targets of ^{197}Au (200 mg cm^{-1}) and ^{12}C (52 mg cm^{-1}). In particular, the reaction products from the ^{20}Ne + ^{12}C collisions provided a wide range of species (elements and isotopes) in the energy range of interest to carry out the calibration of the telescope. A representative result from the calibration is shown in Figure 3.47.

The LET telescope has a relatively wide (half-)opening angle of 27.5°, so that particles incident away from the telescope axis have longer path lengths, and that therefore the particles produce a larger $\mathrm{d}E/\mathrm{d}x$ signal in the first detector D1: $\Delta E(\theta) = \Delta E(0)\,\mathrm{d}/\cos\theta$ where $\Delta E(0)$ is the energy lost by a particle at normal incidence. This effect results in a widening of the range of the $\mathrm{d}E/\mathrm{d}x$ signal for a given particle energy which is absorbed in the second, total energy detector D2. The consequence is a reduction in the species resolution capability of the telescope. However, given that the maximum uncertainty arising from this is $\sim 10\,\%$, this effect does not affect the element resolution capability of the LET but reduces its capability to detect the isotopes of the elements as the atomic number increases. For lower atomic numbers, where the atomic mass m is still a significant fraction of the product $m_1 Z_1^2$ that is determined through the $\mathrm{d}E/\mathrm{d}x$ versus E technique, isotopes such as ^{3}He and ^{4}He can still be resolved by the LET [*Kamermans et al.*, 1980].

[10] After finishing the nuclear physics research activities at VICKSI in the early 1990's research in materials characterization started using modified accelerators as tools.

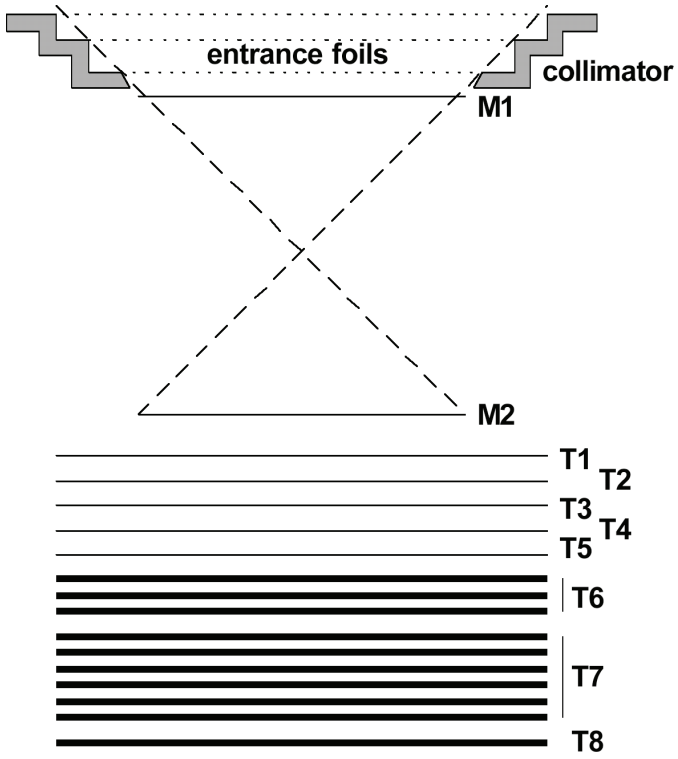

Figure 3.48: Schematic cross section of the Solar Isotope Spectrometer (SIS) on the Advanced Composition Explorer (ACE) mission; the complete instrument consists of two identical telescopes. The SIS instrument measures the isotopic composition of energetic nuclei from He to Zn (nucleonic charge from $Z = 2$ to 30) in the energy range from $\sim$10 MeV/nucleon to $\sim$100 MeV/nucleon. After *Stone et al.* [1998a].

For a greater resolving power in terms of elements and isotopes, path length corrections must be made. This can be achieved through the use of position sensitive detectors which measure both the energy loss of the penetrating particles and their path through the telescope. When using solid-state detectors for this purpose, the necessarily finite thickness of the detectors generally restricts the use of the technique to high energy solar particles and cosmic rays and for high mass resolution for higher atomic number elements, the path of the incident particles needs to be determined. Several high energy telescope systems have used a variety of position sensing detectors for this purpose [*Simpson et al.*, 1992; *von Rosenvinge et al.*, 1995; *Stone et al.*, 1998a], or even, in some instances, non-planar, curved solid-state detectors [*von Rosenvinge et al.*, 1995].

The Solar Isotope Spectrometer (SIS) on the Advanced Composition Explorer, is described in detail by *Stone et al.* [1998a]. The following description of the instrument and its calibration is largely based on that paper. The SIS instrument is used as an example of a high mass-resolution solid-state telescope that incorporates the determination of the trajectory of incident particles. The schematic cross section of one of two identical telescopes is shown in Figure 3.48. The first two "matrix" detectors M1 and M2 are thin

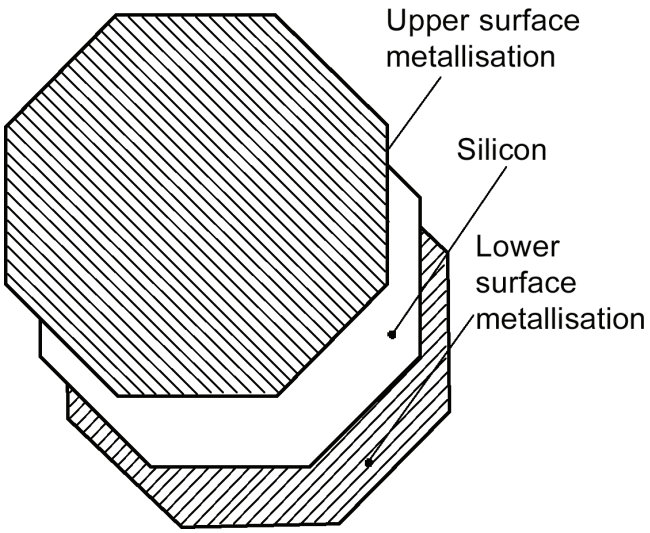

Figure 3.49: A schematic illustration of the position sensitive "matrix" detectors used in the SIS instrument to determine, with high precision, the trajectory of the incident particles. The front and back surfaces of the ∼75 μm detectors have orthogonal metallic strips; each strip is independently pulse height analyzed to locate precisely the point where the incident particle crosses the detector.

($\sim$ 75 μm) silicon detectors, each with 64 metallic strips on both sides that are at right angles to each other as shown schematically in Figure 3.49. Each of the metallic strips is individually pulse height analyzed, so that the point at which the particle crosses the detector can be uniquely determined. Using the two matrix detectors, the path of the incident particle through the telescope is therefore also uniquely determined. The angular resolution of the stack of two matrix detectors is 0.25° (rms) over all angles of incidence. Further solid-state detectors have a thickness of 100 μm (T1 and T2), 250 μm (T3), 500 μm (T4), and 750 μm (T5). Detectors T6 and T7 are made up of stacks of three and five detectors, respectively, giving an equivalent thickness of 2650 μm and 3750 μm; the outputs of the stacks are summed to give the residual energy signals in these two stacks.

The use of the $\mathrm{d}E/\mathrm{d}x$ technique requires that the thickness of the detectors used to determine the energy loss be highly uniform, or at least known to a high precision over the whole sensitive surface of the detectors, if the particle trajectory is determined through the use of position sensitive detectors. In the case of the Ulysses LET, the thickness uniformity requirement was $\sim$ 0.5 μm. For the ACE SIS telescopes, the determination of the isotopes of iron required the knowledge of the thickness to an accuracy of 0.1 %. An important calibration activity consisted in measuring the thickness of the individual detectors and/or obtaining an accurate map of their thickness over the whole sensitive area.

In the case of the detectors used in SIS instrument on ACE, the detectors' thickness was measured using two different techniques. Absolute measurements were made at the Michigan State University's National Superconducting Cyclotron Laboratory, using a ^{36}Ar beam. Measurements were made either at nine selected spots of the detectors, or, for the thicker detectors, using raster scans to obtain complete maps of their thickness. As it was

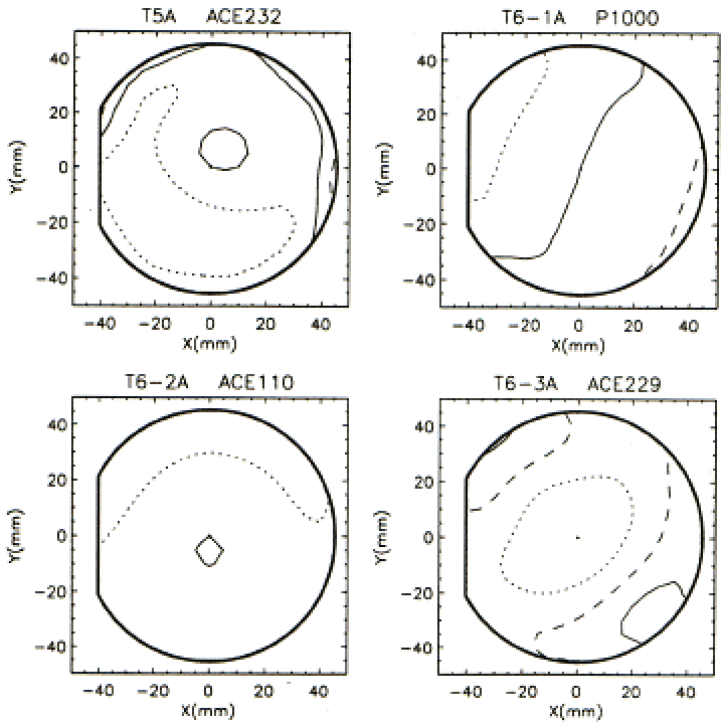

Figure 3.50: Examples of thickness profiles of the detectors used in the SIS instrument. The contours correspond to differences of 1 μm [*Stone et al.*, 1998a].

impossible to test all the detectors using the accelerator, an automated dual laser interferometer technique was also developed for mapping the detectors' thickness profile with the required precision. Examples of thickness profiles are shown in Figure 3.50. In addition to the thickness measurements, the dead layers of the detectors, effectively the electrodes on their upper surfaces, were also determined, using radioactive alpha particle sources. It was found that the dead layers, varying in thickness between 0.1 and 0.6 μm among different detectors, were generally highly uniform, with an uniformity for each detector determined to be within ± 0.05 μm.

Complete SIS flight instrument calibrations were carried out in the Gesellschaft für Schwerionenforschung mbH (GSI) accelerator in Darmstadt, Germany, using several hundred MeV/nucleon ^{18}O and ^{56}Fe ions. Calibrated absorbers were used to generate a range of energies. Polyethylene targets were also used to generate lighter elements through fragmentation of the primary ion. Figure 3.51 illustrates the results of the calibration to validate quantitatively the $\mathrm{d}E/\mathrm{d}x$ versus E technique during the accelerator runs and the clear separation of isotopes by the instrument.

While not discussed specifically in this section, the performance of mass-resolving high energy particle telescopes also depends on the performance of the signal handling electronics. The detectors in the telescopes deliver a pulse, corresponding to the charge collected in the detector as the incident particle produces a large number of electron-hole pairs in the charge-depleted silicon. The charge pulse is amplified to generate first a voltage

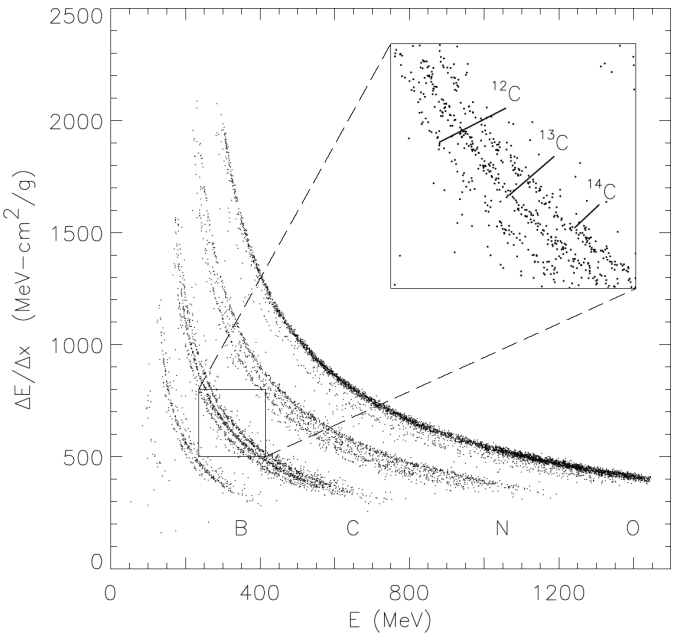

Figure 3.51: Typical calibration result for the SIS instrument, illustrating its ability to clearly resolve isotopes. The figure shows the measured energy loss in the front detectors versus the residual energy measured in the detectors that stop the particles. From *Stone et al.* [1998a].

pulse that is proportional to the collected charge. This voltage pulse is then further processed in diverse ways, depending on whether it is used directly as an input to a counting system, or in a voltage discriminator, or again if it is pulse height analyzed. It is generally possible to perform an independent electronic calibration of the signal processing chain, using calibrated high precision pulse generators. However, the accelerator calibrations described above are normally performed on the complete instrument, which is the telescope and its associated electronics. It is only in this way that the true performance of the instruments can be fully assessed. While ordinarily not a problem with high energy particle solid-state detector telescopes that are usually masked from large fluxes of low energy protons, solid-state detectors are susceptible to radiation damage and loss of performance. This is particularly true if they are exposed to large fluences of low energy protons. The origin and effects of detector radiation damage are discussed in Section 4.2.4.

3.6 Thermal Gas Calibration

Neutral gas mass spectrometers and their gas inlet systems have been described in Section 2.7. There is a substantial difference between the lower atmosphere and upper atmosphere instrumentation. The gas inlet system for lower atmosphere probes is generally more complex than the upper atmosphere instruments. The Cassini Huygens probe to Titan, with a terminal speed of 5–6 m s^{-1}, has a maximum ambient pressure about 1.5 bars

of mainly nitrogen gas [*Lebreton and Matson*, 1997]. For the Galileo probe, the ambient gas pressure was greater than 20 bars, consisting mainly of hydrogen, with a 6 mbar pressure differential between the gas inlet, near the stagnation point, and the gas exit [*Niemann et al.*, 1992]. Differential pumping and pressure reduction have been incorporated in the lower atmosphere Galileo Probe Mass Spectrometer (GPMS) and Huygens Gas Chromatograph Mass Spectrometer (GCMS) [*Niemann et al.*, 1997] instruments in order to analyze the gas at a lower pressure ($< 10^{-4}$ mbar) in the ion source. In these lower atmosphere probes, gas is also "processed" in a more complex gas inlet system. Sputter ion pumps and zirconium-graphite getters are used to maintain a lower pressure in the ion source and mass analyzer region. Ambient samples from specific altitude ranges are also selectively absorbed in enrichment cells, released by heating and analyzed directly or by gas chromatograph columns in the case of GCMS. These lower atmosphere instruments generally operate in the viscous flow range and generally use gas mixtures at the appropriate pressures for simulation of the anticipated results.

In the case of upper atmosphere instruments, which use no pressure reduction, the atmospheric gas is observed directly. To date, all of the mass spectrometers used for planetary atmosphere analysis depend on having the sample as a gas, either thermally accommodated to the inlet surface temperature or measured directly in a molecular beaming mode. Thus, for the calibration we have to reproduce the planetary atmosphere in pressure and temperature, which is the objective of this and following sections. The pressure range is generally in the free molecular flow regime so that single gases can be used for simulation. For the calibration of these instruments one uses thermal (room temperature) gas, with gas either statically contained in the chamber or dynamically flowing into and out of the vacuum test chamber. The discussion on calibration of neutral gas instruments in this book will be confined to upper atmosphere instruments.

In case of instruments on orbiters or planetary flybys, the gas is measured in the spacecraft frame of reference, which has an equivalent energy that depends on the mass of the gas molecule and the spacecraft speed. The gas speed in the spacecraft reference frame ranges from less than 1 km s^{-1} for the Rosetta comet 67P/Churyumov-Gerasimenko orbiter to as high as 68 km s^{-1} for the Giotto flyby at comet Halley. This is an energy range of the order of electron volts to several thousand electron volts. The energy range for each mission depends on the mass range that is desired to be covered and determines the instrument focusing lens potentials when a gas of that speed is being measured directly. It also dictates the gas speed needed for a laboratory simulation. Instruments of this kind have to be calibrated with a neutral beam of the needed energy. In the lower energy range, low-energy neutral beams are used, which are discussed in Section 3.7, at higher energies different techniques are necessary, which are discussed in Section 3.8.

3.6.1 The Quasi-Open Source and Thermal Gas Calibration

For the closed ion source gas inlet, a room temperature gas source can be used for the calibration with non-reactive gases (sensitivity coefficient $K(m)$, see Section 3.1.2) of a mass spectrometer in a moving spacecraft. Once the ambient gas has thermally accommodated to the gas inlet and ion source wall temperature, the gas pressure is analogous to that introduced under laboratory conditions except for possible temperature differences. Source pressures are generally below 10^{-4} mbar with a mean free path greater than 50 cm

for N_2. In this free molecular flow regime molecular collisions with the instrument (and vacuum chamber) surfaces predominate over collisions between molecules.

Tilford [1983] has reviewed many aspects of high vacuum standards and gauging. The determination of the absolute pressure of a gas in a vacuum system has been done by several different methods [see recent review by *Bergoglio and Calcatelli*, 2002]:

- Transfer standards calibrated at various institutions for the gases used:
  - Bayard-Alpert hot-cathode ionization gauges [*Santeler et al.*, 1993; *Tilford*, 1983; *O'Hanlon*, 1989]: Sensitivity depends on the total ionization cross section of the gas; cannot be used for a gas mixture without independent knowledge of the gas composition.
  - Stabil Ion Gauges, which are improved Bayard-Alpert hot-cathode ionization gauges: Absolute precisions below 10 % and repeat precisions down to 3 % are possible, with National Institute of Standards Technology (NIST) traceable calibrations [e.g. *Granville-Phillips*]. Similar systems are offered by other vendors, e.g. the IONIVAC ITR 90 [*Leybold*] or the PBR 260 [*Pfeiffer*]. Knowledge of gas composition is still necessary. *Chung et al.* [1999] calibrated two commercial ion gauges, an extractor gauge and a stabil ion gauge, and found their readings to be accurate well within the specified values.
  - Molecular Drag Gauges (MDG) or Spinning Rotor Gauges (SRG) [*Comsa et al.*, 1980; *McCulloh*, 1983]: Response depends on gas molecular weight and only slightly on accommodation coefficient; lower limit on pressure is about 1×10^{-7} mbar; accuracies are 1 % of measured value with good long term stability; cannot be used for a gas mixture without independent knowledge of the gas composition.
  - Capacitance manometers or Capacitance Diaphragm Gauges (CDG): Response is dependent on the temperature in the free molecular flow regime and gas composition in the transition flow (10^{-4} to 1 mbar) regime [*Poulter et al.*, 1983] because of differing gas molecular diameters [*Takaishi and Sensui*, 1963]; thermal transpiration effects are usually corrected by the manometer electronics readout module.
- Absolute pressure generation:
  - Dynamic flow systems [*Owens*, 1965; *Tilford et al.*, 1988; *Jousten et al.*, 1999]: Gas flows through a restriction into a chamber and is pumped out continuously; background surface outgassing is kept at same level by constant pumping.
  - Static pressure systems [*Hollanda*, 1969; *Jousten et al.*, 1993]: Small amounts of gas are added to a closed, non-pumped system; surface outgassing background continues to rise with time during the pressure run.

It should be noted that in all of these vacuum systems, the instrument sensor and electronics are mounted outside of the chamber rather than in it. This is because even small amounts of gas contamination can affect mass spectrometer neutral gas composition measurements. Many ion and electron spectrometer instruments, on the other hand, mount inside the vacuum chamber [*Ghielmetti et al.*, 1983; *Young et al.*, 1989; *Wüest*, 1999; *Steinacher et al.*, 1995; *Marti et al.*, 2001] although this is not always the case [*Erlandson et al.*, 1994].

3.6.2 Absolute Pressure Thermal Gas Systems

Absolute pressure measurements in the ultra-high vacuum range are difficult. Nevertheless, they have to be done with reference to a primary pressure standard that is maintained by national metrology institutes [see review by *Bergoglio and Calcatelli*, 2002]. A state-of-the-art example of a national primary standard for pressures in the range from 10^{-12} to 10^{-4} mbar has been realized by the Physikalisch Technische Bundesanstalt (PTB) Berlin, Germany, [*Jousten et al.*, 1999]. An earlier example of a primary pressure standard from the National Institute of Standards Technology (NIST) of the USA is described by *Tilford et al.* [1988]. Another pressure standard for pressure range from 5×10^{-9} to 2×10^{-5} mbar has been realized by the Korean Research Institute of Standards and Science (KRISS) [*Chung et al.*, 1999]. However, for calibration of mass spectrometers, i.e., partial pressure gas analyzers, on a tight time schedule these standards are not easily available nor easily duplicated and one has to rely on pressure gauges with calibrations traceable back to a primary standard.

A non-surface reactive thermal gas calibration system [*Pelz et al.*, 1973; *Spencer et al.*, 1973] was used for Atmosphere Explorer , Aeros A and B as well as Dynamics Explorer mass spectrometers, and is based on a system described by *Owens* [1965]. The system was also used to verify the calibration of reference ion gauges used for the OGO-6 (Orbiting Geophysical Observatory) and San Marco 3 mass spectrometer calibrations. The mass spectrometer was attached to a vacuum chamber with a gas inlet in the same plane as a 2.54 cm diameter knife-edged outlet orifice. A liquid helium cooled box coated with zeolite [*Powers and Chambers*, 1971], behind the orifice, provided the primary pumping during calibration and the zeolite surface facilitated pumping of helium gas at liquid helium temperatures. The liquid helium cooled surface condenses molecules coming through the entrance orifice from the vacuum chamber, preventing them from returning back through the orifice. This ensures that the pumping speed calculated from kinetic theory for the orifice is valid. The pressure ranged from 10^{-9} to 10^{-3} mbar. Two independent gas inlets, with two porous Vycor plugs, provide a binary gas mixture. The high pressure in the gas inlets is measured using calibrated capacitance manometers. Gas is admitted to either inlet by means of servo controlled valves driven by an error signal equal to the difference between the desired and actual pressure.

The main vacuum chamber pressure is determined by the balance of the gas flowing in from the high pressure inlet through the porous Vycor plugs and the gas being pumped out through the thin circular orifice [*Santeler et al.*, 1993, pp. 57–62]. The equation of continuity is

$$Q \equiv \frac{\mathrm{d}(PV)}{\mathrm{d}t} = C_{\mathrm{plug}}(P_{\mathrm{inlet}} - P_{\mathrm{chamber}}) = C_{\mathrm{orifice}}(P_{\mathrm{chamber}} - P_{\mathrm{pump}}) \tag{3.119}$$

where P is the pressure, V the volume, "inlet" refers to the high pressure gas inlet, "chamber" refers to the main vacuum chamber to which the instrument is attached, Q to the total gas flow, C_{plug} is the conductance of the porous plug, P_{inlet} is the inlet gas pressure, P_{chamber} the vacuum chamber pressure, P_{pump} the back pressure of the pump, C_{orifice} the conductance of the exit orifice A_{orifice}

$$C_{\mathrm{orifice}} = \frac{\overline{c}}{4}A_{\mathrm{orifice}} = \frac{1}{4}\sqrt{\frac{8k_BT}{\pi m}}A_{\mathrm{orifice}} = \frac{1}{4}\sqrt{\frac{8k_B}{\pi u}}A_{\mathrm{orifice}}\sqrt{\frac{T}{M}} \tag{3.120}$$

with $\bar{c}$ the average speed of the molecules [*Wutz et al.*, 2004] and u is the unified atomic mass unit[11]. Equation 3.120 evaluates to

$$C_{\text{orifice}} = 3.638\ A_{\text{orifice}}\sqrt{\frac{T}{M}} \equiv \mathcal{C}_{\text{orifice}}\sqrt{\frac{T}{M}} \tag{3.121}$$

and A_{orifice} is the area of circular orifice (cm^2), T the gas temperature (K), M the gas molecular weight (u), and C_{orifice} in units of liters per second [*Santeler et al.*, 1993, Equation 5.2]. $P_{\text{pump}} = 0$ for a liquid helium cooled surface and $P_{\text{inlet}} \gg P_{\text{chamber}}$. The plug conductance was determined by the time it took to empty a volume of a given size at a fixed pressure using a volumetric calibrator [*Peggs*, 1976].

$$C_{\text{plug}} = \frac{\mathrm{d}V}{\mathrm{d}t} = \frac{V}{T_{\text{vol}}} \equiv \mathcal{C}_{\text{plug}}\sqrt{\frac{T}{M}} \tag{3.122}$$

where V is the volume of calibrator, T_{vol} the time taken to remove volume V of gas at a fixed pressure, and $\mathcal{C}$ defined by the equations above. If the gas background is negligible and there is no change in the gas composition then the vacuum chamber pressure is

$$P_{\text{chamber}} = \left(\frac{\mathcal{C}_{\text{plug}}}{\mathcal{C}_{\text{orifice}}}\right)\sqrt{\frac{T_{\text{plug}}}{T_{\text{orifice}}}}\ P_{\text{inlet}} \tag{3.123}$$

The chamber pressure is independent of the gas mass for non-reactive gases. For the Pioneer Venus instrument the porous Vycor plugs were replaced with glass capillary arrays.

A similar calibration system has been described by *Nier et al.* [1973] but with one inlet and no zeolite covering the liquid helium cooled surfaces. Figure 3.52 shows a more recent liquid helium cooled system used by *Manning* [1995] to do thermal gas calibrations for the Return Flux Experiment (REFLEX) flown on a sub-satellite of the space shuttle. The chamber pressure calculation is the same as above. Gas inlet pressures were measured by a 1 mbar range Baratron$^{\text{TM}}$ (MKS Instruments, Inc.). The orifice diameter is 1.8 cm in diameter. The fritte conductances were determined by pressure decay of a fixed volume of gas attached to the gas inlet [*Müller*, 1967; *Manning*, 1995]. The pressure behind the leak, as measured by a capacitance manometer, is

$$P(t) = P(0)\ e^{-(C\,t\ /\ V)} \tag{3.124}$$

where $P(t)$ is the pressure at time t, $P(0)$ the pressure at $t = 0$, V the volume behind the fritte, and C being defined in Equation 3.121. A fixed volume of gas is trapped behind the fritte and the pressure observed as function of time as the gas leaks out through the fritte. The slope of the line can be solved for the conductance once the volume is known. A standard volume can be measured by weighing it, filling it with distilled water and weighing it again. Expansion of a gas at known pressure from the standard volume into connecting tubing and subsequently measuring the pressure drop can be used to determine the remainder of the volume.

Vacuum chambers are typically made of metal in the form of cylinders. Metal can be baked to a sufficiently high temperature in order to drive off absorbed water vapor and

[11] $1\ \text{u} = 1.66053886 \times 10^{-27}$ kg.

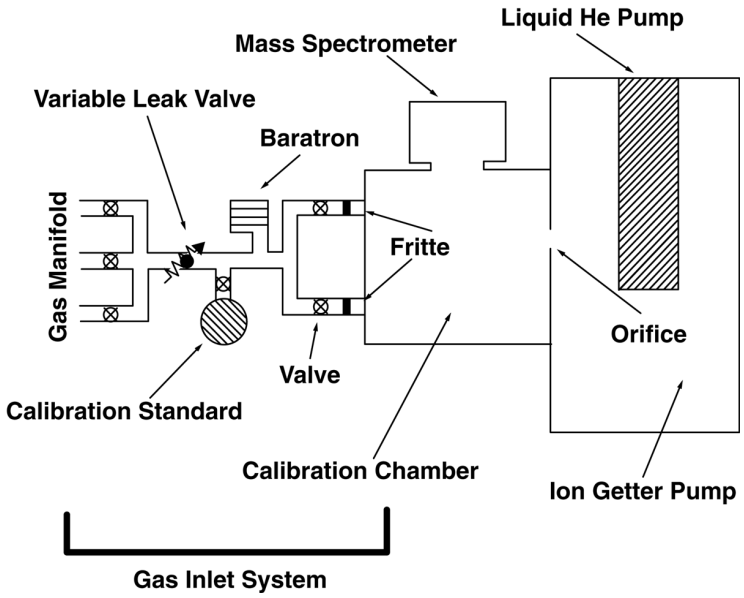

Figure 3.52: System used for the thermal gas calibration of the Return Flux Experiment (REFLEX) flown on a sub-satellite of the space shuttle in 1996. From *Manning* [1995].

other gases. A gas source in a cylindrical vacuum chamber that is in the same plane as the gas exit (pump) orifice, minimizes pressure gradients. A spherical chamber (or a cylinder of such a size as to enclose a sphere) is the best shape for a uniform flux distribution [*Santeler et al.*, 1993, pp. 28–33]. *Holland and Priestland* [1967] have evaluated a system consisting of a spherical vacuum chamber, a spherical entrance chamber for the gas and a baffled pump port. Another example is given by *Nakayama and Hojo* [1974] who used a stainless steel spherical chamber for the calibration of ion gauges. The gas was admitted into the main chamber (diameter 300 mm) through an orifice after being diffused in another smaller spherical chamber (diameter 100 mm) connected to the main chamber. The main chamber pressure was determined by balancing the gas flow into the chamber, as measured by a flow meter, and the gas flow pumped out of the chamber through a 35 mm diameter orifice.

Usually single gases are used for thermal (room temperature) gas calibrations instead of gas mixtures due to the free molecular flow regime where gases act independently of each other. Gases are best mixed directly in the high vacuum chamber or at least a mixture continually flowed past a porous plug or capillary leak and pumped out in the viscous flow regime. For mass spectrometers, a gas mixture could be important if there is an effect on the filament operation or temperature. For example, in the Earth's upper atmosphere, a pure O_2 calibration might give a different sensitivity than an 80 % N_2 and 20 % O_2 mixture because dissociation of O_2 on the filament affects the filament temperature. Moreover, ion-molecule reactions may occur in the ion source, which will be different for different gas mixtures. In this sense, it could be argued that upper atmosphere simulations should

involve gas mixtures similar to those encountered in flight, in the same vein as the lower atmosphere instruments that use gas mixtures.

3.6.3 Transfer Standard Thermal Gas Systems

Generally speaking, the use of a porous plug, capillary tube or very small holes for the gas conductance into a vacuum system with a fixed pumping speed is very reliable. The use of leak valves and other variable leak rate devices generally do not have the needed repeatability for this type of application. There is also a problem with gas mixtures and the various flow regimes (viscous to free molecular flow) that can exist in the valves at different pressures [e.g. *Westermann*, 2000; *Westermann et al.*, 2001; *Graf et al.*, 2004]. NIST vacuum systems typically use a variable leak valve that is set at a fixed value and the pressure behind the valve is changed. A large ballast volume of 8 liters is used behind the leak valve [*Lieszkovszky et al.*, 1990] and the chamber pressure measured with a spinning rotor gauge as a transfer standard. Whereas the systems described in the previous section rely on a computation of the chamber pressure for non-surface reactive gases, direct measurement of the pressure is more desirable.

In a transfer standard system the pressure in the vacuum chamber to which the instrument is attached is determined by a sensor or sensors calibrated by a separate standards institution. The mass spectrometer used on the Midcourse Space Experiment (MSX) mission evaluated spacecraft contamination [*Boies et al.*, 1994]. It was calibrated using transfer standards: a quadrupole partial pressure analyzer, SRG and two Bayard-Alpert ion gauges previously calibrated on the National Institute of Standards Technology (NIST) calibration chamber [*Boies et al.*, 1994]. The 20 cm diameter turbopump was throttled down to 1 cm by an orifice in order to reduce the effects of variable pumping speed on the chamber pressure. Since the MSX mass spectrometer was to measure water contamination, it was calibrated for this species [*Uy et al.*, 1994] using a NIST developed water source [*Tison and Tilford*, 1993] (Figure 3.53).

Like the calibrated Bayard-Alpert ion gauge, the Spinning Rotor Gauge (SRG) is also considered a transfer standard [*Comsa et al.*, 1980; *McCulloh*, 1983]. In the SRG, a small steel sphere, typically 4.5 mm in diameter, is suspended in a permanent magnetic field, spun up electrically to about 400 to 800 Hz and then is allowed to spin freely. The rotational frequency decrease measured over time is the result of momentum transfer to gas molecules colliding with the sphere (molecular drag) and losses due to eddy currents induced in the gauge head by the rotating magnetic field of the sphere (residual drag). The tangential momentum transfer coefficient between the gas molecules and the sphere surface is near unity and varies about 5 % with different gas types [*Comsa et al.*, 1980] with a long term stability of about 4 % [*McCulloh*, 1983]. Modern SRGs can be obtained with accuracies of 1 % and similar long-term stabilities so that recalibration is necessary only at intervals of 1–2 years [*MKS Instruments*]. The accommodation coefficient also depends on the surface finish of the stainless steel sphere [*Comsa et al.*, 1980]. Residual drag at the low pressure and the effect of viscosity at the high pressure limits the range to about 10^{-7} to 10^{-3} mbar. While the basic steel sphere geometry can define the SRG response, the accommodation coefficient must be determined independently from absolute pressure measurements or by comparison with a value on another SRG with a known coefficient.

Gas composition affects the pressure reading of transfer standards [*Poulter*, 1984]. Hot cathode ion gauges have different types of filament materials: typically bare tungsten or

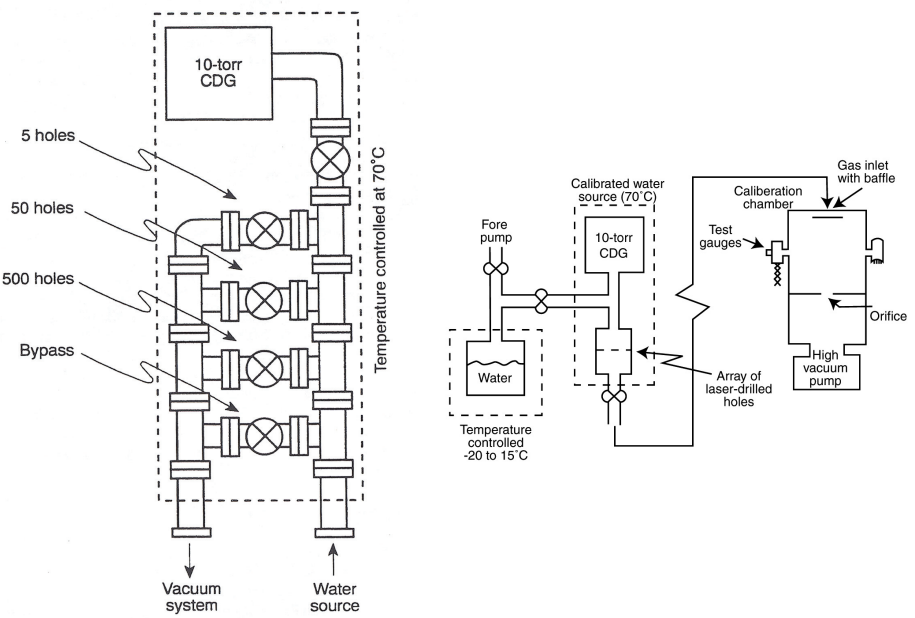

Figure 3.53: Left: The NIST H_2O vapor source. *Right:* Initial comparison of H_2O water vapor source on NIST standard calibration system. From *Uy et al.* [1994].

coated tungsten but also others. Even though the electron emission maybe the same it occurs at very different filament temperatures with different chemical dissociation rates that could give rise to different gas sensitivities; i.e., the specific gauge needs to be calibrated for the gases used. The response of the SRG depends on the molecular weight of the gas, so it is best used with a single gas. *Hinckle and Jacobs* [1993] discuss the use of a SRG for a gas mixture when the ratios of the components are known.

The SRG is useful as a measure of the vacuum chamber pressure only above its residual drag threshold. Extrapolation of the pressure below that level requires tracking the pressure on the high vacuum side with an ion gauge or tracking the higher gas inlet pressure. The latter method has an advantage that ion gauge gas products are not present which could interfere with the mass spectrometer fragmentation patterns.

Figure 3.54 shows a simple schematic of a high-pressure gas inlet source (pressure P_B as measured by a capacitance manometer), capillary leak (free molecular flow conductance C_L), a high vacuum chamber with attached mass spectrometer to be calibrated with a vacuum chamber pressure P_C, and an attached SRG (pressure P_S) with an evacuation pump (speed S). This system is used in the Goddard Atmospheric Experiment Branch with an MKS Instruments, Inc., SRG and Baratron^{TM} capacitance manometer. The conductance C_L has capillaries 5 μm in diameter, so the mean free path at 1 mbar (the maximum pressure range for P_B) is about 10 times the tube diameter. The leak operates in the free molec-

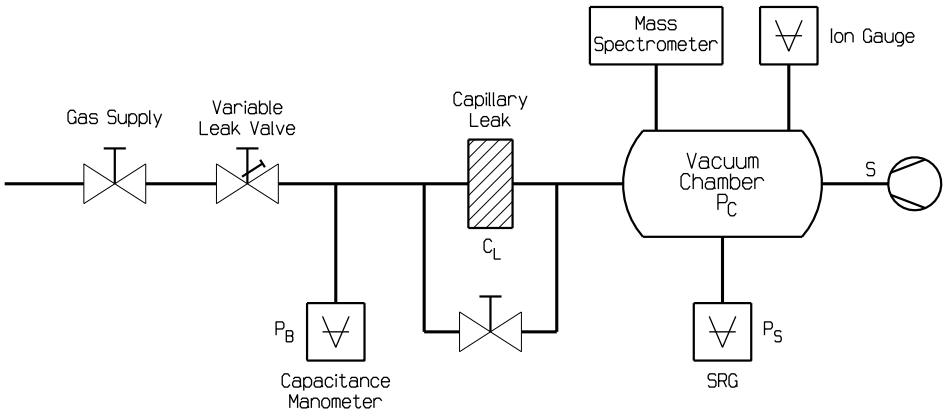

Figure 3.54: Schematic of vacuum system using a capacitance manometer as a high pressure reference (P_B), a capillary leak (C_L) as a flow restriction, a spinning rotor gauge (SRG) with a pressure measurement P_S to measure the chamber pressure (P_C) and a pump with speed of S to evacuate the chamber. The bypass valve around C_L allows pressures higher than 1 mbar to be used with the SRG as a pressure reference.

ular regime and the chamber pressure is a linear function of the capacitance manometer pressure,

$$P_C = G\ P_B \tag{3.125}$$

$$P_C = H\ P_S \tag{3.126}$$

where G and H are constants. The SRG is a transfer standard so the chamber pressure is the SRG pressure and if the pressure in the vacuum chamber is uniform then $H = 1$. At high gas inlet pressure, near 1 mbar where the SRG has valid readings, the slope G is determined from the ratio P_C/P_B. P_C is then extrapolated to lower pressures using this ratio based on the manometer reading, P_B, to lower inlet pressures. The procedure requires that the Baratron^{TM} be linear with pressure, or have a pre-determined non-linearity, and that the pumping speed, S, be constant over the period of the run. For pressures higher than 1 mbar the leak C_L can be by-passed, using only the variable leak and SRG as a pressure reference. The uniformity of pressure between the reference SRG port and the instrument port can be experimentally checked by placing the same ion gauge or SRG on one port and then the other port, and comparing the readings against the common high pressure capacitance manometer pressure used to generate the same pressure.

Figure 3.55, top panel, shows an example run in N_2 on a chamber to which the Cassini INMS engineering unit was attached along with an ion gauge and a SRG. The SRG chamber pressure reading is a linear function of the Baratron inlet pressure reading and is used to determine G (Figure 3.55, top). The chamber density is computed from the chamber SRG pressure and used to determine the mass 28 peak sensitivity (Figure 3.55, bottom). This is the gas sensitivity coefficient, $K(N_2)$, that is used in the equations for the closed source for mass 28 from N_2 (see Section 3.1.2). When the ion gauge is operating on the system it is at its lowest emission (0.1 mA) and for oxygen containing compounds or hydrocarbons it is turned off to prevent generation of gas byproducts due to the hot filaments.

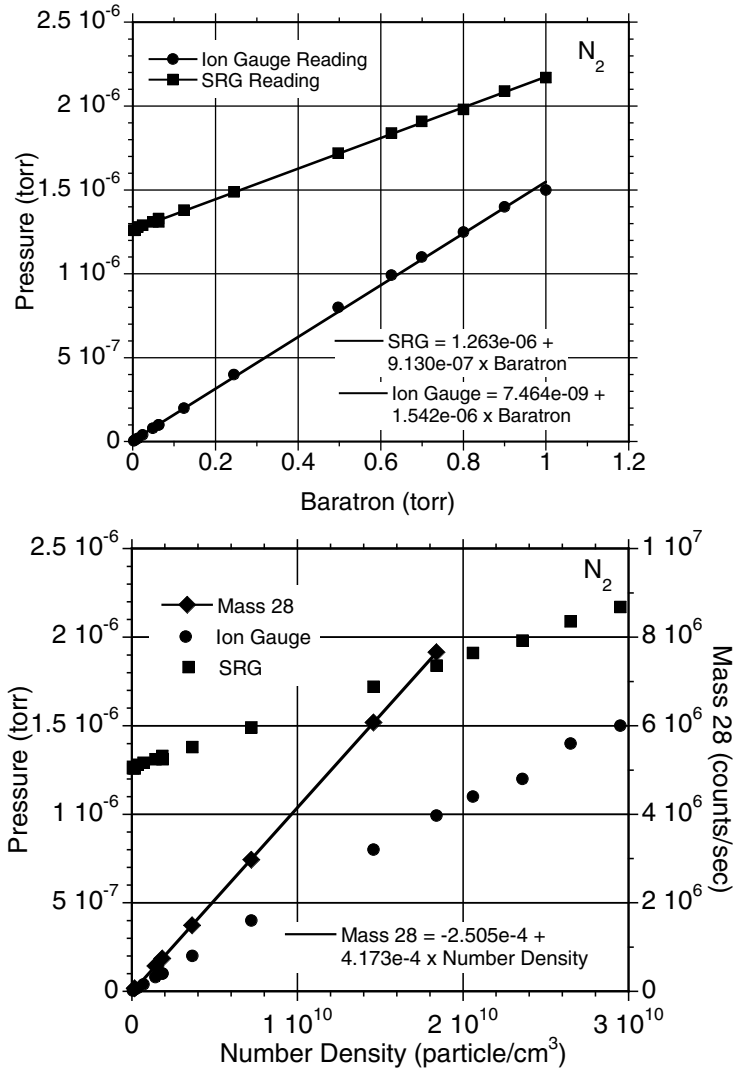

Figure 3.55: Top: Typical data from a molecular nitrogen run on a system similar to that shown in Figure 3.54. The slope of the SRG line as a function of the Baratron (capacitance manometer) reading is used to compute the vacuum chamber number density. The reading of an ion gauge connected to the chamber is also shown. Bottom: The mass 28 sensitivity, in units (counts cm^3)/(particles s), is computed from the slope of the mass 28 peak after correction for gas background and pulse counter pulse-pile-up effects.

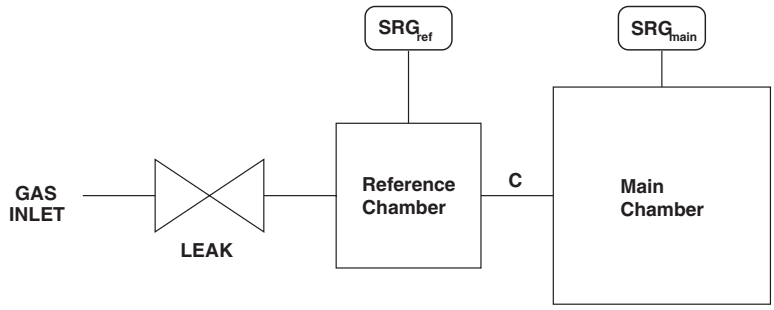

Figure 3.56: The thermal gas pressure system used for the ROSINA instruments [*Westermann*, 2000; *Westermann et al.*, 2001; *Graf et al.*, 2004]. The pressures in the reference chamber and main vacuum chamber are measured with two spinning rotor gauges and are connected with circular orifice. The ratio of the two SRG's is established with an ion gauge.

Lieszkovszky et al. [1990] used a two SRG system for evaluation of partial pressure analyzers. Direct measurement of the chamber pressure from 10^{-6} to 10^{-3} mbar was done with a SRG on the main vacuum chamber. Closing a valve with a small orifice drilled in it, allows an extension of the range from 10^{-9} to 2.5×10^{-5} mbar with the pressure being measured by an SRG on the inlet side.

Westermann [2000] has used a thermally accommodated gas system of similar design for the ROSINA (Rosetta Orbiter Spectrometer for Ion and Neutral Analysis) instrument suite calibration on the Rosetta mission [*Balsiger et al.*, 1998, 2007]. ROSINA consists of three sensors: the Double Focusing Mass Spectrometer (DFMS), the Reflectron Time-of-Flight (RTOF) mass spectrometer, and the COPS (Comet Pressure Sensor). The Rosetta spacecraft is a comet nucleus orbiter. The thermal gas calibration system is shown in Figure 3.56. The pressure in the main (lower pressure) chamber, SRG_{main}, is related to the pressure in the reference (higher pressure) chamber, SRG_{ref}, by

$$SRG_{main} = k \times SRG_{ref} \tag{3.127}$$

where the constant k is established by comparison to a Stabil-Ion^{TM} Bayard-Alpert gauge on the main chamber. A small circular orifice, C, connects the reference chamber to the main vacuum chamber with a conductance of 0.04 l s^{-1}. The pressure range is 10^{-10} to 10^{-5} mbar [*Graf et al.*, 2004].

Figure 3.57 shows a schematic of the gas inlet mixing system that can be used for either the supersonic nozzle or the thermal gas inlet system. The system provides gases or vapors from liquids (e.g. H_2O) with heated lines.

The CASYMIR system (Calibration System for the Mass Spectrometer Instrument ROSINA) used by *Westermann* [2000] includes both a neutral beam system and a thermal gas calibration system on one vacuum station. The Cassini Ion and Neutral Gas Mass Spectrometer (INMS) [*Kasprzak et al.*, 1996], the CONTOUR Neutral and Ion Gas Mass Spectrometer (NGIMS) [*Mahaffy*, 2004] and the Neutral Mass Spectrometer (NMS) on the Nozomi mission [*Niemann et al.*, 1998] were calibrated in the thermal gas mode and characterized for the neutral beaming mode with an ion beam [*Niemann et al.*, 1980a]

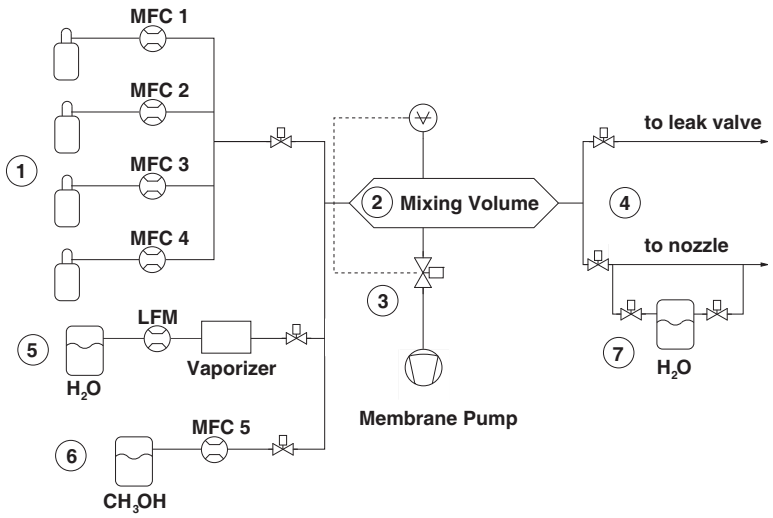

Figure 3.57: Gas mixture inlet system for CASYMIR calibration system with four mass flow controllers (MFC) and separate inlets for water and methyl alcohol [*Westermann*, 2000; *Westermann et al.*, 2001], used for the Rosetta/ROSINA instrument calibrations.

also on a single vacuum station. The INMS flight unit calibration results and current investigation are summarized in [*Waite et al.*, 2004]. Characterization of a flight unit would ideally involve a thermal gas source, an ion beam and a neutral beam ($\sim$ 4.6 km s^{-1} for Nozomi, $\sim$ 6 km s^{-1} for Cassini, $\sim$ 28 km s^{-1} for CONTOUR) all on the same vacuum station. Flight schedules are very constrained in time with calibration/characterization at the end of the development, testing and assembly process. In order to provide a surface clean instrument for calibration, a high temperature bake between 250 °C and 300 °C is needed, requiring many days turn-around. This necessitates testing and calibration on the same vacuum system without bringing the system back to atmosphere pressure.

Figure 3.58 shows a schematic of the vacuum system used to characterize the CONTOUR comet fly-by NGIMS instrument. The vacuum system uses oil free fore-pumps and turbo-molecular pumps. There are two gas inlets for thermally accommodated gas characterization, one for non-condensable gases such as Ar and one for condensable gases such as water. There is an ion gun attached to the wall of the main vacuum chamber in line with the flange on which the instrument is mounted externally. The commercial ion source is from an Extrel^{TM} residual gas analyzer. The instrument flange is attached to a bellows that can be rotated about two perpendicular axes, simulating rotation about the equivalent spacecraft axes.

A 4–500 eV ion beam was used to optimize the ion transmission in both the ion and open source neutral beaming modes of operation (Figure 3.59) with the aid of a SIMPLEX optimization algorithm [*Nelder and Mead*, 1965] using programmable high voltage supplies. The optimum voltages for each ion energy and electrostatic lens were constrained to fit a linear or quadratic polynomial so that they could be computed in real time by the flight computer. One major problem is to establish zero degrees angle relative to the incoming ion beam. This was done to first order mechanically. It was then refined with the

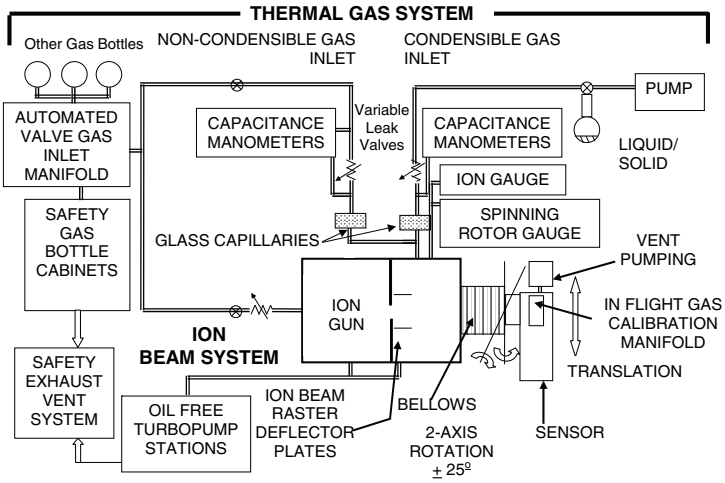

Figure 3.58: The vacuum system used for testing the CONTOUR NGIMS instrument. The instrument is mounted exterior to the system on a bellows. There are two thermal gas inlets, one for permanent gases and one for vapors. An in-line ion beam system is used to characterize the open source. The thermal gas system uses a capacitance manometer as a high pressure reference and spinning rotor gauge as low pressure transfer standard. From *Mahaffy* [2004].

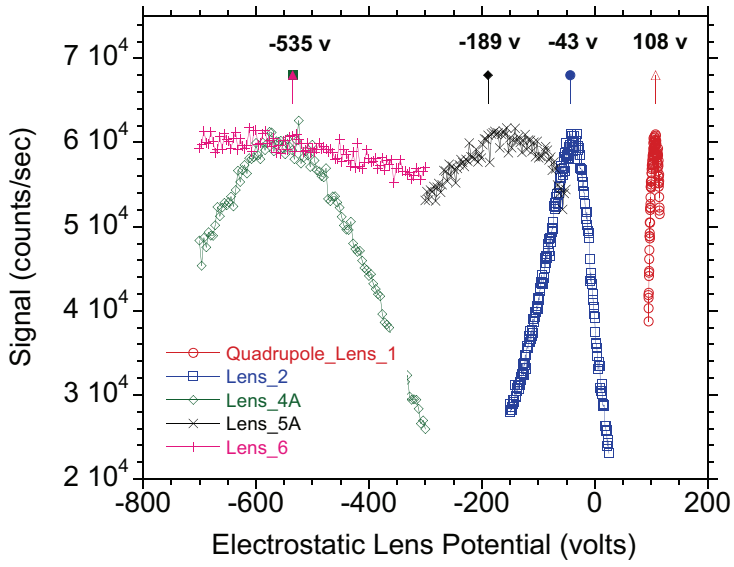

Figure 3.59: An example of ion focusing lens scans for the neutral beaming mode using a 115 eV Ar^+ ion beam. Statistical scatter of points is due the short integration period used. Marked voltages are the final, optimized, voltage values adopted. From *Mahaffy* [2004].

instrument by scanning the quadrupole switching lenses (see Section 2.7.2) as a function of angle with most of the remaining ion lenses set at ground potential for the narrow neutral beaming mode. Mass peak tuning was done using a mixture containing the noble gases krypton, xenon, argon, and helium, as well as perfluorophenanthrene ($C_{14}F_{24}$), a low vapor pressure liquid (see Section 2.7.5). The abundance of mass peaks produced by the calibration mixture allowed characterization of small non-linearities in the mass calibration scale with RF voltage amplitude.

In either thermal gas inlet (Figure 3.58) the gas pressure is measured with a capacitance manometer and the vacuum chamber pressure with a spinning rotor gauge transfer standard. The method of determining the chamber pressure has already been discussed in reference to Figure 3.54. The object of the thermal gas calibration was to determine the sensitivity and fragmentation pattern of a given gas species for each filament and ion source, and verify the linearity of the signal response with pressure. Gases used were based on expected comet species. Ion gauges on the vacuum system were turned off during the calibration with oxygen and hydrogen containing species to prevent contamination or fractionation by the gauge. Normally, the gas pressure in the chamber was increased in steps and data taken. However, oxygen was started at relatively high pressure to insure surface saturation and a few lower pressure points were taken. The vapor inlet was not heated and the relatively large surface area of the vacuum chamber plus sensor provided an adsorbing surface that did not reach equilibrium as was evidenced for water. The ionization cross-section for the production of N_2^+ (mass 28) from N_2 [*Krishnakumar and Srivastava*, 1990] should be about the same as the production of H_2O^+ (mass 18) from H_2O [*Rao et al.*, 1995]. The water sensitivity was considerable lower than that for nitrogen even after allowing the system to stabilize at high pressure. A difference for water and nitrogen was also seen in the MSX water calibration [*Boies et al.*, 1994] where the sensitivity of mass 18 from water was almost an order of magnitude lower than mass 28 from nitrogen. The NIST water source inlet was heated. Generally speaking, in the laboratory mass spectrometers use thermally accommodated gas with heated ion sources to prevent the vapors from condensing. Beaming of the water, as done by *Deckers and Fenn* [1963]; *Westermann* [2000]; *Westermann et al.* [2001], is a better solution although measuring the beam density still involves some small amount of surface area in the flux detector, assuming the instrument is operated in the molecular beaming mode. However, the flux detector must still be calibrated for thermally accommodated water vapor.

For mass spectrometers, the peak heights can change with operating conditions in the analyzer and the ion source. For the Cassini INMS calibration, the same pressure level of N_2 was used to track the mass 28 and 14 u/charge peaks over the period of the calibration. *Holme et al.* [1974] suggests using ratios such as the 20/40 ratio in Ar as a way of monitoring small changes in the quadrupole DC/AC voltage ratio. They also discuss long term data taken over a year with a small quadrupole.

The INMS sensitivity is constant up to the highest pressures used ($\sim 10^{-6}$ mbar) in the calibration procedure when the effects of pulse counter pile-up are removed (Figure 3.55, bottom). However, significant non-linearities were observed at higher pressures by *Lieszkovszky et al.* [1990] for a group of commercial residual gas analyzers operating in the 10^{-5} to 10^{-3} mbar range. *Cowen et al.* [1994] numerically simulated the response of a generic electron impact ionizer with calculations that included the effects of both electron and ion space charge, concluding that most of the nonlinearities arose in the ion source rather in the mass analyzer. Competition between negative and positive space charges leads

to either an increase or a decrease in the relative sensitivity as the gas pressure in the source is raised. It was not necessary to invoke ion-molecule scattering in order to reproduce the trends in the experimental data of *Lieszkovszky et al.* [1990]. Mass spectrometers used in the measurement of the Earth's upper atmosphere [*Hedin and Nier*, 1966] also had non-linearities in the sensitivity with increasing pressure which were empirically represented as a function of the total source number density. Thus, in order to reduce the data the total composition must be estimated and then refined to correct for this effect.

3.6.4 Gases Used for Thermal Gas Calibration

The gases used for characterization/calibration depend on the particular mission as well as the availability and toxic nature (see Appendix A.12). All of the mass spectrometer sensors described here basically ionize a gas using electron impact. Liquids such as water, formaldehyde, and methyl alcohol are still measured in vapor phase even though their parent form under normal temperature and pressure is a liquid or a solid.

It is important to use high purity gases and stainless steel gas lines with either Swagelok^{TM} or VCR^{TM} fittings. Gas bottle regulators can be purchased that allow the regulator to be vacuum pumped back to the gas bottle valve removing air contamination. A valve attached to the regulator that also connects to the system, allows gas to remain in the regulator when the tank and regulator are disconnected from the system as a unit. For toxic gases such as NH_3 or CO, a separately vented gas cabinet can be used for the bottles. For toxic gases, care must be taken to also separately vent the forepump outlets that are the exits for toxic gases. Toxic liquids and solids usually can be loaded into a volume in a fume hood, sealed, carried to the system and attached. Unlike bottled gases, such samples have air contamination. This can be removed using the freeze (at liquid nitrogen temperatures), pump and thaw method, repeated several times. Helium leak checking of the connections can be done with the sample in a frozen state with all valves open. The removal of the air contamination could be done on the same system on which it is to be used or a separate system depending on the closeness of the flight sensor to the inlet for a liquid or solid (cold liquid nitrogen vapors are not sensor friendly).

3.7 Low Energy Neutral Beam Calibration

When the relative speed of the spacecraft with respect to the planet (or comet) is in the range of the thermal speed of the gas or even more, it is necessary to reproduce this relative speed in the calibration, in addition to the temperature and density parameters of the gas. As an example, Figure 3.60 shows the elements of a classical oven (thermal) molecular beam system, with gas effusing through an orifice operating in the free molecular flow regime, and a nozzle (continuum) beam system, operating at higher pressures with gas expanding to form a hypersonic jet [*French*, 1967]. Because nozzle systems operate at much higher pressure, high speed pumping systems are needed to remove the gas to form the jet and to allow operation of lower pressure instruments. There are several types of neutral beam calibration techniques:

- Classical thermal gas oven beam,
- High pressure gas expansion,

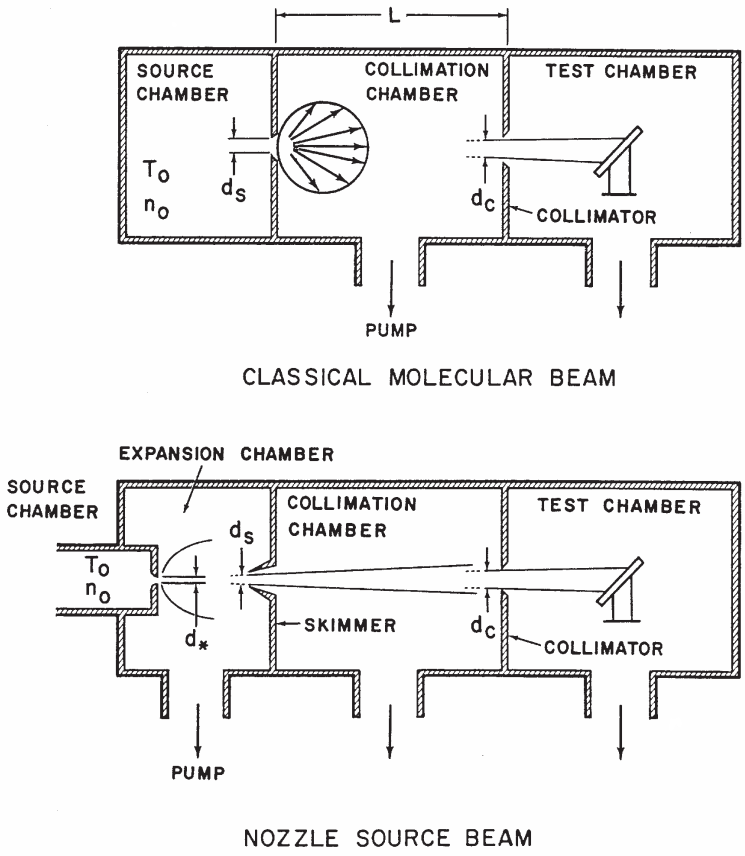

Figure 3.60: Figure showing the elements of the classical free molecular flow beam (top) and the continuum nozzle source beam (bottom). From *French* [1967].

- Atomic and molecular beams,
  - Thermal decomposition of O_2 and H_2,
  - Electron Stimulated Desorption (ESD) as a source of O from O_2,
  - Pulsed laser or supersonic arcs as a source of O from O_2 and N_2O,
  - Photo-detachment of electrons from stable negative ions,
- Specialized systems (e.g. water calibration).

The boundaries or limits for the various beam techniques are not always clear. *French* [1969] lists several: 1) classical oven source of nitrogen at 3000 K has a mean speed less than 2 km s^{-1}; 2) continuum or nozzle beam of nitrogen at 3000 K has a speed of 2.5 km s^{-1}; 3) continuum source seeded beam, 1 % nitrogen, 99 % hydrogen has a theoretical terminal speed of near 9 km s^{-1}; and 4) charge exchange nitrogen beam has a flux about one million times less than a nozzle beam, so the lower limit speed is around

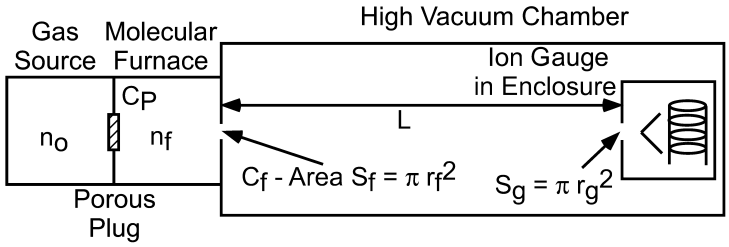

Figure 3.61: Schematic of a thermal gas molecular beam calibration system. From *Fowler and Brock* [1970].

6 km s^{-1} with no upper limit. Techniques involving photo-detachment, which will be discussed in Section 3.8.2 below, can span a larger energy range but are limited to compounds that can form stable negative ions [*van Zyl et al.*, 1976; *Stephen et al.*, 1996].

3.7.1 Thermal Gas Beam Systems

Several thermal gas beam systems have been used for absolute calibration. *Fowler and Brock* [1970] developed a molecular beam system in which a high pressure gas goes through a porous plug restriction into a second chamber (called the molecular furnace) and then goes through a circular orifice as a molecular beam into the main chamber whose surfaces are liquid helium cooled to reduce the scattered gas background and then into the instrument orifice (Figure 3.61).

The upstream pressure was measured by an absolute pressure standard, a rotating piston gauge, the porous Vycor leak was calibrated by pressure decay and the orifice conductance computed from kinetic theory with corrections for transition flow. For an ion gauge in an enclosure the number density, n_g, is given by

$$n_g = \sqrt{\frac{2m}{\pi k_B T_g}}\, C_p\, \frac{n_0}{r_f^2 + r_g^2 + L^2} \tag{3.128}$$

where m is the molecular mass, T_g the gauge enclosure temperature, C_P the conductance of the porous plug, r_f the radius of the furnace orifice, r_g the radius of gauge enclosure and L is the distance from the furnace orifice to the gauge enclosure. For a nude ion gauge, the number density in the beam, n_b, is

$$n_b = \sqrt{\frac{8m}{9\pi^3 k_B T_f}}\, C_p\, \frac{n_0}{L^2} \tag{3.129}$$

Fowler and Brock state that at ordinary molecular beam speeds, the average kinetic energy is not very different from the average ion energy in the ion gauge. Thus, the ion collection efficiency for the beam is nearly the same as for thermally equilibrated gas molecules. A similar system, shown in Figure 3.62, has been used to calibrate the Apollo Lunar Orbital Mass Spectrometer [*Smith*, 1969; *Yaeger et al.*, 1973].

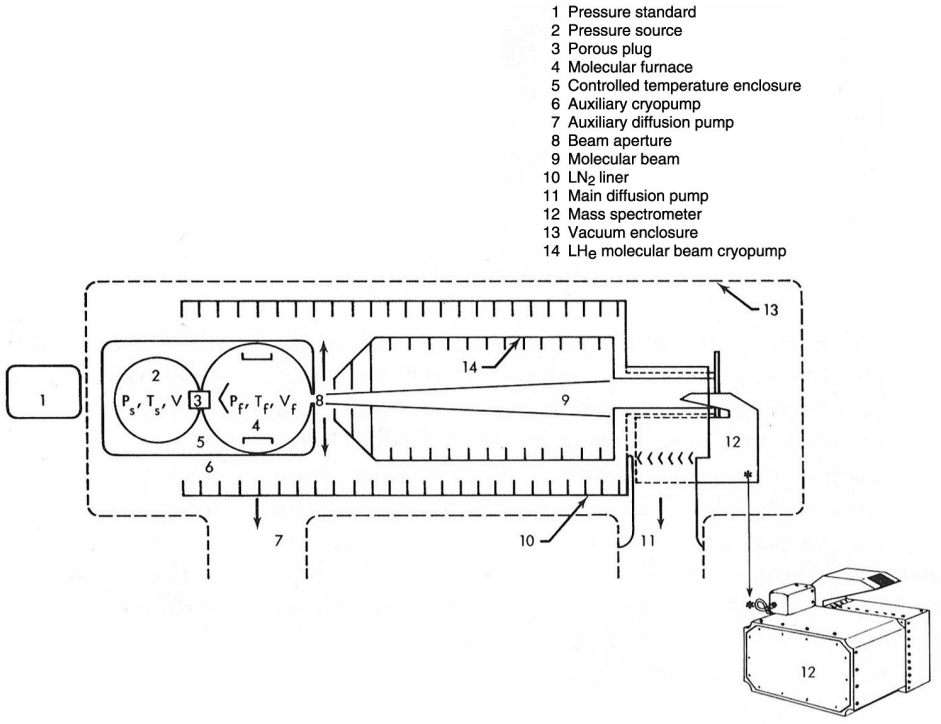

Figure 3.62: Molecular beam system used to calibrate the Apollo Lunar Orbiter Mass Spectrometer. From *Yaeger et al.* [1973].

Mauersberger [1977] presents an instrument designed for stratosphere measurements from a balloon that includes beaming of the ambient gas at 1–20 mbar pressure into a mass spectrometer, with a beam blocking flag and two stages of differential pumping using liquid helium cooled surfaces.

3.7.2 Miscellaneous Low Energy Beam Techniques

Atomic oxygen is a primary constituent in the upper atmospheres of Earth, Venus and Mars. For Earth satellites in the 200–1000 km altitude range and with an orbital speed of about 8 km s^{-1}, the hyperthermal atomic flux is near 10^{15} cm^{-2} s^{-1}. Atomic oxygen can be generated by radio frequency discharges, thermal dissociation and electron impact to generate an equivalent flux but the beam speeds may not match the orbital speeds. In Section 3.8 we will discuss methods to generate faster beams of atoms.

Niemann [1972] developed an O beam system, which is shown in Figure 3.63, to test mass spectrometer response to atomic oxygen. The atomic oxygen is generated by thermal dissociation of molecular oxygen on a hot tungsten filament at 2800 K. The beam is bi-directional so that it can be monitored while an instrument is being tested. Particle fluxes are of the order of 10^{14} cm^{-2} s^{-1} over a 1 cm^2 area with 70–90 % of the beam as O with

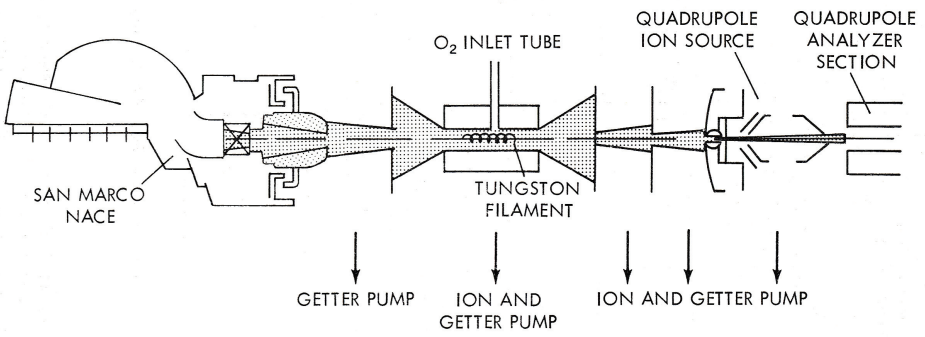

Figure 3.63: An atomic oxygen beam system based on thermal dissociation of molecular oxygen by a hot filament [*Niemann*, 1972; *Pelz et al.*, 1973b]. It was used to test the San Marco NACE instrument. A quadrupole instrument monitors the beam flux in the opposite direction. Maximum beam speed is about 2.2 km s^{-1}.

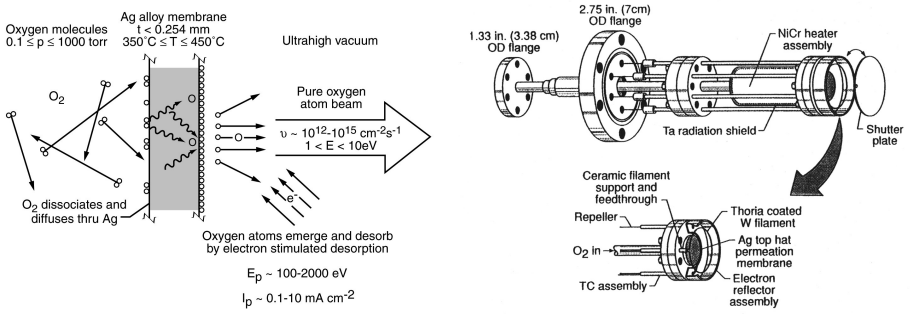

Figure 3.64: Hyperthermal atomic oxygen generator concept (left) and hardware design (right). From *Outlaw and Davidson* [1994].

an average speed of 2.2 km s^{-1}. The system was used to test the San Marco-C neutral gas mass spectrometer and a quadrupole instrument monitored the beam flux in the opposite direction. A similar O source was used to study surface reactions in the Pioneer Venus Bus Neutral Mass Spectrometer (BNMS) instrument [*Hoffman et al.*, 1980].

Outlaw et al. [1987] and *Outlaw and Davidson* [1994] describe an Electron Stimulated Desorption (ESD) source of O from silver (Figure 3.64). The membrane is Ag with 0.5 % Zr, operated below 550 °C, with several hundred mbar of O_2 upstream. The O_2 dissociates into O atoms in the silver and diffuses through the hot membrane, emerging on the vacuum side still as atoms. An incident flux of low energy electrons excite the atoms to anti-bonding states which then desorb as hyperthermal O atoms providing that the membrane temperature is not too high as to permit recombination of O atoms. The desorbing flux of O (^{3}P) is of the order of 4.5×10^{13} neutrals cm^{-2} s^{-1}). The hyperthermal neutral O has an energy 1–10 eV (mean energy is 5 eV, FWHM is 4 eV). The *Outlaw and Davidson* [1994] source maintains the Ag alloy surface at a slightly negative potential (–80 V) to prevent O^+ ions from reaching the target.

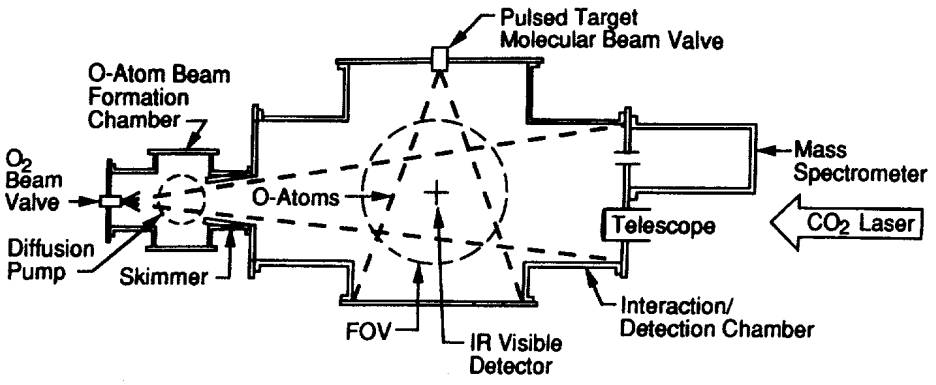

Figure 3.65: Laser pulsed atomic oxygen crossed beam system. From *Upschulte and Caledonia* [1992].

Caledonia et al. [1987] describe a technique for the generation of a high flux of O atoms with a nominal 5 eV energy (equivalent to an Earth spacecraft orbit speed of about 8 km s^{-1}). A laser-induced breakdown of molecular oxygen from a pulsed hypersonic nozzle, followed by rapid expansion of the recombining plasma, produces the O flux. The total production is about 10^{18} atoms per valve pulse with a speed of 5–13 km s^{-1}. The source was developed by Physical Sciences, Inc. (PSI)[12]. *Upschulte and Caledonia* [1992] used this source, which is shown in Figure 3.65, in a crossed-beam mode to study O-atom collisions with CO, CO_2 and CH_4. The beam monitor was a Balzers QMS311/QMA150 quadrupole with a cross-beam electron source and axial electron multiplier. The O beam is "flat" over an 8 cm radius circle 75 cm from the nozzle.

Caledonia et al. [2000] used a similar system (FAST^{TM}-2) as a source of 8 km s^{-1} N(^{4}S) to study reactions with O_2 from a pulsed valve at right angles to the energetic atomic nitrogen beam. The beam source used a 12 J per pulse CO_2 laser to heat and partially dissociate the molecular nitrogen at the exit of the pulsed valve nozzle. The laser pulse induces a plasma breakdown in the high-pressure gas region. The hot plasma gas expansion causes further dissociation of the remaining N_2 and the directed kinetic energy increases as the gas expands and cools. The nozzle limits the expansion to favor ion-electron recombination and inhibit recombination of the nitrogen atoms. The N-beam speed was measured using the N^+ recombination glow by two photomultipliers separated by 7.6 cm downstream of the nozzle. The 1 % ion beam contamination was removed using magnetic coils. Infrared emissions from the collision were measured at right angles to both beams. *Cazaubon et al.* [1996] used a similar technique for producing O and characterized the velocity distribution and flux using optical and quadrupole mass spectrometer time-of-flight measurements. A retarding system in the mass spectrometer was used to reject thermalized gas particles based on SIMION [*Dahl*, 2000] trajectory studies. The 8 km s^{-1} beam consists of 91 % O, 9 % O_2, and ppm amounts of O^+ and O_2^+.

[12] `http://www.psicorp.com/products/services_fast.shtml`

Bischler and Bertel [1993] have described an atomic hydrogen source based on the dissociation of molecular hydrogen by a tungsten tube heated to 1800–2000 K by electron bombardment. About 45 % of the beam is dissociated with a flux of about 10^{14} s^{-1}.

3.7.3 Molecular Beam Techniques

Molecular beam techniques have long been used to simulate flight through planetary atmospheres [*French*, 1967, 1969]. *Fenn* [1967] describes molecular beams in the 1–25 eV range based on various processes: ion sputtering, dipole acceleration, merged beams, mechanical acceleration and very high temperature aerodynamic or electrostatic acceleration. A general review of atomic and molecular beam methods has been given in *Scoles et al.* [1988] and *Anderson* [1974]. *Westermann* [2000] describes the molecular beam method in conjunction with the ROSINA instrument calibration system.

The supersonic nozzle technique for producing molecular beams has been described by *Deckers and Fenn* [1963]. High pressure gas from a nozzle does a free jet expansion into a chamber with a high pumping speed and a pressure of the order of 10^{-2} mbar. The beam then exits the chamber through a skimmer diaphragm into a second chamber, with high pumping speed, and a collimating diaphragm and then into a third chamber, also with high pumping speed, and with a beam detector (Figure 3.60, bottom). The flux intensity, I, is given as

$$I = \frac{A_1 n_0 v_s M}{\left(1 + \frac{1}{2}(\gamma - 1)M^2\right)^3} \left(3 + \gamma M^2\right) \frac{A_2}{2\pi d_{12}^2} \tag{3.130}$$

where A_1 is the area of the skimmer inlet, A_2 the area of the collimating orifice, d_{12} the distance between the skimmer and collimator, n_0 the number density upstream of the nozzle, v_s the speed of sound, γ the specific heat ratio, and M the skimmer entrance Mach number. The detectors were ion gauges. One had an attached tube forming a restriction that results in a greater difference between the background pressure and pressure due to the incoming beam flux. The beam intensity could be mapped by moving the detector in three directions. A beam profile for H_2O molecules was obtained.

Using a supersonic source of hydrogen or helium with small amounts of heavier molecules generates kinetic energies for the heavier molecules in the excess of 1 eV [*Abauf et al.*, 1967]. In a pure gas supersonic expansion,

$$\frac{1}{2} m V^2 \sim c_p \, (T_0 - T) \tag{3.131}$$

where V is the beam speed, m the molecular mass, c_p the specific heat at constant pressure, T_0 the source temperature, and T the final temperature in the jet. Above Mach number $M = 5$, $T \sim 0$. If there is a mixture of a heavy mass, m_h, and a light mass, m_l, then the equation for the heavier mass becomes

$$\frac{1}{2} m V^2 \sim \left(\frac{m_h}{m_l}\right) \langle c_p \rangle \, (T_0 - T) \tag{3.132}$$

where $\langle c_p \rangle$ is the average specific heat for the mixture. The translational kinetic energy is higher than the pure gas case by the ratio (m_h/m_l). In a mixed gas beam, the heavier molecules are focused along the main beam line while the lighter molecules diffuse

more rapidly away from the centerline resulting in the ratio of the heavier to the lighter mass species increasing by a factor of (m_h/m_l). Measurements were made by *Abauf et al.* [1967] for hydrogen and helium carriers with 1 mole percent of CH_4, NH_3, N_2, CO, C_2H_4, C_2H_6, H_2S, C_3H_6, C_3H_8, CO_2, N_2O, C_4H_{10}, SO_2, CH_3Br, Xe and SF_6. Beam speeds were measured using a mechanical chopper and a nude ionization gauge detector. Speeds ranged from about 1.4 km s^{-1} to 3.7 km s^{-1} for the He carrier and 1.8 km s^{-1} to 4.6 km s^{-1} for the hydrogen carrier with source temperatures ranging from 300 K to 1440 K for He carrier and 300 K to 2100 K for hydrogen carrier. Source pressures ranged from 100 mbar to 300 mbar for both carriers. When there was appreciable slip or velocity differences, individual velocities could be observed. However, going to higher source pressures helped alleviate this effect. Fluxes ranged from 10^{16} to 10^{17} molecules per steradian per second. A "pocket-model" of a binary seeded supersonic beam is given in *DePaul et al.* [1993].

French et al. [1972, 1975] describe a collaborative effort between the University of Toronto beam facility and the University of Minnesota aimed at providing ion source design information for the free molecular phase of the Martian entry mass spectrometer on Viking. The concern was 4.5 km s^{-1}, Mach number 15, CO_2 (about 3.8 eV per molecule) impacting the ion source that would need to be focused into the mass analyzer at various pitch and yaw angles in the fly-through, or molecular beaming mode, and the closed source mode. There was a need to identify traces of O or O_2 in the presence of large amounts of CO_2. Velocities of this magnitude can be produced using a high pressure and temperature gas source together with a low molecular weight carrier gas (H_2 or He) seeded with the desired atmospheric gas of interest. The free jet expansion into a vacuum converts about 95 % of the thermal energy into a directed motion of the beam. The maximum beam speed, V, can be calculated for the isentropic expansion of perfect gas from a reservoir [*Cox and Crabtree*, 1965, Equations 1.8 and 1.8a] as

$$\frac{v^2}{v_s^2} = \frac{M^2}{1 + \left(\frac{\gamma - 1}{2}\right) M^2} \tag{3.133}$$

where M is the Mach number, v_s the speed of sound in the reservoir, γ the ratio of specific heats. For high Mach number this reduces to

$$v \sim \sqrt{\frac{\gamma k_B T}{\mu} \frac{2}{\gamma - 1}} \tag{3.134}$$

where k_B is the Boltzmann's constant, T the nozzle temperature, and μ is the mean molecular mass of the beam. The lower the value of mean molecular weight, μ, the faster the beam. This is why hydrogen and helium are frequently used as carriers. If the gas carrier has a low molecular weight and is the major species, then the beam speed is close to that of the carrier alone. Free molecular diffusion after skimming and beam collimation reduces the carrier dilution to less than 50 % [*Klingelhofer and Louse*, 1964; *French et al.*, 1972, 1975]. Flags in front of the ion source are used to intercept the beam so that the local background pressure can be determined. In addition the cavity containing the instrument can be sealed with a plate (Figure 3.66, removable stagnation plate) containing a small orifice to convert it into an ideal closed source for comparison with the standard ion source response in either thermally accommodated or "fly-through" mode. The "fly-through" mode was implemented by applying a slight retarding voltage on the ion source

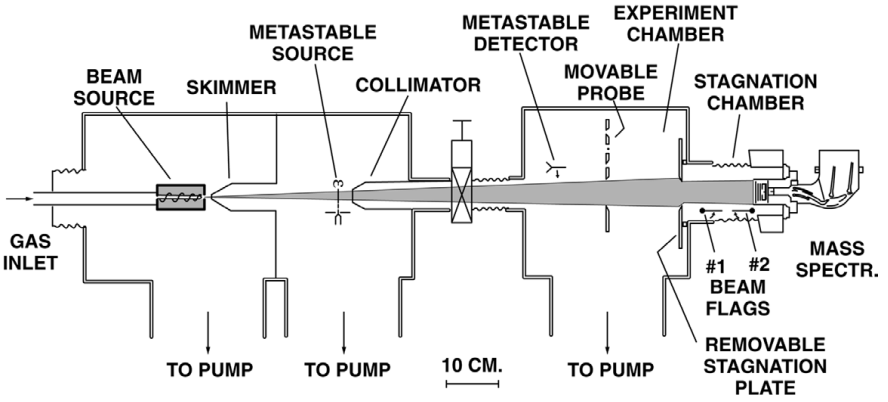

Figure 3.66: The University of Minnesota neutral beam system. From *Ballenthin and Nier* [1981].

extraction plate. The Atmosphere Explorer–C Open Source Spectrometer (OSS) used this technique to separate O and O_2 in the Earth's upper thermosphere [*French et al.*, 1975; *Nier*, 1976].

Figure 3.66 shows a schematic of the Toronto beam system constructed at the University of Minnesota as described by *Ballenthin and Nier* [1981]. The beam speed, for which a measurement is shown in Figure 3.67, was obtained using the metastable time-of-flight technique [*Locke and French*, 1970]. The beam flux can be obtained by converting the spectrometer into a closed source by use of a stagnation plate and a flag blocking the beam. The direct beam signal to background signal could be determined by placing a flag in front of the source (Figure 3.68). The instrument is placed on a bellows so that angular effects on the sensitivity can be determined. The gas inlet consists of four flow meters to generate a gas mixture with one major component (usually He or H_2) and three minor components. This system was also used to test the Pioneer Venus Bus Neutral Mass Spectrometer (BNMS) [*Hoffman et al.*, 1980] (Figure 3.69). Beam speeds of 1.6–6 km s^{-1} with hydrogen beams seeded with He, N_2 or Ar were used to compare the open source number density with the density measured in the closed source mode using the "stagnation" plate. Using the experimentally determined ratios from the neutral beam tests, the theoretically calculated closed source density, as described earlier, can be translated to the actual beam density.

The REFLEX (Return Flux Experiment) instrument is a neutral gas mass spectrometer with a semi-open source geometry designed to measure the return gas flux of gases emitted by a spacecraft [*Manning*, 1995]. It was aboard a free flyer released by the U.S. space shuttle. The REFLEX spectrometer was calibrated on an University of Minnesota neutral beam system [*Ballenthin and Nier*, 1981] since spacecraft speeds were expected to be several km s^{-1} in the Earth's upper atmosphere. The instrument has an ion source, two tandem electrostatic ion analyzers acting as energy filters followed by a Mattauch-Herzog

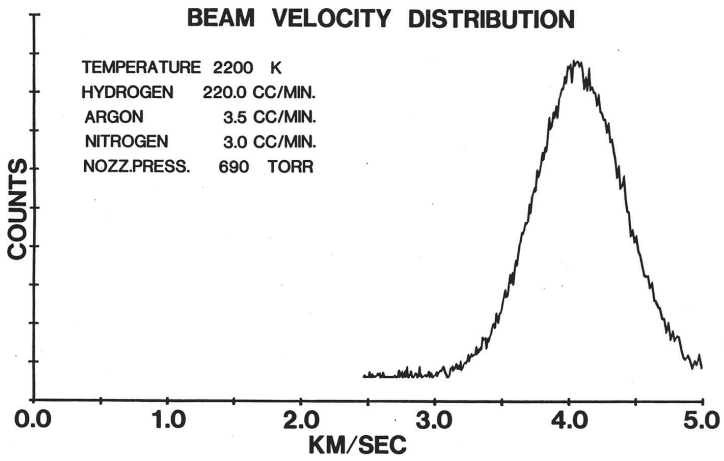

Figure 3.67: A neutral beam distribution obtained from the metastable time-of-flight system for a gas mixture of hydrogen, argon and nitrogen. From *Ballenthin and Nier* [1981].

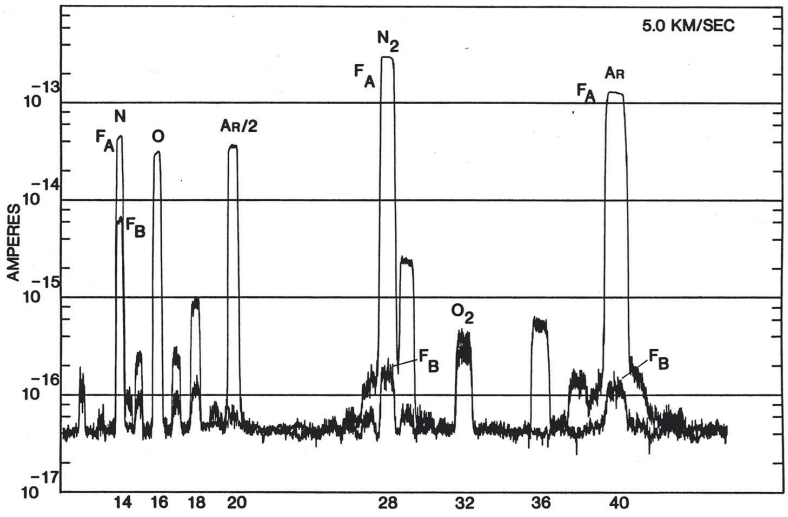

Figure 3.68: Measurements of the direct neutral beam, F_A, and the gas background, F_B, with a flag in front of the ion source. The horizontal scale is the mass-to-charge ratio in u. From *Ballenthin and Nier* [1981].

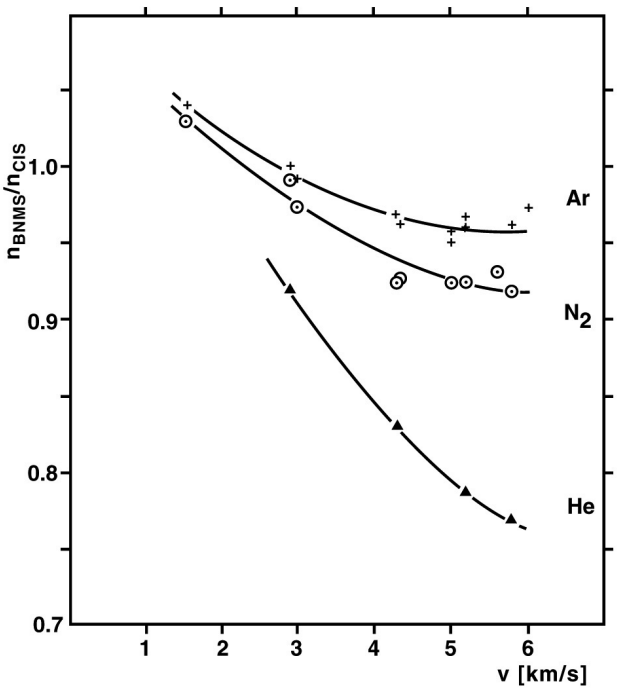

Figure 3.69: The ratio of the measured density n_{BNMS} in the quasi-open ion source to the measured density n_{CIS} in the closed ion source mode as a function of neutral beam speed with the beam direction parallel to the ion source axis. From *Hoffman et al.* [1980].

mass analyzer. To determine the neutral beam density, the flux and beam speed must be measured. Referring to Figure 3.66, the beam flux is

$$F = n_b \, v_b \tag{3.135}$$

where n_b is the number density in the beam and v_b is the mean beam speed. With the stagnation plate in place in front of the instrument and the direct beam blocked by the sensor flag, the thermally accommodated signal is measured (C measurement in Ballenthin's notation), and with the stagnation flag blocking the beam, a background measurement is taken (E measurement). The flux F is also

$$F = \left(\frac{v_g}{4}\right) \frac{(C - E)}{K} \tag{3.136}$$

where C and E are the detector output signals in counts per second, and the average molecular speed in the stagnation chamber is

$$v_g = \sqrt{\frac{8 k_B T_g}{\pi m}}. \tag{3.137}$$

K is the thermal gas sensitivity in units of (counts cm^3 particle^{-1} s^{-1}), which is defined in Section 3.1.2 above, and is determined from a previous thermal gas calibration for the

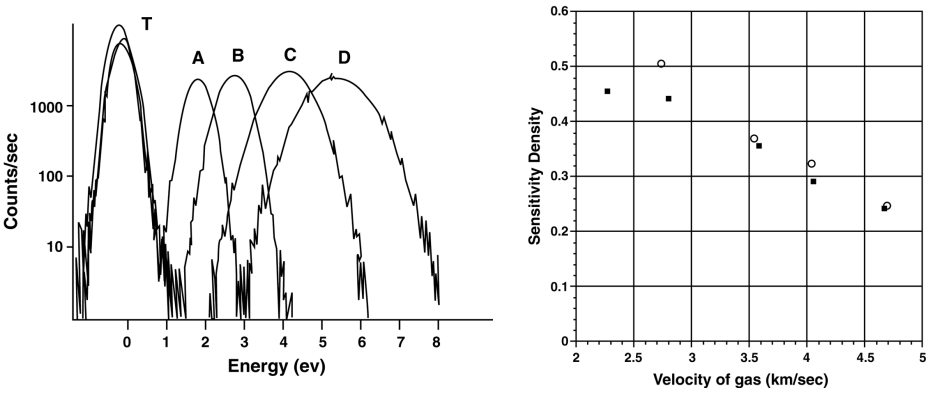

Figure 3.70: Left: Data taken with the REFLEX instrument with a Kr seeded hydrogen beam at various nozzle temperatures. The peak T is the closed source (thermally accommodated) gas present at all nozzle temperatures and the higher energy peaks correspond to various nozzle temperatures: A=25 °C, B=250 °C, C=600 °C, D=1000 °C. *Right:* Argon data for the sensitivity density ((counts s^{-1})/(part cm^{-3})) obtained from a neutral beam facility for various beam speeds on two different days. From *Manning* [1995].

sensor. The beam speed, v_b, is determined from time-of-flight measurement [*Ballenthin and Nier*, 1981] and the beam number density, $n_b(v_b)$, at speed v_b is

$$n_b(v_b) = \frac{F}{v_b} = \frac{(C-E)}{K}\frac{1}{v_b}\sqrt{\frac{k_B T_g}{2\pi m}} \tag{3.138}$$

for gas temperature T_g and molecular mass m. The beam signal is then measured with the both flags retracted (A measurement) and the background density is measured with the sensor flag in place (B measurement). The sensitivity at a given beam speed is

$$K_b(v) = \frac{(A-B)}{n_b(v)}. \tag{3.139}$$

The beam energy as a function of the nozzle temperature is shown in the left panel of Figure 3.70. The values of the sensitivity density, $K_b(v)$, obtained for Ar at various beam speeds are shown in Figure 3.70 (Right). The right panel in Figure 3.70 shows that the sensitivity density decreases from about 0.5 to 0.27 while the mean beam speed increases from 2.5 to 4.5. According to Equation 3.22 the probability for ionization is inversely proportional to the mean beam speed. In this case, the sensitivity density at 4.5 km s^{-1} should be about $0.5 \times (2.5/4.5) = 0.28$, comparable to the measured value of 0.27.

The angular response of the REFLEX instrument to a N_2 beam at 4.96 km s^{-1} was also determined. An example of the 2-dimensional angle variation for a 4.96 km s^{-1} molecular nitrogen beam is shown in Figure 3.71. As can be seen, the observed response is not uniform and is function of both angles.

The Cassini Ion and Neutral Mass Spectrometer (INMS) instrument open source can measure either ions or neutral gas coming in at the spacecraft speed [*Kasprzak et al.*, 1996; *Waite et al.*, 2004]. The calibration system used was similar to that shown in Figure 3.66

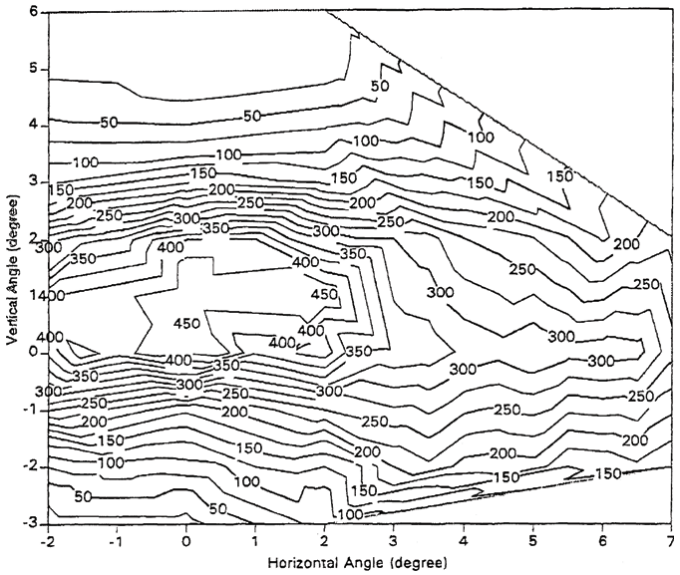

Figure 3.71: The angular response of the REFLEX experiment to a molecular nitrogen beam with a speed 4.96 km s^{-1}. The contour labels are in counts per second. The horizontal angle is the angle in the plane of the ion source, electrostatic analyzer and mass analyzer. The vertical angle is measured normal to this plane. From *Manning* [1995].

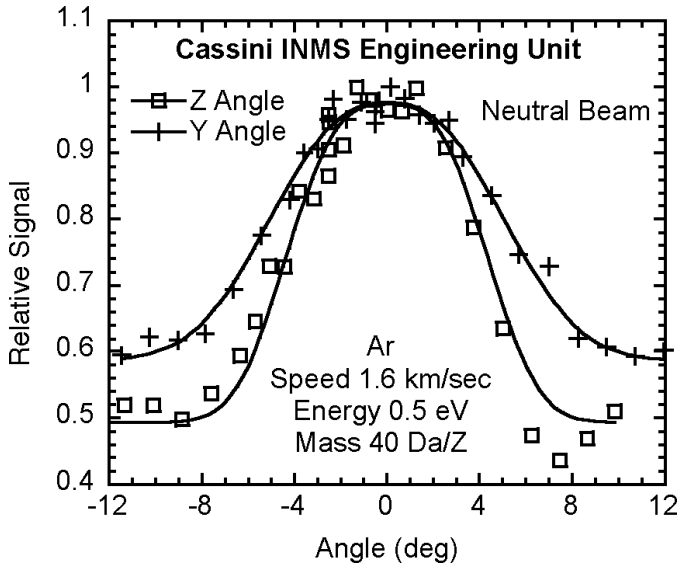

Figure 3.72: The angular response of the Ion and Neutral Mass Spectrometer (INMS) engineering unit (EU) open source to a low energy Ar neutral beam. From *Kasprzak et al.* [1996].

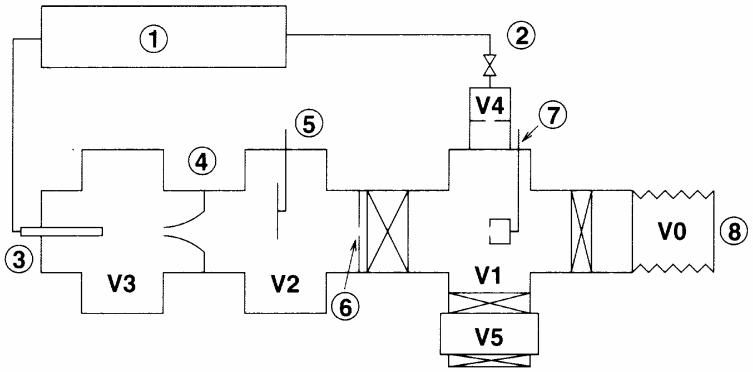

Figure 3.73: A systematic diagram of CASYMIR, showing the bellows chamber V0, the main chamber V1, the collimator chamber V2, the expansion chamber V3, the reference chamber V4 and the chamber V5 which contains a titanium sublimation pump. The other parts are: 1, gas mixing unit; 2, the leak valve used for the static mode; 3, the nozzle used in dynamic mode; 4, the skimmer; 5, the chopper mechanism; 6, the iris diaphragm; 7, the molecular beam analyzer; and 8, the docking plate for the instrument interface.

above. The instrument is mounted on a bellows outside of the vacuum system. An example of the angular response of the open source is shown Figure 3.72 for a low energy neutral Ar beam in two different orthogonal directions. The INMS open source is at right angles to the quadrupole mass analyzer with the ions being deflected by quadrupole "switching" lens. The Y angle refers to angles in the plane of the open source, switching lens and mass analyzer while the Z angle is in the orthogonal direction. For the neutral beam data were only taken on the engineering unit.

Westermann [2000] and *Graf et al.* [2004] describe a neutral beam calibration system, called CASYMIR (see Figure 3.73), very much like that described by *Ballenthin and Nier* [1981]. The thermal gas calibration system is similar to that used by *Lieszkovszky et al.* [1990]. As described earlier, the thermal gas system uses a SRG as a secondary reference standard for thermal gas calibration. The main chamber gas background is about 10^{-10} mbar. A commercial gas-mixing unit can supply up to four gases through separate mass flow controllers to either the thermal gas system or the supersonic nozzle (Figure 3.57). There are separate inlets for water and methyl alcohol (or formaldehyde, ethanol, etc.) to the main chamber inlet and a separate inlet for water vapor in the beam nozzle. The inlets for the vapors can be maintained at a higher than room temperature to prevent condensation. A mechanical beam chopper is used to measure the time-of-flight in combination with a beam analyzer. The beam analyzer consists of an Extrel quadrupole Residual Gas Analyzer (RGA) with an ion source 90° from the axis of the quadrupole and a fast ion gauge (Figure 3.74, Right). The beam density calculation is similar to that described previously. Gas speeds for the comet encounter are near 1 km s^{-1} and can be supplied by the nozzle system having a maximum flux of about 10^{15} particles cm^{-2} s^{-1}. H_2O, CO_2, CH_3OH and CH_4 were tested on the system. Neutral beam widths are determined by scanning the detector across the beam. Long term tests were run on the nozzle with Ar and H_2O which showed the beam was relatively stable over a period of 6 hours. The molecular

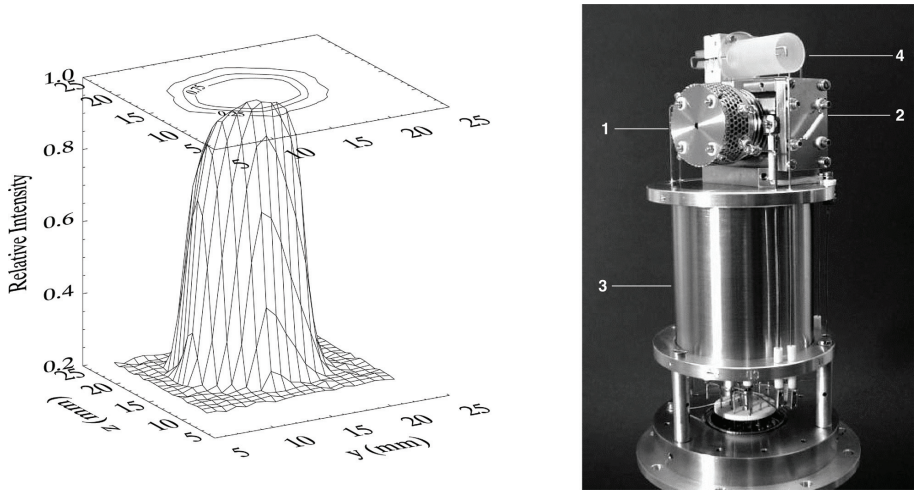

Figure 3.74: Left: Relative intensity of the CASYMIR neutral beam as a function of position. *Right:* The neutral beam analyzer consisting of a residual gas analyzer (1) and a fast ion gauge (4). From *Westermann* [2000]; *Westermann et al.* [2001].

beam nozzle was built by Thermionics, Inc., with 40 μm and 100 μm diameter holes. The collimator is a variable diameter iris diaphragm from PhiTec AG, Germany. Several time-of-flight distributions at different nozzle temperatures are shown in Figure 3.75 for beam velocities ranging from 880 to 1560 km s^{-1} [*Balsiger et al.*, 2007].

Note that the TOF distributions are for a flux detection. The differential number flux j is

$$\mathrm{d}j \sim v^3 \, e^{-a(v-v_0)^2} \mathrm{d}v \tag{3.140}$$

where v is the speed, v_0 is the mean speed of the distribution, and a is the parameter related to the beam temperature and mass. Since $v = L/t$ where L is the path length and t is the time, the time distribution is

$$\mathrm{d}j \sim t^{-5} \, e^{-a\left(\frac{1}{t}-v_0\right)^2} \mathrm{d}t \tag{3.141}$$

Stark and Kinnersley [1988] describe an atomic source using a seeded helium gas carrier generated by an arc-jet. Beam speeds are near 4.5 km s^{-1} and a beam flux of 10^{14} atoms cm^{-2} s^{-1}. Seed gases included O_2 and N_2O. *Silver et al.* [1982] used an atmospheric pressure supersonic nozzle beam source with helium and/or argon seeded with O_2 and produced beam speeds in the range 1.5–4.0 km s^{-1}. A mechanical chopper is used for time-of-flight measurements with a quadrupole mass spectrometer detector.

Brutschy and Haberland [1980] have reported helium beam speeds with 0.35 eV energy (4.5 km s^{-1}) using a high temperature (1600 K), high pressure (100 bar) supersonic gas nozzle beam. The beam speed was measured using time-of-flight with a beam flux about 5×10^{21} He atoms s^{-1} sr^{-1} and a typical speed resolution of 5–8 % FWHM. The vacuum system throughput was 2.6 Pa m^3 s^{-1}.

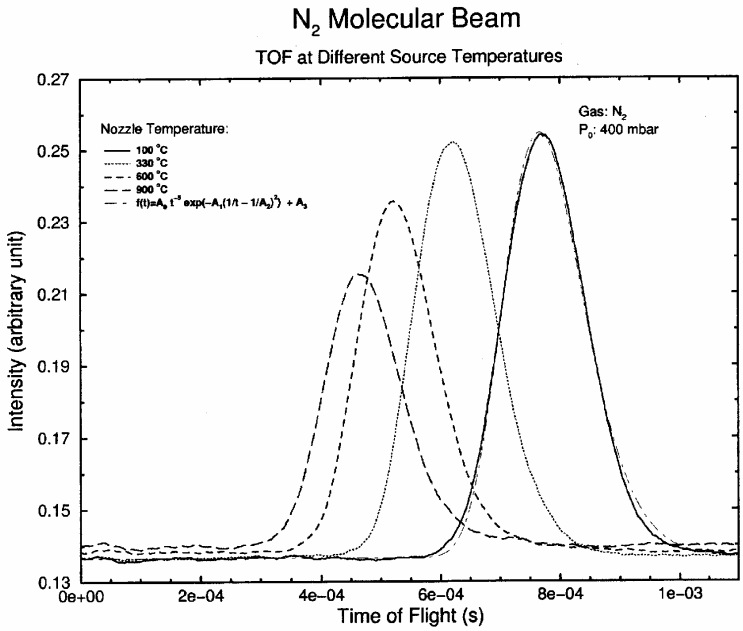

Figure 3.75: Time-of-flight signal curves obtained from the CASYMIR neutral beam system for N_2 molecular beams for nozzle temperatures of 100 °C, 330 °C, 600 °C, and 900 °C at a nozzle pressure of 400 mbar N_2. The time-of-flight path is 0.665 m [*Graf et al.*, 2004; *Balsiger et al.*, 2007].

3.8 ENA Calibrations

The energy range of Energetic Neutral Atoms (ENA) spans $\approx$ 10 eV to about 1 MeV [*Wurz*, 2000]. Sources of these ENAs are where plasma populations coexist with a neutral gas populations and charge exchange between these populations results in the creation of ENAs. Typical examples are planetary magnetospheres and these ENAs are more and more used for imaging various plasma populations of planetary magnetospheres [see review by *Wurz*, 2000, and references therein]. Other examples are the inflow of interstellar gas or comet flybys (such as Giotto and CONTOUR), which can occur at relatively high speed, and the apparent velocity of neutral particles when entering the sensor qualifies them as ENAs. The Giotto mission to comet Halley had a spacecraft speed relative to the comet of 68.4 km s^{-1} [*Krankowsky et al.*, 1986b].

Below approximately 10 eV energy we speak of thermal particles, e.g. a neutral gas, or a comet orbiter (Rosetta). The calibration of such instruments is covered in Section 3.6 above. We speak of ENAs in case of energetic neutral particles in the energy range between about 10 eV and about 1 MeV, with this range being divided into low-, medium-, and high-energy ENAs with respective instruments. This division in energy is somewhat arbitrary and originates from the different instrumentation [*Wurz*, 2000] as well as calibration facilities used in these energy regimes. Above the given ENA energy range neutral particles do not exist, at least not for a long time, because they are ionized through inter-

action with the medium they are propagating in. Note that the labeling of low-, medium-, and high-energy instruments is somewhat different for the ENA instruments than for the charged particle instruments discussed earlier [*Wurz*, 2000].

In principle, there is no fundamental difference in calibrating an instrument for energetic neutral atoms or for charged particles. The performance of ENA instruments is also characterized by a geometric factor, as defined for ion instruments in Section 3.1.1. In many cases instruments for neutral particles can be calibrated in the same way as instruments for charged particles using ion beams, only the charged particle deflection system at the entrance of the ENA instrument has to be disabled. For example the Medium Energy Neutral Atom (MENA) instrument and the High Energy Neutral Atom (HENA) instrument on the IMAGE satellite have been calibrated with positive ions [*Mitchell et al.*, 2000; *Pollock et al.*, 2000; *Henderson et al.*, 2005]. Therefore, everything which has been reported in Sections 3.3 and 3.4 also applies to the calibration of ENA instruments. The additional difficulty for ENA instrumentation is that these instruments are often imaging instruments. Since such instruments often have large geometric factors, which correspond to large entrance apertures and large image pixel sizes, a full geometric factor has to be established for each pixel [*Henderson et al.*, 2005].

Sometimes it is necessary to use a neutral particle beam to calibrate an ENA instrument. The problem of forming a neutral beam that spans the energy range from a few eV to a hundreds of keV is not simple. The main difficulties here are the production of a neutral beam at the desired energy and composition, and knowing its properties (energy, flux, spatial distribution, and so forth). Three different approaches to produce energetic neutral beams have been reported in the literature as quoted in the following sections. All these techniques start out with an ion beam, which can be well characterized, and that eventually becomes neutralized.

3.8.1 Charge Exchange Gas Cells

A fairly simple and widely used method to produce an energetic neutral beam is the use of charge-exchange between an ion beam and a neutral gas. *Utterback and Miller* [1961] investigated fast molecular nitrogen beams in the energy range 5–1000 eV. The beam flux ranged from 10^8 to 10^{10} molecules s^{-1} for this energy range. In charge exchange, an energetic ion, A^+_{fast}, collides with a thermal, e.g. room temperature, neutral gas atom or molecule, B, picking up an electron via

$$A^+_{\text{fast}} + B \rightarrow A_{\text{fast}} + B^+ \tag{3.142}$$

with A exiting as a fast neutral atom or molecule, A_{fast}. Note that this is the same process that is responsible for the emission of ENAs from planetary magnetospheres. Neutralization efficiencies as high as 10 % can be obtained provided that the suitable charge capture partners can be found (e.g. A and B the same species for resonant charge exchange). The usual apparatus is that of an ion beam facility consisting of sections for gas ionization, ion acceleration, ion selection and focusing, and finally neutralization via charge exchange. Thereby, the primary, mass-selected, ion beam of the desired energy is guided through a cell filled with a gas [*Utterback and Miller*, 1961; *Schmidt*, 1993; *Brüning*, 1996]. For the applications under consideration here preferably noble gases are used, since they are inert and will not interfere with the instrumentation. Originally, N_2 has been used to neutralize

a N_2^+ ion beam via resonant charge capture, i.e., A and B are the same species [*Utterback and Miller*, 1961]. Laboratory calibrations to determine the absolute sensitivities for the Giotto neutral mass spectrometer (NMS) used neutral beams of N_2 and Ne at 69 km s^{-1} [*Krankowsky et al.*, 1986b] generated by charge exchange. Recently, neutral beams generated by charge exchange were used for testing and calibrating components for space instrumentation [*Wurz et al.*, 1998; *Jans et al.*, 2001; *Wieser et al.*, 2002b].

The neutralization chamber is a tube in line with the ion beam having small entrance and exit orifices, filled with the charge exchange gas, followed by a set of deflection electrodes to remove the remaining primary ions, or negative ions arising from two electrons being exchanged, from the emerging particle beam. Since most charge-exchange collisions occur at large impact parameters and only single collisions occur, a negligible change in direction and energy of the primary ion, then energetic neutral, occurs. Geometrical dimensions and pressure inside the gas cell have to be such that the probability of an ion hitting a gas atom is significant, preferably close to one. Since the pressure in the vacuum chamber has to be kept below a certain level, only small apertures for entering and exiting of the beam can be used. Also, the limiting pumping speed of the vacuum system sets an upper limit for the cell pressure. Typical cell pressures are some 10^{-5} mbar. Under optimal operation conditions neutralization efficiencies of about 10 % can be achieved [*Schmidt*, 1993].

Knowing the precise neutralization rate and flux of neutral atoms is difficult, since it depends on a pressure measurement in the charge-exchange cell. Product ions can be collected in the neutralization chamber with a Faraday cage for a measurement of the total charge B^+. Another method to characterize the beam flux is to compare the secondary emission from the surface produced by the neutral beam with that produced by a known ion flux assuming comparable emission coefficients. This still does not characterize quantum state although this is not important for calibrations of ENA instrumentation.

Alternatively, instead of the gas cell the charge exchange can be realized with a molecular beam from a nozzle oriented at right angles to the fast ion beam with energies in the range of 500 eV to 1500 eV [*Devine et al.*, 1963]. The flux detector was an ion gauge with a narrow entrance orifice on a movable carriage and a time-of-flight detector was used for the neutral beam speed.

3.8.2 Photo-Detachment Sources

Photo-detachment of an electron from negatively charged ions is an elegant way to produce an energetic neutral beam [*van Zyl et al.*, 1976; *Stephen et al.*, 1996; *Stephen and Peko*, 2000]. Negative ions are extracted from a modified Colutron^{TM} ion source, typically at $1000\,eV$ beam energy and the species of interest is selected by a Wien filter. A schematic drawing of the experimental apparatus is given in Figure 3.76 (left). The ion beam is then bent by 9° to remove neutral particles produced upstream of the beam (see Figure 3.76, right). Ion-optical focussing and final energy setting occurs just before the photo-detachment region. Photo-detachment is realized with a strong argon-ion-laser (Spectra Physics 2040E, typical wavelengths 488–512 nm, kW level power). Ground state $O(^3P)$ is produced from O^- by using photons with an energy less than 3.43 eV (wavelength greater than 361 nm). At the available laser intensities the neutralization is in the percent range, the remaining ions are removed electrostatically from the beam into an ion collector. Hydrogen and oxygen beams with energies from $4\,eV$ to $1000\,eV$ have been

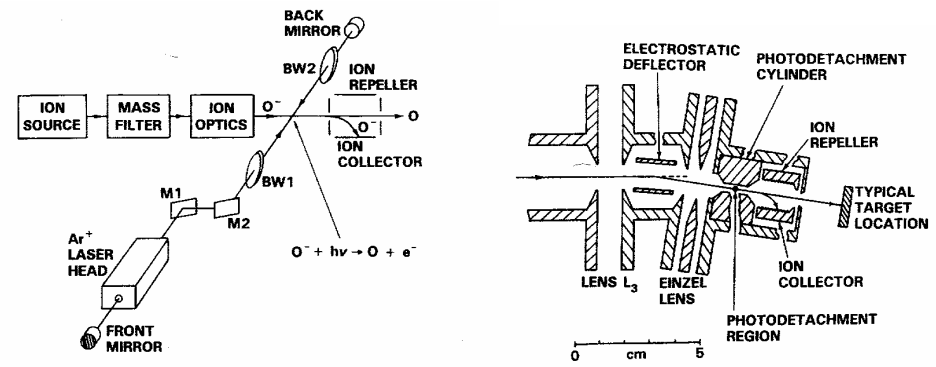

Figure 3.76: Left: Schematic of University of Denver O^- photo-detachment system for producing neutral O atoms. *Right:* Schematic of lens system and window for laser beam source. From *Stephen et al.* [1996].

realized, with an energy spread of $1.5\,eV$ given by the ion source. Beam intensities are up to 10^{11} atoms s^{-1}. The beam flux scales as the square root of the inverse velocity for photo-detachment efficiency. The beam intensity is measured by chopping the laser beam that results in a modulation of the measured current in the ion collector. With a lock-in amplifier system the amplitude of this current modulation can be measured, which is the neutral beam intensity. This facility was used for calibrating the Low-Energy Neutral Atom (LENA) imager of the IMAGE mission [*Moore et al.*, 2000] with the instrument mounted on a two-axis turntable in a vacuum chamber that intercepted the neutral beam of either ground state H or O. In addition, the facility was used for the absolute calibration of microchannel plates for H, H^-, H^+, H_2^+ and H_3^+ [*Peko and Stephen*, 2000] and O, O^- and O^+ [*Stephen and Peko*, 2000] in the energy range 30–1000 eV. The major drawback of the photo-detachment technique is that it is limited to compounds that can form stable negative ions.

3.8.3 Surface Neutralization

When ions are scattered off solid surfaces at shallow angles of incidence specular deflection of incoming beam will result if the surface is sufficiently flat on an atomic scale, i.e., surfaces with a roughness of ≈ 1 nm_{rms} and better. In addition, charge exchange reactions between the projectile and the metal surface will take place, especially Auger neutralization, resonance neutralization, and quasi-resonant processes, resulting in an efficient neutralization of the scattered particle [*Eckstein*, 1981]. The small angle deflection ensures a sufficiently long time for charge exchange, thus guaranteeing an efficient high neutralization rate of the projectile ions. Typically, the neutral fraction in the scattered particles is close to 100 % [*Eckstein*, 1981]. Surface neutralization works well for almost all elements as long as the ionization potential of the projectile atom is larger than the work function of the surface. If this is not the case, e.g. for scattering of alkali ions from surfaces, neutralization yields may drop to about 10 %, thus reducing the fluxes available for calibration.

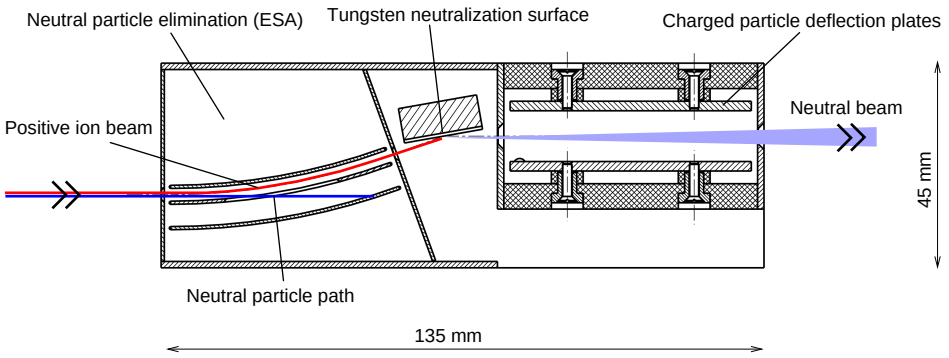

Figure 3.77: Cross section of the ion beam neutralizer used at the University of Bern, Switzerland [*Wieser and Wurz*, 2005; *Wieser*, 2005].

Therefore, surface scattering can be used to design a simple ion beam neutralizer, which allows the use of a conventional ion beam facility as a neutral beam facility. Neutral atomic beams can be produced for every species for which an ion beam can be generated with the available neutral particle fluxes being about the same as the initial ion fluxes (see above). One needs metal surfaces highly polished to a roughness of less than 1 nm_{rms}, preferably single crystals, with small atom spacings at the surface are desired. Furthermore, to optimize scattering in azimuth angle one wants to avoid alignment of the ion beam direction with a low-index crystal orientation [*Losch and Niehus*, 1999a]. Such a neutralizer can be built relatively small, is easy to operate and even can be made portable to other ion beam facilities or be attached to the instrument to be calibrated. Moreover, no extra pumping is required unlike gas neutralization cells. The disadvantage of this technique is that energy loss will occur as a result of the scatter process and the resulting neutral beam will have some angular divergence and energy spread, which have to be known to interpret the calibration results.

Recently, *Losch and Niehus* [1999a, b] used a Pt(111) surface to convert an ion beam into a neutral atom beam for surface science studies in an UHV environment. They used a grazing angle of incidence 4.5° for the particle scattering. Any remaining ions are removed by an ion deflector. The energy loss in this setup was about 100 eV with an energy spread < 40 eV for 3 keV He scattered from a Pt single crystal [*Losch and Niehus*, 1999a]. Going to larger angles of incidence will cause larger energy loss and larger energy and angular scatter.

Such an ion-beam neutralizing system was developed for the ion calibration facility at the University of Bern (see Appendix A.4.2) [*Ghielmetti et al.*, 1983; *Steinacher et al.*, 1995]. The neutralizer system, uses an electrostatic analyzer to deflect the ion beam onto the neutralizing surfaces. Before entering the electrostatic analyzer the ions are decelerated to the desired energy for calibration. A schematic drawing of this neutralizer is shown in Figure 3.77 and a photograph of the whole system in operation is shown in Figure 3.78 (see also Appendix A.4.2 for more information). The ion deflection serves two purposes. One purpose is to remove a possible neutral component in the ion beam, and the second purpose is that this neutralizer design only causes a lateral displacement of the beam, but not a change in beam angle with respect to the incident ion beam. The latter is important,

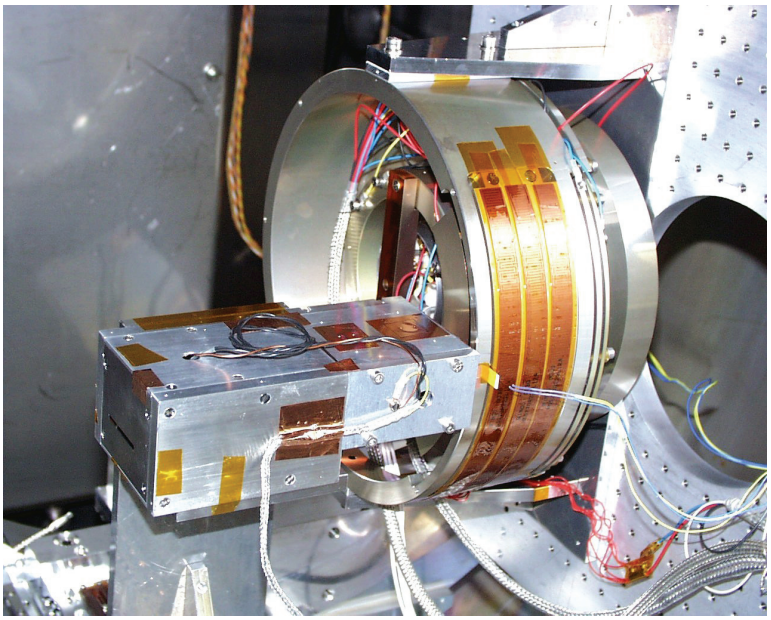

Figure 3.78: Ion beam neutralizer, the rectangular box in the center, is installed in the CASYMS calibration facility of the University of Bern, Switzerland [*Steinacher et al.*, 1995]. The ion beam comes from the left and enters the narrow rectangular slit of the neutralizer. The installed instrument is the IBEX-Lo prototype [*Wieser and Wurz*, 2005; *Wieser*, 2005] for IBEX mission [*McComas et al.*, 2004].

since the instrument accommodation and movement inside the calibration chamber are designed for the ion beam direction. The neutralization surfaces that are used are a set of highly-polished single-crystal tungsten (110) plates. Particles scattered off the surfaces have to pass ion-deflection electrodes, removing all remaining charged particles, before they exit through an aperture from the neutralizer unit [*Wieser and Wurz*, 2005; *Wieser*, 2005]. The beam neutralizer is small and therefore can be moved easily to an other ion-beam calibration facility. It was used for calibration of a prototype ENA instrument for the detection of the interstellar gas [*Wieser et al.*, 2002a, 2005].

3.9 Cross-Calibration between the Flight Model and Laboratory Model

Occasionally, a second instrument (a flight spare or a laboratory instrument) is used in calibration as a proxy to simulate the flight instrument under conditions similar to the space environment as an aid for the interpretation of flight sensor results. To do that, i.e., to transfer the calibration from one instrument to another, one needs to cross calibrate the flight instrument with the proxy instrument sufficiently well to ascertain that both have the same performance or to understand the differences between them in sufficient detail. Cross-calibration basically means that the flight instrument and the proxy undergo the

same calibration procedure. Once a cross-calibration has been established calibration results from one instrument (typically the proxy instrument) may be transferred to the other instrument (typically the flight instrument). At best, these differences are found in calibration before launch to avoid surprises, at least it has to be foreseen to perform the same calibrations with the proxy instrument after launch.

The need to transfer a calibration arises, for example, when the time for a complete calibration of the flight instrument is not sufficient, which does happen regularly because of the often tight delivery schedules, and the calibration is completed with a proxy instrument. Also, the transfer of calibration becomes necessary when conditions in space occur that had not been anticipated before launch and thus were not covered by the flight instrument calibration. A typical example is a different thermal environment in space where the instrument is operated at temperatures much higher or lower than in the laboratory calibrations. Sometimes an instrument unexpectedly delivers a signal for a stimulus it was not designed for nor intended for, like the fortuitous measurement of iron ions in fast solar wind streams. For the quantitative interpretation of these measurements a calibration of the backup instruments had to be performed and applied to the data collected during flight [*Mitchell and Roelof*, 1980; *Mitchell et al.*, 1981]. Other, more specific examples, are given in Sections 3.9.1 to 3.9.3 below. A time varying response of the instrument, e.g. because of aging or exposure, can be assessed by using a proxy on ground with which these effects can be duplicated and thus a time- or exposure-dependent calibration can be established. Such effects are not investigated with the flight instrument for obvious reasons. Moreover, in case of a discovery, one typically lacks a suitable calibration and then a post-launch calibration with a suitable proxy is necessary.

In the ideal case for the transfer of a calibration a flight model and a flight spare model are available and are cross-calibrated well. The flight model is the instrument which is actually on a spacecraft collecting in space the scientific data to be interpreted. The flight spare instrument remained on ground, and is, ideally, identical to the flight instrument. If available, the flight spare instrument is fully qualified to be used in space instead of the flight model should that need occur. Often the flight model and the flight spare model are built almost at the same time. In principle these two instruments should be identical, but in practice this is rarely fully accomplished because of the complexity of modern instruments and the small number of units being built. Interestingly, the designated flight spare instrument (during hardware phase) is sometimes the one actually used in space (thus becoming the flight instrument) and the designated flight instrument stays on ground (thus becoming the flight spare). Occasionally, the flight spare model is called backup model, and sometimes this designation indicates that it is only almost as good as the flight instrument.

When a flight spare instrument is not available a laboratory model is often used for the transfer of calibration. The term laboratory model may cover a wide range of instrument workmanships, from a real flight spare instrument, to an engineering model (flight-like in performance but not flight quality hardware), or even a prototype. Transfer of calibrations between a flight instrument and a laboratory instrument can be done to an extent depending on closeness to the actual flight instrument with a cross-calibration that maps out the differences well. Typically, some sub-components of the laboratory instrument are flight-quality or flight-like (in terms of performance) and a calibration on component level may be transferred from the laboratory model to the flight model (e.g. detectors or power supplies). This assumes that the instrument response function can be factorized to a level where the cross-calibration of a component or sub-unit is independent of the remaining

instrument performance. A particle detector is a typical example for cross-calibration on the sub-unit level.

3.9.1 Solar Wind Instrumentation

An example for the transfer of calibration from the flight spare to the flight instrument is the MTOF sensor of the CELIAS instrument [*Hovestadt et al.*, 1995] of the SOHO mission, which measures the solar wind elemental and isotopic composition. For the interpretation of data from the MTOF sensor, calibrations for some solar wind species were done after launch of SOHO because the MEFISTO calibration facility was not yet capable to provide these species before launch of SOHO. This calibration was performed later using the MTOF flight spare sensor once the upgrade of the calibration facility was accomplished [*Marti et al.*, 2001]. Since the flight sensor and the flight spare sensor of MTOF were calibrated at this facility the two models and their differences were well understood, and the calibration could easily be transferred from the flight spare to the flight sensor [*Wurz et al.*, 2003].

Actually, calibrations of flight spare instruments after launch, which are then transferred to the flight instrument, are quite common in this research field. The flight spare of the SWICS instrument was calibrated thoroughly for the measurement of ^{3}He at the University of Bern long after the launch of the Ulysses mission [*Bodmer*, 1996]. This calibration was then used for the SWICS instrument on the Ulysses spacecraft for the successful interpretation of the ^{3}He data [*Gloeckler and Geiss*, 1998].

Similar plans exist for the PLASTIC instrument of the STEREO mission [*Galvin et al.*, 2006; *Blush et al.*, 2005]. STEREO was launched in October 2006. The two PLASTIC flight units have been calibrated at the University of Bern. Since one rarely has a complete set of calibration data it is planned to join the flight spare entrance system with the EQM TOF section and electronics to get an instrument that performance-wise is very close to a flight spare instrument.

3.9.2 Cometary Instrumentation

On the Giotto mission both mass spectrometers, the Ion Mass Spectrometer (IMS) [*Balsiger et al.*, 1986] and the Neutral gas Mass Spectrometer (NMS)[*Krankowsky et al.*, 1986a] are examples of successful post-launch calibrations using flight spare instruments, which were considered identical to the flight instruments. For IMS the time before launch was too short to perform a full calibration, which then was performed after launch using the identical flight spare instrument [*Meier*, 1988a]. The NMS flight spare instrument was used to calibrate the detection efficiencies for ions at $m/q = 28$ arising mainly from ionization of N_2 and CO at different electron energies in the electron-impact ion source of NMS [*Meier*, 1988b]. These data were used for the interpretation of the NMS data collected during comet Halley encounter [*Eberhardt et al.*, 1987].

For the two mass spectrometers of the ROSINA instrument [*Balsiger et al.*, 2007] on the Rosetta mission it is even necessary to have and maintain flight spare sensors for the entire mission duration since these mass spectrometers will perform measurements in mass ranges exceeding that of previous cometary missions by far and ground-based observations are limited as well. Thus, it is difficult to design a calibration program that completely covers the measurements to be done at the comet. Moreover, the Rosetta spacecraft will be

placed very close to the comet, down to a few cometary radii at best, which is deep inside its atmosphere, and the physical conditions may be different from what we now think they are. In addition to the flight spare sensors this also necessitates the upkeep of the dedicated calibration facility [*Graf et al.*, 2004]. This is particularly challenging since the launch of the mission was 2 March 2004 and the arrival at the comet 67P/Churyumov-Gerasimenko is planned for May 2014, thus the sensors, the calibration facility and the know-how have to be preserved for more than ten years.

3.9.3 Pioneer Venus ONMS Backup Sensor Calibration

The Pioneer Venus (PV) Orbiter Neutral Gas Mass Spectrometer (ONMS) [*Niemann et al.*, 1980a] was designed to perform neutral gas composition measurements in the thermosphere of Venus [*Niemann et al.*, 1980b]. The flight instrument (the Flight Unit, FU), was calibrated for CO_2, O_2, N_2, Ar, and He. Atomic nitrogen was discovered to be present in the upper atmosphere [*Kasprzak et al.*, 1980] and in the instrument it was measured as NO, resulting from the recombination of atomic nitrogen with atomic oxygen on the ion source surfaces. CO, also present in the upper atmosphere of Venus, and NO contribute to the electron impact fragmentation at mass (short for mass per charge) 14 along with molecular nitrogen. Post launch calibration of the backup instrument, referred to as DVU (Design Verification Unit), was done to estimate the fragmentation ratios for CO and NO. The sensitivity values (in units of [(counts cm^3)/(s particles)]) for the major fragmentation mass peaks of CO (mass 28) and NO (mass 30) were estimated separately from their ionization cross sections relative to the ionization cross section of mass 28 from N_2 [*Kieffer and Dunn*, 1966] and the known sensitivity of mass 28 from N_2 for the FU. Figure 3.79 illustrates the procedure for determining the fragmentation ratios of CO and NO relative to the major mass peak using the DVU. With the sensor set in its normal "tuned" (maximum sensitivity) state, mass peak ratios of 14/30 and 16/30 due to NO, 12/28, 14/28 and 16/28 due to CO and 14/28 from N_2 were measured (circles in Figure 3.79). The next step involved changing ("detuning") the electrostatic focusing lenses between the ion source and the entrance to the quadrupole mass analyzer such that 14/28 ratio for N_2 was reduced from 0.11 to 0.082 (squares in Figure 3.79), closer of the FU value of 0.073 (symbol "X" in Figure 3.79). The ratios between the normal "tuned" state and the "detuned" state were then used to estimate the fragmentation ratios for the FU CO and NO (filled diamonds in Figure 3.79) based on the desired FU 14/28 ratio for N_2 (symbol "X" in Figure 3.79).

3.9.4 Cassini IMNS Backup Sensor Calibration

The Cassini Ion and Neutral Gas Mass Spectrometer (INMS) [*Waite et al.*, 2004; *Kasprzak et al.*, 1996] has been making measurements of low energy neutral gas and ions since orbit insertion around Saturn in July, 2004. The limited calibration data for the flight unit (FU) has been augmented by additional data obtained from the backup engineering unit (EU) in the laboratory. Calibration gases for the FU were N_2, Ar, He, H_2, Kr, CH_4, C_2H_4 and C_2H_2 in 1997. The EU calibration gases included those for the flight unit and added Ne, O_2, CO, CO_2, C_2H_6, C_3H_8 and C_6H_6 in 1998. Another calibration in 2006 includes exotic gases such as HCN and C_2N_2. Since the two units were not identical, for each filament and electron energy, the sensitivity of the major mass spectral peak of a gas was normalized to the major peak sensitivity of N_2, removing first order differences

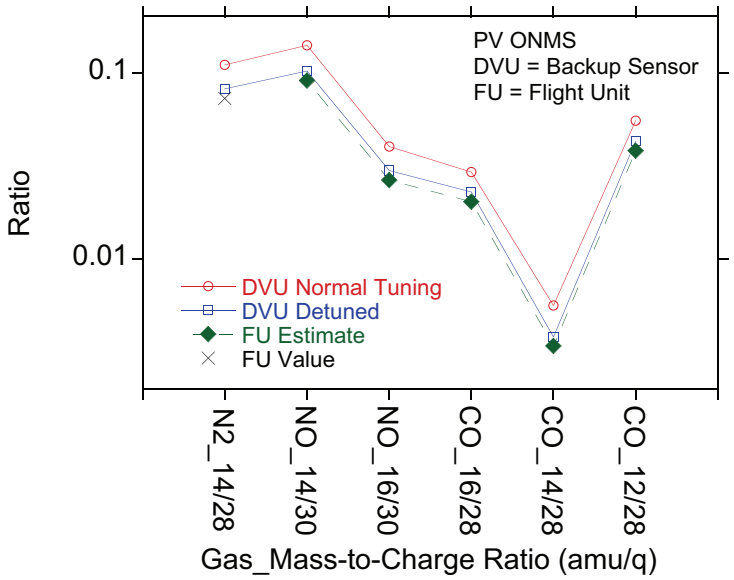

Figure 3.79: Estimating the mass peak fragmentation branching ratios of CO and NO for the PV ONMS flight unit (FU) sensor using the backup unit (DVU) sensor [*Niemann et al.*, 1980b].

between the FU and EU data sets, and a relationship determined between the two data sets. The ratios of the fragment peaks to the major peak of the same gas species for the FU were also related to those of the EU. To extrapolate to gas species that were not calibrated for either the EU or FU an effective sensitivity was calculated using total ionization cross sections and fragmentation patterns or branching ratios (see Appendix A.12: Neutral Gas Mass Spectrometer: Fragmentation Patterns, Total Ionization Cross-Sections). The ion mode sensitivity (counts s^{-1})/(particle cm^{-3}) was determined by EU characterization and verified by the few data points available from the FU. Since the ion energy is predicted from the incoming particle mass and spacecraft speed, this relationship is verified using in-flight data with the initial settings determined in the laboratory.

Acknowledgements

We acknowledge the following people who made calibration data available that has not been published: K. Altwegg and S. Graf, from University of Bern, Switzerland, R. Frahm, from Southwest Research Institute, TX, USA, and D. Kataria, from Mullard Space Science Laboratory, University College London, UK. PW acknowledges support for graphics from J. Fischer from University of Bern, Switzerland. WL acknowledges the partial financial support by NASA under contract NAS5-30302.

Bibliography

Abuaf, N., J.B. Anderson, R.P. Andres, J.B. Fenn, and D.G.H. Marsden, Molecular beams with energies above one electron volt, *Science*, **156**, 997–999, 1967.

Adams, L. and A. Holmes-Siedle, The development of an MOS dosimetry unit for use in space, *IEEE Trans. Nucl. Sci.* **25**, 1607–1612, 1978.

Aellig, M.R., A.J. Lazarus, J.C. Kasper, and K.W. Ogilvie, Rapid measurements of solar wind ions with the Triana PlasMag Faraday cup, *Astrophys. Space Sci.*, **277(1/2)**, 305–307, 2001.

Allegrini, F., The PLASTIC sensor on STEREO: Design of the entrance system / energy analyzer and numerical simulations of solar wind measurements, Ph.D. thesis, University of Bern, 2002.

Alton, G.D., Ion sources for accelerators in materials research, *Nucl. Instrum. Methods B*, **73**, 221–288, 1993.

Anderson, J.B., Molecular beams from nozzle sources, in *Molecular Beams and Low Density Gasdynamics*, P.P. Wegener, Ed., Marcel Dekker, Inc., New York, 1–91, 1974.

Angelopolous, V., U. Auster, C.W. Carlson, K.-H. Glassmeier, G.T. Delory, W. Baumjohann, R.P. Lin, R. Nakamura, S. Mende, K. Schwingenschuh, F.S. Mozer, J. Buechner, G. Parks, O. Le Contel, T.D. Phan, A. Roux, M.A. Temerin, E. Donovan, K.K. Khurana, P. Escoubet, M.G. Kivelson, H. Laakso, J. Raeder, M. Fujimoto, C.T. Russell, C.J. Jacquey, R.E. Ergun, D. LeQueau, X. Li, J. Samson, A.T.Y. Lui, I. Voronkov, D. Sibeck, V. Sergeev, and H.J. Singer, `http://sprg.ssl.berkeley.edu/themis/`, 2006.

August, L.S., R.R. Circle, J.C. Ritter, and J.S. Tobin, A MOS dosimeter for use in space, *IEEE Trans. Nucl. Sci.* **30**, 508–511, 1983.

Ballenthin, J.O. and A.O. Nier, Molecular beam facility for studying mass spectrometer performance, *Rev. Sci. Instrum.*, **52**, 1016–1024, 1981.

Balsiger, H., K. Altwegg, F. Bühler, J. Fischer, J. Geiss, A. Meier, U. Rettenmund, H. Rosenbauer, R. Schwenn, J. Benson, R. Hemmerich, K. Säger, G. Kulzer, M. Neugebauer, B.E. Goldstein, R. Goldstein, E.G. Shelley, T. Sander, D. Simpson, A.J. Lazarus, and D.T. Young, The Giotto ion mass spectrometer, *ESA Special Publication*, **SP-1077**, ESA Publications Divison, Noordwijk, 129–148, 1986.

Balsiger, H., K. Altwegg, E. Arijs, J.-L. Bertaux, J.-J. Berthelier, P. Bochsler, G.R. Carignan, P. Eberhardt, L.A. Fisk, S.A. Fuselier, A.G. Ghielmetti, F. Gliem, T.I. Gombosi, E. Kopp, A. Korth, S. Livi, C. Mazelle, H. Rème, J.A. Sauvaud, E.G. Shelley, J.H. Waite, B. Wilken, J. Woch, H. Wollnik, P. Wurz, and D.T. Young, Rosetta Orbiter Spectrometer for Ion and Neutral Analysis—ROSINA, *Adv. Space Res.*, **21(11)**, 1527–1535, 1998.

Balsiger, H., K. Altwegg, P. Bochsler, P. Eberhardt, J. Fischer, S. Graf, A. Jäckel, E. Kopp, U. Langer, M. Mildner, J. Müller, T. Riesen, M. Rubin, S. Scherer, P. Wurz, S. Wüthrich, H. Rème, C. Aoustin, C. Mazelle, J.-L. Médale, J.A. Sauvaud, E. Arijs, S. Delanoye, J. De Keyser, E. Neefs, D. Nevejans, J.-J. Berthelier, J.-L. Bertaux, L. Duvet, and J-M. Illiano, T.I. Gombosi, B. Block, G.R. Carignan, L.A. Fisk, F. Gliem, B. Fiethe, S.A. Fuselier, A.G. Ghielmetti, T. Magoncelli, E.G. Shelley, A. Korth, K. Heerlein, H. Lauche, S. Livi, A. Loose, B. Wilken, J.H. Waite, D.T. Young, and H. Wollnik, ROSINA – Rosetta Orbiter Spectrometer for Ion and Neutral Analysis, *Space Sci. Rev.*, **128**, 745–801, doi:10.1007/s11214-006-8335-3, 2007.

Bennett, W.H., Radio-frequency mass spectrometer, *J. Appl. Phys.*, **21**, 143–149, 1950.

Berger, M.J., S.M. Seltzer, S.E. Chapell, J.C. Humphreys, and J.W. Motz, Response of silicon detectors to monoenergetic electrons with energies between 0.15 and 5.0 MeV, *Nucl. Instrum. Methods*, **69**, 181–193, 1969.

Bergoglio, M. and A. Calcatelli, The physical measurement of pressure in SI units and its extension to lower pressures, *Vacuum*, **64**, 153–162, 2002.

Bergoz Instrumentation, Espace Allondon Ouest, 01630 Saint Genis Pouilly, France.

Berthelier, J.-J. and J.-F. Roussel, A study of the electrical charging of the Rosetta orbiter: 2. Experimental tests in a laboratory plasma, *J. Geophys. Res.*, **109**, A01105, doi:10.1029/2003JA009834, 2004.

Betz, G. and K. Wien, Energy and angular distributions of sputtered particles, *Int. J. Mass Spectr.*, **140**, 1–110, 1994.

Bevington, P.R. and D.K. Robinson, *Data Reduction and Error Analysis for the Physical Sciences*, 3^{rd} Ed., McGraw-Hill, New York, 2003.

Biddle, A.P. and J.M. Reynolds, Integrated development facility for the calibration of low-energy charged particle flight instrumentation, *Rev. Sci. Instrum.*, **57(4)**, 572–582, 1986.

Bischler, U. and E. Bertel, Simple source of atomic hydrogen for ultrahigh vacuum applications, *J. Vac. Sci. Technol. A*, **11**, 458–460, 1993.

Blush, L., Private communication, University of Bern, 2004.

Blush, L.M., P. Bochsler, H. Daoudi, A. Galvin, R. Karrer, L. Kistler, B. Klecker, E. Möbius, A. Opitz, M. Popecki, B. Thompson, R.F. Wimmer-Schweingruber, and P. Wurz, Development and calibration of major components for the STEREO/PLASTIC (plasma and suprathermal ion composition) instrument, *Adv. Space Res.*, **36(8)**, 1544–1556, 2005.

Bodmer, R., The Helium Isotopic Ratio as a Test for Minor Ion Fractionation in the Solar Wind Acceleration Process: SWICS/Ulysses Data Compared with Results from a Multifluid Model, Ph.D. thesis, University of Bern, 1996.

Boies, M.T., R.C. Benson, J.D. Kinnison, J.S. Morgan, T.E. Phillips, O.M. Uy, and W. Wilkinson, Comparative sensor calibration: Mid-course space experiment (MSX) neutral mass spectrometer and total pressure sensor, *Proc. SPIE*, **2261**, 208–217, 1994.

Bordoni, F., Channel electron multiplier efficiency for 10–1000 eV electrons, *Nucl. Instrum. Methods*, **97**, 405–408, 1971.

Brinton, H.C., L.R. Scott, M.W. Pharo, and J.T. Coulson, The Bennett ion-mass spectrometer on Atmosphere Explorer-C and E, *Radio Sci.*, **8**, 323–332, 1973.

Brown, I.G., Ed., *The Physics and Technology of Ion Sources*, Wiley-VCH Verlag GmbH & Co., Weinheim, 2004.

Brüning, K., Streuung und Dissoziation langsamer Moleküle an Oberflächen, Diploma Thesis, University of Osnabrück, 1996.

Brutschy, B. and H. Haberland, A high-temperature, high-pressure supersonic nozzle beam, *J. Phys. E: Sci. Instrum.*, **13**, 150–151, 1980.

Burch, J.L., J.D. Winningham, V.A. Blevins, N. Eaker, W.C. Gibson, and R.A. Hoffman, High-altitude plasma instrument for Dynamics Explorer-A, *Space Sci. Instrum.*, **5**, 455–463, 1981.

Caledonia, G.E., R.H. Krech, and B.D. Green, A high flux source of energetic oxygen atoms for material degradation studies, *AIAA Journal*, **25**, 59–63, 1987.

Caledonia, G.E., R.H. Krech, D.B. Oakes, S.J. Lipson, and W.A.M. Blumberg, Products of the reaction of 8 km s^{-1} $N(^4S)$ and O_2, *J. Geophys. Res.*, **105**, 12833–12837, 2000.

Camanzi, B., A.G. Holmes-Siedle, and A.K. McKemey, The dose mapping system for the electromagnetic calorimeter of the BaBar experiment at SLAC, *Nucl. Instrum. Methods A*, **457(3)**, 476–486, 2001.

Carlson, C.W., D.W. Curtis, G. Paschmann, and W. Michael, An instrument for rapidly measuring plasma distribution functions with high resolution, *Adv. Space Res.*, **2(7)**, 67–70, 1983.

Carlson C.W. and J.P. McFadden, Design and application of imaging plasma instruments, in *Measurement Techniques in Space Plasmas: Particles*, R. Pfaff, J. Borovsky, and D.T. Young, Eds., Geophys. Monogr. Ser., **102**, American Geophysical Union, Washington, D.C., 125–140, 1998.

Carlson, C.W., J.P. McFadden, R.E. Ergun, M. Temerin, W. Peria, F.S. Mozer, D.M. Klumpar, E.G. Shelley, W.K. Peterson, E. Moebius, R. Elphic, R. Strangeway, C. Cattell, and R. Pfaff, FAST observations in the downward auroral current region: Energetic upgoing electron beams, parallel potential drops, and ion heating, *Geophy. Res. Lett.*, **25(12)**, 2017–2020, 1998.

Carlson, C.W., J.P. McFadden, P. Turin, D.W. Curtis, and A. Magoncelli, The electron and ion plasma experiment for FAST, *Space Sci. Rev.*, **98**, 33–66, 2001.

Carrington, A., H.W. Nicholson, and J. Krivichic, Electron backscattering from a silicon detector from 0.182 to 0.579 MeV, *Nucl. Instrum. Methods A*, **248**, 425–428, 1986.

Cazaubon, B., A. Paillous, J. Siffre, and R. Thomas, Five-electron-Volt atomic oxygen pulsed-beam characterization by quadrupolar mass spectrometry, *J. Spacecraft and Rockets*, **33**, 870–876, 1996.

Chao, C.K. and S.-Y. Su, On accuracy of RPA measurements of ion fluxes, *Adv. Space Res.*, **23(8)**, 1537–1540, 1999.

Chung, K.H., S.S. Hong, Y.H. Shin, J.Y. Lim, S.K. Lee, and S.Y. Woo, Hot cathode ionization gauge calibration with the KRISS ultra-high vacuum standards, *Metrologia*, **36**, 675–679, 1999.

Coffey, V.N., T.E. Moore, and C.J. Pollock, The scanning thermal ion composition spectrometer (STICS), in *Measurement Techniques in Space Plasmas: Particles*, R.-Pfaff, J.-Borovsky, and D.T.-Young, Eds., Geophys. Monogr. Ser., **102**, American Geophysical Union, Washington, D.C., 175–180, 1998.

Cohen, H.A., Free molecular gas flow through a moving absorbing cylindrical tube, *J. Vac. Sci. Technol.*, **5**, 200–204, 1968.

Comsa, G., J.K. Fremerey, B. Linenau, G. Messer, and P. Rohl, Calibration of a spinning rotor gas friction gauge against a fundamental vacuum pressure standard, *J. Vac. Sci. Technol.*, **17**, 642–644, 1980.

Cowen, M.C., W. Allison, and J.H. Batey, Non-linearities in sensitivity of quadrupole pressure analyzers operating at higher gas pressures, *J. Vac. Sci. Technol. A*, **12**, 228–234, 1994.

Cox, R.N. and L.F. Crabtree, *Elements of Hypersonic Aerodynamics*, Academic Press, New York, 1965.

Curtis, D.W., C.W. Carlson, R.P. Lin, G. Paschmann, G. Rème, and A. Cros, On-board data analysis techniques for space plasma particle instruments, *Rev. Sci. Instrum.*, **60**, 372–380, 1989.

Dahl, D.A., SIMION 3D Version 7.0 User's Manual, Idaho National Engineering and Environmental Laboratory, **INEEL-95/0403**, 2000.

Daoudi, H., Private communication, University of Bern, 2005.

Deckers, J. and J.B. Fenn, High intensity molecular beam apparatus, *Rev. Sci. Instrum.*, **34**, 96–100, 1963.

DePaul, S., D. Pullman, and B. Friedrich, A pocket model of seeded supersonic beams, *J. Phys. Chem.*, **97**, 2167–2171, 1993.

Devine, F.M., B. Crave, J. Souquet, and R. Clapier, Experiments on charge and momentum exchange between ions and molecules in the development of high-speed molecular beams, in *Advances in Applied Mechanics, Proc. 3rd International Symposium on Rarefied Gas Dynamics*, J.A. Laurman, Ed., Academic Press, New York, **1**, 363–386, 1963.

Dichter, B.K., J.O. McGarity, M.R. Oberhardt, V.T. Jordanov, D.J. Sperry, A.C. Huber, J.A. Pantazis, E.G. Mullen, G. Ginet, and S.G. Gussenhoven, Compact Environmental Anomaly SEnsor (CEASE): A novel spacecraft instrument for *in situ* measurements of environmental conditions, *IEEE Trans. Nucl. Sci.* **45**, 2758–2764, 1998.

Donley, J.L., The thermal ion and electron trap experiments on the Explorer 31 satellite, *Proc. IEEE*, **57**, 1061–1067, 1969.

Eberhardt, P., D. Krankowsky, W. Schulte, U. Dolder, P. Lammerzahl, J.J. Berthelier, J. Woweries, U. Stubbemann, R.R. Hodges, J.H. Hoffman, and J.M. Illiano, The CO and N_2 abundance in comet P/Halley, *Astro. Astrophys.*, **187**, 481–484, 1987.

Eckstein, W., Charge fractions of reflected particles, in *Inelastic Particle-Surface Collisions*, E. Taglauer and W. Heiland, Ed., *Chemical Physics*, **17**, 157–183, 1981.

Eidelman, S., K.G. Hayes, K.A. Olive, M. Aguilar-Benitez, C. Amsler, D. Asner, K.S. Babu, R.M. Barnett, J. Beringer, P.R. Burchat, C.D. Carone, S. Caso, G. Conforto, O. Dahl, G. D'Ambrosio, M. Doser, J.L. Feng, T. Gherghetta, L. Gibbons, M. Goodman, C. Grab, D.E. Groom, A. Gurtu, K. Hagiwara, J.J. Hernández-Rey, K. Hikasa, K. Honscheid, H. Jawahery, C. Kolda, Y. Kwon, M.L. Mangano, A.V. Manohar, J. March-Russell, A. Masoni, R. Miquel, K. Mönig, H. Murayama, K. Nakamura, S. Navas, L. Pape, C. Patrignani, A. Piepke, G. Raffelt, M. Roos, M. Tanabashi, J. Terning, N.A. Törnqvist, T.G. Trippe, P. Vogel, C.G. Wohl, R.L. Workman, W.-M. Yao, and P.A. Zyla, Review of particle physics, *Phys. Lett. B*, **592**, 1–1109, 2004.

Erlandson, R.E., M.T. Boies, and O.M. Uy, The MSX ion mass spectrometer: Measurement of contaminant and ambient ions, *Proc. SPIE*, **2261**, 181–187, 1994.

Evans, D.S. and M. Greer, Polar Orbiting Environmental Satellite Space Environment Monitor - 2: Instrument descriptions and archive data documentation, NOAA Technical Memorandum, **OAR SEC-93**, 2000.

Fenn, J.B., Molecular beam engineering at intermediate energies, *ENTROPIE*, **18**, 11–21, 1967.

Fowler, P. and F.J. Brock, Accurate, wide range ultrahigh-vacuum calibration system, *J. Vac. Sci. Techol.*, **7**, 507–516, 1970.

Frahm, R., Private communication, Southwest Research Institute, TX, 2005.

French, J.B., Molecular beams for rarified gasdynamic research, **AGARDograph 112**, North Atlantic Treaty Organization, Advisory Group for Aerospace Research, Technical Editing and Production Ltd., Hartford House, London, 1967.

French, J.B., Planetary atmosphere simulation using molecular beams, IES/AIAA/ASTM 4th Space Simulation Conference, Los Angeles, Calif., **AIAA Paper No. 69–1031**, 1969.

French, J.B., N.M. Reid, A.O. Nier, and J.L. Hayden, Molecular beam simulation of planetary atmospheric entry — Some recent results, IES/AIAA/ASTM Space Simulation Conference, NASA Goddard Space Flight Center, Greenbelt, MD, **Paper No. 63**, 687–

702, 1972.

French, J.B., N.M. Reid, A.O. Nier, and J.L. Hayden, Rarified gas dynamic effects on mass spectrometric studies of upper planetary atmospheres, *AIAA Journal*, **13**, 1641–1646, 1975.

Gaitskell, R.J., L.C. Angrave, N.E. Booth, A.D. Hahn, G.L. Salmon, and A.M. Swift, A measurement of the beta spectrum of Ni-63 using a new type of cryogenic detector, *Phys. Lett. B*, **370**, 163–167, 1996.

Galvin, A., E. Abrams, L. Blush, P. Bochsler, C. Farrugia, M. Granoff, L. Kistler, B. Klecker, M. Lee, E. Möbius, M. Popecki, J.M. Quinn, B. Thompson, S. Turco, R. Wimmer-Schweingruber, and P. Wurz, The PLasma And Supra Thermal Ion Composition (PLASTIC) instrument on STEREO, *Space Sci. Rev.*, in preparation, 2006.

Gao R.S., P.S. Gibner, J.H. Newman, K.A. Smith, and R.F. Stebbings, Absolute and angular efficiencies of a microchannel-plate position-sensitive detector, *Rev. Sci. Instrum.*, **55(11)**, 1756–1759, 1984.

Geller, R., *Electron Cyclotron Resonance Ion Sources and ECR Plasmas*, Inst. Physics Publ., Bristol, 1996.

Ghielmetti, A.G., H. Balsiger, R. Banninger, P. Eberhardt, J. Geiss, and D.T. Young, Calibration system for satellite and rocket-borne ion mass spectrometers in the energy range 5 eV/charge to 100 keV/charge, *Rev. Sci. Instrum.*, **54**, 425–436, 1983.

Gloeckler, G. and K.C. Hsieh, Time-of-flight technique for particle identification at energies from 2–400 keV/nucleon, *Nucl. Instrum. Methods*, **165**, 537–544, 1979.

Gloeckler, G., F.M. Ipavich, W. Stüdemann, B. Wilken, D.C. Hamilton, G. Kremser, D. Hovestadt, F. Gliem, R.A. Lundgren, W. Rieck, E.O. Tums, J.C. Cain, L.S. Masung, W. Weiss, and P. Winterhof, The charge-energy-mass spectrometer for 0.3–300 keV/e ions on the AMPTE CCE, *IEEE Trans. Geosci. Remote Sens.*, **GE-23**, 234–240, 1985.

Gloeckler, G., J. Geiss, H. Balsiger, P. Bedini, J.C. Cain, J. Fischer, L.A. Fisk, A.B. Galvin, F. Gliem, D.C. Hamilton, J.V. Hollweg, F.M. Ipavich, R. Joos, S. Livi, R.A. Lundgren, U. Mall, J.F. McKenzie, K.W. Ogilvie, F. Ottens, W. Rieck, E.O. Tums, R. von Steiger, W. Weiss, and B. Wilken, The solar wind ion composition spectrometer, *Astron. Astrophys. Suppl. Ser.*, **92**, 267–289, 1992.

Gloeckler, G., and J. Geiss, Measurement of the abundance of Helium-3 in the Sun and in the local interstellar cloud with SWICS on Ulysses, *Space Sci. Rev.*, **84**, 275–284, 1998.

Gloeckler, G., J. Cain, F.M. Ipavich, E.O. Tums, P. Bedini, L.A. Fisk, T. Zurbuchen, P. Bochsler, J. Fischer, R.F. Wimmer-Schweingruber, J. Geiss, and R. Kallenbach, Investigation of the composition of solar and interstellar matter using solar wind and pickup ion measurements with SWICS and SWIMS on the ACE Spacecraft, *Space Sci. Rev.*, **86**, 497–539, 1998.

Goldan, P.E., E.J. Yadlowsky, and E.C. Whipple, Errors in ion and electron temperature measurements due to grid plane potential non-uniformities in retarding potential analyzers, *J. Geophys. Res.*, **78**, 2907–2916, 1973.

Gosling J.T., J.R. Asbridge, S.J. Bame, and W.C. Feldman, Effects of a long entrance aperture upon the azimuthal response of spherical electrostatic analyzers, *Rev. Sci. Instrum.*, **49**, 1260–1268, 1978.

Graf, S., K. Altwegg, H. Balsiger, A. Jäckel, E. Kopp, U. Langer, W. Luithardt, C. Westermann, and P. Wurz, A cometary neutral gas simulator for gas dynamic sensor and mass spectrometer calibration, *J. Geophys. Res.*, **109(E7)**, doi:10.1029/2003JE002188, 2004.

Granville-Phillips, a division of Brooks Automation, Inc., Chelmsford, MA 01824, USA.

Grebowsky, J.M., H.A. Taylor, M.W. Pharo III, and N. Reese, Thermal ion perturbation observed in the vicinity of the space shuttle, *Planet. Space Sci.*, **35**, 501–513, 1987.

Grebowsky, J.M. and A. Schaefer, Ion mass spectrometer measurements from the Space Shuttle, *Indian J. Radio Space Phys.*, **19**, 49–61, 1990.

Grohmann, K., D. Hechtfischer, J. Jakschik, and H. Lübbig, A cryodevice for induction monitoring of dc electron or ion beams with nano-ampere resolution, in *Superconducting quantum interference devices and their applications*, H.D. Hahlbohm and H. Lubbig, Eds., Walter de Gruyter & Co., Berlin, 311, 1977.

Grunn, R., Designing system grounds and signal, *Control Engineering*, May, 1987.

Gussenhoven, M.S., R.C. Filz, K.A. Lynch, E.G. Mullen, and F.A. Hanser, Space radiation dosimeter SSJ* for the Block 5D/Flight 7 DMSP satellite: calibration and data presentation, Air Force Research Laboratory publication, **AFGL-TR-86-0065**, 1986.

Gussenhoven, S., E.G. Mullen, J.T. Bell, D. Madden, and E. Holeman, APEXRAD: Low altitude orbit dose as a function of inclination, magnetic activity and solar cycle, *IEEE Trans. Nucl. Sci.*, **44**, 2161–2168, 1997.

Hanser, F.A. and B. Sellers, Measurement of totally depleted silicon solid-state detector thickness by X-ray attenuation, *Rev. Sci. Instrum.*, **45**, 226–231, 1974.

Hanser, F.A. and B.K. Dichter, Space radiation dosimetry, in *Biological Effects and Physics of Solar and Galactic Cosmic Radiation*, C.E. Swenberg, G. Horneck and E.G. Stassinopoulos, Eds., Plenum Press, New York, 135–151, 1993.

Hanson, W.B., D.R. Frame, and J.E. Midgley, Errors in retarding potential analyzers caused by nonuniformity of the grid-plane potential, *J. Geophys. Res.*, **77**, 1914–1922, 1972.

Hao, L., J.C. Gallop, J.C. Macfarlane, and C. Carr, HTS cryogenic current comparator for non-invasive sensing of charged-particle beams, *Physica C*, **368**, 114–118, 2002.

Harvey, I.K., A precise low temperature dc ratio transformer, *Rev. Sci. Instrum.*, **43**, 1626–1629, 1972.

Hedin, A.E., C.P. Avery, and C.D. Tschetter, An analysis of spin modulation effects on data obtained with a rocket-borne mass spectrometer, *J. Geophys. Res.*, **69**, 4637–4648, 1964.

Hedin, A.E. and A.O. Nier, A determination of the neutral composition, number density, and temperature of the upper atmosphere from 120 to 200 kilometers with rocket-borne mass spectrometers, *J. Geophys. Res.*, **71**, 4121–4131, 1966.

Henderson, M.G., M.F. Thomsen, R. Skoug, M.H. Denton, and C.J. Pollock, Calculation of IMAGE/LENA geometric factors and conversion of images to units of integral and differential flux, *Rev. Sci. Instrum.*, **76**, doi:10.1063/1.1884190, 2005.

Hinkle, L.D. and R.P. Jacobs, Accuracy and applicability of the spinning rotor gauge to calibration in gas mixture environments, *J. Vac. Sci. Technol. A*, **11**, 261–263, 1993.

Hoffman, J.H., K. Pelka, U. von Zahn, D. Krankowsky, and D. Linkert, The Pioneer Venus bus neutral gas mass spectrometer, *IEEE Trans. Geosci. Remote Sens.*, **GE-18**, 122–126, 1980.

Holland, L. and C. Priestland, Measurement of the variation of molecular impact rate within a spherical calibration vessel, *Vacuum*, **17**, 461–468, 1967.

Hollanda, R., *Evaluation of a Volume-Ratio System for Vacuum Gauge calibration for* 10^{-8} *to* 10 *Torr*, NASA Technical Note, **TN D-5406**, NASA, Washington, D.C., 1969.

Holme, A.E., W.J. Thatcher, and J.H. Leck, A small analytical quadrupole mass spectrometer designed for operation in high and ultra high vacuum systems, *Vacuum*, **24**, 7–11,

1974.

Holmes-Siedle, A. and L. Adams, RADFET: A review of the use of metal-oxide-silicon devices as integrating dosimeters, *Int. J. Rad. Appl. Instrum.* **28(2)**, 235–244, 1986.

Horowitz, R. and H.E. La Gow, Upper air pressure and density measurements from 90–220 kilometers with the Viking 7 rocket, *J. Geophys. Res.*, **62**, 57–78, 1957.

Hovestadt, D., M. Hilchenbach, A. Bürgi, B. Klecker, P. Laeverenz, M. Scholer, H. Grünwaldt, W.I. Axford, S. Livi, E. Marsch, B. Wilken, P. Winterhoff, F.M. Ipavich, P. Bedini, M.A. Coplan, A.B. Galvin, G. Gloeckler, P. Bochsler, H. Balsiger, J. Fischer, J. Geiss, R. Kallenbach, P. Wurz, K.-U. Reiche, F. Gliem, D.L. Judge, K.H. Hsieh, E. Möbius, M.A. Lee, G.G. Managadze, M.I. Verigin, and M. Neugebauer, CELIAS: The charge, element, and isotope analysis system for SOHO, *Solar Physics*, *162*, 441–481, 1995.

Hughes, P.C. and J.H. De Leeuw, Theory for the free molecular impact probe at an angle of attack, Rarified Gas Dynamics, 4^{th} Symposium, **1**, 653–675, 1965.

Humphries, S. Jr., *Charged Particle Beams*, John Wiley & Sons, Inc., New York, 1990.

Jans, S., P. Wurz, R. Schletti, K. Brüning, K. Sekar, W. Heiland, J. Quinn, and R.E. Leuchtner, Scattering of atoms and molecules from barium zirconate surfaces, *Nucl. Instrum. Methods B*, **173**, 503–515, 2001.

Johnson, G.W., *LabVIEW Graphical Programming*, McGraw-Hill, Inc., 1994.

Johnstone, A.D., C. Alsop, S. Burge, P.J. Carter, A.J. Coates, A.J. Coker, A.N. Fazakerley, M. Grande, R.A. Gowen, C. Gurgiolo, B.K. Hancock, B. Narheim, A. Preece, P.H. Sheather, J.D. Winningham, and R.D. Woodliffe, PEACE: A plasma electron and current experiment, *Space Sci. Rev.*, **79**, 351–398, 1997.

Jousten, K. and G. Rupschus, The uncertainties of calibration pressures at PTB, *Vacuum*, **44**, 569–572, 1993.

Jousten, K., H. Menzer, D. Wandrey, and R. Niepraschk, New, fully automated, primary standard for generating vacuum pressures between 10^{-10} Pa and 3×10^{-2} Pa with respect to residual pressure, *Metrologia*, **36**, 493–497, 1999.

Kamermans, R., J. Henrion, R.G. Marsden, T.R. Sanderson, and K.-P. Wenzel, Element and isotope separation for a heavy ion cosmic ray telescope with large geometric factor, *Nucl. Instrum. Methods*, **171**, 87–92, 1980.

Karrer, R., Ion-optical calibration of PLASTIC/STEREO, Ph.D. thesis, University of Bern, 2006.

Kasprzak, W.T., D. Krankowsky, and A.O. Nier, A study of the day-night variations in the neutral composition of the lower atmosphere, *J. Geophys. Res.*, **73**, 6765–6782, 1968.

Kasprzak, W.T., A.E. Hedin, H.B. Niemann, and N.W. Spencer, Atomic nitrogen in the upper atmosphere of Venus, *Geophys. Res. Lett.*, **7**, 106–108, 1980.

Kasprzak, W.T., H.B. Niemann, and P. Mahaffy, Observations of energetic ions on the nightside of Venus, *J. Geophys. Res.*, **92**, 291–298, 1987.

Kasprzak, W.T, H. Niemann, D. Harpold, J. Richards, H. Manning, E. Patrick, and P. Mahaffy, Cassini orbiter ion and neutral mass spectrometer instrument, *Proc. SPIE*, **2803**, 129–140, 1996.

Kataria, D., G. Watson, P.J. Carter, A.N. Fazakerley, A.M. James, and R.J. Wilson, In-flight monitoring and optimisation of MCP performance on multi-spacecraft missions, *Proc. SPIE*, **4796**, 115–125, 2003.

Kataria, D., Private communication, Mullard Space Science Laboratory, University College London, 2005.

Kayser, D.C., L.H. Johnson, W.E. Potter, and A.O. Nier, Theory of the fly-through mode for neutral mass spectrometers, *Space Sci. Instrum.*, **4**, 339–350, 1979.

Keithley Instruments, Inc., *Low Level Signal Handbook*, 6th Ed., 28775 Aurora Road, Cleveland, Ohio 44139, USA, 2006.

Kieffer, L.J. and G.H. Dunn, Electron impact ionization cross-section data for atoms, atomic ions, and diatomic molecules: 1. Experimental data, *Rev. Mod. Phys.*, **38**, 1–35, 1966.

Klingelhofer, R. and P. Louse, Production of fast molecular beams using gaseous mixtures, *Phys. Fluids*, **7**, 379–381, 1964.

Knoll, G.F., *Radiation Detection and Measurement*, John Wiley and Sons, New York, pp. 389–391, 2000.

Knudsen, W.C., Evaluation and demonstration of the use of retarding potential analyzers for measuring several ionospheric quantities, *J. Geophys. Res.*, **71**, 4669–4678, 1966.

Knudsen, D.J., T.D. Phan, M.D. Gladers, and M.J. Greffen, Thermal electron temperature measurements from the Freja cold plasma analyzer, in *Measurement Techniques in Space Plasmas: Particles*, R.-Pfaff, J.-Borovsky, and D.T.-Young, Eds., Geophys. Monogr. Ser., **102**, American Geophysical Union, Washington, D.C., 91–96, 1998.

Knudsen, D., `http://www.phys.ucalgary.ca/lab_CPCF.html`, 2004.

Krankowsky, D., P. Lammerzahl, D. Dörflinger, I. Herrwerth, U. Stubbemann, J. Woweries, P. Eberhardt, U. Dolder, J. Fischer, U. Herrmann, H. Hofstetter, M. Junck, F.O. Meier, W. Schulte, J.J. Berthelier, J.M. Illiano, M. Godefroy, G. Gogly, P. Thévenet, J.H. Hoffman, R.R. Hodges, and W.W. Wright, In situ gas and ion measurements at comet Halley, *ESA Special Publication*, **SP-1077**, ESA Publications Division, Noordwijk, 109–128, 1986a.

Krankowsky, D., P. Lammerzahl, I. Herrwerth, J. Woweries, P. Eberhardt, U. Dolder, U. Herrmann, W. Schulte, J.J. Berthelier, J.M. Illiano, R.R. Hodges, and J.H. Hoffman, In situ gas and ion measurements at comet Halley, *Nature*, **321**, 326–329, 1986b.

Krishnakumar, E. and S.K. Srivastava, Cross sections for the production of N_2^+, $N^+ + N_2^{2+}$, and N^{2+} by electron impact on N_2, *J. Phys. B: At. Mol. Opt. Phys.*, **23**, 1893–1900, 1990.

Krueger, F.H., *Partial Discharge Detection in High-Voltage Equipment*, Butterworths, Temple Press, London, 1989.

Lebreton, J-P. and D.L. Matson, *The Huygens Probe: Science, Payload and Mission Objectives*, *ESA Special Publication*, **SP-1177**, ESA Publications Division, Noordwijk, 1997.

Lessard, M., G.P. Garbe, and R.L. Arnoldy, A calibration source for low energy electron detectors, in *Measurement Techniques in Space Plasmas: Particles*, R.-Pfaff, J.-Borovsky, and D.T.-Young, Eds., Geophys. Monogr. Ser., **102**, American Geophysical Union, Washington, D.C. 301–306, 1998.

Leybold Vakuum GmbH, Bonnerstraße 498, Cologne, D-50968, Germany.

Lieszkovszky, L., A.R. Fillippelli, and C.R. Tilford, Metrological characteristics of a group of quadrupole partial pressure analyzers, *J. Vac. Sci. Technol. A*, **8**, 3838–3854, 1990.

Lin, R.P., K.A. Anderson, S. Ashford, C. Carlson, D. Curtis, R. Ergun, D. Larson, J. McFadden, M. McCarthy, G.K. Parks, H. Rème, J.M. Bosqued, J. Coutelier, F. Cotin, C. D'Uston, K.-P. Wenzel, T.R. Sanderson, J. Henrion, J.C. Ronnet, and G. Paschmann, A three-dimensional plasma and energetic particle investigation for the Wind spacecraft, *Space Sci. Rev.*,**71**, 125–153, 1995.

Locke, J.W. and J.B. French, Critical evaluation of the metastable time-of-flight technique for obtaining molecular velocity distributions, *J. Vac. Sci. Technol.*, **7**, 46–49, 1970.

Losch, A. and H. Niehus, NICASS—A new method for surface structure analysis, *Phys. Stat. Sol.*, **173**, 117–121, 1999a.

Losch, A. and H. Niehus, Structure analysis of the KBr(100) surface: An investigation with a new method for surface analysis of insulators, *Surf. Sci.*, **420**, 148–156, 1999b.

Mahaffy, P.R. and K. Lai, An electrostatic quadrupole deflector for mass spectrometer applications, *J. Vac. Sci. Technol. A*, **8**, 3244–3246, 1990.

Mahaffy, P.R., Private communication, Code 699, NASA Goddard Space Flight Center.

Manning, H.L.K, The Development and Calibration of a New Mass Spectrometer for Upper Atmospheric Research, Ph.D. thesis, University of Minnesota, Minneapolis, 1995.

Marsden, R.G., J. Henrion, T.R. Sanderson, K.-P. Wenzel, N. de Bray, and H.P. Blok, Calibration of a space-borne charged particle telescope using protons in the energy range 0.4 to 20 MeV, *Nucl. Instrum. Methods in Phys. Res.*, **221**, 619–626, 1984.

Marti, A., R. Schletti, P. Wurz, and P. Bochsler, Calibration facility for solar wind plasma instruments, *Rev. Sci. Instrum.*, **72(2)**, 1354–1360, 2001.

Mauersberger, K., Mass spectrometer beam system for applications in the stratosphere, *Rev. Sci. Instrum.*, **48**, 1169–1173, 1977.

McCarthy, M.P. and J.P. McFadden, Measurement of 0–25 eV ions with a retarding potential analyzer on the Cluster ion spectroscopy experiment, in *Measurement Techniques for Space Plasmas: Particles*, R. Pfaff, J. Borovsky, and D.T. Young, Eds., Geophys. Monogr. Ser., **102**, American Geophysical Union, Washington, D.C., 97–103, 1998.

McComas, D.J., S.J. Bame, W.C. Feldman, J.T. Gosling, and J.L. Philips, Solar wind halo electrons from 1 – 4 AU, *Geophys. Res. Lett.*, **19(12)**, 1291–1294, 1992.

McComas, D., F. Allegrini, P. Bochsler, M. Bzowski, M. Collier, H. Fahr, H. Fichtner, P. Frisch, H. Funsten, S. Fuselier, G. Gloeckler, M. Gruntman, V. Izmodenov, P. Knappenberger, M. Lee, S. Livi, D. Mitchell, E. Moebius, T. Moore, D. Reisenfeld, E. Roelof, N. Schwadron, M. Wieser, M. Witte, P. Wurz, and G. Zank, The interstellar boundary explorer (IBEX), *AIP Conf. Proc.*, **719**, 162–181, 2004.

McCulloh, K.E., Calibration of molecular drag vacuum gauges, *J. Vac. Sci. Technol. A*, **1**, 168–171, 1983.

McDonald, F.B. and V.S. Ptuskin, Galactic cosmic rays, in *The Century of Space Science*, J.A.M. Bleeker, J. Geiss, and M.C.E. Huber, Eds., Kluwer Acad. Publ., Dordrecht, 677–697, 2001.

McEntire, R.W., E.P. Keath, D.E. Forth, A.T.Y. Lui, and S.M. Krimigis, The medium-energy particle analyzer (MEPA) on the AMPTE CCE spacecraft, *IEEE Trans. Geosci. Remote Sens.*, **GE-23**, 230–233, 1985.

McGarity, J.O., A. Huber, J. Pantazis, M.R. Oberhardt, D.A. Hardy, and W.E. Slutter, Compact ion/electron analyzer for spaceflight or laboratory use, *Rev. Sci. Instrum.*, **63**, 1973–1977, 1992.

Meier, A., Eichung des für die Untersuchung der inneren Koma des Kometen Halley verwendeten Ionenmassenspektrometers Giotto-IMS, Ph.D. thesis, University of Bern, 1988a.

Meier, R., Labormessungen mit dem Giotto-Neutralgasmassenspektrometer: Nacheichung des Zweitinstrumentes mit Kohlenmonoxid und Stickstoff, Diploma thesis, University of Bern, 1988b.

Mitchell, D.G. and E.C. Roelof, Thermal iron ions in high speed solar wind streams: Detection by the IMP 7/8 energetic particle experiment, *Geophys. Res. Lett.*, **7**, 661–664, 1980.

Mitchell, D.G., E.C. Roelof, W.C Feldman, S.J. Bame, and D.J. Williams, Thermal iron ions in high speed solar wind streams, 2. Temperatures and bulk velocities, *Geophys. Res. Lett.*, **8**, 827–830, 1981.

Mitchell, D.G., S.E. Jaskulek, C.E. Schlemm, E.P. Keath, R.E. Thompson, B.E. Tossman, J.D. Boldt, J.R. Hayes, G.B. Andrews, N. Paschalidis, D.C. Hamilton, R.A. Lundgren, E.O. Tums, P. Wilson IV, H.D. Voss, D. Prentice, K.C. Hsieh, C.C. Curtis, and F.R. Powell, High Energy Neutral Atom (HENA) imager for the IMAGE mission, *Space Sci. Rev.*, **91**, 67–112, 2000.

MKS Instruments, Six Shattuck Road, Andover, Massachusetts 01810, USA.

Möbius, E., G. Gloeckler, D. Hovestadt, F.M. Ipavich, B. Klecker, M. Scholer, H. Arbinger, H. Höfner, E. Künneth, P. Laeverenz, A. Luhn, E.O. Tums, and H. Waldleben, The time-of-flight spectrometer SULEICA for ions of the energy range 5–270keV/charge on AMPTE IRM, *IEEE Trans. Geosci. Remote Sens.*, **GE-23**, 274–2279, 1985.

Möbius, E., L.M. Kistler, M.A. Popecki, K.N. Crocker, M. Granoff, Y. Jiang, E. Sartori, V. Ye, H. Rème, J.A. Sauvaud, A. Cros, C. Aoustin, T. Camus, J.-L. Médale, J. Rouzaund, C.W. Carlson, J.P. McFadden, D. Curtis, H. Heetderks, J. Croyle, C. Ingraham, B. Klecker, D. Hovestadt, M. Ertl, F. Eberl, H. Kästle, E. Künneth, P. Laeverenz, E. Seidenschwang, E.G. Shelly, D.M. Klumpar, E. Hertzberg, G.K. Parks, M. McCarthy, A. Korth, H. Rosenbauer, B. Gräve, L. Eliasson, S. Olsen, H. Balsiger, U. Schwab, and M. Steinacher, The 3-D plasma distribution function analyzers with time-of-flight mass discrimination for Cluster, FAST, and Equator-S, in *Measurement Techniques in Space Plasmas: Particles*, R.-Pfaff, J.-Borovsky, and D.T.-Young, Eds., Geophys. Monogr. Ser., **102**, American Geophysical Union, Washington, D.C., 243–248, 1998.

Moore, J.H., C.C. Davis, and M.A. Coplan, *Building Scientific Apparatus*, Addison-Wesley Publishing Company, Inc., 1983.

Moore, T.E., C.R. Chappell, M.O. Chandler, S.A. Fields, C.J. Pollock, D.L. Reasoner, D.T. Young, J.L. Burch, N. Eaker, J.H. Waite, Jr., D.J. McComas, J.E. Nordholdt, M.F. Thomsen, J.J. Berthelier, and R. Robson, The thermal ion dynamics experiment and plasma source instrument, *Space Sci. Rev.*, **71**, 409–458, 1995.

Moore, T.E., C.J. Pollock, and D.T. Young, Kinetic core plasma diagnostics, in *Measurement Techniques in Space Plasmas: Particles*, R. Pfaff, J. Borovsky, and D.T. Young, Eds., Geophys. Monogr. Ser., **102**, American Geophysical Union, Washington, D.C., 105–123, 1998.

Moore, T.E., D.J. Chornay, M.R. Collier, F.A. Herrero, J. Johnson, M.A. Johnson, J.W. Keller, J.F. Laudadio, J.F. Lobell, K.W. Ogilvie, P. Rozmarynowski, S.A. Fuselier, A.G. Ghielmetti, E. Hertzberg, D.C. Hamilton, R. Lundgren, P. Wilson, P. Walpole, T.M. Stephen, B.L. Peko, B. van Zyl, P. Wurz, J.M. Quinn, and G.R. Wilson, The low-energy neutral atom imager for IMAGE, *Space Sci. Rev.*, **91**, 155–195, 2000.

Morrison, R., *Grounding and Shielding Techniques in Instrumentation*, Wiley-Interscience, New York, 1986.

Moss, S.J. and E. Hyman, Minimum variance technique for the analysis of ionospheric data acquired in satellite retarding potential analyzer experiments, *J. Geophys. Res.*, **73**, 4315–4323, 1968.

Müller, D., Ein einfaches Gas-Einlaßsystem zur präzisen Herstellung niedriger Drucke, *Z. Angew. Phys.*, **23(6)**, 467–470, 1967.

Müller-Mellin, R., H. Kunov, V. Fleißner, E. Pehlke, E. Rode, N. Röschmann, C. Scharmberg, H. Sierks, P. Risznyak, S. McKenna-Lawlor, I. Elendt, J. Sequeiros, D. Meziat,

S. Sanchez, J. Medina, L. Del Peral, M. Witte, R. Marsden, and J. Henrion, COSTEP—Comprehensive suprathermal and energetic particle analyser, *Solar Physics*, *162*, 483–504, 1995.

Nakayama, K. and H. Hojo, Relative ion gauge sensitivities to various hydrocarbon gases, *Japan. J. Appl. Phys.*, **Suppl 2(11)**, 113–116, 1974.

Nelder, J.A. and R. Mead, A simplex method for function minimisation, *Comp. Jou.*, **7**, 308–313, 1965.

Niemann, H.B., An atomic oxygen beam system for the investigation of mass spectrometer response in the upper atmosphere, *Rev. Sci. Instrum.*, **43**, 1151–1161, 1972.

Niemann, H.B., J.R. Booth, J.E. Cooley, R.E. Hartle, W.T. Kasprzak, N.W. Spencer, S.H. Way, D.M. Hunten, and G.R. Carignan, Pioneer Venus orbiter neutral gas mass spectrometer experiment, *IEEE Trans. Geosci. Remote Sens.*, **GE-18**, 60–65, 1980a.

Niemann, H.B., W.T. Kasprzak, A.E. Hedin, D.M. Hunten, and N.W. Spencer, Mass spectrometric measurements of the thermosphere and exosphere of Venus, *J. Geophys. Res.*, **85**, 7817–7827, 1980b.

Niemann, H.B., D.N. Harpold, S.K. Atreya, G.R. Carignan, D.M. Hunten, and T.C. Owen, The Galileo probe neutral mass spectrometer, *Space Sci. Rev.*, **60**, 111–142, 1992.

Niemann, H.B., S. Atreya, S.J. Bauer, K. Biemann, B. Block, G. Carignan, T. Donahue, L. Frost, D. Gautier, D. Harpold, D. Hunten, G. Israel, J. Luhnine, K. Mauersberger, T. Owen, F. Raulin, J. Richards, and S. Way, The gas chromatograph mass spectrometer aboard Huygens, *ESA Special Publication*, **SP-1177**, ESA Publications Division, Noordwijk, 1997.

Niemann, H.B., D.N. Harpold, S. Feng, W.T. Kasprzak, S.H. Way, S.K. Atreya, B. Block, G.R. Carignan, T.M. Donahue, A.F. Nagy, S.W. Bougher, D.M. Hunten, T.C. Owen, S.J. Bauer, H.J. Hayakawa, T. Mukai, Y.N. Miura, and N. Sugiura, The Planet-B neutral gas mass spectrometer, *Earth Planets Space*, **50**, 785–792, 1998.

Nier, A.O., W.E. Potter, D.R. Hickman, and K. Mauersberger, The open-source neutral-mass spectrometer on atmosphere explorer-C, -D, and -E, *Radio Sci.*, **8**, 271–276, 1973.

Nier, A.O., Planetary atmosphere with mass spectrometers carried on high-speed probes or satellites, *10^{th} International Symposium on Rarified Gas Dynamics*, **Paper No. 2**, Aspen Colorado, 1255–1275, 1976.

Nyffenegger, O., M. Mildner, P. Wurz, K. Altwegg, and H. Balsiger, Influence of electric charging on the ROSINA instrument in the plasma environment of comet 46P/Wirtanen, in *Proc. 7^{th} Spacecraft Charging Technology Conference*, *ESA Special Publication*, **SP-476**, ESA Publications Division, Noordwijk, 203–206, 2001.

O'Hanlon, J.F., *A User's Guide to Vacuum Technology*, 2nd Ed., John Wiley & Sons, New York, 1989.

Ogilvie, K.W., D.J. Charnay, R.J. Fritzenreiter, F. Hunsaker, J. Keller, J. Lobell, G. Miller, J.D. Scudder, E.C. Sittler Jr., R.B. Torbert, D. Bodet, G. Needell, A.J. Lazarus, J.T. Steinberg, J.H. Tappan, A. Mavretic, and E. Gergin, SWE, a comprehensive plasma instrument for the Wind spacecraft, *Space Sci. Rev.*, *71*, 55–77, 1995.

Østgaard, J.O., Measurement of channel electron multiplier efficiency using a photoemission electron source, *J. Phys. E*, *12*, 1106–1108, 1979.

Owens, C.L., Ionization gauge calibration system using a porous plug and orifice, *J. Vac. Sci. Technol.*, **2**, 104–108, 1965.

Outlaw, R.A., W.K. Peregoy, G.B. Hofland, and G.R. Corallo, Electron stimulated desorption of atomic oxygen from silver, NASA Technical Paper, **2668**, 1987.

Outlaw, R.A., and M.R. Davidson, Small ultrahigh vacuum compatible hyperthermal oxygen generator, *J. Vac. Sci. Technol. A*, **12**, 854–860, 1994.

Pages L., E. Bertel, H. Joffe, and L. Sklaventis, Energy loss, range and bremstrahlung yield for 10 keV to 100 MeV electrons in various elements and chemical compounds, *Atomic Data*, **4**, 1–127, 1972.

Parker, L.W. and E.C. Whipple Jr., Theory of spacecraft sheath structure, potential, and velocity effects on ion measurements by traps and mass spectrometers, *J. Geophys. Res.*, **75**, 4720–4733, 1970.

Paschmann, G., A.N. Fazakerley, and S.J. Schwartz, Moments of plasma velocity distributions, in *Analysis Methods for Multi-spacecraft Data*, G. Paschmann and P.W. Daly, Eds., *ISSI Scientific Report*, **SR-001**, ESA Publications Division, Noordwijk, 125–158, 1998.

Patterson, T.N.L., Deduction of ionospheric parameters from retarding potential analyzers, *J. Geophys. Res.*, **74**, 4799–4801, 1969.

Peggs, G.N., The measurement of gas throughput in the range 10^{-4} to 10^{-10} Pa m^3 s^{-1}, *Vacuum*, **26**, 321–328, 1976.

Peko, B.L. and T.M. Stephen, Absolute detection efficiencies of low energy H, H^-, H^+, H_2^+ and H_3^+ incident on a multichannel plate detector, *Nucl. Instrum. Methods B*, **171**, 597–604, 2000.

Pelz, D.T., C.A. Reber, A.E. Hedin, and G.R. Carignan, A neutral-atmosphere composition experiment for the Atmosphere Explorer-C, -D, and -E, *Radio Sci.*, **8**, 277–285, 1973.

Pelz, D.T., G.P. Newton, W.T. Kasprzak, and T.D. Clem, The San Marco III neutral atmosphere composition experiment, **NASA X-623-73-143**, Goddard Space Flight Center, Greenbelt, MD, 1973.

Peters, A., H. Reeg, P. Forck, W. Vodel, and R. Neupert, Recent improvements of a cryogenic current comparator for nA ion beams with high intensity dynamics, in *Proc. 4^{th} European Workshop on Beam Diagnostics and Instrumentation for Particle Accelerators (DIPAC)*, Chester, 109–111, 1999.

Pfeiffer Vacuum AG, Berliner Straße 43, D-35614 Asslar, Germany.

Pollock, C.J., K. Asamura, J. Baldonado, M.M. Balkey, P. Barker, J.L. Burch, E.J. Korpela, J. Cravens, G. Dirks, M.-C. Fok, H.O. Funsten, M. Grande, M. Gruntman, J. Hanley, J.-M. Jahn, M. Jenkins, M. Lampton, M. Marckwordt, D.J. McComas, T. Mukai, G. Penegor, S. Pope, S. Ritzau, M.L. Schattenburg, E. Scime, R. Skoug, W. Spurgeon, T. Stecklein, S. Storms, C. Urdiales, P. Valek, J.T.M. van Beek, S.E. Weidner, M. Wüest, M.K. Young, and C. Zinsmeyer, Medium energy neutral atom (MENA) imager for the IMAGE mission, *Space Sci. Rev.*, **91**, 113–154, 2000.

Poulter, K.F., M.-J. Rodgers, P.J. Nash, T.J. Thompson, and M.P. Perkin, Thermal transpiration correction in capacitance manometers, *Vacuum*, **33**, 311–316, 1983.

Poulter, K.L., Effect of gas composition on vacuum measurement, *J. Vac. Sci. Technol. A*, **2**, 150–158, 1984.

Powers, R.J. and R.M. Chambers, A clean cryo-vacuum system with high pumping speeds for all gas species, *J. Vac. Sci. Technol.*, **8**, 319–323, 1971.

Rao, M.V.V.S., I. Iga, and S.K. Srivastava, Ionization cross section for the production of positive ions from H_2O by electron impact, *J. Geophys. Res.*, **100**, 26421–26425, 1995.

Read, F.H., N.J. Bowring, P.D. Bullivant, and R.R.A. Ward, Penetration of electrostatic fields and potentials through meshes, grids, or gauzes, *Rev. Sci. Instrum.*, **69(5)**, 2000–2006, 1998.

Reames, D.V., Particle acceeration at the Sun and in the heliosphere, *Space Sci. Rev.*, **90**, 413–491, 1999.

Redus R., Private communication, Amptek Inc., Bedford, MA, 2002.

Rème, H., F. Cotin, A. Gros, J.L. Medale, and J.A. Sauvaud, The Giotto electron plasma experiment, *J. Phys. E*, **20**, 721–731, 1987.

Rème, H., J.M. Bosqued, J.A. Sauvaud, A. Cros, J. Dandouras, C. Aoustin, J. Bouyssou, Th. Camus, J. Cuvilo, C. Martz, J.L. Medale, H. Perrier, D. Romefort, J. Rouzaud, C. D'Uston, E. Möbius, K. Crocker, M. Granoff, L.M. Kistler, M. Popecki, D. Hovestadt, B. Klecker, G. Paschmann, M. Scholer, C.W. Carlson, D.W. Curtis, R.P. Lin, J.P. McFadden, V. Formisano, E. Amata, M.B. Bavassano-Cattaneo, P. Baldetti, G. Belluci, R. Bruno, G. Chionchio, A. di Lellis, E.G. Shelley, A.G. Ghielmetti, W. Lennartsson, A. Korth, H. Rosenbauer, R. Lundin, S. Olsen, G.K. Parks, M. McCarthy, and H. Balsiger, The Cluster ion spectrometry (CIS) experiment, *Space Sci. Rev.*, **79**, 303–350, 1997.

Rice, R.F. and Jun-J. Lee, Some Practical Universal Noiseless Coding Techniques, Part II, JPL Publication, **83-17**, 1983.

Roussel, J.-F., V. Viel, and J. Bernard, Characterization of a multicomponent plasma in an ionospheric plasma simulation chamber, in *Proc. 23rd International Conference on Phenomena in Ionized Gases*, Univ. Paul Sabatier, Toulouse, 1997.

Roussel, J.-F. and J.-J. Berthelier, A study of the electrical charging of the Rosetta orbiter: 1. Numerical model, *J. Geophys. Res.*, **109**, A01104, doi:10.1029/2003JA009836, 2004.

Santeler, D.J., D.H. Hokelboer, D.W. Jones, and F. Pagano, *Vacuum Technology and Space Simulation*, American Institute of Physics (AIP) Press, Washington, D.C., 1993.

Schmidt, K., Untersuchung der Dissoziation einfacher Moleküle und Molekülionen bei der Streuung an Metalloberflächen, Ph.D. thesis, University of Osnabrück, 1993.

Schultz, F.V., N.W. Spencer, and A. Reifman, Atmosphere Pressure and Temperature Measurements between Altitudes 40 and 110 km, University of Michigan Research Institute, Upper Atmosphere Report, **No. 2**, Air Material Command, July 1, 1948.

Scoles, G., D. Bassi, U. Buck, and D. Laine, *Atomic and Molecular Beam Methods*, **1**, Oxford University Press, New York, 1988.

Seltzer, S.M. and M.J. Berger, Transmission and reflection of electrons by foils, *Nucl. Instrum. Methods*, **119**, 157–179, 1974.

Shelley, E.G., A.G. Ghielmetti, H. Balsiger, R.K. Black, J.A. Bowles, R.P. Bowman, O. Bratschi, J.L. Burch, C.W. Carlson, A.J. Coker, J.F. Drake, J. Fischer, J. Geiss, A. Johnstone, D.L. Kloza, O.W. Lennartsson, A.L. Magoncelli, G. Paschmann, W.K. Peterson, H. Rosenbauer, T.C. Sanders, M. Steinacher, D.M. Walton, B.A. Whalen, and D.T. Young, The toroidal imaging mass-angle spectrograph (TIMAS) for the Polar mission, *Space Sci. Rev.*, **71**, 497–530, 1995.

Shirkov, G.D. and G. Zschornack, *Electron Impact Ion Sources for Highly Charged Ions*, Vieweg & Sohn Verlagsges., Brauschweig, 1996.

Silver, J.A., A. Freedman, C.E. Kolb, A. Rahbee, and C.P. Dolan, Supersonic nozzle beam source of atomic oxygen produced by electric-discharge heating, *Rev. Sci. Instrum.*, **53**, 1714–1718, 1982.

Simons, D.P.L., A.J.H. Maas, P.H.A. Mutsaers, and M.J.A. de Voigt, Study of localised radiation damage to PIPS detectors by a scanning microprobe: Measured effects and the consequences for STIM analysis, *Nucl. Instrum. Methods B*, **130**, 160–165, 1997.

Simpson, J.A., J.D. Anglin, A. Balogh, M. Bercovitch, J.M. Bouman, E.E. Budzinski, J.R. Burrows, R. Carvell, J.J. Connell, R. Ducros, P. Ferrando, J. Firth, M. Garcia-Munoz, J. Henrion, R.J. Hynds, B. Iwers, R. Jacquet, H. Kunow, G. Lentz, R.G. Marsden, R.B. McKibben, R. Müller-Mellin, D.E. Page, M. Perkins, A. Raviart, T.R. Sanderson, H. Sierks, L. Treguer, A.J. Tuzzolino, K.P. Wenzel, and G. Wibberenz, The Ulysses cosmic ray and solar particle investigation, *Astro. Astrophys. Suppl. Series*, **92(2)**, 365–399, 1992.

Smith, A., Analysis of a molecular beam system utilizing a known pressure source, NASA Technical Note, **NASA TN D-5308**, 1969.

Spjeldvik, W.N. and P.L. Rothwell, The Radiation Belts, in *Handbook of Geophysics and the Space Environment*, A.S. Jursa, Ed., Airforce Geophysics Laboratory, Chapter 5, 1985.

Spencer, N.W., H.B. Niemann, and G.R. Carignan, The neutral-atmosphere temperature instrument, *Radio Sci.*, **8**, 287–296, 1973.

Stark, J. and M. Kinnersley, The development of low power, high velocity oxygen source, *Rarified Gas Dynamics: Space Related Studies*, **116**, 156–170, 1988.

Steinacher, M., F. Jost, and U. Schwab, A modern and fully automated calibration system for space ion mass spectrometers, *Rev. Sci. Instrum.*, **66(8)**, 4180–4187, 1995.

Stephen, T.M., B. van Zyl, and R.C. Amme, Generation of a fast atomic-oxygen beam from O^- ions by resonant cavity radiation, *Rev. Sci. Instrum.*, **67**, 1478–1482, 1996.

Stephen, T.M. and B.L. Peko, Absolute calibration of a multichannel plate detector for low energy O, O^- and O^+, *Rev. Sci. Instrum.*, **71**, 1355–1359, 2000.

Stone, E.C., C.M.S. Cohen, W.R. Cook, A.C. Cummings, B. Gauld, B. Kecman, R.A. Leske, R.A. Mewaldt, M.R. Thayer, B.L. Dougherty, R.L. Grumm, B.D. Milliken, R.G. Radocinski, M.E. Wiedenbeck, E.R. Christian, S. Shuman, and T.T. Rosenvinge, The solar isotope spectrometer for the Advanced Composition Explorer, *Space Sci. Rev.*, **86**, 357–408, 1998a.

Stone, E.C., C.M.S. Cohen, W.R. Cook, A.C. Cummings, B. Gauld, B. Kecman, R.A. Leske, R.A. Mewaldt, M.R. Thayer, B.L. Dougherty, R.L. Grumm, B.D. Milliken, R.G. Radocinski, M.E. Wiedenbeck, E.R. Christian, S. Shuman, H. Trexel, T.T. Rosenvinge, W.R. Binns, D.J. Crary, P. Dowkontt, J. Epstein, P.L. Hink, J. Klarmann, M. Lijowski, and M.A. Olevitch, The cosmic-ray isotope spectrometer for the Advanced Composition Explorer, *Space Sci. Rev.*, **86**, 285–356, 1998b.

Sullivan, J.D., Geometrical factor and directional response of single and multi-element particle telescopes, *Nucl. Instrum. Methods*, **95**, 5–11, 1971.

Swaminathan, V., R. Alig, W. Murray, and D. Sarnoff, Design of an improved miniature ion neutral mass spectrometer for NASA applications, NASA Contract, **NAS5-32823**, 1996.

Takaishi, T. and Y. Sensui, Thermal transpiration effect of hydrogen, rare gases and methane, *Transactions of the Faraday Society*, **59**, 2503–2514, 1963.

Taylor, J.R., *An Introduction to Error Analysis: The Study of Uncertainties in Physical Measurements*, 2^{nd} Ed., University Science Books, CA, 1997.

Taylor, H.A. Jr., H.C. Brinton, and C.R. Smith, Positive ion composition in the magnetosphere obtained from the OGO-A satellite, *J. Geophys. Res.*, **70**, 5769–5781, 1965.

Taylor, H.A., Jr., H.C. Brinton, M.W. Pharo III, and N.K. Rahman, Thermal ions in the exosphere: Evidence of solar and geomagnetic control, *J. Geophys. Res.*, **73**, 5521–5533, 1968.

Taylor, H.A., H.C. Brinton, T.C.G. Wagner, B.H. Blackwell, and G.R. Cordier, Bennett ion mass spectrometers on the Pioneer Venus bus and orbiter, *IEEE Trans. Geosci. Remote Sens.*, **GE-18**, 44–49, 1980.

Tilford, C.R., Reliability of high vacuum measurements, *J. Vac. Sci. Technol. A*, **1**, 152–162, 1983.

Tilford, C.R., S. Dittmann, and K.E. McCulloh, The National Bureau of Standards primary high-vacuum standard, *J. Vac. Sci. Technol. A*, **6**, 2853–2859, 1988.

Tison, S.A. and C.R. Tilford, Low Density Water Vapor Measurements: The NIST Primary Standard and Instrument Response, NIST Internal Report, **NISTIR 5241**, 19–29, 1993.

Tsein, H., Superaerodynamics, mechanics of rarefied gases, *J. Aeron. Sci.*, **13**, 653–664, 1946.

Torsti, J., E. Valtonen, M. Lumme, P. Pletonen, T. Eronen, M. Louhola, E. Riihonen, G. Schultz, M. Teittinen, K. Ahola, C. Holmlund, V. Kelhä, K. Leppälä, P. Ruuska, and E. Strömer, Energetic particle experiment ERNE, *Solar Physics*, *162*, 505–531, 1995.

Troy, B.E. Jr. and E.J. Maier, Effect of grid transparency and finite collector size on determining ion temperature and density by the retarding potential analyzer, *J. Geophys. Res.*, **80(16)**, 2236–2240, 1975.

Tuszewski, M.G., T.E. Cayton, and J.C. Ingraham, A new numerical technique to design satellite energetic electron detectors, *Nucl. Instrum. Methods A*, **482**, 653–666, 2002.

Unser, K., A toroidal DC beam current transformer with high resolution, *IEEE Trans. Nucl. Sci.*, **NS-28(3)**, 2344–2246, 1981.

Upschulte, B.L. and G.E. Caledonia, Laboratory measurements of infrared excitation cross sections of fast O-atom collisions with CO, CO_2, and CH_4, *J. Chem. Phys.*, **96**, 2025–2033, 1992.

Utterback, N.G. and G.H. Miller, Fast molecular nitrogen beam, *Rev. Sci. Instrum.*, **32**, 1101–1106, 1961.

Uy, O.M., R.C. Benson, M.T. Boies, J.D. Kinnenson, J.S. Morgan, S.A. Tison, A.R. Fillippelli, and C.R. Tilford, Use of the NIST-developed water calibrator for the Midcourse Space Experiment (MSX) mass spectrometer, *Proc. SPIE*, **2214**, 316–324, 1994.

Vályi, L., *Atom and Ion Sources*, John Wiley & Sons, London, UK, 1977.

Van Zyl, B., N.G. Utterback, and R.C. Amme, Generation of a fast atomic hydrogen beam, *Rev. Sci. Instrum.*, **47**, 814–819, 1976.

Vasyliunas, V.M., Deep space plasma measurements, in *Methods of Experimental Physics*, **9B**, 49–88, 1971.

Vilppola, J.H., J.T. Keisala, P.J. Tanskanen, and H. Huomo, Optimization of hemispherical analyzer manufacturing with respect to resolution requirements, *Rev. Sci. Instrum.*, **64**, 2190–2194, 1993.

Vilppola, J.H., P.J. Tanskanen, H. Huomo, and B.L. Barraclough, Simulations of the response function of a plasma ion beam spectrometer for the Cassini mission, *Rev. Sci. Instrum.*, **67**, 1494–1501, 1996.

Vilppola, J.H., P.J. Tanskanen, B.L. Barraclough, and D.J. McComas, Comparison between simulations and calibrations of a high resolution electrostatic analyzer, *Rev. Sci. Instrum.*, **72**, 3662–3669, 2001.

Vodel, W., S. Nietzsche, R. Neubert, R. Nawoldt, A. Peters, K. Knaack, M. Wendt, and K. Wittenburg, SQUID based cryogenic current comparator for measurements of the dark current of superconducting cavities, in *Proc. 7^{th} European Workshop on Beam Diagnostics and Instrumentation for Particle Accelerators (DIPAC)*, Lyon, 163–165,

2005.

von Rosenvinge, T.T., L.M. Barbier, J. Karsch, R. Liberman, M.P. Madden, T. Nolan, D.V. Reames, L. Ryan, S. Singh, H. Trexel, G. Winkert, G.M. Mason, D.C. Hamilton, and P. Walpole, The energetic particles: acceleration, composition, and transport (EPACT) investigation on the Wind spacecraft, *Space Sci. Rev.*, *71*, 155–206, 1995.

von Steiger, R., Composition of the Solar Wind, Habilitation thesis, University of Bern, 1994.

von Zahn, U., Composition studies in the thermospere by means of mass spectrometers, in *Structure and Dynamics of the Upper Atmosphere*, F. Veriani, Ed., Developments in Atmospheric Science, Elsevier, Publishing Co, Amsterdam, **1**, 389–434, 1974.

Wadley, W.G., Magnetic shielding with multiple cylindrical shells, *Rev. Sci. Instrum.*, **27**, 910–916, 1956.

Waite, J.H., W.S. Lewis, W.T. Kasprzak, V.G. Anicich, B.P. Block, T.C. Cravens, G.G. Fletcher, W.-H. Ip, J.G. Luhmann, R.L. McNutt, H.B. Niemann, J.K. Parejko, J.E. Richards, E.M. Walter, R.L. Thorpe, and R.V. Yelle, The Cassini ion and neutral mass spectrometer (INMS) investigation, *Space Sci. Rev.*, **114**, 113–231, 2004.

Westermann, C.B., A Novel Calibration System for the Simulation of Cometary Atmospheres, Ph.D. thesis, University of Bern, 2000.

Westermann, C.B., W. Luithardt, E. Kopp, T. Koch, R. Liniger, H. Hofstetter, J. Fischer, K. Altwegg, and H. Balsiger, A high precision calibration system for the simulation of cometary gas environments, *Meas. Sci. Technol.*, **12(9)**, 1594–1603, 2001.

Whipple, E.C. Jr., J.W. Hirman, and R. Ross, A satellite ion-electron collector: Experimental effects of grid transparency, photoemission, and secondary emission, ESSA Tech. Rep., **ERL 99-ALI**, Environ. Res. Lab., NOAA, Boulder, CO, 1968.

Wieser, M., P. Wurz, P. Bochsler, E. Moebius, J. Quinn, S.A. Fuselier, J. DeFazio, and T.M. Stephen, Direct mass spectrometric measurement of interstellar neutral gas, *Proceedings of the Week of Doctoral Students 2002*, J. Safránková and A. Kanka Eds., Charles University, Prague, 275–280, 2002a.

Wieser, M., P. Wurz, K. Brüning, and W. Heiland, Scattering of atoms and molecules off a magnesium oxide surface, *Nucl. Instrum. Methods B*, **192**, 370–380, 2002b.

Wieser, M., Detection of Energetic Neutral Atoms and its Application to Heliospheric Science, Ph.D. thesis, University of Bern, 2005.

Wieser, M., P. Wurz, P. Bochsler, E. Moebius, J. Quinn, S.A. Fuselier, A. Ghielmetti, J. DeFazio, and T.M. Stephen, NICE: An instrument for direct mass spectrometric measurement of interstellar neutral gas, *Meas. Sci. Technol.*, **16**, 1667–1676, 2005.

Wieser, M. and P. Wurz, Production of a low energetic neutral particle beam using surface neutralization, *Meas. Sci. Technol.*, **16**, 2511–2516, 2005.

Wilken, B. and W. Stüdemann, A compact time-of-flight mass-spectrometer with electrostatic mirrors, *Nucl. Instrum. Methods*, **222**, 587–600, 1984.

Wilken, B., W.I. Axford, I. Daglis, P. Daly, W. Güttler, W.H. Ip, A. Korth, G. Kremser, S. Livi, V.M. Vasyliunas, J. Woch, D. Baker, R.D. Belian, J.B. Balke, J.F. Fennel, L.R. Lyons, H. Borg, T.A. Fritz, F. Gliem, R. Rathe, M. Grande, D. Hall, K. Kecsuméty, S. McKenna-Lawlor, K. Mursula, P. Tanskanen, Z. Pu, I. Sandahl, E.T. Sarris, M. Scholer, M. Schulz, P. Søraas, and S. Ullaland, RAPID – The imaging energetic particle spectrometer on Cluster, *Space Sci. Rev.*, **79**, 399–473, 1997.

Winningham, J.D., J.L. Burch, N. Eaker, V.A. Blevins, and R.A. Hoffman, The Low Altitude Plasma Instrument (LAPI), *Space Sci. Instrum.*, **5**, 465–475, 1981.

Wolf, B., Ed., *Handbook of Ion Sources*, CRC Press Inc., Boca Raton, FL, 1995.

Wüest, M., The calibration of satellite particle sensors, *Adv. Space Res.*, **23**, 1533–1536, 1999.

Wurz, P., T. Fröhlich, K. Brüning, J. Scheer, W. Heiland, E. Hertzberg, and S.A. Fuselier, Formation of negative ions by scattering from a diamond (111) surface, *Proceedings of the Week of Doctoral Students 1998*, J. Safránková and A. Kanka Eds., Charles University, Prague, 257–262, 1998.

Wurz, P., Heavy Ions in the Solar Wind: Results from SOHO/CELIAS/MTOF, Habilitation thesis, University of Bern, Bern, 1999.

Wurz, P., Detection of energetic neutral particles, in *The Outer Heliosphere: Beyond the Planets*, K. Scherer, H. Fichtner, and E. Marsch, Eds., Copernicus Gesellschaft e.V., Katlenburg-Lindau, 251–288, 2000.

Wurz, P., P. Bochsler, J.A. Paquette, and F.M. Ipavich, The calcium abundance in the solar wind, *Astrophys. Jou.*, **583**, 489–495, 2003.

Wutz, M., H. Adam, and W. Walcher, *Handbuch Vakuumtechnik*, 8^{th} Ed., Vieweg Verlag, Braunschweig, 2004.

Yeager, P.R., A. Smith, J.J. Jackson, and J.H. Hoffman, Absolute calibration of Apollo lunar orbital mass spectrometer, *J. Vac. Sci. Technol.*, **10**, 348–354, 1973.

Young, D.T., J.L. Burch, and J.A. Marshall, Ion accelerators in space plasma mass spectroscopy, *Nucl. Instrum. Methods B*, **41**, 750–754, 1989.

Zeman, H.D., Deflection of an ion beam in the two-dimensional electrostatic quadrupole field, *Rev. Sci. Instrum.*, **48**, 1079–1085, 1977.

Zhang, H., *Ion Sources*, Springer-Verlag, Berlin, 1999.

— 4 —

In-Flight Instrument Calibration and Performance Verification

JAMES P. MCFADDEN[1], DAVID S. EVANS[2], WAYNE T. KASPRZAK[3], LARRY H. BRACE[4], DENNIS J. CHORNAY[3], ANDREW J. COATES[5], BRONISLAW K. DICHTER[6], WALTER R. HOEGY[3], ERNEST HOLEMAN[7], KATHERINE KADINSKY-CADE[6], JUSTIN C. KASPER[8], DHIREN KATARIA[5], LYNN KISTLER[9], DAVIN LARSON[1], ALAN J. LAZARUS[8], FORREST MOZER[1], TOSHIFUMI MUKAI[10], KEITH W. OGILVIE[3], GÖTZ PASCHMANN[11], FRED RICH[6], YOSHIFUMI SAITO[10], JACK D. SCUDDER[12], JOHN T. STEINBERG[13], MARTIN WÜEST[14], AND PETER WURZ[15]

[1]*Space Sciences Laboratory, University of California, Berkeley, CA, USA*
[2]*Space Environment Center, NOAA, Boulder, CO, USA*
[3]*Goddard Space Flight Center, NASA, Greenbelt, MD, USA*
[4]*Leelanau Research, Empire, MI, USA*
[5]*Mullard Space Science Laboratory, Holmbury St. Mary, Dorking, Surrey, UK*
[6]*Air Force Research Laboratory, Hanscom Air Force Base, MA, USA*
[7]*Institute for Scientific Research, Boston College, Chestnut Hill, MA, USA*
[8]*Massachusetts Institute of Technology, Cambridge, MA, USA*
[9]*EOS, University of New Hampshire, Durham, New Hampshire, USA*
[10]*Institute of Space and Astronautical Science, Sagamihara, Japan*
[11]*International Space Science Institute, Bern, Switzerland*
[12]*University of Iowa, Iowa City, IA, USA*
[13]*Los Alamos National Laboratory, Los Alamos, NM, USA*
[14]*INFICON Ltd., Balzers, Liechtenstein*
[15]*Physikalisches Institut, University of Bern, Bern, Switzerland*

4.1 Introduction

In-flight calibrations are an essential component of any experiment plan for space-based instruments. These calibrations are necessary not only to verify instrument response and correct for instrument degradation, but also to identify unforeseen changes in response. Verifying proper operation after launch is necessary since the instrument has just experienced large stresses, both thermal and mechanical. In addition, post-launch is often the first time the instrument will experience the full spectrum of spaceflight perturbations, UV photon exposure, and particle flux levels. These perturbations result from the space environment, on-board subsystems, other experiments, or from some combination of these. The experimenter must develop procedures for in-flight testing and calibration of the instrument to assure its proper operation and to provide reliable data to the scientific community.

Once an instrument is launched into space, the science team will spend several weeks in a "commissioning phase" where instrument turn on is done step by step, proper instrument operation confirmed at each step, and inter-experiment compatibility verified. The extended time for this check-out reflects both the limits of real time ground communication, and a general caution during instrument commanding since any mistake could be catastrophic. This check-out does not end with the commissioning phase. Several months of intense data monitoring are normally required just to confirm that the instrument is operating as planned. For interplanetary missions, this commissioning may take place several years after launch. Once proper operation has been confirmed, the instrument team must perform in-flight calibration checks to both confirm and possibly refine the calibrations determined on the ground. In-flight calibrations may be a one-time event to confirm a pre-launch value, or may be an ongoing effort throughout the life of the mission. These calibrations may include "relative calibrations" that account for variations in instrument sensitivity with look direction or particle energy, and "absolute calibrations", which are used to determine overall sensitivity and accuracy of the particle flux measurements.

For some instruments, in-flight calibrations may be the only absolute calibrations possible. Absolute calibration done before launch often requires support facilities with relatively high costs, and may not be practical for some experiments. For other instruments whose absolute calibration is known to change over time, determination of the pre-launch absolute calibration may be an unnecessary step. In this case procedures should be developed to conduct an in-flight calibration that can determine the instrument sensitivity to the accuracy required. The needed accuracy of an instrument can be in the percent range (composition, isotope ratios) all the way to tens of percent. For example, for many single spacecraft missions, absolute calibrations to better than $\sim$30 % may not be necessary in order to fulfill the mission requirements. If the primary measurement is energy spectral shape rather than absolute flux values, an accurate absolute calibration may not be required as long as the instrument relative response can be verified within some general range. However, for multi-spacecraft missions where differences in measurements between spacecraft are critical to the science, careful in-flight absolute calibrations are essential.

This chapter is structured in the following fashion. The first section identifies known sources of instrument degradation, noise and spurious responses that necessitate in-flight calibrations for data validation. The material in this section includes descriptions of problems and, when known, explanations of their origin. Separate sub-sections concentrate on different types of instrumentation.

The next section in this chapter deals with the in-flight procedures and techniques that have been used to expose and correct some of the forms of instrument degradation that were described in the first section. Examples of the results obtained from implementing these procedures on space-flight instruments are provided.

While some missions, for example routine monitoring missions, may require little more than correcting for instrument degradation and spurious sensor response, other missions may require the more difficult step of in-flight determination of absolute instrument calibration. The subsequent sections in this chapter describe the in-flight calibration techniques designed to establish the much more difficult absolute calibration and accuracy of space plasma and particle sensors. Separate sections are devoted to the procedures for establishing the absolute calibration of plasma ($<$30 keV), energetic particles ($>$30 keV), and neutral gas experiments. The material also provides examples of in-flight calibrations that have been performed on single- and multi-spacecraft missions.

Throughout the chapter the material is infused with much of the current "lore" and "experience" gained by those individuals who have performed these tasks. The material points out where in-flight calibrations may fail and where one can be fooled by false agreements. A major objective of the chapter is not only to present useful calibration techniques but also to describe pitfalls and problems in performing these tasks.

For those who attempt these tasks in the future, here is a word of caution: If one can explain away a calibration disagreement, what do agreements tell you? Calibrations require a continuing effort to understand and explain the data.

4.2 Sources of Instrument Degradation, Noise, and Spurious Responses

This section identifies various sources of instrument degradation and discusses how this degradation affects an instrument's response. Degradation is the primary reason that periodic in-flight calibrations are required. Since degradation may manifest itself in the form of noise and since noise removal is required before performing in-flight calibrations, sources of spurious or background noise are also discussed, including those not related to degradation. This material is a necessary prelude to the discussions of in-flight calibration because unforeseen noise will often accompany an instrument's first operation in the harsh environment of space. To the extent possible the problems are characterized quantitatively and, when possible, solutions are provided. Where appropriate, diagnostics that could help identify problems on future experiments are suggested. Much of this discussion centers on the detectors and how radiation, contamination, and extended use affect their life. However, information is also provided on analyzers and associated electronics, in particular how those can contribute to instrument degradation and noise.

The first two sections discuss electrostatic analyzers and electron multiplier (MCP and CEM) detectors, which form the heart of most plasma instruments. A separate section on time-of-flight systems addresses problems associated with these more complex instruments that incorporate carbon foils. These sections are followed by a compact summary of well-known problems with energetic particle detectors. Problems specific to neutral gas instruments and ENA instruments, which incorporate many of the same analyzer and detector systems, are discussed separately. Separate sections are included for Faraday cups, which are frequently used to measure the intense solar wind ion flux, and Langmuir probes that are often used to infer plasma density. This section closes with some examples of unexpected sources of noise that warrant a more extended discussion.

4.2.1 Electrostatic Analyzers (ESAs)

There is no known mechanical degradation experienced by ESAs other than catastrophic failure due to vibration at launch. However, there are a number of processes that give rise to spurious, undesirable, and unexpected responses associated with ESAs.

Response to ultraviolet photons. Electrostatic analyzers do allow several forms of background "noise" to reach the plasma detectors. Perhaps the most serious form of spurious response experienced by ESA plasma instruments is caused by photons that scatter in the

analyzer to reach the detector. In particular, solar UV often produces large background responses in sensors whose aperture faces the Sun. Proper analyzer design must include serrating (or scalloping) the outer analyzer surface and blackening both surfaces. Scalloping the outer plate was found to reduce scattered UV by an order of magnitude in a gold-blackened, top-hat analyzer designed to require a photon to make two reflections to reach the detector [*Carlson and McFadden*, 1998]. Serrating (scalloping) the inner plate was not necessary because three reflections were required to reach the detector from the inner plate.

The Cluster HIA top-hat ion analyzer [*Rème et al.*, 1997] (with $\Delta R/R$=0.065, $R \sim$ 4 cm, scalloped outer sphere, Cu_2S blackening of both spheres) had extremely low solar UV response ($\sim$50 counts s^{-1} peak rate), demonstrating that the technique was adequate. In contrast, the FAST ion analyzers ($\Delta R/R$=0.075, $R \sim$4 cm, scalloped outer plates) and electron analyzers ($\Delta R/R$=0.060, $R \sim$4 cm, scalloped outer plates) used gold-black and experienced peak solar UV background count rates as high as $\sim$650 s^{-1} and $\sim$400 s^{-1}, respectively, indicating gold-black is not as effective. *Zurbuchen et al.* [1995] provided a comprehensive analysis of blackening techniques and concluded that CuO and Cu_2S provide the lowest UV reflectivity.

The electron and ion analyzers in the Low-Energy Particle (LEP) experiment on Geotail [*Mukai et al.*, 1994] used both serrated analyzer plates and carbon blackening (Aerodag G) to reduce the efficiency of counting solar EUV photons by a factor of 10^7. Even then the sensors had a residue response to solar EUV when the Sun was in the field of view that was significant when the instrument was in a low-density plasma regime. In this case modeling, based on laboratory calibrations, permitted a subtraction of the remaining EUV response from the sensor measurements to correct the data.

As the experience with the CELIAS-STOF instrument on SOHO shows, Lyman-α is not alone in producing solar photon background in detectors. STOF was designed to reduce Lyman-α background but was still swamped with spurious response from other UV light that made the sensor usage much more complicated. Although Lyman-α is the most intense solar line, other UV lines can contribute substantially. The integral of the UV intensity from $\lambda = 0$ to 250 nm (corresponding to the work function of carbon) is about a factor of 300 larger than the Lyman-α intensity. *Bamert* [2004] discusses the ground processing correction for solar UV contamination and, after significant effort, STOF can provide usable data.

Other instruments have introduced UV light traps at the ESA entrance aperture, either in lieu of serrated analyzer plates or to add to the UV suppression provided by plate serration. Among those are the PEACE electron instrument on Cluster [*Johnstone et al.*, 1997] and the ASPERA-3 electron spectrometer (ELS) on the Mars Express mission [*Barabash et al.*, 2004].

In addition to spurious responses from photon scatter, solar UV will produce photoelectrons within the ESA whenever the sensor aperture faces the Sun. These photoelectrons will produce a response in detectors when the analyzer is operated to select low-energy electrons. Elimination of this background is probably not possible and necessitates special data handling that can reduce its impact on the measurements. Section 4.4.3 describes in detail how the effect of photoelectrons from the Geotail satellite was handled in the computation of total ion and electron densities.

Scattered Electrons. Scattered and secondary electrons introduce still another form of background in electron ESAs. Electrons impinging at low angle of incidence on the analyzer plate surface have a 50 % or higher probability of scattering with little energy loss and can result in an out-of-energy-band response in ESA detectors. For an incident monoenergetic unidirectional electron beam this scattering can produce a spurious detector response at ESA angles and energies other than the incident beam angle and energy. The magnitude of the problem depends upon details of the ESA design. It often appears in an ESA designed for high geometric factor, such as top-hat analyzers, whose small deflection angle ($<90°$) permits electrons outside the selected energy pass band to pass through with a single scatter.

For these sensors, the amplitude of the response in the wings may be a few percent of that at the nominal central beam energy and extend from about half to twice the beam energy before the analyzer structure forces a second bounce. For broad electron energy spectra, this scattering has a negligible effect. For steep spectra, the sensor response due to electron scattering will set an upper limit to the resolution of high-energy tails in the spectra. For highly peaked spectra, as found in the Earth's auroral zones, internal scattering and secondary electron production can also produce an apparent low-energy component to the electron spectrum. This component is difficult to distinguish from atmospheric secondary electrons and may require complex ground processing for its removal. Ground testing should be undertaken to measure the extent that electrons can gain access to the detector by scattering in the analyzer.

Scattered electrons can also lead to spurious response in ESAs operated to measure positive ions. Top-hat design ion ESAs on the FAST spacecraft experienced increased background counts when intense fluxes of 10 keV electrons were present. Intense electron fluxes below 2–3 keV generally do not pose a problem for ion sensors since the front surface of the detectors (MCPs or CEMs) are typically biased negative at 2–3 kV, preventing these electrons from reaching them.

Scattered Ions. Problems similar to those arising from scattered electrons may also occur for scattered ions. Ions entering an ESA with energies outside the selected passband or angles outside the nominal ESA field-of-view may strike the analyzer plate at glancing incidence and have a small probability of being specularly reflected. Such ions would have a non-zero probability of passing through the analyzer to the detector despite having an incorrect energy-to-charge ratio. This process would diminish, or smear the instrument energy resolution and could produce ghost peaks in the ion energy spectrum. The application of a rough surface coating to the analyzer plates, or employing serrated analyzer plates, would minimize specular reflection by reducing the area exposed for small-angle scattering. *Wüest and Bochsler* [1992] have shown that the application of a CuS_2 coating to the analyzer plates reduces the ion scattering by about an order of magnitude, more so at the extremes of the energy passband than towards the center (Figure 4.1).

Field Emission. Field emission of low-energy electrons from exposed insulating surfaces within the ESA structure can be still another source of spurious response in the particle detector. This can arise when highly insulating metal oxide surfaces (aluminum or magnesium oxide, for example) are directly exposed to fluxes of hot plasma and acquire a surface charge. The electric field strength between the charged surface and the underlying

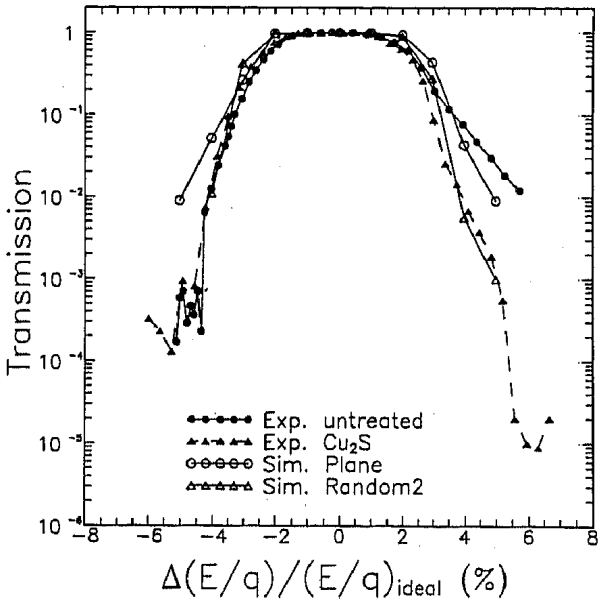

Figure 4.1: Transmission of He^{2+} through a spherical section analyzer (Wind/MASS ESA prototype) as function of the deviation from the nominal incidence energy. The results of experimental measurements, using an untreated and a copper sulfide treated analyzer, are compared to theoretical results obtained from a Monte Carlo simulation that included particle scattering from the analyzer plates. From *Wüest and Bochsler* [1992].

conducting metal can become so large that electrons are field emitted from the surface [*Malter*, 1936] and counted by the particle detector. Care must be taken in the choice of materials and to insure that insulating surfaces within an ESA are not exposed to incident plasma or viewed directly by the particle detector positioned behind the ESA plate structure.

High Voltage Problems. Noise counts associated at the highest energy steps of top-hat ESAs have been observed in several instruments. These counts were observed in relatively compact analyzers (R=4 cm), both ion and electron, and when the deflection voltage was $\sim$4 kV. The magnitude of these noise counts varied from zero to several hundred counts per second among essentially identical analyzers. Field emission or electrical discharges within the ESA is believed to be the cause, possibly due to microscopic variations in blackening. Other than replacing an entire unit, no solution was found for this problem. In what may be a related problem, during thermal vacuum testing for the FAST spacecraft, operator error resulted in several ESAs having their high voltage turned on in poor vacuum resulting in internal arcing. During subsequent operation in high vacuum, these sensors showed a high noise level that increased with the higher deflection plate voltage. Inspection showed that the insulator supporting the inner hemisphere of the analyzer had discoloration streaks due to surface arcing. Once a surface arc path is formed, there continues

to be an arcing problem even in high vacuum. Noise from this arcing was capacitively coupled to the charge sensitive preamplifiers to produce a spurious response. Cleaning the insulators eliminated this source of noise.

ESA electrical failures typically involve the loss of the high voltage sweep supply and hence the complete loss of the instrument. However, there have been partial electrical failures that result in degraded operation. The ISEE-3 electron electrostatic analyzers were designed to sweep in energy from 1.2 to 16 keV. During post-launch testing, the CEM count rates above 8 keV particle energy were observed to be independent of ESA energy setting, whereas it was known that the electron flux decreased dramatically at higher energies. There were no diagnostics available to check the high voltage output. It was postulated that the sweep high voltage supply was prevented from reaching its maximum voltage due to excessive leakage current while the lower energy portion of the sweep worked properly. An extrapolation of the solar wind spectra (measured by a separate instrument) to higher energies was consistent with the 1.2–8.0 keV measurements and dispersion analysis of solar electrons during Type III events confirmed that the lower energy channels were operational. This partial failure, whose cause was never unambiguously determined, was an indication of future troubles and the high voltage supply failed completely after $\sim$15 months. Modern experiments should include diagnostics that directly measure the sweep supply voltage and current to confirm proper operation and diagnose malfunctions.

Opto-coupler degradation. Some of the more recent ESA plate voltage sweep designs incorporate opto-couplers to obtain fast plate voltage sweeps and voltage resets (e.g., *Carlson et al.* [2001]). Historically, ESAs swept particle energy by using a rapid analyzer plate charge to high voltage followed by a slow, exponential (or pseudo-exponential) voltage decay during which particle data were taken. The charging time represented a period when useful data were not collected. Opto-couplers are devices that incorporate light emitting diodes (LED) operated at low voltage to control the conductance of photodiodes that, in turn, govern the charging (or discharging) current delivered from a high voltage supply to the ESA plates. The light signal from the LED is coupled to the photodiode by a light pipe thereby providing electrical isolation between the low and high voltage portions of the system. The LED can be driven by a low voltage signal to modulate the conductance of the photodiode and so tailor the voltage profile imposed on the ESA plates. In FAST two separate opto-coupler systems are used; the first to control the charging of the analyzer plates, which can be made very rapid because of the very high conductance capability of the photodiode, and the second to control a slower discharge phase during which particle data are obtained. Radiation damage to opto-couplers and their drive circuits is a concern. Radiation damage can decrease the conductance of the photodiode for a given illumination, can change the light emission from the LED for a given drive signal, or can change the transparency of the light pipe.

The FAST satellite utilized 24 pairs of opto-couplers (AMPTEK HV601B) in a radiation environment anticipated to be $\sim$20–30 kRad per year after shielding. Ground testing showed the opto-couplers to be fairly rugged, with only a 13 % drop in photodiode conductance after a 98 kRad dose in 8 hours. After 7 years on orbit, all FAST opto-coupler circuits are still functioning although they have experienced degradation. Analyzer plate charge times have increased from pre launch values of $<$1 ms to between 3 and 8 ms.

In the case of the 8 ms charging time constant, the analyzer plate voltage only reached ∼40 % of the available voltage indicating that the opto-coupler transconductance had decreased by at least a factor of 20. The opto-coupler circuits with the most degradation were those circuits that experienced the largest drive currents. The two most degraded circuits were operated to sweep the ESA from 8 to 30 keV (∼30 mA drive current) every 6.4 ms continuing in that mode at a ∼40 % sweep duty cycle for 3 years. During the remaining 4 years those circuits operated in a less stressful mode where the ESA plate voltages remained fixed for about half the time with much reduced photodiode current demand.

In comparison, the two circuits that operated the 2 to 8 keV ESA energy sweep during the same period had their transconductance decreased by only about a factor of ∼10. The remaining circuits, which were operated at still lower voltages, retained about 1/3 of their initial conductance for the recharge opto-couplers. There was also evidence that a plate voltage discharge opto-coupler in one of the most highly stressed circuits (8–30 keV ESA energy sweep) has degraded enough ($<$1/20 the initial conductance) that the sweep voltage slew rate was affected over a limited energy range.

These results suggest that opto-coupler degradation is not just a function of the radiation environment but also depends upon the drive current. In the case of FAST, this degradation affected the higher energy steps of the ESA making data analysis difficult. For experiments with opto-couplers that require large drive currents in a high radiation environments, designing in the ability to increase the plate voltage charge time by ground command will help alleviate the loss of high-energy channels.

4.2.2 Gain Degradation in Electron Multiplier Detectors

While other types of electron multiplier particle detectors have been used in the past (such as the Johnston discrete dynode multiplier), microchannel plate (MCP) and Channel Electron Multiplier (CEM) detectors (see Section 2.2.3) are currently the most common low-energy particle detectors used in plasma sensors. Both devices operate as electron multipliers, with typical output charge pulses of $\sim 10^6$ electrons for chevron configuration MCPs and $>10^7$ for CEMs for a registered ion or electron. Their properties depend on the manufacturing process (glass type, chemical treatment, etc.) and any exposure to contaminants. In general, MCP and CEM properties are similar enough that the following discussions will treat them together. Properties peculiar to one or the other will be pointed out.

MCP and CEMs are known to age. This aging manifests itself in two ways, and both effects must be identified and compensated for in order to maintain the integrity of the observations throughout a space mission. The first is a decrease in electron gain that depends upon total extracted charge and results in a decrease in pulse counting efficiency. This gain decrease is discussed in greater detail below.

The second is a decrease in the efficiency for an incident particle to produce secondary electrons at the entrance aperture of the device necessary to initiate a detectable output pulse. This decrease is primarily related to hydrocarbon contamination. Such contamination may not be initially detectable because a contaminated MCP or CEM may have particle conversion efficiencies similar to clean devices. However, under UV or particle bombardment, hydrocarbon chains may form on the sensitive area of the input face of the device, effectively changing its properties. An efficiency decrease may be observed with fewer than 10^{13} counts cm^{-2} for MCPs, which may be less than a mission lifetime.

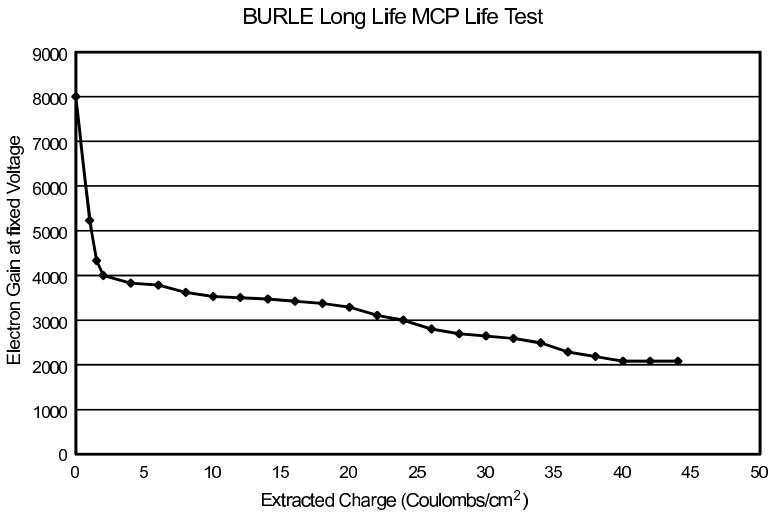

Figure 4.2: MCP gain vs. extracted charge.

To avoid these problems we strongly suggest washing all detectors in a 50:50 mixture of isopropanol and methanol, followed by baking at 100 °C for ∼30 minutes.

New MCPs and CEMs show an abrupt decrease in gain early in their life. This initial decrease is believed to be related to changes on the interior surface where contaminants (adsorbed gases, water vapor, etc.) are slowly scrubbed away by electron bombardment. Typically the detector bias voltage must be raised several times during the first few months or years of operation to compensate for this gain decrease. After the initial scrubbing period, the devices exhibit a rather slow decrease in gain that will still require monitoring, but usually with less frequent changes in bias voltage required. The initial gain decrease can be avoided by performing scrubbing prior to launch [*Martin et al.*, 2003], but this will necessitate subsequently maintaining the detectors isolated in a high vacuum or a dry nitrogen purge.

Because of their large collecting area and ability to resolve the spatial location of an event on the surface of the device, MCPs have become the low-energy particle detector of choice on recent space missions. However, MCPs also have a finite operating life. Testing indicates that the total charge per unit area that can be extracted from the MCP is between 10 and 100 C cm^{-2} before the device becomes unusable (Figure 4.2). This limit appears to be due to changes in the micro-pore glass due to alkali metal migration. While the progressive decrease in MCP gain can be compensated by increases in the bias voltage, eventually the voltage capability of the bias supply may reach its limit or voltage breakdown within the MCP may occur. This suggests that it is better to operate the MCP at the lowest acceptable gain to maximize lifetime.

MCPs have been used in a number of experiments and scientific missions in recent years. Considerable, and very diverse, experience has been accumulated concerning MCP lifetimes in terms of total charge extracted from the device leading to some possible insight into those factors that govern total lifetime. Among those factors that may play a role are the selection of bias voltage to optimize the pulse height distribution (PHD), the length

to diameter ratio (L/D) of the MCP pores, and the MCP resistivity that is often tailored to improve the count rate dynamic range of the device. The following details some representative examples of MCP lifetime and makes suggestions for procedures that may improve operating lifetime.

The MCPs in the Wind 3D Plasma (1994 launch) and FAST ESA (1996 launch) instruments continue to function normally after many years on orbit. The Wind 3D Plasma, EESA-L, sensor (180° FOV) has experienced the largest integrated fluxes, with a total count estimated as of late 2003 to be $\sim 10^{14}$ or $\sim$8 C cm^{-2} of charge extracted from the device active area. The EESA-L sensor used MCPs manufactured by Mullard (currently Photonis) in the form of half-annulus rings L/D=80 with resistivities of $\sim$400 MΩ cm^{-2}. Bias voltages were increased several times during the first two years of operation (from 2.2 kV to 2.4 kV), but no further increases have been required in recent years. These MCPs were not scrubbed prior to flight, so the initial voltage increase was likely necessitated by gain loss from in-flight scrubbing. The Wind high voltage supply currently has an additional 1.2 kV of capability for future voltage increases.

The FAST analyzers used Galileo (currently Burle), higher-current, larger-pore MCPs ($\sim$180 MΩ cm^{-2}, L/D=40) with the same overall dimensions as the MCP used in the EESA-L instrument. MCP bias voltages were initially set between 1.7 and 1.9 kV, and were increased to 1.9–2.15 kV after 7 years operation. Typically the major increase in bias voltages on the FAST MCPs were required during the first and second year of operation with additional increases not required until much later in mission life. The required voltage increases varied among individual MCPs with the smallest bias voltage increases (100–150 V) associated with those MCPs that started the mission at higher voltage. The largest bias voltage increase ($\sim$400 V) was for a sensor that experienced identical fluxes to a sensor with the lowest bias increase ($\sim$100 V), suggesting that the MCP gain loss was not strictly a function of integrated counts. Both these sensors currently have similar bias voltages indicating that the primary difference between those two MCPs was their change in response during early orbit scrubbing. The MCP in the FAST electron ESA (360° FOV) has experienced an integrated count of $\sim 8\times10^{12}$, or $\sim$0.34 C cm^{-2} extracted from the MCP active area, with no signs of degradation. This sensor required a $\sim$250 V increase in bias voltage during the first two years, with only an $\sim$100 V increase during the following 4 years. The rather small gain loss after initial scrubbing was typical of all 16 MCPs on FAST indicating gain losses occur rather slowly for the fluxes encountered during this mission.

Unlike the FAST and Wind MCPs, the Cluster/PEACE MCPs required significant bias voltage increases during the first 2 years of operations. Figure 4.3 shows the gain history of the LEEA and HEEA MCPs on one of the Cluster spacecraft. The periodic increases in MCP gain are associated with bias voltage adjustments. In the absence of such adjustments, the MCP gains decrease by nearly a factor of 10 over several months of operation.

The PEACE electron plasma analyzers used Philips (currently Photonis), chevron-configuration MCPs with 12.5 μm pores, L/D of 80, and pore bias angles of 13°. The plates were not scrubbed prior to flight. Initial bias voltages of 2.8 kV were required for an average gain of $\sim 2\times10^6$. During the first two years of operation, the sensors have seen total counts estimated at 2.6–3.6$\times10^{12}$ (currently being corrected for counts below threshold) for the Low-Energy Electron Analyzers (LEEAs) and 3.6–4.4$\times10^{12}$ for the High-Energy Electron Analyzers (HEEAs). Corresponding charge extraction is estimated at 0.38-0.6 C and 0.47–0.84 C (0.042–0.067 and 0.052–0.093 C cm^{-2}). Significant gain

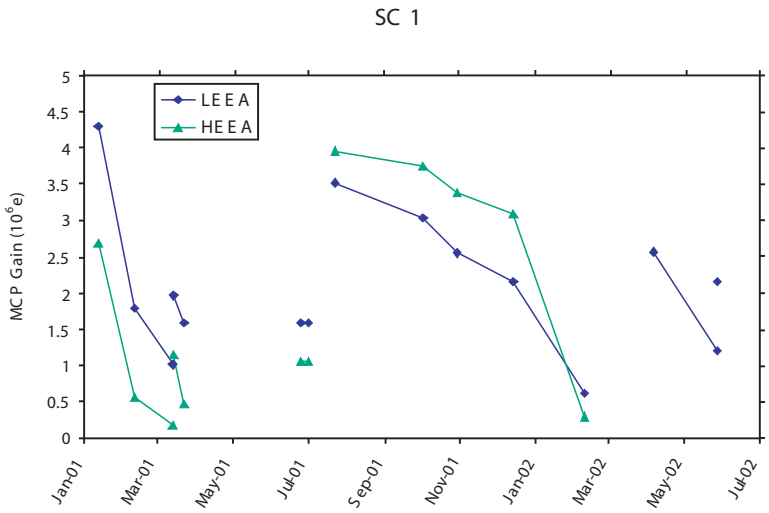

Figure 4.3: The time history of the MCP gains in the PEACE LEEA and HEEA analyzers on Cluster SC1. The periodic increases in gain are due to changes in MCP bias voltages. These MCPs suffered significant gain losses over periods of only a few months of operation.

drops were observed and compensated by voltage changes, which were between 450–570 V for the LEEAs and 570–800 V for the HEEAs. In general, larger changes were required for MCPs with lower gain. This relatively rapid decrease in gain has required MCP bias voltages to be increased to near the HV supply limits. To increase instrument's lifetime, the sensors are no longer operated at their full duty cycle, with some sensors turned off in high flux regions such as the magnetosheath.

What has caused the unexpected degradation of the Cluster/PEACE MCPs? The results of *Martin et al.* [2003] on the scrubbing profile of MCPs (Figure 4.4) show that scrubbing continues until more than 0.1 C cm^{-2} charge has been extracted. Since the charge extracted from the PEACE MCPs was rather small (<0.1C cm^{-2}), those devices should have been still experiencing scrubbing and not have been anywhere near the lifetime charge extraction limit.

Similar MCP cleaning and contamination control (dry N_2 purge) were implemented for all these projects. Internal insulators were similar low outgassing materials, such as PEEK (Polyetheretherketone), Kapton, Polyimide, Glass Laminate, Vespel, Ultem, and Macor. In addition, the Cluster/HIA sensors experienced identical pre-launch environments as PEACE but have shown no signs of degradation other than early orbit scrubbing. A possible and likely explanation is that the PEACE design required too high an MCP bias voltage at the mission start, and that subsequent voltage increases to compensate for scrubbing quickly used up the additional range of the HV supplies. PEACE used microchannel plates with L/D=80, which require higher bias voltage in the Chevron configuration than plates with L/D=40 would for the same gain. This lower gain can be compensated by either using a thin spacer (∼0.025 mm) between the plates to increase the number of microchannels firing in the second plate, or by increasing the bias voltage. The PEACE team

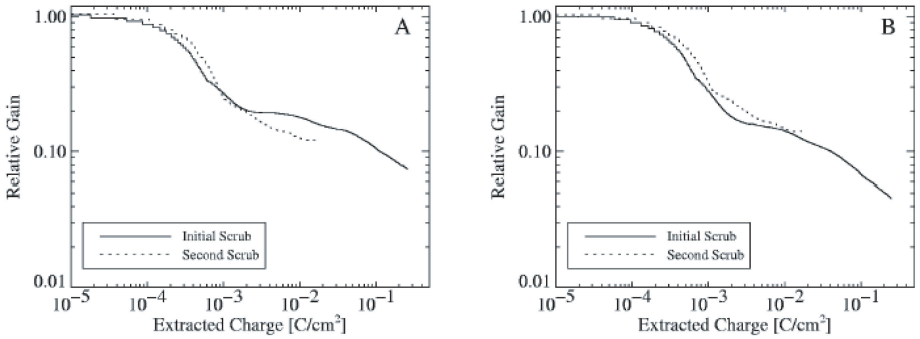

Figure 4.4: Relative gain as a function of charge extracted for the scrubs of the two MCP segments A and B of the COS-FUV01 instrument on HST. From *Martin et al.* [2003].

chose to increase the bias voltage because this resulted in narrower MCP pulse height distributions (see PHD, Section 2.2.4 for a discussion) at mission start, and therefore better performance with fewer charge pulses near their preamplifier threshold. However, a high bias voltage ($\sim$1.4 kV per plate) was required to get the peak in the PHD ($\sim 2 \times 10^6$) well above their preamplifier threshold ($\sim 4 \times 10^5$), which meant the plates were being driven near their gain limit. Subsequent small drops in gain due to scrubbing required large voltage increases to compensate, resulting in some sensors being driven at the HV supply upper limit after only $<$0.1 C cm^{-2} charge extraction. In retrospect, a better solution may have been to use a spacer between the MCPs and accept less than ideal PHDs early in the mission. We note that for plates with L/D=40 in Chevron configuration, spacers are not required for gains of $\sim 2 \times 10^6$ with modest ($\sim$1 kV per plate) bias voltages.

Monitoring and compensating for gain loss in MCP detectors is complicated by the fact that gain loss is often not uniform over the sensitive area of the device. For example, a solar wind ion detector may have the bulk of its count rate confined to a small portion of the MCP area, as is the case for the Wind 3D Plasma and Cluster/HIA sensors. This can cause the gain to decrease more rapidly over a part of the detector requiring an increase in bias voltage. However, this leads to excessively high gain in other parts of the MCP and may result in higher noise levels. This problem can be mitigated with proper laboratory MCP scrubbing, however it may be better to avoid this problem by designing the instrument so that the MCP sensitive area is more uniformly exposed to the incident particles. For example, a top-hat ion ESA could be designed so its 360° planar FOV responds to solar wind ions in a spacecraft spin plane oriented to correspond to the ecliptic plane. This would produce a uniform dose on the MCPs since the solar wind is generally confined to the ecliptic plane. Deflectors at the ESA entrance could be used to provide a small out-of-plane measurement of the solar wind. In principle, this arrangement could also provide extremely fast measurements of the solar wind independent of spacecraft spin.

A final point of caution. Instruments that incorporate MCPs are often designed with safety features that shut off the experiment if too much detector current is drawn. The threshold current level for these features should be adjustable in-flight since MCP currents change substantially during the mission, for example with increases in MCP bias voltages

to compensate for gain loss. MCP resistance also decreases with increased temperature, so currents will rise when the instrument gets hot with the potential for destructive thermal runaway . To prevent this problem, current trips or limiters should be included in the high voltage supply design together with adequate heat sink capability in the MCP mounting structure.

Section 4.2.9 describes in greater detail some instances of subtle and, as yet, unexplained, cases of noise counts arising from MCP and CEM detectors.

4.2.3 Time-of-Flight Detector Systems

Time-of-flight (TOF) systems are inherently less susceptible to noise because of the coincidence requirements for a measurement. In order to count as a valid event, two or three signals must be triggered within a set time window. For example, an ion must trigger a "start," a "stop" and perhaps also a "position" or "energy" detector. Thus, a random penetrating particle from the radiation belts that results in a single count on one detector is not counted as an event, and so does not create background. Only when the rates are high enough that random counts are measured for "start" and "stop" and "position" will they actually be counted as an event in the instrument. Cluster/CODIF measures singles rates of 30,000 counts per second (cps) from penetrating ions from the radiation belts. Despite this high rate, CODIF can still measure the ion composition, while the background severely degrades the Cluster/HIA electrostatic analyzer measurements.

Time-of-flight mass spectrometers typically use thin carbon foils, which are traversed by the particle to be registered, to create a start signal. The passing particle (an energetic ion or atom) releases secondary electrons both on the entrance and the exit side of the carbon foil. Depending on instrument design either the entrance or exit electrons are guided to a detector for the start pulse. The yield of secondary electrons depends strongly on the chemical nature of the surface (the outer-most layer). When at air all surfaces are covered with a thin water layer, possibly creating a thin oxide layer. Other residues from processing the carbon foil may also be present initially. Typically, these surface coatings increase the secondary electron yield. Since this layer is thin it evaporates with time in vacuum (e.g. during the mission) or is sputtered away and the secondary electron yield is reduced by a factor two to six when reaching a clean carbon surface. This results in a degradation of the start efficiency or total electron yield and cannot be separated from a gain reduction of the start MCP. For example, for the MTOF sensor of the CELIAS instrument on SOHO the start rate decreased by a factor of 3 during the first 2 years of operation, which is mostly attributed to the decrease in secondary electron yield of the carbon foil (F. Ipavich, private communication).

Time-of-flight instruments are limited in their maximum count rate for two reasons. First, the dead time is significantly longer for TOF instruments because of the length of time required to process each event. For Cluster/CODIF, the time to process an event is 5.25 μs, including acquiring the event, calculating the time-of-flight, and validating the coincidence requirements. Dead time effects are evident at 20,000 cps, but can be corrected up to 200,000 counts per second (see Section 3.1.3 for discussions of dead time). The larger problem at high rates is a background generated by false coincidences. If the rate is high enough, more than one ion may enter the instrument during a measurement and there is no way to determine if the "start" signal and "stop" signal come from the same ion. As the rates get higher, a background of false coincidences is generated from unrelated starts

and stops. This effect is worse if the individual efficiencies are low, since there is a larger chance to have "start" with no "stop," or a "stop" with no "start." Cluster/CODIF exhibits these types of background events contaminating the minor ions when it observes proton rates of about 5000 counts per seconds at one angle and energy. These rates are commonly observed when using CODIF's high geometric factor section within the magnetosheath. There is almost always a background generated in the magnetosheath which contaminates the measurements of minor ions like O^+ at the energy and direction of the main flow.

In addition, time-of-flight systems use Micro Channel Plates for their "start" and "stop" signals, and these detectors are subject to degradation as was discussed earlier. Systems that use the same MCP for the "start" and "stop" signal can have the problem of non-uniform gain degradation. In the design used for the FAST/Cluster/Equator-S series of instruments, focused electrons generate the start signal, while the stop signal is generated by the ion impacting the MCP. Because the ion scatters in the entrance foil, the position of the ion on the MCP is much less focused than the position of the electrons. As a result, the start efficiency degrades faster than the stop efficiency. For Cluster/CODIF, the stop efficiency is still at 80–90 % of its initial value after the first three years of the mission, while the start efficiency has degraded by ∼50 %. As a result, the MCP voltage cannot be raised any further because that leads to too high a current for the stop signal, which disables the high voltage power supply. Therefore the instrument is forced to operate with reduced efficiencies. Using separate MCPs with separate control voltages would alleviate this problem. Similarly, the TEAMS instrument on FAST suffered greater MCP degradation in the positions that looked in the ram-direction of the spacecraft. Since the degradation was not uniform, the MCP voltages could not be raised enough to compensate without disabling the high voltage power supply.

The methods used for verifying MCP gain are described in Section 4.3.1.

4.2.4 Energetic Particle Detectors

Silicon solid-state detectors (SSDs) used to detect energetic particles suffer damage from the very particles that they are designed to measure. The damage can be classified into two types: bulk and surface damage. The first type occurs when an incident particle collides with a Si atom in the crystal lattice displacing the atom from its location in the lattice. The displaced atom and the resulting vacancy form a defect in the lattice (sometimes termed a Frenkel defect), that is capable of trapping a charge carrier for periods of time ($\sim$ ms) long compared to the charge collection time for the circuit reading out the Si detector ($\sim \mu$s). These defects, scattered through the volume of the sensor, decrease the ability for ion-electron pairs produced by an incident particle to be completely collected during the circuit integration time resulting in misidentification of particle energy. In space applications, lower energy protons are the primary cause of lattice defects both because they are plentiful and because their damage is concentrated near the surface of the detector. Protons, even with energies of only a few keV, create defects readily. In fact, incident protons can create clusters of many defects along their stopping path. Electrons, on the other hand, require at least 250 keV to have an appreciable chance of creating a defect, with a very small probability of creating a second one. Since the proton damage is predominantly near the surface of the detector, the reduced charge collection primarily affects the lower energy particles being measured, effectively increasing the detector's dead layer.

The production of bulk lattice defects also results in increased leakage currents through the detector. The primary effect of increased leakage current is degradation of detector energy resolution. A large enough leakage current can result in noise appearing in the lowest energy channels. Increased leakage current can also result in a lowering of the bias voltage applied across the detector because of an increased voltage drop across the series bias resistor in the voltage supply. The reduced detector bias voltage reduces the depletion layer thickness and contributes to lowering the fraction of the charge collected. This latter problem can be mitigated by designing for bias voltage increases during the mission.

The second type of defect, a surface defect, is also produced by the impact of particles on the detector structure but is localized at or near the surface electrode. The net result of a surface defect can be increased leakage currents, increased dead layers, or damage to the detector junction. The energy broadening due to increased surface leakage current introduced by surface defects can be nearly eliminated by detector designs that use separate metal rings at the detector edge to collect these edge currents. High fluxes of low-energy ions that penetrate only the outer exposed surface increase the dead layer (as discussed above) causing the detector noise to increase with time. Most detector designs have the blocking or junction surface facing inward, reducing radiation damage to the device. Operating with the junction surface exposed to space can have the beneficial effect of reducing the dead layer and decreasing the minimum detectable particle energy. However, this will be at the expense of increasing the device's exposure to intense low-energy ion fluxes that may eventually cause the detector to fail.

A population of protons stopping near the surface can cause both types of degradation to occur. Low-energy protons are particularly damaging because of their short ranges in Si. Protons with energies below 100 keV have a range less than 1 μm in Si resulting in both surface and lattice defects. Significant degradation effects can be expected after an irradiation of 10^{12}–10^{13} protons cm^{-2} [*Knoll*, 2000]. In contrast, 10^{14} protons cm^{-2} with energies $>$ 250 keV will result in similar degradation.

Particle radiation damage can impact other types of solid-state detectors in exactly the same way as occurs in energetic particle SSDs. An example of such degradation was observed in an instrument on NASA's Chandra X-ray observatory. After only a few weeks on orbit, a solid-state Si CCD began to suffer performance degradation. The problem was traced to proton damage of the highly sensitive surface region of a CCD containing thousands electronic circuits deposited on the Si chip. Calculations showed that protons with energies above 80 keV had access to the device by undergoing grazing angle scattering from the X-ray mirrors resulting in surface and bulk defects. Further degradation was avoided by moving the detector into a shielded region whenever the spacecraft was exposed to high fluxes of low-energy protons in the radiation belts [*Dichter and Woolf*, 2003].

In summary, radiation damage to solid-state detectors can, over time, lead to greatly increased detector noise and degraded energy response. Section 4.3.3 describes in more detail the evidence for radiation damage in the performance of the solid-state detectors on the NOAA/POES satellites. Examples are given of both the impact of increased noise on the response of one solid-state detector telescope and the impact of reduced charge collection on the performance of detectors exposed to fluxes of low-energy protons. Section 4.3.3 also shows examples of the magnitude of the changes experienced in detectable proton energies as a result of this damage, deduced from inter-satellite comparisons of sensor responses between newly launched and long-operating instruments.

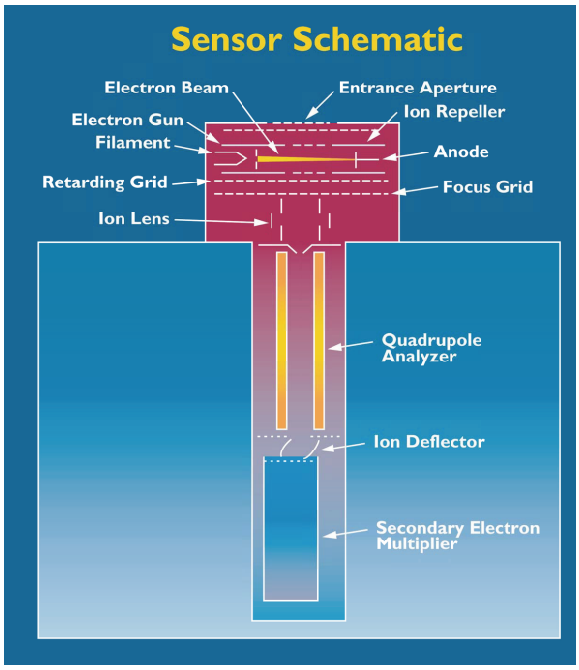

Figure 4.5: Schematic of the ONMS instrument.

4.2.5 Neutral Gas Instruments

The neutral gas mass spectrometer is designed to measure the ambient gas composition. These instruments use MCP and CEM detectors and so are subject to some of the same problems described in Section 4.2.2. Identifying and correcting for degradation of those sensors would follow the procedures discussed in Section 4.3.1 and an example specific to the Cassini INMS is described there. Anomalies have also been encountered in neutral gas mass spectrometer data while operating in space that are beyond the mainstream experience with similar instruments and warrant further discussion.

Niemann et al. [1980b] has described a problem encountered in low altitude (near or below 150 km) thermosphere measurements with the Pioneer Venus Orbiter Neutral Mass Spectrometer (ONMS). As seen in Figure 4.5 this instrument has a series of grids in the ion source [*Niemann et al.*, 1980a] with the ion repeller grid near +40 volts. Other grids between the grounded entrance aperture and the ion repeller reject ambient low-energy electrons. At low altitudes where the CO_2 density was high, the spacecraft speed of 9.8 $\mathrm{km\,s^{-1}}$ produced a high CO_2 flux that sputtered trace alkali metal ions (Na^+, K^+ and Ca^+) from the gold plating of the positively charged ion repeller grid. The variation of the instrument signal as a function of the angle between the normal to the entrance aperture and the spacecraft velocity vector was significantly different from that expected for the ambient gas. The ions were detected whenever the velocity vector was nearly aligned with the instrument axis. This variation along with the observed mass-to-charge ratios formed a diagnostic tool for the anomaly.

An additional spurious ion signal was observed in the ONMS data at a mass-to-charge ratio of 19. This signal was most likely due to fluorine (F) desorbed from grids and surfaces under electron bombardment or from the filament itself. The signal was not spin modulated or related to the ambient atmospheric flux but did gradually increase in magnitude over the 14-year life of the instrument. Similarly designed instruments with filament ionization sources also show this characteristic mass 19 peak.

Another type of problem arises when background gases are emitted from the surrounding ion source surfaces at mass-to-charge ratios that interfere with those produced by ambient gases. In this case it is necessary to subtract the background contributions due to the desorbing species. Usually there is a drop in the magnitude of surface outgassing over time. Typical background gases in the ONMS ion source, after the source was opened prior to entry into the ambient atmosphere, were H_2, CH_4, H_2O, CO, and CO_2 at very low count level. However, many of the background contaminant gases were renewed each orbit from surface reactions as a result of low altitude exposure to ambient atomic oxygen. In fact, not all surface reactions are necessarily bad. For ONMS [*Niemann et al.*, 1980b; *Kasprzak et al.*, 1980] the reaction O(wall) + O(gas) $\rightarrow$ O_2(gas) and O(wall) + N(gas) $\rightarrow$ NO(gas) stabilized after about 20 orbits such that O_2 and NO were used as a measure of O and N, respectively, in the ambient atmosphere.

Ultraviolet light can also be a source of background. The ONMS instrument had its ion source, quadrupole mass analyzer and Cu-Be, box and grid, multiplier detector on a co-linear axis. The spacecraft orbit was nearly polar with a spin axis normal to the ecliptic plane and the ONMS axis at 30° angle with respect to the spin axis. On the dayside of Venus during certain parts of the spin period and orbit, the sensor detected a background signal due to ultraviolet light scattered from the planet's clouds. This signal was of the order of several counts per second and independent of the mass-to-charge ratio. A similar signal seen near midnight was correlated with an intense UV emission observed by the Ultraviolet Spectrometer. Geometry calculations confirmed that the signal was observed only when light from the planet could enter along the instrument axis, unaffected by the quadrupole mass analyzer, and reach the detector.

Another source of background was observed when the INMS instrument sampled close to Saturn. Laboratory calculations indicated that measurements of low densities in Saturn's magnetosphere by the INMS [*Kasprzak et al.*, 1996; *Waite et al.*, 2004] would be difficult due to radiation background contaminating the CEM detectors. A tantalum shield was placed around the detector housing to reduce the background radiation level. Backgrounds of this type are identified as a mass independent signal when a mass scan is performed with the quadrupole mass analyzer and must be subtracted from the data in all mass channels.

Desorbing gas species from the exterior of the satellite can also interfere with the measurement of ambient species. Generally speaking, a gas inlet design whose field of view (field of response) does not include satellite surfaces precludes this from happening in a free molecular flow regime. However, in the case of INMS, the original mounting of the instrument on the Cassini spacecraft was on the same surface as a forward firing thruster. Earlier, *Scialdone* [1972] performed calculations on the condensation region in front of a satellite that resulted from impinging neutral ambient particles. These reflected particles form a stagnation region ahead of the satellite and potentially can contaminate ambient gas measurements. An experimental test on the Atmosphere Explorer satellite AE-D using a mass spectrometer and a neon gas jet source was done to determine the return flux due to scattering [*Scialdone et al.*, 1978]. Using a similar calculation technique, it was shown that

at low altitudes on Titan (high gas densities), Cassini orbiter thruster gas products would be scattered backward into the INMS field of view [*Waite et al.*, 2004]. The thrusters were relocated on an orthogonal axis to circumvent this problem.

Although instrument mechanical misalignments are not properly an anomaly, they can cause measurement problems in instruments with narrow fields of view (FOV). The CONTOUR (COmet Nucleus TOUR) Neutral Gas and Ion Mass Spectrometer (NGIMS) [*Mahaffy et al.*, 2002] has an open ion source that was designed to measure both ion and neutral species at high flyby speeds (28 km s^{-1} for comet Encke). The FOV of the source is only 6° by 2°. As mounted on the spacecraft, the bore sight of the open source was misaligned with the main spacecraft axis by ∼0.6° (specified to be ±0.1° rotational alignment about the spacecraft axes). The bore sight of the open source was measured optically relative to a fixed optical cube on the sensor and later referenced to the master optical cube on the spacecraft. An analysis of the data demonstrated that a misalignment of 0.6° resulted in nearly a factor of 2 loss in signal compared to that at 0°. Mechanical methods of correcting the problem were not feasible because the instrument was already mounted in the dust shield of the spacecraft when the comparison with the master cube was made and there was no time left in the integration schedule. Eventually a solution was adopted that involved the reorientation of the spacecraft near closest approach, with minimal impact on the optical instrument pointing. The determination of the alignment of instruments such as the NGIMS with a narrow field of view is important both in the laboratory during calibration as well as when mounted on the spacecraft.

4.2.6 ENA instruments

Energetic Neutral Atom (ENA) instruments have many components in common with ion instruments, however at lower particle energies additional elements for registering or ionizing an ENA are necessary [*Wurz*, 2000]. As final step in the particle registration, ENA instruments also use MCP, CEM and solid-state detectors and thus are also subject to the same problems described in Sections 4.2.2 and 4.2.4.

At the lowest energies, 10–1000 eV, neutrals must be ionized for successful detection and analysis. Ionization of ENAs is done via surface ionization where an electron is transferred from a specially selected conversion surface to the neutral particle when scattering off this surface under a glancing angle forming a negative ion [*Wurz*, 2000]. This ionization process is very sensitive to the chemical nature of the conversion surface. For example, the LENA instrument on the IMAGE mission used a tungsten conversion surface covered with a thin water-oxide layer, like most metals that have been exposed to air [*Moore et al.*, 2000]. This thin layer improved the ionization efficiency by about a factor of 3. In space the water-oxide layer would have disappeared by evaporation and sputtering except that the perigee of the IMAGE satellite was low enough so that exospheric oxygen replenished the oxide layer on the conversion surface and maintained constant ionization efficiency for the mission duration.

Because ENA instruments have straight entrance systems, they are much more susceptible to contamination by UV light. Since ENA instruments typically have large geometric factors due to low ENA fluxes, UV light from stars and interstellar Lyman-α background causes a noise signal that may be in the same range as the actual signal. If ENA instruments are also imaging instruments, the susceptibility to UV light can be used to check and improve the knowledge of the instrument in space. For example, the pointing knowledge

of the GAS instrument on Ulysses has been improved using the UV signal from 70 stars with positions well known from star catalogues [*Witte et al.*, 2004]. Another example of the UV susceptibility of an ENA instrument is the Neutral Particle Detector (NPD) of the ASPERA-3 instrument on Mars Express [*Barabash et al.*, 2004], which is a TOF instrument designed to register ENAs in the energy range of 100 eV to 10 keV. The singles rates are typically 10^4 s^{-1} for the start and 10^3 s^{-1} for the stop detector because of the registered UV photons. The actual ENA counts (TOF coincidence) are in the range up to a few 10 s^{-1} with a UV background in the range of 0.1–1 s^{-1} because of accidental coincidences. The susceptibility of the NPD sensor for UV photons could even be used to measure the UV air glow of the Martian exosphere [*Galli et al.*, 2006]. Finally, most of the UV sources in the sky are relatively constant over time, thus the signal resulting from registering UV photons can be used to check on the time dependence of the instrument efficiency, e.g., start and stop detector gains.

4.2.7 Faraday Cup Instruments

As pointed out in Sections 2.2.1 and 2.4, plasma measurements that employ Faraday cups do not require electron multiplier particle detectors whose properties depend critically on surfaces that change with time. The stability of a properly designed Faraday cup instrument depends, essentially exclusively, upon the stability of electronic circuits and components that, with careful design and component choice, can be achieved. Faraday cup sensors can achieve great long-term stability as is shown in Section 4.3.6.

Nevertheless, Faraday cups are susceptible to mechanical noise that can couple to their suppressor grid. Vibration of the suppressor grid will introduce small currents at the collector plate due to $V\mathrm{d}C/\mathrm{d}t$, where V is the grid voltage and C is the capacitance between the grid and collector plate. Vibrations change the gap between these surfaces that changes the capacitance. Currents as large as $(2\text{–}3)\times10^{-13}$ A were experienced by one of the two Faraday cups on Wind when an adjacent tape recorder was in use. This noise introduced negligible errors in the density measurements since it was 2–3 orders of magnitude below typical currents measured looking into the plasma flow. (Eventually that recorder failed, and the other recorder introduced negligible vibrations probably due to its greater distance from the instruments).

A similar problem was experienced by the PLS experiment on the Voyager spacecraft. In that case, a stepper motor for the LECP cosmic ray telescope introduced vibrations as the telescope changed its orientation. This was unfortunate because the vibration could have easily been reduced had the stepper motor manufacturer known about the concern for mechanical noise. The vibrations induced in the PLS grids are damped quickly enough that the issue was resolved simply by pausing PLS measurements during the actual movement of the LECP motor.

For spacecraft containing Faraday cups, a mechanical noise cleanliness specification is advised, and it is important that the spacecraft builders be reminded of its existence. If a spacecraft is known to produce mechanical noise, there are mechanical approaches that can reduce the problem. For the ALSEP lunar mission, grids were made from perforated thin metal sheet, producing much stiffer grids that would experience negligible deformation. This solution has some drawbacks including mass and reduced transparency. For the Triana mission the Faraday cup was to be placed near the filter wheel for the main telescope, which contained a stepper motor. Mechanical isolators, essentially mounting

bolts enclosed in steel wool, were used to damp vibrations from the spacecraft. Another approach is to reduce the sensor's response to frequencies in the acceptance band of the electronics. On the Wind spacecraft, care was taken to control the resonant frequencies of the grids by adjusting their tension. The modulator ran near 200 Hz and the resonant frequencies and their harmonics of the sensor grids were adjusted to be lower than that frequency. It is important to realize that the quality factor, Q, of the grid vibration may be increased in a vacuum where damping is reduced. On Voyager, the measured Q of early design grids, were increased by factors of 100 compared to their Q at normal pressures. The grids for Wind were made of knitted tungsten wire and did not show an appreciable change in Q in vacuum. In any case, it is important to measure the vibration response of grids as part of the calibration effort.

4.2.8 Langmuir Probes

The use of Langmuir probes to measure the local plasma environment may conveniently be divided into two plasma regimes, high-density low-temperature ionospheres and low-density higher-temperature regions. In the first regime the Langmuir probe is normally operated in a mode where the collection current is measured as a function of an impressed voltage (Section 2.3). The current-voltage relation provides information about both the electron density and temperature. In the second regime the current-voltage relation does not reflect the local plasma properties because currents are dominated by photoemission currents from the probe, or by collection of photo-electron currents from surfaces adjacent to the probe or from the spacecraft. In low-density regimes, Langmuir probes are generally driven at a fixed current corresponding to 10 %–50 % of the photoemission current. The probe then floats to within 1–2 volts of the plasma potential and the probe potential is measured relative to the spacecraft. The spacecraft potential is primarily a function of the ambient electron density, with a weak electron temperature dependence [*Escoubet et al.*, 1997]. Instrument degradation in these two regimes are discussed in turn below. Section 4.3.7 provides a discussion of in-flight techniques for identifying these problems.

4.2.8.1 Current-Measuring Probes

As pointed out in Section 2.3 describing the design and operation of Langmuir Probes (LP), the basic data obtained is the curve relating the voltage applied to the probe and the current collected. For a plasma in thermal equilibrium, there always should be a characteristic current-voltage ($I - V$) curve as described earlier. Contamination on the surface of the probe, that may introduce a non-uniformity in the work function of the probe surface, can distort the ($I - V$) curve. This, in turn, can introduce errors in recovering the plasma parameters.

While the collectors may have been cleaned prior to launch, they can be re-contaminated during the launch phase or by outgassing from the spacecraft after orbit has been achieved. The contaminating material then can experience chemical changes under the action of solar EUV radiation and exposure to thermospheric atomic oxygen. If the resulting contaminating layer is a poor conductor and is not uniformly distributed, different areas of the surface may charge to different potentials, thus producing energy smearing of the electron retarding region that significantly affects the T_e determination as described above. Surface contamination has its greatest effect at high densities because the correspondingly

larger currents produce larger voltage drops across the insulating surface layers. While the voltage drop may be smaller at low densities, the discharge time of the insulating layer will be longer because the ion and electron fluxes from the ionosphere are lower. This effect can be seen as an exponential discharge signature in I_i at the beginning of the ion saturation region immediately following the retrace of the saw tooth sweep (from positive to negative). Such signatures were observed in curves from the AE-E probes later in that mission. The use of redundant LP sensors made it easier to detect the presence of surface contamination, since the different probe locations may lead to different degrees of contamination and different delays in their onset.

In anticipation of the possibility of contamination, the AE-C, D and E probes were designed to be heated by internal filaments. However, due to high radiative heat loss, the available electrical power was insufficient to achieve and maintain effective bake-out temperatures ($>300\,°C$). One of the AE-C collectors developed symptoms of contamination about 6 weeks after launch, while the other remained free of contamination throughout the 5-year mission. Both of the collectors on AE-D and E eventually became contaminated to some degree, and the internal heating could not improve the quality of the $I - V$ curves. Eventually these probes became useful only for measuring N_i, which is not affected by contamination.

The ineffectiveness of collector heating experienced with some of the AE probes led *Brace* [1998] to use an electron bombardment technique instead. The DE-2 mission employed ionospheric electrons to bombard the probe surfaces. The cleaning was achieved by applying +150 V to one of the probes as the spacecraft traversed the denser parts of the ionosphere [*Krehbiel et al.*, 1981]. This method is simpler than internal heating, requires less power, is faster, and has been proven more effective. The probe was cleaned about 6 days into the mission by electron bombardment for a full orbit. No evidence of patchiness or hysteresis was evident in the $I - V$ curves at that time, since the cleaning did not change the quality of the curves. The probe was cleaned again 18 month later just before the end of the mission, with the same result. The $I - V$ curves from the other DE-2 probe, which was not designed to be cleaned, began to show evidence of contamination several weeks after launch, and its effects were evident throughout the remainder of the mission.

These two results led the instrument team to conclude that both probes had become contaminated prior to or during the launch, and that the initial cleaning of the first probe was successful in removing the contamination before exposure to solar EUV and chemically active atoms (O and O^+) could reduce the conductivity of the contaminating layer. From this limited experience we have concluded that electron bombardment should be used early in the mission to clean the probes before they have experienced extended exposure to the space environment.

As illustrated in Figure 4.6, a cleaning procedure of the type used on DE-2 was not required for the Langmuir probes on the Pioneer Venus Orbiter (PVO) mission [*Brace et al.*, 1988]. The figure shows that early in the PVO mission, when the periapsis altitude was low, the photoelectron yield of the Langmuir probe was low. Presumably this was because encounters of the satellite with Venus' thermosphere deposited a surface layer of O_2 on the probe. Later in the mission, when the periapsis altitude was raised and the satellite was exposed continuously to the solar wind, the photoelectron yield increased by a factor of two and stabilized. This improvement in performance is believed due to the cleaning of the surface of the probe by the impact of solar wind ions. (Exposure to solar UV may also contribute to surface cleaning.) One might expect similar ion and electron sputtering to

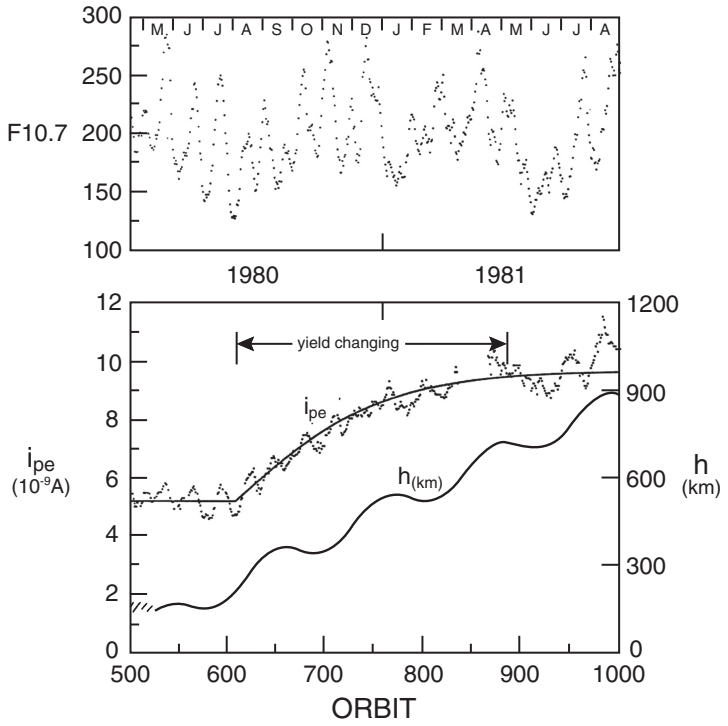

Figure 4.6: The photoelectron yield from the Langmuir probe on the PVO spacecraft, together with the periapsis altitude of the spacecraft, are plotted as a function of time during the mission. The improvement in photoelectron yield is well correlated with the rise in periapsis altitude and is thought due to reduced exposure to atmospheric oxygen that forms a poor photoemission layer on the probe surface. The solar F10.7 flux data are used to correct the photoelectron yield for changing solar ultraviolet fluxes. From *Brace et al.* [1988].

occur in high inclination Earth orbits that encounter energetic ions and electrons at high latitudes. This kind of natural in-flight cleaning could account for the absence of Langmuir probe contamination in the early missions that did not dip into the atmosphere and were in high inclination orbits (Explorers 17, 22, 31, 32, Alouette-2, ISIS-1, and ISIS-2.)

4.2.8.2 Voltage-Measuring Probes

Langmuir probes operated in voltage mode and used to infer plasma density based on spacecraft potential experience two primary changes with time: 1) the leakage current of the probe's preamplifier will increase with radiation damage and 2) photoemission currents from the probe and spacecraft generally increase during the first 2–4 months on orbit. Leakage current changes depend upon the radiation tolerance of the probe preamplifier, the radiation environment, and the amount of shielding. Leakage current problems with the FAST probes resulted in noticeable instrument degradation after ∼3 years, with severe

degradation after ∼5 years. This was quite good for a mission in a high radiation environment, and designed for a 1 year nominal life. In contrast, the Polar spacecraft's Langmuir probes continue to perform well after 8 years in a similar radiation environment, with no signs of leakage current problems.

The increases in photoemission currents result from an evaporation of surface contaminants and generally requires an increase in the bias current applied to the probes to maintain a constant probe-to-plasma potential. The increased photoemission of the spacecraft means that the plasma density versus spacecraft potential relationship will change as surface contaminants are removed. A related change in photoemission properties can occur if the spacecraft orbit takes it close to a planet, in particular less than ∼600 km for the Earth. In this case probe and spacecraft surfaces can absorb enough oxygen to change the photoemission properties. On-board thrusters can also contaminate surfaces and change the photoemission properties.

In addition to these overall changes, there are several periodic variations in photoemission that affect the inferred plasma density. Since spacecraft are generally asymmetric about their spin axis, the amount of surface area exposed to sunlight will change as the spacecraft rotates, causing small changes in spacecraft potential. Often the largest variations come from the Langmuir probes' deployment wires, whose outer conducting jacket is typically tied to spacecraft ground. For Cluster, spacecraft potential modulations of ∼0.4 V and ∼1.5 V were observed superimposed on average spacecraft potentials of ∼5 V and ∼30 V, resulting in inferred plasma density variations of ∼12 % and ∼20 %, respectively.

Since the inferred plasma density is obtained from a difference measurement between the spacecraft and a Langmuir probe, variations in probe-to-plasma potential will affect that result. Small variations in probe-to-plasma potential caused by plasma density changes or by spacecraft produced electric fields, which scale with plasma density, will not introduce errors since these variations are included in the in-flight cross-calibration between plasma density and spacecraft-to-probe potential. However, the probe-to-plasma potential can change with spin due to variations in the probe's photoemission or due to geophysical electric fields. To reduce Langmuir probe emission variations, probes are normally spherical, coated with a graphite paint (Dag 213, Acheson Colloids) to provide uniform photoemission, and carefully handled to prevent any non-uniform contamination. However, should a non-uniform surface be present, as might occur from a fingerprint, then a spin period modulation of the probe-to-plasma potential may be observed. These contamination problems often clean up as the probe is exposed to sunlight and/or intense particle bombardment from the plasma. The Cluster mission uses spherical probes that are attached by a fine wire. The exposed area of the wire is ∼10 % of the probe's surface area, resulting in small variations in photoemission with spin. Spin-frequency probe-potential variations induced by contamination or varying solar illumination on the fine wire are smaller than the spacecraft potential variations with spin. Probe operation is also influenced by solar illumination and therefore brief entry into the spacecraft shadow will result in a brief spike in potential at the spin period. Shadow problems can generally be avoided by tipping the spacecraft spin axis away from the normal to the Earth-Sun line. In addition, any geophysical electric fields will create modulations of the probe-to-spacecraft potential. The use of two (or four) probes located on opposite sides of the spacecraft will eliminate these electric-field-induced problems unless the scale size of the fields is small compared to the probe antenna lengths.

Since plasma densities inferred from the spacecraft potential are made for low density regimes, it is generally assumed that the plasma current to the probes is small and has little impact on the probe-to-plasma potential, which is mainly controlled by the probe's bias current. However, when plasma densities are greater than a few particles per cm^3, or when intense electron fluxes are present such as in aurora, the plasma currents can become significant. In this case a change of the plasma current as a probe goes into the spacecraft wake or onto the same magnetic field line as the spacecraft, can briefly change the probe's floating potential. In these higher density regimes, the inferred plasma density is a stronger function of relative potential between the probe and spacecraft, so that small variations in probe-to-plasma potential may significantly affect the inferred density. In addition, intense fluxes of energetic electrons, as observed in the aurora or at times in the magnetosheath, may cause a deviation from the nominal spacecraft potential versus local plasma density curve, even if electron thermal corrections are included. When the spacecraft potential is small, these energetic electrons will also produce secondary electrons that will complicate the inferred density versus potential relation.

4.2.9 Unexpected Sources of Noise

Often an instrument will encounter unexpected sources of noise, background, or spurious sensor responses. Unless on-board diagnostics are capable of identifying and eliminating these effects that can obscure the intended measurements, data analysis efforts can be greatly complicated. This section presents several examples of unexpected noise that illustrate real problems encountered in flight. The purpose is both to provide a forum where these problems can be recorded for future reference and to suggest design modifications and laboratory testing that allow identification of similar problems before they are discovered again during the next missions.

Both CEMs and MCP exhibit several forms of background noise or spurious counts that instrument designers should be aware of. For example, MCPs produce background counts from radioactive decay in the glass, edge effects, and through a process called "after-emission". Radioactive decay will contribute a background rate of $\sim$0.2–1.0 count s^{-1} cm^{-2} of MCP area. The edges of MCPs are always a source of noise and care should be taken to design the MCP mounting so that collection anodes do not collect charge from within 2 mm of the MCP edge.

Penetrating radiation, in particular MeV electrons, from the radiation belts and energetic solar particles are the most obvious source of unwanted background. Penetrating radiation can affect all types of detector systems from low-energy plasma instruments to solid-state detector instruments. Other than increasing the thickness of material around the detector, which is normally precluded by limited mass resources, little can be done to prevent this background. If mass is available, the use of graded-Z material is preferred [*Robertson*, 2003]. Graded-Z material not only reduces the flux of penetrating MeV electrons, but also reduces the bremsstrahlung X-rays produced in the shielding that can also trigger the detector. An alternate technique employs a guard scintillator surrounding the detector and coincidence rejection to eliminate background response from penetrating radiation. Such a system was developed for the Wind 3D Plasma sensors [*Lin et al.*, 1995]. For Wind 3D Plasma this background removal allowed better measurements of the tenuous flux in the solar wind suprathermal tail [*Lin et al.*, 1998]. A drawback of coincidence detection is a reduction of the capability to handle high counting rates. For instruments that

will experience both low and high background rates, the ability to disable the coincidence feature is preferred.

Background count rates in the MCP detectors from penetrating radiation (or radioactive decay in the glass) will produce an exponential PHD since the pulses are initiated throughout the device and not at the entrance aperture. Because the exponential distribution is more sensitive to MCP voltage changes near the pre-amplifier threshold, variation in MCP bias voltage can affect the background rates more than they affect the efficiency for counting particles. Therefore it is better to keep the MCP bias voltage at a lower level. For a Gaussian PHD, a reasonable value for the peak of the PHD is about five times the preamplifier threshold, where the preamplifier threshold is set high enough to avoid any electronic noise. The primary sources of penetrating radiation seen in the FAST sensors are from the inner and outer radiation belts, and from energetic solar protons associated with large flares. FAST does not collect data inside the inner belt due to high background (>40 kHz). Background rates of 1–10 kHz are observed in the outer MeV electron belt. Solar proton events can produce high background rates. The solar proton event of November, 2000 had a maximum of >30 kHz background count rate in the FAST instrument and noticeable background lasted several days. These sources of background responses appear as slowly varying, analyzer-energy-independent low-level count rates.

The "after-emission" phenomenon in an MCP is when a microchannel continues to produce output pulses after the original stimulus has been removed [*Lees et al.*, 1990]. After the stimulus is removed, the probability of such after-emission is observed to decrease with a power law time constant, t^{-m}, where m may range from 0.5–1.0 depending upon the stimulus. The elevated noise levels may last for hours. The source of this noise is not understood but its similarity to the increase in background counts seen at operating pressures in the 10^{-4} to 10^{-5} mbar range suggest that it may result from an increase in pressure at the back of the MCPs due to vaporization of surface contaminates by the charge pulses. This type of noise is particularly noticeable when an incident flux varies from a large value to near zero in a short interval. For example, solar wind ion instruments, which measure a large flux over a small portion of a spacecraft spin, may observe after-emission for the remainder of the spin.

After-emission from CEM's, similar to the MCP artifact discussed above, has been observed in the TED instruments on NOAA-10 and NOAA-14. This curious phenomenon was initiated when the satellite encountered intense auroral particle fluxes that produced large count rate responses in the TED particle sensors. The elevated CEM responses continued after exiting the region of auroral particle fluxes, both in data taken during the ESA energy sweep and during the short period at the beginning of each sweep when the analyzer plate voltage was forced to zero so that a background CEM response could be obtained. Figure 4.7 illustrates this effect as it appeared simultaneously in two CEM systems on NOAA-14. The counts from the two CEMs accumulated in 16 consecutive background intervals (1.23 seconds every 32 seconds) are shown for an entire transit over the auroral zone. The shaded area indicates where intense natural aurora was encountered. The CEM background unexpectedly increased during those encounters and required some minutes to decay to normal levels after the auroral stimulus had been removed.

The explanation for the long-lived spurious count phenomenon on NOAA-14 remains unknown. The problem did not appear until after about six months of on orbit operation. It was suspected at the time that the problem arose from the Malter effect [*Malter*, 1936], the field emission of electrons from an exposed aluminum oxide surface that had charged

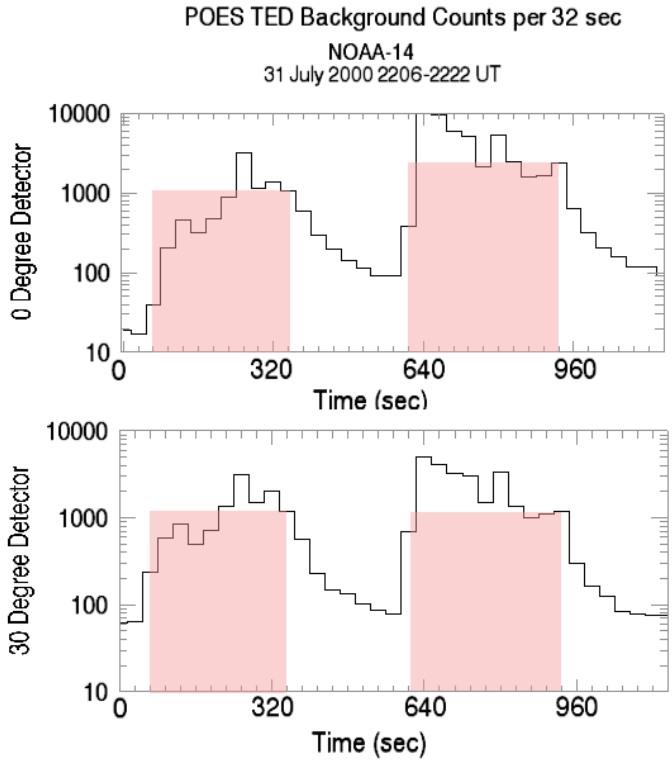

Figure 4.7: Background counts from two NOAA-14 TED electron analyzers, with Channeltron detectors, as a function of time. Background counts were accumulated over 1.23 seconds of a 32 second period containing 16 consecutive analyzer energy sweeps. Background counts were registered during a portion of the energy sweep when zero bias voltage was applied to the analyzer plates. The shaded areas mark periods when large auroral electron fluxes were measured and which correlate with large increases in background counts. After exiting these intense aurora, the background counts decay away with a time constant the order of one minute.

under the impact of auroral particles entering the ESA. The six-month time constant was explained as being the time required to erode away a protective black coating, perhaps by atomic oxygen impact. However, late in the NOAA-14 mission, the signal threshold discriminator level was increased in order to eliminate an electrical noise source from being counted. Astonishingly, this step virtually eliminated the after-emission phenomenon and demonstrated that the source of the CEM response must originate from within the CEM itself rather than from electrons field emitted from an exterior surface. The CEM design used in the NOAA-14 instrument was a two-stage device with a separately biased "pre-amplifier" stage feeding charge pulses into a "post-amplifier" stage. The two sections of the CEM were joined using a conducting epoxy (of unknown manufacture, but perhaps aluminum based) that served also as the electrical contact for the bias voltage. One explanation of the NOAA-14 CEM after-emission phenomenon could be a Malter effect field

emission process from the epoxy. CEM pulses originating from that location would not have undergone the full gain of the device and, so, would have amplitudes that would fall below the increased threshold level.

The Wind 3D Plasma PESA-H ion sensor experienced unexpected MCP noise counts in look directions near the ecliptic plane where no counts above background were expected. The noise counts were modulated at twice the ESA energy sweep rate, producing a two-humped spectrum with a factor of four count rate modulation. The noise counts scaled with solar wind flux and were confined to those anodes that were exposed to the intense solar wind protons when the sensor faced sunward.

The PESA-H sensor was not designed to measure the intense solar wind protons, but rather the supra-thermal tail of the ion distribution. PESA-H was expected to saturate when facing the Sun, and to recover quickly to make the off-sunward measurement. Although this noise is not completely understood, it appears to be related to "after-emission" [*Lees et al.*, 1990] in the MCPs after being exposed to high solar wind ion fluxes. To reduce these background counts, the PESA-H sweep was modified to perform only a partial sweep when facing the Sun, avoiding the solar wind protons. This eliminated the problem and allowed more accurate measurements of the solar wind's suprathermal tail.

The modulation at twice the PESA-H energy sweep rate is most puzzling. This modulation is at the same sweep rate as an adjacent PESA-L sensor, however arbitrary phase shifts are observed in this modulation that appear unrelated to any identifiable instrument operations. One possibility is that the MCP pulse height distribution (PHD) of the "after-emission" signals is near the fixed discriminator thresholds ($\sim 2 \times 10^5$ electrons) of the PESA-H preamplifiers. In this case a few percent modulation of the MCP high voltage could produce a significant change in counts above threshold. No evidence of such high voltage modulation was recorded during the ground testing, and no test data exists on the "after-emission" PHDs in the PESA-H MCPs since this phenomenon was not recognized as a potential problem until after the sensor was on orbit. This explanation requires a PHD near the discriminator threshold, which differs from that described in *Lees et al.* [1990], so the nature of this noise problem is still a mystery.

Although the PESA-H noise problem is still not understood, its observation suggests several tests and design modifications. Raw HV supplies for MCPs should be tested and shown to have a voltage ripple of $<1\,\%$, otherwise noise near the discriminator threshold may be modulated, making its removal difficult. Sensors should be designed with adjustable threshold discriminator levels since new forms of noise may manifest themselves on orbit. For sensors exposed to high fluxes, ground tests of after-emission should be performed to characterize it, including determination of its PHD. Finally, designing in the ability to eliminate exposure to high fluxes would allow sensors to provide more accurate measurements of weak fluxes.

4.3 Identification of Instrument Degradation, Noise, and Spurious Responses

This section details the in-flight calibration procedures and techniques that are used to identify instrument and particle sensor degradation. A major sub-section concentrates upon the identification of gain degradation in electron multipliers that are the sensor of choice in space plasma instruments. Numerous examples of gain loss in these devices,

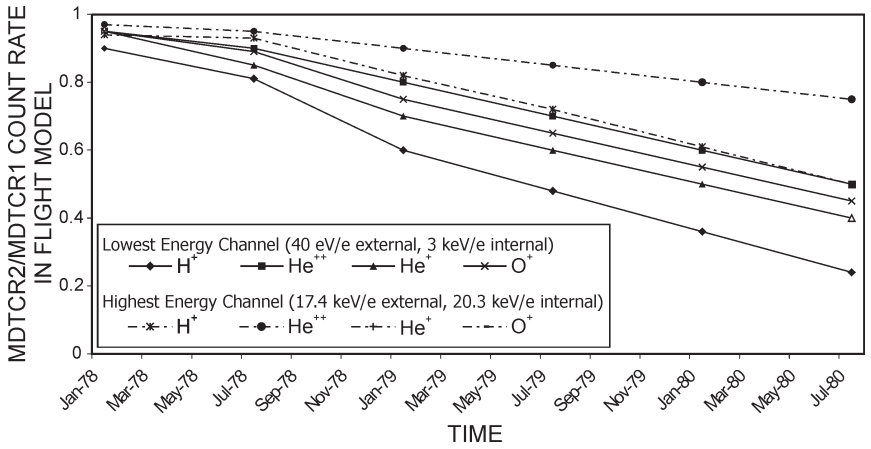

Figure 4.8: Ratio of the count rate at high discrimination level (MDTCR2) and the count rate at low discrimination level (MDTCR1) on the ISEE-1 Ion Mass Spectrometer over the course of approximately 2.5 years. The degradation is species dependent and energy dependent. Note that the high-energy He^+ and He^{2+} data points are superimposed on the high-energy O^+ curve.

as exposed by various types of in-flight calibration procedures, are provided as well as examples of gain restoration by increasing sensor bias voltage. Separate sub-sections are devoted to identifying and quantifying degradation and noise in time-of-flight, solid-state, and neutral gas instruments. Additional sub-sections are used to demonstrate the long-term stability of Faraday cups and to identify degradation in Langmuir probes. The last section describes use of artificial signal injection to test for degradation.

4.3.1 Identifying Gain Degradation in Electron Multiplier Detectors

Early examples of instrument degradation due to gain loss in electron multipliers can be found in missions prior to ∼1980 that often incorporated fixed high voltage supplies. Electron multiplier gain degradation was anticipated in the design of the ISEE-1 Ion Mass Spectrometer [*Shelley et al.*, 1978]. To maximize the geometric factor, this instrument used the Johnston electron multiplier [*Stickel et al.*, 1980; *Peart and Harrison*, 1981] with a fixed high voltage supply. The signal processing employed two discrimination levels, differing by about a factor of 2.0, for recording counts. By monitoring the ratio between the high discrimination and low discrimination level count rates, an estimate of gain degradation in the multiplier could be obtained and corrections made. As seen in Figure 4.8, the high discrimination level rate declined significantly with respect to the low level, and after about 2.5 years only the low discrimination level count rate could be used. Further degradation, as sensed by the low discrimination level rate, was not detected during the instrument's remaining two years of life. As can be seen in Figure 4.8, the gain degradation was species and energy dependent. This is consistent with known efficiency and gain variations for ion detection by electron multipliers [*Keller and Cooper*, 1996; *Oberheide et*

al., 1997] since higher-mass and higher-energy ions tend to eject more secondary electrons resulting in larger gain.

A significant gain loss was experienced by the CEMs in the electron and proton ESA spectrometers on the SCATHA satellite [*Fennell*, 1982]. The CEM bias supply in this instrument could be commanded to one of three voltage levels. In normal operation the bias voltage was kept at the lowest level. However, periodically, at locations in the magnetosphere where particle fluxes were expected to be constant, the CEM bias voltage was increased for a short time to each of the two higher levels. During those tests the ratio of sensor count rate at the lowest bias to that at each of the two higher levels was determined, as well as the ratio of sensor count rate at the mid-point bias level to that at the highest. Figure 4.9 shows the evolution with time during the mission of these three ratios for the electron ESA and proton ESA CEM, respectively. All three count rate ratios were initially close to 1.0 indicating that the CEM gains were sufficiently high even at the lowest bias voltage. With time each of these ratios declined, the most serious decline being in the ratios that compared the CEM response at the lowest bias and highest bias levels. Functional fits were made to these experimental data and used to correct the SCATHA observations for CEM gain degradation.

Later instruments generally incorporated detector bias supplies whose voltages could be increased with time to restore electron multiplier gain. In addition, the more recent instruments are able to cycle the signal electronic discrimination through multiple levels to obtain information on the detector's pulse height distribution and the degree of multiplier gain loss. The Total Energy Detector (TED) in the Space Environment Monitor on the POES satellites uses such a system to track the gain loss in the CEM particle detectors. Figure 4.10 shows an example of this procedure and the effect of raising the CEM bias voltage to restore the electron gain. The CEM response is plotted as the threshold discriminator cycled through four steps, the level at each step increasing by a factor of 2.0 over the previous step. The top panel in Figure 4.10 shows significant decrease in sensor response with increasing discriminator level, indicating insufficient CEM gain. The bottom panel shows the results after the bias voltage had been increased. The variation in sensor response with discriminator setting is much decreased and is largely dominated by temporal variations in the natural auroral electron flux at the time. It should be noted that in routine operation, the threshold discriminator is always set to its lowest level.

Data from the SSJ4 precipitating particle spectrometers of the Defense Meteorological Satellite Program (DMSP) are provided by the Air Force Research Laboratory and are widely used. The calibrations are done as carefully as possible in a vacuum chamber before flight, however the laboratory calibration data do not account for the on-orbit degradation of the Channeltron detectors. Comparisons of in-flight auroral particle data from newly launched spacecraft with data from similar instruments on older spacecraft in the same orbit plane have been problematic because two spacecraft almost never cross the auroral zones simultaneously.

In a promising new technique, the flux of MeV particles in the South Atlantic Anomaly (SAA) region has been used as a standard for determining the degradation of the detectors. The SSJ4 instruments were not built with the intention of detecting and measuring MeV particles. However the MeV particles are capable of penetrating the sides of the instrument case and reaching the Channeltron detectors. The SAA is a source of particles that exhibits almost no variation in flux from day to day and month to month, but does vary with respect to the 11-year solar cycle. While the pulse height distribution (PHD) of a CEM from

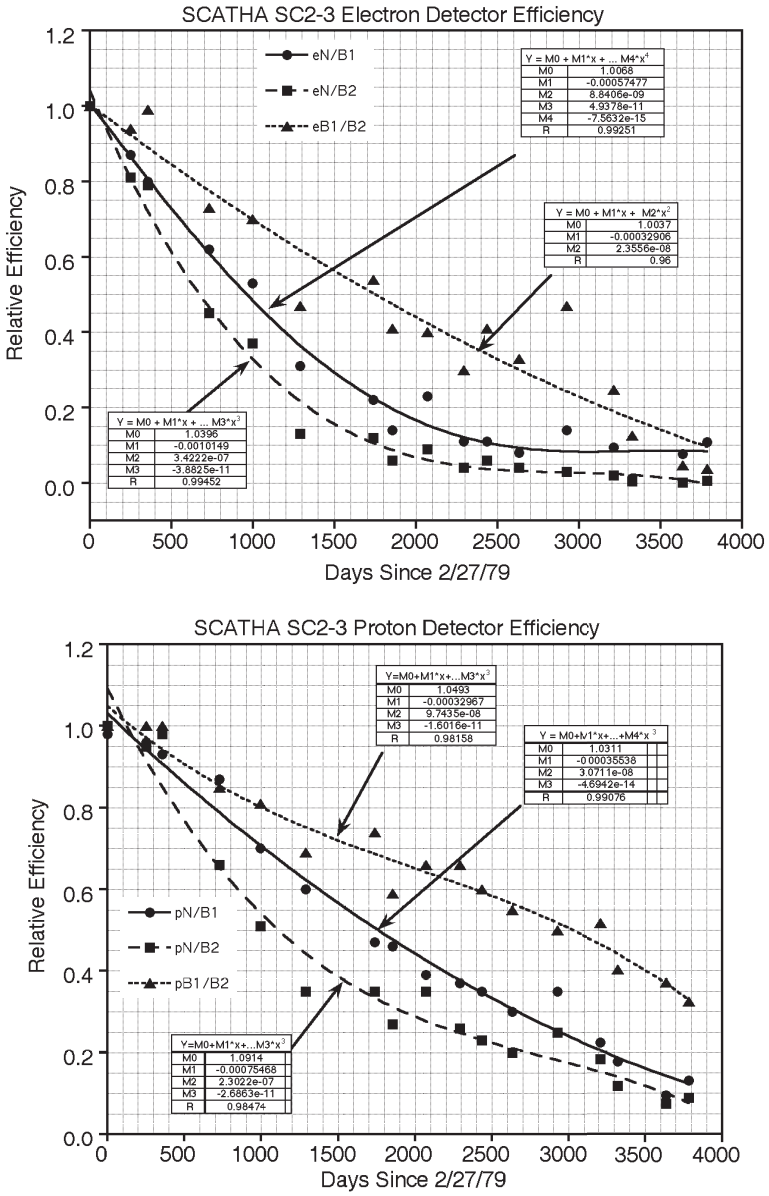

Figure 4.9: The figure illustrates the decrease in CEM detector efficiency in the electron (top) and proton (bottom) ESA spectrometers on the SCATHA satellite. The parameter eN/B1 in the top part is the ratio in electron ESA CEM response between the lowest bias setting and the mid-point bias setting. eN/B2 is the response ratio between the lowest bias setting and the highest. eB1/B2 is the ratio between the mid-point and highest bias setting. The parameters in the bottom part that characterize the CEM in the proton ESA have a similar meaning.

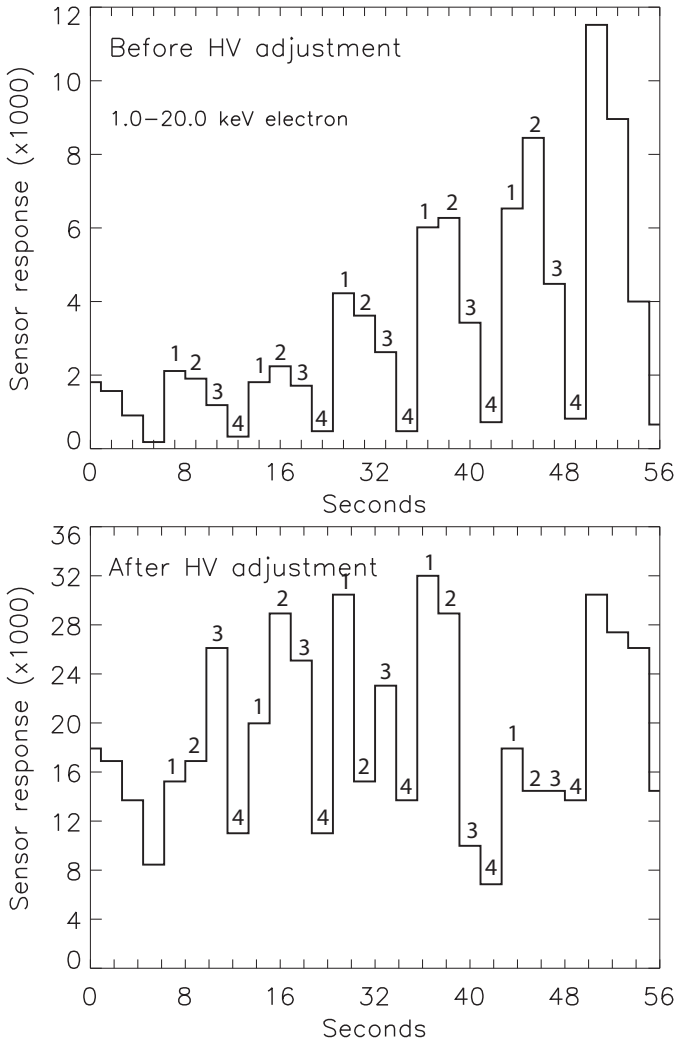

Figure 4.10: The top panel displays the integrated energy flux response of one of the 1.0–20 keV TED electron sensors on NOAA-16 as a function of time. 56-seconds of data are shown. Each discriminator level is held constant for 2-seconds and adjusted through four settings as labeled on the figure. Level 4 is the highest discriminator setting. The dramatic decrease in response at levels 3 and 4 (the highest level in each sequence) indicates insufficient CEM gain. The lower panel displays that sensor's response after the CEM high voltage was adjusted upwards, illustrating a much less systematic decrease in counts with increased threshold indicating sufficient CEM gain.

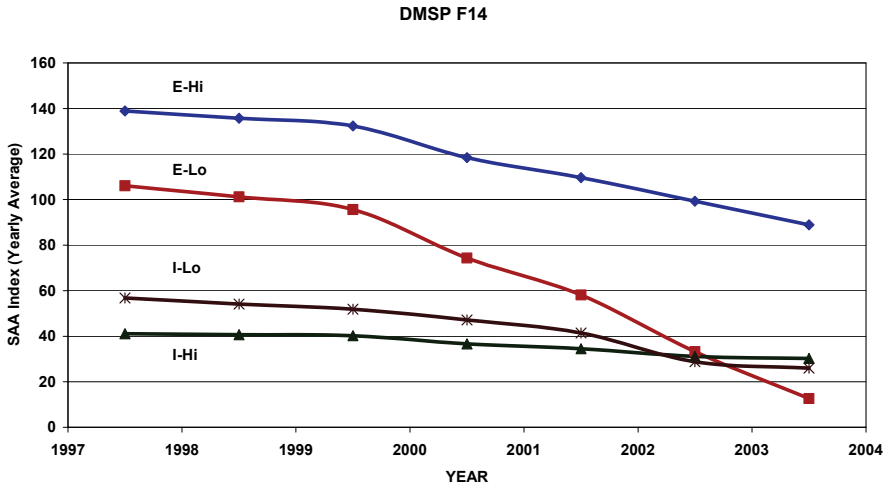

Figure 4.11: Time variation of SAA index for the four detectors in the SSJ4 instrument on DMSP F14, without normalization.

penetrating particles is not optimum, if carefully used the SAA particles can be used as a standard because the flux is a much steadier source of particles than any other location available.

Ten SSJ4 instruments have been flown on DMSP spacecraft, from DMSP/F6 (launched December 1982) to DMSP/F15 (launched December 1999). Each instrument includes a pair of electrostatic analyzers (ESAs) for electrons and a pair for ions. The high-energy ESA in each pair has 10 energy channels ranging from 30 keV (channel 1) to 950 eV (channel 10). The low-energy ESA in each pair has 10 energy channels ranging from 950 eV (channel 11) to 30 eV (channel 20). A Channeltron detector is used in conjunction with each ESA. Two resulting 20-point spectra are generated each second (one each for electrons and ions).

To determine the SAA index, the daily average of count rates in four energy channels is summed (channels 2, 4, 6, 8 for high-energy ESA; channels 12, 14, 16, 18 for low-energy ESA) while the instrument is traveling through the SAA region. The instrument goes through the SAA 7 to 8 times per day. The SSJ4 sensor experiences spurious responses at SAA locations during some seasons of the year. In order to minimize the effect of the spurious response in the SAA index, yearly averages are used. Figure 4.11 shows the time variation of the SAA index for the SSJ4 instrument on DMSP F14. The plot includes curves from the high- and low-energy electron ESAs (E-Hi and E-Lo), and the high and low-energy ion ESAs (I-Hi and I-Lo). The high-energy ion data are more stable over time than the low-energy ion data or the electron data. This is observed for all of the SSJ4 instruments. Figure 4.12 is a composite SAA index for the F8, F9, F13, F14, and F15 SSJ4 high-energy ion ESAs. The dependence of the SAA on the solar cycle is clear from this figure. Based on Figure 4.12, the low-energy ion data and the electron data in Figure 4.11 are normalized by the high-energy ion curves for all SSJ4s to remove the solar cycle variation. The normalized SAA index then reflects the time deterioration of the CEMs.

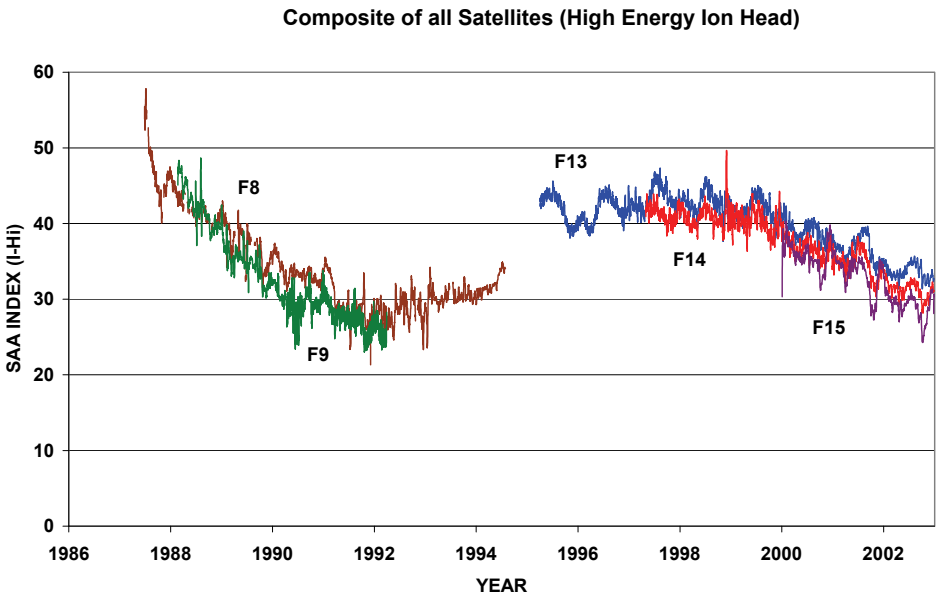

Figure 4.12: Solar cycle variation of composite SAA index for high-energy ion ESAs.

The INMS neutral gas instrument for the Cassini mission uses a similar, but more sophisticated method for tracking and compensating gain degradation in the CEM detectors that are used. The pulse height discriminator can be cycled through sixteen different levels while the detector bias voltage is cycled through three settings. Figure 4.13 shows the integrated pulse height data for the three different bias voltage levels chosen for the INMS flight configuration at five different times during the instrument's life history. It can be seen that as time progresses, the slope of the curves above discriminator level 4 changes the greatest for a bias voltage of 2500 V and the least for 2900 V. An estimate of the effect of multiplier gain change on a change in absolute sensor sensitivity indicates that a 20 % change in sensitivity will occur for a multiplier gain change from 2×10^7 to 1×10^8 [*Waite et al.*, 2004].

Estimates of the efficiency or electron gain loss in the Wind 3D Plasma Experiment were obtained by inter-comparing solar wind densities inferred from the ion and electron ESAs with the Wind SWE detector. When efficiency or gain loss was detected, the MCP bias voltage was increased to compensate. MCP voltage adjustments were also commanded for short periods to look for changes in calculated density at the MCP voltage change boundaries. However these methods were not very reliable for exposing MCP gain loss since small variations due to the efficiency changes were often masked by larger variations in the actual solar wind density.

Using a method similar to that employed in the INMS instrument, the MCP efficiency decreases in the FAST ESAs are detected by adjusting the preamplifier discriminator threshold at several MCP bias voltages near the currently programmed value. This procedure involves toggling the discriminator threshold between its normal operating level just above the system noise and a test level near the peak in an optimal MCP PHD. The

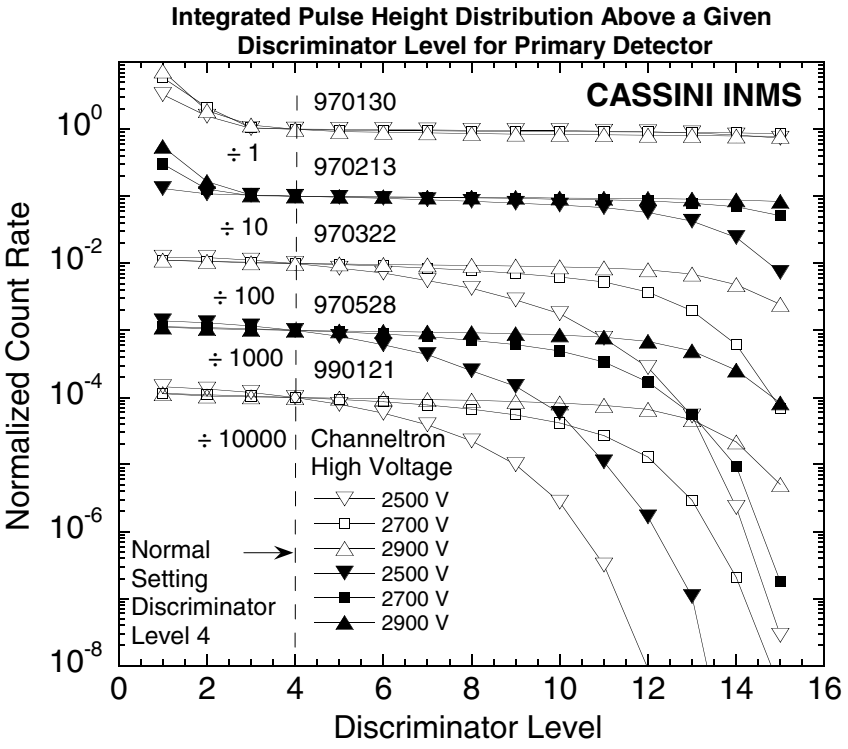

Figure 4.13: Plot of the integrated pulse height distributions for the 3 high voltage levels (Low, Medium, High) used for the Cassini INMS flight unit. The data are for 5 different dates: 970130 (beginning of the CEM laboratory characterization period), 970213 (end of characterization period), 970322 (after environmental testing), 970528 (spacecraft level test) and 990121 (instrument checkout after launch.) Level 4 is the normal level used. Data for 970130 and 970213 used mass 28 from N_2, while 970322, 970528, and 990121 used mass 40 from Ar. For ease of display, the curves have been normalized to discriminator level 4 and the 3 sets of data for each date have been divided by the values shown just below the curves on the left-hand side of the dashed line. The date 970130 is interpreted as year 1900+97=1997, month 01 (January) and day of month 30. From *Waite et al.* [2004].

MCP bias voltage is adjusted until the MCP count rate varies by a factor of two as the discriminator level varies. For a nominal Gaussian PHD from the MCP, this procedure insures that the bias voltage is sufficient that virtually all the MCP pulses will be registered.

The PEACE (Plasma Electron And Current Experiment) instruments on the Cluster mission employed MCPs and ESAs to obtain 3-D distributions of electrons. Post-launch procedures established for PEACE included gain monitoring of each sensor, comparison between the two sensors on the same spacecraft, comparison with sensors on the other spacecraft and finally, comparing with other instruments such as WHISPER. PEACE did not include the ability to determine MCP pulse height distributions after launch using variable pulse threshold levels in the signal electronics although it did have the capability to vary the individual MCP bias voltages.

Advantage was taken of the fact that the PEACE instrument contained two analyzers (HEEA and LEEA) that had overlap in the measured electron energy range and differed only in geometric factor. The procedure for tracking MCP performance involved commanding the LEEA and HEEA to perform energy sweeps over the same electron energy range so that their expected responses would differ only by the ratio of geometric factors. The MCP bias voltage in one of the analyzers (either the LEEA or HEEA) would be held constant at its normal operating value while the bias voltage for the MCP in the other analyzer was stepped through a wide range below and above its normal operating value. The response of the one MCP as a function of changing bias voltage compared to the MCP whose voltage was fixed provided information about the adequacy of that MCP gain relative to the fixed discrimination level. The procedure was repeated but the role of the two analyzers reversed to provide information about the gain of the second MCP. In this manner gain degradation was monitored and MCP bias voltages increased as needed.

A few space instruments have integrated a UV lamp with CEM detectors to provide a standard stimulus to electron multipliers that could be periodically commanded on from the ground and thereby track detector gain over time. This approach was first used in the Plasma Experiment on the Helios-1 and -2 missions [*Schwenn et al.*, 1975; *Rosenbauer et al.*, 1981]. Because the pulse discriminator threshold in the Helios instruments was maintained well below the amplitude of the charge pulse from the CEM (insuring all output pulses were counted), a simultaneous measurement of the CEM count rate from the UV lamp and the integrated current output from the CEM would immediately yield an average charge per pulse (the CEM gain). Early in the mission the gain decreased due to scrubbing but was restored with a single increase in bias voltage and remained very stable for remaining five years of this mission.

A second, more elaborate, implementation of a UV calibration lamp system was used in the SWE Vector Electron Ion Spectrometer (VEIS) on Wind [*Ogilvie et al.*, 1995] and again in the Hydra experiment on board Polar [*Scudder et al.*, 1995]. In the Hydra instrument individual light pipes coupled the output from a single UV lamp to 12 separate sensor heads thus providing a common stimulus for all the electron multiplier detectors. In principle this approach would not only track degradation of individual detectors but would permit adjusting individual detector bias voltages so that all sensors had the same sensitivity. After the launch of Polar use of this system was deferred until it had been verified that all the electron multipliers were operating in a saturated mode. Unfortunately during this period of time radiation damage to the light pipes reduced the UV transmission by different, and unknown, factors so that the intended function of calibration of separate sensors from a common, well-defined source, was compromised (Scudder, private communication).

A useful report on the design and use of UV lamps for in-flight calibration of a variety of sensors used in space experiments is provided by *Morrow et al.* [1993].

4.3.2 Identifying Degradation in Time-of-Flight Detector Systems

The CODIF time-of-flight instruments on the Cluster satellites require routine monitoring of the MCPs that are used to generate start signals, stop signals and MCP position information. In order to be counted as a valid event, an event needs to have a start signal, a stop signal, and a single position signal. Thus the overall efficiency is a combination of the start efficiency, the stop efficiency, and the probability of getting a single position.

The start efficiency depends on the number of electrons emitted from the carbon foil, and the MCP gain of the start detector. The stop efficiency depends on how much scattering occurs in the carbon foil, as well as the MCP gain of the stop detector. The probability of measuring a single position can be effected by the MCP gain, and the amount of cross-talk between positions. These efficiencies depend on position within the instrument, and on the ion species and energy.

The count rate of individual signals and coincidence signals are used to give an absolute measurement of the efficiencies of the different contributions. For example, the start rate tells exactly how many events triggered the time-of-flight system (but not how many total ions hit the start MCP), independent of the start efficiency. The start-stop coincidence rate tells how many of the ions that gave a start (i.e., triggered the time-of-flight system), also gave a stop. Thus, the ratio between the start rate and the start-stop coincidence rate is an exact measurement of the stop efficiency. Similarly, the ratio of the stop rate to the start-stop coincidence is a measure of the start efficiency (see also Section 3.4.2.4). Thus the rate ratios can be used to track the efficiency changes during the mission. This analysis should be carried out in regions where background is low to minimize spurious start or stop signals.

To use this method, it is important that the rates reliably reflect the signals actually used by the time-of-flight electronics. On Cluster/CODIF, for example, the start rate measures exactly the same signal that is used to start the time-of-flight measurement and the start-stop coincidence rate also comes directly from the time-of-flight circuitry. Thus the ratio of these two rates exactly gives the stop efficiency for the time-of-flight measurement. The stop rate, while generated from the same charge pulse, is processed with different electronics than the stop pulse as it goes into the time-of-flight electronics. Thus the threshold for the stop rate can be different from the threshold for the stop used by the time-of-flight system. If the threshold is different, then the start efficiency determined by taking the ratio of the start-stop coincidence rate to the stop rate is only an approximation to the true start efficiency. Only one of the 3 operating CODIF instruments has a stop rate close enough to the "real" stop threshold to be used for reliable "start" efficiency measurements.

4.3.3 Identifying Noise and Radiation Damage in Solid-State Detectors

The in-flight identification of noise in the electronics of a solid-state detector system is done by introducing pulses of known frequency and with amplitude that increases monotonically with time into the charge sensitive amplifier and pulse discriminator chain. The pulse amplitude range over which each detector's lowest energy threshold discriminator transitions from no response to full response to the injected pulses provides a measure of noise generated by each solid-state detector. This procedure also verifies that the electronic pulse height discriminator levels are proper and correspond to the energy band edges that were set prior to flight. If the solid-state detector noise level becomes large, the ability to identify discriminator levels is much degraded and ultimately becomes impossible. The procedure does not verify the proper operation of the solid-state detector itself, for example, whether all the charge deposited in the detector by a particle was, in fact, collected by the amplifier, because the pulse insertion point is just after the SSD.

The noise levels of individual solid-state detectors can increase over time, occasionally very abruptly. When a solid-state detector noise level increases, the data become degraded,

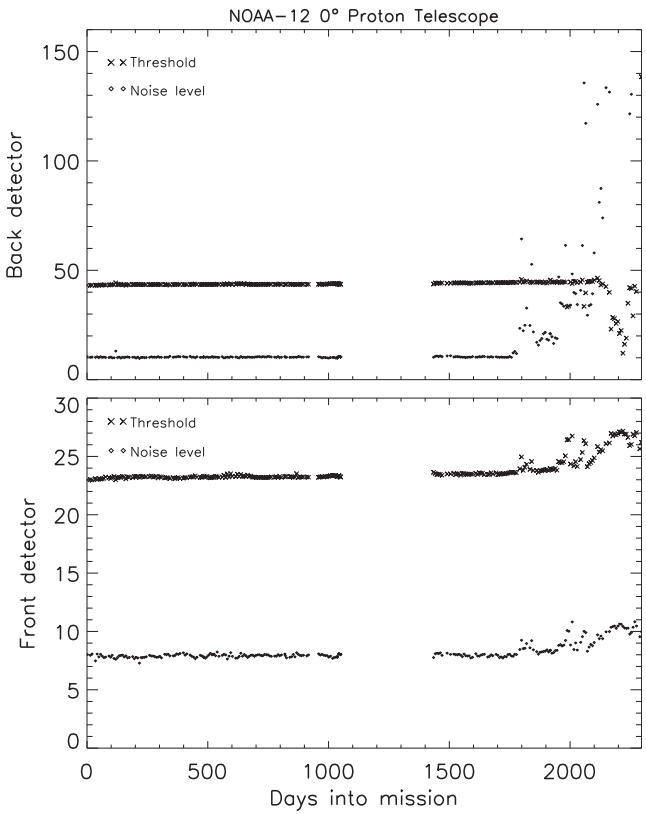

Figure 4.14: A history of the detector noise levels and discriminator threshold levels in terms of keV equivalent energy loss for the front and back solid-state detectors in a NOAA-12 dual detector telescope system. The noise level in the back detector, normally much less than the threshold, increased dramatically after 1800 days of operation and rendered the data from this detector telescope unusable. The gap in the plot was a period when NOAA-12 in-flight calibrations were not exercised.

sometimes to the point of no value at all. For this reason, the detector noise levels must be monitored continually. Figure 4.14 shows the 30 keV threshold discriminator level (in terms of keV equivalent energy loss in the solid-state detector) for a MEPED (Medium Energy Proton and Electron Detectors) proton telescope flown on NOAA-12 over the course of many years. Also plotted in Figure 4.14 is the noise level originating from the back solid-state detector in this proton detector telescope, also in units of keV. These data show that after many years of operation, the noise level from this detector suddenly increased in a sporadic fashion. Signals from the back solid-state detector in the two-detector proton telescope assembly are used to "veto" pulses from the front detector in order to provide data on high-energy protons that deposit energy in the front detector but pass entirely through to deposit energy in the back detector as well. When the back detector in this proton telescope became noisy, virtually all the response from the front detector (from low-energy protons stopping in that detector) was vetoed. The instrument count rates or-

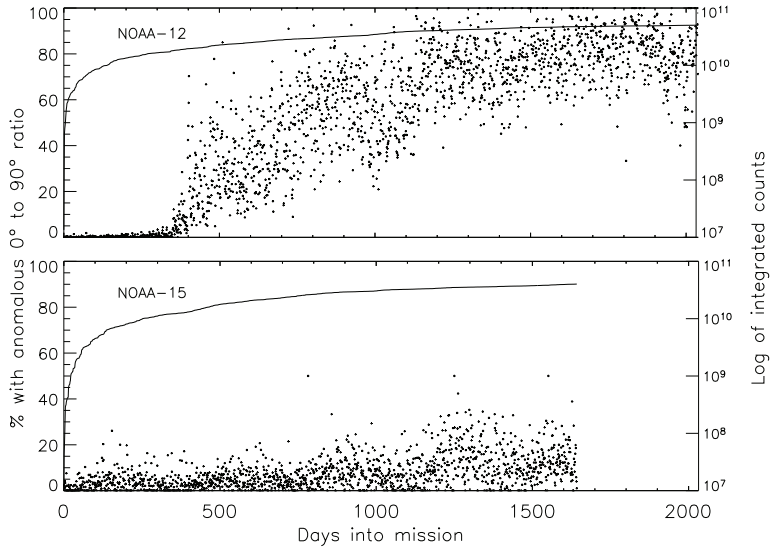

Figure 4.15: The effect of radiation damage to solid-state detectors demonstrated by the probability of anomalous proton pitch angle distributions observed each day during the NOAA-12 mission (top panel) and the NOAA-15 mission (bottom panel.) Also plotted in each panel is the running total of counts accumulated by the 90° proton detector during each mission. It is unclear why the two instruments behaved so differently to this radiation damage. However, the detectors were procured from different lots, stored differently, and launched years apart, so details of the manufacturing, storage, and radiation environment might be required to explain differences in damage caused by regular use.

dinarily produced by 30 keV to 2500 keV proton fluxes became very low, and often zero, and that telescope became non-operational.

The first indication that the solid-state detectors in the MEPED proton telescopes on the NOAA satellites suffered radiation damage arose from observations of anomalous proton pitch angle distributions. Previous scientific studies of the radiation belt and auroral zone proton populations at low altitude demonstrated that, while the >30 keV proton population may become isotropic (intensities in the atmospheric loss cone comparable with those at high pitch angles) the loss cone fluxes were never significantly higher than the trapped fluxes. Such field-aligned pitch angle distributions are regarded as unphysical and, if observed, might indicate problems with the MEPED proton telescope instruments. MEPED proton telescope observations are routinely surveyed to expose instances of this type of angular distribution. This revealed a subtle, but potentially devastating, solid-state degradation problem.

The analysis of proton angular distributions was restricted to observations in the radiation belts, at L-values between 2.0 and 7.0, and considered only instances where the zenith-viewing detector count rate (averaged over 16-seconds) was greater than 200 counts per second. The number of instances each day that these criteria were satisfied was tabulated, as well as the subset of those instances where the ratio in count rates between the zenith-viewing and horizon-viewing proton telescopes exceeded 1.5 (a field-aligned angu-

lar distribution). The upper panel of Figure 4.15 shows the percentage of instances each day that the NOAA-12 MEPED >30 keV proton observations displayed a field-aligned angular distribution, with the linear scale on the left. The running total of counts registered by the horizon-viewing proton telescope is also plotted in the top panel of Figure 4.15, with the logarithmic scale on the right. The bottom panel of Figure 4.15 shows similar, although less dramatic, behavior on the part of the proton telescope detectors on NOAA-15.

These data make it clear that very significant degradation is occurring in one or both proton telescope detectors. It is certain that this degradation is a consequence of radiation damage to the structure of the solid-state detectors by the impact of low-energy protons stopping in the detector. Damage near the detector surface has reduced the charge mobility to the point that only a fraction of the charge is collected within the integration time of the amplifier (see Section 4.2.4). While detectors in the zenith and horizon-viewing MEPED telescopes must both undergo damage with time, the horizon-viewing detector is more rapidly damaged because the proton fluxes are typically largest at the higher pitch angles. Consequently, the effective threshold proton energy sensed by the horizon-viewing detector increases more rapidly and the integral count rate above that threshold decreases more rapidly than for the zenith-viewing telescope. Eventually, the differences in threshold proton energies between the two are such that the zenith-viewing instrument regularly exhibits a higher count rate than the horizon-viewing telescope.

The precise changes in effective energy thresholds on the part of the MEPED proton telescopes cannot be easily determined. There is no standard proton distribution, with a well defined and time invariant spectrum and intensity available to calibrate the net effects of the radiation damage. Only comparisons of sensor responses between newly launched instruments and ones that have been operating for some time can provide this information.

The first attempt of such a comparison was made between MEPED proton telescope observations on NOAA-15 shortly after the launch of that satellite (when radiation damage to the detectors would have not yet occurred) and the proton observations on NOAA-12 after almost 7 years of operation. While NOAA-15 and NOAA-12 were in essentially the same orbits with almost identical orbital periods, there was roughly one-half an orbit difference in their positions at the same time. The two satellites never sampled the same energetic particle environment at the same time. Thus careful selection of observational data situations, where it was likely that very similar, if not identical, energetic proton populations were sampled, was required so that a comparison between sensor responses could be made. The criteria used to select those cases are described below.

The data selection for both satellites was restricted to locations in the center of the low altitude extent of the outer radiation belt, L-values between 4.0 and 6.0 and in the same hemisphere. Each NOAA-12 transit through the selected location was bracketed in time by a pair NOAA-15 transits, roughly 3000 seconds earlier and 3000 seconds later. Because of the sun-synchronous nature of the satellite orbits, the magnetic local time would be nearly the same for all three data samples. Of the full set of such triads of satellite passes, a reduced database was created by selecting cases where the >30 keV proton telescope responses were significant (more than 1000 cps) at the same L-value location on both the NOAA-15 transits as well as the bracketed NOAA-12 transit. In order to minimize the effect of time variations in the energetic particle population, the criterion was that the proton telescope responses during the bracketing pair of NOAA-15 transits could not differ by more than a small factor. The final database included about 20 cases of favorable comparisons obtained over the course of the first 60 days of NOAA-15 operation.

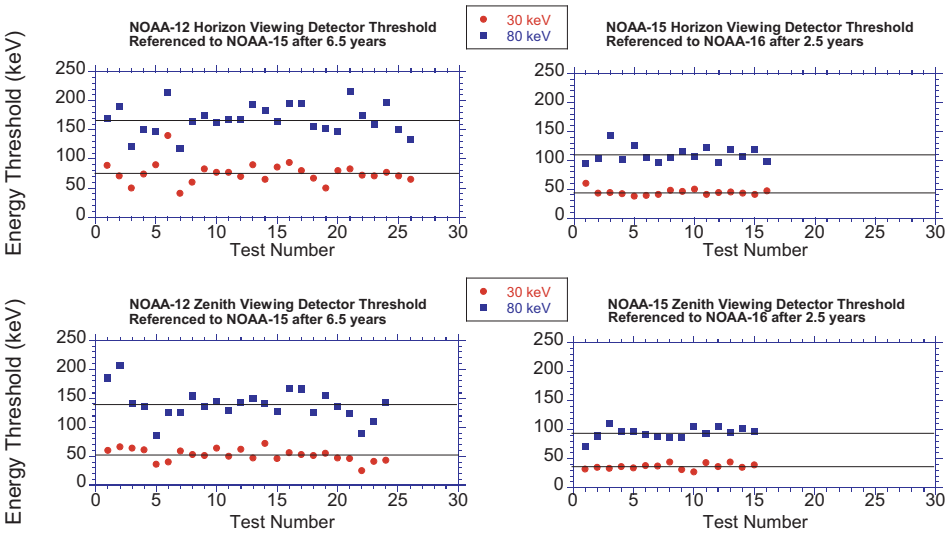

Figure 4.16: Comparisons between the effective proton energy thresholds of newly launched solid-state detector telescopes and telescopes after years of operation. The left pair of panels show the change in the nominal 30 keV and 80 keV energy thresholds in the NOAA-12 instrument after 6.5 years of operation as inferred from comparisons with the newly launched NOAA-15 instrument. The solid-state detector in the zenith-viewing telescope suffered less radiation exposure and less degradation of the threshold. The right pair of panels show the results of a similar comparison between the NOAA-15 instruments after 2.5 years of operation as referenced to the newly launched NOAA-16 instruments.

For each case selected, the NOAA-15 proton telescope responses obtained during the pair of transits were averaged together and used to construct integral proton energy spectra of three functional forms: a power law integral spectrum, an exponential integral spectrum, and an integral spectrum assuming that the differential energy spectrum was Maxwellian. Because the NOAA-15 detectors were newly launched, it was assumed that no radiation damage had occurred and the proton energy spectra constructed from those data would well represent the proton energy distributions sampled by the NOAA-12 proton telescope systems during the intervening time. The proton integral energy spectra defined from the NOAA-15 observations were then applied to the NOAA-12 proton telescope responses and the proton energy thresholds consistent with those spectra calculated.

The left pair of panels in Figure 4.16 shows the results of about 25 separate energy threshold comparisons between NOAA-12 and NOAA-15 horizon- and zenith-viewing telescope pairs. The nominal energy thresholds at the beginning of life of NOAA-12 would have been 30 keV and 80 keV. While there is considerable variability from case to case, it is clear that radiation damage has at least doubled the effective proton energy thresholds on the NOAA-12 horizon viewing instruments from their original values (30 and 80 keV) to approximately ∼75 and ∼165 keV, respectively. The zenith viewing detectors have also suffered considerable damage (∼50 keV and ∼130 keV thresholds) in spite of their total radiation dose being significantly less.

The right pair of panels in Figure 4.16 show results of a similar comparison done between the NOAA-15 proton telescope instruments after 2.5 years of operation and the NOAA-16 telescopes soon after that satellite was launched. Early in the life of NOAA-16, the orbits of the two satellites crossed one another at nearly the same time when instruments on both satellites observed significant proton fluxes. The NOAA-16 to NOAA-15 comparisons thus were less compromised by possible temporal or spatial variation in the energetic particle population between observations. Over the 2.5 years, the nominal 30 keV and 80 keV energy in the NOAA-15 zenith viewing telescope had increased to about 45 keV and 110 keV while the thresholds in the zenith viewing telescope had increased to only 36 keV and 94 keV, respectively. It is clear that after only 2.5 years of operation, the solid-state detectors in the NOAA-15 proton telescopes were already suffering the effects of radiation damage.

As can be appreciated, whenever the actual proton energy thresholds of proton detector telescopes are uncertain to a factor of 2 or more, estimates of energetic particle fluxes and energy deposition into the atmosphere will be greatly in error. This error could be as much as a factor of 10 or more depending on the steepness of the proton energy spectrum. Therefore the uncertainty in the energy response of solid-state detectors produced by radiation damage is a serious problem.

4.3.4 Identifying Degradation in Neutral Gas Instruments

The primary elements in neutral gas instruments that should suffer in-fight degradation are the CEM or MCP detectors. The method for tracking degradation in those detectors would generally replicate the techniques described in Section 4.3.1. In addition it is known that ion sources experience a loss in efficiency with operation time, especially in the presence of reactive gases. Reactive gases and radicals produced in the ion source change the surface properties of the electrode surfaces, perhaps resulting in insulating layers on electrodes, which can charge up during operation and distort the electric fields. Also, hot wire filaments (e.g. tungsten-rhenium) change their shape with operation time, becoming thinner because of evaporation and chemical attack which may result in a degradation of the ion source efficiency. Other electron emitters, such as cold electron emitters (e.g. microtips), also suffer from degradation with time due to the reactive chemical environment and ion bombardment. Identifying and tracking this degradation is usually performed by designing the source to have a constant ionization current of electrons, and by monitoring the voltage required to maintain this current. However, distortion of the filament with age may result in not all of the emitted electrons arriving in the volume where the gas should be ionized. Since the filament current is generally not measured at the place where the ions are created, this degradation may not be easily identifiable and might not be distinguished from a degradation of the detector performance. In addition, electrodes in the ion source may be contaminated from radicals or material entering the source resulting in insolated patches forming on the electrodes which can degrade the collection, trapping, and transfer of the created ions into the mass analyzer. Again this degradation is difficult to separate from degradation of the detectors that register the particles.

As an example of degradation tracking in neutral gas instruments, consider the Double Focusing Mass Spectrometer (DFMS) of the ROSINA instrument that is included in the Rosetta comet mission. The DFMS is unique in that it includes MCPs, CEMs, and a Faraday cup in its detector system. The extreme stability of the Faraday cup detector

serves as the standard for identifying and tracking degradation in the far less stable CEM and MCP detectors, as well as degradation of the ion source. Since the operation range of these three detectors is different, cross-calibration between them can only be performed for the limited pressure range of overlap. Linearity of the detectors outside the band of cross-calibration has to be assumed, which is very reasonable since the extrapolation is towards lower gas pressures. During the ground calibration of the DFMS sensor, several cross-calibrations between the three detectors were performed for CO_2, Ne, and Xe in the pressure range 10^{-8}–10^{-6} mbar using electron emission currents in the ion source between 2 and 200 μA. In all cases each of the two filaments was used. As an example of the intercalibration, for 20 μA emission current and 4×10^{-8} mbar CO_2 one obtains a current of 40 fA in the Faraday cup. The same current gives 22,500 cps in the CEM and 21,900 cps on the MCP detector. In flight, a gas mixture in the pressure range of 10^{-8}–10^{-6} mbar can be released into the ion source from a reservoir to track degradation over the mission duration of ~12 years (see Section 4.6 and *Balsiger et al.* [2007]). In addition, the ROSINA instrument has two total pressure sensors (Bayard-Alpert type) to aid the absolute calibration of the two mass spectrometers [*Balsiger et al.*, 2007].

There are several sources of background whose identification may not be possible until in-flight measurements are made. These can include sputtering of ions from grids by a high speed gas flux, de-absorption of gases from grids or walls, UV light contamination, penetrating background radiation, and backscatter from thrusters. Thruster backscatter will be correlated with thruster firings making identification simple. Hydrazine ($C_2H_8N_2$) thrusters produced a mass 2 peak (H_2) in the INMS on Cassini. Mass independent background generally means that the signal originates in the detector section, after the mass analyzer, and is due to an uncharged particle (photon) or energetic particle not affected by the mass analyzer. Radiation will produce a mass-independent background that can be modulated with detector orientation if the radiation source is not isotropic or the detector shielding not complete. Similarly, UV contamination produces a mass-independent background whose signal should correlate with a UV source such as a planetary atmosphere clouds. (Neutral gas instruments are generally not oriented where direct sunlight has access to the entrance aperture.) A geometry calculation is normally required to determine the linear configuration of the entrance aperture and detector and the projection of the line of sight to the background source. UV light that gains access to surfaces near the detector can release electrons at the multiplier that do not originate in the mass analyzer or ion source section.

Background can also originate in or near the ionization source. The Pioneer Venus Orbiter Neutral Mass Spectrometer (ONMS) detected alkali metal ions that were being sputtered from the grids by an intense CO_2 flux at low altitudes (see also Section 4.2.5). The ions were focused forward into the ion source. This produced an undesirable background signal that raised the threshold for the detection of atmospheric species, in this case ^{40}Ar and ^{20}Ne which were expected or might be expected in the atmosphere of Venus. Identification of these counts as background was made by examination of the angle variation of the signal which did not have the expected cosine dependence for an incoming gas species but displayed a much narrower, forward sputtering angular dependence. In addition, the mass peak width was much wider than usual for the atmospheric gas species due to the higher energy of the sputtered ions and due to the instrument's response to these high energy ions. An additional diagnostic peak indicating sputtering was the mass 23 peak due to sodium, also observed at high pressure in laboratory calibrations.

Desorption of gases from the grids and instrument walls is a final source of background counts in neutral gas experiments. These gases are emitted under electron bombardment in the ion source, or can be emitted directly from the hot filament. Desorption signals are not spin modulated or related to ambient atmospheric flux, and may increase in magnitude over the life of the instrument. These signals are often identified during ground testing as was the fluorine (F) signal in the Pioneer Venus ONMS instrument. Similarly designed instruments with filament ionization sources also show the characteristic mass 19 peak. Other background gases in the ONMS ion source, after the source was opened prior to entry into the ambient atmosphere, were H_2, CH_4, H_2O, CO, and CO_2 at very low count level. Background contaminant gases can also be renewed each orbit from surface reactions as a result of low altitude exposure to ambient atomic oxygen. Carbon and hydrogen desorbing from various metal parts or the filament along with just normal outgassing are the source. The desorbed gases can also react with each other and other surfaces including the hot filament. The desorption backgrounds are identified by comparing the inbound composition and the outbound composition very far away from the atmosphere. The fact that the same species may show up 24 hours later on an inbound pass, albeit at a lower signal level, confirms that they have been entrained on the metal surfaces and are desorbed by the hot filament thermally or by electron bombardment.

4.3.5 Identifying Degradation and Noise in ENA Instruments

The primary elements in the Energetic Neutral Atom (ENA) instruments that suffer in-flight degradation are the CEM or MCP detectors in medium and low energy ENA instruments, and the SSDs in high energy ENA instruments. The methods for tracking degradation in those detectors would generally replicate the techniques described in Sections 4.3.1 and 4.3.3. For ENA instruments that use time-of-flight (TOF), monitoring changes in the start and stop pulse efficiency can be found in section 4.3.2. The primary degradation experienced by ENA instruments that has not been discussed involves low energy ENA detection. These instruments use kinetic secondary electron emission or surface ionization as part of the detection processes. Kinetic secondary electron emission involves an ENA striking a "start surface" where it releases a secondary electron that produces a "start" pulse. The scattered ENA continues until it is absorbed by the "stop" detector. The time difference is used to determine the particle velocity. Surface ionization is where an electron is transferred from a specially selected "conversion surface" to the neutral particle which scatters off the surface under a glancing angle [*Wurz*, 2000]. The negative ion is then analyzed and accelerated to a detector. Degradation of both the "start surface" and "conversion surface" will impact instrument sensitivity.

Degradation of a conversion surface generally means that the chemical composition of the top-most monolayer of the surface changes because of adsorption of gases on the active surface, which reduces the conversion efficiency. However, some instruments rely on an active monolayer to increase efficiency and degradation occurs with the removal of this active layer by sputtering or evaporation. An example of the latter is the LENA instrument on the IMAGE satellite [*Moore et al.*, 2000]. LENA used a highly polished tungsten conversion surface. Like all metals exposed to air, the tungsten was covered with a thin water/oxide layer, which improved the ionization efficiency by a factor of about three. However, that layer was lost when exposed to high vacuum in space. Fortunately, the perigee of the IMAGE satellite carried it low enough that exospheric oxygen replen-

ished the oxide layer and maintained constant ionization efficiency during the mission. Nowadays, conversion surfaces are used that do not degrade by losing their active layer [*Wurz*, 2006]. The only method of degradation of such surfaces is the adsorption of gases and their possible decomposition by UV photons. This can be mitigated by a stringent cleanliness program and low outgassing of the instrument. In particular the instrument should spend several days in high vacuum to eliminate any surface contaminants before UV light is allowed to illuminate the conversion surface.

Identifying degradation of "start surface" kinetic secondary electron emission yields can be made in a manner similar to other time-of-flight efficiency determinations. By monitoring the ratio of valid start-stop combinations to single event stops, one can determine the start efficiency (see Section 4.3.2). However, this monitoring requires that the single event stops are dominated by actual ENAs and not the result of other singles background such as UV photons or penetrating radiation. Start surfaces that are currently used are very flat high-Z material that often have a multi-layer coating to suppress forward scattering of UV light [*Barabash et al.*, 2004] and thereby facilitate this efficiency calibration. Degradation of the "stop detector" can also be monitored in the same manner at time-of-flight stop detectors by measuring the ratio of valid events to single starts (see Section 4.3.2). Again this monitoring requires that the single's start rate be dominated by ENA and not by other sources of background.

ENA instruments experience similar background from UV photons and penetrating radiation as neutral gas instruments, with the background arising from UV photons typically being the most important source. Both types of instruments have straight entrance systems that eliminate most charged particles through electrostatic deflection, but are susceptible to contamination by UV light. Both have detectors that can register UV photons and penetrating radiation. ENA instruments incorporate UV light absorbing materials on their internal surface to reduce this background. For ENA instruments with CEM or MCP detectors, background due to radioactive decay in the glass may also be important.

Background in ENA instruments is exacerbated by the low intensity fluxes that are measured, where signal to noise may be small. Therefore background subtraction is an important part of the ENA data analysis. UV light from stars can be significant, but can also be used to monitor the instrument's susceptibility to this background since stars generally have constant light output. This UV background signal can also be used to derive the relative start and stop detection efficiencies during the instrument's operation in space. If the single events are dominated by UV and not by ENAs (as is the case for the simpler ENA instruments) and the UV source (stars, backscattered Lyman-α, etc.) stays constant with time, the single event rate will vary only with detector efficiency. Since the absolute detection efficiencies for Lyman-α photons and particles are different, only relative information of the detector efficiency with time is derived. The absolute relationship can be established early in the mission when the detection efficiency for particles is known from the ground calibration. For ENA instruments that use time-of-flight, coincidence timing will eliminate single event background unless this background becomes comparable to the detector cycle time for an event, which may happen in ENA instruments. Background from penetrating radiation will generally introduce a slowly varying, spin-dependent, single event rate that is independent of any analyzer dependent settings.

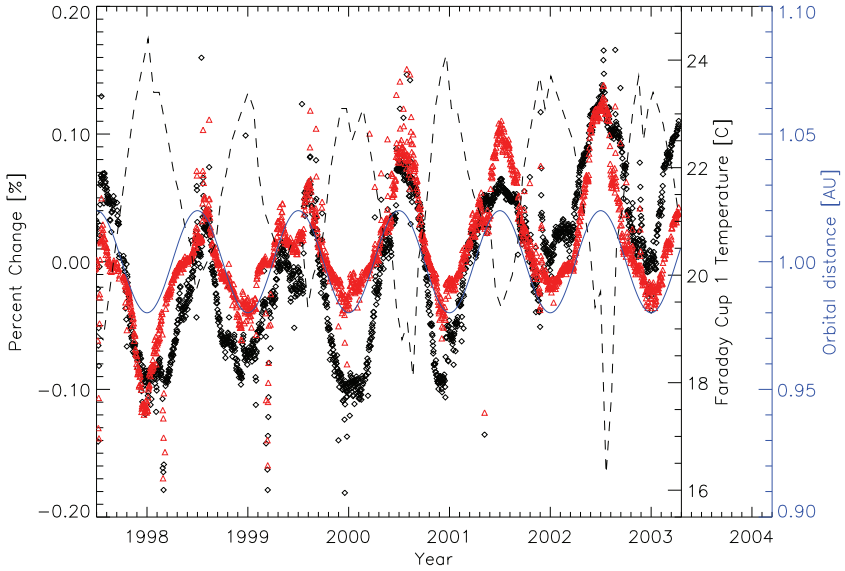

Figure 4.17: The variation in the response of the two Faraday cups on the Wind spacecraft over nearly 6 years as determined by the internal current calibration. The symbols are the percent variation in the instrument responses, and the dashed line is the temperature of the instruments obtained from housekeeping data. The orbital distance of Earth, and hence the spacecraft, from the Sun is shown as the solid line. Adapted from *Kasper et al.* [2006].

4.3.6 Identifying Degradation in Faraday Cup Instruments

As pointed out in Section 4.2.7, the long term stability of a Faraday cup instrument depends on the stability of the electronics. The stability of the electronics can be tested by an internal calibration system that can inject known currents at the input of the measurement chain to stimulate the entire system including the analog to digital conversion circuits. The injected currents can be stepped over the entire dynamic range of the instrument and provide complete end-to-end characterization of the electronics. A full description of the internal calibration system used in the Wind Faraday cup experiment is given in Chapter 3.

An internal calibration of the two Faraday cup (FC) instruments on Wind was performed every 92 seconds. Figure 4.17 is a plot of the percent change over time in the response of the two FCs to the nominally-same internal calibration current (each generated independently by that instruments's calibration system.) The symbols in the figure indicate the evolution over time of the response of each instrument to the same calibration signal. Note that there is a <0.1 % variation in the reported current with a period of one year which is seen independently by both instruments.

The solid line in Figure 4.17 is the orbital distance of the Earth from the Sun, which suggests that there is a change in the instrument response due to a temperature variation of the instruments as the distance to the Sun changes. Preflight thermal testing of the instrument did indicate that the RC circuit of the log analog-to-digital circuit had a one-

part in a thousand per degree C temperature variation. Since this effect appears to be in the RC circuit, the internal calibration system could be used to remove this 0.1 % effect. In addition, there appears to be a 0.04 % overall gradual variation in the instrument response to the internal calibration signal.

4.3.7 Identifying Degradation in Langmuir Probes

4.3.7.1 Current-Measuring Probes

The primary method for identifying degradation or other problems arising in the operation of Langmuir probes in a high-density environment is a simple internal consistency check. The simple exponential relationship (Section 2.3.1) between the electron temperature T_e and the measured current I_e, $I_e(V) \sim \exp(eV/kT_e)$, when the Langmuir probe bias, V, is negative provides a powerful test of the validity of the T_e measurements. If the retarding region is not exponential, that measurement can be assumed to be invalid and should be discarded. *Brace et al.* [1971] showed that the ISIS-1 probes exhibited retarding regions that were exponential over a range of 6 or 7 kT_e.

Surface contamination (the main source of probe degradations) of the collector may introduce T_e errors, as discussed in the implementation section (Section 2.3.5). The accuracy of the electron and ion density, N_e and N_i, measurements can be of the order of 10 % after corrections of N_e for certain systematic errors. Errors can be detected and assessed most readily by comparing the N_e and N_i measurements from the same $I - V$ curve. N_e and N_i are independently measured because they come from different regions of the $I - V$ curve. Since plasma neutrality requires N_e to equal N_i, we are free to use either as a measure of the density. The N_e measurements extend to lower densities because the electron saturation current is about a factor of 50 greater than the ion saturation current for the same density. However, the N_i measurements are more accurate, at least in the F-region of the ionosphere, because the ion saturation current is almost exclusively due to the sweeping up of heavy ions by the known cross sectional area of the probe. In high density plasmas, major departures of the observed $I - V$ curve from the theoretical functional dependence, or significant disagreements between the independent measures of N_e and N_i, are indications of an instrument problem, possibly due to probe contamination.

A final method of assessing Langmuir probe operation is through comparisons between the measurements of two independent Langmuir probes on the same rocket or satellite. This may identify additional measurement errors that do not show up in the internal consistency checks. Systematic differences may arise from mechanical failure, surface contamination of one or both probes, or differences in mounting location.

4.3.7.2 Voltage-Measuring Probes

Radiation damage to the probe's preamplifier is the primary source of degradation and may be ascertained in three ways. First, the current required to balance the apparent photoemission may increase because of increased leakage currents in the damaged circuit. Second, the signal output of an electric field measurement may decrease with time because of the voltage divider effect of the plasma sheath and the decreasing input impedance of the preamplifier. Third, the preamplifier output may be forced to one of its power inputs and become locked rather than track the plasma potential.

A determination of changes in the photoemission current can be made by examining the current-voltage relation of the Langmuir probes. In particular, if the probe is biased very negative (~tens of volts) with respect to the nearby plasma, all photoelectrons will escape the probe while fewer plasma electrons will be captured. Thus the current to a probe at very negative potentials will provide a measure of the photoemission current, after a small correction due to the thermal plasma. This test can be run occasionally to monitor photoemission, however care must be taken not to drive the spacecraft to large positive voltages during the test, such that the probe-to-plasma potential becomes small. Generally this means performing the test on one probe at a time, with the other probes monitoring spacecraft potential.

4.3.8 The Use of Artificial Signal Injection for Instrument Performance Verification

Thus far the material in Section 4.3 has dealt primarily with determining the proper performance of the front-end detector portions of various types of instrumentation for observing particles and plasmas in space. However, it is equally important that these instruments are capable of in-flight testing and verification that the down-stream processing of the signals from the sensor heads is done properly. Modern detector systems invariably test the system performance by injecting pulses of varying amplitude, frequency, and phasing at various points in the data processing chain to perform this function.

For example, many instruments designed to observe energetic particles use multi-element solid-state detector assemblies. Pulse height analyzes of the signals produced in coincidence from each of the detectors are used to identify both the energy and the species of the particle that transited the detectors. Artificially injecting pulses of various amplitudes simultaneously at each of the sensor signal inputs will verify that the pulse height analysis required of such detectors is being performed properly and that the requirement for coincidence in signals from multiple sources is satisfied. The MEPED instrument on POES (described above) is one such example. Similar use of pulse stimulation is described by *Fritz and Cessna* [1975] for the ATS-6 instrument, by *Weiss and Wilken* [1987] for the Implanted Ion Spectrometer instrument flown on the Giotto mission, by *Williams et al.* [1994] for the EPIC (Energetic Particles and Ion Composition) instrument on Geotail, and by *Sharber et al.* [1996] for the PEM (Particle Environment Monitor) on the UARS satellite. *Wilken et al.* [1997] have a thorough explanation of the complex and encompassing use of artificial pulse injection to perform in-flight testing of the RAPID instrument for the Cluster mission.

Time-of-Flight instrumentation has similar requirements for testing the processing of signals generated from the sensors (MCPs and solid-state detectors) with the added complexity of accurately determining the time interval between two independent signals. Again, the artificial injection of pulses at selected points in the signal processing chain with, possibly, variable phasing, is the most effective way of verifying proper operation of the on-board analysis of the multiple signals. *Rème et al.* [1993, 1997] describe the use of artificial pulses to verify proper operation of the Cluster CIS instrument while *Klumpar et al.* [2001] describe the use of this method for a similar TOF instrument flown on the FAST satellite.

Amplitude and frequency variable pulse injection was used in the plasma instrument on AMPTE-IRM not only to test threshold discriminators but, by slaving the pulse frequency

to the ESA plate voltage, also verified the analyzer sweep voltage profile. In the same instrument other pulse modes were used to check the data gathering logic and the on-board computation of plasma moments [*Paschmann et al.*, 1985].

Even the simplest plasma instruments benefit from injecting artificial pulses into the amplifier-discriminator electronics. This is especially valuable when the threshold discrimination levels can be stepped in order to obtain a PHD from CEMs or MCPs. Among the numerous space particle instruments that have utilized artificial pulse injection for this purpose are the Helios plasma experiment [*Rosenbauer et al.*, 1981], the Interstellar Neutral-Gas Experiment on Ulysses [*Witte et al.*, 1992], the Solar Wind Ion Composition Spectrometer, also on Ulysses [*Gloeckler et al.*, 1983], the particle analyzers on FAST [*Carlson et al.*, 2001], and the TED sensor in the POES SEM-2 instrument [*Evans and Greer*, 2000].

4.4 Relative and Absolute Calibration of Plasma Instruments

4.4.1 Introduction

The necessity for accurate in-flight calibration of plasma sensors is becoming critical to the solution of many of the space plasma physics problems that require multi-spacecraft missions to resolve gradients in the plasma. The Cluster mission (launched in 2000) and the proposed Magnetospheric Multi-scale Mission (scheduled launch in 2013) both involve four spacecraft flying in close formation in order to resolve small scale (10–1000 km) structures in the plasma. The accuracy of gradient determination, and the new physics that can be learned from these missions, ultimately depends upon the accuracy of in-flight calibrations. For these types of science missions, measurement accuracies to better than 5 % are highly desirable.

Other spacecraft platforms, such as the DMSP and NOAA satellites, require periodic in-flight calibrations in order to provide effective long-term monitoring of Earth's auroral zones. The accuracy required of these calibrations efforts depends upon goals of the mission, with ∼30–50 % accuracy often being adequate. However, even these more relaxed calibration goals still require periodic testing of the sensors. Single spacecraft missions also require careful in-flight calibrations for proper interpretation of the observations. Interpretation of the local physical process and placement of the local observations in a global context typically require in-flight calibrations to better than 30 %.

Before embarking on determining either absolute or relative calibration of plasma sensors, the data set must be thoroughly qualified. As discussed in Sections 4.2 and 4.3, plasma instruments that include MCP or CEM detectors must verify that the detector gains are proper. Any sources of background or spurious responses should have been identified and the data corrected. If those responses are not corrected, those data should not be used in establishing relative or absolute calibrations.

Laboratory calibrations of the instruments may have exposed slight differences in analyzer characteristics, temperature variations of one sort or another, and other peculiarities of individual sensor systems. For example, non-concentric analyzer plates can introduce variations in both energy (a few %) and sensitivity (10–20 %) with look direction. Thermal drifts of resistors and offset drifts in operational (OP) amplifiers may lead to drifts in

energy response. All variations in analyzer characteristics, temperature effects, and other factors exposed in laboratory calibrations must be introduced before in-flight calibrations are attempted. This section assumes the plasma data have been fully qualified and all known corrections have been made.

The efficiency of MCPs (or CEMs) may vary across the detector. The magnitude of these variations generally depends upon details of the pulse height distribution and the preamplifier discriminator threshold, and may depend upon accumulated flux. In addition, efficiency variations are also caused by changing the angle between the particle velocity and MCP pore bias angle [*Gao et al.*, 1984]. For example, the top-hat analyzer RPA-1 on the Giotto spacecraft utilized a 360° annulus MCP chevron pair for detection [*Rème et al.*, 1987]. Because the electrons exited from the analyzer at an angle not perpendicular to the MCP plane, there was an azimuthal dependence of the average electron velocity relative to the individual microchannels. This problem was avoided on later missions (Wind, Mars Surveyor, FAST, Cluster) by splitting the MCPs into 180° C-shaped segments, with the bias angle direction centered on the C. Simulations and ground testing showed this was effective in eliminating the majority of MCP bias angle skewing. Even with this arrangement, pre-acceleration between the analyzer and detectors may introduce additional small efficiency variations due to changes in angle between particle velocity and pore bias.

The energy dependence of the MCP efficiency is also a part of relative calibrations. These variations in response are much more difficult to determine. The efficiency of an MCP varies much more for electrons (∼60 %) than for ions (∼20 %) over the energy range of most plasma instruments (0–30 keV) when nominal pre-accelerations of up to several hundred volts for electrons and 2–3 kV for ions are used. Attempts to determine the energy dependent efficiency based upon in-flight calibrations have been made for instruments on Geotail, Wind and Polar and are described in the following sections.

It is important to understand how errors in the determination of relative efficiencies effect the measurements. The dependence of detector efficiency on incident particle energy is generally noticed in the even moments (density, pressure). For multi-spacecraft missions where density or pressure gradients are important, the use of the same functional dependence on energy and cross-calibration of the sensors on different spacecraft reduces the chance that errors in this dependence will introduce significant errors in the gradients. Errors are more likely to be detected when comparing plasma parameters from different instrument types, such as electron and ion sensors, or by spectral comparisons between different instruments.

Variations in efficiency with look-direction will impact primarily the odd moments (velocity, heat flux). Since much of the physics is often tied to particle or energy flows, determination of the relative efficiency with look direction is often more critical. This relative efficiency can be determined by comparing sensor counting rates during times of isotropic particle distributions, or at similar pitch angles at times when the distributions are anisotropic. If convective flows are present, care must be taken to transform the distribution before pitch angle comparisons are made. Since the transformation to the proper reference frame will often depend upon the uncalibrated data, it is best to minimize these transformations to avoid any feedback in the process. Spacecraft charging must also be properly accounted for, especially if the potentials are large enough to significantly affect particle trajectories. Problems introduced by both flows and spacecraft charging favor performing these calibrations using the more energetic portion of the particle population.

When performing such calibrations, care should be taken to avoid regions where pressure gradients can introduce flows or where non-gyrotropic distributions are present.

This section first describes the physical principles governing plasmas in space that are used as a basis for determining relative and absolute calibration of plasma sensors. The limitations in the use of those principles are discussed as well as advice on the proper choice of physical location and conditions that are most conducive to obtaining high quality calibrations. A number of specific examples illustrating the use of these physical principles for calibration of various types of plasma sensors on a variety of missions is then provided.

The reader will appreciate that similar calibration procedures are used for different instruments and for similar instruments on different science missions, so there may be unavoidable duplication in the following material.

4.4.2 Physical Principles

In this section, we will describe methods for in-flight calibration of plasma instruments that are based on independent determinations of the plasma density, on quasi-neutrality of the plasma, on constraints on the ion and/or electron distributions imposed by gyrotropy and the direction of the magnetic field, and on pressure balance. The examples of in-flight calibrations described in the subsequent sections are largely based on applications of one or more of these methods.

4.4.2.1 Use of Wave-Determined Plasma Densities

One of the most common methods of checking a plasma instrument's response is by comparing the local plasma density inferred from wave measurements to the density determined by integrating the distribution of particles. This method is used to determine the "absolute calibration" or "integral sensitivity" of the instrument. The accuracy of the method depends upon the plasma instrument's relative calibration, the measurement of all significant plasma components, the proper identification and correction for ion mass and spacecraft charging, and the accuracy of the density determined from the data of the wave instrument. Whereas relative calibrations are typically stored as a set of numbers approximately equal to one, representing small variations in instrument response with angle and energy, the absolute calibration is stored as a single number that provides an integral sensitivity (or total geometric factor) for the instrument. The combinations of absolute and relative calibrations are then used to scale count rates to obtain absolute flux values.

The simplest wave determined density calibration involves identification of the plasma frequency,

$$\omega_p = 2\pi f_p = \sqrt{\frac{N_e e^2}{m_e \epsilon_0}} \tag{4.1}$$

from naturally occurring Langmuir waves. For $f_p \gg f_{ce} = eB/(2\pi m_e)$, as is the case in the solar wind and magnetosheath, the Langmuir wave dispersion relation can be approximated as $\omega^2 = \omega_p^2 + \frac{3}{2}k^2 v_e^2$ where v_e is the electron thermal velocity and k the wavenumber. Short-wavelength waves, for example those produced in the electron foreshock, may have frequencies that deviate from f_p due to finite k effects and/or Doppler

shifts. In addition, electromagnetic waves may be present and dominate the spectra. The EM wave field typically has a broad frequency spectrum with cutoff near f_p. Therefore what is commonly used as a proxy for f_p is the sudden drop in wave power near f_p. The accuracy of this method ultimately depends upon the frequency resolution of the measured wave spectrum, the relative sampling between wave spectra and particle density, and the presence of long wavelength waves. The finite k effects can be alleviated by the use of a relaxation sounder as described in Section 2.10.

Recent observations within the Earth's magnetosphere have shown that cold plasma can dominate the local density in the dayside plasmasheet [*Sauvaud et al.*, 2001], nightside plasmasheet [*Seki et al.*, 2003], plasmasheet boundary layer [*Etcheto and Saint-Marc*, 1985], lobes [*Hirahara et al.*, 1996], polar cap [*Su et al.*, 1998] and plasmasphere [*Lemaire and Gringauz*, 1998]. Cold ions in these low density regions are not detected by plasma instruments due to the spacecraft charging (unless flows are large, see *Sauvaud et al.* [2001]), and so care must be taken when selecting times for magnetospheric density calibrations. Note that even in small quantities, such cold ions can affect the wave modes, or in case of oxygen, have a major effect on the mass density of the plasma.

Cold electrons can also be a significant component in the magnetosphere, especially within the plasmasphere, lobes and plasmasheet boundary layer. These electrons are difficult to separate from spacecraft photo-electrons since most instruments tend to mix these populations in the energy channel that corresponds to the spacecraft potential.

Magnetospheric measurements may also have significant concentrations of heavy ions (O^+, He^+) and proper integration of the ion distribution functions requires knowledge of particle mass. For non-mass resolving sensors, care must be taken in the selection of calibration times and locations in order to minimize high-mass components. In the near-Earth environment, relative calibrations are often determined within the magnetosphere where bulk plasma flows are generally lower and particle distributions are both hotter and more isotropic. However, density inter-calibrations are better performed within the magnetosheath or solar wind where cold plasma is not present and the contribution from heavy mass ions (He^{2+}) can be estimated from solar wind spectra.

In comparing wave and particle determined densities, care must be taken to perform the particle integrals correctly. The most common errors involve mistreatment of spacecraft charging, the exclusion of some portion of the plasma, or the failure to properly account for different mass ions. In Section 4.4.2.2 we present a discussion on how to properly integrate a distribution, accounting for spacecraft charging. To minimize the impact of different mass ions, density calibrations within the magnetosphere should avoid magnetic storm periods where ionospheric O^+ and He^+ outflows contribute significantly to the density.

For measurements by non-mass-resolving ion sensors in the solar wind or magnetosheath, the assumption of H^+ introduces a fractional underestimation of the inferred density used for inter-comparison with wave determined density (N_e),

$$\frac{N_{H^+} + N_{He^{2+}}/\sqrt{2}}{N_{H^+} + 2N_{He^{2+}}} \approx 1 - 1.29\frac{N_{He^{2+}}}{N_{H^+}} \tag{4.2}$$

for $N_{He^{2+}} \ll N_{H^+}$. The error results from the estimated number density using the incorrect mass/charge, where calculated density is proportional to $(m/q)^{0.5}$, and including the dual charge on the He^{2+}. If composition data are available, the correction should be made. This error is of similar magnitude to errors in wave-determined density.

4.4.2.2 Calculating Particle Moments and Correcting for Spacecraft Charging

Many of the techniques described in subsequent sections involve the comparison of the particle moments with other measured physical quantities. Discussions of unit conversion from count rate to differential flux or distribution function can be found in Chapter 1, along with an overview of particle moment computation (see also Appendix A.7.3). However an aspect of these calculations that is not addressed is the correction for spacecraft charging. Corrections for particle acceleration from the plasma to the spacecraft are often either incorrectly performed or ignored. For most geophysical plasmas, these corrections are essential for accurate moment computations, therefore we provide a brief description of this process.

To understand the correct methodology for correcting plasma moments for spacecraft potential, we recall the basics of plasma instruments. A plasma sensor measures a count rate, R. The instrument's geometric factor, G, sets the open area, energy and angle range accepted by the detector. G has nominal units of (cm^2 sr eV). Dividing R by G gives differential number flux, J',

$$J'(E', \Omega') = \frac{R(E', \Omega')}{G(E', \Omega')} \tag{4.3}$$

with units of $(\mathrm{s\,cm}^2\,\mathrm{sr\,eV})^{-1}$. Here we use $'$ to distinguish the internal analyzer energy, solid angle and differential flux, E' and Ω', and J' from the values far from the spacecraft, E and Ω and J.

Since an analyzer's internal relative voltages do not depend upon spacecraft charging, the measured differential fluxes represents the plasma at the entrance aperture after it has undergone any accelerations by the spacecraft potential. This differential flux measurement can then be converted into units of phase space density, which again defines the plasma at the instrument's entrance aperture. It is important that this conversion to distribution function, $f'(E', \Omega')$, use the analyzer energy, E', and not the particle energy far from the spacecraft, E.

$$f'(E', \Omega') = \frac{m^2}{2E'} J'(E', \Omega') \tag{4.4}$$

where m is the particle mass. Since phase space density is conserved in electrostatic accelerations, internal phase space densities are the same as phase space densities far from the spacecraft,

$$f'(E', \Omega') = f(E, \Omega) \tag{4.5}$$

with the plasma being transformed from E, Ω to E', Ω' as it accelerates through the spacecraft potential. Corrections for spacecraft charging are reduced to mapping energy and solid angle. For calculating plasma moments, we recall that Nth order moments involve integrals over $f(v, \Omega)$

$$\mathsf{M}^N_{lmn\ldots} = m \int_\Omega \int_0^\infty (\boldsymbol{s}_l \boldsymbol{s}_m \boldsymbol{s}_n \ldots) v^N f(v, \Omega) v^2 \, \mathrm{d}v \, \mathrm{d}\Omega \tag{4.6}$$

where the number of subscripts $(l, m, n \ldots)$ is N, and each subscript varies over x, y, and z. The $\boldsymbol{s}_l$ are unit vectors: $\boldsymbol{s}_x = \boldsymbol{i}\cos\theta\cos\varphi, \boldsymbol{s}_y = \boldsymbol{j}\cos\theta\sin\varphi, \boldsymbol{s}_z = \boldsymbol{k}\sin\theta$. We transform the dependence of this equation from velocity to energy:

$$\mathsf{M}^N_{lmn\ldots} = m\int_\Omega\int_0^\infty (\boldsymbol{s}_l\boldsymbol{s}_m\boldsymbol{s}_n\ldots)\left(\frac{2}{m}\right)^{(N+1)/2} E^{(N+1)/2} f(E,\Omega)\frac{\mathrm{d}E}{m}\,\mathrm{d}\Omega \tag{4.7}$$

assuming a non-relativistic transformation. We now transform from the unmeasured E, Ω to the measured analyzer values of E', Ω':

$$\begin{aligned}\mathsf{M}^N_{lmn\ldots} = m\int_{\Omega'}\int_{-q\Omega}^\infty (\boldsymbol{s'}_l\boldsymbol{s'}_m\boldsymbol{s'}_n\ldots)\left(\frac{2}{m}\right)^{(N+1)/2}(E'+q\Phi)^{(N+1)/2}\\ \cdot f'(E',\Omega')\frac{\mathrm{d}E'}{m}\,\mathrm{d}\Omega'\end{aligned} \tag{4.8}$$

where q is the particle charge and Φ is the spacecraft potential relative to the plasma. The energy integral is limited to values $> -q\Phi$ to prevent inclusion of spacecraft generated particles. For $q\Phi > 0$, the lower limit of the integral is set to zero and a portion of the distribution is not measured. This may result in significant moment calculation errors if a cold component is not measured by the sensor. Note that angular deflections of particles will result in a functional dependence of $\boldsymbol{s'}_l$ on Φ and E [i.e., $\boldsymbol{s}_l(\theta,\varphi) = \boldsymbol{s'}_l(\theta',\varphi',E',\Phi)$]. If spacecraft charging introduces significant deflection of incident particles and if the distribution function is anisotropic, accurate moment calculations may require a ray tracing effort to determine the $\boldsymbol{s}_l$ to $\boldsymbol{s'}_l$ mapping.

Finally we convert distribution function back to measured count rate,

$$\begin{aligned}\mathsf{M}^N_{lmn\ldots} = m\int_{\Omega'}\int_{-q\Phi}^\infty (\boldsymbol{s'}_l\boldsymbol{s'}_m\boldsymbol{s'}_n\ldots)\left(\frac{2}{m}\right)^{(N+1)/2}(E'+q\Phi)^{(N+1)/2}\\ \cdot\left(\frac{m^2}{2E'}\right)\frac{R(E',\Omega')}{G(E',\Omega')}\frac{\mathrm{d}E'}{m}\,\mathrm{d}\Omega'\end{aligned} \tag{4.9}$$

and rearrange some terms to get:

$$\begin{aligned}\mathsf{M}^N_{lmn\ldots} = 2\left(\frac{m}{2}\right)^{(3-N)/2}\int_{\Omega'}\int_{-q\Phi}^\infty (\boldsymbol{s'}_l\boldsymbol{s'}_m\boldsymbol{s'}_n\ldots)(1+q\Phi/E')^{(N+1)/2}\\ \cdot (E')^{(N-1)/2}\frac{R(E',\Omega')}{G(E',\Omega')}\,\mathrm{d}E'\,\mathrm{d}\Omega'\end{aligned} \tag{4.10}$$

Equation 4.10 provides a general formula that corrects particle moments for a spacecraft potential. When these measurements are made by top-hat electrostatic analyzers with microchannel plate or CEM detectors, the geometric factor can often be approximated as:

$$G_{\mathrm{ESA}}(E',\Omega') = gE'\varepsilon(E')\alpha(\Omega') \tag{4.11}$$

where g is a constant, $\varepsilon(E')$ represents the energy dependence of the detector, and $\alpha(\Omega')$ the angle dependence of the combined analyzer-detector. Both $\varepsilon(E')$ and $\alpha(\Omega')$ are nominally close to unity. $\varepsilon(E')$ is generally a slowly varying function of E' as discussed in

Sections 2.2.3 and 2.2.4. $\alpha(\Omega')$ includes the small changes in sensitivity resulting from detector non-uniformity or variations in analyzer open area. Substituting we get:

$$\begin{aligned} \mathsf{M}^N_{lmn\ldots} = \frac{2}{g}\left(\frac{m}{2}\right)^{(3-N)/2} \int_{\Omega'}\int_{-q\Phi}^{\infty} (\boldsymbol{s'}_l \boldsymbol{s'}_m \boldsymbol{s'}_n \ldots)(1+q\Phi/E')^{(N+1)/2} \\ \cdot (E')^{(N-1)/2} \frac{R(E',\Omega')}{\varepsilon(E')\alpha(\Omega')} \frac{\mathrm{d}E'}{E'} \mathrm{d}\Omega' \end{aligned} \tag{4.12}$$

For most practical computations, the integral is replaced by a sum and becomes:

$$\begin{aligned} \mathsf{M}^N_{lmn\ldots} = \frac{2}{g}\left(\frac{m}{2}\right)^{(3-N)/2} \sum_{E'>-q\Phi} \sum_{\Omega'} \Big[(1+q\Phi/E')^{(N+1)/2} (E')^{(N-1)/2} \\ \cdot \varepsilon(E')^{-1} \frac{\mathrm{d}E'}{E'}\Big] R(E',\Omega') \Big[(\boldsymbol{s'}_l \boldsymbol{s'}_m \boldsymbol{s'}_n \ldots)\alpha(\Omega')^{-1} \mathrm{d}\Omega'\Big] \end{aligned} \tag{4.13}$$

where we have explicitly ordered the energy and angle dependence within the sum. If angle deflections can be assumed to be small so that $\Omega' \sim \Omega$ and $\boldsymbol{s'}_l \sim \boldsymbol{s}_l$, then the above sum is rather straight forward and readily calculated. For top-hat style sensors viewing primarily radial rather than tangential to spacecraft surfaces, and especially if the instrument is deployed on a short boom away from spacecraft surfaces, the small deflection approximation ($\Omega' \sim \Omega$) will be valid except for the lowest energy particles. In this case, accurate moments are relatively simple as long as the bulk of the plasma is observed at $E' > -q\Phi$ and as long as accurate measurements of spacecraft potential are available.

When an independent measurement of spacecraft potential is available, as from a Langmuir probe, the energy mapping is relatively simple. A current biased Langmuir probe will float near the plasma potential and measure the spacecraft-to-probe potential difference (see Sections 2.3.7). The energy shift should include an additional potential shift of ~1–2 V that represents the probe-to-plasma potential. When an independent measurement of spacecraft potential is not available, a distinguishing feature in the particle spectra can be used to determine the spacecraft potential. These corrections are generally most important for high-altitude, low-density plasmas where spacecraft charging varies from ~5 V to >40 V. The most easily resolved features in these regions are the spectral inflections that mark the boundary between spacecraft photoelectrons and plasma electrons.

Distribution function corrections are more difficult when angle deflections of the particles approaching the spacecraft are significant. For a sensor that views radially away from the spacecraft, angle deflections should be negligible. However, for fields-of-view that are near tangent to spacecraft surfaces, angle deflections may be significant, especially at energies just above the cutoff energy determined by charging. Detailed ray tracing using the spacecraft and sensor geometries may be required. These deflections cause the largest problems when significant cold populations are present. For electrons these corrections can in principle be made since positively charged spacecraft do not exclude any of the distribution from access to the instrument. For ions the retarding potential may eliminate a significant fraction of the ion population. If cold plasma measurements are important for the science goals, the best solution is to minimize the problem by deploying the sensor on a boom away from the spacecraft and biasing the sensor near the plasma potential.

4.4.2.3 Charge Neutrality

Except on very small spatial scales, space plasmas are neutral. Charge density equality is a powerful tool for establishing instrument relative and absolute calibration. Of course, care must be taken that such comparisons are only made when there is evidence that the distributions of ions and electrons are measured completely, no photoelectrons contaminate the electron measurement, and no cold ion species are being missed.

4.4.2.4 Gyrotropy

For distributions that are gyrotropic (i.e., have cylindrical symmetry around the magnetic field direction in the bulk velocity frame), the 3-D distribution becomes 2-D (pitch-angle and energy). A set of sensors rotating with the spacecraft will observe particles at a range of pitch angles depending on the orientation of the magnetic field relative to the spacecraft spin axis. A large and overlapping range of pitch angles is often sampled by the different sensors. If the data are pitch angle sorted as a function of energy, one can intercompare the measured response for the times when different sensors sample the same pitch angles. If those times are not too far apart, one can assume the input fluxes have not changed and the response should be the same. In this way one can calibrate the relative geometric factors, including detection efficiencies as a function of energy.

The gyrotropy assumption is quite commonly fulfilled for electrons. For electrons one may be able to ignore the velocity transformation into the plasma bulk frame. However if the electron spectrum is steep, even small velocities much less than the electron thermal velocity can cause significant differences in count rate between the flow and anti-flow directions so care should be taken. For ions, it is critical to go into the bulk velocity frame, or more conveniently, to select times where bulk velocities are negligible. For ions, one must also avoid the vicinity of plasma boundaries where finite gyro radius effects introduce non-gyrotropy to the distributions.

For low altitude satellites, plasmasheet population outside the loss cones generally provides the most isotropic fluxes suitable for detector inter-comparisons. The auroral regions should be avoided because there are significant spatial structures that can be crossed in a single spacecraft rotation that give rise to ambiguities in the comparisons. For interplanetary missions, variations in the magnetic field direction and the relatively high electron thermal velocities allow look-direction relative calibrations for electron plasma sensors. In-flight calibrations of ion plasma sensors in the solar wind are more difficult because of the high drift to thermal velocity ratio. If these calibrations are crucial to the mission success, it may warrant performing spacecraft maneuvers that allow the sensor field-of-view to rotate through the solar wind flow direction in order to calibrate its response.

Another approach is based on the effect of gyrotropy on the ion or electron pressure (or temperature) tensors. These tensors can always be diagonalized through a major-axis transformation, with diagonal elements P_{11}, P_{22}, P_{33} and zero off-diagonal terms. For distributions that are gyrotropic, but have a significant anisotropy, one of the major axes should be aligned with the magnetic field. Any misalignment is thus an indicator of imperfect calibration. Similarly, one could use the computed heat flux. As the magnetic field impedes heat flow in the perpendicular direction, the heat flux vector is expected to be aligned with the magnetic field. From a large data base of pressure anisotropies or heat

fluxes (and associated magnetic field directions) one could thus derive an improved (relative) calibration.

The gyrotropy principle was used in the in-flight calibration of plasma instruments on Geotail (Section 4.4.3), Polar (Section 4.4.4), and Cluster (Section 4.4.6.2). A similar approach was used for particle sensors on board the AE-D satellite and those results are described by *Lin and Hoffman* [1979].

4.4.2.5 Pressure Balance

For one-dimensional, time-stationary plasma boundaries, momentum conservation implies constancy of the total pressure, plasma plus magnetic, across that boundary. So comparing the total pressure on the two sides of such a boundary provides a check of the (absolute) calibration factors behind the (perpendicular) plasma pressure, provided the magnetic field strengths are significantly different on the two sides. This technique is generally appropriate for ions only, because the electron pressure is usually a small (10 %) fraction of the plasma pressure. However, both electron and ion pressures should be included in the pressure balance calculation. Pressure balance has been used in the calibration of the CIS/CODIF mass spectrometer on Cluster, as described in Section 4.4.6.3.

4.4.2.6 Alfvén Waves

Alfvén waves are characterized by a quantitative relation, $\Delta \boldsymbol{V} = \Delta \boldsymbol{B}/\sqrt{\rho\mu_0}$, between the magnitude and direction of the wave-associated variations, where $\Delta \boldsymbol{V}$ and $\Delta \boldsymbol{B}$ are variations in the plasma bulk velocity and magnetic field, with ρ being the mass density of the plasma and μ_o the permeability constant. This relation is routinely used for identifying Alfvén waves, but to our knowledge has only been applied once for calibration purposes. During the encounter with comet Halley, magnetic field and plasma observations on board the Giotto spacecraft revealed in-phase perturbations that were assumed to be Alfvén waves, produced by the interaction of the comet with the solar wind. The variations in the instantaneous plasma bulk flow velocities, calculated from measurements by the three-dimensional positive ion analyzer on Giotto, displayed a near-linear dependence on the simultaneously measured variations in the wave's magnetic field, as expected [*Johnstone et al.*, 1987]. This result provided confidence that the plasma bulk flow velocity was being properly retrieved from the raw plasma measurements provided by the instrument.

4.4.2.7 Intra-Satellite versus Inter-Satellite Calibrations

While the calibration principles described above involve comparisons between sensors or instruments on the same spacecraft, and most of the mission specific examples in the following sections are in that category, the Cluster multi-spacecraft mission and the NOAA/POES missions described in Sections 4.4.6 and 4.4.7 are exceptions.

Multi-spacecraft missions provide the opportunity for cross-calibrations of identical instruments on different spacecraft that can be a powerful tool for obtaining relative calibrations. Naturally, this can only be done in situations where there is reasonable confidence that the plasma environments (densities, temperatures, etc.) are as nearly identical as possible at the spacecraft locations. The Cluster mission is particularly suited for both intra- and inter-satellite calibrations because its instruments are identical on all four spacecraft

and the spacecraft often in close proximity exposing them to the same particle environment. An example of such an inter-satellite calibration for Cluster is presented in Section 4.4.6.4.

4.4.3 Geotail

The constraint for density equality is a powerful tool for establishing instrument relative and absolute calibration since the local density of ions and electrons cannot differ by more than 1 part in 10^6 in the magnetosphere. This constraint was effectively used to perform the Geotail LEP (low energy plasma) in-flight calibratons. The following discusses the approach used to calibrate the EAi (Energy Analyzer for ions) instrument using ion moments, followed by a more detailed discussion of the EAe (Energy Analyzer for electrons) calibrations using electron moments.

The Geotail LEP instrument obtained angular distributions by using multiple detectors: seven MCPs in the ion instrument and seven CEM's in the electron instrument. There are certain corrections that must first be made to both the ion and electron data. These are for spurious response from penetrating particles (cosmic rays) and for the sensor responses to solar EUV, especially when the Sun is in the sensor field of view. The correction for cosmic ray response follows from the background response in locations where little or no low-energy plasma is present. The correction for EUV is based upon laboratory measurements and modeling. Once these background counts were removed, the ion and electron data were corrected for differences in relative efficiencies among these MCP and CEM detectors. Comparing detector responses when different detectors viewed the same particle energy and pitch angle (Section 4.4.2.4) established this correction.

Once these corrections were applied to the data from the EAi instrument, the computation of the moments was a straightforward integration of the 3-D distribution obtained from the instrument. The ion sensor's MCP efficiency was assumed to be independent of incident ion energy. The absolute calibration of the LEP ion instrument was then determined by comparing the density moment thus obtained with the plasma density obtained from the cutoff frequency of the continuum radiation as described also in Section 4.4.2.1. This comparison was made in regions of varying plasma densities and temperatures including the plasmasheet, the lobe, and the magnetosheath.

Implementing a similar procedure for electron moments is considerably more complex because of the influence of spacecraft potential and the photoelectron cloud produced at the spacecraft. For this reason, a more comprehensive discussion of the procedures for obtaining the electron moments is warranted.

The LEP electron data are significantly contaminated by instrumental photoelectrons and secondary electrons, especially at low energies ($<$60 eV) and when viewing in the sunward direction. Figure 4.18 shows omni-directional electron and ion energy-time spectrograms obtained on 14 October, 1993 when the Geotail spacecraft was in the distant tail lobe region ($X_{GSE} = -140\,R_E$.) The upper panel shows the spectrogram for electrons. Before 0946 UT significant fluxes of spacecraft photoelectrons were observed below 40 eV. According to a simultaneous Langmuir probe measurement, the spacecraft potential was +36 V at this time. Geotail has the capability to control the spacecraft potential using an Ion Emitter (IE) [*Tsuruda et al.*, 1994]. When the IE was turned on at 0946 UT, the spacecraft potential changed to about +2 V relative to the probe, or about +3 V to +4 V relative to

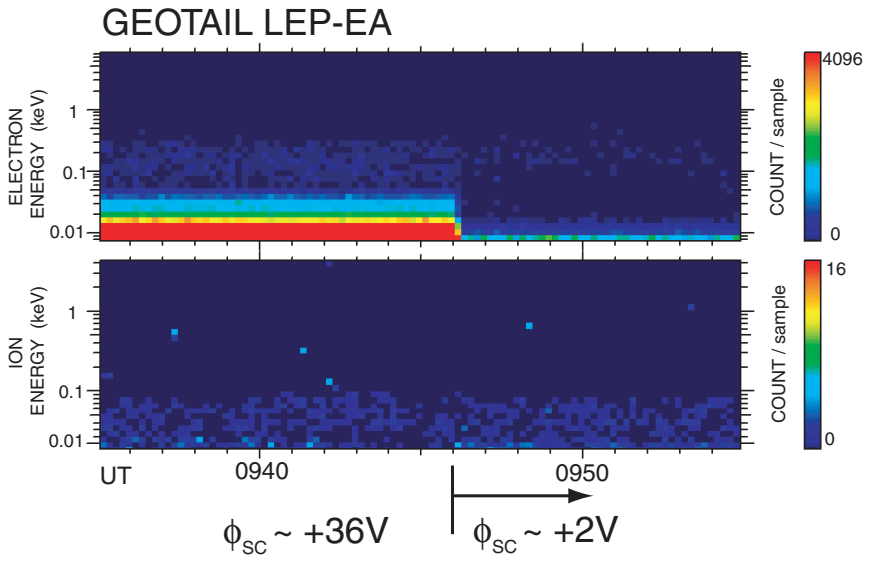

Figure 4.18: Electron and ion energy spectrograms spanning the time when the Ion Emitter was turned on and changed the spacecraft potential from ∼36 V to ∼2 V.

the plasma. At the same time the energy where the photoelectrons were detected decreased to below 10 eV.

When the spacecraft potential was +36V, spacecraft photoelectrons were detected at almost all directions although the flux was most intense when the analyzer was viewing the Sun. When the spacecraft potential decreased to ∼+2 V, relative to the Langmuir probes, intense photoelectron fluxes were observed only in the Sun viewing sector. These latter photoelectrons are produced internal to the analyzer. Figure 4.19 shows detailed distribution functions observed when the LEP EAe sensor was viewing anti-sunward (left panels) and toward the Sun (right panels.) All four data sets were taken when the spacecraft potential was ∼+2 V relative to the Langmuir probes.

Photoelectrons detected by the EAe instrument will greatly affect the computation of the electron velocity moments, especially the absolute value of the electron density. For this reason the contribution of photoelectrons generated at the spacecraft surface and within the analyzer were removed from the instrument response before such calculations were attempted. This was done by extrapolating the 50–100 eV plasma electron distribution back to lower energies assuming a thermal distribution. The dashed green curves in Figure 4.19 illustrate this extrapolation (straight line on a $\log(f)$ versus energy).

Once the EAe CEM responses were corrected for background, photoelectrons, and relative efficiencies, the computation of velocity moments up to third order proceeded in much the same fashion as for the ion data from the EAi instrument. The electron energies were corrected for the spacecraft potential as measured by the Langmuir probes. A large number of simultaneous electron and ion densities were obtained during measurement intervals in the plasmasheet and the averages of those densities $\langle n_e \rangle$ and $\langle n_i \rangle$ were calculated. Since electron and ion densities are equal, and since ion data were already cal-

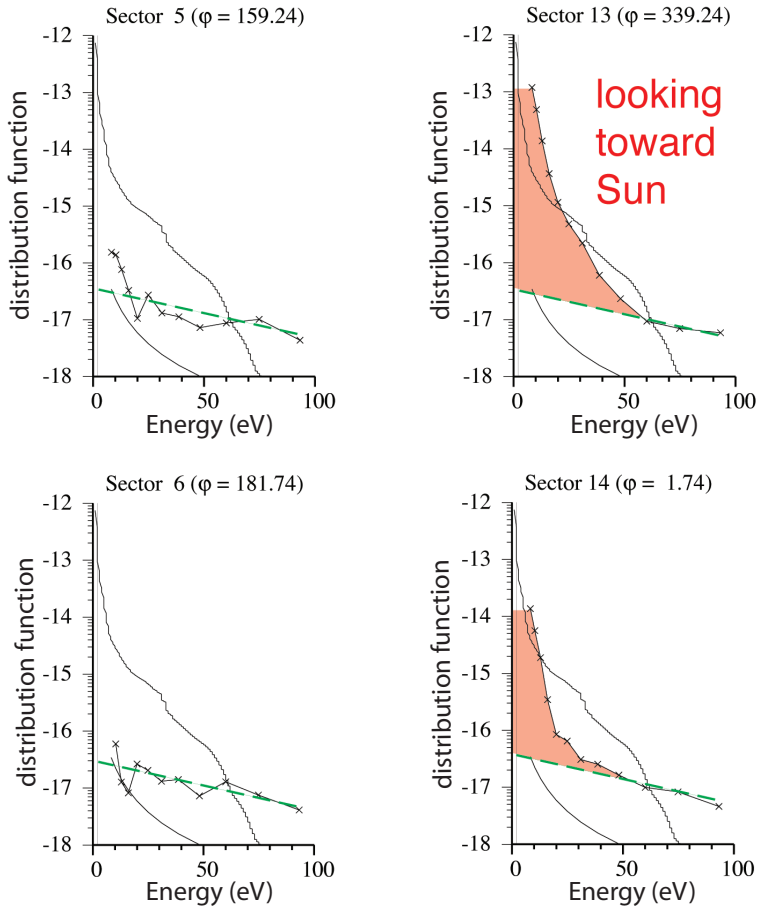

Figure 4.19: The sub-panels display details of the electron distribution functions in terms of phase space densities for four selected viewing sectors in the plane normal to the Geotail spin axis when the spacecraft potential was +2 V relative to the Langmuir probes. The sub-panels on the left are from sectors when the EAe instrument was viewing anti-sunward and in the shadow of the spacecraft while the sub-panels on the right are from sectors when the instrument was viewing toward the Sun and on the sunlit side of the satellite. The cross symbols in each panel are the electron distribution function obtained directly from the LEP EAe observations while solid line in the lower left of each panel marks the one count level of the detector system response. The second solid line in each panel, extending to very high value at low electron energy, is the modeled distribution of spacecraft generated electrons. The green dashed line in each panel is the extrapolation to lower energy of the electron distribution function observed at higher energies where photoelectrons would not contribute to the sensor response.

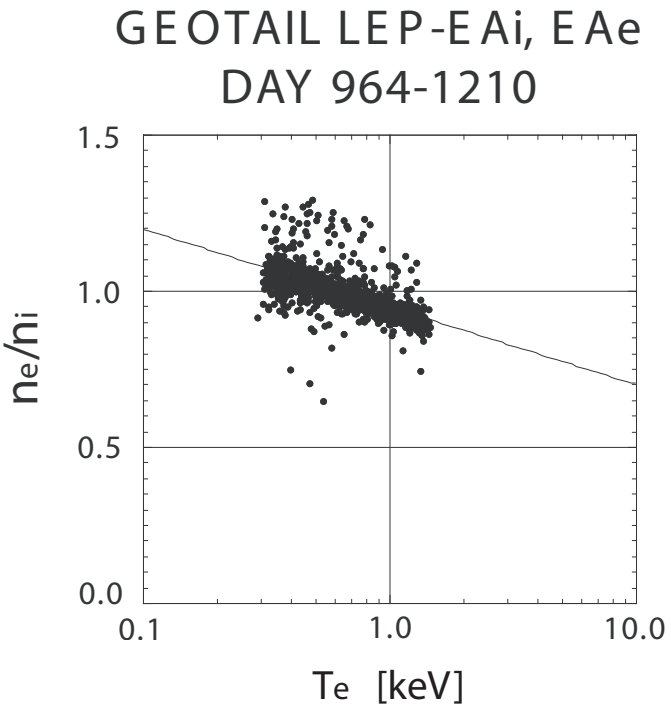

Figure 4.20: The ratio n_e/n_i as a function of electron temperature (in keV) obtained from many observations in the plasmasheet. The data have been corrected for photoelectrons and for differences among analyzers. While the data points cluster about 1.0, there is a clear dependence of the ratio upon electron temperature that demonstrates the need to account for the energy dependence of the CEM for detecting electrons.

ibrated, the ratio $\langle n_e \rangle / \langle n_i \rangle$ must represent the average efficiency of the EAe's CEMs for detecting electrons. To correct for the average CEM efficiency, each computed electron density was multiplied by $\langle n_i \rangle / \langle n_e \rangle$ to obtain a final value of electron density. Figure 4.20 shows the ratio between n_e (corrected in this manner) and n_i as a function of electron temperature T_e for a data set obtained in the plasmasheet when T_e was >300 eV. If there were no energy dependence in the CEM electron counting efficiency, the n_e/n_i ratios would cluster about 1.0 with the scatter being a measure of the overall experimental uncertainties in computing plasma densities. However, Figure 4.20 shows that the n_e/n_i ratio decreases with increasing electron temperature. This decrease is caused by the energy dependence in the efficiency of electron detection by the CEMs that had not yet been applied.

Figure 4.21 shows the energy dependence of CEM electron counting efficiency applied to the electron instrument EAe to remove the slope in Figure 4.20. This energy dependence is similar to the measured efficiency reported by *Archuleta and DeForest* [1971]. The energy dependent efficiency was applied only for electrons above 300 eV since a 250 V accelerating voltage is applied to the input of the EAe CEMs and the counting efficiency of a CEM is reported to be a maximum for a 300 eV, $\pm$200 eV, electron. The curve was derived by an iterative procedure of varying the energy dependent efficiency curve, re-

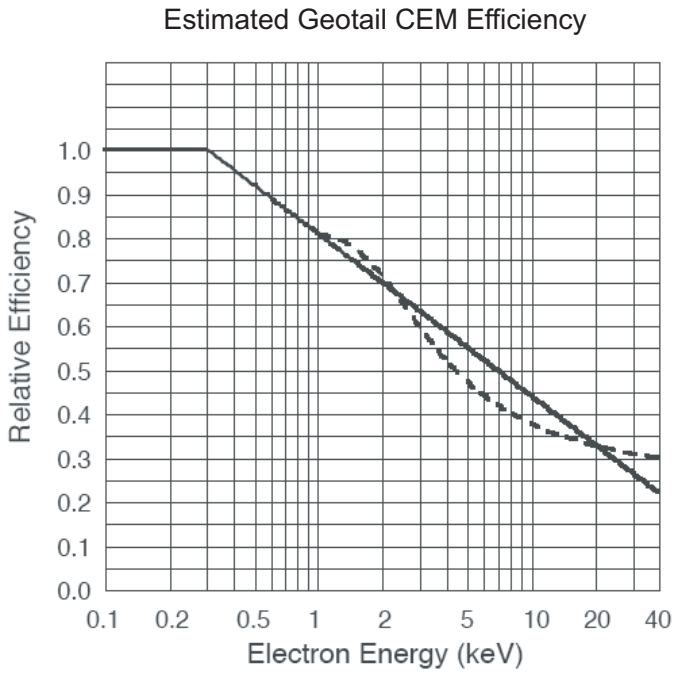

Figure 4.21: The solid line is the energy dependence of the CEM efficiency used to correct the Geotail LEP electron observations and eliminate the energy dependence in the n_e/n_i ratio in Figure 4.20. For comparison, the dashed line shows a fit of the energy dependence between 1 keV and 50 keV, normalized to 0.8 at 1 keV, reported by *Archuleta and DeForest* [1971].

calculating electron velocity moments and reevaluating the dependence of n_e/n_i upon T_e until the n_e/n_i ratio was no longer dependent on electron temperature in the plasmasheet.

As described in Section 4.4.2.4, the relative efficiencies of the seven CEMs in the EAe instrument were established under the assumption of the angular distribution of electrons being gyrotropic. However, a careful analysis of the electron bulk velocity parallel to the Geotail spin axis (which was nearly perpendicular to the ecliptic plane) and its dependence upon electron temperature revealed the necessity for an additional, but very minor, correction to those relative efficiencies. Figure 4.22 displays scatter plots of the simultaneous measurements of that component of electron bulk velocity, V_{ez}, and electron temperature T_{ezz}. The red points are for the case where the original CEM relative efficiencies were used in the analysis and show an unphysical dependence of bulk velocity upon electron temperature. If there remained a slight difference in relative efficiency between different CEMs, the averaged V_{ez} will deviate from zero, especially when the electron energies are high. Slight modifications to the relative CEM efficiencies were then assumed to remove the energy dependence of V_{ez} upon T_{ezz}. These final corrections were as small as a few percent. The different colors of the data points in Figure 4.22 correspond to the results that were obtained for different final corrections, the green points showing the most favorable result.

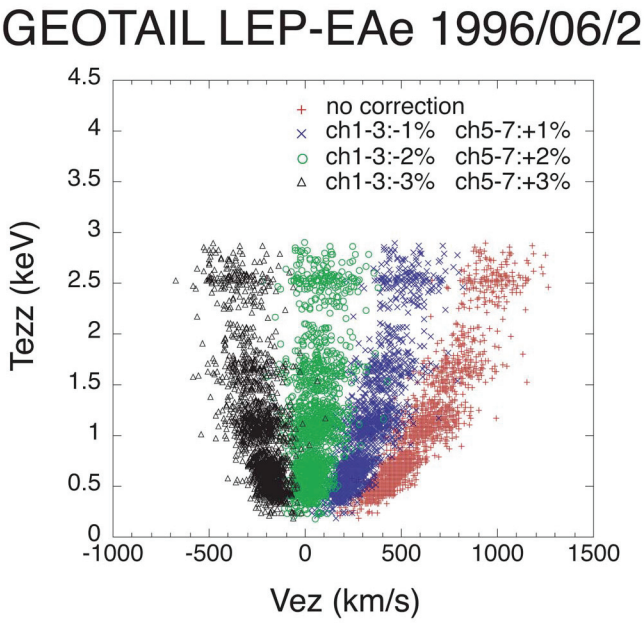

Figure 4.22: A scatter plot of the electron flow speed normal to the ecliptic plane as a function of electron temperature. The red points are the results obtained after introducing all the prior instrument corrections. The dependence of the flow speed on temperature indicated the need for small additional corrections to the analyzer responses. Corrections of only a few percent to some analyzers removed that dependence and the final results are shown in green.

In conclusion, excellent in-flight calibrations were obtained for the Geotail LEP instrument using the described procedures to obtain consistent electron and ion velocity moments. It was more difficult to calibrate the electron sensor than the ion sensor because of contamination by photoelectrons and the effects of spacecraft potential. The final electron densities agree to within 10 % in most cases as illustrated by the scatter in the n_e to n_i ratios in Figure 4.20.

4.4.4 Polar-Hydra

The Hydra plasma investigation has been described by *Scudder et al.* [1995]. The following discussion describes the intracalibration work performed to balance the responses of the separate sensors that make up this instrument. Hydra contains 12 cylindrical electrostatic analyzers mounted with anti-collinear fields of view in two separate boxes on opposite faces of the spacecraft. Six analyzers are in each box with their own stepping and detector bias supplies. Each analyzer has two, permanently biased channeltrons of the Sjuts type at its exit aperture, one for electrons and one for ions. The polarity of voltage sweeps on the spectrometer deflection plates are alternately reversed to transmit ions or

electrons through the optics. All analyzers measure one complete energy sweep of electrons followed by a complete energy sweep of ions.

The Hydra calibration required that these analyzers measure a statistically significant, cylindrically symmetric distribution function when in hot plasmas and during periods when convection was not important. Thus the intracalibration involves making the data set statistically consistent with gyrotropy of the particle distribution function. Accordingly, convenient periods of time (1 week's data) were searched for intervals when different spectrometers measured particles of the same energy and pitch angle and when convection signatures were weak. All such matched measurements, regardless of counting rates should fall on a common line through the origin, where the slope determines the relative counting efficiency. By insisting that the different detectors measure the same energy and pitch angle (but in general different gyrophase) different pairs of measurements can be compared. Measurements are considered to have the same pitch angle so long as both elements in any given pair agree within the half-angle of the aperture acceptance, which is 5° . Measurement pairs by the j'th and k'th sensors are consolidated and sorted by energy to allow calculations of relative efficiency variation as a function of energy.

Appropriate attention must be given to the Poisson statistics involved for each counting rate in the pairwise comparisons of detectors. The least squares problem involves finding the appropriate proportionality constant $\mu_{j,k}$ between the k'th and j'th measurements. This determination reduces to finding the minimum chi-square dispersion from the prediction of the product of two Poisson probabilities of the observed rates. This procedure is a non-linear least-squares problem. In short, we desire a set of proportionality constants $\mu_{k,j}$ such that the probabilities $P(C_k)P(\mu_{k,j}C_j)$, $j \neq k$ as a theoretical distribution predicts in a least squares sense the occurrence distribution of the count pairs $(C_k(t_l), C_j(t_l))$, where both measurements are at the same time interval, the same energy, and same pitch angle.

A sample page of the results of such a calibration is shown in Figure 4.23. Each subpanel illustrates the correlation at a particular energy between Analyzer 7 and the reference analyzer numbered 12. All the correlations were acquired during one week's observations. Data from the radiation belt were excluded because of high background. The best fit parameter of the joint probability above determines the slope of the line of proportionality through the origin with slope $\langle\mu_{7,12}\rangle$, where $\mu_{7,12}$ depends on particle energy, E_q. The size of the dots reflects the relative number of individual readings in that location for that panel. The high degree of organization seen in these examples is common across all possible combinations of the 12 sensors. Such a statistical and over-determined approach also affords an estimate for the uncertainties involved. Variations in these slopes were used over the life of the mission to motivate changes in the post acceleration voltages.

The above procedure implemented between all possible analyzer pairs yields $\langle\mu_{k,12}(E_q)\rangle$ so that all analyzers have calibration factors relative to one reference analyzer's measurement efficiency as a function of energy. The next step in the calibration procedure was to adopt a form for the relative efficiency versus energy of the reference analyzer's measurement. For electrons, the energy dependent efficiency given by the manufacturer (Sjuts) was used. Since the Hydra preacceleration of electrons was small (20–40 V), including the low energy variation of the CEM efficiency was crucial for obtaining accurate densities. For ions, the CEM efficiency was assumed to have no energy dependence above the post acceleration energy.

The final step in the calibration was the determination of the absolute quantum efficiency of the entire reference measurement. The absolute calibration requires cross checks

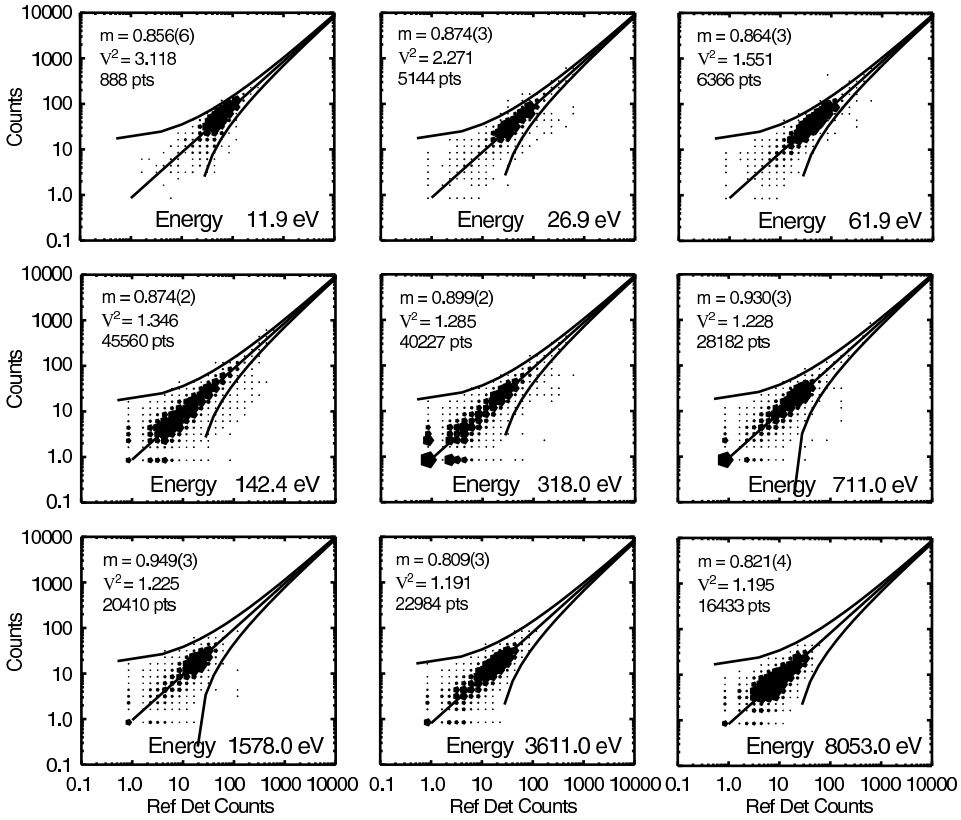

Figure 4.23: Scatter plots of the simultaneous response between Hydra Analyzer 7 and Hydra Reference Analyzer 12 after all intra-analyzer corrections have been made. The 9 panels correspond to 9 different electron energies.

with geophysical occurrences using measurement from other instruments. Examples are the Walén test [*Scudder et al.*, 1999] at Alfvénic structures where the absolute proportionality constant depends on the absolute density. Comparisons with solar wind Faraday cup measurements when Polar is in the solar wind have also been used to corroborate these determinations. Statistical cross checks have been made between electron and ion measurements to verify that the densities are tracking one another. Cross checks are also made with other more absolute measures such as plasma line or spacecraft floating potential predictions. Finally, the spacecraft return current, calculated from electron measurements, were organized against determinations of the floating potential to illustrate that the data are well organized and that the prediction of the photoemission properties of the spacecraft are reasonable. These comparisons have been summarized in *Scudder et al.* [1999].

The Hydra instrument was launched in 1996 and after 11 years is still operational. The degradation in efficiency has been carefully monitored by comparing Hydra predicted densities, after all intracalibrations have been completed, with the predictions of the local plasma density from a floating potential density relation. That relationship was determined early in flight in regions like the magnetosheath where the return currents conditions and

calibration curves were well documented. The degradation in photoemission is much less severe than the channeltron gain degradation, and very satisfactory renormalizations have been made by referencing the overall efficiency of each analyzer to that of the reference analyzer (12). Selecting the absolute detection efficiency usually brings the overall variation of the Hydra-determined plasma density into good agreement with that predicted from the spacecraft potential. For a recent example of this see *Scudder et al.* [2000].

4.4.5 Wind 3D Plasma

The Wind 3D Plasma experiment contained two electron (EESA-L, EESA-H) and two ion (PESA-L, PESA-H) plasma sensors covering the energy range from a few eV to 30 keV, and a set of solid-state detectors that extended the supra-thermal energy range to 400 keV for electrons and ∼11 MeV for ions [*Lin et al.*, 1995]. The -L and -H refers to low and high sensitivity analyzers, with both high sensitivity sensors having anti-coincidence scintillators to reduce background from penetrating radiation. Three of the ESAs used the same basic spherical top-hat design with $\Delta R/R = 0.075$ and inner hemisphere radius of R=3.75 cm. The fourth, EESA-H, had R=8 cm but the same $\Delta R/R = 0.075$ so that all sensors had the same basic energy resolution, analyzer energy constant, and angular resolution perpendicular to the planar FOV. The PESA-L sensor had a pinhole attenuator, which reduced the incident flux by a factor of 50, but maintained the same energy-angle response. Sensors had anode angular resolution that varied from 5.6° near the spin plane, to 11.2° at ∼45° from the spin plane, to 22.5° near the spin axis. Both low sensitivity sensors were half-analyzers with 180° FOVs whose center look direction direction was perpendicular to the spin axis. The high sensitivity sensors had 360° FOVs whose planes were rotated 90° from the low sensitivity FOVs. Electron and ion sensor pairs were mounted on short (0.5 m) booms on opposite sides of the spacecraft to reduce FOV obstructions and particle deflections due to spacecraft charging. All ESA sensors used MCP detectors.

The in-flight calibration effort for the Wind 3D Plasma experiment offered several challenges. The Wind spacecraft spends the majority of its orbit in the solar wind, which generally restricts the type of in-flight calibrations that are possible. The high solar wind flows ($\sim$400 km s^{-1}) result in both an extremely narrow ion beam distribution and anisotropy in the relatively cool (T_e ∼10 eV) electron distribution. Typical ion beam widths are near the analyzer resolution, have high count rates that require dead-time corrections, and have enough alpha content to require an algorithm that does not assume moments are dominated by protons. Although an occasional burst mode provides some 3-D data at the spin period (3s), generally data rate restrictions only allow moments calculated on board to be transmitted at this rate, limiting the ability to make ground based corrections to the data. Electrons are the most difficult to measure quantitatively since the combination of photo-electrons and variable spacecraft potential result in on-board moment calculations that are qualitative at best. 3-D count rate distributions are available at a lower cadence, typically once every 8, 16 or 32 spins. It is the 3-D data that allow the most accurate data corrections using in-flight calibration techniques described below. Generally only those calibrations that were required for science goals were attempted. Below we outline the various calibration efforts for each plasma sensor head.

One of the primary tasks of in-flight calibrations is to maintain an optimal bias voltage to the MCP detectors. The AMPTEK A111 preamplifiers had a fixed charge threshold level and precluded cycling the threshold level to determine the MCP's pulse height dis-

tributions. Instead the MCPs were stepped through a series of bias voltages with ∼50 V increments while the instrument count rate was monitored. The set of voltages started ∼100 V below the current MCP bias voltage and extended to ∼100 V above the current value. The sensor remained in its nominal energy sweep mode and a plateau in the average count rate was used to determine the optimal bias voltage. MCP bias changes were made a few times during the first four years as the MCPs were scrubbed. They have remained at these voltages for the remaining ∼10 years.

PESA-L is a solar wind sensor that uses a set of eight 5.625° anodes near the spin plane to measure the core H^+ and He^{2+} angular distributions. 64 energy sweeps per spin provide 5.625° spin plane resolution, which is about the analyzer intrinsic resolution. A 14 energy step sweep with dynamic range, $E_{\max}/E_{\min}$, of ∼10 is adjusted every spin so E_{min} is about 2/5 of the peak count rate in order to track the solar wind velocity to provide a high-energy-resolution measurement. Tracking is performed with software using computed moments. A core 8×8 solid angles × 14 energies are used for moment calculations each spin period and a 5×5 solid angle × 14 energy snapshot (one spin) distribution is transmitted every eight spins. On-board moment calculations use the relative energy shift between H^+ and He^{2+} to separate the different particle moments. PESA-L complements the Wind SWE Faraday cup measurements (see Section 4.4.9) by providing much higher time resolution measurements of the solar wind core. Since SWE does not include detectors that change with age, and since it was carefully cross-calibrated with measurements of the plasma frequency, f_p, by the WAVES experiment (see Section 4.4.11), PESA-L used the SWE data to perform its in-flight absolute calibration. This allowed cross-calibration of plasma density over long periods, during times when dead-time corrections were negligible, and when f_p was not well measured. In-flight calibration checks of the analyzer energy constant showed a 2 % systematic difference in solar wind flow velocity between SWE and PESA-L. With no way of determining the absolute flow velocity and source of the error, PESA-L data analysis software used the laboratory determined analyzer energy constant. Without an isotropic particle distribution available for in-flight relative sensitivity calibrations, the PESA-L 5.625° anodes were assumed to have the identical response determined by laboratory calibrations. MCP energy efficiency was assumed flat, which is reasonable for a limited energy sweep range (typically 0.4–4.0 keV) and ∼2.3 kV preacceleration.

The primary in-flight calibration effort for PESA-L was the determination of electronic dead time. Due to the high solar wind fluxes, dead-time corrections are critical for quantitative measurements particularly during cold or dense solar wind conditions. The Wind 3D Plasma sensors used AMPTEK A111 preamplifiers that do not have well defined dead times. The A111 dead time depends upon the amplitude of both the initial and trailing charge pulse, with larger initial pulses requiring longer recovery times before a second pulse can be registered. Dead time correction therefore requires a complex average that depends upon the MCP pulse height distribution. Since the MCP pulse height distribution can droop during high count rates as microchannels recover, the dead time is also a function of count rate history. For corrections to 3-D arrays of count rate data, the average dead time was determined from density comparison with SWE and incorporated in the ground calculation programs that converted rate data to physical units. Such corrections are not possible for on-board moment computations, so a method was developed to correct the on-board ion moments for dead time effects. Since the peak ion count rate in an ideal analyzer in response to a drifting Maxwellian is proportional to $N_i v_d^4/v_{th}^3$, this quantity was used as

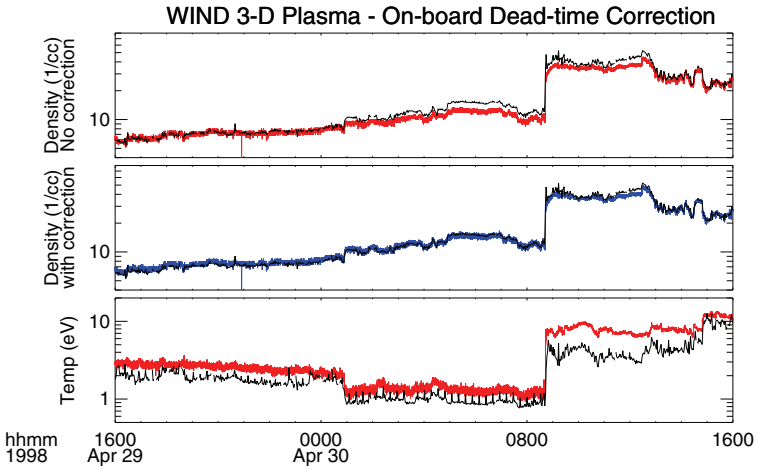

Figure 4.24: The figure demonstrates an effective method for dead-time correcting the on-board calculated density moments from the Wind 3D Plasma PESA-L sensor. The top panel shows uncorrected PESA-L density (red) and SWE determined density (black). The second panel illustrates that the dead-time corrected PESA-L density (blue) and SWE density (black) have good agreement. The bottom panel shows the ion temperature from PESA-L (red) and SWE (black). Since the peak count rate of a drifting Maxwellian is proportional to $N_i v_d^4/v_{th}^3$, this formula was used as a proxy for count rate in a dead-time correction algorithm that operated on the on-board calculated density moments. Note that the dead-time corrections are not the largest where the density is highest, but rather where the temperature is lowest.

a proxy for the rate in the dead time corrections, $N_{i,\mathrm{corr}} = (EFF \cdot N_i)/(1 - DT \cdot N_i v_d^4/v_{th}^3)$, where the ion number density, N_i, the solar wind velocity, v_d, and the ion thermal speed, v_{th}, are the moments calculated on board, and the *EFF* and *DT* are the absolute counting efficiency and dead time, respectively. *EFF* and *DT* are determined from fits between PESA-L and SWE densities. Variations in both *EFF* and *DT* are observed over the mission as MCPs aged or as bias voltages were changed indicating that the dead time was not exclusively a preamplifier dead time effect. Figure 4.24 shows a comparison of the uncorrected and corrected solar wind densities from PESA-L and the SWE density during a period where dead time corrections were important. The third panel shows the uncorrected temperature from 3DP and SWE. Note that dead time corrections can be most important during periods where the ions are cold, and not necessarily where the density is high, due to the $1/v_{th}^3$ in the peak count rate of a drifting Maxwellian.

PESA-H is a high sensitivity ion sensor for measuring the solar wind suprathermal tail and ions reflected at the Earth's bow shock. PESA-H has a 30 energy step sweep covering ~80 eV to ~30 keV, 16 times a spin. 3-D distributions (typically 96 solid angles by 15 energies) averaged over 16 or 32 spins are its primary data product. The PESA-H sensor calibrations were primarily restricted to cross checks of the analyzer energy constant with PESA-L. Since PESA-H saturates in the solar wind, and since PESA-L only makes limited

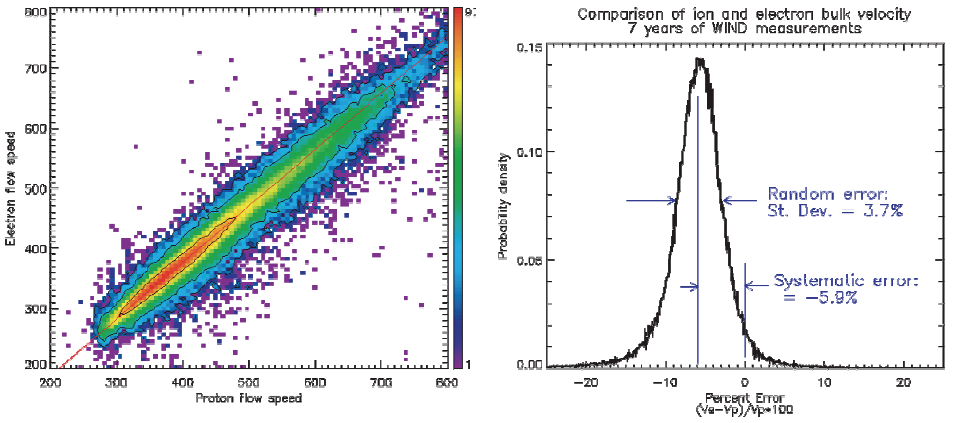

Figure 4.25: Left: a histogram of the Wind 3D Plasma electron velocity versus ion velocity; *Right:* a histogram of electron velocity errors. A ∼6 % systematic error was present that is likely due to errors in analyzer energy constants determined on the ground. Random errors had a standard deviation of only 3.7 %.

measurements in the solar wind direction, no in-flight cross-calibrations of sensitivity were made between them. PESA-H relies on laboratory calibration determinations. It may be possible to find periods during Wind perigee passes in the magnetosphere where PESA-H relative and absolute in-flight calibrations could be made, however no science objectives have driven this requirement. In-flight testing did drive one operational change in PESA-H. As discussed in Section 4.2.9, the sensor experienced high background counts in the equatorial anodes due to problems with "after-emission" caused by the high solar wind flux. To avoid this problem in the measured distribution, the sensor's energy sweep was limited to a 3 keV to 30 keV range when the sensor looked in the solar wind direction. Since the sensor had a 360° FOV, the truncated sweep was required twice a spin. However, this avoidance meant the sensor would not be able to cover the entire energy range when looking Earthward. To retain full energy coverage when looking Earthward, the energy sweep truncation was only applied once a spin and data taken from the sensor half-with after-emission were discarded.

The EESA-L sensor provides the solar wind electron plasma measurement on Wind. Its energy sweep from ∼6 eV to 1.3 keV covers the primary solar wind core and suprathermal tails, as well as photo-electrons under typical conditions. On-board moment calculations provide spin period data, however, since these algorithms do not allow corrections for spacecraft potential, spin period data are qualitative at best. Relative anode sensitivity uses laboratory determined values to account for variations that are not geometrical. These are due primarily to double counting at the anode edges which makes the smaller anodes have a larger effective sensitivity. (Double counting occurs when the MCP charge cloud is split between two anodes, resulting in both preamplifiers registering counts.) The laboratory determined value of the analyzer energy constant was used. Comparison of EESA-L and PESA-L solar wind velocity (Figure 4.25) shows that a small (∼6 %) systematic shift is observed between these two measurements. Possible sources for this difference are errors in the analyzer energy constants, offset errors in the EESA sweep, particle deflections

associated with spacecraft charging, or a systematic error introduced by the fitting routine described below. Neglecting this systematic error, the figure demonstrates that anisotropy in the measured electron distribution caused by the bulk flow is adequate to allow accurate velocity measurements even though the drift velocity of the solar wind is a small fraction of the electron thermal velocity. The MCP efficiency is assumed to be independent of electron energy, which is a reasonable approximation for a ~0.4 kV pre-acceleration and electron energies of 0.4–1.7 keV at the front of the MCP. The absolute MCP efficiency was determined via cross-calibration with PESA-L and required a complex ground-based calculation algorithm to correct for spacecraft potential and eliminate photo-electrons.

The primary EESA-L in-flight calibration effort involved determining the spacecraft potential and any temperature-produced offsets in the HV sweep. A sweep mode was operated several times that allowed the inner hemisphere voltage to be driven negative. A dropout in the photo-electron flux signaled the value where inner hemisphere voltage crossed through zero, and therefore determined the sweep HV offset. Since the Wind spacecraft rarely experiences eclipse, its temperature is stable and the HV offset was assumed constant. Spacecraft potential determination on Wind was difficult given no direct measurement from DC electric field probes. Since the electron density and temperature both impact the spacecraft potential, a fitting algorithm was developed that assumed the measured electrons could be fit to a combination of a drifting bi-Maxwellian core and suprathermal tail, plus a fixed photo-electron spectrum. For primarily radial electron trajectories, the spacecraft potential marks the boundary between photo-electrons generated from the spacecraft and the ambient plasma electrons. The photo-electron spectra were determined from measurements in the low density magnetotail lobe regions that extended out to ~60 eV. The fitting assumes the actual finite energy width of measurement bins as determined from folding the analyzer response with the change in sweep energy during a counter accumulation. Using the actual energy response was critical since the energy resolution was relatively coarse across the boundary between photo-electrons and plasma electrons. The fitting algorithm is primarily a minimization of the difference between the measured counts and functional fit with several parameters: spacecraft potential, N_e, v_d, $T_{e\parallel}$, $T_{e\perp}$, and optionally a suprathermal drifting Kappa or bi-Maxwellian. The fit is limited to energies below $\sim 3T_e$ and does not rely on any other sensor measurements. Excellent agreement between calculated electron and ion densities and flow velocities have provided confidence in the technique. Figure 4.26a shows an example spectra (+ symbols) along with results of the fitting algorithm (solid curves). The algorithm does not include terms to fit the solar wind strahl, and therefore has poor agreement at higher energies along the magnetic field (purple). In principle, additional parameters could be included to fit the strahl, but they are not required for accurate determination of the spacecraft potential and core moments. Figure 4.26b shows a time series comparison between the fitted electron moments and ion moments indicating an accurate determination of spacecraft potential using this technique. Without an accurate spacecraft potential, electron moments would be qualitative at best.

EESA-H is used to provide a higher sensitivity monitor of the solar wind electrons' suprathermal tail. Because of saturation problems at low energies, the EESA-H energy sweep extended from ~100 eV to 30 keV. Its primary data product is a 3-D count array (88 solid angles × 30 energies). Ground calibration determined values of relative sensitivity and analyzer energy constant were used. The absolute sensitivity was determined by intercomparison with EESA-L over their common energy range. To reduce background noise

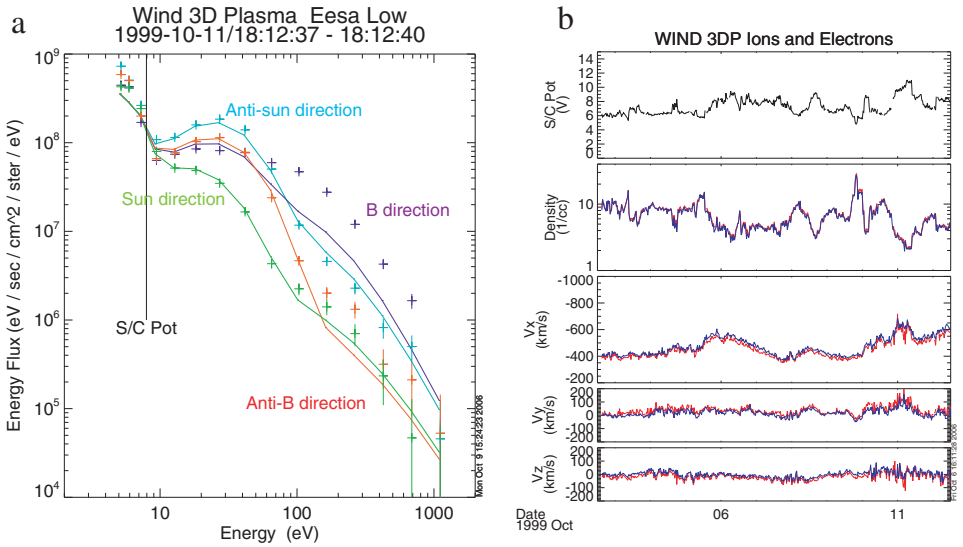

Figure 4.26: (a) The figure shows sample electron spectra (+ symbols) at four pitch angles along with the results of a fitting algorithm (solid curves) that determined the spacecraft potential from the break in the spectra between photo-electrons and plasma electrons. For details of the algorithm, see the text. The algorithm does not contain terms for solar wind strahl and therefore does not fit the field aligned suprathermal tail. (b) Figure is a time series comparison between the fitted electron moments (blue) and ion moments (red) indicating an accurate determination of spacecraft potential using this technique. The top panel shows the spacecraft potential determined from the fitting algorithm.

problems, several of the anodes were not used in 3-D array accumulations due to noise from the edges of the MCPs. The primary in-flight calibration came from observations that the high energy EESA-H spectra did not align with the electron spectra determined from the solid-state detectors (SSDs). This was due to the assumption that the MCP counting efficiency was independent of electron energy. Since a determination of the actual energy dependent efficiency was not possible, an efficiency dependence was developed based on the published equations in *Goruganthu and Wilson* [1984]. Figure 4.27 shows the energy dependent efficiency curve used which assumed the 0.4 kV pre-acceleration. The estimated efficiency at 30 keV is about 45 % of the maximum at low energy resulting in a significant spectral shift. This correction reduced the spectral mismatch between EESA-H and the SSDs to about the measurement error as shown in Figure 4.28.

4.4.6 Cluster CIS

In this section, various in-flight calibration techniques for the CIS/CODIF mass spectrometer instrument on Cluster are described. CODIF consists of a toroidal top-hat electrostatic analyzer combined with a carbon-foil time-of-flight velocity analyzer (Section 2.6.4). Ions and carbon foil electrons are detected with microchannel plates.

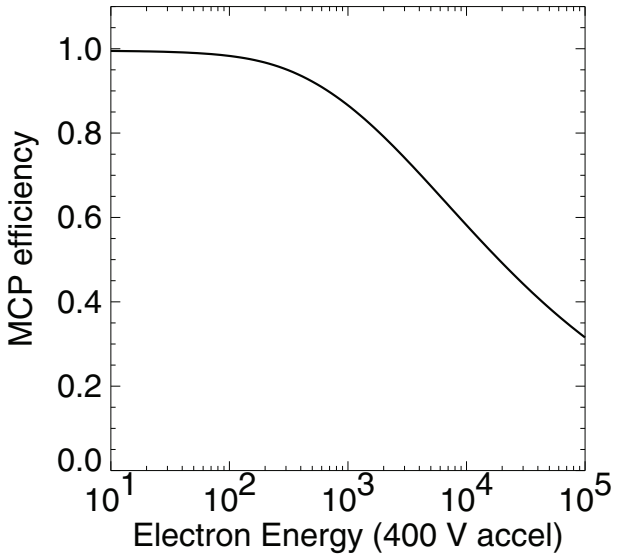

Figure 4.27: MCP energy dependent efficiency used to correct the Wind 3D Plasma electron measurements. The curve is based on published results by *Goruganthu and Wilson* [1984].

4.4.6.1 Absolute Efficiencies

The raw counters used for these measurements count any ion that enters the instrument. There is no a priori way to know the ion species. Thus the only way to determine the efficiencies for different ion species in-flight is to use time periods when a particular ion species dominates. Since the dominant ion in the magnetosphere is H^+, it is relatively easy to find time periods to use to determine the efficiencies for H^+. Over the polar cap there are time periods when the dominant population is a beam of O^+ ions. These time periods can be used to determine the O^+ efficiencies. Similarly, there are times during magnetic storms when O^+ dominates in some energy ranges.

As described in Section 4.3.2, the count rates of individual signals and coincidence signals are used to give an absolute measurement of the efficiencies of each signal. The individual count rates and coincidence rates are determined for time periods when one ion species dominates and the distribution is relatively isotropic, so that the efficiency is representative of all positions in the instrument.

Figure 4.29 shows the change in the start and stop efficiencies for H^+ on spacecraft 1 (SC1). The circles are for ions at 1 keV, and the squares for ions at 11 keV. The overall change is about the same, independent of energy. Clearly, the start efficiency degraded significantly more than the stop efficiency. On the figure the vertical lines connected by the solid bars mark the time periods when the spacecraft is routinely entering the magnetosheath. The most significant degradation occurred during these times. The increases that are observed after these time periods are due to increases in the MCP voltage. The intense magnetosheath flux contributed significantly to the MCP degradation over time.

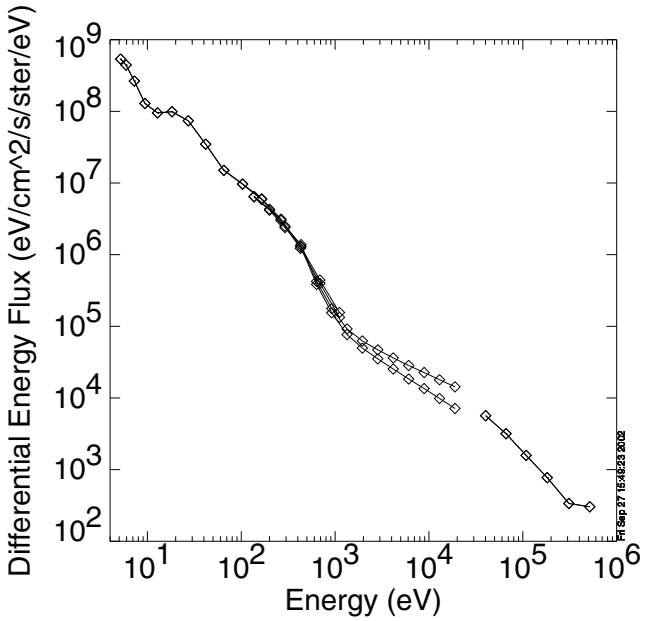

Figure 4.28: Wind 3D Plasma electron spectra determined by the EESA-L (6 eV to 1.3 keV), EESA-H (0.2 to 20 keV) and SSD (>40 keV) sensors. The two curves between 1 and 20 keV represent electron spectra assuming no MCP energy dependent efficiency (lower) and the energy dependent efficiency in Figure 4.27 (upper). Although at a given time spectral features could be present that would result in a break in the slope, it was found that the spectra were more continuous across this measurement boundary for the assumed efficiency in Figure 4.27.

To determine the efficiency changes for O^+, we identified time periods when O^+ dominated. These were mainly periods when the spacecraft was over the polar cap and observed O^+ beams. The ions normally are observed in one energy step and one position on the MCP. Thus the rate data for that time period is used to give the O^+ efficiency for that energy and position. Then, using the relative efficiencies (as described in the next section), we can determine the O^+ efficiency for all the positions.

4.4.6.2 Relative Efficiencies

To determine the relative efficiencies of individual detector positions within an instrument, we identified time periods when the ion pitch angle distribution was expected to be gyrotropic (see Section 4.4.2.4). Since this was done using data that had been classified by composition, it was performed independently for each ion species, even when that species was not dominant. The only requirement was to have sufficient count rate for the particular ion species to get a statistically valid pitch angle distribution.

For Cluster we chose time periods in the inner magnetosphere, as close to perigee (4 R_E) as possible while avoiding regions where radiation belt contamination was a problem. For each identified time period, we calculated a fit to the pitch angle distribution for one

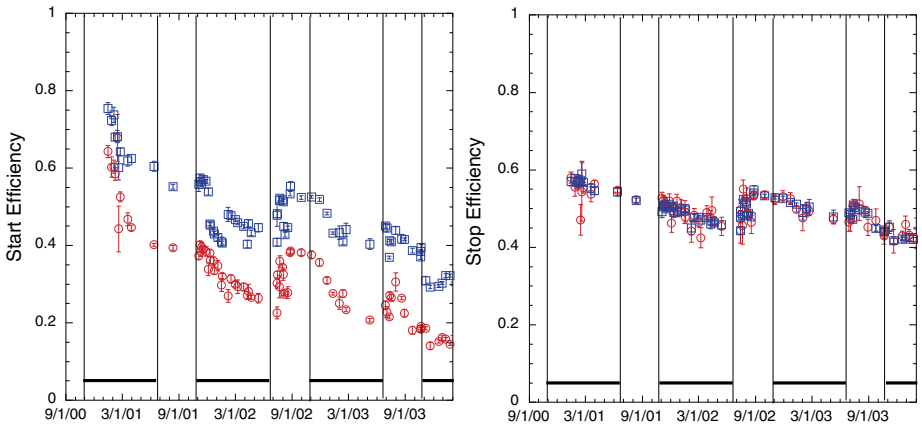

Figure 4.29: The CODIF event start and event stop identification efficiencies on Cluster spacecraft 1 as a function of time. Circles (red) are for protons at 1 keV and squares (blue) for protons at 11 keV. Most of the degradation occurred in the magnetosheath whose crossings are indicated by the bars on the bottom. Increases in efficiency are due to changes in MCP bias voltage.

detection position in the analyzer, which has good statistics and covered a range of pitch angles. The distribution was fit to the function: $f = A \sin^n \Theta$, where Θ is the pitch angle. Then, the same fit function was used to normalize the other detection positions, so that each position had the same value at 90° pitch angle as the original position. The resulting normalized distributions are visually inspected to assure that all positions now agree over the full pitch angle range. This method is similar to that used for the HIA anode calibrations and, like that method, works well when there is good overlap between the pitch angles measured at different detection positions in the analyzer.

Figure 4.30 shows this technique applied to O^+ for a time period in February 2003, when the relative efficiencies for S/C 4 had degraded at different rates. As the figure shows, there is good agreement between the different detection positions after the normalization.

4.4.6.3 Pressure Balance

Checking for pressure balance allows a final verification on the efficiencies and geometric factor. This was performed using observations in the magnetotail (when the spacecraft moves frequently from the magnetic field dominated lobe to the plasma dominated plasmasheet), in the cusp, and at the magnetopause. Checking pressure balance from year to year and during different phases of the mission validated the efficiency changes with time that we found from the other methods and identified an overall factor by which the flux needed be adjusted.

Figure 4.31 shows an example of a pressure balance check during a plasmasheet pass in July, 2001. In all cases, the increases and decreases in the plasma pressure were offset by decreases and increases in the magnetic pressure, so that the total pressure profile was relatively smooth throughout the time period, confirming the calibration of the CODIF

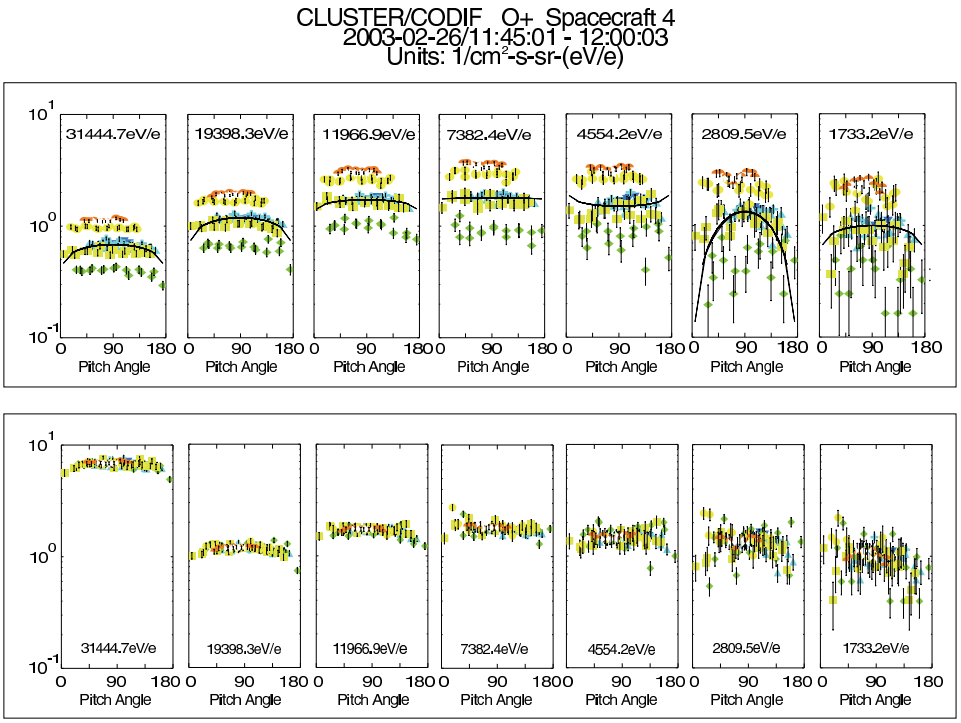

Figure 4.30: Relative efficiency determination for CODIF on Cluster 4. The panels in the top half show the pitch angle distribution for a range of energies before the new normalization factors were determined. The different colors and symbols indicate different anodes within the instrument. Also shown, with the black line, is the fit which was used for the normalization. The panels in the bottom half show the pitch angle distribution after the normalization for the same time period.

instrument. In addition, the total pressures measured on three spacecraft were compared and found to be in good agreement.

4.4.6.4 Three-Spacecraft Check of Calibrations

To test the inter-calibration of the three Cluster spacecraft, we calculated and compared average ion moments from the 3-D distributions for time periods in the magnetotail. Figure 4.32 shows the comparison of daily averages of the proton density and velocity in the plasmasheet for the 2001 tail season. SC3 had one MCP on the high sensitivity side (4 out of 8 positions) with very low efficiencies, a factor of ∼100 less than the other 4 positions. As a result, the calibration for SC3, particularly for the velocity in the z direction, was difficult, and there were larger differences between the velocities measured on SC3 and the other spacecraft. The average densities agreed on the three spacecraft within 4 %. The mean velocity values in the x direction were 23.8, 31.4, and 27.8 km s^{-1}, for SC1, SC3, and SC4, respectively. The standard deviations of the differences in the daily values from SC1 were 21.5 km s^{-1} for SC3 and 8 km s^{-1} for SC4. The mean velocity values in y

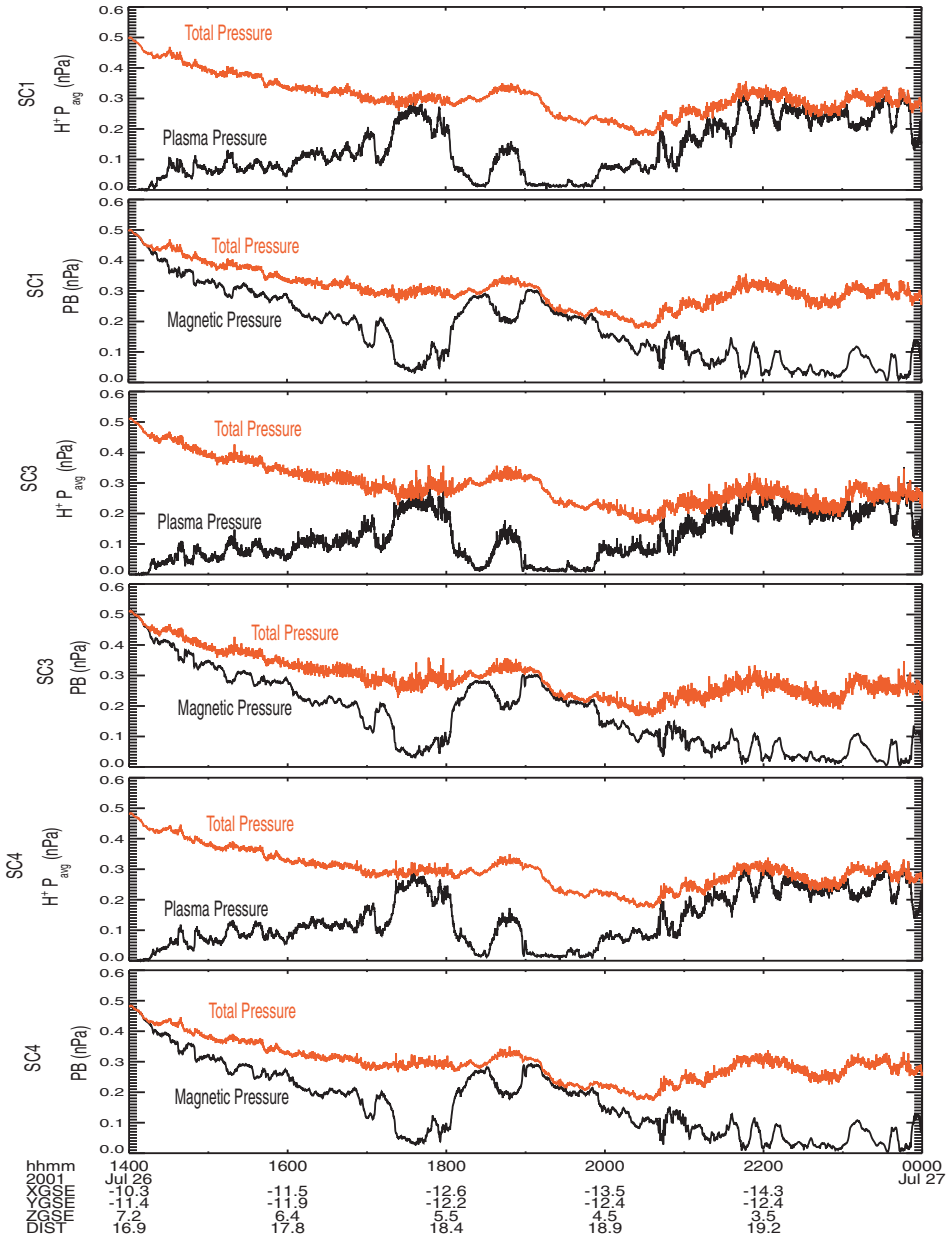

Figure 4.31: Pressure balance check for CODIF on Cluster 1, 3, and 4. The top panel shows (in red) the total pressure (magnetic plus plasma) and the plasma pressure (black), the second panel the total pressure (red) and the magnetic field pressure (black), both for spacecraft 1. The third and fourth panels show the same parameters for spacecraft 3, and the fifth and sixth show the same parameters for spacecraft 4.

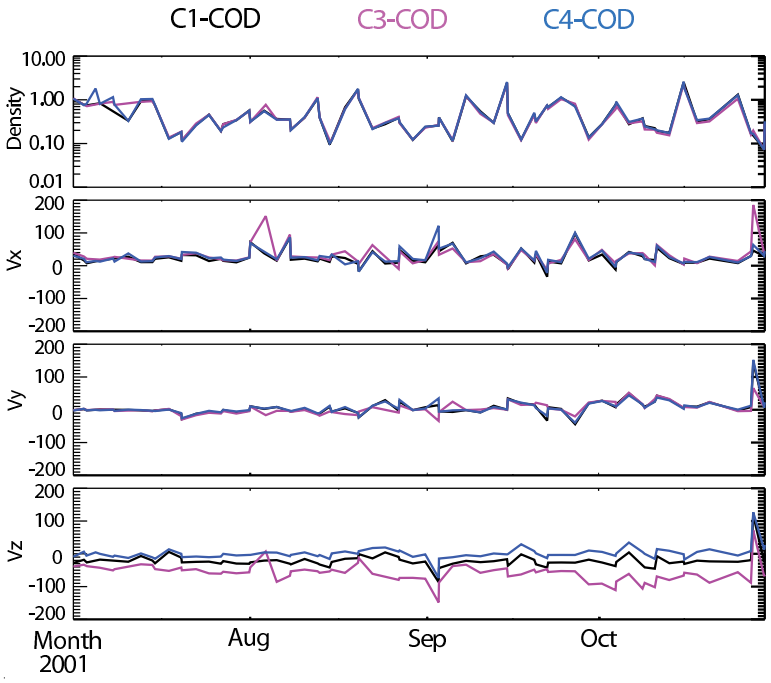

Figure 4.32: Comparison of daily averages of the proton density and velocity from CODIF on Cluster 1, 3, and 4 in the plasmasheet for the 2001 tail season.

were 6.2, 3.7 and 6.7 km s^{-1}, with the standard deviation of the differences in the daily values of 14.5 km s^{-1} and 4 km s^{-1} for SC3 and SC4. The velocity in the z direction is the most difficult parameter, because it relies on having a very good calculation of the relative efficiencies of the different positions. It had the biggest offset between the three spacecraft, with average mean values of -21.7, -58.2, and 1.0 km s^{-1} for the three spacecraft. The standard deviation of the differences in the daily values (km s^{-1}) from SC1 was 20.5 for SC3 and 8.0 for SC4.

4.4.7 NOAA-POES

The Total Energy Detector system in the Space Environment Monitor on board the 3-axis stabilized NOAA POES operational satellites is designed to monitor the energy flux carried into the atmosphere by electrons and ions below 20 keV energy. The instrument set contains ESA plasma detectors of conventional design that view at 0° and 30° to the spacecraft vertical. There are locations along the orbit of these satellites where these two view directions are at the same angle with respect to the local magnetic field vector and permit an inter-comparison to be made between the instrument responses (providing the local particle fluxes are sufficiently large). The top panel in Figure 4.33 summarizes the results of numerous such comparisons between sensors on the NOAA-15 spacecraft. The integrated energy fluxes (both electrons and protons) over the energy range 1000–20000 eV agree to within 10 % between the sensor systems. The comparisons of electron energy

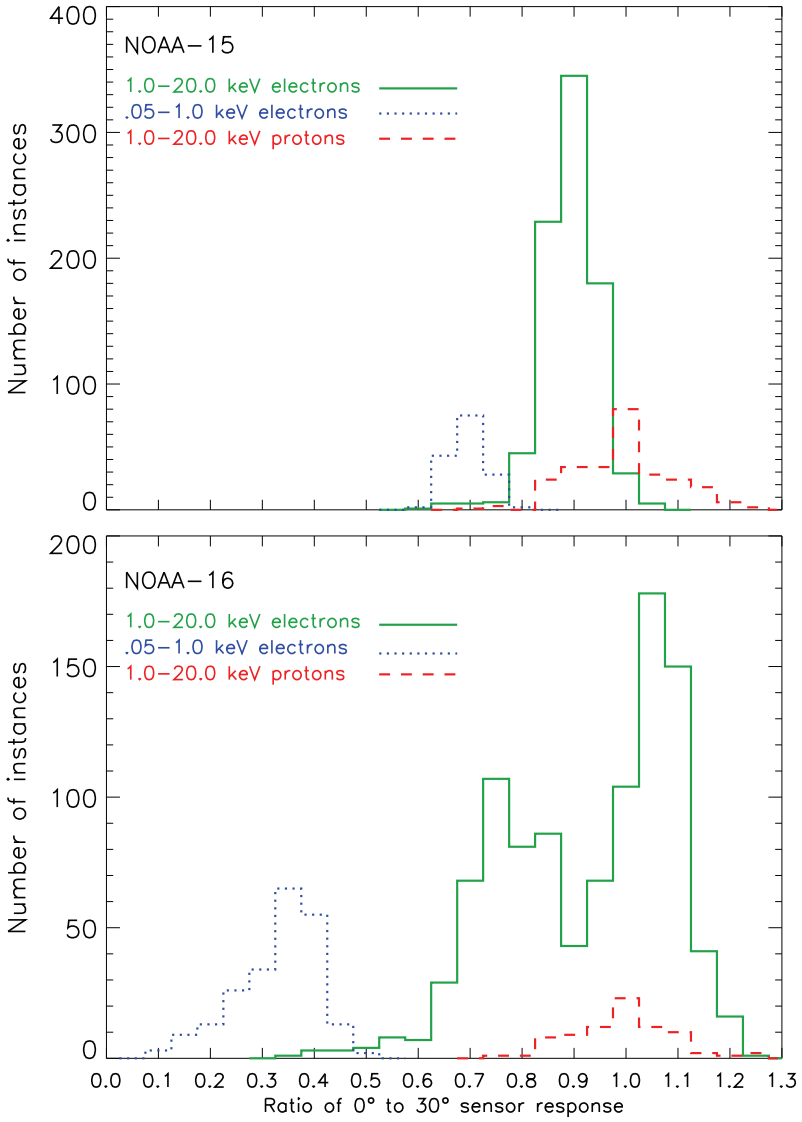

Figure 4.33: The distribution in the ratio of integrated particle energy flux as measured by the 0° and 30° TED detectors when both view particles at the same pitch angle. The data in the top panel (a) are for NOAA-15 while the bottom panel (b) are for NOAA-16. If the relative calibration of the detector systems were well known, the ratio should always be close to 1.0. Any departure of the mean ratio from 1.0 is a measure of the uncertainty in absolute calibration while a distribution of ratios around a mean value may reflect variations in Channeltron gain with time. The very low value of 0.35 for the NOAA-16, 0.5–1.0 keV electron sensor comparison is almost certainly because of inadequate Channeltron gain on the part of the 0° detector.

fluxes integrated between 50–1000 eV agree less well between the 0° and 30° instruments (proton energy fluxes integrated over the low-energy range were too small to permit a comparison.) The lower panel in Figure 4.33 is a similar comparison between TED instruments on NOAA-16. Here the comparisons between the two sets of electron sensor systems is poorer, especially in the case of the two low-energy electron sensors where the zenith viewing instrument typically reports an integrated energy flux of less than 50 % of the off-zenith instrument in spite of observing identical electron populations. The exact reason for the disagreement is not known although the likely cause is too low a CEM bias voltage for the zenith-viewing instrument resulting in inadequate gain.

The fact that several NOAA POES satellites are in operation simultaneously provides the opportunity to obtain relative inter-calibrations between TED instruments on different spacecraft. The orbits of the NOAA polar orbiting satellites intersect at high latitudes and seemingly would provide many opportunities. However, it is rare that the intersection occurs both at the same time and in a region where auroral particle fluxes are large enough that a comparison between instruments on the two satellites is possible. Nevertheless, such occasions do occur and present the opportunity to perform direct comparisons between TED instruments. Figure 4.34 shows one such case where the NOAA-15 and NOAA-16 satellites intersected at nearly the same location (in invariant magnetic latitude and magnetic local time) within a few tens of km and within a few tens of seconds. In this case there was satisfactory agreement between the energy flux observations made on one satellite and those on the other.

However, because auroral phenomena are very dynamic in time and structured in space, comparisons of this sort are of marginal value in verifying the performance of one TED instrument against another. Cases of good agreement can be found but, equally often, are cases of poorer agreement. Those cases of poor agreement can easily be accounted for by the highly structured, in space and time, auroral particle precipitation together with the 2.0-second cadence of the TED energy flux measurements that translates to about 10 km motion across the magnetic field (referenced to 120 km.) The validity of such comparisons is further compromised because the satellite orbits at the intersection point are oblique to one another and do not perform identical transits through the auroral energy flux region.

In the case of the TED instrument, inter-satellite comparisons are also done using the estimated hemispheric power inputs that are calculated for each satellite's complete transit across the polar regions [*Fuller-Rowell and Evans*, 1987]. The history of such power estimates is available on the Internet (URL address `http://www.sec.noaa.gov/ftpdir/list/hpi/`.) The estimates of hemispheric power input rely on the TED energy flux measurements obtained during the transit through the polar region together with a set of global statistical patterns of auroral particle energy fluxes. The hemispheric power estimates are compromised during dynamic times when the actual global pattern of auroral energy input may depart significantly from any statistical pattern. However, the estimates have been shown to be, on the average, a reasonable indicator of the level of polar auroral activity.

The inter-satellite comparisons of hemispheric power use daily averages of the individual estimates obtained from each satellite's pass over the polar regions (about 30 estimates per satellite per day) rather than comparing individual estimates. Moreover, by combining daily averages over a period of months the influences introduced by the time varying and spatially structured aurora might be averaged out and a lowest order estimate of the overall sensitivity of one TED instrument compared to another is obtained. When this procedure

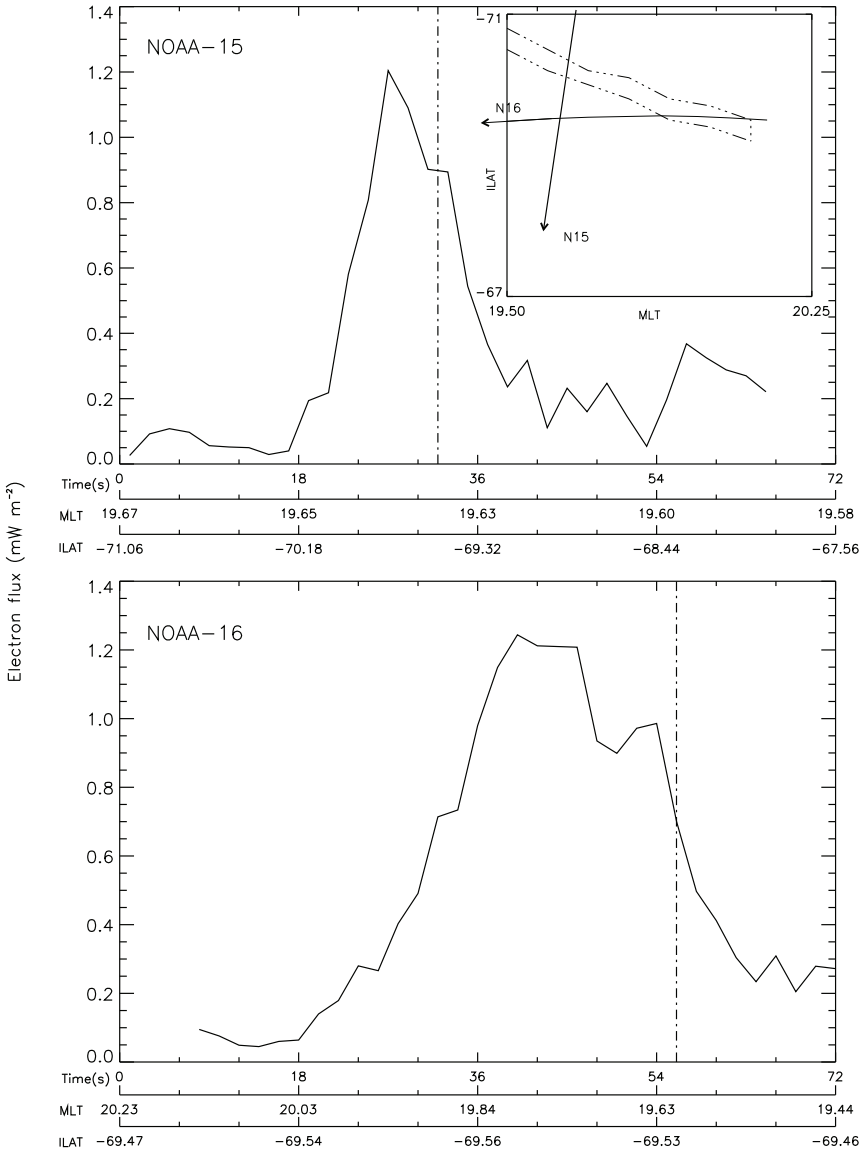

Figure 4.34: The integrated (50–20000 eV) electron energy fluxes observed by the NOAA-15 and NOAA-16 TED instruments plotted against time and location in magnetic coordinates for an inter-satellite conjunction near an auroral arc. The insert displays the tracks of the two satellites (solid lines) and the suspected orientation of the auroral precipitation feature. The two vertical dashed lines in each main panel mark the point in space where the two satellites intersected about 22 s apart in time. The agreement between the two TED sensor responses to this common auroral feature appears to be satisfactory.

was applied to TED observations from NOAA-15, NOAA-16, and NOAA-17, the results showed the overall NOAA-16 TED sensitivity to be 1.38 times that of NOAA-15 and the overall NOAA-17 TED sensitivity to be 1.04 that of NOAA-15. These values are in addition to the laboratory calibrated TED instrument sensitivities but are consistent with the variability in instrument sensitivities and rough estimates of the absolute uncertainties in instrument calibration.

Modest attempts have been made to obtain an in-flight absolute sensitivity calibration for the TED sensor systems. This is fraught with difficulty because there are no independent and accurate measurements of auroral particle energy fluxes that would represent a standard for comparison.

Comparisons between TED energy flux observations and ground-based observations of auroral forms have been made in the course of scientific studies. However, these comparisons yielded little more than confirmation that TED observations replicated the location and spatial extent of the aurora observed from the ground. It was not possible to make the quantitative comparison between auroral brightness and the energy fluxes observed from the satellite that might have constituted an independent verification of the TED energy flux calibrations.

Incoherent scatter radar measurements of ionospheric electron density profiles in the aurora can, in principle, be converted to altitude dependent ion production rates and thence to the parent auroral particle energy spectrum and integrated energy fluxes. Those results can be compared to the energy flux measurements made by the TED instrument during overflights of the radar facility. One such comparison [*Basu et al.*, 1987] between observations from Chatanika and observations made by an earlier TED instrument on the NOAA-6 satellite showed reasonable agreement. However, given uncertainties both in treating the radar data and in the TED observations, this comparison did not constitute an absolute verification of the TED calibration.

Finally, comparisons have been made between TED observations of auroral electron and proton energy flux into the atmosphere and observations from the IMAGE satellite of the resulting ultraviolet and far ultraviolet emissions from the atmosphere [*Hubert et al.*, 2002]. The TED auroral particle observations were used as input to model the intensity of emissions from the atmosphere and the modeled intensities compared to the IMAGE observations. The modeled emissions were in good agreement with those observed indicating that the TED energy flux observations were valid to within a factor of two. It should be pointed out, however, that this study was as much directed toward verifying the IMAGE calibrations as the TED calibration and was not a verification of either calibration against an absolute standard.

In summary, analysis of post-launch data from the TED instrument can verify that the analyzer systems are responding in the expected manner to auroral particle energy fluxes and not responding to spurious effects. Comparisons between sensor systems viewing different directions can be performed, and differences in sensor responses identified and corrected. Inter-satellite comparisons of TED observations are difficult to make on a case-by-case basis, but simultaneous data taken over long periods can be used to obtain comparisons between sensitivities of different instruments that are valid on a statistical basis. Currently, it is not possible to obtain an independent verification of the absolute sensitivity calibrations of the TED sensor systems because there is no absolute standard available for comparison.

4.4.8 FAST

In-flight calibrations of plasma detectors on low altitude satellites often pose a problem because the dominant plasma components are cold and therefore poorly resolved. For electrons, this problem is exacerbated by spacecraft photo-electrons and secondary electrons which appear at 90° pitch angles because of deflection by the strong geomagnetic field. Intense auroral electron fluxes also produce low-energy secondary electrons within the analyzers. If the satellite altitude is high enough to pass into the auroral acceleration region (generally >3000 km), comparisons can be made between plasma densities estimated from separate ion, electron and wave observations. This is possible because the auroral acceleration region accelerates the cold ionospheric ions to create beams that are easily resolved, and excludes cold ionospheric electrons leaving only the energized precipitating and trapped populations, with the admixture of spacecraft-produced photo and secondary electrons.

McFadden et al. [1999] made comparisons between ion and electron densities in the auroral acceleration region on 11 passes of the FAST satellite. FAST contains top-hat electrostatic analyzers that are oriented to continuously measure the 2-D pitch angle distributions. Particles are detected with microchannel plates. After an initial correction for relative efficiencies between ion and electron sensors determined on a single orbit, they were able to obtain N_e/N_i density ratios of $\sim 1.0 \pm 0.2$ for ten additional orbits. The calculations included corrections for composition and only included hot (>100 eV) electrons. Figure 4.35 shows an example of this density comparison. The measurements allowed them to conclude that a significant (>20 %) cold electron population was not present. The primary source of error in this analysis stems from a combination of 2-D measurements and large $\boldsymbol{E} \times \boldsymbol{B}$ drifts within electrostatic shocks. These drifts were large enough to shift the field-aligned ion beams off the magnetic field direction resulting in errors in the calculated ion beam density. A 3-D measurement could have avoided drift problems in ion density calculations, however, auroral ion beams often change faster than the spacecraft spin period so 3-D measurements would likely have been plagued by time aliasing.

In-flight cross-calibrations between wave inferred plasma density and measured plasma density can also be attempted in the auroral acceleration region. *Strangeway et al.* [1998] used fits of the parallel to perpendicular electric field ratio, $E_\parallel/E_\perp$, to determine the resonance cone angle of the Langmuir/whistler dispersion, assuming a cold fluid dispersion with a thermal correction. Density estimates using this wave technique were estimated to be not much better than a factor of 2. This is less accurate than preflight calculations of the plasma instrument sensitivity and therefore not adequate for calibration purposes but perhaps adequate for determining significant sensitivity losses due to degradation. Higher altitude satellites may be able to employ this or other wave techniques with more accuracy depending on the wave environment. However any plasma instruments observing particle fluxes on magnetic field lines that connect to the Earth are likely to encounter significant cold plasma that must be carefully accounted for.

Another cross-calibration test that can be performed on auroral data is a comparison between the inferred current from magnetic field deflections, and direct current measurements from auroral electron fluxes. Integral comparisons are found in *Carlson et al.* [1998, Figure 2] and *McFadden et al.* [1998a, Figure 1] and *McFadden et al.* [1998b, Figure 1]. Such comparisons are sensitive to many factors; for example, the orientation of the arc, the presence of electrons below the spectral peak, the low-energy electron cutoff of the sen-

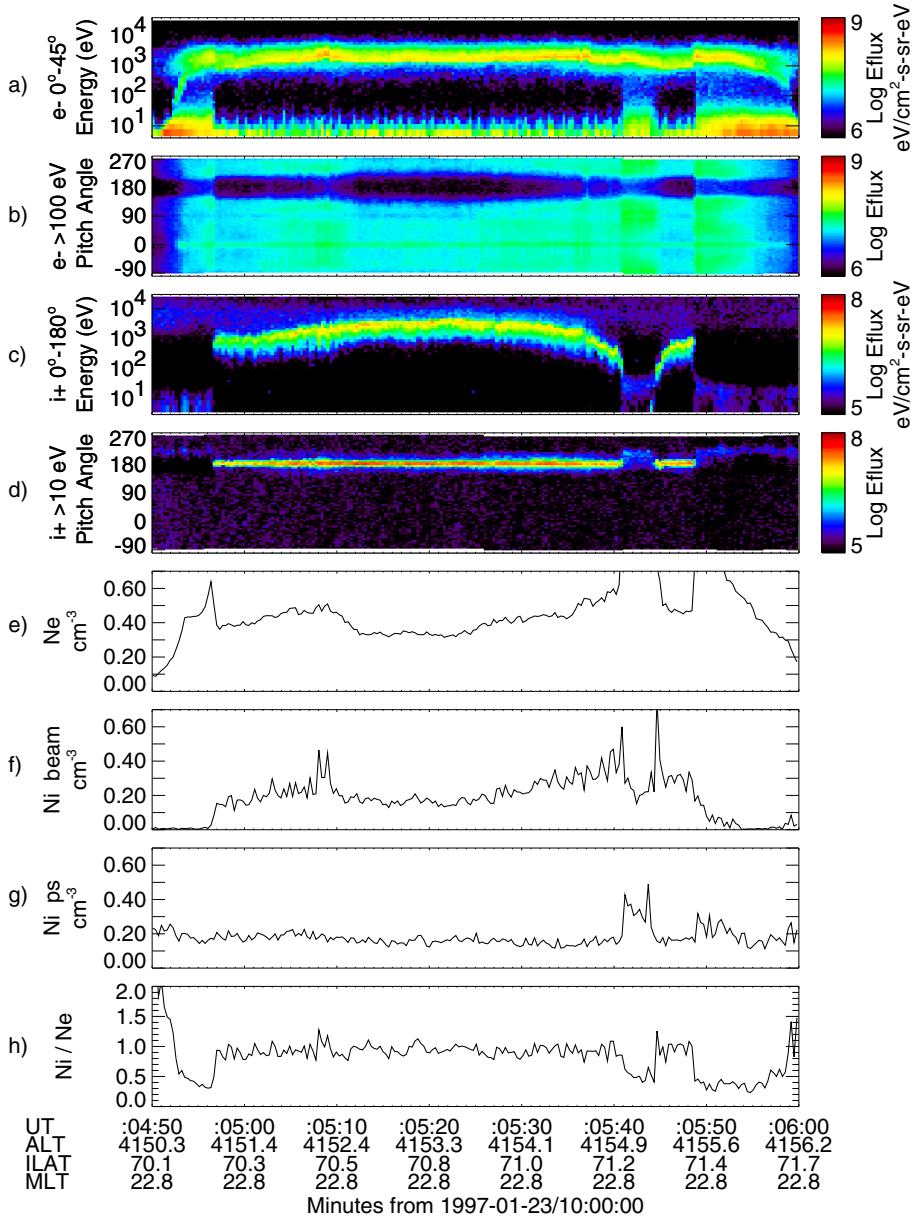

Figure 4.35: FAST ion and electron density comparison. Panels from top to bottom show: (a-d) energy and pitch angle spectrograms for electrons and ions; (e-g) density of electrons, beam ions, plasmasheet ions; (h) ion-electron density ratio. This last panel illustrates that the electron and ion densities agree to within ∼20 % inside the auroral acceleration region where no cold plasma is present. These comparisons provide a test of the relative calibrations between ion and electron sensors. From *McFadden et al.* [1999].

sor, and asymmetries in the spacecraft photo-electrons into the sensor. Since auroral arc orientation can vary dramatically during active periods, these comparisons are best made during quieter periods, when the spacecraft crosses normal to the oval, and within broad arc structures. The particle measurements in the upward current region can generally be improved by introducing a cutoff energy slightly below the spectral peak. This is because field-aligned electron fluxes below the spectral peak generally do not participate in the overall current. These electrons result from upwelling ionospheric electrons that are subsequently trapped and accelerated downward by EMIC waves [*McFadden et al.*, 1998b, and references therein], with no contribution to the net current. If electrons below the spectral peak are included in the accounting, the upgoing ionospheric electrons are often missed due to their low-energy while the energized downgoing ionospheric electrons are counted leading to an overestimate of the upward current. Introduction of this energy cutoff also avoids problems associated with asymmetries in the photoelectron and secondary electron populations measured by the spacecraft.

Good plasma sensor calibrations are also important for comparisons between precipitating electron and/or proton fluxes and the light detected by auroral imagers. Several studies estimated the mean energy and flux of precipitating auroral particles from space using Polar-UVI and IMAGE-FUV [*Lummerzheim et al.*, 1997; *Chua et al.*, 2001; *Frey et al.*, 2001; *Gérard et al.*, 2001]. The comparison with simultaneous plasma measurements showed agreement within 20–50 %. This agreement is reasonably good given the many simplifications and assumptions of quantitative estimates from UV images. All optical inversion methods depend on models of the atmospheric composition, assumptions about the pitch angle distributions, energy spectra, and temporal stability of the precipitation. Furthermore, plasma measurements are always very localized investigations while the size of an image pixel can easily reach 100×100 km^2. As in the case of wave comparisons, comparisons between imager estimates and measured precipitating flux suggest that remote sensing is not adequate for plasma sensor calibrations but may be adequate for detecting significant plasma sensor degradation. Since stars easily can be used to provide continuous in-flight monitoring of imager sensitivity [*Frey et al.*, 2003], any significant deviation between inversion results from an imager and a plasma sensor would then point to changes in the plasma sensor sensitivity.

Techniques, similar to the IMAGE-FAST comparisons described above, were utilized by the UARS satellite but with the advantage that the remote sensing and local observations involved in the comparison were on the same satellite. The Particle Environment Monitor instrument suite on the UARS satellite included an electron spectrometer and an X-ray imager designed to observe bremsstrahlung X-rays produced from the atmosphere by precipitating auroral electrons [*Sharber et al.*, 1996]. The combination of these two instruments provided the opportunity to cross check one instrument's performance against the other. The energy spectrum of auroral electrons incident on the atmosphere could be constructed from the measurement of the X-ray energy spectrum. The imaging capability of the X-ray imager permitted the close connection between the *in situ* observations of precipitating auroral electrons and the location where the resultant X-ray production occurred, thus allowing a comparison to be made between the directly measured and reconstructed electron spectra. While this procedure did not provide for the absolute in-flight calibration of either of the two instruments, the general good agreement between measured and inferred energy spectra did provide confidence in the quality of both the particle and X-ray observations.

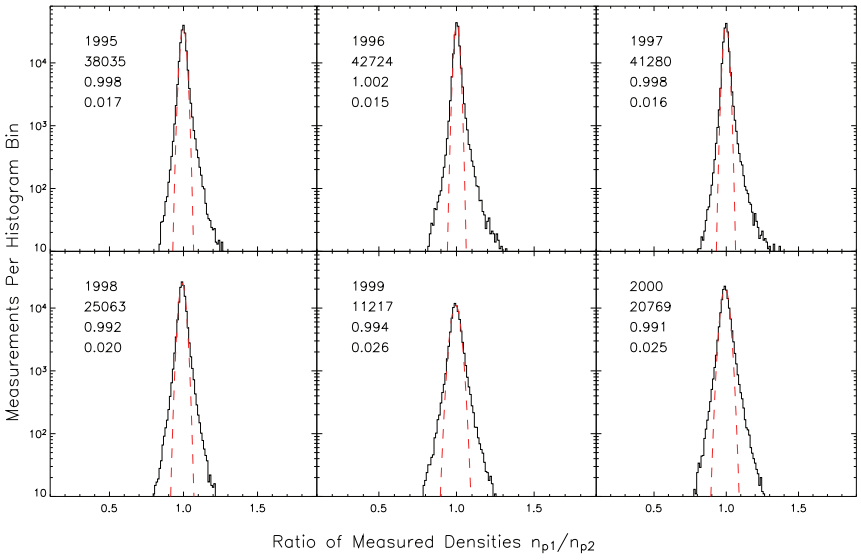

Figure 4.36: Histograms of the ratios of the proton number densities determined independently by the two Faraday cup instruments on the Wind spacecraft over a six-year period from 1995–2000. Each of the six panels is the data for one year. The dashed red lines are the best-fit Gaussian distributions to each year of data. The column of numbers in each panel are: the year, the number of measurements in the histogram, the center of the Gaussian, and the standard deviation.

4.4.9 Wind Faraday Cups

The long-term stability of the electronic portion of the Faraday cups (FC) on the Wind satellites has been described earlier. There are two independent FC instruments on the Wind spacecraft, so a comparison of the solar wind ion parameters deduced separately by the two instruments is a possible way to detect an end-to-end variation in the relative calibration of either instrument over the course of the mission. Figure 4.36 shows histograms of the ratio of the proton number densities determined through a moment analysis of the observations by each FC. The red curves are a best fit of a Gaussian distribution to the histograms. Each panel has the year, the number of spectra that went into the histogram, the center of the best-fit Gaussian, and the width of the distribution. On average, the two instruments agree to one part in a thousand, with only very minor variations of the center of the distribution around a ratio of 1.0, or in the width of the distributions over a period of six years.

4.4.9.1 SWE/FC and Waves

Absolute calibrations of the FCs on Wind have also been performed through comparisons with wave measurements. This study uses another instrument on the Wind spacecraft

that measures the total electron number density in a completely independent manner. The Thermal Noise Receiver (TNR) instrument portion of the WAVES experiment measures the power spectra of electromagnetic fluctuations at a high cadence of 0.2–4.5 seconds in the frequency range from $4 - 300$ kHz [*Bougeret et al.*, 1995]. The solar wind plasma fluctuates at and above the electron plasma frequency $\omega_p^2 = n_e q^2/m_e \epsilon_o$, a quantity which is only a function of the total electron number density n_e and which varies from $50 - 300$ kHz in typical solar wind conditions. A neural network identifies the plasma frequency from a single TNR power spectrum and determines the electron number density. An extensive comparison of Ulysses/SWOOPS plasma data and Ulysses/URAP wave data using this technique has been presented by *Issautier et al.* [2001] for in-ecliptic and polar solar wind conditions.

In this section we compare a predicted value for the electron number density n_e based on the FC observed proton n_p and alpha n_α number densities with the TNR measurements. Since hydrogen and helium are fully ionized in the solar wind, the total electron number density due to protons and alphas is $n_p + 2n_\alpha$. However, we need to take into account the contribution of other ion species in the solar wind. Approximately 0.1–0.2 % of the solar wind by number density is composed of heavy ions like oxygen and iron. While these heavy ions are rare, the typical charge states observed are large, for example O^{+7} and Fe^{+10}, so a small heavy ion abundance results in a contribution to n_e of ∼1 %. A detailed study by *Kasper et al.* [2006] showed heavy ion contributions to n_e ranged from 0.8 to 1.5 % depending upon the source (inter-stream or coronal hole). If n_e is the total electron number density measured by TNR, and all of the measurements were exact, then the fraction F_m of n_e due to heavy ions would be,

$$F_m \equiv 1 - \frac{n_p + 2n_\alpha}{n_e} \tag{4.14}$$

However, even after taking into account the heavy ions, *Kasper et al.* [2006] found that systematic errors resulted in errors to F_m of ∼4.7 %.

The mean value of F_m over the entire selected data set was 5.9 %, with a standard deviation of 5.1 %. The standard deviation is in agreement with the observations of *Maksimovic et al.* [1995], although $F_m = 5.9$ % is larger than was reported in that same study. That difference can be attributed to a refined analysis of the TNR data [Maksimovic, private communication, 2002] and to the use of proton number densities derived from a bi-Maxwellian analysis which yields results about 1 % smaller than the key-parameter number densities which were used in the 1995 study.

The width of the distribution of F_m over the mission was identified in part as being due to dependencies on time and on solar wind speed. The determination of the average value of F_m as a function of speed and year, and the estimate of the natural variation of the heavy ion component, are detailed in Figure 4.37. The center of the F_m distribution is plotted as a function of speed for each of the years from 1995–2000. Measurements in the same speed window have been offset horizontally by several km s^{-1} to avoid confusion. The two dashed lines indicate the estimated range of F_m. There are variations in F_m with speed which should be compared with more detailed predictions.

In summary, a combination of the estimates of F_m, the TNR electron measurements, and the SWE/FC proton and alpha number densities agree to within ∼4.7 %. Similar agreements were reported for Ulysses for the velocity and the electron core temperature [*Issautier et al.*, 2001]. The widths of the F_m distributions are consistent with the derived

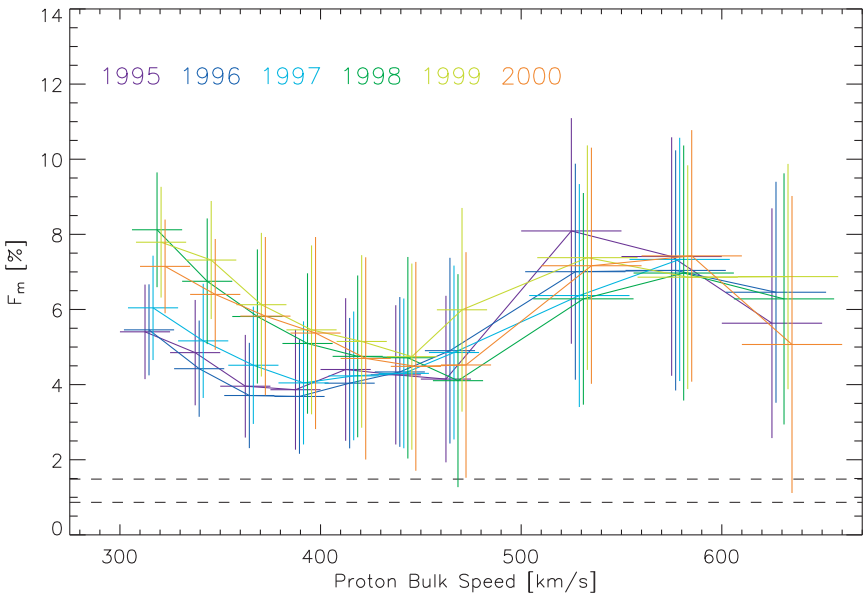

Figure 4.37: Center of F_m distributions and best-fit Gaussian widths (the vertical error bars) as a function of speed and year. Dashed lines indicate estimates of the expected contribution of heavy ions to the total electron number density. Modified from *Kasper et al.* [2006].

uncertainties in the proton and alpha number densities being less that 1 %. Furthermore the agreement between F_m and theory is consistent with the Wind Faraday cups having correct and stable density calibrations within a few percent of the absolute values.

4.4.9.2 SWE/FC and MFI

To identify the uncertainty in proton and alpha velocity measurements, we compare the alpha-proton differential flow vector, $\Delta \boldsymbol{V}_{\alpha p}$,

$$\Delta \boldsymbol{V}_{\alpha p} \equiv \boldsymbol{V}_{\alpha} - \boldsymbol{V}_{p} \tag{4.15}$$

with the direction of the ambient magnetic field $\boldsymbol{B}$ measured by the Magnetic Field Investigation (MFI) on Wind. The FC on Wind is able to separately determine the proton and alpha velocities using the procedures outlined in *Aellig et al.* [2001]. In order for a differential flow between the two species to be stable, the flow must be parallel or anti-parallel to the field. Defining the angle between the differential flow and the magnetic field as,

$$\Delta\theta \equiv \arccos\left(\frac{\Delta \boldsymbol{V}_{\alpha p} \cdot \boldsymbol{B}}{|\Delta \boldsymbol{V}_{\alpha p}||\boldsymbol{B}|}\right) \tag{4.16}$$

we look at the range in θ seen as a function of the magnitude of the differential flow. As long as the individual measurements of $\boldsymbol{V}_{\alpha}$ and $\boldsymbol{V}_{p}$ are sufficiently accurate, $\Delta\theta$ will

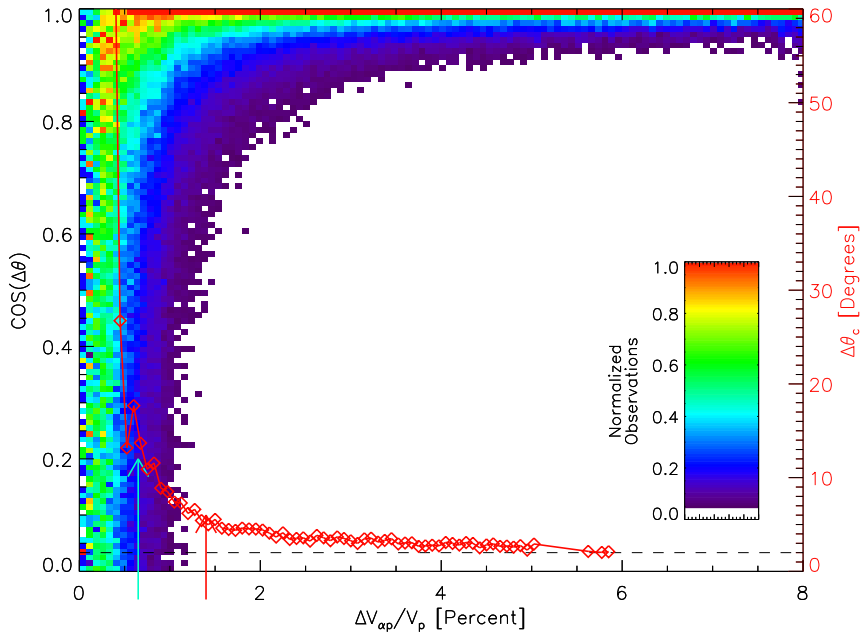

Figure 4.38: Determination of the uncertainty in hydrogen and helium velocity measurements by comparing the direction of the differential flow vector and the magnetic field. The colored squares are a two-dimensional histogram of the distribution of the measured values of cos $\Delta\theta$ as a function of the ratio of differential flow to proton bulk speed, $|\Delta \boldsymbol{V}_{\alpha p}|/V_p$. The diamonds are the average value of $\Delta\theta$ as a function of $|\Delta \boldsymbol{V}_{\alpha p}|/V_p$. Since the differential flow should only be parallel to the magnetic field, and therefore cos $\delta\theta$ should equal 1, the plot demonstrates accurate determination of both proton and alpha flow velocities. However, when the differential flow is less than $\sim$1 % of V_p, accurate comparisons are not possible.

be close to either 0° or 180°. We expect that for sufficiently small values of $\Delta \boldsymbol{V}_{\alpha p}$ the direction of the differential flow will become uncertain and the range of $\Delta\theta$ will grow.

The results of this study are shown in Figure 4.38, which is a two-dimensional histogram of the measured values of cos $\Delta\theta$ as a function of the ratio of the differential flow to proton bulk speed, $|\Delta \boldsymbol{V}_{\alpha p}|/V_p$. For large values of $|\Delta \boldsymbol{V}_{\alpha p}|/V_p$, the flow vector is aligned to within 2° of the magnetic field. For $|\Delta \boldsymbol{V}_{\alpha p}|/V_p \lesssim 1.5\,\%$, the spread in $\Delta\theta$ begins to increase as expected, and in the range of $0.5-1.4\,\%$ the distribution in $\Delta\theta$ becomes isotropic. If the uncertainty in $\Delta \boldsymbol{V}_{\alpha p}$ arises equally from the hydrogen and the helium velocity measurement, then this result implies that the uncertainty in the ion velocities is between 0.5 and 0.7 %.

4.4.9.3 CELIAS/MTOF Proton Monitor with SWE/FC

The proton monitor, (PM), a small subsensor of the CELIAS instrument on SOHO was designed to measure solar wind plasma parameters to assist the data analysis of the

other CELIAS sensors [*Ipavich et al.*, 1998]. Two methods have been used to derive solar wind speed, kinetic temperature, density, and out-of-ecliptic angle from the PM measurements. One method involved the calculation of many synthetic spectra. From the spectra that agreed best with a measurement the four solar wind parameters that determined the spectra were taken. The other method used was a moment analysis to derive the solar wind parameters. To decide which method was best, the solar wind parameters were compared to Wind/SWE measurements, considering the different locations of the two spacecraft [*Ipavich et al.*, 1998]. It turned out that both methods had advantages, depending on investigated parameter, thus in the final analysis of PM data a mixture of both methods was employed. Furthermore, the SWE data were used to refine the PM data analysis so that data derived from the PM sensor are calibrated to give absolute values with modest error bars. In a later study comparing many more measurements from PM and SWE, the same conclusion was derived [*Coplan et al.*, 2001].

4.4.9.4 Moment versus Non-Linear Analysis Methods

Each of the more than two million ion spectra measured by the Faraday cup instruments on the Wind spacecraft up to 2003 has been analyzed using both a preferred non-linear fitting method and the method of moments. Velocities and number densities agreed to within one percent. The largest differences are in the thermal speeds. Two-dimensional histograms of the distribution of temperatures determined from moments versus non-linear methods are shown in Figure 4.39.

Although it was found that the two methods generally agree, the moment-thermal-speeds are generally slightly larger. In addition, a speed-dependent trend was identified in the average ratio of the two thermal speeds. This trend was investigated further through the use of a series of Monte Carlo simulations of solar wind spectra and Faraday cup measurements. Simulations of solar wind ions were made and the resulting moment-thermal-speeds and non-linear-thermal-speeds compared. The initial simulation was based solely on the contribution of protons to the total signal produced in the Faraday cup instruments. At large thermal speeds the moment-thermal-speeds were smaller than the non-linear-thermal-speeds, as observed in the data. It is thought that this is because at large thermal speeds the instrument would not see the entire distribution, and as a result the second moment would be underestimated.

In a more complex simulation of FC ion spectra, alpha particles were allowed to stream along field lines, as is commonly observed at 1 AU. This result, shown by the curves in Figure 4.40, is in good agreement with the observed ratios. The diamonds are the observed variation of the ratio of moment to non-linear thermal speeds. We can conclude for the Faraday cups that the two major sources of discrepancies are 1) not measuring the entire distribution at large thermal speeds and 2) contamination from alpha particles at small thermal speeds.

4.4.10 In-Flight Testing in Special Circumstances

There are several cases where an instrument team took advantage of special circumstances that arose during a mission to conduct additional testing and verification of the instrument performance. One of the prime objectives of the Deep Space 1 mission was to

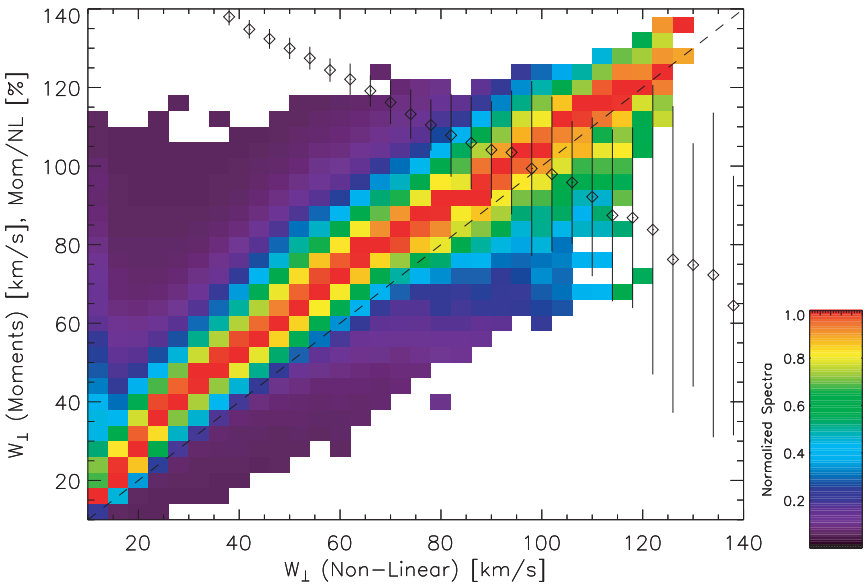

Figure 4.39: Comparison of moment and non-linear calculations of the perpendicular thermal speeds using Wind Faraday cup observations. Colored bins indicate the normalized distribution of the observations; compare with the dashed line indicating equality. Diamonds indicate 100 times the average ratio as a function of speed.

test the ion propulsion technology. The spacecraft included a comprehensive plasma instrument, PEPE (Plasma Experiment for Planetary Exploration) to monitor the local plasma environment during the mission. Resource limitations prevented a complete ground calibration of PEPE and analysis of in-flight data was required to establish instrument performance [*Young et al.*, 2000]. However, after launch solar wind bulk velocities, densities, and temperatures computed from the PEPE observations were compared to similar parameters obtained from the well-calibrated SWE on Wind when the two spacecraft were within 10^6 km of one another. The comparisons between the two agreed to within 10 %. The time-of-flight portion of the PEPE instrument also responded as expected to the ion propulsion system (IPS) propellant Xe^+ and to Mo^+ that sputtered from the IPS grid structures during IPS operation.

In order to provide gravity assist to the orbit, the Cassini spacecraft performed an Earth swing-by in August 1999. This provided the opportunity to compare plasma observations by the Cassini Plasma Spectrometer (CAPS) and energetic particle observations by the Low-Energy Magnetospheric Measurement System (LEMMS) with the relatively well characterized plasma and particle environment in Earth's magnetosphere [*Rymer et al.*, 2001; *Lagg et al.*, 2001]. Unfortunately, the encounter occurred at a time of high magnetospheric activity with Earth's magnetosphere in a dynamic state that precluded detailed comparisons between the instrument observations and models based upon a quiescent magnetosphere. However, the Cassini instrumentation did respond as expected to crossing various regions of Earth's magnetosphere (e.g. the bow shock, the magnetopause,

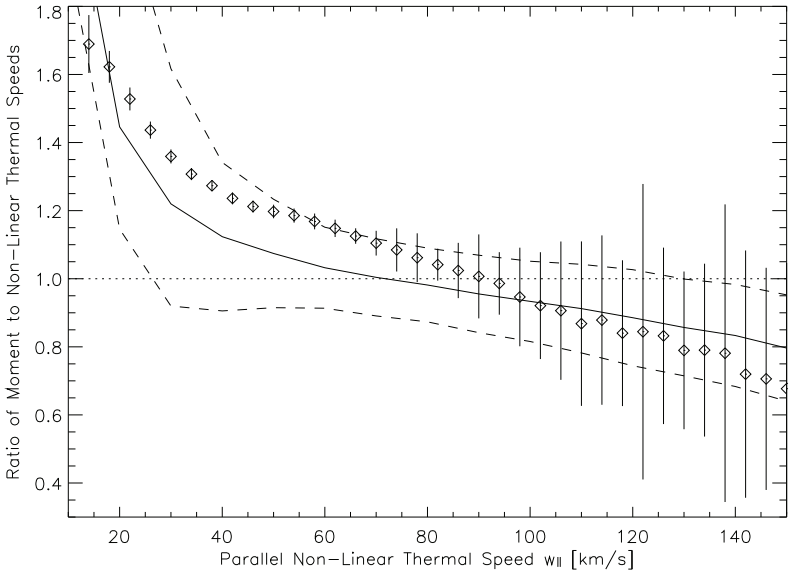

Figure 4.40: Comparison of the observed variation (diamonds) of the ratio of moment-thermal-speed to non-linear-thermal-speed calculations with a Monte Carlo simulation of that ratio, as a function of thermal speed. The center line is the average value of the ratio determined from the Monte Carlo simulation, and the upper and lower dashed lines indicate the one-sigma width to the distribution of simulated ratios.

low latitude boundary layer, tail lobe, plasmapause, and radiation belts) that qualitatively confirmed a proper instrument performance.

The Galileo spacecraft performed Earth swing-byes in December 1990 and in December 1992. On both occasions energetic proton observations by a LEMMS instrument as the satellite rapidly transited through Earth's radiation belts were converted to phase space densities as a function of the particle's magnetic moment and L-value [*Alinejad and Armstrong*, 1997]. Those results were compared to the AP8 radiation belt model with good agreement and so verified the performance of the LEMMS instrument and of the analysis procedures that yielded the phase space densities.

4.4.11 Langmuir Probes

In-flight relative and absolute calibrations of Langmuir probes (LPs) operated at high plasma densities may be established either by inter-comparisons with other instruments on the same spacecraft or by comparisons with simultaneous ground based observations. As mentioned earlier, comparisons between Langmuir probes on the same spacecraft not only expose degradation or problems, but those comparisons can also provide confidence in the measurements. In the late 1960s, multiple long-wire probes were flown on the same rocket to determine if the type of metal coating on the collector had any affect upon the T_e

measurements [*Brace et al.*, 1971]. They found good agreement in the T_e measurements made by long-wire probes made of different metals or having different surface coatings. Comparisons among the measurements by different types of plasma instruments on the same satellites offered other insights into the validity of the various techniques. *Donley et al.* [1969] found good agreement among the measurements made by the cylindrical and planar LPs and the planar retarding potential analyzers on the Explorer 31 satellite. *Brace and Findley* [1969] found excellent agreement when comparing measurements from identical Langmuir probes on satellites with distinctly different physical configurations (Explorer-31 and Alouette-2) while they were orbiting in close proximity. *Miller et al.* [1984] also found very good agreement between the measurements of N_e, N_i, and T_e made by the Langmuir probe and the retarding potential analyzer on the PVO spacecraft.

Comparisons between space-borne and ground observations provide another method of establishing probe calibration. In 1968, two rockets were launched near the Arecibo radar facility in Puerto Rico to allow comparisons of LP and incoherent scatter measurements. *Brace et al.* [1969] reported that the daytime T_e measurements were in excellent agreement with the radar measurements, but the probe temperatures were slightly higher on the nighttime flight. The T_e measurements by a platinum and a stainless steel probe on the nighttime flight disagreed by 10 %; a difference that was not present in the daytime measurements. The inherently large surface patchiness of the stainless steel probe may have led to the slightly higher values of T_e from that probe. More extensive incoherent radar and LP comparisons were reported by *McClure et al.* [1973] based on overflights of OGO-6. The long-wire LP measurements from OGO-6 yielded T_e values about 15 % higher than the radar measurements [*McClure et al.*, 1973]. Much better agreement was reported by *Benson et al.* [1977], who compared AE-C short probe measurements with those made simultaneously by the Millstone Hill, Chatanika, St. Santin, and Arecibo radars. The single disagreement was at Millstone Hill where the radar T_e measurements were lower than the probe measurements by an average of 11 %. These comparisons were valuable because they uncovered a systematic difference between the radar measurements from Millstone and the other locations. The generally better T_e agreement between the radars and the short probes suggests that the accuracy of the earlier long probe measurements may have suffered from a combination of surface patchiness and geomagnetically induced potentials, both of which cause energy smearing of the electron retardation regions at very low T_e. These effects are described in Section 2.3. While these comparisons among *in situ* and remote measurements have demonstrated the validity of the LP technique in a wide variety of space applications, they do not obviate the need to avoid implementation errors in any new mission.

4.5 In-Flight Relative and Absolute Calibration for Energetic Particles

Instruments designed to measure energetic particles encompass a number of different designs. Among these are simple solid-state detectors directly exposed to space or located under an energy degrader or absorber, multiple element solid-state detector systems capable of identifying both particle energy and mass, Cherenkov detector systems for detecting very high-energy particles and scintillation detector systems. A combination of detector techniques may be used in the same instrument to suppress background (anti-coincidence

guard scintillators, Cherenkov detectors together with solid-state detector telescopes for particle species separations, etc.). In all cases both relative and absolute calibration of such detector systems must utilize either known properties of the natural radiation environment or radioactive sources in the instrument. This section describes several such techniques that can be used to perform such in-flight calibrations.

Cosmic rays provide an opportunity to perform an absolute flux calibration for instruments sensitive to high-energy protons. At high altitudes, geosynchronous and above, the cosmic ray flux is isotropic. Thus it is possible to calibrate both dosimeters, with a 4π sr field of view, or telescopes with a narrow field of view using natural cosmic rays.

Cosmic rays consist of 83 % protons, 13 % α-particles, 1 % heavy nuclei and 3 % electrons. At geosynchronous altitude, the Earth's magnetic field is sufficiently weak that it no longer provides an effective barrier to cosmic rays with energies above 87 MeV [*Stassinoupoulos*, 1989]. Thus the incident proton spectrum ranges in energy from about 100 MeV to tens of GeV.

Energy loss of high-energy protons varies slowly with kinetic energy. At 100 MeV the energy loss is 5.8 MeV g^{-1} cm^{-2} and it decreases slowly to the minimum ionizing value of 2 MeV g^{-1} cm^{-2} at 1 GeV and stays at this value at higher energies. Consequently any high-energy proton detector will respond to cosmic rays. In addition, some high-energy electron detectors that depend on energy loss measurements will also respond to very high-energy protons because their energy loss is also at the minimum ionizing value of 2 MeV g^{-1} cm^{-2}.

Cosmic ray intensity varies inversely with solar activity reaching 4 protons cm^{-2} s^{-1} at solar minimum and decreasing to 2 protons cm^{-2} s^{-1} at solar maximum. Since the solar cycle variation can be modeled [*Smart and Shea*, 1985], the actual, isotropic flux can be determined to about 10–20 %. Even without the solar cycle correction, the flux value may be set to an intermediate value of 3 protons cm^{-2} s^{-1}, with an error of not more than 33 %.

Proton instruments on high altitude spacecraft can make measurements of cosmic ray count rate and, using the known cosmic ray flux, convert the count rates to absolute flux response. This procedure can be used to perform an end-to-end check of the instrument response as well as to track that response with time. This technique can only be used when the high-energy proton population from sources other than cosmic rays is low, a condition met at geosynchronous altitudes except during solar proton events. This technique may also be used at low Earth orbits with data collected when the spacecraft is out of the inner belt, including the South Atlantic Anomaly, and not in the horns of the outer belt. Be aware that the effect of the Earth shielding the spacecraft must be considered for spacecraft in low-Earth orbits.

Lastly we point out that in-flight determination of energy degradation due to changes in dead layer and lattice defects, as described in Section 4.3.3, is rather difficult. This is primarily a problem for ion detectors whose energy range may extend down to <30 keV. The simplest solution may be to include a separate calibration detector which remains shielded from exposure during most of the mission and whose aperture can be opened periodically to cross-calibrate the primary sensor. When resources are available, this will provide the most reliable in-flight absolute and relative calibration for the primary sensor.

4.5.1 Absolute Energy Response Calibration

The measurement of energy response of a detector provides an end-to-end measurement of the gain of the system (detector and electronics). In some cases, the absolute energy response of a detector can be measured in-flight by a radiation source. The source can be either mounted in fixed position, so as to illuminate the sensor at all times, or be placed on a movable arm so that its radiation strikes the detector only during calibration periods. The disadvantage of the first method is that the signal due to the source may be a significant and continuous background. The disadvantage of the second method is that it requires a motion mechanism, which adds significant complexity to the instrument design.

In spite of additional complexity, some space instruments have included radioactive sources to monitor instrument performance. The Particle Environment Monitor (PEM) experiment on the UARS satellite included an ^{241}Am α-source to track the in-flight performance of the solid-state detectors in that instrument [*Sharber et al.*, 1996]. The Medium Energy Particle Analyzer (MEPA) on the AMPTE CCE satellite included an alpha source to monitor both MCP and solid-state detector performance in that time-of-flight instrument [*McEntire et al.*, 1985]. Both the Energetic Particle Detector on the Galileo mission [*Williams et al.*, 1992] and the EPIC instrument on Geotail [*Williams et al.*, 1994] included Am alpha emitting sources to monitor performance. The use of the alpha source proved particularly helpful in monitoring the performance of the MCP that was used to detect the secondary electrons created when an ion transited the "start" foil in the TOF component of these instruments [McEntire, private communication]. In locations where natural background was low and the alpha source dominated the response of the TOF instrument, the rate of "start" signals produced when the alpha transited the foil should be equal to the rate of "stop" signals produced when the alpha was absorbed by the solid-state detector. A ratio of significantly less than 1.0 indicates insufficient gain in the MCP and the requirement for an adjustment of the MCP bias voltage. The Electron, Proton, and Alpha Monitor (EPAM) on ACE [*Gold et al.*, 1998] used a variety of radioactive sources mounted on the reclosable telescope covers for in-flight calibration.

Sources that emit mono-energetic α-particles can be used to calibrate a single Si solid-state detector or a scintillator detector. The reason why only a single detector may be calibrated is that a typical 6 MeV α-particle has a range of 21 μm in silicon and will be stopped in the first detector it hits. Although radiation sources provide α-particles only in the energy range of 4 to 6 MeV, a lower energy may be obtained by placing a thin foil over the source. The energy of the emitted α-particles will be reduced at a cost of increased spread of the energy distribution. For a list of available α-particle sources see *Knoll* [2000].

Most β-particle sources provide electrons with a continuum of energies up to an end-point value. This is due to the physics of the process that produces them. Weak decay β-particles are produced in three-body process that also produces a neutrino, which carries away some of the available energy. The result is that the β-particle can have any energy from 0 to the end point value, which is unique to each β emitting isotope. Due to this property, the detector being calibrated with a β source will be exposed to β-particles with a continuum of energies. However, since the shape of the energy spectrum is constant in time, it may be possible to get some information about the gain of the system by monitoring ratios of count rates from key channels. There are a few electron conversion sources that produce mono-energetic electron lines, accompanied by γ-rays. A list of useful line and continuum β-particle sources is shown in Table 4.1

Table 4.1: List of β sources

Isotope	Source Type	E(keV)
^{3}He	Endpoint	18.6
^{14}C	Endpoint	156
^{36}Cl	Endpoint	714
^{63}Ni	Endpoint	67
^{90}Sr/^{90}Y	Endpoint	546/2270
^{99}Tc	Endpoint	292
^{137}Cs	Line	624, 656
^{207}Bi	Line	482, 554, 976, 1048

Sources that emit γ-rays can be used to calibrate Si solid-state detectors, particularly the ones with thicknesses range of hundreds of microns (see Section 3.5). The difficulty of this type of calibration is that solid-state detectors have low probability of interacting with a γ-ray and are not efficient in capturing its full energy. However, γ-ray sources are extremely useful in checking the calibration of scintillators. The relatively large size and the high density of scintillator sensors results in a high probability of an interaction with the γ-ray and a good probability of total absorption of the γ-ray energy. This results in a well defined peak at the γ-ray energy. The measured position of the peak can be used to track the end-to-end gain of the system. A list of useful γ-ray sources is shown in Table 3.1.

While, for the reasons given above, γ-ray sources are rarely included in space experiments, the cosmic ray electron experiment on Pioneer-10 made use of 2.6 MeV γ-rays originating from the RTG power source on that satellite to assess and correct for detector degradation that had occurred during the encounter with Jupiter's radiation belts [*Eraker*, 1982].

4.5.2 Relative Flux Response (Multi-Spacecraft)

Solar proton events generate high fluxes of very energetic protons. Near Earth, these protons appear both at high altitudes and in low-Earth orbit at high L values. As long as there are no high-energy electrons associated with the event, these protons provide a means of cross calibrating detectors on more than one spacecraft. Presence of high-energy electrons can be determined using real-time data from the POES electron sensor, available from the NOAA web site: `www.sel.noa.gov/data/`. An example of data from such cross-calibration is shown in Figure 4.41. Data plotted in the figure demonstrate a comparison between responses of identical Si solid-state detector dosimeters [*Dichter et al.*, 1998] in low-Earth (TSX-5 mission) and geosynchronous (DSP mission) orbits for the same L values of 6.5 to 6.7. It is evident that the proton data for both detectors are in good agreement, while the electron data are not well correlated. This is as expected since the dynamics of trapped electrons are very different at the two altitudes. It is clear that solar event protons can provide a means to cross calibrate proton-sensing instruments.

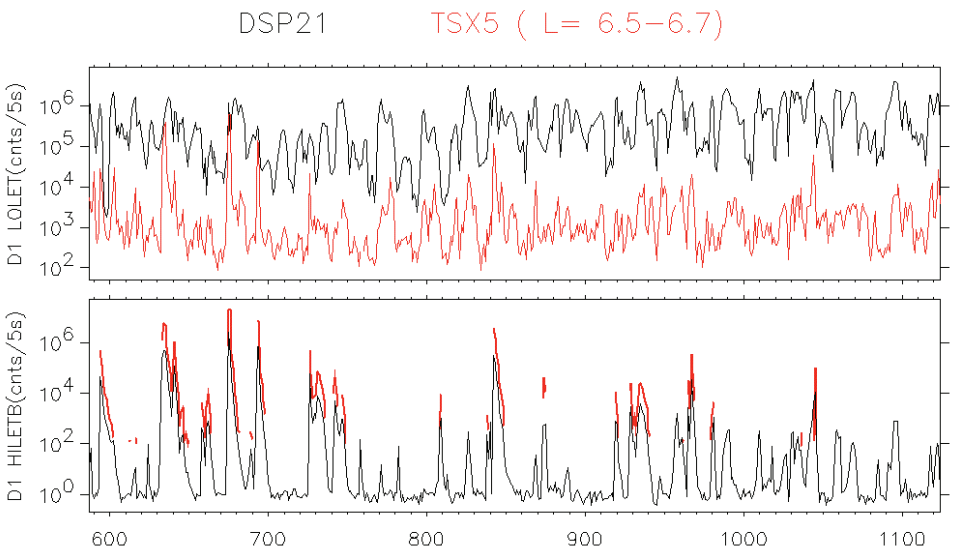

Figure 4.41: Daily averages of proton and electron dosimeter data, for L-Shells 6.6 to 6.7, for DSP and TSX-5 missions. HILETB is the proton dose and LOLET the electron dose. TSX-5 data are multiplied by 10 for clarity. Proton data (lower plot) show good correlation between the low altitude TSX-5 and geosynchronous DSP satellite. Energetic electron data do not correlate well due to different dynamics of the trapping process.

The TSX-5 spacecraft spends very little time in the L-shell region of the geosynchronous DSP, thus accounting for the proton data gaps. Therefore, the comparison should be made by binning the data in multiple orbit bins, such as daily averages. The process of cross-calibration is easier with identical sensors, however, it is still possible to perform the task with different sensors. The daily averages may not have the same values but the timing and relative height of the observed structures should be in good agreement. Furthermore, the relative height of the structure should not vary with time, providing a method for long term calibration.

4.6 In-flight Relative and Absolute Calibration for Neutral Gas Sensors

One of the problems with calibration of neutral gas mass spectrometers is that once the process is finished, the instrument is bundled up in final flight configuration, exposed to thermal vacuum and vibration testing, launched and then left sealed for an extended period of time, sometimes in very hostile environments. The question then becomes: how relevant is the pre-launch calibration to the current flight operation of the instrument? Questions of interest for the pre-launch versus post-launch flight instrument include:

- What is the gas sensitivity?

- If mass peak jumping is used to increase the sample rate rather than more detailed mass spectral scanning, is the jump point on the top of the peak or on its side?
- What is the mass peak resolution?
- Are the focusing lenses in the ion beam path at their optimum transmission values?

Most, if not all, neutral gas mass spectrometers are sealed off in a vacuum prior to final delivery and testing. The advantage of a sealed mass spectrometer is that there is usually some background gas which can be used for full spectrometer sensor testing with the ion source filaments operating and with either vacuum or atmospheric pressure on the flight electronics. Some sensors even carry a low pressure atmosphere deliberately introduced to enhance the testing procedure [*Mahaffy et al.*, 2002; *Boies et al.*, 1994]. The other advantage of a sealed sensor is that it can be kept clean during maneuvers such as orbit insertion and thruster firings. The sensors can also be actively pumped by an ion pump or a getter material requiring no electrical power from the spacecraft.

Having arrived at its destination, the sensor is opened to its environment using a variety of different methods. For example, the Open Source Spectrometer instruments [*Nier et al.*, 1973] for the Atmosphere Explorer satellites were maintained under vacuum by an ion pump and opened by a cutter-wheel device [*Thorness and Nier*, 1962]. The Pioneer Venus Orbiter Neutral Mass Spectrometer [*Niemann et al.*, 1980a] vacuum was maintained by a small getter pump and the metal-ceramic break-off cap removed by a pyrotechnic actuator which cracks the ceramic band, allowing the cap to be ejected. The ROSINA Double Focusing Mass Spectrometer [*Balsiger et al.*, 2007, 1998] and Reflectron Time-of-Flight sensors are evacuated through pump-out valves that are closed prior to launch. The system maintained a low level vacuum ($< 10^{-5}$ mbar) until it was opened pyrotechnically. After opening the cover can be closed by a motor. While sealed, this internal gas provides a means of evaluating the optimum operational voltages of many of the electrostatics lens systems, the integrated pulse height distribution of secondary multipliers, and the mass peak tuning. Repeated use of the same test script tracks instrument performance from initial sealing, through vibration and thermal vacuum tests, and into the post-launch period until the cover is ejected. This type of testing checks instrument performance but does not necessarily track its absolute sensitivity.

One example of a problem is described in *Kasprzak et al.* [1993] where the neutral mass spectrometer made measurements in the upper atmosphere of Venus from Dec. 1978 to Aug. 1980. After that period the periapsis of the orbit was not actively controlled and neutral density measurements were not possible until June 1992 to October 1992. It was discovered that the instrument had a different mass peak tuning for masses near 44 u/charge (CO_2) than that of the earlier period. The only gas available for mass tuning was ambient CO_2 that is abundant on the night side only at very low altitudes. The desire to sample all gas species at high time resolution (i.e., mass peak jumping) was in conflict with the desire to determine the proper instrument tuning due to the low telemetry data rate, the limited instrument modes available, the low neutral density, a spinning spacecraft and the short time period (several minutes) available per periapsis pass for diagnostics. If an independent gas source were available for checking mass tuning at places other than at periapsis, the process would have been much easier. Since the instrument was retuned, there was also the possibility that the individual mass peak sensitivities could have changed as a result.

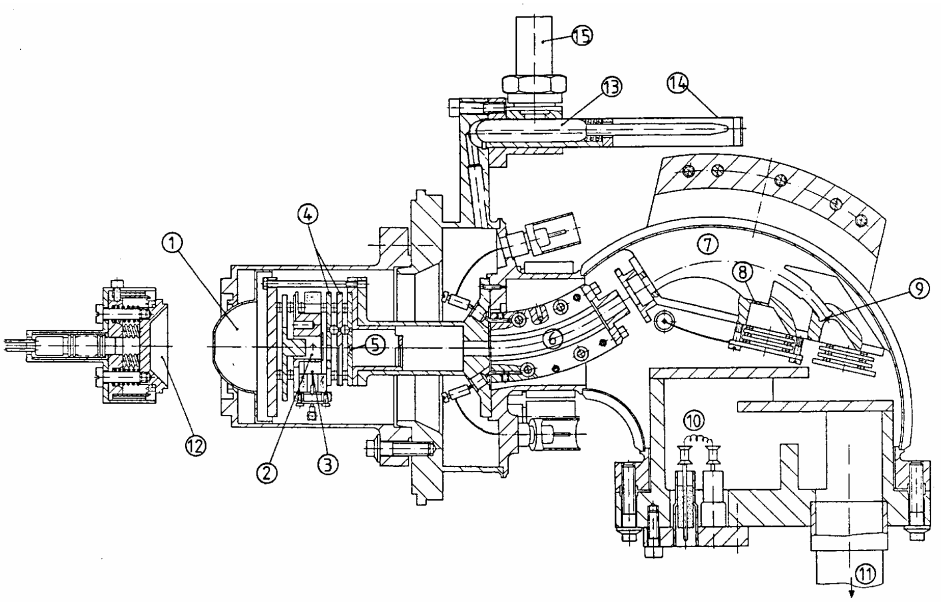

Figure 4.42: The BUGATTI mass spectrometer. The In-Flight Calibration cell (IFC) consists of a glass vial (13) attached to a metal tube (14) that is broken by a squib (15) releasing gas into the ion source (2, 3, 4) and antechamber (1) that has an ejectable cover (12). From *von Zahn et al.* [1990].

Chereji et al. [1978] describe a device to supply a constant reproducible amount of deuterium into an entrance of a mass spectrometer open to space using a palladium valve that is temperature controlled. The flow rate is 3×10^{-4} to $3\times10^{-3}\mu$l s^{-1}. *Outlaw et al.* [1971] describe a metal-gas binary system that uses hydrogen dissolved in erbium. The temperature of the system determines the equilibrium hydrogen pressure.

The Pioneer Venus Bus Neutral Gas Mass Spectrometer (BNMS) [*Hoffman et al.*, 1980b] carried a small glass vial of a calibration gas (He). With the instrument still sealed in launch configuration and four days before entry into the Venus atmosphere, a pyrotechnic device was fired crushing the vial, expanding a known quantity of gas into the mass spectrometer with closely estimated volume. This was done to check the gain of the low mass continuous channel multiplier which could not be checked with a direct current measurement as could the high mass channel. The Pioneer Venus Sounder Probe Neutral Gas Mass Spectrometer [*Hoffman et al.*, 1980a] carried a calibration gas mixture of methane and ^{136}Xe to provide mass peaks at 15 u/charge (CH_3^+), 68 u/charge ($^{136}Xe^{2+}$) and 136 u/charge ($^{136}Xe^+$).

The BUGATTI experiments [*von Zahn et al.*, 1990] used instruments with a double-focusing Mattauch-Herzog electric and magnetic deflection mass spectrometer with an in-flight calibration system (Figure 4.42). To protect the stability of the mass spectrometer calibration, an ion source cover is attached to the instrument while it is still under vacuum inside the calibration system. Shortly before the ion source cover is ejected after launch, an in-flight calibration for N_2, O_2 and Ar is performed with gases stored in a glass vial

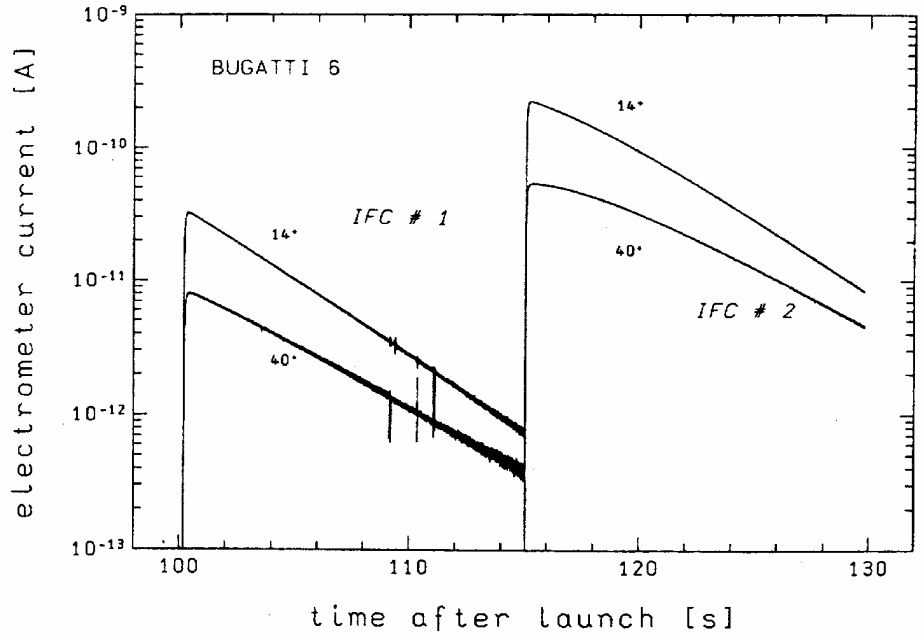

Figure 4.43: The In-Flight Calibration volume pressure decays for IFC #1 (volume 1) and IFC #2 (volume 2). From *von Zahn et al.* [1990].

that is broken. An ion getter pump slowly removes the released gas. Two volumes were used for each instrument (0.14 mbar and 1.44 mbar of 79.1 % N_2, 19.8 % O_2, and 1.08 % Ar to match the assumed gas composition at 100 km on Earth). The lower pressure vial is broken first and the higher pressure vial 15 seconds later. The curves (Figure 4.43) are extrapolated back to zero time in order to establish the absolute pressure based on the initial filling pressure and the vial to ion source volume ratio.

The Midcourse Space Experiment (MSX) contamination mass spectrometer [*Boies et al.*, 1994] was backfilled with trace amounts of He, Ar, Kr, and Xe. The gas mix was used as a means of tracking the instrument sensitivity and mass linearity from instrument integration and testing through launch until cover break off. After break off, a comparison was made with a total pressure sensor measuring similar contamination gases. For orbital instruments, comparison with orbital drag measurement of the total density can also be used [*Hedin et al.*, 1983].

The NGIMS [*Mahaffy et al.*, 2002] instrument aboard the CONTOUR spacecraft has a gas reservoir with two valves: 1) a rupture valve that maintains the gas in the volume until it is pierced by a lance; and 2) a standard valve that can be commanded open or closed (Figure 4.44). Both valve types are used in the GCMS instrument aboard Huygens Probe [*Niemann et al.*, 1997, 2002]. A Kulite pressure sensor monitors the volume pressure. The gas mixture is 9.2 % of ^{129}Xe, 18.6 % of Ar and 72.2 % of Ne contained in a volume of 5.6 cm^3 at an initial pressure of 466.6 mbar. Isotopic ^{129}Xe is used in order to prevent confusion with possible comet Xe at other isotopes. The same mixture was used to backfill the sensor at very low pressure before final sealing. The mixture in the gas reservoir is

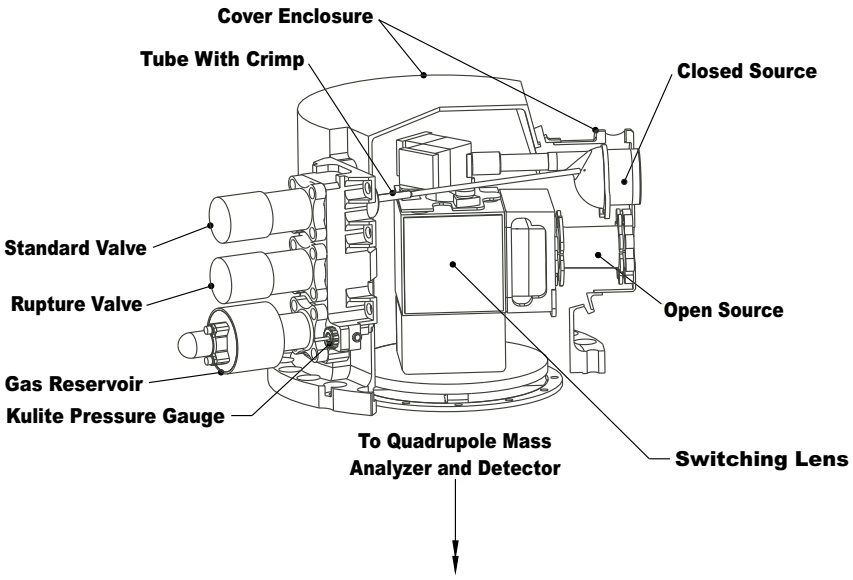

Figure 4.44: The CONTOUR NGIMS ion source with in-flight gas calibration volume. From *Mahaffy et al.* [2002].

admitted to the ion source volume by a small tube with a crimp in it for gas flow restriction. A dome covers the volume containing the open source and closed source. A small hole in the antechamber wall allows gas into the closed source. The purpose of the gas mixture is to allow a check of mass peak tuning for middle and low frequencies of the three frequency quadrupole system. It also allows scans of the electric potentials on the programmable ion focusing elements to confirm optimum transmission settings after a comet encounter. Relative sensitivity changes before and after comet encounters can also be detected. The noble gases were chosen since they are chemically inert, with no surface adsorption. The disadvantage for NGIMS is that the isotopic mass of Xe only goes up to 129 u/charge, while the instrument mass range is up to 300 u/charge.

The ROSINA instrument package for the Rosetta Mission [*Balsiger et al.*, 2007, 1998] has both a double focusing mass spectrometer (DFMS), mass range 12–100 u/charge, and a time-of-flight mass spectrometer (RTOF), mass range 1–300 u/charge. The DFMS has one ion source and the RTOF two ion sources (an orthogonal source and an ion storage source). Each instrument has two in-flight gas calibration units (GCU) with a connecting tube to each ion source (Figure 4.45). The reservoir volume is about about 10 cm^3 and contains a gas mixture at about 5 bars pressure. The mixture for DFMS consists of 4.5 % Ne, 93 % CO_2 and 2.5 % Xe while that for the RTOF consists of 33.3 % He, 33.4 % CO_2 and 33.3 % Kr by weight. There is a high pressure gauge for the gas reservoir and a mini-Pirani low pressure gauge (range 0.2–0.04 mbar). The valve is a non-commercial design with a flow rate that is temperature controlled and operates below 60 °C. The gas flow into the ion source is dependent on the conductivity and the flow system in the capillary and

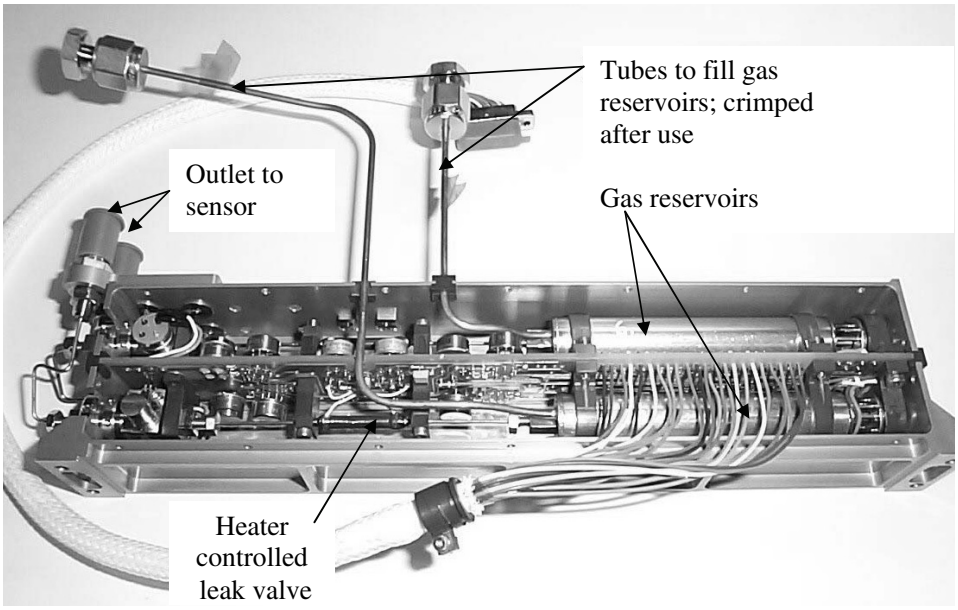

Figure 4.45: The ROSINA DFMS in-flight gas calibration unit (GCU) [*Balsiger et al.*, 2007, 1998].

tube to the ion source. The ion source pressure with the calibration gases should be below 3×10^{-6} mbar.

No problems, such as premature gas leaks or chemical changes in the test gases, have been encountered with the use of trace gas releases to check post-launch calibrations of neutral gas spectrometers.

4.7 In-Flight Relative and Absolute Calibration for ENA Instruments

In-flight calibration of Energetic Neutral Atom (ENA) instruments is difficult for two reasons. First, there are no "well-calibrated" neutral particle sources in space that can be used to establish an absolute in-flight calibration. Second, since ENAs are neutral particles, a Faraday cup detector, which is a very reliable detector for cross-calibrating charged particle detectors, can not be used. The ENA instrument in-flight calibration generally relies on comparisons with plasma measurements. ENA instruments have a charged particle rejection system at their entrance and their detectors generally react to charged particles in a manner similar to neutrals. Therefore when the rejection system is switched off, ions can enter the ENA instrument and be detected in the same way as neutral particles. This generally requires the ion spectra to have relatively low fluxes in the energy range of the ENA instrument to prevent the ENA instrument's saturation. This often limits the periods where cross-calibration can be performed to those when the plasma sensor, which has much smaller geometric factor, has a count rate slightly above its background rate. By

using ion distributions established through cross-calibration with a plasma instrument on the same spacecraft, one can establish an absolute in-flight calibration for the ENA instrument. This method also assumes that the plasma instrument's absolute calibration has been determined, which usually requires cross-calibration with a third instrument.

For a relative calibration of an ENA instrument with look direction, one can often make use of the detector's sensitivity to UV photons. For mass resolving sensors that incorporate microchannel plates (MCPs) in their time-of-flight detectors, a UV photon entering the instrument can trigger either the start or the stop detector with a certain probability (in the range of 10^{-3} to 10^{-2}). Since many UV sources, e.g. stars, are sufficiently constant with time, monitoring these UV-induced background rates over the mission allows assessment of sensor degradation. Corrections for that degradation can be made by increasing the MCP bias voltages. Furthermore, stars are point sources and thus they can be used to establish the imaging quality of the ENA instrument and to derive the minimum point spread function. This provides only an estimate of the point spread function because registered ENAs suffer a degradation of their energy and flight direction in the course of their detection in the instrument [*Wurz*, 2000; *Henderson et al.*, 2005]. Lastly, the absolute pointing of the ENA instrument can be established using the UV signal from stars, as was performed with the GAS instrument on Ulysses [*Witte et al.*, 2004].

An additional method of testing ENA instrument calibration is through a comparison of the model determined source distribution of plasma with *in situ* plasma data from a spacecraft located in the source region. ENA imaging instruments record a 2-D image of a three-dimensional plasma population, where the third dimension is collapsed into a line-of-sight integral [*Wurz*, 2000]. To interpret ENA images, one needs an inversion model to establish the three dimensional structure of the plasma population. This evaluation has been performed for the terrestrial ring current where *in situ* plasma measurements by the CIS instruments on Cluster have been compared with ENA images recorded with HENA on IMAGE. *Vallat et al.* [2004] found mixed agreement between these two measurements, with three of the four high flux ($> 10^5$ cm^{-2} sr^{-1} s^{-1} keV^{-1}) measurements within the HENA error bars, and two low flux measurements outside the HENA error bars. The study also identified several limitations to using the inversion technique including finite angular resolution of the camera, limited precision of the exospheric hydrogen and magnetic field models, and averaging caused by the line-of-sight integral response. All of these contributed to a scatter of the calculated fluxes with respect to the measured fluxes.

4.8 Conclusion

As the material in this chapter has made abundantly clear, unexpected spurious responses and post-launch changes in performance on the part of space plasma instrumentation are very much the rule and only rarely the exception. It is important to anticipate at the earliest stage of an experiment program that this will happen and devise instrument design features and post-launch operating procedures that will mitigate, identify, and correct for instrument changes and spurious responses.

Proper instrument shielding, aperture and analyzer structure design, and choice of materials and surface coatings are important factors in minimizing spurious instrument responses. Even then, situations may occur in space when the physical parameter that is to be measured is of such low intensity relative to sources of spurious response, that the

spurious instrument response dominates. Thought must be given as early as possible to procedures that would serve to identify such situations so that those data would be excluded from analysis.

Detector variations and degradation with time appears to be an unavoidable feature of space plasma instrumentation. It is very important that instrument design and operating procedures include features that serve to identify and correct for these effects. While not an inclusive list, at the very least instruments using CEMs or MCPs should be designed with ground commandable pulse counting threshold setting that permit detector pulse height distributions to be determined and commandable bias voltage settings that compensate for detector gain losses. The ability to command a plasma instrument to measure, for example, a fixed particle energy or limited energy range can also be valuable in identifying instrument performance anomalies. For energetic particle detectors, having a radioactive source or flying a calibration detector that experiences minimal exposure to degradation, can greatly simplify the in-flight calibration process. Similarly, including a mechanism for releasing calibration gases into neutral gas detectors can reduce uncertainties in the in-flight calibration effort.

In closing, addressing the problems described in this chapter at the instrument design stage and developing procedures to handle post-launch instrument performance at the earliest possible time in the program is vital to a successful experiment.

Acknowledgements

The authors would like to thank Sue Greer for creating the figures displaying data from the SEM on the POES satellites, Joseph Fennell for supplying and explaining the SCATHA figure and Walter Lennartsson and Edward Shelley for supplying and explaining the ISEE-1 ion mass spectrometer figure.

Bibliography

Aellig, M., A. Lazarus, and J. Steinberg, The solar wind helium abundance: Variation with wind speed and the solar cycle, *Geophys. Res. Lett.*, **28**, 2767–2770, 2001.

Alinejad, N. and T.P. Armstrong, Galileo energetic particle detector observations of geomagnetically trapped protons, *J. Geophys. Res.*, **102**, 27053–27068, 1997.

Archuleta. R. J. and S.E. DeForest, Efficiency of channel electron mulipliers for electrons 1–50 keV, *Rev. Sci. Instrum.*, **42**, No. 1, 89–91, 1971.

Balsiger, H., K. Altwegg, E. Arijs, J.-L. Bertaux, J.-J. Berthelier, B. Block, P. Bochsler, G.R. Carignan, L. Duvet, P. Eberhardt, B. Fiethe, J. Fischer, L.A. Fisk, S.A. Fuselier, A.G. Ghielmetti, F. Gliem, T.I. Gombosi, M. Illiano, T. Koch, E. Kopp, A. Korth, K. Lange, H. Lauche, S. Livi, A. Loose, T. Magoncelli, C. Mazelle, M. Mildner, E. Neefs, D. Nevejans, H. Rème, J.A. Sauvaud, S. Scherer, A. Schoenemann, E.G. Shelley, J.H. Waite, C. Westermann, B. Wilken, J. Woch, H. Wollnik, P. Wurz, and D.T. Young, Rosetta Orbiter Spectrometer for Ion and Neutral Analysis-ROSINA, *Adv. Space Res.*, **21**, 1527–1535, 1998.

Balsiger, H., K. Altwegg, E. Arijs, J.-L. Bertaux, J.-J. Berthelier, B. Block, P. Bochsler, G.R. Carignan, L. Duvet, P. Eberhardt, B. Fiethe, J. Fischer, L.A. Fisk, S.A. Fuselier, A.G. Ghielmetti, F. Gliem, T.I. Gombosi, M. Illiano, T. Koch, E. Kopp, A. Korth,

K. Lange, H. Lauche, S. Livi, A. Loose, T. Magoncelli, C. Mazelle, M. Mildner, E. Neefs, D. Nevejans, H. Rème, J.A. Sauvaud, S. Scherer, A. Schoenemann, E.G. Shelley, J.H. Waite, C. Westermann, B. Wilken, J. Woch, H. Wollnik, P. Wurz, and D.T. Young, Rosetta Orbiter Spectrometer for Ion and Neutral Analysis-ROSINA, *Space Sci. Rev.*, 128, 745–801, doi:10.1007/s11214-006-8335-3, 2007.

Bamert, K., Suprathermal particles associated with coronal mass ejections, Ph.D. thesis, University of Bern, 2004.

Barabash, S., R. Lundin, H. Andersson, J. Gimholt, M. Holström, O. Norberg, M. Yamauchi, K. Asamura, A.J. Coates, D.R. Linder, D.O. Kataria, C.C. Curtis, K.C. Hsieh, B.R. Sandel, A. Fedorov, A. Grigoriev, E. Budnik, M. Grande, M. Carter, D.H. Reading, H. Koskinen, E. Kallio, P. Riihela, T. Saeles, J. Kozyra, N. Krupp, S. Livi, J. Woch, J. Luhmann, S. McKenna-Lawlor, S. Orsini, R. Cerrulli-Irelli, A. Mura, A. Milillo, E. Roelof, D. Williams, J.-A. Sauvaud, J.-J. Thocaven, D. Winningham, R. Frahm, J. Scherer, J. Sharber, P. Wurz, and P. Bochsler, The Analyzer of Space Plasmas and Energetic Atoms (ASPERA-3) for the Mars Express Mission, *ESA Special Publication*, **SP-1240**, ESA Publications Division, Noordwijk, 121–139, 2004.

Basu, B., J.R. Jasperse, R.M. Robinson, R.R. Vondrak, and D.S. Evans, Linear transport theory of auroral proton precipitation: a comparison with observations, *J. Geophys. Res.*, **92**, 5920–5932, 1987.

Benson, R.F., P. Bauer, L.H. Brace, H.C. Carlson, J. Hagen, W.B. Hanson, W.R. Hoegy, M.R. Torr, R.H. Wand, and V.B. Wickwar, Electron and ion temperatures - A comparison of ground based incoherent scatter and AE-C measurements, *J. Geophys. Res.*, **82**, 36–42, 1977.

Boies, M.T., R.C. Benson, J.D. Kinnison, J.S. Morgan, T.E. Phillips, O.M. Uy, and W. Wilkinson, Comparative sensor calibration: Mid-course Space Experiment (MSX) neutral mass spectrometer and total pressure sensor, *Proc. SPIE*, **2261**, 208–217, 1994.

Bougeret, J.-L., M.L. Kaiser, P.J. Kellogg, R. Manning, K. Goetz, S.J. Monson, N. Monge, L. Friel, C.A. Meetre, C. Perche, L. Sitruk, and S. Hoang, Waves: The radio and plasma wave investigation on the Wind spacecraft, *Space Sci. Rev.*, **71**, 231–263, 1995.

Brace, L.H., W.R. Hoegy, and R.F. Theis, Solar EUV measurements at Venus based on photoelectron emission from the Pioneer Venus Langmuir probe., *J. Geophys. Res.*, **93**, 7282–7296, 1988.

Brace, L.H., H.C. Carlson, and K.K. Mahajan, Radar backscatter and rocket probe measurements of electron temperature over Arecibo, *J. Geophys. Res.*, **74**, 1883–1885, 1969.

Brace, L.H. and J.A. Findlay, Comparison of cylindrical electrostatic probe measurements on Alouette II and Explorer 31 satellites, *Proc. IEEE*, **57**, 1057–1060, 1969.

Brace, L.H., G.R. Carignan, and J.A. Findlay, Evaluation of ionospheric electron temperature measurements by cylindrical probes, *Space Res.*, **11**, 1079–11051, 1971.

Brace, L.H., Langmuir probe measurements in the ionosphere, in *Measurement Techniques for Space Plasmas: Particles*, R. Pfaff, J. Borovsky, and D.T. Young, Eds., Geophys. Monogr. Ser., **103**, American Geophysical Union, Washington, D.C., 23–35, 1998.

Carlson, C.W., J.P. McFadden, R.E. Ergun, M. Temerin, W. Peria, F.S. Mozer, D.M. Klumpar, E.G. Shelley, W.K. Peterson, E. Möbius, R. Elphic, R. Strangeway, C.A. Cattell, and R. Pfaff, FAST observations in the downward auroral current region: Energetic upgoing electron beams, parallel potential drops, and ion heating, *Geophys. Res. Lett.*, **25**, 2017–2020, 1998.

Carlson, C.W. and J.P. McFadden, Design and applications of imaging plasma instruments, in *Measurement Techniques in Space Plasmas: Particles*, R.-Pfaff, J.-Borovsky, and D.T.-Young, Eds., Geophys. Monogr. Ser., **102**, American Geophysical Union, Washington, D.C., 125–140, 1998.

Carlson, C.W., J.P. McFadden, P. Turin, D.W. Curtis, and A. Magoncelli, The electron and ion plasma experiment for FAST, *Space Sci. Rev.*, **98**, 33–66, 2001.

Chereji, I., G. Toderean, V. Mercea, and V. Istomin, Device for in-flight calibration of mass spectrometer, *Space Sci., Instrum.*, **4**, 107–110, 1978.

Chua D., G. Parks, M. Brittnacher, W. Peria, G. Germany, J. Spann, and C. Carlson, Energy characteristics of auroral electron precipitation: A comparison of substorms and pressure pulse related auroral activity, *J. Geophys. Res.*, **106**, 5945–5956, 2001.

Coplan M.A., F. Ipavich, J. King, K.W. Ogilvie, D.A. Roberts, and A.J. Lazarus, Correlation of solar wind parameters between SOHO and Wind, *J. Geophys. Res.*, **106**, 18615–18624, 2001.

Dichter, B.K., J.O. McGarity, M.R. Oberhardt, V.T. Jordanov, D.J. Sperry, A.C. Huber, J.A. Pantazis, E.G. Mullen, G. Ginet, and S.G. Gussenhoven, Compact Environmental Anomaly Sensor (CEASE): A novel spacecraft instrument for in situ measurements of environmental conditions, *IEEE Trans. Nucl. Sci.*, **45**, 2758–2764, 1998.

Dichter, B.K. and S. Woolf, Grazing angle proton scattering: effects on Chandra and XMM-Newton X-ray telescopes, *IEEE Trans. Nucl. Sci.*, **50**, 2292–2295, 2003.

Donley, J.L., L.H. Brace, J.A. Findlay, J.H. Hoffman, and G.L. Wrenn, Comparison of results of Explorer XXXI direct measurement probes, *Proc. IEEE*, **57**, 1078–1084, 1969.

Eraker, J.H., Origins of the low-energy relativistic interplanetary electrons, *Astrophys. J.*, **257**, 862–880, 1982.

Escoubet, C.P., A. Pedersen, R. Schmidt, and P.A. Lindqvist, Density in the magnetosphere inferred from ISEE 1 spacecraft potential, *J. Geophys. Res.*, **102**, 17595–17609, 1997.

Etcheto, J. and A. Saint-Marc, Anomalously high plasma densities in the plasma sheet boundary layer, *J. Geophys. Res.*, **90**, 5338–5344, 1985.

Evans, D.S. and M.S. Greer, Polar Orbiting Environmental Satellite Space Environment Monitor-2: Instrument descriptions and archive data documentation, NOAA Technical Memorandum, **OAR SEC-93**, 2000.

Fennell, J.F., Description of P78-2/SCATHA/ satellite and experiments, *The IMS Source Book: Guide to the International Magnetospheric Study Data Analysis*, C.T. Russell and D.J. Southwood, Eds., American Geophysical Union, Washington, D. C., 65–81, 1982.

Frey, H.U., S.B. Mende, C.W. Carlson, J.C. Gérard, B. Hubert, J. Spann, R. Gladstone, and T.J. Immel, The electron and proton aurora as seen by IMAGE-FUV and FAST, *Geophys. Res. Lett*, **28**, 1135–1138, 2001.

Frey, H.U., S.B. Mende, T.J. Immel, J.-C. Gérard, B. Hubert, S. Habraken, J. Spann, G.R. Gladstone, D.V. Bisikalo, and V.I. Shematovich, Summary of quantitative interpretation of IMAGE far ultraviolet auroral data, *Space Sci. Rev.*, **109**, 255–283, 2003.

Fritz, T.A. and J.R. Cessna, ATS-6 NOAA low energy proton experiment, *IEEE Trans. Aerospace and Electronic Sys.*, **AES-11**, No. 6, 1145–1154, 1975.

Fuller-Rowell, T.J. and D.S. Evans, Height-integrated Pedersen and Hall conductivity patterns inferred from the TIROS-NOAA satellite data, *J. Geophys. Res.*, **92**, 7606–7618, 1987.

Galli, A., P. Wurz, H. Lammer, H.I.M. Lichtenegger, R. Lundin, S. Barabash, A. Grigoriev, M. Holmström, and H. Gunell, The hydrogen exospheric density profile measured with

ASPERA-3/NPD, *Space Sci. Rev.*, **126**, 447–467, 2006.

Gao, R.S., P.S. Gibner, J.H. Newman, K.A. Smith, and R.F. Stebbings: Absolute and angular efficiencies of a microchannel-plate position-sensitive detector, *Rev. Sci Instrum.*, **55**, 1756–1759, 1984.

Gérard, J.-C., B. Hubert, M. Meurant, V.I. Shematovich, D.V. Bisikalo, H. Frey, S. Mende, G.R. Gladstone, and C.W. Carlson, Observation of the proton aurora with IMAGE FUV imager and simultaneous ion flux in-situ measurements, *J. Geophys. Res.*, **106**, 28939–28948, 2001.

Gloeckler, G., J. Geiss, H. Balsiger, L.A. Fisk, F. Gliem, F.M. Ipavich, K.W. Ogilvie, W. Stüdemann, and B. Wilken, The ISPM Solar-Wind Ion Composition Spectrometer, *ESA Special Publication*, **SP-1050**, ESA Publications Division, Noordwijk, 77–103, 1983.

Gold, R.E., S.M. Krimigis, S.E. Hawkins III, D.K. Haggerty, D.A. Lohr, E. Fiore, T.P. Armstrong, G. Holland, and L.J. Lanzerotti, Electron, proton, and alpha monitor on the Advanced Composition Explorer spacecraft, *Space Sci. Rev.*, **86**, 541–562, 1998.

Goruganthu, R.R. and W.G. Wilson, Relative electron detection efficiency of microchannel plates from 0-3 keV, *Rev. Sci. Instrum.*, **55**, 2030–2033, 1984.

Hedin, A.E., H.B. Niemann, W.T. Kasprzak, and A. Seiff, Global Empirical Model of the Venus Thermosphere, *J. Geophys. Res.*, **88**, 73–83, 1983.

M.G. Henderson, M.F. Thomsen, R. Skoug, M.H. Denton, R. Harper, H.O. Funsten, and C.J. Pollock, Calculation of IMAGE/MENA geometric factors and conversion of images to units of integral and differential flux, *Rev. Sci. Instrum.*, **76**, 043303-1–043303-24, 2005.

Hirahara, M., T. Mukai, T. Terasawa, S. Machida, Y. Saito, T. Yamamoto, and S. Kokubun, Cold dense ion flows with multiple components observed in the distant tail lobe by Geotail, *J. Geophys. Res.*, **101**, 7769–7784, 1996.

Hoffman, J.H., R.R. Hodges, W.W. Wright, V.A. Blevins, K.D. Duerksen, and L.D. Brooks, Pioneer Venus Sounder Probe Neutral Gas Mass Spectrometer, *IEEE Trans. Geosci. Remote Sens.*, **GE-18**, 80–84, 1980a.

Hoffman, J.H., K. Pelka, U. von Zahn, D. Krankowsky, and D. Linkert, The Pioneer Venus Bus Neutral Gas Mass Spectrometer, *IEEE Trans. Geosci. Remote Sens.*, **GE-18**, 122–126, 1980b.

Hubert, B., J.C. Gérard, D.S. Evans, M. Meurant, S.B. Mende, H.U. Frey, and T.J. Immel, Total electron and proton energy input during auroral substorms: remote sensing with IMAGE-FUV, *J. Geophys. Res.*, **107**, SMP 15-1 to SMP 15-12, 2002.

Ipavich, F.M., A.B. Galvin, S.E. Lasley, J.A. Paquette, S. Hefti, K.-U. Reiche, M.A. Coplan, G. Gloeckler, P. Bochsler, D. Hovestadt, H. Grünwaldt, M. Hilchenbach, F. Gliem, W.I. Axford, H. Balsiger, A. Bürgi, J. Geiss, K.C. Hsieh, R. Kallenbach, B. Klecker, M.A. Lee, G.G. Managadze, E. Marsch, E. M"obius, M. Neugebauer, M. Scholer, M.I. Verigin, B. Wilken, and P. Wurz, Solar wind measurements with SOHO: The CELLAS/MTOF proton monitor, *J. Geophys. Res.*, **103**, 17205–17214, 1998.

Issautier, K., R.M. Skoug, J.T. Gosling, S.P. Gary, and D.J. McComas, Detailed comparison between the URAP and SWOOPS experiments, *J. Geophys. Res.*, **106**, 15665–15675, 2001.

Johnstone, A.D., A.J. Coates, B. Wilken, W. Studemann, W. Weiss, R.C. Ireli, V. Formisano, H. Borg, S. Olsen, J.D. Winningham, D.A. Bryant, and S.J. Kellock, The Giotto three-dimensional positive-ion analyzer, *J. Phys. E*, **20**, 795–805, 1987.

Johnstone, A.D., C. Alsop, S. Burge, P.J. Carter, A.J. Coates, A.J. Coker, A.N. Fazakerley, M. Grande, R.A. Gowen, C. Gurgiolo, B.K. Hancock, B. Narheim, A. Preece, P.H. Sheather, J.D. Winningham, and R.D. Woodliffe, Peace: a Plasma Electron and Current Experiment, *Space Sci. Rev.*, **79**, 351–398, 1997.

Kasper, J.C., A.J. Lazarus, J.T. Steinberg, K.W. Ogilvie, and A. Szabo, Physics-based test to identify the accuracy of solar wind ion measurements: A case study with the Wind Faraday cup, *J. Geophys. Res.*, **111**, doi:10.1029/2005JA011442, 2006.

Kasprzak, W.T., A.E. Hedin, H.B. Niemann, and N.W. Spencer, Atomic nitrogen in the upper atmosphere of Venus, *Geophys. Res. Lett.*, **7**, 106–108, 1980.

Kasprzak, W.T., H.B. Niemann, A.E. Hedin, S.W. Bougher, and D.M. Hunten, Neutral composition measurements by the Pioneer Venus neutral mass spectrometer during Orbiter re-entry, *Geophys. Res. Lett.*, **20**, 2747–2750, 1993.

Kasprzak, W.T., H. Niemann, D. Harpold, J. Richards, H. Manning, E. Patrick, and P. Mahaffy, Cassini Orbiter ion and neutral mass spectrometer instrument, *Proc. SPIE*, **2803**, 129–140, 1996.

Keller, C.A. and B.H. Cooper, Quantitative detection of low energy positive and negative ions with a channel electron multiplier, *Rev. Sci. Instrum.*, **67**, 2760–2764, 1996.

Klumpar, D.M., E. Möbius, L.M. Kistler, M. Popecki, E. Hertzberg, K. Crocker, M. Granoff, Li Tang, C.W. Carlson, J. McFadden, B. Klecker, F. Eberl, E. Künneth, H. Kästle, M. Ertl, W.K. Peterson, E.G. Shelley, and D. Hovestadt, The Time-of-flight Energy, Angle, Mass Spectrograph (TEAMS) experiment for FAST, *Space Sci. Rev.*, **98**, 197–219, 2001.

Knoll, G.F., *Radiation Detection and Measurement*, John Wiley & Sons, New York, 2000.

Krehbiel, J.P., L.H. Brace, R.F. Theis, W.H. Pinkus, and R.B. Kaplan, The Dynamics Explorer Langmuir probe instrument, *Space Sci. Instr.*, **5**, 493–502, 1981.

Lagg, A., N. Krupp, S. Livi, J. Woch, S.M. Kirmigis, and M.K. Dougherty, Energetic particle measurements during the Earth swing-by of the Cassini spacecraft in August 1999, *J. Geophys. Res.*, **106**, 30209–30222, 2001.

Larson, D.E., R.P. Lin, and J. Steinberg, Extremely cold electrons within the January 1997 magnetic cloud, *Geophys. Res. Lett.*, **27**, 157–160, 2000.

Lees, J.E., G.W. Fraser, and J.F. Pearson: 1990, After emission in Microchannel Plate detectors, in *EUV, X-Ray, and Gamma-Ray Instrumentation for Astronomy*, O.H. Siegmund, H.S. Hudson, Eds., *Proc. SPIE*, **1344**, 333–339, 1990.

Lemaire, J.E. and K.I. Gringauz, with contributions from D.L. Carpenter and V. Bassolo, *The Earth's Plasmasphere*, Cambridge Atmospheric and Space Science Series, Cambridge University Press, 1998.

Lin, R.P., K.A. Anderson, S. Ashford, C. Carlson, D. Curtis, R. Ergun, D. Larson, J. McFadden, M. McCarthy, G.K. Parks, H. Rème, J.M. Bosqued, J. Coutelier, F. Cotin, C. d'Uston, K.-P. Wenzel, T.R. Sanderson, J. Henrion, J.C. Ronnet, and G. Paschmann: A three-dimensional plasma and energetic particle experiment for the Wind spacecraft, *Space Sci. Rev.*, **71**, 125–153, 1995.

Lin, R.P., D. Larson, T. Phan, R. Ergun, J. McFadden, K. Anderson, C. Carlson, M. McCarthy, G.K. Parks, R. Skoug, R. Winglee, H. Rème, N. Lormant, J.M. Bosqued, C. d'Uston, T.R. Sanderson, and K.-P Wenzel, Wind observations of suprathermal particles in the solar wind, in *Geospace Mass and Energy Flow: Results From the International Solar-Terrestrial Physics Program*, J.L. Horwitz, D.L. Gallagher, and W.K. Peterson, Eds., Geophys. Monogr. Ser., **104**, 1–12, American Geophysical Union, Wash-

ington, D.C., 1998.

Lin, C.S. and R.A. Hoffman, Characteristics of the inverted-V event, *J. Geophys. Res.*, **84**, 1514–1524, 1979.

Lummerzheim D., M. Brittnacher, D. Evans, G.A. Germany, G.K. Parks, M.H. Rees, and J.F. Spann, High time resolution study of the hemispheric power carried by energetic electrons into the ionosphere during the May 19/20, 1996 auroral activity, *Geophys. Res. Lett.*, **24**, 987–990, 1997.

Mahaffy, P.R., personal communication, Code 699, Goddard Space Flight Center: Mahaffy, P.R., W.T. Kasprzak, D. Harpold, H.B. Niemann, R. Bitzel, B. Block, J. Demick, S. Feng, C. Gunderson, S. Leake, J. Maurer, R. Miller, T. Owen, E. Patrick, M. Paulkovich, E. Raaen, J. Richards, F. Tan, S. Schwinger, S. Way, and J. Winchester, The Neutral Gas and Ion Mass Spectrometer for the CONTOUR Mission, originally prepared for *Space Sci. Rev.*, 2002.

Maksimovic, M., S. Hoang, N. Meyer-Vernet, M. Moncuquet, J.-L. Bougeret, J.L. Phillips, and P. Canu, Solar wind electron parameters from quasi-thermal noise spectroscopy and comparison with other measurements on Ulysses, *J. Geophys. Res*, **100**, 19881–19892, 1995.

Malter, L., Thin film field emission, *Phys. Rev.*, **50**, 48–58, 1936.

Martin, A., J. Vallerga, J. McPhate, and O. Siegmund, Further scrubbing and quantum efficiency results of the HST-COS Far-Ultraviolet Detector, *Proc. SPIE*, **4854**, 526–531, 2003.

McClure, J.P., W.B. Hanson, A.F. Nagy, R.J. Cicerone, L.H. Brace, M. Baron, P. Bauer, H.C. Carlson, J.V. Evans, G.N. Taylor, and R.F. Woodman, Comparisons of Te and Ti from OGO-6 and from various incoherent scatter radars, *J. Geophys. Res.*, **78**, 197–205, 1973.

McEntire, R.W., E.P. Keath, D.E. Fort, A.T.Y. Lui, and S.M. Krimigis, The Medium-Energy Particle Analyzer (MEPA) on the AMPTE CCE Spacecraft, *IEEE Trans. Geosci. Remote. Sens.*, **GE-23**, 230–233, 1985.

McFadden, J.P., C.W. Carlson, R.E. Ergun, F.S. Mozer, M. Temerin, W. Peria, D.M. Klumpar, E.G. Shelley, W.K. Peterson, E. Möbius, L. Kistler, R. Elphic, R. Strangeway, C. Cattell, and R. Pfaff, Spatial structure and gradients of ion beams observed by FAST, *Geophys. Res. Lett.*, **25**, 2021–2024, 1998a.

McFadden, J.P., C.W. Carlson, R.E. Ergun, C.C. Chaston, F.S. Mozer, M. Temerin, D.M. Klumpar, E.G. Shelley, W.K. Peterson, E. Möbius, L. Kistler, R. Elphic, R. Strangeway, C. Cattell, and R. Pfaff, Electron modulation and ion cyclotron waves observed by FAST, *Geophys. Res. Lett.*, **25**, 2045–2048, 1998b.

McFadden, J.P., C.W. Carlson, R.E. Ergun, D.M. Klumpar, and E. Möbius, Ion and electron characteristics in auroral density cavities associated with ion beams: No evidence for cold ionospheric plasma, *J. Geophys. Res.*, **104**, 14671–14682, 1999.

Miller, K.L., W.C. Knudsen, and K. Spenner, The dayside Venus ionosphere. I. Pioneer Venus retarding potential analyzer experimental observations, *Icarus*, **57**, 386–409, 1984.

Moore, T.E., D.J. Chornay, M.R. Collier, F.A. Herrero, J. Johnson, M.A. Johnson, J.W. Keller, J.F. Laudadio, J.F. Lobell, K.W. Ogilvie, P. Rozmarynowski, S.A. Fuselier, A.G. Ghielmetti, E. Hertzberg, D.C. Hamilton, R. Lundgren, P. Wilson, P. Walpole, T.M. Stephen, B.L. Peko, B. van Zyl, P. Wurz, J.M. Quinn, and G.R. Wilson, The low-energy neutral atom imager for IMAGE, *Space Sci. Rev.*, **91**, 155–195, 2000.

Morrow, M.L., W.H. Morrow, and L.N. Majorana, UV and VUV sources for in-flight calibration of space experiments, Space Astronomical Telescopes and Instruments II, *Proc. SPIE*, **1945**, 478–483, 1993.

Mukai, T., S. Machida, Y. Saito, M. Hirahara, T. Terasawa, N. Kaya, T. Obara, M. Ejiri, and A. Nishida, The Low Energy Particle (LEP) instrument onboard the Geotail satellite, *J. Geomag. Geoelectr.*, **46**, 669–692, 1994.

Niemann, H.B., J.R. Booth, J.E. Cooley, R.E. Hartle, W.T. Kasprzak, N.W. Spencer, S.H. Way, D.M. Hunten, and G.R. Carignan, Pioneer Venus Orbiter neutral gas mass spectrometer experiment, *IEEE Trans. Geosci. Electr. Remote Sens.*, **GE-18**, 60–65, 1980a.

Niemann, H.B., W.T. Kasprzak, A.E. Hedin, D.M. Hunten, and N.W. Spencer, Mass Spectrometric Measurements of the Thermosphere and Exosphere of Venus, *J. Geophys. Res.*, **85**, 7817–7827, 1980b.

Niemann, H.B., S. Atreya, S.J. Bauer, K. Biemann, B. Block, G. Carignan, T. Donahue, L. Frost, D. Gautier, D. Harpold, D. Hunten, G. Israel, J. Luhnine, K. Mauersberger, T. Owen, F. Raulin, J. Richards, and S. Way, The gas chromatograph mass spectrometer aboard Huygens, *ESA Special Publication*, **SP-1177**, ESA Publications Division, Noordwijk, 1997.

Niemann, H.B., S.K. Atreya, S.J. Bauer, K. Biemann, B. Block, G.R. Carignan, T.M. Donahue, R.L. Frost, D. Gautier, J.A. Haberman, D. Harpold, D.M. Hunten, G. Israel, J.I. Luhnine, K. Mauersberger, T.C. Owen, F. Raulin, J.E. Richards, and S.H. Way, The gas chromatograph mass spectrometer for the Huygens Probe, *Space Sci. Rev.*, **104**, 553–591, 2002.

Nier, A.O., W.E. Potter, D.R. Hickman, and K. Maurersberger, The open-source neutral-mass spectrometer on Atmosphere Explorer-C, -D, and -E, *Radio Sci.*, **8**, 271–276, 1973.

Oberheide, J., P. Wilhelms, and M. Zimmer, New results on the absolute ion detection efficiencies of a microchannel plate, *Meas. Sci. Technol.*, **8**, 351-354, 1997.

Ogilvie, K.W., D.J. Chornay, R.J. Fritzenreiter, F. Hunsaker, J. Keller, J. Lobell, G. Miller, J.D. Scudder, E.C. Sittler, R.B. Torbert, D. Bodet, G. Needell, A.J. Lazarus, J.T. Steinberg, J.H. Tappan, A. Mavretic, and E. Gergin, SWE, A comprehensive plasma instrument for the Wind spacecraft, *Space Sci. Rev.*, **71**, 55–77, 1995.

Outlaw, R.A. and R.E. Stell, An In-Situ, Metal-Gas, Secondary Standard Assembly for Ultrahigh-Vacuum Instrumentation, *J. Vac. Sci. Technol.*,**8**, 608–610, 1971.

Paschmann, G., H. Loidl, P. Obermayer, M. Ertl, P. Laborenz, N. Sckopke, W. Baumjohann, C.W. Carlson, and D.W. Curtis, The plasma instrument for AMPTE IRM, *IEEE Trans. Geosci. Remote Sens.*, **GE-23**, 262–266, 1985.

Peart, B. and M.F.A. Harrison, Measurements of the ion detection efficiencies of Johnston electron multipliers, *J. Phys. E: Sci. Instrum.*, **14**, 1374, 1981.

Rème, H., F. Cotin, A. Cros, J.L. Medale, and J.-A. Sauvaud, The Giotto electron plasma experiment, *J. Phys. E - Sci. Instrum.*, **20**, 721–731, 1987.

Rème, H., M. Bosqued, J.A. Sauvaud, A. Dros, J. Dandouras, C. Aoustin, Ch. Martz, J.L. Medale, J. Rouzaud, E. Möbius, K. Crocker, M. Granoff, L.M. Kistler, D. Hovestadt, B. Klecker, G. Paschmann, M. Ertl, E. Künneth, C.W. Carlson, D.W. Curtis, R.P. Lin, J.P. McFadden, J. Croyle, V. Formisano, M. Di Lellis, R. Bruno, M.B. Bavassano-Cattaneo, B. Baldetti, G. Chionchio, E.G. Shelley, A.G. Ghielmetti, W. Lennartsson, A. Korth, H. Rosenbauer, I. Szemerey, R. Lundin, S. Olsen, G.K. Parks,

M. McCarthy, and H. Balsiger, The Cluster ion spectrometry experiment, Cluster: Mission, Payload and Supporting Activities, W. R. Burke, Ed., European Space Agency, Paris, *ESA Special Publication*, **SP-1159**, ESA Publications Division, Noordwijk, 133–161, 1993.

Rème, H., J.M. Bosqued, J.A. Sauvaud, A. Cros, J. Dandouras, C. Aoustin, J. Bouyssour, Th. Camus, J. Cuvilo, C. Martz, J.L. Medale, H. Perrier, D. Romefort, J. Rouzaud, C. d'Uston, E. Möbius, K. Crocker, M. Granoff, L.M. Kistler, M. Popecki, D. Hovestadt, B. Klecker, G. Paschmann, M. Scholer, C.W. Carlson, D.W. Curtis, R.P. Lin, J.P. McFadden, V. Formisano, E. Amata, M.B. Bavassano-Cattaneo, P. Baldetti, G. Belluci, R. Bruno, G. Chionchio, A. Di Lellis, E.G. Shelley, A.G. Ghielmetti, W. Lennartsson, A. Korth, H. Rosenbauer, R. Lundin, S. Olsen, G.K. Parks, M. McCarthy, and H. Balsiger, The Cluster Ion Spectrometer (CIS) experiment, *Space Sci. Rev.*, **79**, 303–350, 1997.

Robertson, D.W., Building a new kind of graded-Z shield for Swift's burst alert telescope, *Proc. SPIE*, **4851**, 1374–1381, 2003.

Rosenbauer, H., R. Schwenn, H. Miggenrieder, B. Meyer, H. Grünwaldt, K.-H. Mühlhäuser, H. Pellkofer, and J.H. Wolfe, Die Instrumente des Plasmaexperiments auf den HELIOS-Sonnensonden, **BMFT-FB-W 81-015**, Max-Planck-Institut für Aeronomie, Katlenburg-Lindau, 1981.

Rymer, A.M., A.J. Coates, K. Svenes, G.A. Abel, D.R. Linder, B. Narheim, M. Thomsen, and D.T. Young, Cassini Plasma Spectrometer Electron Spectrometer measurements during the Earth swing-by on August 18, 1999, *J. Geophys. Res*, **106**, 30117–30198, 2001.

Sauvaud, J.-A., R. Lundin, H. Rème, J.P. McFadden, C. Carlson, G.K. Parks, E. Möbius, L.M. Kistler, B. Klecker, E. Amata, A.M. Di Lellis, V. Formisano, J.M. Bosqued, I. Dandouras, P. Décréau, M. Dunlop, L. Eliasson, A. Korth, B. Lavraud, and M. McCarthy, Intermittent thermal plasma acceleration linked to sporadic motions of the magnetopause, first Cluster results, *Ann. Geophys.*, **19**, 1523–1532, 2001.

Schwenn, R., H. Rosenbauer, and H. Miggenrieder, The plasma experiment on board Helios, *Raumfahrtforschung*, **19**, 226–232, 1975.

Scialdone, J.J., Self-Contamination and Environment of an Orbiting Satellite,*J. Vac. Sci. Technol.*, **9(2)**, 1007–1015, 1972.

Scialdone, J.J., A.E. Hedin, and C.J. Rice, Comparison of Satellite Self-Contamination Experiments and Scattering Return Flux Calculations, *J. Geophys. Res.*, **83**(A1), 195–198, 1978.

Scudder, J.D., F. Hunsaker, G. Miller, J. Lobell, T. Zawistowski, K.W. Ogilvie, J. Keller, D. Chornay, F. Herrero, R. Fitzenreiter, D. Fairfield, J. Needell, D. Bodet, J. Googins, C. Kletzing, R. Torbert, J. Vandiver, R. Bentley, W. Fillius, C. McIlwain, E. Whipple, and A. Korth, Hydra - A 3-Dimensional Electron and Ion Hot Plasma Instrument for the Polar Spacecraft of the GGS Mission, *Space Sci. Rev.*, **71**, 459–495, 1995.

Scudder, J.D., P.A. Puhl-Quinn, F.S. Mozer, K.W. Ogilvie, and C.T. Russell, Generalized Walén tests through Alfvén waves and rotational discontinuities using electron flow velocities, *J. Geophys. Res.*, **104**, 19817–19834, 1999.

Scudder, J.D., X. Cao, and F.S. Mozer, Photoemission current-spacecraft voltage relation: Key to routine, quantitative low-energy plasma measurements, *J. Geophys. Res.*, **105**, 21281–21294, 2000.

Seki, K., M. Nirahara, M. Hoshino, T. Terasawa, R.C. Elphic, Y. Saito, T. Mukai, H. Hayakawa, H. Kojima, and H. Matsumoto: Cold ions in the hot plasma sheet of Earth's magnetotail, *Nature*, **422**, 589–592, 2003.

Sharber, J.R., R. Link, R.A. Frahm, J.D. Winningham, D. Lummerzheim, M.H. Rees, D.L. Chenette, and E.E. Gaines, Validation of UARS particle environment monitor electron energy deposition, *J. Geophys. Res.*, **101**, 9571–9582, 1996.

Shelley, E.G., R.D. Sharp, R.G. Johnson, J. Geiss, P. Eberhardt, H. Balsiger, G. Haerendel, and H. Rosenbauer, Plasma composition experiment on ISEE-A, *IEEE Trans. Geosci. Electr.*, **GE-16**, 266–270, 1978.

Smart, D.F. and M.A. Shea, Galactic cosmic radiation and solar energetic particles, in *Handbook of Geophysics and the Space Environment*, A. S. Jursa, Ed., National Technical Information Service, Springfield, VA,, 6-1 – 6-29, 1985.

Stassinoupoulos, E.G., High-Energy Radiation Background in Space, A.C. Rester and J.I. Trombka, Eds., *AIP Conf. Proc.*, **186**, American Institute of Physics, New York, 1989.

Stickel, R.E., Jr., F.G. Kellert, K.A. Smith, F.B. Dunning, and R.F. Stebbings, Low energy ion counting efficiency of a Johnston electron multiplier, *Rev. Sci. Instrum.*, **51**, 396–397, 1980.

Strangeway, R.J., L. Kepko, R.C. Elphic, C.W. Carlson, R.E. Ergun, J.P. McFadden, W.J. Peria, G.T. Delory, C.C. Chaston, M. Temerin, C.A. Cattell, E. Möbius, L.M. Kistler, D.M. Klumpar, W.K. Peterson, E.G. Shelley, and R.F. Pfaff, FAST observations of VLF waves in the auroral zone: Evidence of very low plasma densities, *Geophys. Res. Lett.*, **25**, 2065–2068, 1998.

Su, Y.J., J.L. Horwitz, T.E. Moore, B.L. Giles, M.O. Chandler, P.D. Craven, M. Hirahara, and C.J. Pollock, Polar wind survey with the thermal ion dynamics experiment plasma source instrument suite aboard POLAR, *J. Geophys. Res.*, **103**, 29305–29337, 1998.

Thorness, R.B. and A.O. Nier, Device for Remote Opening of a Vacuum System, *Rev. Space Sci. Instrum.*, **3**3, 1005–1007, 1962.

Tsuruda, K., H. Hayakawa, M. Nakamura, T. Okada, A. Matsuoka, F.S. Mozer, and R. Schmidt, Electric field measurements on the GEOTAIL satellite, *J. Geomag. Geoelectr.*, **46**, 693–671, 1994.

Vallat, C., I. Dandouras, P.C. Brandt, R. DeMajistre, D.G. Mitchell, E.C. Roelof, H. Rème, J.-A. Sauvaud, L. Kistler, C. Mouikis, M. Dunlop, and A. Balogh, First comparisons of local ion measurements in the inner magnetosphere with energetic neutral atom magnetospheric image inversions: Cluster-CIS and IMAGE-HENA observations, *J. Geophys. Res.*, **109**, A04213, doi:10.1029/2003JA010224, 2004.

von Zahn, U., F.-J. Lubken, and C. Putz, BUGATTI experiments: Mass spectrometric studies of lower thermosphere eddy mixing and turbulence, *J. Geophys. Res.*, **95**, 7443–7465, 1990.

Waite, Jr., J.H., W.S. Lewis, W.T. Kasprzak, V.G. Anicich, B.P. Block, T.C. Cravens, G.G. Fletcher, W.-H. Ip, J.G. Luhmann, R.L. McNutt, H.B. Niemann, R.L. Thorpe, and R.V. Yelle, The Cassini Ion and Neutral Mass Spectrometer (INMS) investigation, *Space Sci. Rev.*,**114**, 113–231, 2004.

Weiss, W. and B. Wilken, The Giotto implanted ion spectrometer, (ISS): Principles of the electronic operation and data collection, *J. Phys. E: Sci. Instrum.*, **20**, 1510–1516, 1987.

Wilken, B., W.I. Axford, I. Daglis, P. Daly, W. Güttler, W.H. Ip, A. Korth, G. Kremser, S. Livi, V.M. Vasyliunas, J. Woch, D. Baker, R.D. Belian, J.B. Blake, J.F. Fennell, L.R. Lyons, H. Borg, T.A. Fritz, F. Gliem, R. Rathje, M. Grande, D. Hall, K. Kec-

suemety, S. McKenna-Lawlor, K. Mursula, P. Tanskanen, Z. Pu, I. Sandahl, E.T. Sarris, M. Scholer, M. Schultz, F. Søraas, and S. Ullaland, RAPID, The imaging energetic particle spectrometer on Cluster, *Space Sci. Rev.*, **79**, 399–473, 1997.

Williams, D.J., R.W. McEntire, S. Jaskulek, and B. Wilken, The Galileo energetic particle detector, *Space Sci. Rev.*, **60**, 385–412, 1992.

Williams, D.J., R.W. McEntire, C. Schlemm, A.T.Y Lui, G. Gloeckler, S.P. Christon, and F. Gliem, Geotail energetic particles and ion composition instrument, *J. Geomag. Geolectr.*, **46**, 39–57, 1994.

Witte, M., H. Rosenbauer, E. Kepler, H. Fahr, P. Hemmerich, H. Lauche, A. Loidl, and R. Zwick, The interstellar neutral-gas experiment on Ulysses, *Astron. Astrophys. Suppl. Ser.*, **92**, 333–348, 1992.

Witte, M., M. Banaszkiewicz, H. Rosenbauer, and D. McMullin, Kinetic temperature of interstellar neutral helium: updated results from the Ulysses/GAS-instrument, *Adv. Space Res.*, **34** 61–65, 2004.

Wüest, M. and P. Bochsler, Simulation of ion backscattering from rough surfaces, *Nucl. Instrum. Methods B*, **71**, 314–323, 1992.

Wurz, P., Detection of energetic neutral particles, in *The Outer Heliosphere: Beyond the Planets*, K. Scherer, H. Fichtner, and E. Marsch, Eds., Copernicus Gesellschaft e.V., Katlenburg-Lindau, 251–288, 2000.

Wurz, P., J. Scheer, and M. Wieser, Particle scattering off surfaces: application in space science, *J. Surf. Sci. Nanotechn.*, **4**, 394–400, 2006.

Young, D.T., J.E. Nordholt, and J.J. Hanley, Plasma Experiment for Planetary Exploration (PEPE), DS1 Technology Validation Reports, JPL Publication, **00-10**, Pasadena, CA, 2000.

Zurbuchen, T.H., P. Bochsler, and F. Scholze, Reflection of ultraviolet light at 121.6 nm from rough surfaces, *Opt. Eng.*, **34**, 1303–1315, 1995.

— 5 —

Summary and Outlook

MARTIN WÜEST[1], DAVID W. ROBINSON[2], AND DENNIS DECOSTE[3]
[1]*INFICON Ltd., Balzers, Liechtenstein*
[2]*National Physics Laboratory, Teddington, Middlesex, UK*
[3]*Jet Propulsion Laboratory, Pasadena, CA, USA*

5.1 Summary of Previous Chapters

Calibration is defined as a set of operations that establish, under specified conditions, the relationship between the values of quantities indicated by a measuring instrument or measuring system and the corresponding values realized by standards. Calibration of an instrument means determining by how much the instrument reading is in error by checking it against a measurement standard of known error.

Space physics particle instrumentation needs to be calibrated on the ground and in-flight to insure that the data can be properly interpreted.

On the ground, calibration is performed by exposing the instrument to a well characterized incident particle beam. Not only the nominal range of parameters the instrument is designed to measure should be calibrated but the instrument should also be exposed to out-of-band exposure such as higher energies, angles outside of the nominal field-of-view and susceptibility to ultraviolet radiation.

There are several challenges to laboratory calibration on the ground. The beam must be well characterized in energy, angle, mass and position. The particle flux must be uniform over the whole aperture area of the instrument to be calibrated. The beam must be very stable in time and space. One of the difficulties arises that in order to measure the incident particle flux the beam monitor is placed upstream in front of the instrument thereby blocking the incident beam and interrupting the beam detection by the device under test. A beam monitor placed outside of the field-of-view of the instrument to be calibrated is often in a region at the fringes of the beam where the beam is not very stable. This basically prevents the measuring of the same beam with a trusted reference detector and the instrument under test at the same time. Further, highly sensitive instruments are calibrated at flux levels too low to be detected with stable Faraday cup detectors. Present day windowless electron multiplier detectors are able to measure the low flux levels but are sensitive to degradation as a function of contamination and the amount of extracted charge. Windowless electron multipliers are therefore not very stable reference detectors. This makes it difficult to obtain a reliable absolute calibration traceable to a national measurement institute.

Calibration is still a time consuming process. It involves testing the instrument at component, subsystem and integrated level. It is important that the instrument is not only operated using a special calibration configuration to save time, but also in its full flight configuration exercising the full path of the data through data compression and telemetry. Very

seldom there is enough time available to calibrate all the desired points in parameter space. Usually only a subset can be calibrated for schedule and economic reasons. The number of calibration points is often further reduced since the available calibration time is cut due to development schedule slip and a fixed launch date. This increases the uncertainties as more parameters have to be interpolated or extrapolated. Calibration data should be evaluated preferably in near-real time to prevent losing valuable calibration time if something in the instrument or facility is not working properly. Computer simulation models should be used to obtain a thorough understanding of the actual flight instrument.

In flight the instrument performance degrades due to contamination (outgassing), environmental effects (atomic oxygen, radiation) or aging. One of the most sensitive parts in today's instrument are their detectors. Microchannel plate detectors degrade as function of the extracted charge. Solid-state detectors experience radiation damage which increases their noise and the lower energy detection threshold.

The goal of the in-flight calibration is to determine this instrument degradation. Calibration is then performed by comparing measurements taken with different bias voltage or discriminator threshold settings. If possible, the instrument data is compared with other sensors covering the same or at least a part of the same measurand on the same or on a different spacecraft. In-flight calibration is not easy, as no absolute calibration standard for particles exist in space and measuring the same physical quantity with two different spacecraft at the same environmental conditions is very challenging.

5.2 Future Calibration Needs

A particular problem in present day space physics instrumentation are the windowless electron multiplier detectors currently used in many space missions. They experience gain degradation as a function of extracted charge. It is essentially this detector degradation which prevents a stable calibration and which makes building standard candles so difficult. But at this time there are no other alternatives available for flight.

Basically, to improve sensor accuracy long-term stable detectors and in-flight calibration standards are needed and the traceability of the instrument and facility calibration to the national measurement institute need to be improved.

Methods at speeding up calibration need also to be found. In particular for the envisioned cluster missions, where tens or hundreds of the same instrument are deployed, current calibration methods will quickly be too time consuming and uneconomical.

The next two sections will present an attempt of possible solutions for the two topics.

5.3 Absolute Calibration and Traceability

This section focuses on the requirements of traceability to a measurement institute reference standard and methods of calibration transfer.

In order to improve on the calibration of space particle instruments one has to reflect on the traceability of the calibration and why calibration is needed in the first place.

Calibration is a process whereby the bounds of uncertainty of a particular measurement are established with respect to a pre-established absolute reference. This may be by comparing the measurements from one instrument with respect to another under the same

conditions or in relation to measuring the properties of a "known" specimen. Where the reference is to a realization of a quantity that is accepted as being the top level standard in a country's National Measurement Institute (NMI) (that has itself been intercompared with other NMI standards), this is a calibration directly to a primary standard. If the calibration is against a secondary standard which itself has been compared with a primary standard, then the measurements will have a known "unbroken chain of traceability" back up to the primary standard. In practice this is not always the case and if calibrations are carried out in a system where the traceable route to the primary realization at an NMI cannot be established, then the confidence in the measurement will be affected.

For the greatest confidence in any particular measurement, at any particular level of uncertainty, not only should the traceable chain be clearly established, but in addition the measurement strategies at each stage of the comparison chain should be agreed and understood. In other words, traceability is not the purchase of an artifact, but the demonstration of its use in a consistent way.

5.3.1 The Importance of Traceability to the Space Community

For the space industry, "getting it right first time" is an absolute requirement. There are no cost free second chances in launching and operating spacecraft for commercial, regulatory or scientific applications, and history has a catalog of operational failures to illustrate the point. This places high demands on the confidence that systems will operate correctly but also that the data they supply are correct and consistent. Confidence in the results is vital so that future research can be based on the measurements taken in space. Data obtained from various instruments on different spacecraft launched at different times are often integrated into models or maps. This can only realistically occur if all the data is fully quality assured and has associated with it a valid uncertainty statement.

End user customers of data from space need to have confidence that what they pay for is what they get. As the customer for space data moves from being national agencies and their scientists to companies and the public become the end users, as is the case in space weather, they will demand third party accredited quality standards, not supplier driven test plans. This is the experience of the terrestrial markets where competition between suppliers drives the need for measurement standards.

Space users now need "good data", not just "data". As a result "consumer" confidence in the use of space based systems will grow as they start to achieve a consistency of quality and reliability from a range of service providers. This may also be enhanced by some form of "quality stamp" for space data, akin to the accreditation of terrestrial calibration and testing activities by an accreditation service provider.

5.3.2 Lack of Adequate Standards

A particular problem in space physics is the lack of adequate standards for ionizing and charged particle radiation.

Standards are important in the area of space plasma measurements. There is evidence that data in the literature are inconsistent between experiments. We need strategies to improve the traceable calibration of such instruments. Standards in the general area of ionizing radiation for space is important also to predict the life of electronic components on satellite and for regulation compliance where human exposure occurs.

NMIs maintain a wide range of ionizing radiation facilities to support industry and health care services to enable regulations to be met. These facilities include gamma-ray, X-ray, neutron facilities, and accelerators.

These facilities are used to provide traceable links to primary ionizing radiation standards. Research at NMIs may also be able to help with providing a common traceable link for space research instruments where the levels of particle fluxes needed for a successful calibration are very low and are a challenge for traditional radiation calibration routes. Recent research on the use of superconducting non-contact ion current measurement at NPL provides a possible route for traceable measurements with quantum limited accuracy [*Hao et al.*, 2001a, 2002, 2003a, b]. For more details on this detector see Subsection 5.4.2.

5.3.3 Summary and Recommendation

It is clear from the above analysis that absolute measurements are a key to designing space qualified systems that are "right first time". Absolute measurement (at whatever level of uncertainty) can only be assured if an un-broken chain of traceability can be established and demonstrated, when calibrating instruments for use in space, or for use in validating and testing the performance of space instruments prior to launch.

Traceable standards (where there is a common approach linked to NMIs and consistent across nations), enables end users to have confidence in the reliability and consistency of data produced from space systems. This is essential if commercial markets for space data are to grow beyond the current (more limited) range of applications. The space industry can benefit from more than 100 years of activity by the network of NMIs in developing a globally harmonized system of measurement.

It is therefore recommended that National Measurement Institutes are involved at all levels in the validation of space instrumentation and ground test facilities - to access the benefits of established terrestrial standards programmes. This should involve identifying centers of excellence to quality assure space physics and other data.

5.4 Calibration Transfer Standard

There is a need for an easy transportable charged particle flux calibration standard. Such a transfer calibration standard would be calibrated at a NMI and transported to the calibration facility, where it would serve as a calibrated reference against which the facility beam monitor would be calibrated.

At high fluxes a simple Faraday cup with a bundled electrometer serves as a reasonably stable flux detector.

However, at lower fluxes where traditionally continuous electron multipliers or multichannel plates are used, the situation is already much more complicated. Those windowless electron multiplier obtain their secondary electron multiplication properties from their detector surfaces. These detector surfaces are easily contaminated by e.g. different amounts of water vapor or hydrocarbons in the air during transport or installation. The transfer standard would therefore need to be transported under vacuum and never exposed to atmosphere or poor vacuum conditions.

Even under clean conditions windowless electron multipliers degrade with time as the degradation is a function of the extracted charge. Regular calibrations against the national standard are therefore required to assure high confidence in the performance.

Recently, *Hao et al.* [2005b] have described an interesting device which eventually could prove useful as a detector in a beam monitor for the measurement of a charged particle beam. This device is a cryogenic transition-edge bolometric detector which is inherently capable of simultaneous detection and energy resolution of single particles. The incoming radiation causes dissociation of a number of Cooper-pairs, producing an almost simultaneous transient in the inductance. This induced change in inductance of the sensitive element is inductively coupled to a SQUID.

5.4.1 Cross-Calibration Between Facilities

All instruments and devices of a calibration facilities should carry a valid calibration traceable to a national measurement institute.

In order to facilitate the calibration of the beam parameters it is suggested to build an electrostatic analyzer with high energy and angle resolution which could be calibrated at a national measurement institute. Such a high resolution beam analyzer could consist of a 127°-sector electrostatic analyzer with narrow entrance and exit apertures to achieve a narrow field-of-view. The detector could be a continuous electron multiplier packaged together with its associated electronics.

It is suggested that a national measurement institute, a space agency or an enterprising company build a small series of such a high resolution beam analyzer and calibrate it at a national measurement institute or a designated reference facility. After calibration the instruments are distributed to the individual calibration facilities, where the high resolution beam monitor serves as a transfer standard to characterize the beam. Calibration would be maintained by regular common calibration campaigns where the instrument is sent back to the reference facility. Alternatively, a high fidelity standard could be sent on a round robin calibration campaign.

5.4.2 Non Beam Blocking Current Meter

Calibration facility beams can show some form of flux instability or slow drift in a parameter. Beam monitors are currently inserted into the beam to measure the beam flux. The beam monitor thereby blocks the beam to the instrument under calibration. Particle beams are usually not wide enough and not homogeneous enough to place a beam monitor at the fringes of the beam outside the field of view of the instrument. The fringes of the beam is also a place where the beam is more unstable. It is therefore difficult to obtain simultaneous flux measurement by a beam monitor measuring the incoming flux into the instrument and by the instrument under calibration. What is needed is a reference monitor that measures exactly the same flux that goes into the entrance aperture of the instrument under calibration. Such a beam monitor can therefore not block the incident particle beam. Either a remote sensing of the beam is required or the beam must pass through a hollow structure to be analyzed.

An interesting development in this regard is the current comparator described by [*Hao et al.*, 2001a, b, 2002, 2003a, b] (see Figure 5.1). Its operation is based on the Meissner effect in bulk superconductors. A charged particle beam is passed along the axis of a

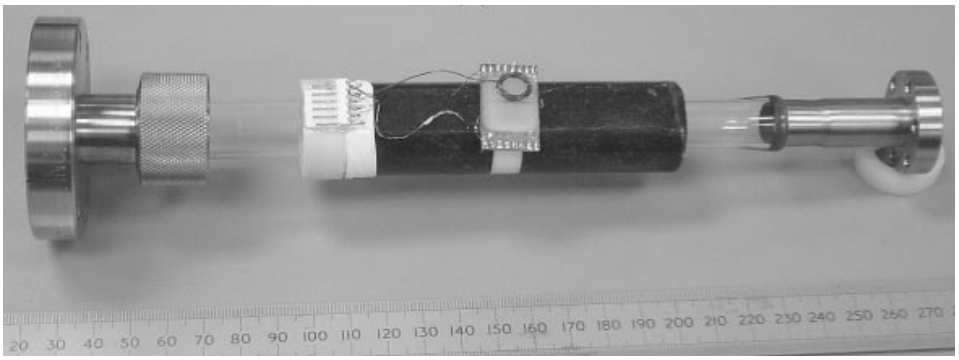

Figure 5.1: High temperature superconducting current concentrator as beam monitor. From *Hao et al.* [2003b].

superconducting tube and the Meissner effect causes a shielding current to flow in the opposite direction, along the inside surface of the tube, to screen the magnetic field arising from the charged particle beam from the interior of the bulk superconductor. This screening current returns along the outside surface of the tube, producing a magnetic field which can be detected by a SQUID. Such a prototype high temperature superconducting cryogenic current comparator with a high temperature superconducting planar gradiometer SQUID has been successfully demonstrated as a means of noninvasively sensing charged particle beams in the current range 1 μA–3.5 A. Its limiting sensitivity is presently estimated to be less than 0.1 nA or even 10 pA [*Hao et al.*, 2003b, 2005a]. If such sensitivities can be achieved in the future such a current comparator could become a very useful beam monitor design for calibration facilities.

5.4.3 Internal Reference Standard

In order to improve the in-flight calibration a reference standard is desired. Optical space instruments have stars that have been calibrated from the ground which serve as transfer standards. Remote sensing instruments have ground truth sites available for radiometric calibration. High energy instruments can carry radioactive sources with them (see Section 4.5) and neutral gas instruments can carry calibration gas sources (see Section 4.6) as internal in-flight calibration reference, but there is no such reference available to low and medium energy in situ space physics instrumentation.

5.5 New Techniques to Improve Calibration

Many instruments have already been built that have multiple sensor heads, e.g., IMAGE/MENA [*Pollock et al.*, 2000], Polar/Hydra [*Scudder et al.*, 1995], or are part of programmatic missions (a continuous program delivering the same instrument for several sequential missions), e.g., GOES, DMSP, TIROS/NOAA, NPOESS or LANL spacecraft. Further, multi-spacecraft missions are to become more common (e.g. Cluster II (4 spacecraft), THEMIS (5 spacecraft), or the planned Magnetospheric Multiscale Mission (originally planned as four spacecraft with four identical dual ion spectrometer instruments on

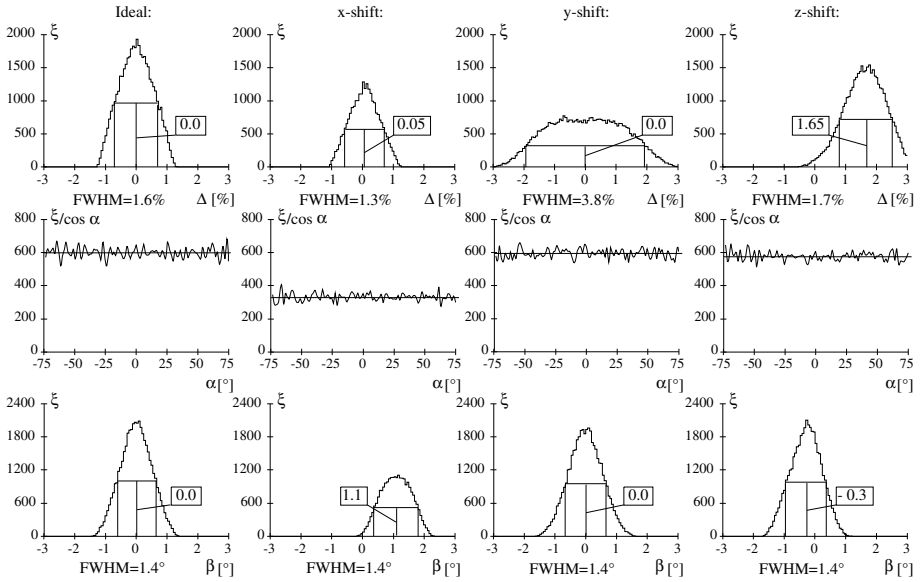

Figure 5.2: The energy, α- and β-distributions in an ideal case of a hemispheric electrostatic analyzer and in cases when a 60 μm misalignment in either x-, y-, or z-direction has occurred. FWHM values and averages of energy and β-distributions are shown. $\Delta = (E - E_0)/E_0$ where E_0 is the nominal kinetic energy. ξ is the number of transmitted particles per bin. The bin widths are $\mathrm{d}E = 0.06\,\%$, $\mathrm{d}\alpha = 1.5°$ and $\mathrm{d}\beta = 0.06°$. From *Vilppola* [1998].

each spacecraft for a total of 16 flight instruments). Some of these planned missions envision tens or even hundreds of instruments (e.g. Magnetospheric Constellation [*NASA*, 2001] with 30 to 100 nanosatellites, carrying magnetometers, plasma velocity and energetic particle analyzers). Today, calibration of a space instrument usually takes several weeks. There will not be sufficient time available at a single facility using standard one-at-a-time calibration methods to calibrate these large numbers within a reasonable time. The traditional options are then to either reduce the number of calibration points, work faster, use increased automation or split the calibration up by using calibration time at different facilities in parallel. New methods to speed up calibration while maintaining the accuracy need to be developed. These new methods could involve artificial intelligence methods. Each of the options present their own challenges.

5.5.1 Challenges for Small Series Production

The challenge for small series production rests in keeping the tolerances under control. For example Figure 5.2 displays the simulated effect of minute manufacturing misalignment in a hemispheric electrostatic analyzer. It is relatively easy to build one or two working instruments. This can be achieved by selecting parts with the proper tolerances and by matching of parts. When producing a small series, tolerances usually increase, es-

pecially if manual operations are involved. The parts matching then gets quickly too time consuming and costly. To produce dedicated automated machines, or program equipment for manufacturing or assembly, the number of units produced is often too small to justify the expense.

In order to keep the accuracy, tolerances and repeatability of the measurement within the required specifications, the instrument needs to be designed for ease of manufacturabiliy and assembly by different persons, adjustment, and calibration. Assembly jigs could contribute at keeping tolerances in control.

5.5.2 Instrument Response Modeling

Throughout the chapters of this book it was stressed that simulating the instrument is a valuable, if not essential technique. Raytracing has been dealt with in some detail in Appendix A.1 and A.3. Taking into account detector efficiencies and data compression performed on the instrument complete instrument response models can be developed. Calibration data taking could then be restricted to obtain the data needed to establish the support data points for the model.

5.5.3 Statistical methods

If the manufacturing tolerances are under control, then statistical methods could be used to reduce the amount of calibration data needed to take. A sampling of the parameter space could be calibrated and appropriate interpolation and extrapolation to the calibration data performed. There are several statistical methods which could be used in a calibration context. Among them are: Design of Experiments (DoE), parameter estimation, multi-variate analysis (multiple, non-linear), regression, correlations, and statistical process control.

5.5.4 Artificial Intelligence Methods

Artificial intelligence methods is a vast class of methods that could be useful in future calibration work. An example of the usefulness of neural networks is given by *Waldemark and Norqvist* [1995]. They taught neural network filters to normalize in-flight data by determining sensitivity coefficients for each of 32 angular sectors of a three-dimensional ion composition spectrometer, based on calibration measurements for one selected reference sector. This allowed for simple calibrations, accounting for the fact that sensitivity actually varies for each sector, by developing simple transfer functions between the sensitivity of the reference sector and the sensitivity of the other sectors. In order to do that, they systematically gathered a large training set of about 1000 samples, across many orbits for each of 16 ion energy levels.

5.6 Machine Learning Methods for Automated Calibration

This section describes an approach for autonomously calibrating devices which minimizes the number of (typically expensive and difficult to obtain) calibration measurements

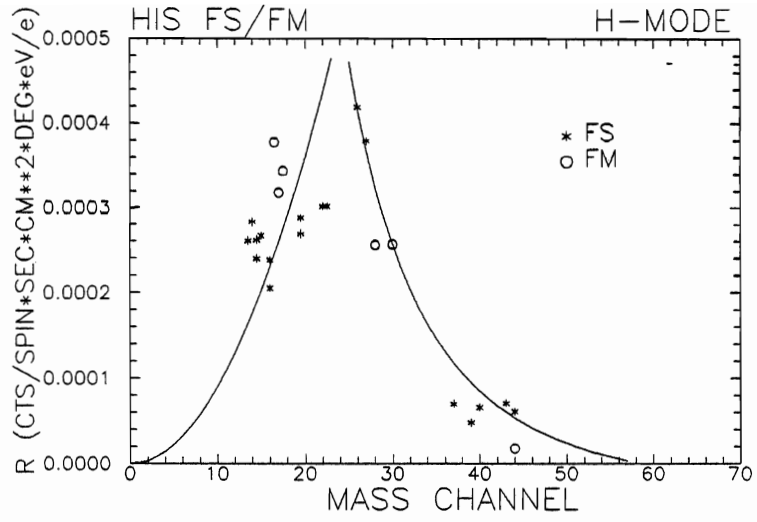

Figure 5.3: Giotto Ion Mass Spectrometer/High Intensity Spectrometer mass dependence of the instrument response R, which is normalized with the size and the sensitivity of the channel electron multipliers. FM stands for flight model, FS for flight spare. Differences between the two instruments are clearly visible. From *Meier* [1988].

required on the device. This essentially involves adapting knowledge learned from measurements of similar devices (such as ground spares, simulators, the first in a series, or similar onboard devices) to inform which measurements on the new device would be "most informative" given existing measurements so far.

The basic approach involves learning both a model of the similar device from operational data (including data gathered actively based on automated suggestions) as well as a model for mapping predictions of the first model into predictions for the next device being calibrated. Whereas there are typically only a small and fixed set of (pre-launch) calibration data points available for the main or first device, a second, spare or similar device can often be sampled with fewer calibration data points. This leads to a cost and time savings.

The idea of using an engineering model (e.g., a high-fidelity software simulation or a physical device similar to the flight instrument) to improve the calibration process is central to this method. As one example, an engineering model can be used to make additional calibration measurements after the launch of a flight instrument. Figure 5.3 shows data for the Giotto Ion Mass Spectrometer flight instrument as well as for a nominally identical flight spare. Clearly, there are systematic differences between the data produced by each instrument. The question now becomes how to transfer the calibration factors obtained with the engineering model to the flight instrument.

5.6.1 Current State-of-the-Art and Related Work

Currently, re- and cross-calibration with a spare unit is done in a time consuming and labor intensive fashion (e.g. *Meier* [1988]) (see also Section 3.9). Individual parameters are fitted manually and conversion factors established. In the case of post-launch degradation

(e.g. as happened with Polar/TIMAS), re-calibration is often attempted by using numerical ray-tracing methods and by intercomparison with other instruments on the same spacecraft [*Wüest*, 1999].

The techniques we outline here can be viewed as a more automated and comprehensive approach to this problem. The transfer learning approach actively samples the available data source (engineering model) to optimize the value of the lab measurements that are made. Such active sampling is critical to minimizing cost (e.g., technician labor) and time (e.g., lag between instrument readiness and launch). Transfer learning originated within the robotics community [*Thrun and Mitchell*, 1995; *Thrun*, 1998] as a way to incorporate new observations into existing models.

5.6.2 Machine Learning Methods

Figure 5.4 outlines the basic framework for one automated calibration scenario. There are three primary machine learning elements: (1) model learning, (2) transfer learning, and (3) active learning. Each learning element is discussed in more detail below.

5.6.2.1 Model Learning

The first step is to learn an approximate regression function for each instrument (flight unit and engineering model) from an initial set of measurements. Each regression function predicts the instrument output given the input parameters (Energy E, Mass M_i, etc.). For particle instruments, determining the regression function amounts to establishing estimators for the energy-geometric factor, G_i, which was referred to in earlier chapters. In Figure 5.4 the resulting estimators are labeled `f0_flight` and `f0_spare`. These estimators are based on initial data sets that are gathered "passively", i.e., from tests already performed or from simple uniform sampling of parameter space. Indeed, in cases where these methods are not initiated until after launch, such passive data is all that will be available for the flight device.

Given the relatively small amount of initial data (typically 10^2 to 10^3 parameter space positions) that calibration tasks tend to provide, support vector machines (SVMs) [*Schölkopf and Smola*, 2001] are used to learn the estimators [*DeCoste and Levine*, 2000; *DeCoste and Schölkopf*, 2002]. SVMs provide an especially good theoretical basis for active learning techniques as well (see below).

Traditionally, the tradeoff cost of enjoying the improved accuracy and robustness offered by SVMs has been that they tend to be much slower to compute than their nearest-competitor models (such as neural networks). *DeCoste* [2002] describes methods for speeding up SVMs to reach the speed of neural networks. Such efficiency enables state-of-the-art kernel-based models, such as SVMs, to be practical for embedding on spacecraft or real-time ground operations, ensuring that the approach both achieves the best possible accuracy as well as being practical for use in calibration contexts, even with limited computing power.

5.6.2.2 Transfer Learning

The second step is to incorporate `f0_spare` into `f0_flight` using transfer learning. Since more measurements can be obtained with the engineering model (e.g. no hard launch

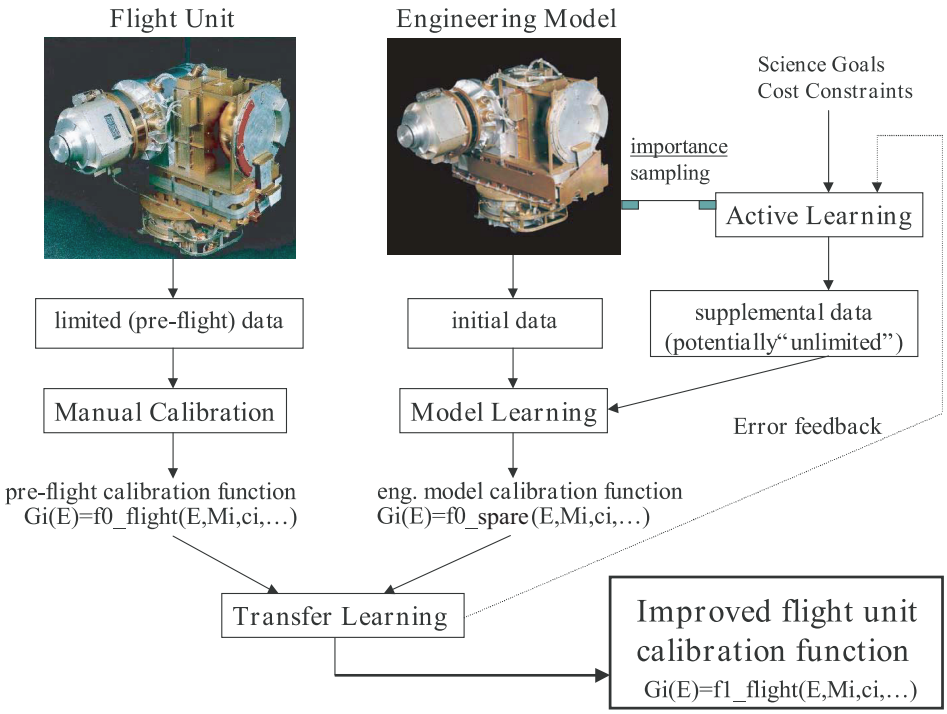

Figure 5.4: Framework for automated calibration using transfer learning. In this scenario, the flight unit is calibrated based on limited pre-launch data. The engineering model is calibrated using more extensive measurements, which leads to a more complete and accurate calibration of the engineering model. The engineering model calibration function cannot be directly applied to the flight unit, but it can be adapted via transfer learning. Error feedback is used to drive an active learning process that decides which new measurements on the engineering model would be most informative. Science goals and cost constraints can also be incorporated in this framework. The end result is a calibration function for the flight unit that is better than the initial pre-flight calibration function.

deadline), it can be more thoroughly calibrated. The idea then is to adapt the detailed understanding of `f0_spare` into `f0_flight`, by focusing on regions of parameter space where overlapping measurements were obtained. The result is a function `f1_flight`, which is a better estimator of the flight unit's behavior than `f0_flight`. A machine-learning cross-validation procedure, in which hold-out subsets of the available data from the flight device are used to evaluate how much and what aspects of `f0_spare` can safely be incorporated into `f0_flight`, without making the estimates produced by `f1_flight` match the hold-out data worse than the estimates produced by `f0_flight`. One basic approach for doing this is to have the regression model for `f1_flight` involve two inputs, one being `f0_flight` and another being `f0_spare`, with the relative weighting of those two inputs being determined by what works best across the entire cross-validation process (e.g. where various random subsets of the observations are in turn only used to evaluate

the error in the candidate regression model and not used to train the model weights). More complex methods can be explored, including learning transformations (i.e. rescalings of the model weights) within the `f0_flight` and `f0_spare` models which, when again using both models as inputs to `f1_flight`, yield a `f1_flight` model with the best cross-validated accuracy (while trying to preserve, i.e. "transfer", weights as close to the values of the original `f0_flight` and `f0_spare` as possible). The essential idea is that those transformed aspects of `f0_spare` that can be safely transferred are likely to provide good hints about how the flight unit will respond on regions of parameter space that were not explicitly tested in the pre-flight calibration process. A statistically rigorous cross-validation model search process will ensure that we transfer knowledge between models only when it is helpful to do so.

5.6.2.3 Active Learning

The algorithm then iteratively improves the estimators, by determining which regions of parameter space are well-understood by the current estimators and which regions require additional measurements. This drives the process of intelligent "active" data gathering. Before flight, such active data gathering can be performed on the flight unit as well, allowing one to make maximal use of the limited time available for (pre-flight) calibration. Over the course of the mission, however, active sampling can be most extensively applied to the engineering model (i.e. `f0_spare`), potentially improving the calibration throughout the mission (by incorporating the more extensive calibration results obtained for the engineering model into the flight estimator (`f1_flight`), via transfer learning as discussed earlier).

To actively learn what regions of parameter space are most critically in need of additional data, probing both `f0_spare` and `f0_flight` at various parameter input values to identify the settings for which the two estimators most disagree, either in relative values or in levels of certainty. Another method involves gathering data for those regions in which either estimator's estimated level of uncertainty (e.g. statistical error variance), evaluated against the actual observed outputs of their respective (spare or flight) hardware devices, is highest. These two approaches should prove complementary — the first strives to reduce relative disagreement, while the second strives to reduce absolute predictive uncertainty.

5.6.3 Other methods

There are a few optimization techniques available to speed up calibration. They essentially fall into three classes: The first class involves parallelization, the second is to reduce the amount of data taken and the third is to work faster.

Into the first category falls the concept of calibrating several instruments during the same pump down. This saves pumpdown time on successive instrument calibrations as the pump down of a large calibration facility can take many hours or even a few days. This concept works only for small instruments, as the calibration beam is not usually very large in area. If one instrument is kept as a reference instrument in the calibration chamber when calibrating successive batches of instruments, a relative calibration between the sensors is established.

Another concept in the same class is to calibrate at several institutions in parallel. Here problems arise because the facilities do not have exactly the same capabilities e.g.

in energy range or beam area, thereby possibly restricting the parameter space that can be commonly calibrated. Further, as has been mentioned above, the inter-calibration of facilities will be important in order to reduce the absolute calibration error.

Into the class of reducing the amount of calibration data taken falls the concept of performing a detailed calibration on one instrument of a series and on the other instruments only an azimuthal and an energy scan is performed. One instrument is calibrated in more detail, while the others are basically only checked at one or two parameters. This procedure assumes that the instrument are all identical. The uncertainties of the measurement will be increased. Although the central portion of the energy-angle acceptance will be similar, there is usually noticeable deviation on the fringes which affect the geometrical factor and the differential-directional number flux.

Another method to reduce the time required for a calibration is to increase the pumping speed of the facility's vacuum system by adding additional pumps. For example adding cryopumps to turbomolecular pumps increases the pumping for water vapor, a major constituent in a high vacuum residual atmosphere. This will reduce the time to reach high vacuum conditions needed to operated windowless electron multipliers.

Increased automation can be used to reduce the comparatively slow human interaction with adjusting beam parameters or facility settings.

5.7 Summary

This book describes the importance of an accurate calibration. It describes for different instrument classes methods, processes and pitfalls to calibrate in situ particle instruments on the ground pre-flight and post-launch in flight. It also provides a few hints how the calibration could be improved in the future.

Bibliography

Cohn, D.A., Z. Ghahramani, and M.I. Jordan, Active learning with statistical models, *J. Artificial Intelligence Research*, **4**, 129–145, 1996.

DeCoste, D., Anytime interval-valued outputs for kernel machines: Fast support vector machine classification via distance geometry, in *Proc. 19th Int. Conf. on Machine Learning (ICML)*, C. Sammut and A.G. Hoffmann, Eds., Morgan Kaufmann, 99–106, 2002.

DeCoste, D. and M. Levine, Automated event detection in space instruments: A case study using IPEX-2 data and support vector machines, *SPIE Conference Astronomical Telescopes and Instrumentation*, March 2000.

DeCoste D. and B. Schölkopf, Training invariant support vector machines, *Machine Learning*, **46**, 161–190, 2002.

Hao, L., J.C. Gallop, J.C. Macfarlane, C. Carr, and G.B. Donaldson, HTS flux concentrator for non-invasive sensing of charged particle beams, *Supercond. Sci. Technol.*, **14**, 1–4, 2001a.

Hao, L. J.C. Macfarlane, D.A. Peden, R.A.M. Lee, J.C. Gallop, and C. Carr, Design and performance of an HTS current comparator for charged-particle-beam measurements, *IEEE Trans. Appl. Supercond.*, **11**, 635–638, 2001b.

Hao, L., J.C. Gallop, J.C. Macfarlane, and C. Carr, HTS cryogenic current comparator for non-invasive sensing of charged-particle beams, *Physica C*, **368**, 114–118, 2002.

Hao, L., J.C. Gallop, J.C. Macfarlane, and C. Carr, HTS cryogenic current comparator for non-invasive sensing of charged-particle beams, *IEEE Trans. Instrum. Meas.*, **52**, 617–620, 2003a.

Hao, L., J.C. Macfarlane, C. Carr, and J.C. Gallop, HTS current concentrator for remote sensing of charged particle beams, *IEEE Trans. Appl. Supercond.*, **13**, 739–742, 2003b.

Hao, L., J.C. Macfarlane, S. Haining, and J.C. Gallop, HTS superconducting current comparator: dynamic range and noise limits, *IEEE Trans. Instrum. Meas.*, **54**, 584–587, 2005a.

Hao, L., J.C. Macfarlane, S.K.H. Lam, C.P. Foley, P. Josephs-Franks, and J.C. Gallop, Inductive sensor based on nano-scale SQUIDs, *IEEE Trans. Appl. Supercond.*, **15**, 514–517, 2005b.

Meier A., Eichung des für die Untersuchung der inneren Koma des Kometen Halley verwendeten Ionenmassenspektrometers Giotto-IMS-HIS, Ph.D. thesis, University of Bern, 1988.

NASA, The Magnetospheric Constellation Mission, Dynamic Response and Coupling Observatory (DRACO): Understanding the Global Dynamics of the Structured Magnetotail, Report of the NASA Magnetospheric Constellation Science and Technology Definition Team, **NASA/TM-2001-209985**, NASA Goddard Space Flight Center, Greenbelt, MD, 2001.

Pollock, C.J., K. Asamura, J. Baldonado, M.M. Balkey, P. Barker, J.L. Burch, E.J. Korpela, J. Cravens, G. Dirks, M.-C. Fok, H.O. Funsten, M. Grande, M. Gruntman, J. Hanley, J.-M. Jahn, M. Jenkins, M. Lampton, M. Marckwordt, D.J. McComas, T. Mukai, G. Penegor, S. Pope, S. Ritzau, M.L. Schattenburg, E. Scime, R. Skoug, W. Spurgeon, T. Stecklein, S. Storms, C. Urdiales, P. Valek, J.T.M. van Beek, S.E. Weidner, M. Wüest, M.K. Young, and C. Zinsmeyer, Medium energy neutral atom (MENA) imager for the IMAGE mission, *Space Sci. Rev.*, **91**, 113–154, 2000.

Schölkopf, B. and A. Smola, *Learning with Kernels*, MIT Press, Cambridge, MA, 2001.

Scudder, J.D., F. Hunsaker, G. Miller, J. Lobell, T. Zawistowski, K.W. Ogilvie, J. Keller, D. Chornay, F. Herrero, R. Fitzenreiter, D. Fairfield, J. Needell, D. Bodet, J. Googins, C. Kletzing, R. Torbert, J. Vandiver, R. Bentley, W. Fillius, C. McIlwain, E. Whipple, and A. Korth, Hydra - A 3-Dimensional Electron and Ion Hot Plasma Instrument for the Polar Spacecraft of the GGS Mission, *Space Sci. Rev.*, **71**, 459–495, 1995.

Thrun, S. and T.M. Mitchell, Learning one more thing, in *Proc. 14th Int. Joint Conf. On Artificial Intelligence (IJCAI)*, Morgan Kaufmann, San Mateo, CA, 1217–1225, 1995.

Thrun S., Lifelong Learning Algorithms, in *Learning to Learn*, S. Thrun and L.Y. Pratt, Eds., Kluwer Academic Publishers, 181–209, 1998.

Vilppola, J.H., Cassini Mission and the Cassini/IBS Instrument, Licentiate thesis, University of Oulu, 1998.

Waldemark, J. and P. Norqvist, Multiple neural network filtering for in-flight calibration of satellite measurements, *IEEE Int. Conf. on Neural Networks*, **1**, 507–510, 1995.

Wüest, M., The calibration of satellite particle sensors, *Adv. Space Res.*, **23**, 1533–1536, 1999.

— A —

Appendices

A.1 Raytracing in Instrument Design

JAMES P. MCFADDEN

Space Sciences Laboratory, University of California, Berkeley, CA, USA

Computer programs for simulating an instrument's response are essential tools in the design of modern plasma sensors. These programs calculate the electric and magnetic fields used to separate various particle populations, and perform particle ray tracing to test and characterize the analyzer optics. They also allow the developer to visualize the particle motion and the impact of analyzer components on that motion. Once a basic optics design is selected, simulations allow rapid evaluation of the complete analyzer response. Simulation of sophisticated optics speeds instrument development, eliminating costs associated with prototypes and allowing evaluation of design tolerance requirements. In addition, once a sensor is fabricated, instrument performance during calibrations is generally compared with the simulated response to determine whether the analyzer is operating properly or contains any defects in its construction.

The starting point for plasma instrument design is a general understanding of particle optics, not the simulation code. Therefore, before proceeding with a discussion of computer-aided design, it is important for the developer to be familiar with the literature on analyzer characteristics and particle optics. Analytic calculations of the response of spherical and cylindrical electrostatic analyzers (ESAs) can be found in *Paolini and Theodoridis* [1967] and *Theodoridis and Paolini* [1968]. These papers illustrate energy and angle focusing of standard electrostatic analyzer geometries and provide a basis for understanding more complex geometries. *Coplan et al.* [1984] describes second order focusing in magnetic spectrometers as required for high-resolution mass spectrometers. *Carlson et al.* [1983] provided the first description of "top-hat" electrostatic analyzers whose symmetric, 360° planar field-of-view form the basis of most modern plasma sensors. A more complete discussion of "top-hat" parameterization and design can be found in *Carlson and McFadden* [1998]. Lastly the Geophysical Monograph: "Measurement Techniques in Space Plasma Physics" [*Pfaff et al.*, 1998] provides articles on a variety of plasma instrument geometries, discussions of their optics, and descriptions of analyzer simulations and calibrations.

The above references provide a good knowledge base for the creation of new analyzer concepts. Ray tracing codes can then be used for a quick testing, or sanity check of the optics. However, once an optics concept is selected, it is recommended that a preliminary mechanical design be developed prior to implementing any extensive ray tracing efforts. This is because mechanical constraints often become driving factors in the instrument design. For example, it is easy to simulate an analyzer containing a suspended sphere that has no mechanical support, however constructing such an instrument would be impossible.

The design effort should pay particular consideration to insulator requirements, locating them away from particle trajectories to prevent any charging and the subsequent impact on particle motion. Once a mechanical concept is developed, particle ray tracing can be used to refine the optics design.

Most current space plasma instruments utilize electric fields rather than magnetic fields to analyze particles. The reasons are primarily for mass savings and to avoid perturbations to spacecraft magnetometers. Therefore, this appendix will focus on descriptions of ray tracing techniques involving electrostatic optics. However, the programming elements and implementation are similar for magnetic optics, and the ideas discussed below should be easily adapted to magnetic analysis. For a more detailed discussion of numerical solutions for electric and magnetic fields see *Binns et al.* [1992].

Numerical simulation of analyzers requires three main components: a field solving module, a particle ray tracing module, and plotting/display routines. For a specified set of boundary conditions, the first module solves Maxwell's equations for the electric and magnetic fields. The ray tracing module uses the equations of motion [$\mathrm{d}x/\mathrm{d}t = v$ and $\mathrm{d}v/\mathrm{d}t = (q/m)(E + \boldsymbol{v} \times \boldsymbol{B})$] to calculate particle trajectories in the analyzer and to record information about those trajectories. Plotting software allows the user to display particle trajectories within the analyzer or to characterize a large number of recorded trajectories. For those who wish to develop their own code, the basic electrostatic field solving and ray tracing algorithms are rather simple and discussed below. The primary development effort involves simplifying the input of boundary conditions and the generation of an interface to the plotting/display routines. There are also several techniques that speed up the calculations of both the fields and particle ray tracing that are described below. For those less interested in programming, there are several commercial packages available as described in Appendix A.2.

For simple electrostatic analyzers, the field solving module reduces to solving the Laplace Equation, $\nabla^2 U = 0$, to obtain the electrostatic potential field, U, which is then used to calculate the electric field ($E = -\nabla U$). The Laplace solver operates on a 2-D or 3-D grid in the given coordinate system. The selection of a coordinate system to reflect the symmetry of the analyzer can reduce the calculation time and simplify input of boundary conditions. The normal methodology involves assigning fixed potential values to the grid points located at the instrument's surfaces (Dirichlet boundary conditions) and then applying the Laplace solver to determine the potential on other grid points. Alternatively, the gradient of the potential (von Neumann boundary conditions) could be specified. However for space plasma instruments surface potentials are generally controlled, not the potential gradient, therefore we do not discuss this alternate boundary condition specification.

A.1.1 Electric Field Solving Program

Consider a simple 2-D square grid where $\Delta x = \Delta y$. For a finite grid, the Laplace equation reduces to a finite difference equation. The second derivative of the potential function $U(x, y)$ with respect to x reduces to:

$$\frac{\mathrm{d}^2 U}{\mathrm{d}x^2} \Rightarrow \frac{U_{i+1,j} + U_{i-1,j} - 2U_{i,j}}{\Delta x^2} \tag{A.1}$$

Here we maintain standard programming notation for integer array indices, $U_{i,j}$, where $i = 0, 1, 2, \ldots, N_i - 1$ and $j = 0, 1, 2, \ldots, N_j - 1$.

The 2-D Laplace equation reduces to:

$$\frac{U_{i+1,j} + U_{i-1,j} - 2U_{i,j}}{\Delta x^2} + \frac{U_{i,j+1} + U_{i,j-1} - 2U_{i,j}}{\Delta y^2} = 0 \tag{A.2}$$

which can be rewritten as:

$$U_{i,j} = \frac{U_{i+1,j} + U_{i-1,j} + U_{i,j+1} + U_{i,j-1}}{4} \tag{A.3}$$

when $\Delta x = \Delta y$. In 3-D with $\Delta x = \Delta y = \Delta z$, the solution is simply

$$U_{i,j,k} = \frac{U_{i+1,j,k} + U_{i-1,j,k} + U_{i,j+1,k} + U_{i,j-1,k} + U_{i,j,k+1} + U_{i,j,k-1}}{6} \tag{A.4}$$

These formulas make it clear that the solution to Laplace's equation has values for potential at any point equal to the average of the points that surround it. The essence of the Laplace equation is that there are no local minima or maxima and the potential at the center of a box is the average of the potential on the box's surfaces.

For a rectangular 2-D grid where $\Delta x \neq \Delta y$, we write the general form of (A.3) as:

$$U_{i,j} = \frac{K_1(U_{i+1,j} + U_{i-1,j}) + K_2(U_{i,j+1} + U_{i,j-1})}{K_0} \tag{A.5}$$

where $K_1 = \Delta y^2$, $K_2 = \Delta x^2$ and $K_0 = 2(\Delta x^2 + \Delta y^2)$. The Laplace equation gives the potential at the center of a box from the average potential on its surface. For a rectangular box, some surfaces are larger and the constants K_0, K_1, and K_2 are weighting factors that correct for varying surface area. Note that the above solutions cannot be applied at the outer boundaries of the grid since the formula calls on undefined points. This can be handled by using periodic boundary conditions or requiring fixed boundary conditions at the grid limits.

Most current plasma sensor designs have cylindrical symmetry, therefore a cylindrical coordinate system is generally chosen. For 2-D cylindrical coordinates and $U(r, z)$, the finite difference Laplace equation reduces to:

$$U_{i,j} = \frac{K_1\left[(1 + \frac{1}{2i})U_{i+1,j} + (1 - \frac{1}{2i})U_{i-1,j}\right] + K_2\left[U_{i,j+1} + U_{i,j-1}\right]}{K_0} \tag{A.6}$$

where $K_1 = \Delta r^2$, $K_2 = \Delta z^2$ and $K_0 = 2(\Delta r^2 + \Delta z^2)$. One generally chooses $\Delta r = \Delta z$, and (A.6) simplifies to:

$$U_{i,j} = \frac{(1 + \frac{1}{2i})U_{i+1,j} + (1 - \frac{1}{2i})U_{i-1,j} + U_{i,j+1} + U_{i,j-1}}{4} \tag{A.7}$$

Unlike the square and rectangular grids, the radial coordinate's inner and outer boundaries cannot be made periodic, and the $i = 0$ surface cannot generally be made a fixed boundary condition. Instead the outer radial boundary must be a fixed potential (or fixed gradient potential) and the inner boundary must be solved using a separate equation. The simplest inner boundary solution is to use the square grid approximation in 3-D and set

$$U_{i=0,j} = \frac{4U_{i=1,j} + U_{i=0,j+1} + U_{i=0,j-1}}{6} \tag{A.8}$$

where we again assumed $\Delta r = \Delta z$.

For 3-D cylindrical coordinates and $U(r, z, \phi)$, the finite difference Laplace equation becomes:

$$U_{i,j,k} = \Big\{ K_1 \Big[\big(1 + \tfrac{1}{2i}\big) U_{i+1,j,k} + \big(1 - \tfrac{1}{2i}\big) U_{i-1,j,k} \Big] + K_2 \big[U_{i,j+1,k} + U_{i,j-1,k} \big] + K_3 \big[U_{i,j,k+1} + U_{i,j,k-1} \big] \Big\} / K_0 \tag{A.9}$$

where $K_1 = \Delta r^2$, $K_2 = \Delta z^2$, $K_3 = (1/i\Delta\phi)^2$, $K_0 = 2\Delta r^2 + 2\Delta z^2 + 2(1/i\Delta\phi)^2$ and $\Delta\phi$ is the azimuthal resolution.

If the simulation spans the entire 2π azimuthal range, then $\Delta\phi = 2\pi/N_\phi$, where N_ϕ is the number of azimuthal grid points. At the azimuthal limits, $k = 0$ and $k = N_\phi - 1$, periodic boundary conditions are assumed for continuity. Most instruments will have some periodic symmetry in the azimuthal direction, therefore it is useful to build the azimuthal range of "ϕ" as a pie slice with periodic boundary conditions that span a fraction of 2π in order to reduce the number of grid points. If the simulation has M_ϕ periodic symmetry, then use $\Delta\phi = 2\pi/(N_\phi M_\phi)$. The azimuthal resolution should be chosen so that $i\Delta\phi$ resolves the boundary conditions where azimuthal symmetry is broken. Finally, as with the 2-D solution, a different formulation is required along the symmetry axis. The 3-D analog to (A.8) is:

$$U_{i=0,j,0} = \frac{\left[\dfrac{4}{N_\phi} \displaystyle\sum_{k=0}^{N_\phi - 1} U_{i=1,j,k} \right] + U_{i=0,j+1,0} + U_{i=0,j-1,0}}{6} \tag{A.10}$$

and $U_{i=0,j,k} = U_{i=0,j,0}$.

Other coordinate systems can be used for the Laplace solver, however even rather common coordinate systems such as spherical coordinates generally prove to be arduous. This is because boundary specification becomes difficult in anything but rectangular and cylindrical coordinates. Since most mechanical drawings are in these coordinates, most instrument surfaces project to simple line segments or circular curves in these coordinate systems.

Now that the basic finite difference Laplace equations are specified, we can write a Laplace solver algorithm. The Laplace solver is actually the diffusion equation, $\mathrm{d}U/\mathrm{d}t = D\nabla^2 U$, which produces the Laplace solution through an iterative relaxation. The simple 2-D the finite difference diffusion equation is:

$$\frac{U_{i,j}^{t+1} - U_{i,j}^{t}}{\Delta t} = \frac{D\left[U_{i+1,j}^{t} + U_{i-1,j}^{t} - 2U_{i,j}^{t}\right]}{\Delta x^2} + \frac{D\left[U_{i,j+1}^{t} + U_{i,j+1}^{t} - 2U_{i,j}^{t}\right]}{\Delta y^2} \tag{A.11}$$

where we use a t superscript to track the array with each iteration of the diffusion equation. Equation (A.11) can be rewritten as:

$$U_{i,j}^{t+1} = U_{i,j}^{t} + \frac{D\Delta t}{\Delta x^2}\left[U_{i+1,j}^{t} + U_{i-1,j}^{t} + U_{i,j+1}^{t} + U_{i,j-1}^{t} - 4U_{i,j}^{t}\right] \tag{A.12}$$

where we have assumed $\Delta x = \Delta y$ for simplicity. The $(D\Delta t/\Delta x^2)$ term is a user selectable parameter and allows control of the diffusion rate. With each iteration, values of the potential at each point are corrected by the right side term, with weight given by $(D\Delta t/\Delta x^2)$.

If this term is chosen too large, the iteration will be unstable and not converge. If the term is too small, the convergence is slow.

There are several related schemes that produce solutions to the Laplace equation. *Potter* [1973] shows that "Over Relaxation" schemes converge the fastest. Successive over relaxation introduces a parameter, W, to the diffusion equation that speeds up the convergence. The method involves using weighted averages of both newly calculated points at iteration $t+1$ and the points at the previous iteration t.

Consider rewriting (A.12) as follows:

$$U_{i,j}^{t+1} = \left(1 - 4D\frac{\Delta t}{\Delta x^2}\right) U_{i,j}^{t} + 4D\frac{\Delta t}{\Delta x^2}\frac{U_{i+1,j}^{t} + U_{i-1,j}^{t} + U_{i,j+1}^{t} + U_{i,j-1}^{t}}{4} \quad \text{(A.13)}$$

Over relaxation involves using two of the newly calculated array elements along with two of the previous array elements to determine the new value at each grid point. With over relaxation, (A.13) becomes:

$$U_{i,j}^{t+1} = (1-W)U_{i,j}^{t} + W\frac{U_{i+1,j}^{t} + U_{i-1,j}^{t+1} + U_{i,j+1}^{t} + U_{i,j-1}^{t+1}}{4} \quad \text{(A.14)}$$

where W plays the role of the diffusion term ($4D\Delta t/\Delta x^2$). Over relaxation produces much faster convergence since grid points are influenced by distant boundary conditions on each iteration through use of the forward time ($t+1$) terms. Note that (A.14) will produce an asymmetry in the diffusion rate with potentials on boundary conditions near the $i=0$, $j=0$ corner diffusing faster. This can be made symmetric by alternating the iteration order and using:

$$U_{i,j}^{t+1} = (1-W)U_{i,j}^{t} + W\frac{U_{i+1,j}^{t+1} + U_{i-1,j}^{t} + U_{i,j+1}^{t+1} + U_{i,j-1}^{t}}{4} \quad \text{(A.15)}$$

W must be less than 2 or the iteration formula is unstable and $W=1$ results in no over relaxation. W coefficients from 1.7 to 1.9 work well for nominal grid sizes and boundary surface spacing (15 to 60 grid points between different potential surfaces) typical for electrostatic deflectors.

For 2-D cylindrical coordinates where $\Delta r = \Delta z$, the over relaxation algorithm becomes:

$$U_{i,j}^{t+1} = (1-W)U_{i,j}^{t} + W\frac{(1+\frac{1}{2i})U_{i+1,j}^{t+1} + (1-\frac{1}{2i})U_{i-1,j}^{t} + U_{i,j+1}^{t+1} + U_{i,j-1}^{t}}{4} \quad \text{(A.16)}$$

For 3-D cylindrical coordinates, the over relaxation algorithm is:

$$U_{i,j,k}^{t+1} = (1-W)U_{i,j,k}^{t} + W\Big\{K_1\Big[\big(1+\tfrac{1}{2i}\big)U_{i+1,j,k}^{t} + \big(1-\tfrac{1}{2i}\big)U_{i-1,j,k}^{t+1}\Big] + K_2\Big[U_{i,j+1,k}^{t} + U_{i,j-1,k}^{t+1}\Big] + K_3\Big[U_{i,j,k+1}^{t} + U_{i,j,k-1}^{t+1}\Big]\Big\}/K_0 \quad \text{(A.17)}$$

where $K_1 = \Delta r^2$, $K_2 = \Delta z^2$, $K_3 = (1/i\Delta\phi)^2$, $K_0 = 2\Delta r^2 + 2\Delta z^2 + 2(1/i\Delta\phi)^2$.

Once the Laplace solver has been implemented in code, the user needs a means of determining the level of convergence. A simple method is to record the largest difference

potential at each iteration, $U_{i,j,k}^{t+1} - U_{i,j,k}^{t}$, and monitor the convergence until the level of change is negligible.

Three additional modifications to this approach can reduce the calculation time for determining an electrostatic potential solution. First, for problems that involve more than one potential (other than zero potential) applied to instrument surfaces, and where the ratios of these potentials vary, the approach should take advantage of the linearity of the Laplace equation for a fixed boundary geometry. Initially use the Laplace solver to determine the solutions for each independent boundary potential, with all other boundaries set to zero potential. With this set of independent solutions, a general solution can be obtained by just scaling and adding the separate solutions. This allows the user to quickly vary the relative surface potentials without having to reapply the Laplace solver. The time savings from this approach can be enormous.

Second, for problems that require a large number of grid points, a rapid solution can be obtained by initially solving the problem on a coarse grid, then scaling to a finer mesh. The procedure applies boundary conditions to a coarse grid, iterates to convergence, then doubles all array dimensions using interpolation to determine potential for new grid points, re-applies the boundary conditions to take advantage of the finer mesh, then iterates to convergence again. For very large grids, the doubling can be performed several times and the convergence time can be reduced by a factor of $\sim$4 for each doubling.

Third, for some instruments there may be large sections of the analyzer that particles do not ever transit. For example, in top-hat analyzers, there are no trajectories that transit the volume inside the inner hemisphere. For regions with no particle trajectories, one can write a Laplace solver that allows the user to disable the iteration algorithm in regions of no interest. Generally this only results in a modest improvement in calculation time, probably $\sim$50 % depending upon the geometry.

When operating the Laplace solver, it is important to have display code to monitor the solution. Displays should allow the user to check that his or her boundary condition specification is correct, and to provide a means for examining the regions where convergence is poorest.

In addition to the Laplace solver, the electric field solving program must include a method for specifying boundary conditions and maintaining those boundary condition values during the iteration process. One method is to maintain a separate "boundary array" that has identical dimensions as the potential array and keeps track of boundary points. This array could be a simple byte array, with "0" for non-boundary points and "1" for boundary points. During the Laplace iteration, a conditional statement is applied to the "boundary array" grid point to determine whether the equivalent potential grid point changes with the iteration. The "boundary array" can also be used by the plotting program to draw the boundaries, and by the ray tracing algorithm to determine when a particle strikes a surface.

Effort should be taken to make the input of boundary conditions convenient. Most boundary conditions can be specified with a minimal number of parameters. For example, a flat surface on a 2-D rectangular grid can be specified by the two end points. The boundary condition algorithm then determines those grid points that lie "close" to the line connecting the points and sets their boundary array values to 1. "Close" is generally chosen to be either within 1/2 or $1/\sqrt{2}$ of the grid spacing, depending upon the ray tracing algorithm that senses when a particle strikes a boundary (see the following section). In 3-D, planar surface specification requires 6 coordinates, with four coordinates used to specify a

line segment (X_1, X_2, Z_1, Z_2), and a third pair of coordinates (Y_1, Y_2) used to specify the extent in the third dimension. The input algorithm should allow for selection of the symmetry direction. In addition, the same 6 coordinates could be used to specify a volume, so a separate input algorithm is advised. In a manner similar to planar surfaces, curved surfaces can be specified by a few parameters (center of curvature, a radius, and one or two pairs of angles). For complex designs, one may also want to develop a program that can translate a mechanical drawing directly into boundary condition specification.

Once the potential distribution is calculated, the electric field must then be determined and stored as an array to be used by the particle ray tracing algorithm. Depending upon the accuracy of the ray tracing algorithm, one may need to calculate the electric field gradients for interpolation between grid points and/or higher order field derivatives. These additional terms reduce errors caused by discontinuities in the calculated fields as particles are traced between grid points.

Finally, in addition to the relaxation method, other methods are available for determining the electric potential distribution given a set of boundary conditions. Modeling techniques such as the boundary element method or the finite element method can be found in *Binns et al.* [1992], *Yildir et al.* [1993],*Beer* [2001], or *Zienkiewicz et al.* [2005].

A.1.2 Particle Ray Tracing Program

Particle ray tracing uses a finite difference algorithm to solve the equations of motion [$\mathrm{d}x/\mathrm{d}t = v$ and $\mathrm{d}v/\mathrm{d}t = (q/m)(E+\boldsymbol{v}\times\boldsymbol{B})$] for a particle traveling through predetermined electric and magnetic fields. The fields are determined by the field solvers as described above. Information about the trajectory is either recorded in a file or presented in real time plots for visualization. The ray tracing algorithm must calculate trajectories in 3-D even if the fields are only 2-D due to symmetry. The code must include methods for stopping a particle when it hits a boundary or falls outside the region of interest. The program should provide a method to monitor the accuracy of the tracing algorithm. The user interface to this program must allow selection of the initial position, velocity, and q/m of a particle. Normally more than one particle trajectory will be run at a time, so a simple method of defining a set of input particles is desired. The interface should also provide control over the visualization tools to allow quick feedback to the designer. Details of the ray tracing programs, including features that enhance performance, are described below.

For those interested in designing their own ray tracing program, there are several approaches to the tracing algorithms. The simplest finite difference algorithm is Euler's method:

$$\begin{aligned} X^{t+1} &= X^t + \Delta X = X^t + \Delta t V^t \\ V^{t+1} &= V^t + \Delta V = V^t + \Delta t A(X^t, V^t) \end{aligned} \tag{A.18}$$

where X, V, and A are the position, velocity, and acceleration vectors, and the forward time step is produced using the velocity and acceleration at the previous point. The acceleration is determined from the electric and magnetic field arrays. This formulation may be adequate for some computations, however a relatively small Δt may be required to achieve the desired accuracy. For a large number of trajectories, it is worthwhile to use a more accurate algorithm that allows for larger time steps. Runge-Kutta, leap-frog, and predictor-corrector algorithms all provide more accurate calculation methods. The decreased calculation time with larger Δt more than offsets the increased calculation time for the more

complex algorithms. Below we describe the Runge-Kutta algorithm which provides an adequate engine for simulation of particles in instruments.

Runge-Kutta provides a higher order approximation to the fields experienced by a particle during the integration time step. In its simplest form, "2nd order" Runge-Kutta estimates the average velocity and acceleration over at the interval from the midpoint value:

$$\begin{aligned}
\Delta X_1 &= \Delta t(V^t) & \Delta V_1 &= \Delta t A(X^t, V^t) \\
\Delta X_2 &= \Delta t(V^t + \Delta V_1/2) & \Delta V_2 &= \Delta t A(X^t + \Delta X_1/2, V^t + \Delta V_1/2) \\
X^{t+1} &= X^t + (\Delta X_1 + \Delta X_2)/2 \\
V^{t+1} &= V^t + (\Delta V_1 + \Delta V_2)/2
\end{aligned} \tag{A.19}$$

Higher order Runge-Kutta use successive applications of (A.18) to build more accurate approximations. The 4^{th} order Runge-Kutta is most commonly used.

$$\begin{aligned}
\Delta X_1 &= \Delta t(V^t) & \Delta V_1 &= \Delta t A(X^t, V^t) \\
\Delta X_2 &= \Delta t(V^t + \Delta V_1/2) & \Delta V_2 &= \Delta t A(X^t + \Delta X_1/2, V^t + \Delta V_1/2) \\
\Delta X_3 &= \Delta t(V^t + \Delta V_2/2) & \Delta V_3 &= \Delta t A(X^t + \Delta X_2/2, V^t + \Delta V_2/2) \\
\Delta X_4 &= \Delta t(V^t + \Delta V_3) & \Delta V_4 &= \Delta t A(X^t + \Delta X_3, V^t + \Delta V_3) \\
X^{t+1} &= X^t + \Delta X_1/6 + \Delta X_2/3 + \Delta X_3/3 + \Delta X_4/6 \\
V^{t+1} &= V^t + \Delta V_1/6 + \Delta V_2/3 + \Delta V_3/3 + \Delta V_4/6
\end{aligned} \tag{A.20}$$

This formulation provides more than adequate accuracy for analyzer simulations. If time-dependent fields are incorporated into the analyzer, where $A = A(t, X, V)$, the ΔV_1, ΔV_2, ΔV_3, ΔV_4 terms are evaluated at t, $t + \Delta t/2$, $t + \Delta t/2$, $t + \Delta t$, respectively.

Using a higher order ray tracing algorithm will reduce calculation errors, but not eliminate them. Calculation errors primarily result from too large a time step, especially in regions where the field gradients are large. Singularities in the coordinate system are another source of calculation errors. For example, particles passing near the symmetry axis of a cylindrical or spherical coordinate system will experience a rapid change in angle coordinates requiring either very small time steps or a temporary coordinate transformation that eliminates the singularity. To deal with these changing conditions, the time step is generally adjusted throughout the trajectory to maintain the required accuracy.

In addition to errors introduced by the ray tracing algorithm, the discreteness of the field array also becomes a source of error. As a test particle moves from grid cell to grid cell within the field array, different sets of grid points are used to calculate the local field. At the boundaries between grid cells, discontinuities in the calculated potential and fields will result. These errors can be reduced by incorporating higher order field interpolation or by decreasing grid spacing with a larger array. Both require increased calculation time. These field-grid induced errors are often most noticeable in particles that pass near surface boundaries. This is due to both the surface roughness producing large field gradients, and by changes in the field interpolation algorithm near these boundaries. For example, grid points inside a conducting boundary cannot be used in the electric field interpolation at the boundary surface, requiring electric field interpolation that is not centered on the test particles as they approach a boundary. A method of monitoring these errors and determining whether they are acceptable is required.

A simple method of error monitoring is to perform an additional calculation at twice the time step for comparison with the result after two nominal time steps. These comparisons can be made at each time step, with the resulting error used to adjust the subsequent time step. Alternatively, integral trajectories with different time step resolutions can be used to estimate errors based on differences in the final positions and velocities.

An alternate method of error monitoring is to track a known constant of the motion. If the ray tracing algorithm does not explicitly conserve energy, comparison of initial and final particle total energy provides a direct means of measuring calculation errors. This has the advantage that it captures finite-grid interpolation errors in addition to errors caused by large time steps. Making energy conservation a selectable feature of the tracing algorithm can also be beneficial. An initial run without conservation can be used determine a step size that results in acceptable errors, then a second run with conservation produces a more accurate result.

Generally the time step is not held fixed for the tracing algorithm, but is continuously adjusted to produce a calculated trajectory that has a small constant level of error. This requires an algorithm that decreases the time step when accelerations are large or when the velocity changes rapidly due to coordinate singularities. If the field grid has no large gradients, a simple "adaptive time step" algorithm can be used that fixes the fractional grid space traveled in a time step:

$$\Delta t = \Delta s/(|V| + V_{\min}) \tag{A.21}$$

where Δs is the fractional grid spacing and is generally kept less than 0.5. The term $V_{\min}$ is introduced to prevent too large a time step when particles reflect as $V \rightarrow 0$. More complex "adaptive time step" algorithms can be found in *Press et al.* [1992].

We point out that the increased accuracy provided by higher order algorithms may not produce a significant increase in computational speed. The reason is that the boundary crossing algorithm may require particle motion to be incremented by <0.5 grid spacings during a time step in order to detect a particle striking a surface. For nominal array dimensions with 10-60 grid points between different potential surfaces, (A.19) is fairly accurate for time steps producing motion of ~ 0.1 grid spacing.

Once an algorithm for integrating the equations of motion is selected, a boundary crossing algorithm needs to be developed. Details of this algorithm depend upon how boundary conditions are stored. A simple and fast algorithm can be developed that relies on the "boundary array" (see "Electric Field Solving Algorithm" in Section A.1.1). The "boundary array" records surface boundary points using a "1" for boundary points and "0" for non-boundary points. This algorithm requires that all grid points within $1/\sqrt{2}$ of the ideal boundary condition be assigned a "1" and that particle motion be limited to <0.5 of the grid spacing per time step. After each time step, the boundary crossing algorithm tests the nearest "boundary array" grid point. If "0", the algorithm goes to the next time step. If "1" and the grid is 3-D (2-D) it tests the additional three (two) nearest "boundary array" grid points that form a tetrahedron (triangle) containing the particle. If all are "1", the particle is defined to have crossed a surface boundary. This algorithm maintains a surface roughness similar to the grid resolution. For analyzer geometries where particles skim along the analyzer surfaces, such as electrostatic analyzers, one can reduce errors caused by surface roughness by defining the curved surfaces with slightly larger or smaller radii to compensate, leaving the surface peaks near the ideal radii. If higher accuracy is required,

one can use the above algorithm to trigger a more complex surface crossing algorithm. The more complex algorithm need only be called when the particle is near a boundary.

In addition to the ray tracing and boundary crossing algorithms, the ray tracing programs needs a user interface. The user interface should make it convenient to input initial conditions and to display the results of a simulated particle trajectory. Input parameters include the initial position, X_0, initial velocity, V_0, and q/m. For multiple trajectories one should be able to select the incremental change in the initial position and velocity, ΔX_0 and ΔV_0. The user should have control over the time step, Δt (or Δs), and the program should indicate the level of "error" for each trajectory. The code generally requires both an interactive mode with real-time display capability, and batch mode for running numerous particles during instrument characterization. The display should plot surfaces in a variety of projections with selectable plotting limits, along with the trajectories projected onto the plotting surface. A file of output of trajectories should contain initial and final conditions (X_0, V_0, X_f, V_f) along with a measure of the error. We also suggest including a measure of the time-of-flight of the particle, which can be useful in mass spectrometer designs. Lastly, it is useful if the output file of one simulation run can be used as the input to a subsequent run, allowing an instrument to be designed in stages.

Once a set of boundary conditions have been determined and interactive testing completed, a complete characterization of the analyzer response is needed. This amounts to finding the phase space volume of initial conditions that produce successful trajectories. Often symmetry of the analyzer can be used to reduce the dimension of the phase space of initial conditions. For example in 2-D cylindrical coordinates (z, r, ϕ, V_z, V_r, V_ϕ), characterization of symmetric top-hat electrostatic analyzers can be achieved by either varying z, ϕ, V_z, V_r or by varying z, V_z, V_r, V_ϕ. Symmetry makes varying the azimuthal coordinate ϕ and azimuthal velocity V_ϕ equivalent. Due to the large number of computations involved in analyzer characterization, the ray tracing program is generally operated in a batch mode that requires no user interaction.

The brute force method of characterizing a sensor's total response is to determine the overall limits to the initial conditions, followed by setting up a batch job to test all trajectories in the phase space volume. This method of characterization generally leads to a rather small portion of trajectories (a few %) that actually transit the analyzer and requires significant computation time for analyzer characterization. An alternative is to use a Monte Carlo approach that randomly selects trajectories within the initial condition phase space, but again the fraction of trajectories passing through the analyzer is generally small.

A much faster and uniform analyzer characterization can be obtained with a smart particle selection algorithm. This algorithm starts with an initial condition that produces a successful trajectory. It then selects its nearest neighbors in initial condition phase space and runs these trajectories. Of those trajectories that are successful, it again selects their neighbors in initial condition phase space, eliminating any trajectories already run. The mapping is complete when the last successful trajectory has no neighbors that have not been run. This method quickly maps out a contiguous volume in initial condition phase space of successful trajectories. For typical electrostatic analyzer designs, we find $\sim$50 % of the attempted trajectories are successful. For complex analyzers optics, one may need to determine whether the response has more than one contiguous volume in phase space requiring additional initial conditions to be found in these separate regions.

To optimize computing speed, the smart particle selection method must have a fast algorithm for testing whether a trajectory has been run. A simple method is to create an "already-run" array with dimensions that match the limits of the initial conditions. For example, consider initial conditions specified in a mixed coordinate system where we define position in terms of cylindrical coordinates, (z, r, ϕ), and velocity in pseudo-spherical coordinates, (E, α_v, ϕ_v), where E is energy, α_v is elevation angle and ϕ_v is the azimuthal angle. (See Figure 2.30 for pseudo-spherical coordinates). This mixed system of initial conditions can be convenient for comparison with theory or test data where the sensor has cylindrical symmetry but the testing apparatus produces rotations in spherical coordinates. Note that although the initial conditions are specified in one coordinate system, the ray tracing algorithm can use another coordinate system with a coordinate transformation at the start and end of a trajectory. If the initial condition phase space spans $z = \{30, 50\}$, $\phi = \{-30, 30\}$, $E = \{1.2, 1.9\}$, $\alpha_v = \{-10, 10\}$, with $\Delta z = 0.5$, $\Delta\phi = 2$, $\Delta E = 0.02$, $\alpha_v = 0.5$, the "already-run" array would require dimensions [41,31,36,33]. Once a trajectory has been run, a "1" is assigned to the array at the corresponding index. For example, initial condition $z = 34$, $\phi = 16$, $E = 1.52$, $\alpha_v = -5$ corresponds to index [8,23,16,5], where we start our indexing at zero. By indexing in this way, initial conditions can be quickly tested for a previous run. Since only "1"s and "0"s are needed, the "already-run" array can be a byte array to save memory.

The trajectory batch mode approach described above is used to characterize the total analyzer response. Its output is a file of successful trajectories containing initial and final conditions, along with other diagnostics of the run. Display programs needed to analyze these trajectories and characterize the instrument response are described below.

A.1.3 Display Programs for Characterizing Analyzers

In addition to the plotting routines required by the Field Solving and Ray Tracing Programs to display surfaces, field contours, and particle trajectories, the ray tracing package needs a program that can produce summary plots of instrument response in order to characterize the analyzer. The input data to these plotting routines are the output files from the batch programs that have determined the phase space volume of successful trajectories. These files generally contain a list the initial and final conditions (position and velocity) for each successful trajectory, along with any additional information such as travel time through the analyzer. Most of the required plots are rather straight forward weighted histograms or contour plots. However, plotting routines that can convolve the particle's input or output conditions with some function are also highly useful both for comparisons with calibration data and for designing aspects of the instrument such as collimation. Useful plotting routines are described below.

Chapter 3 has provided several examples of the use of analyzer simulations in a calibration effort. Transmission versus particle energy or angle of incidence, as seen in Figure 3.6b and 3.6c, are the most common weighted histograms used to characterize an analyzer. These plots provide a simple data set for comparison with calibration data. They also provide the designer with information about how the analyzer behaves in a non-ideal sense to broaden a measurement. For example, most electrostatic analyzers have a roughly Gaussian response in both energy and angle (see Figure 3.6b,c), which will result in a factor of $\sqrt{2}$ broadening of beams with similar energy or angle widths. On the other hand, weighted contour plots as shown in Figure 3.6a and 3.8 are generally used to identify the

coupling between input parameters such as energy-angle coupling. This type of coupling can result in a complex distortion of narrow beams, such as the solar wind, which may require de-convolution to extract a correct pressure tensor. If the particle distribution is much broader than this measurement resolution, this broadening can generally be ignored and the instrument response treated as ideal.

We use the term "weighted" when referring to transmission and contour plots to make it clear that all test particles that successfully transit an analyzer do not have equal weight in the analyzer response. The weighting depends on the projected area in the direction of the particle motion. For example, input particles with velocities $\boldsymbol{v}_i = (v_{xi}, v_{yi}, v_{zi})$ that are confined to an area bordered by $x = x_1, x = x_2, y = y_1, y = y_2$, with Δx and Δy spacing uniformly sampled, must used the projected area along the velocity vector, $\Delta x \Delta y (v_{zi}/|\boldsymbol{v}_i|)$, when calculating their contribution to the geometric factor. The program should also produce the weighted total of all the trajectories which can then be trivially converted to an analyzer geometric factor by scaling by the input resolution. For example consider a cylindrically symmetric top-hat sensor where initial conditions are stored as mixed cylindrical (z, r, ϕ) and pseudo-spherical (E, α_v, ϕ_v) coordinates (see Figure 2.30 for pseudo-spherical, where E is energy, $\alpha_v = \theta_v - 90°$ is elevation angle, and θ_v, ϕ_v are standard spherical coordinates). In the simulation, let z, ϕ, E, α_v be varied by Δz, $\Delta\phi$, ΔE, $\Delta\alpha_v$ with r, ϕ_v fixed. Each successful trajectory would be weighted by an area, $\Delta z(r\cos(\phi - \phi_v))(\pi\Delta\phi/180°)$, an energy range, ΔE, and a solid angle, $2\pi(\pi\Delta\alpha_v/180°)\cos(\alpha_v)$. Since successful trajectories will have $(\phi - \phi_v) \sim 0$ and $\alpha_v \sim 0$, these trajectories receive nearly equal weights of approximately $2\pi r\Delta z\Delta\phi\Delta E\Delta\alpha_v (\pi/180°)^2$. The total geometric factor is the sum of these individual weights.

Be aware that this calculated geometric factor may have small errors due to finite grid size that require corrections. For example, if the simulated analyzer surfaces protrude into the analyzer gap due to finite grid effects and result in the loss of particles, errors of the order of $(\delta R/\Delta R)^3$ may result, where δR is the grid resolution and ΔR is the gap. On the other hand, if the surface radii in the simulation are purposely chosen larger (or smaller) to prevent this type of loss, a small error in the calculated analyzer energy constant of the order of $\delta R/\Delta R$ could result (see Section 2.5.5.2 for definition of analyzer energy constant).

The transmission and contour plots should also be designed to work with both initial and final conditions of the trajectories. Whereas initial conditions are often uniformly spaced providing a natural binning resolution, output final conditions are generally random requiring determination of the binning resolution. Therefore the code needs to contain a mechanism to select both the range and resolution of this binning. It is also useful to include fitting routines, especially Gaussian fits, to provide a quantitative measure of analyzer energy and angle response.

Another useful plotting routine is to hold one or two input variables constant while plotting weighted transmission or contour response curves as a function of other variables. These types of plots are often useful for understanding subtle aspects of instrument response or the coupling between various input parameters. Since calibrations are generally performed with a spatially uniform, mono-energetic and parallel beam, a single calibration measurement has two input parameters fixed. An example of the usefulness of these plots occurred during calibration efforts for the Cluster/CODIF sensor. It was discovered that this toroidal top-hat analyzer (see Figure 2.33) could produce two separate image spots at the exit plane when illuminated with a monoenergetic parallel beam. There was a concern

that either the beam was non-uniform or that the analyzer was misbehaving, possibly containing surfaces that were charging and distorting the beam. A quick check of the simulated response showed the sensor was behaving normally. However, when averaged over all input beam energies and angles, the separate image spots merged into a single contiguous image.

There are several functional convolutions of the trajectory data that are useful in analyzer designs. One of the most useful and simplest is the projection of trajectories into regions near the starting or ending points. Generally the starting or ending points for successful trajectories are field free regions. In this case the trajectories can be trivially propagated around these locations to determine the spatial response at different locations without the need to perform a new batch simulation. In particular, projection of trajectories is extremely useful in designing analyzer collimation. For example, after batch characterization without including entrance collimation, one can: 1) select a collimator location and properties, 2) project the trajectories to the collimator location, 3) introduce spatial filtering that eliminates trajectories outside the collimation, and 4) plot the projected trajectories using standard plotting routines described above. This procedure can be quickly repeated until optimal collimation is determined.

This procedure was used in the design of the collimator/attenuator for the Mars Observer Electron Reflectometer [*Acuña et al.*, 1992]. This top-hat electrostatic analyzer was required to contain an attenuator that could reduce the flux by a factor of $\sim$40 at low energies while maintaining uniform response over the 360° field of view. The solution involved using a grid triplet in the main aperture, with the center grid biased to repel low energy particles. When the retarding voltage was applied, these grids were bypassed by thin slits in the support posts that suspended the upper portion of the analyzer. The key to the design was determining the radius and number of the support posts that could provided a uniform response over the azimuthal field of view. As the sensor was rotated through a parallel beam, the fall off in response at one slit required an increasing response at an adjacent slit so the total count rate would remain nearly constant. A single simulation of the analyzer without collimation, combined with plotting routines that projected and filtered successful trajectories, allowed a quick optimization of the collimator/attenuator design.

Another useful functional convolution calculates the response of the analyzer for selectable input distributions. Typical input distributions are drifting Maxwellians (such as the solar wind) or narrow-angle broad-energy beams (as found in auroral downward current regions). These convolution routines are particularly useful if the measurement requirements for angular or energy resolution are close to the expected analyzer response. These convolutions allow the designer to directly observe the distortion caused by finite energy and angle resolution, or by the energy-angle coupling, and thereby make adjustments to the design if needed before cutting metal. An additional useful feature is to design the convolution routines to produce simulated output count arrays that mimic the analyzer data files expected to be transmitted to the ground. These output arrays of counts should include expected statistical fluctuations. One can then use data analysis software to extract required measurement parameters, such as pressure, and compare these extracted parameters to the original input parameters.

Bibliography

Acuña, M., J. Connerney, P. Wasilewski, R. Lin, K. Anderson, C. Carlson, J. McFadden, D. Curtis, H. Rème, A. Cros, J. Medale, J. Sauvaud, C. d'Uston, S. Bauer, P. Cloutier, M. Mayhew and N. Ness The Mars Observer magnetic fields investigation, *J. Geophys. Res.*, **97**, 7799–7814, 1992.

Beer, G., *Programming the Bundary Element Method*, John Wiley & Sons, New York, 2001.

Binns, K.J., P.J. Lawrenson, C.W. Trowbridge, *The Analytical and Numerical Solution of Electric and Magnetic Fields*, John Wiley & Sons, New York, 1992.

Carlson, C.W., D.W. Curtis, G. Paschmann, and W. Michael, An instrument for rapidly measuring plasma distribution functions with high resolution, *Adv. Space Res.,* **2**, 67–60, 1983.

Carlson, C.W., and J.P. McFadden, Design and applications of imaging particle instruments, in *Measurement Techniques in Space Plasmas: Particles*, R. Pfaff, J. Borovsky, and D.T. Young, Eds., Geophys. Monogr. Ser., **102**, American Geophysical Union, Washington, D.C., 125–140, 1998.

Coplan, M.A. J.H. Moore, R.A. Hoffman, Double focusing ion mass spectrometer of cylindrical symmetry, *Rev. Sci. Instrum.*, **55**, 537–541, 1984.

Paolini, F.R., and G.C. Theodoridis, Charged particle transmission through spherical plate electrostatic analyzers, *Rev. Sci. Instrum.,* **38**, 579–589, 1967.

Pfaff, R.F., J.E. Borovsky, D.T. Young, Eds., *Measurement Techniques in Space Plasmas: Particles*, Geophys. Monogr. Ser., **102**, American Geophysical Union, Washington, D.C., 1998.

Potter, D., *Computational Physics*, John Wiley & Sons, London, 1973.

Press, W.H., B.P. Flannery, S.A. Teukolsky, and W.T. Vetterling, *Numerical Recipes in C: The Art of Scientific Computing*, 2^{nd} Ed., Cambridge University Press, 1992.

Theodoridis, G.C., and F.R. Paolini, Charged particle transmission through cylindrical plate electrostatic analyzers, *Rev. Sci. Instrum.*, **39**, 326–331, 1968.

Yildir, Y.B., K.M. Prasad, and D. Zheng, Computer aided design in electromagnetic systems: Boundary element method and applications, *Control and Dynamics Systems*, **59**, 167–223, 1993.

Zienkiewicz, O.C., R.L. Taylor, and J.Z. Zhu, *The Finite Element Method: Its Basis and Fundamentals*, 6^{th} Ed., Butterworth-Heinemann, Oxford, 2005.

A.2 Raytracing Software

MARTIN WÜEST
INFICON Ltd., Balzers, Liechtenstein

This section describes a selection of computer simulation packages that have been used in designing particle instruments. The emphasis of this list has been on packages for which support is available by the distributor or vendor. Additional software packages may be found at `laacg1.lanl.gov/laacg/software`

ANSYS

ANSYS Inc. provides both quasi static (low frequency) and full wave (high frequency) electromagnetics analysis capabilities across several finite element based products like ANSYS Emag, or ANSYS Multiphysics.

Simulation Method: Finite element
Operating System: Unix, Microsoft Windows

Vendor:
ANSYS Inc.
Southpointe
275 Technology Drive
Canonsburg, PA 15317
Phone: +1 724 514 3304
Fax: +1 724 514 9494
email: `info@ansys.com`
web: `www.ansys.com`

CPO Ltd

Fully relativistic calculation of electrostatic/magnetic fields and the trajectories of charged particles through those fields. Particle scattering and losses due to grid, background gas or secondary emissions can be simulated. Available in 2 and 3-D versions including support for space charge.

Simulation Method: Boundary Element Method
Operating System: Microsoft Windows

Vendor:
Charged Particle Optics (CPO) Ltd
Fax: +44 1625 615 011
email: `cpo@electronoptics.com`
web: `www.electronoptics.com`

Field Precision

Finite element code for electromagnetic simulation. Available modules: OmniTrack, AMaze (advanced 3-D electromagnetics), Trak, TriComp (Advanced 2-D electromagnetics).

Simulation method: Finite element
Operating System: Microsoft Windows, Linux

Vendor:
Field Precision
PO Box 13595
Albuquerque, New Mexico 87192
USA
Phone: +1 505 220 3975
Fax: +1 505 294 0222
email: techninfo@fieldp.com or sales@fieldp.com
web: www.fieldp.com

Infolytica

ElecNet and MagNet are graphical user interface based software packages that solve electrostatic, magnetostatic, DC current flow, time-harmonic and transient 2-D and 3-D problems subject to assigned electrode and boundary conditions. ElecNet solves Laplace's equation subject to assigned boundary conditions (usually assigned potentials-Dirichlet problem). Can model problems with complex model geometries and with different material properties. The Trajectory Evaluator Assistant module is used to simulate particle trajectories. The OptiNet module allows to optimize the design based on an evolutionary strategy.

Simulation method: Finite element
Operating System: Microsoft Windows

Vendor:
Infolytica Corp.
300 Leo Pariseau
Montréal, QC, H2X 4B3
Canada
Tel: +1 514 849-8752
Fax: +1 514 849-4239
email: info@infolytica.com
web: www.infolytica.com

Integrated Engineering Software

The different packages listed below use the boundary element method which allows modeling of large open field analysis and true geometry curvature rather than straight line

approximations required by other methods. 2-D modules: Electro (electrostatic analysis), Magneto (magnetostatic analysis), Oersted (time harmonic), Lorentz (particle trajectory) 3-D modules: Coulomb (electrostatic analysis), Amperes (magnetostatic analysis), Faraday (time harmonic), Lorentz (particle trajectory), Singula (high frequency).

Simulation Method: Boundary Element, Finite Element, and Hybrid Method
Operating System: Microsoft Windows

Vendor:
Integrated Engineering Software Sales Inc.,
1220-1821 Wellington Avenue
Winnipeg, Manitoba R3H 0G4
Canada
Phone: +1 204 632 5636
Fax: +1 204 633 7780
email: info@integratedsoft.com
web: www.integratedsoft.com

PBGuns

The particle beam gun simulation (PBGUNS) code is a fully interactive program for the simulation of axisymmetric 2-D electron and ion beams.

Simulation Method: iterative relaxation technique on a rectangular array of squares
Operating System: Microsoft Windows

References: *Boers* [1993, 1996]

Vendor:
Thunderbird Simulations
4724 Downey Street NE
Albuquerque, NM 87109
USA
Fax: +1 505 830 0532
Email: jeboers@comcast.net
web: thunderbirdsimulations.com

Poisson Superfish

POISSON SUPERFISH is a group of codes that solve Poisson's equation and are used to calculate static and RF electromagnetic fields in 2-D Cartesian coordinates or axially symmetric cylindrical coordinates.

Simulation Method: Finite difference method
Operating System: VMS, Unix, DOS/MS-DOS 3.3 or above, Microsoft Windows

References : *Halbach and Holsinger* [1976], *Menzel and Stokes* [1987], *Poisson User's Guide* [1981], *Poisson Manual* [1987]

Contact:
James H. Billen and Lloyd M. Young
Los Alamos National Laboratory
Group LANSCE-1
Mailstop H817
Los Alamos, NM 87545
Phone: +1 505 667 6627
Fax: +1 505 665 2904
email: jbillen@lanl.gov
web: laacg1.lanl.gov/laacg/services/psann.html

or

U.S. Department of Energy
Office of Scientific and Technical Information
Energy Science and Technology Software Center
P.O. Box 1020 175
Oak Ridge Turnpike
Oak Ridge, TN 37831-1020
Phone: +1 865 576 2606
Fax: +1 865 576 6436
email: ESTSC@adonis.osti.gov
web: www.osti.gov/estsc/

Simion

Simion Version 8 is a 3-D Microsoft Windows based ion optics program. Electrostatic and Magnetic fields are determined by numerically solving the Laplace equation via finite difference techniques. These techniques make use of over-relaxation and skipped point refining techniques to obtain solution times that are proportional to n (where n is the number of points in the array). A highly modified Runge-Kutta method is used to calculate ion trajectories in these fields. Automatically self-adjusting time steps make use of curvature and edge detection along with binary boundary approach methods to minimize the number of integration steps required to maintain ion trajectory accuracy. It can model complex problems using Laplace equation solutions for potential fields. The code can use up to 2 GB memory and supports array sizes up to 200 million points. Electrostatic and magnetic potential arrays can be studied with this software to determine their effect on ion trajectories.

Simulation Method: Finite difference
Operating System: Microsoft Windows

References: *Dahl et al.* [1990]

Vendor:
Ion Source Software
P.O.Box 2726
Idaho Falls, ID 83403
USA Phone/FAX +1 208 522 2224
E-mail: `simion@srv.net`
web: `www.srv.net/~klack/simion.html`

or

Scientific Instrument Services, Inc
1027 Old York Road
Ringoes, NJ 08551
USA
Phone: +1 908 7885550
FAX: +1 908 8066631
E-Mail: `sis@sisweb.com`
web: `www.sisweb.com`

Vector Fields

OPERA-3D is a pre and post-processor environment developed to analyze electromagnetic design problems in three dimension. At the core of the program is one of several modules such as TOSCA (3-D statics analysis), ELECTRA (3-D dynamic analysis), CARMEN, SCALA (3-D space charge analysis) or SOPRANO (high-frequency electromagnetic fields).

Simulation Method: Finite element
Operating System: Unix, Microsoft Windows

Vendor:
Vector Fields Ltd
24 Bankside
Kidlington
Oxford OX5 1JE
UK
Tel: +44 (0)1865 370151
Fax: +44 (0)1865 370277
Email: `Info@vectorfields.co.uk`
Web: `www.vectorfields.com`

Bibliography

Boers, J.E., PBGUNS: A digital computer program for the simulation of electron and ion beams on a PC, in *Proc. Internat. Conf. on Plasma Science (ICOPS)*, Vancouver, BC, 213, 1993.

Boers, J.E., An interactive version of the PBGUNS program for the simulation of axisymmetric and 2-D, electron and ion beams and guns, in *IEEE Proc. of the 1995 Particle Accelerator Conf.*, 2312–2313, 1996.

Dahl, D.A., J.E. Delmore, and A.D. Appelhans, SIMION PC/PS2 electrostatic lens design program, *Rev. of Sci. Instrum.*, **61**, 607–609, 1990.

Halbach, K., R.F. Holsinger, SUPERFISH - A computer program for evaluation of RF cavities with cylindrical symmetry, *Particle Accelerators*, **7**, 213–222, 1976.

Menzel, M.T. and H.K. Stokes, User's Guide for the POISSON/SUPERFISH Group of Codes, Los Alamos Accelerator Code Group, **LA-UR-87-115**, Los Alamos National Laboratory, Los Alamos, NM, 1987.

POISSON/SUPERFISH Group of Codes Manual, Los Alamos Accelerator Code Group, **LA-UR-87-126**, Los Alamos National Laboratory, Los Alamos, NM, 1987.

POISSON Group Programs User's Guide, Los Alamos National Laboratory Memorandum, Los Alamos National Laboratory, Los Alamos, NM, 1981.

A.3 High Energy Instrument Modeling

BRONISLAW K. DICHTER AND MICHAEL J. GOLIGHTLY
Air Force Research Laboratory, Hanscom Air Force Base, MA, USA

Sensor design, calibration and computer modeling are three interwoven elements of instrument development. As the design work proceeds, computer modeling and particle calibrations are used to provide feedback on the design work, which in turn leads to more complex models and calibrations. Monte Carlo codes, which simulate instrument response using stochastic methods and detailed physics models, play a key role in this effort. These codes, capable of detailed modeling of radiation interactions within the instrument, can provide highly precise computations of the instrument response. Great care, however, is called for in their use both in terms of available computer time and in terms of the errors introduced into the calculations that lead to reasonable looking but incorrect answers. The great precision that can be achieved with the modeling results does not ensure their accuracy. For example, if an instrument model contains an error or the distribution of incident particles is not correct, running a larger number of trajectories through the instrument will provide a precise answer (small statistical error) but an incorrect one (large systematic error). Confidence in the modeling accuracy and fidelity can only be achieved through comparison to calibration measurements under controlled conditions. If sufficient care is used, instrument computer models are an invaluable tool for the instrument development. In this appendix, we will describe how the sensor modeling fits into the instrument development process, give a general overview of Monte Carlo codes used for modeling instruments, and, finally discuss some problems with Monte Carlo modeling.

A.3.1 Instrument Development Process

Although a typical development process will be described below in a linear fashion, it really is a spiral process with numerous feedbacks among design, calibrations and simulations. In the end, instrument models usually must be used in extracting useful data from the measured signal because most of the situations that occur on orbit cannot be tested for or calibrated in the lab. Sensor modeling itself is a multilevel process ranging from simple semi-empirical models of key sensor features to a detailed 3-D computer model that includes all aspects of the mechanical design and sensor response to all relevant particles.

The types of instruments that benefit from modeling range from simple, single sensor, dosimeter behind a shield to complex multi-element detectors such as shown in Figure 2.20. For example, while a measurement of received radiation dose, in physical units, can be performed without any computer modeling of a dosimeter, the incident flux inferred by this measurement does require this type of modeling for a correct interpretation. This is because of a complex interrelationship of energy loss of particles with different energies and different angles of incidence. Multi-element instruments often require extensive modeling to convert counts in various sensor channels to particle fluxes. Energy losses and angular scattering effects are complicated for such detectors and stochastic events such as large angle scattering events and nuclear interactions may also be important.

Real detectors have responses that are characterized by limited acceptance, transformation and finite resolution. An example of transformation is the measurement of energy deposited in a Si solid-state detector. The quantity that is actually measured is the integral

of the current caused by the passage of a particle through the detector. It is necessary to transform the current measurement to an energy measurement. In an ideal system these quantities would be in direct proportion. However, non-linear effects due to sensor radiation damage or a high nuclear charge of the particle can have significant effects. Finite resolution of the measuring apparatus also adds to measurement uncertainty. As a result, there is only a statistical relationship between the true value of the quantity being sought and the quantity measured by the detector [*Blobel*, 2002]. This limitation must be understood before a significant modeling effort is undertaken.

The first step of the development process is the rudimentary design of the sensor and its mechanical envelope based on measurement requirements. Simple models of the key aspects of the instrument are then developed. These aspects include number, thickness and type (Si solid-state, scintillator, Cherenkov radiator, etc.) of sensors, the geometry of sensor placement in the instrument, shielding and energy degrading materials. Initial models consisting of an idealized sensor and its shielding and are used to determine the response to in-aperture particles of interest and some out-of-aperture particles that will be present the background signal.

Typical model calculations at this stage can be performed as "back of the envelope" calculations or using simple computer codes written by the developer. Public domain Monte Carlo codes such as SRIM [*Ziegler et al.*, 1985] can also be used at this point, to determine the energy loss of ions in key instrument elements. Energy deposition by electrons is highly complicated and usually requires a Monte Carlo code to accurately account for it. A public domain program such as CASINO [*Hovington et al.*, 1997] is an example of such a code for simple planar geometries. Nevertheless, useful results for electron energy deposition can be obtained using range-energy tables [*Pages et al.*, 1972] as well as reflection and angular scattering information [*Seltzer and Berger*, 1974]. The results at this stage are used to develop the prototype design. The prototype instrument is then constructed and subjected to initial calibration tests to verify the design and its modeling. The comparison of simulation and testing is then used to refine the instrument design and to develop an engineering model and a realistic geometric model of the entire instrument. Codes such as SRIM and CASINO only permit planar geometry and so cannot be used to study detailed response of geometrically complex instruments.

To model complex geometries, one turns to existing Monte Carlo codes such as ITS, GEANT, MCNPX, PENELOPE or EGS (see Section A.3.8) to determine the instrument response to incident particles. Comparisons are made with tests of the engineering model under well understood conditions using particle beams or radioactive particle sources to validate the computer models [*Galica et al.*, 2001a, b]. Results of modeling are used to further refine the instrument design in terms of sizes and geometries of its sensors and lead to the development of a fully geometrically realistic instrument model. Some Monte Carlo codes include the electronics chain and the data processing path of the instrument in the model. Electronics modeling is performed to study the influence of electronic noise on the instrument performance. As a final step, the data processing algorithm used to derive spectral information from the raw data, including ground post processing, can be modeled and the output compared to the input particle spectra.

At this point the flight or proto-flight instrument is built and undergoes final testing and calibration. The computer model is again validated using the calibration data. If there is a disagreement between the calibration data and the calculated response, both the instrument and model need to be investigated to determine the cause of the difference (see

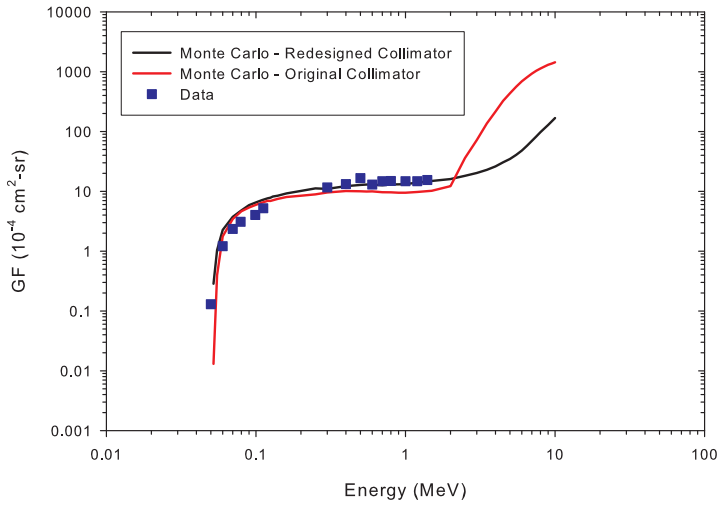

Figure A.1: Comparison of experimentally determined CEASE telescope electron geometric factors and those calculated using ITS Monte Carlo code. The red line shows the modeled response with the original collimator. The collimator geometry and composition were changed to reduce the effect of high energy (> 2 MeV) electrons on lower energy electron measurements. The modeled response of the redesigned collimator is shown with the black line.

Section A.3.6 on problems in using Monte Carlo simulations). The validated model is then used to determine the instrument response for cases where the instrument response cannot be measured due to limitations of calibrations facilities, schedule or budget. Once the instrument is on orbit, the full model of the instrument is used in converting counts into physical units and is a crucial element in the subtraction of background from the measured signal.

An example of instrument modeling impacting instrument design occurred in the development of the collimator for the Compact Environmental Anomaly Sensor (CEASE) [*Dichter et al.*, 1998]. One of the detectors of this instrument, a two element telescope with a collimator, was designed to make engineering measurements of high energy electrons responsible for deep dielectric charging. Electrons were detected and differentiated from protons by the pattern of energy deposition in the telescope detectors (dE/dx technique). An effort was made to extract scientific data on high energy electrons from the telescope counts. The unit was calibrated, using electron beams up to 1.4 MeV and data were compared to a Monte Carlo instrument simulation (Figure A.1). The energy dependence of the geometric factor at the lowest energies is limited by the transmission of the low energy electrons through a 9 μm entrance Al foil. At intermediate energies, the geometrical factor is determined by the collimator geometry. At the highest energies, the electrons penetrate the collimator and the geometric factor is determined by the geometry of the front and back detectors in the telescope.

Agreement between calibration data and calculated results was good up to the maximum measured energy. However, modeled results showed that above about 2 MeV the

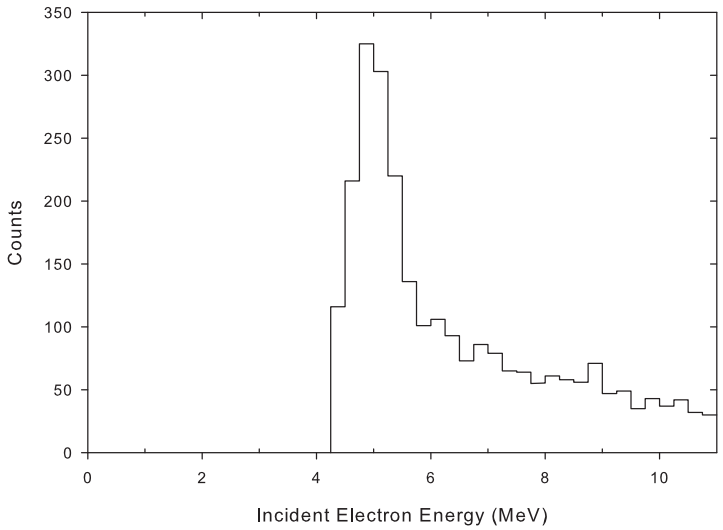

Figure A.2: A simulated spectrum of electrons contributing to the 5 MeV energy deposition channel in the GSO scintillator calculated using the GEANT code. High energy electrons contribute due to large angle scattering which causes them to leave the scintillator before depositing their full energy. This necessitates the use of spectrum unfolding techniques to obtain meaningful on-orbit data.

instrument responded to electrons with an increased sensitivity. This out-of-band response caused even small fluxes of high energy electrons to contaminate the measurements of low energy electrons, making these measurements difficult, if not impossible, under many environments expected on-orbit. The out-of-band response was traced to the design of the collimator, adequate for the engineering function of the instrument but not the secondary scientific function. After the first units were flown, the collimator was re-designed for the upcoming US Air Force Demonstration and Science Experiment mission (DSX) to 1) reduce the large energy sensitivity for high energy electrons and 2) to increase the threshold energy of that increased sensitivity (Figure A.1). The new collimator design used tungsten instead of copper, it was made thicker and its opening angle was decreased from 45° to 31°. The new collimator will allow improved low energy electron measurements under most conditions encountered on-orbit.

Another example of the use sensor simulation in the design of an instrument occurred in the development of a high energy ($1.5 < E < 12$ MeV) electron spectrometer proposed for the NASA Radiation Belt Strom Probe (RBSP) mission. The central element of the instrument was a cylinder of a high density Gadolinium Silicate (GSO) scintillator. GEANT simulation was used to evaluate various geometries of the GSO and determine the optimal dimensions, resulting in a GSO element minimized in size and mass and maximized in the probability of detecting the full electron energy. Results from GEANT modeling analysis determined the size of the GSO crystal such that increasing its dimensions did not significantly improve the amount of collected light. The GEANT analysis also showed that, due to backscattering from the crystal, at any incident energy there is a non-negligible probability that an electron will leave the crystal before depositing its full energy there,

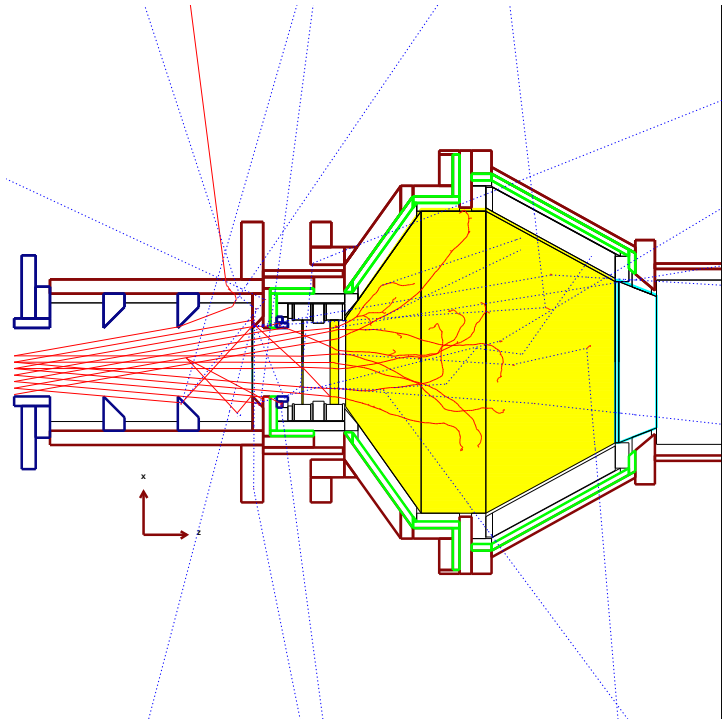

Figure A.3: A cutaway view of the entire HIST simulated geometry, overlaid with 10 MeV electron tracks (red) at 0°, -5° and +10°. Sections of the instrument, from left to right are: entrance collimator, detector stack, scintillator, and photomultiplier tube. Note the >10 keV photons (blue dashed), bremsstrahlung emission and Compton scattering within the scintillator. Each axis vector represents 2 cm. From `http://www.bu.edu/dbin/csp/`.

leading to an energy deposition spectrum such as shown in Figure A.2. This kind of spectrum clearly shows the effects of "smearing" the response to a particular energy electron into multiple data channels and points to the need for the application of spectral unfolding techniques to derive electron energy spectra from the raw data. GEANT can utilize user-developed algorithms to compute output light spectra which can be used to devise and test deconvolution algorithms well before the instrument is built and calibrated. Figure A.3 [*Contos*, 1997] graphically depicts results of a GEANT simulation of electron trajectories in the HIST instrument similar to the proposed RBSP electron spectrometer.

A.3.2 Monte Carlo Codes

The Monte Carlo process simulates real world events based on the probability of their occurrence and determines the average behavior of a system by observing a large number of such trials. As an example, consider the motion of a proton through a solid medium. Protons interact with the medium in two different ways. They lose energy to distant atomic electrons through many very small interactions in the medium. Although the process is

probabilistic, the large number of these events can be treated as a continuous process, well described by an analytic formula. Protons can also directly strike atomic nuclei in a low-probability, stochastic process; such events and their various outcomes must be determined by the collision cross section probabilities using suitably chosen random numbers. After a nuclear interaction, the incident proton is scattered, losing energy and significantly changing its direction of motion while the target atom recoils, possibly even breaking up into several fragments. The computer code then tracks and propagates the original scattered projectile proton and recoil(s) using the same algorithms as for the original proton, although with different collision cross sections.

The process of small energy losses to distant atomic electrons (continuous slowing down approximation or CSDA), is described by the Bethe-Bloch formula (see Equations 2.1 and 2.2) which shows that the rate of energy loss of an ion in matter is proportional to the electron density of the target and square of the effective ion charge and inversely proportional to the ion kinetic energy, times a complex function of relativistic and target material corrections. A slightly different version of the Bethe-Bloch formula, valid up to ultra relativistic energies, is used in the GEANT code. This program can also simulate complex proton-nucleus interaction processes such as large angle scattering and nuclear reactions. Repeating the process for a large number of incident protons, distributed in energy and angle over the entrance aperture of the instrument, provides the average in-aperture response. Just as importantly, modeling incident particles distributed over all incident angles over the entire surface of the instrument provides the out-of-aperture background. Clearly, the more incident protons are modeled, the more accurate the calculation, although care must be taken to avoid a random number generator which begins to repeat numbers prior to the maximum number of events. The number of incident protons that are modeled represents a compromise between the level of accuracy and the available computer time.

Electron trajectories in a material are more complex than proton trajectories. These particles also lose some energy through the CSDA as given by the Berger-Seltzer formula [*ICRU Report 37*, 1984] which is similar to the Bethe-Bloch formula. However, because scattering of equal mass particles efficiently transfers energy and momentum, electrons readily undergo large angle scattering events. This results in very complex electron trajectories, including back scattering. In addition, other processes such as bremsstrahlung, electron-positron pair creation and energetic knock-on electron production (delta rays) have to be included. For a complete discussion see the GEANT Physics Manual (`http://geant4.web.cern.ch/geant4/UserDocumentation/UsersGuides/PhysicsReferenceManual/html80/PhysicsReferenceManual.html`).

A.3.3 Numerical Issues

In the early stages of development, where simple, symmetric geometries are used, the instrument developer has a choice of writing their own custom Monte Carlo code to simulate instrument response or using a code such as GEANT from the outset. The choice of whether to pursue the custom code is a matter of personal preference. The advantage of the custom approach is that it forces the designer to develop a detailed understanding of the instrument and an appreciation of its functionally important elements. Writing a custom Monte Carlo code also provides a good introduction to the concepts and techniques used by more complete codes.

A.3.4 Random Number Generation

At the core of any Monte Carlo code is generation of random numbers. For someone writing a custom code, a thorough understanding of this process is a necessary prerequisite. Even if a code like GEANT is being used, an understanding of random number generation, according to different distributions, is important so that the code is not simply a black box.

Random variables are used throughout the code. At the start of an event, the location and direction of motion of the incident particle are chosen. Depending on the particle source used, these can be deterministic or chosen using random numbers. As the particle moves through a detector, after every short segment, the probability of a direct interaction is evaluated using a random variable. If there is no interaction, the particle loses energy according to a deterministic Bethe-Bloch or Seltzer formula. If there is an interaction, for example a nuclear reaction, random variables are used to determine the type, number and direction of the resulting fragments as well the lifetimes of all excited particles. Clearly, the complexities of the processes being modeled in the code requires other random number distributions in addition to uniformly distributed random numbers.

There exist many computer techniques for obtaining random numbers uniformly distributed over an interval [*Press et al.*, 1992]. However, random variable distributions of interest in Monte Carlo codes include those distributed according to other functions. For example, we may wish to simulate the energy resolution of a detector by choosing a Gaussian distributed random variable.

In addition to different types of distributions, there are often multiple, independent algorithms for generating the same type of distribution. Each features a different strength, such as speed, uniqueness of generated "seed" number and repeat periodicity. Attention should be given to ensure that the one selected will not introduce bias into the analysis. As an example of the variety of available random number generating functions, algorithms that can be used in the Monte Carlo program GEANT4 include the following options: uniformly distributed (flat) distributions using the James algorithm, the drand48(), srand48(), rand() and srand() system functions from the C standard library, the RANECU algorithm and GEANT's own RandFlat routine; an exponential distribution, given a user-provided mean value; a Gaussian distribution, given a user-provided mean and (optionally) deviation; a Poisson distribution, given a user-provided mean value and the Breit-Wigner algorithm (Toolkit Developer's Guide, II.12, "Class Design", `http://geant4.web.cern.ch/geant4/`, under "User Support").

There are both analytic and numerical methods of converting a uniformly distributed random variable to another type of distribution. Following *Press et al.* [1992], the analytical transformation technique useful for simple distributions can be written as follows. Begin with a uniform probability distribution $p(x)$

$$p(x) = \begin{cases} \mathrm{d}x & 0 < x < 1 \\ 0 & \text{otherwise} \end{cases} \tag{A.22}$$

This distribution is properly normalized $\int_{-\infty}^{+\infty} p(x)\,\mathrm{d}x = 1$. Generate a random number from the uniform $p(x)$ distribution and take a function $y(x)$ of it. The probability distribution of y, $p(y)$, is given by the fundamental transformation law of probabilities

$$|p(y)\,\mathrm{d}y| = |p(x)\,\mathrm{d}x| \tag{A.23}$$

If we require to generate random y's according to an arbitrary distribution $p(y) = f(y)$, where f is a positive function, normalized to unity on the interval $-\infty$ to $+\infty$, then

$$\frac{\mathrm{d}x}{\mathrm{d}y} = f(y) \tag{A.24}$$

Solving for x yields $x = F(y)$, where $F(y)$ is the indefinite integral of $f(y)$. If the inverse function of F^{-1} exists, then the properly distributed y is given by $y = F^{-1}(x)$.

Example 1: Interaction probability
The normalized probability, f, of an interaction by a particle moving a small distance z in a medium is given by

$$f(z) = \frac{1}{\lambda} \exp\left[\frac{-z}{\lambda}\right] \tag{A.25}$$

where λ is the mean free path and $\lambda \gg z$, by assumption. In order to get a random variable distributed according to $f(z)$, first compute the integral F,

$$F(y) = \int_0^y f(z)\,\mathrm{d}z = \int_0^y \frac{1}{\lambda} \exp\left[\frac{-z}{\lambda}\right] \mathrm{d}z = 1 - \exp\left[\frac{-y}{\lambda}\right] \tag{A.26}$$

Setting $x = F(y)$ and rearranging terms yields

$$1 - x = \exp\left[\frac{-y}{\lambda}\right] \tag{A.27}$$

If x is uniformly distributed between 0 and 1 (see Equation A.22), then $1 - x$ is also uniformly distributed on the same interval and has the same probability distribution. In effect, $1 - x$ is the same random variable as x so that instead of Equation A.27 it is possible to write

$$x = \exp\left[\frac{-y}{\lambda}\right] \tag{A.28}$$

The inverse function,F^{-1}, is the natural log and applying it both sides of Equation A.28 gives

$$y = -\lambda \ln(x) \tag{A.29}$$

This is the transformation that must be applied to a uniformly distributed random number x to get a random number distributed according to Equation A.25.

Example 2: Uniform distribution on a circular aperture
Suppose that an instrument model requires particles to be uniformly incident on a circular aperture with a radius of R. An efficient method, using the rotational symmetry of the aperture, leads to selecting values for the polar angle θ and the radius r. All values of θ on the interval 0 to 2π are equally probable so that a uniformly distributed random variable can be used to pick a value of θ. The values of r are not uniformly distributed on the

interval 0 to R. This is because the points must be uniformly distributed per unit area and, since the differential area element is $\mathrm{d}A = 2\pi r \mathrm{d}r$, the larger the value of r the larger the area it represents.

Since the area of the circular aperture as a function of its radius is $A(r) = 2\pi r^2$, it follows that

$$A(r) = 2\pi r^2 = \int_0^{2\pi} \mathrm{d}\theta \int_0^r f(z)\mathrm{d}z \tag{A.30}$$

Then, by inspection, the normalized probability distribution $f(z) = 2z/R^2$. Integrating $f(z)$ in a manner analogous to Equation A.26 yields

$$F(r) = r^2/R^2 = x \tag{A.31}$$

so that $r = R\sqrt{x}$ is the required transformation to get the uniform distribution on the entrance aperture.

If analytical inverse of the indefinite integral cannot be computed, the rejection method can be used. This method provides a random variable characterized by an arbitrary distribution function. For details the reader is referred to Sections 7.1 and 7.2 of [*Press et al.*, 1992].

A.3.5 Reduction of Variance

The result of a Monte Carlo calculation has an associated statistical uncertainty. This is most significant in studying rare events for which the statistical uncertainty is the largest. In general, rare events can be ignored in spacecraft instrumentation. However, if the in-aperture signal is small and the out-of aperture background due to penetrating particles is large, then even rare events coming from the out-of-aperture particles can be important. Simple "brute force" technique of increasing the number of events can be very costly in computer time, most of which would be spent on "normal" events, of little interest to the designer. Some techniques to solve this problem including truncation, population control and probability modification are described below. For a complete discussion of these techniques see *Rubinstein* [1981] and *Fishman* [1996].

Truncation involves ignoring elements that are not relevant to the problem. For example, when studying rare background events, e.g. when an incident particle and an energetic recoil strike two co-located detectors and generate a coincidence signal, only the geometry near the two detectors need be considered. This geometry model might include the two detectors and some nearby shielding. In this way the code is not wasting large amounts of time analyzing events occurring far away from the region of interest. Other examples include energy truncation (stop following a particle track once it gets below the energy of interest) and geometrical truncation (stop following a particle track once it reaches a certain detector zone).

Population control involves sampling important parts of the population more than less important ones. For example, in studying the response of a certain sensor to background radiation, a particle striking the shielding near the sensor would be split into m particles, each assigned a weight of $1/m$. Each of the m particle histories would then be tracked and included in the Monte Carlo results. Since the weight of each of these particles is $1/m$, the

splitting does not alter the overall statistical results to change. It does, however, allow for a more detailed sampling of a more important set of trajectories.

Probability modification involves sampling from fictitious, convenient distributions rather than from the true distribution and weighing the results to remove the introduced bias. In the example above, penetrating background particles near the sensor of interest, may be generated with a higher frequency, rather than simply generating them uniformly. This sampling scheme allows the most important histories to be tracked more often and, as long as the results are weighed accordingly, it does not bias the overall statistical results.

A.3.6 Problems in Using Monte Carlo Simulations

An important issue in using sophisticated codes such a GEANT is the accuracy of the instrument geometric model. These models tend to be complex, with numerous geometrical volumes representing individual sensors and shielding components. "Complex" does not necessarily imply "accurate" and complicated models may contain subtle errors. Incorrect zone dimensions or errors in identifying the zone material can lead to significant errors in computing the expected signal or signal-to-noise ratio. It is usually impractical to model the entire spacecraft; so that instrumental effects due to particles scattering from the spacecraft structures cannot always be studied. Therefore, it is vital that sophisticated instrument models be validated, to the extent possible, against simpler models and calibration and test results.

One example of the impact of a simple error in a complex geometric model involved an instrument designed to measure high energy (E $>$ 20 MeV) protons [*Redus et al.*, 2002]. Results of modeling of the instrument's response, using MCNPX, initially showed a very low response to high energy electrons and somewhat lower than expected response to protons. A follow-on analysis using a simple, semi-analytical model of the three first sensors of the instrument (D1, D2 and S1 in Figure 2.20), and using empirical electron angular scattering distributions [*Seltzer and Berger*, 1974] indicated that the electron response should be much greater. Subsequently, a dimensional error was found during a detailed study of the geometric model of the instrument used with MCNPX. Correcting the error led to good agreement between the electron response results from the two analyses. Perhaps even more importantly, the correction led to a change in the predicted high-energy proton response. Typically, data analysis occurs many years after an instrument is calibrated at a time when important details of the earlier analyses and measurements may be lost or are very hard to recover. Proper validation of instrument response modeling should be done prior to an instrument's launch in order to obtain meaningful on-orbit measurements.

The most subtle and insidious error in Monte Carlo based approaches is sampling random numbers from incorrect distributions. The earlier example of choosing points randomly distributed over a disk illustrates this problem. Unless great care is used, sampling the wrong distribution can lead to incorrect results. The errors are subtle because the code would appear to run properly and the erroneous results would appear to be reasonable. This particular error might not be caught on the ground if sufficient calibrations were not performed; this again illustrates the importance of validating the instrument models as much as possible using high quality calibration data.

A common error when modeling an instrument's response to penetrating background radiation is selecting a sampling algorithm that provides a uniform distribution of the pop-

ulation from the inner surface of a sphere. If a standard coordinate system is used with polar (Θ) and azimuthal (φ) angles, the initial approach might be to choose distributions uniform in both angles. This is, in fact, incorrect because while φ is uniformly distributed on [0,2π], it is the cos Θ that is uniformly distributed on the interval [-1,1].

Finally, if the response modeling involves particles moving toward the instrument's entrance aperture, then the effective area of the aperture A_{eff}, as a function of the angle of incidence, Θ, must be considered. Noting that A_{eff} is a function of cos(Θ) only, the normalized function f can be written as

$$f(\cos\Theta) = 2\cos\Theta. \tag{A.32}$$

By analogy to example 2,

$$x = 2\int_0^{\cos\Theta} \cos\phi \, \mathrm{d}\cos\phi \tag{A.33}$$

and the transformation, yielding the proper distribution in the angle Θ, is $\cos\Theta = \sqrt{x}$.

A.3.7 Conclusions

Requirements for successfully modeling an instrument's response to radiation using Monte Carlo methods include:

1. Understanding the mathematical basis of the approach, its advantages and shortcomings.
2. Clearly stating and conceptualizing the problem. What are the key elements of the model? What populations of particles are relevant to the problem?
3. Devising variance reduction techniques appropriate to the problem at hand.
4. Determining the correct random number distributions to sample in various parts of the calculation.
5. Testing the approach on a problem whose answer is known analytically, semi-analytically or from previous calibrations and experimental tests.
6. Recognizing that sophisticated programs often contain subtle errors.

A.3.8 Some Available Monte Carlo Codes

GEANT
Simulates full 3-D geometry of the detector. Protons, alpha particles, heavy ions and electrons as incident particles. Available energies (a few keV to thousands of MeV) cover the entire range of interest for energetic space particle detectors. Generates all relevant secondary particles including neutrons. Can be used to track particle coincidences in various detector segments. GEANT offers capability of simulating experimental resolution of the detector. Reference: `http://geant4.web.cern.ch/geant4/`. The GEANT physics reference manual is at `http://geant4.web.cern.ch/geant4/UserDocumentation/UsersGuides/PhysicsReferenceManual/html80/PhysicsReferenceManual.html`

MCNPX
Simulates full 3-D geometry of the detector. Protons, alpha particles, and electrons as incident particles. Available energies (a few keV to thousands of MeV) cover the entire range of interest for energetic space particle detectors. Generates all relevant secondary particles including neutrons. Can be used to track particle coincidences in various detector segments. Reference: `www-rsicc.ornl.gov`, Code number C00730.

SRIM
Simulates proton, alpha particle and heavy ion trajectories in planar geometry target material. Compute energy losses and energy loss straggling, range and range straggling and angular scattering in multiple material layers. Computes the damage to, and sputtering yields from, detector materials. Energy range spans from eV to GeV.
Reference: `http://www.srim.org/`

CASINO
Simulates electron trajectories in a planar geometry target material. Multiple target layers are accommodated. Visual display of electron tracks is provided as are useful histograms with information on the depth of penetration into sample, backscattered and transmitted energy. Energy range spans from eV to MeV.
Reference: `www.gel.usherbrooke.ca/casino/`

ITS 3.0
Calculates electron and photon transport through 3-D detector geometry. Incident electron energy range is 1 keV to 1 GeV. Reference: `www-rsicc.ornl.gov`. Code number C00467.

PENELOPE
Performs Monte Carlo simulation of coupled electron-photon transport in arbitrary materials and complex quadric geometries. A mixed procedure is used for the simulation of electron and positron interactions (elastic scattering, inelastic scattering and bremsstrahlung emission), in which 'hard' events (i.e. those with deflection angle and/or energy loss larger than pre-selected cutoffs) are simulated in a detailed way, while 'soft' interactions are calculated from multiple scattering approaches. Electron kinetic energies must be in the range from 100 eV to 1 GeV. Reference: Kim Buckner, U. S. Department of Energy Energy Science and Technology Software Center, P.O. Box 1020, OAK RIDGE, TN 37831-1020 U. S. A. E-mail: `ESTSC@adonis.osti.gov`

EGS
General purpose package for the Monte Carlo simulation of the coupled transport of electrons and photons in an arbitrary geometry for particles with energies from a few keV up to several TeV. Reference: `http://www.slac.stanford.edu/egs/`

A useful listing and comparison of heavy ion codes can be found in *ICRU Report 73* [2005].

Bibliography

Blobel, V., An Unfolding Method for High Energy Physics Experiments, Contribution to the Conference on Advanced Statistical Techniques in Particle Physics, Durham, 18–22 March 2002, Report-no: DESY 02-078, June 2002. Available at `http://www.arxiv.org/abs/hep-ex/0208022`.

Contos, A.R., Complete description and characterization of the high sensitivity telescope (HIST) onboard the POLAR satellite, M.S. thesis, 223 pp., Boston University, Boston, MA, 1997.

Dichter, B.K., J.O. McGarity, M.R. Oberhardt, V.T. Jordanov, D.J. Sperry, A.C. Huber, J.A. Pantazis, E.G. Mullen, G. Ginet and M.S. Gussenhoven, Compact Environmental Anomaly Sensor (CEASE): a novel spacecraft instrument for in situ measurements of environmental conditions, *IEEE Trans. Nucl. Sci.*, **45**, 2758–2764, 1998.

Fishman, G.S., *Monte Carlo, concepts, algorithms and applications*, Springer Verlag, New York, 1996.

Galica, G.E., B.D. Green, F. Scire-Scapuzzo, H.E. Spence, J.D. Sullivan, B.K. Dichter and D.L. Cooke, Scintillator-based ring current imager for nano-satellites, 39^{th} American Institute of Aeronautics and Astronautics Aerospace Sciences Meeting, Reno, NV, **AIAA-2001-0237**, 2001.

Galica, G.E., B.D. Green, F. Scire-Scappuzzo, H.E. Spence, J.D. Sullivan, B.K. Dichter, D.L. Cooke, Scintillator-based low energy particle imaging spectrometer for nanosatellites, in *Spacecraft Charging Technology, Proceedings of the 7^{th} International Conference*, R.A. Harris, Ed., *ESA Special Publication*, **SP-476**, ESA Publications Divison, Noordwijk, 287–295, 2001.

Hovington, P., D. Provin and R. Gauvin, CASINO: A new Monte Carlo code in C language for electron beam interactions, *Scanning*, **19**, 1–14, 1997.

ICRU Report 37, Stopping Powers for Electrons and Positrons, 1984.

ICRU Report 73, Stopping of Ions Heavier than Helium, Journal of the ICRU, **5**(1), 2005.

Pages, L., E. Bertel, H. Joffre and L. Sklaventis, Energy loss range and brehmstrahlung yield for 10 keV to 100 MeV electrons in various elements and chemical compounds, *Atomic Data*, **4**, 1–127, 1972.

Press, W.P., S.A. Teukolsky, W.T. Vetterling and B.P. Flannery, *Numerical Recipes, The Art of Scientific Computing*, 2^{nd} Ed., Volume 1 of Fortran Numerical Recipes, Cambridge University Press, New York, 1992.

Redus R.H., B.K. Dichter, M.R. Oberhardt, J.O. McGarity, J. Dalcomo, S. Woolf, A.C. Huber and J.A. Pantazis, Design, development and calibration of a high energy proton telescope for space radiation studies, *Nucl. Instrum. and Methods A*, **482** 281–296, 2002.

Rubinstein R.Y., *Simulation and the Monte Carlo method*, John Wiley & Sons, New York, 1981.

Seltzer, S.M. and M.J. Berger, Transmission and reflection of electrons by foils, *Nucl. Instrum. and Methods*, **119**, 157–179, 1974.

Sullivan, J.D., private communication, 2006.

Ziegler, J.F., J.P. Biersack and U. Littmark, *The Stopping and Range of Ions in Solids*, Pergamon Press, New York, 1985.

A.4 Calibration Facilities

WAYNE T. KASPRZAK[1] AND MARTIN WÜEST[2]
[1]*Goddard Space Flight Center, NASA, Greenbelt, MD, USA*
[2]*INFICON Ltd., Balzers, Liechtenstein*

This appendix presents an overview of most calibration facilities for space plasma instruments available in the world.

A.4.1 Summary of Calibration Facilities

First, each facility is listed in a one-line summary in Table A.1 for ion calibration facilities, Table A.2 for electron calibration facilities, Table A.3 for other calibration facilities, and Table A.4 for neutral calibration facilities. This is followed by Tables A.5–A.8 listing the abbreviations used in Tables A.1–A.4.

Second, each facility listed in the previous subsection is presented in some more detail in a two-page summary with a table giving a general description of the facility, its particle source, vacuum system, instrument mounting and rotation, ground support equipment, beam monitors, and also providing contact information. This is supplemented with a second page giving a schematic and/or some pictures of the facility.

Table A.1: Ion calibration facilities

Facility	Energy Range	Ion Source Type	Mass-to-Charge Selector	Source of Ions or Ion Species	Beam Current, Current Density	Beam Diameter, Area	Axis Position System	Maximum Instrument Size	Maximum Instrument Weight
CESR-1	50 – 30000 eV	EI	MAGMS	Gases 1–50 u	$<1\times10^{7}$ s^{-1} cm^{-2}	120 mm	2-R, 2-T	30 × 30 × 50 cm	10 kg
CESR-2	5 – 800 eV	EI	QUAD	Gases 1–50 u	$<1\times10^{7}$ s^{-1} cm^{-2}	10 mm	2-R, 2-T	40 × 40 × 40 cm	15 kg
CETP-IPSL	1 – 500 eV	EI	WFIL	H_2,He,N_2, CH_4,Ar	<10 pA cm^{-2}	2 cm	3-R, 1-T	30 × 30 × 30 cm	15 kg
GSFC-AEB	1 – 900 eV	EI	None	H_2,He,Ne, N_2,Ar,Kr, Xe	0.5-10 pA	1.2 cm	2-R, 1-T	23V × 61L × 28B cm	25 kg
GSFC-IPB-1	10 – 20,000 eV	EI	WFIL	H_2,He,Ne, N_2,O_2,Ar, CH_4,O,N, C_2H_6	<∼100 pA	5–50 mm	2-R, 2-T	91.4D × 91.4L cm	∼25 kg
GSFC-IPB-2	10 – 20,000 eV	DCD	WFIL	N_2	<∼100 pA	5–50 mm	2-R, 2-T	91.4D × 96.5L cm	∼25 kg
GSFC-REF-1	35 keV – 1.7 MeV	RF	EMAG	H^+,He,C^+, N^+,O^+,Ne, Ar,Kr,Xe	10^{-9} – 1 μA cm^{-2}	0.05 – 1.27 cm (in 9 steps); 5.08 cm (no aperture)	1-R, 1-T 1-R, 1-T 2-R, 1-T	1: 49.5 × 49.5 × 58.4V cm 2: 43.2D × 76.2V cm 3: 76.2D × 96.5V cm	1: 11.3 kg 2: 23-34 kg 3: 45.4 kg
GSFC-REF-2	1 – 130 keV	RF	EMAG	H^+,He,C^+, N^+,O^+,Ne, Ar,Kr,Xe	10^{-9} – 1 μA cm^{-2}	0.05 – 1.27 cm (in 9 steps); 5.08 cm (no aperture)	1-R, 1-T 2-R, 1-T	1: 49.5 × 49.5 × 58.4V cm 3: 76.2D × 96.5V cm	1: 11.3 kg 3: 45.4 kg

Table A.1: Ion calibration facilities (continued)

Facility	Energy Range	Ion Source Type	Mass-to-Charge Selector	Source of Ions or Ion Species	Beam Current, Current Density	Beam Diameter, Area	Axis Position System	Maximum Instrument Size	Maximum Instrument Weight
HAFB	20 eV – 20 keV	EI	None	N_2,O_2,Ar, Xe	0.05 – 1 pA cm^{-2}	12 cm	2-R, 1-T	30 × 35 × 40 cm	10 kg
IRF-1	30 eV – 50 keV	DP	WFIL	H^+,H_2^+, He^+,N^+, Ne^+,N_2^+,Ar^+	100 fA – 10 nA	8 cm	2-R, 2-T	365D × 400L	15 kg
IRF-2	100 eV – 30 keV	DP	WFIL	H^+,H_2^+, He^+,N^+, Ne^+,N_2^+,Ar^+	100 fA – 10 nA	10 cm	2-R	365 × 300 × 200	15 kg
ISAS-Ion-1	1 keV – 30 keV	EI	PMAG	H – Ar (gases only)	<10 pA	50 mm	3-R, 1-T	300 × 400 × 400 mm	15 kg
ISAS-Ion-2	1 eV – 10 keV	EI	EMAG	H – Zn	<20 μA	1 mm	3-R	250 × 250 × 250 mm	10 kg
ISL	<∼1 MeV – 800 MeV (Au) 3.5 MeV/n, $m/q = 6$ 6 MeV/n, $m/q = 4$ 70 MeV	ECR, VDG, 200 kV RFQ, CYCL	RMAG	p,d,Li,C,N, O,F,Ne,Cl,S, Ar,Kr,Xe,Au $^3He^+$,$^{12}C^+$ $^{18}O^+$,$^{36}Ar^+$ $^{84}Kr^+$,^{132}Xe $^{12}C^+$,$^{18}O^+$ $^{20}Ne^+$,$^{40}Ar^+$ $^{84}Kr^+$,^{132}Xe p for air experiments	∼100 part/sec – 1 μA	2 mm to 35 × 35 mm^2, 70 mm line, w/sample motion 300 × 300 mm^2	3-R	330 × 350 × 50 mm	4 kg

Table A.1: Ion calibration facilities (continued)

Facility	Energy Range	Ion Source Type	Mass-to-Charge Selector	Source of Ions or Ion Species	Beam Current, Current Density	Beam Diameter, Area	Axis Position System	Maximum Instrument Size	Maximum Instrument Weight
LMATC	~250 eV – 100 keV	DP	RMAG	H – Xe	~1 fA cm^{-2} – ~10 nA cm^{-2}	10 cm	2-R	30R cm	10 kg
LANL-ISR1	0.2 – 50 keV	MW	EMAG	H,D,H_2,He, C,CH_4,N,O, H_2O,Ne,CO, N_2,O_2,CO_2, Ar,Kr,Xe	<1 pA cm^{-2} – 0.1 μA cm^{-2}	1 mm – 2 cm	2-R, 1-T	50 × 50 × 50 cm	11 kg
MSFC-LEEIF	1 – 3000 eV	EI		H – Xe	0.01 – 100 pA cm^{-2}	2.5 – 20 mm	2-R, 2-T	46 × 46 × 30 cm	18 kg
SwRI-IDCF	≈500 eV – 51 keV	DP	WFIL	H – Xe positive, negative, ions	1 fA cm^{-2} – 1 nA cm^{-2}	10 cm	2-R, 2-T	70L × 120D cm	30 kg
UBern-CASYMS	5 eV – 100 keV	EI	RMAG	H_2,C_xH_y, N_2,CO_2,..., He – Xe	10^7 – 10^8 cm^{-2} s^{-1}	10×10 cm^2	3-R, 2-T	60 × 50 × 80 cm	50 kg
UBern-MEFISTO	3 – 100 keV/q	MW	WFIL	H_2,C_xH_y, N_2,CO_2,..., He – Xe, Na,Mg,Al, Ca,Cr,Fe,Zn	fA – μA	0.1 – 8 mm, pencil	2-R, 2-T	60 × 60 × 60 cm	20 kg
UCalgary-ASIF	1 eV – 10 keV	EI	WFIL	He,Ne,Ar, N_2,O_2, others possible	<1 μA	0.05 – 3 cm	2-R, 2-T	28 × 28 × 28 cm	10 kg

Table A.1: Ion calibration facilities (continued)

Facility	Energy Range	Ion Source Type	Mass-to-Charge Selector	Source of Ions or Ion Species	Beam Current, Current Density	Beam Diameter, Area	Axis Position System	Maximum Instrument Size	Maximum Instrument Weight
UCBerkeley-SSL	2 – 50 keV	DP	WFIL	H^+,He^+, Ne^+,O^+, N^+,Ar^+	$10^2 - 10^9$ part/s/cm^2	1 –10 cm	2-R, 1-T	16R cm 20L cm to FOV	15 kg
UDenver-1	20 – 3000 eV	DP	EMAG	H^+,H_2^+, H_3^+,He^+ H^-	0.5 – 50 μA (species dependent)	<2 mm	N/A	15.2B × 20.3W × 25.4V cm	15 kg
UDenver-2	3 – 1000 eV	EI	WFIL	positive, negative ions, <100 u, some metals	1 pA – 0.1 μA (species dependent)	<2 mm	2-R	50.8B × 50.8W × 50.8V cm	50 kg balanced
UMichigan-MASS-SPEC	500 eV – 30 keV	EI	WFIL	H–Ar	1.5 nA	2 cm	2R, 1T	30 × 30 × 30 cm	15-20 kg (balanced)
UNHampshire-1a-SIG	≤2 keV	EI	PMAG	Residual Gas	Variable	2.5 cm	1-R	30 × 30 × 50 cm	20 kg
1b-BIG	≤50 keV	EI	PMAG	Residual Gas	50 – 200 μA	≤2.5 cm	1-R	30 × 30 × 50 cm	20 kg

Table A.2: Electron calibration facilities

Facility	Energy Range	Electron Source	Beam Current, Current Density	Beam Diameter, Area	Axis Position System	Maximum Instrument Size	Maximum Instrument Weight
CESR-1	20 – 1000 eV 20 – 3000 eV	EG UV	$< 1\times10^{8}$ s^{-1} cm^{-2} $< 1\times10^{9}$ s^{-1} cm^{-2}	2 ×15 mm ^{2} 100 mm	2-R, 2-T 2-R, 2-T	30 × 30 × 50 cm	10 kg
GSFC-IPB-1	20 – 5000 eV	CEG	variable to ∼1 nA	5 – 15 mm	2-R, 2-T	91.4D × 91.4L cm	∼25 kg
GSFC-IPB-2	20 – 5000 eV	CEG	variable to ∼1 nA	5 – 15 mm	2-R, 2-T	91.4D × 96.5L cm	∼25 kg
GSFC-REF-1	35 keV – 1.7 MeV	ACC	10^{-9} – 1 μA cm^{-2}	0.05 – 1.27 cm (in 9 steps); 5.08 cm (no aperture)	1-R, 1-T 1-R, 1-T 2-R, 1-T	1: 49.5 × 49.5 × 58.4V cm 2: 43.2D × 76.2V cm 3: 76.2D × 96.5V cm	1: 11.3 kg 2: 23-34 kg 3: 45.4 kg
GSFC-REF-2	1 – 130 keV	ACC	10^{-9} – 1 μA cm^{-2}	0.05 – 1.27 cm (in 9 steps); 5.08 cm (no aperture)	1-R, 1-T 2-R, 1-T	1: 49.5 × 49.5 × 58.4V cm 3: 76.2D × 96.5V cm	1: 11.3 kg 3: 45.4 kg
HAFB	3 eV – 30 keV	UV(Au)	0.01 - 0.3 pA cm^{-2}		2-R, 1-T	30 × 35 × 40cm	10kg
IRF-1	100 eV – 100 keV	CEG	100 fA – 10 nA	8 cm	2-R, 2-T	365D × 400L	15 kg
IRF-2	100 eV – 60 keV	CEG	100 fA – 10 nA	10 cm	2-R	365 × 300 × 200	15 kg
MSFC-LEEIF	1 – 1000 eV 67 keV max, 17 keV avg	CEG ^{63}Ni	1 nA – 400 μA	variable	2-R, 2-T	46 × 46 × 30 cm	18 kg
MSSL-ECF	<5 eV – 15 keV	UV(Au)	4 orders magnitude, <few pA cm^{-2}		2-R		
RPI-LINAC	8 – 70 MeV	ACC	variable to >100 μA	1 – 50 cm	Remotely controlled	N/A	N/A

Table A.2: Electron calibration facilities (continued)

Facility	Energy Range	Electron Source	Beam Current, Current Density	Beam Diameter, Area	Axis Position System	Maximum Instrument Size	Maximum Instrument Weight
SwRI-ECF	< 1 – 30 keV	UV (Au)	variable $\sim 10^{-4}$ erg cm^{-2} sr^{-1} s^{-1} eV^{-1}	< 1.9 cm	2-T, 2-R	11.4D × 8.9V cm	500 g
UCBerkeley-SSL	100 eV – 30 keV	UV (Cr)	$< 10^6$cm^{-2} s^{-1}	∼ 10 cm	2-R, 1-T	16R cm 20L cm to FOV	15 kg
UCalgary-ASIF	5 eV – 1 keV	TES	< 1 μA	0.05 – 0.5 cm	2-R, 2-T	28 × 28 × 28 cm	10 kg
UNHampshire	5 eV – 15 keV	UV (Cr)	3 pA cm^{-2}	15 cm	3-R, 2-T	20 × 20 × 20 cm	5 kg

Table A.3: Other accelerator calibration facilities

Facility	Energy Range	Particle(s)	Source	Beam Current, Current Density	Beam Diameter, Area	Name Telephone Number E-Mail
AFRL/VSSE	0.33 – 1 Mev	Electrons	Dynamitron			William Kemp +1-505-846-6889 william.kemp@kirtland.af.mil
Brookhaven National Laboratory	1 – 29 Mev	Protons	Van de Graaff			Sandy +1-631-344-4581 ccarlson@bnl.gov
Boeing Space & Defense Systems	0.2 – 2.8 Mev 0.2 – 2.8 Mev	Protons Electrons	Dynamitron Dynamitron	∼hundreds μA $\leq$10 mA	15.2 cm 38.1 cm	Jerry Wert +1-206-544-5409 jerry.wert@boeing.com
Indiana University	40 – 200 Mev	Protons	Cyclotron			Barbara von Przewoski +1-812-855-2913 przewoski@iucf.indiana.edu
NASA Jet Propulsion Laboratory	0.15 – 1 Mev	Electrons	Dynamitron			Len Dorsky +1-818-354-4455 Leonard.I.Dorsky-103069@jpl.nasa.gov
NIST Radiation Interactions and Dosimetry	few keV to 300 keV 0.5 to 2.5 MeV 7 – 32 MeV	Electrons Electrons Electrons	DCCR Van de Graaff Linac			Fred Bateman +1-301-975-5580 fred.bateman@nist.gov
NRL	0.5 – 6 Mev	Protons	Van de Graaff			Kenneth Grabowski +1-202-767-5738 kenneth.grabowski@nrl.navy.mil
The Northeast Proton Therapy Center (NPTC) at Massachusetts General Hospital Center	100 – 230 MeV; down to 20 MeV w/energy degrader	Protons	ACC	$\leq$80 nA cm^{-2}	0.5 – 20 cm	Ethan Cascio +1-617-724-9529 ecascio@partners.org

Table A.3: Other accelerator calibration facilities (continued)

Facility	Energy Range	Particle(s)	Source	Beam Current, Current Density	Beam Diameter, Area	Name Telephone Number E-Mail
University of California Davis Crocker Laboratory	12 – 68 MeV 15 – 45 MeV 5 – 90 MeV 6 – 130 MeV	Protons Deuterons Alphas ^{3}He	ACC	$\leq$ 20 μA $\leq$ 20 μA $\leq$ 30 μA $\leq$ 1 μA	several mm – 7 cm	Carlos M. Castaneda +1-530-752-4228 Castaneda@Crocker.UCDavis.edu
University of Massachusetts Lowell Radiation Laboratory	1 – 5.5 MeV 1 – 5.5 MeV 2 – 11 MeV 2 MeV	H,D He^+ He^{2+} O	Van de Graaff	20 μA cm^{-2} 1 μA cm^{-2} 0.5 μA cm^{-2} 1 μA cm^{-2}		David DeSimone +1-978-934-3281 David.DeSimone@uml.edu
Western Michigan University	1 – 12 MeV	Protons	Van de Graaff			S. M. Ferguson +1-616-387-4957 steve.ferguson@wmich.edu
Yale Wright Nuclear Structure Laboratory	7.5 – 31 MeV	Protons	ACC			R. Casten +1-203-432-3090 rick@riviera.physics.yale.edu

Table A.4: Neutral gas calibration facilities

Facility	Speed, Energy, Temperature	Source	Gas or Ion Species	Beam Flux, Number, Current Density; Pressure Range	Beam Diameter, Area	Axis Position System	Maximum Instrument Size	Maximum Instrument Weight
GSFC-AEBa	300 K	TNG	H_2,He,Ne,N_2,Ar, Kr,Xe,CH_4,C_2H_2, C_2H_4,C_2H_6,NH_3, C_3H_4,C_3H_8,CO, CO_2,O_2,H_2O, CH_3OH,HCHO	$10^{-10} - 10^{-4}$ hPa	N/A	2-R, 1-T	23V × 61L × 28B cm	25 kg
GSFC-AEBb	0.5 – 4 km/s (1 % Ar in H_2)	HPBE	Trace gas in H_2 or He carrier			2-R, 1-T	23V × 61L × 28B cm	25 kg
GSFC-REF-1	35 keV – 1.7 MeV	CEX	H^+,He,C^+, N^+,O^+,Ne, Ar,Kr,Xe	10^{-9} – 1 μA cm^{-2} ∼30 % of beam are neutrals below 100 kev	0.05 – 1.27 cm (in 9 steps); 5.08 cm (no aperture)	1-R, 1-T 1-R, 1-T 2-R, 1-T	1: 49.5 × 49.5 × 58.4V cm 2: 43.2D × 76.2V cm 3: 76.2D × 96.5V cm	1: 11.3 kg 2: 23-34 kg 3: 45.4 kg
GSFC-REF-2	1 – 130 keV	CEX	H^+,He,C^+, N^+,O^+,Ne, Ar,Kr,Xe	10^{-9} – 1 μA cm^{-2} ∼30 % of beam are neutrals below 100 kev	0.05 – 1.27 cm (in 9 steps); 5.08 cm (no aperture)	1-R, 1-T 2-R, 1-T	1: 49.5 × 49.5 × 58.4V cm 3: 76.2D × 96.5V cm	1: 11.3 kg 3: 45.4 kg
LANL-1	2 to >7 km/s (∼1 to >4 eV)	LSD	O,N,H,He,Ar,Ne, Xe	10^{17} cm^{-2} s^{-1}	5.1 cm	3-T, 2-R	internal: 0.5 m^3 eternal: <1.3 m ground to beam axis	variable

Table A.4: Neutral Gas Calibration Facilities (continued)

Facility	Speed, Energy, Temperature	Source	Gas or Ion Species	Beam Flux, Number, Current Density; Pressure Range	Beam Diameter, Area	Axis Position System	Maximum Instrument Size	Maximum Instrument Weight
LANL-2	0.5 – 5.0 km/s	HPBE	O_2,N_2,CO_2,H_2O, SO_2, others	$\leq 10^{17}$ cm^{-2} s^{-1}	<1 cm^2	3-T, 1-R	internal: 0.2 m^3 external: <1.3 m ground to beam axis	variable
SwRI-IDCF	≈500 eV – 51 keV	CEX	H – Xe	1 fA cm^{-2} – 1 nA cm^{-2} ∼2 % of ion beam converted to neutrals	10 cm	2-R, 2-T	70L × 120D cm	30 kg
UBern-CASYMIR	2 – 150 K 0.3 – 4 km/s 0.07 – 7.5 eV	TNG HPBE	All gases, liquid/solid vapors, gas mixing manifold, H_2O boiler	$10^{-10} - 10^{-5}$ hPa $10^{12} - 10^{15}$ cm^{-2}s^{-1}	3 cm	2-R, 3-T	Instrument externally mounted, platform diameter 350 mm	100 kg
UBern-MEFISTO	15 eV – 3 KeV	IBN	H,O,C,N,...	$10^5 - 10^{10}$ cm^{2}s^{-1}	2 mm	2R, 2T	60 × 60 × 60 cm	20 kg
UDenver-1	20 – 3000 eV	DP LPD	H (100 % ground state)	$\leq 6\times10^{11}$ s^{-1} @ 50 eV, 1/v scaling	<2 mm	N/A	15.2B × 20.3W × 25.4V cm	15 kg
UDenver-2	3 – 3000 eV	EI LPD	O (100 % ground state) H (100 % ground state)	2×10^8 s^{-1} @ 50 eV, 1/v scaling	<2 mm	2-R	50.8B × 50.8W × 50.8V cm	50 kg balanced

Table A.5: Abbreviations-Source

Abbreviation	**Name**
ACC	Accelerator
BIG	Large Ion Gun
CEG	Commercial Electron Gun
CEX	Charge Exchange
CYCL	Cyclotron
DCCR	Direct-Current Cascaded Rectifier
DCD	DC Discharge
DP	Duo-Plasmatron
ECR	Electron Cyclotron Resonance
EG	Electron Gun
EI	Electron Impact
EMAG	Electromagnet
HPBE	High Pressure Beam Expansion, skimmer system
IBN	Ion Beam Neutralization
KLY	Klystron
LPD	Laser Photo Detachment
LSD	Laser Sustained Plasma Discharge
MAG	Magnet
MAGMS	Magnetic Mass Spectrometer
MW	Microwave
NB	Neutral Beam
PEN	Penning discharge
PMAG	Permanent Magnet
RF	Radio Frequency
RFQ	Radio Frequency Quadrupole
RMAG	90° Bending Magnet
SIG	Small Ion Gun
TES	Thermionic Emission Source
TNG	Thermal Neutral Gas
UV	Ultraviolet
VDG	van de Graaff accelerator
WFIL	Wien Filter ($\boldsymbol{E} \times \boldsymbol{B}$)

Table A.6: Abbreviations-Facility

Abbreviation	Name
AEB	Atmospheric Experiment Branch (NASA GSFC)
AFRL	Air Force Research Laboratory
ASIF	Advanced Space Instrumentation Facility
CAPS	Cassini Auroral Plasma Spectrometer
CASYMIR	Calibration System for the Mass Spectrometer Instrument ROSINA
CASYMS	Calibration for Mass Spectrometers
CESR	Centre d'Etude Spatiale des Rayonnements
CETP	Centre d'étude des Environnements Terrestre et Planétaires
ECF	Electron Calibration Facility
GSE	Ground support equipment
GSFC	Goddard Space Flight Center
HAFB	Hanscom Air Force Base
IDCF	Instrument Development and Calibration Facility
IKI	Space Research Institute
IPB	Interplanetary Physics Branch (NASA GSFC)
IPSL	Institut Pierre Simon Laplace
IRF	Institutet för Rymdfysik (Institute of Space Physics), Kiruna, Sweden
ISAS	Institute of Space and Astronautical Science
ISL	Ionenstrahllabor, Berlin
LANL	Los Alamos National Laboratory
LEEIF	Low Electron Energy and Ion Facility
LMATC	Lockheed-Martin Advanced Technology Center
MEFISTO	MEsskammer für FlugzeitInStrumente und Time-Of-Flight
MSFC	Marshall Space Flight Center
MSSL	Mullard Space Science Laboratory
NASA	National Aeronautics and Space Administration
NIST	National Institute of Standards and Technology
NPTC	Northeast Proton Therapy Center at Massachusetts General Hospital
NRL	Naval Research Laboratory
QUAD	Quadrupole
REF	Radiation Effects facility
RPI	Rensselaer Polytechnic Institute
SSL	Space Sciences Laboratory
SwRI	Southwest Research Institute
UBern	University of Bern
UCBerkeley	University of California, Berkeley
UCalgary	University of Calgary
UDenver	University of Denver
UNHampshire	University of New Hampshire
UMichigan	University of Michigan
UTDallas	University of Texas, Dallas
VSSE	Space Vehicles Directorate/Space Electronics and Protection Branch (AFRL)

Table A.7: Abbreviations-Position

Mnemonics	**Name**
N-R	N=number of axes; R=rotation
N-T	N=number of axes; T=translation
D	Diameter
L	Length
V	Vertical
W	Width
B	Along beam
R	Radius

Table A.8: Abbreviations-Miscellaneous

Mnemonics	**Name**
CEM	Channel Electron Multiplier
MCP	Multi-Channel Plate
Channeltron	Channel Electron Multiplier
GPIB	General Purpose Interface Bus
DAC	Digital-to-Analog Convertor
ADC	Analog-to-Digital Convertor
NI	National Instruments
PC	Personal Computer
PCI	Peripheral Component Interface
GSE	Ground Support Equipment
FOV	Field Of View

A.4.2 Description of Calibration Facilities

Table A.9: Centre d'Etude Spatiale des Rayonnements Facility: CESR-1,2

Category	Ion and electron beam.
Description	High vacuum characterization and calibration facility for testing space plasma instruments with electrons and ions.
Vacuum System	System 1: Stainless steel chamber with terrestrial magnetic field reduction to 200 nT in a volume $30\times30\times30$ cm^{-3} System 2: Small chamber.
Ion Source	System 1: Electron impact source with energy range 50 eV to 30,000 eV. Mass range 1-50 u using a magnetic mass spectrometer. Beam diameter is 150 mm. Beam intensity kept constant to within 5 %. System 2: Movable ion beam with energy range 5 eV – 800 eV and beam diameter of 10 mm. Mass selection by quadrupole mass spectrometer.
Electron Source	System 1: Electron production by heated filament, beam covers an area of 2×15 mm^2 with an energy range 20 eV to 1 keV. Second electron source production by UV photoemission over an energy range 20 – 3,000 eV with a beam diameter of 100 mm.
Instrument Mounting	System 2: Turntable.
Rotation, Translation	
GSE	Computer control and data acquisition.
Monitors	System 1: Electron flux monitored by photocathode current or the current collected by a cylindrical anode. System 2: Ion flux measured by Faraday cup.
Contact	Jean-André Sauvaud Centre d'Etude Spatiale des Rayonnements 9, avenue du colonel Roche 31028 Toulouse cedex 4 France Tel: +33 (0)5 61 55 66 76 Fax: +33 (0)5 61 55 67 01 E-mail: `Jean-Andre.Sauvaud@cesr.fr`
Reference	

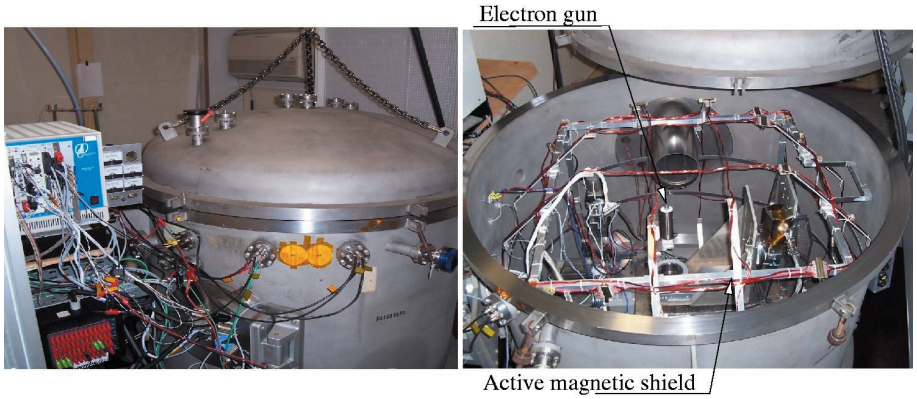

Figure A.4: Photograph of CESR calibration facility for low energy ions and electrons.

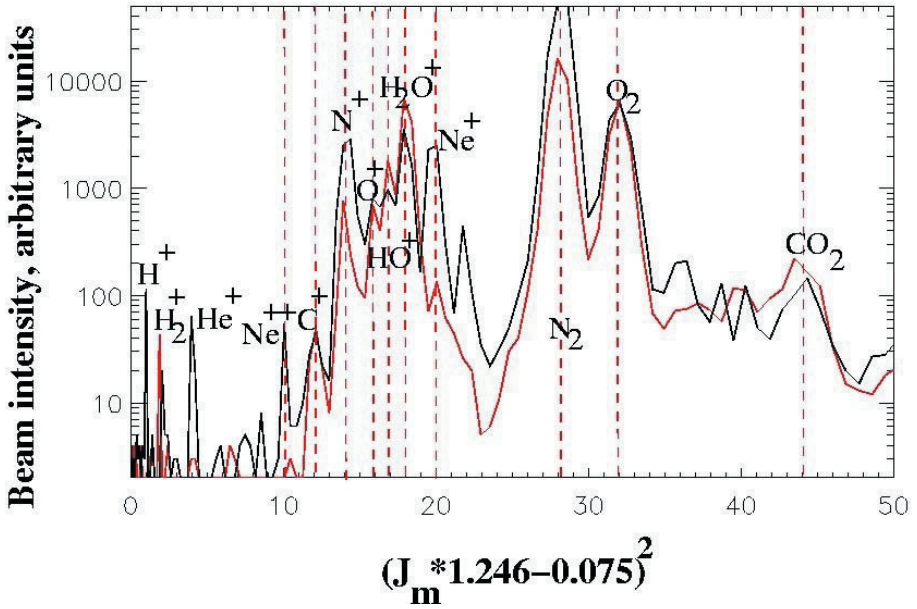

Figure A.5: Calibration of the ion beam in the large vacuum chamber (System 1). The horizontal axis is the mass-to-charge ratio derived from the ion gun magnet current, J_m (A).

Table A.10: Centre d'Etude des Environnements Terrestre et Planétaires Facility: CETP-IPSL

Category	Low energy ion beam.
Description	Ion calibration facility used for the development and calibration of ion mass spectrometers used for space research.
Vacuum system	The ion source is connected to a cylindrical (Diameter = Length = 1.2 m) stainless steel chamber. The main chamber door is also 1.2 m in diameter. All feedthrough connections are located on ConFlat^{TM} flanges. A clean vacuum of $\sim 5\times10^{-6}$ Pa ($\sim 5\times10^{-8}$ mbar) is obtained with turbo-molecular and cryogenic pumps.
Ion Beam	The Colutron^{TM} ion source has an energy range 1–500 eV, a maximum flux 10 pA cm^{-2}, a beam diameter of 2 cm (energy dependent) and has a Wien filter as a mass selector. Gases used include H_2, He, N_2, CH_4 and Ar.
Instrument mounting	The instrument sits on a table that can be rotated $\pm 80°$ around the main vertical axis and the instrument can be rotated $\pm 20°$ with respect to this direction around one vertical and one horizontal axis located in a plane at a variable distance (0 to 12 cm) from the main axis. This allows placement of individual windows of a spectrometer in front of the beam and allows a change in the direction of the ion flux at the entrance. All movements are computer controlled and can be simultaneously activated. Maximum instrument size is $30 \times 30 \times 30$ cm and maximum weight is 15 kg.
Monitors, Gauges	A totally independent moving system supports a monitor detector (Retarding Potential Analyzer with MCP detection) which measures the beam energy and uniformity in the two dimensions (vertically and horizontally) perpendicular to the beam direction, just in front of the instrument entrance aperture. Bayard-Alpert hot filament ion gauges are used to measure the chamber pressure.
Contact	Jean-Marie Illiano CETP/IPSL 4 Avenue de Neptune 94100 St-Maur France Tel: +33-1-45114276 Fax: +33-1-48894433 E-mail: `Jean-Marie.Illiano@cetp.ipsl.fr`
Reference	

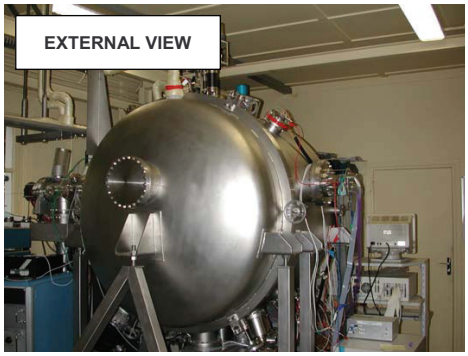

Figure A.6: External chamber view.

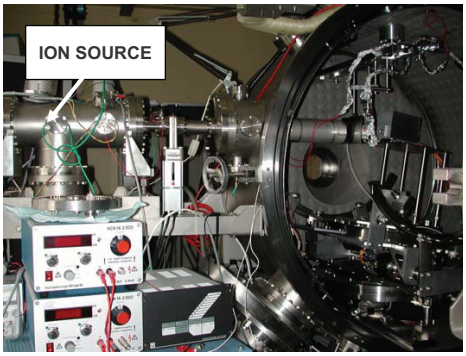

Figure A.7: View of ion source.

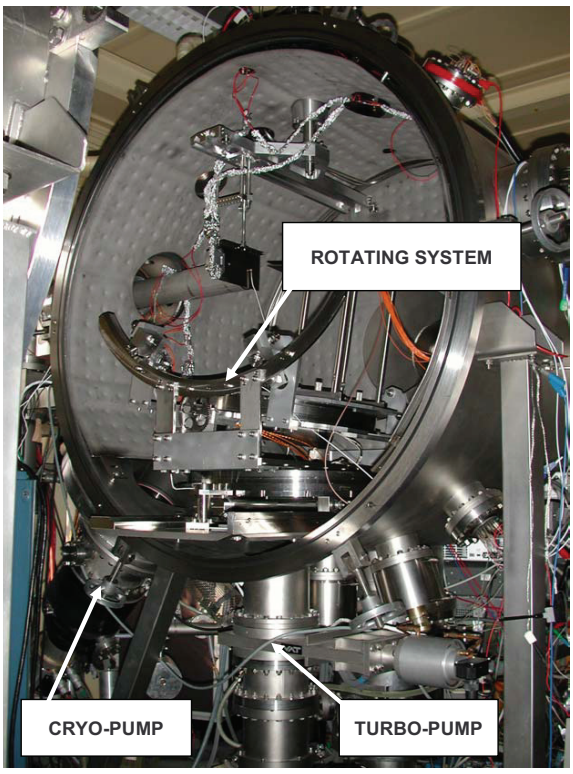

Figure A.8: Interior of vacuum chamber.

Table A.11: NASA Goddard Space Flight Center Facility: GSFC-AEB

Category	Neutral thermal gas, neutral gas beam and ion beam.
Description	High vacuum, gas calibration system for thermal gas and ion beam characterization of upper atmosphere mass spectrometers used for direct in situ sampling.
Vacuum System	All metal, bakeable to 300°C with oil-free turbopumps and forepumps.
Ion Beam	Commercial Extrel^{TM} ion source has a 1–900 eV energy range with a ΔE$\sim$40 V at 500 eV. The beam can be rastered and the beam diameter is less than 1.2 cm.
Thermal Gas	Permanent gas and liquid/vapor inlets use variable leaks, glass capillary leaks and capacitance manometers. The main chamber pressure range is $10^{-10} - 10^{-4}$ mbar. There is a separate gas inlet for the ion gun.
Neutral Beam	Hypersonic high pressure vacuum expansion of a carrier gas (usually He or H_2) with one or more trace amount seed gases. Beam speed $\sim$4 km s^{-1} for 1 % Ar in H_2.
Monitors, Gauges	The main chamber has a spinning rotor gauge, Bayard-Alpert ion gauges and a Dycor^{TM} residual gas analyzer. Metastable time-of-flight system for neutral beam.
Instrument Mounting	External to the vacuum system on bellows attached to a Conflat^{TM} flange. The maximum space inside cradle is 23 cm vertical $\times$ 61 cm horizontal $\times$ 28 cm along beam line. The maximum weight is 25 kg.
Rotation, Translation	Rotation is $\pm$25° about two orthogonal axes normal to ion beam line. Translation is $\pm$ 2.5 cm horizontally.
GSE	Computer control and readout of ion gun and system sensors with optimization of controlled ion source lenses.
Miscellaneous	Automatic overpressure protection system and protection in the event of a forepump failure. Gas cylinder safety cabinets and separate venting for forepump effluent is used for toxic gases.
Contact	Hasso Niemann NASA Goddard Space Flight Center Code 915, Atmospheric Experiment Branch Greenbelt, MD 20771, USA Tel: +1-301-614-6381 Fax: +1-301-614-6406 E-Mail: `Hasso.B.Niemann@nasa.gov`
Reference	

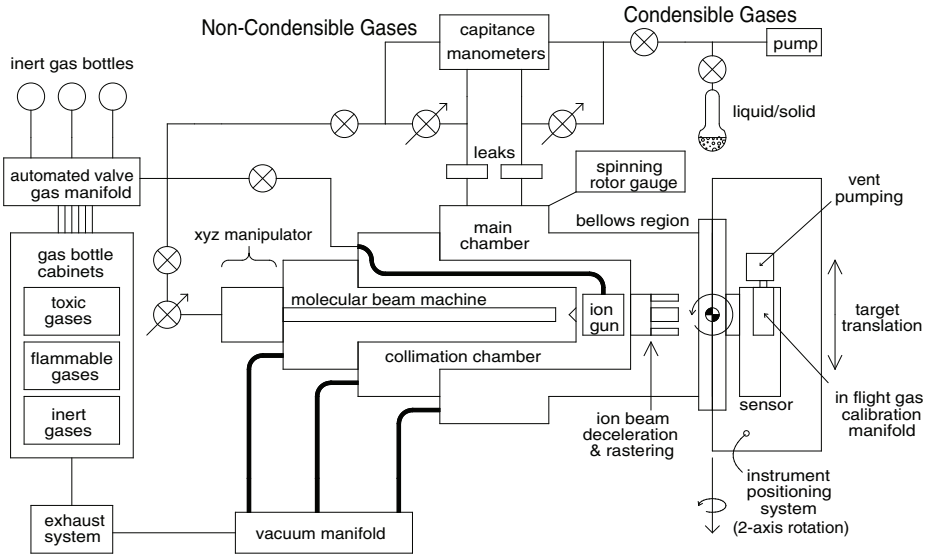

Figure A.9: Schematic of vacuum system.

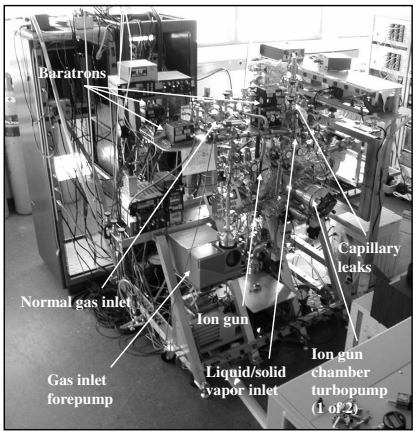

Figure A.10: Schematic of gas inlet system.

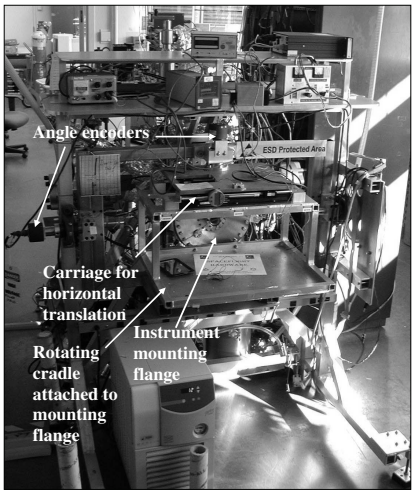

Figure A.11: Instrument cradle.

Table A.12: NASA Goddard Space Flight Center Facility: GSFC-IPB-1

Category	Ion and Electron Beam.
Description	Versatile, high vacuum calibration facility for ion and electron beam characterization of space plasma physics detectors/instruments.
Vacuum system	Chamber 1 is a cylindrical chamber, 91.4 cm diameter by 91.4 cm in length. Totally dry pumping system with a pressure of $\sim 1 \times 10^{-7}$ mbar using (2) 20.3 cm cryogenic pumps.
Ion Beam	The electron impact ionization source has an energy of 10-20,000 eV, a width $<$0.5 eV and a beam size 5 mm to 50 mm in diameter. Mass selection is done using a Wien filter with a resolution of $\sim$30. The beam intensity is $\sim$100 pA.
Electron Beam	A commercial electron gun (Comstock) with an energy range of 20–5000 eV, an energy width of $<$0.7 eV and a beam diameter of $\sim$5–15 mm. The electron beam is orthogonal to the ion beam.
Monitors, Gauges	Beam monitors consist of a 40 mm diameter 2-D imaging system (Quantar) and a Faraday cup with a Keithley 6517A electrometer.
Instrument Mounting	Stages are configured to accommodate the instrument under test (maximum weight $\sim$25 kg). Multiple SHV, BNC, Triaxial and SMA feedthroughs are available.
Rotation, Translation	Two rotation and two translation stages are computer controlled. Two additional translation stages are used for mounting beam monitors.
GSE	Computer control of all stages, power supplies, digital and analog I/O. Readout and recording of stage position, chamber pressure, beam monitor etc., together with sensor data. CAMAC system for fast A/D and TOF data acquisition using Sparrow KMAX software.
Miscellaneous	Automatic chamber pump down from atmosphere with overpressure protection circuit for failsafe shutdown. Other components include Helmholtz coil system, a SRS 200 Residual Gas Analyzer and a solar intensity UV source (Opthos).
Contact	Dennis Chornay NASA Goddard Space Flight Center Code 692, Interplanetary Physics Branch Greenbelt, MD 20771, USA Tel: +1-301-286-7307 Fax: +1-301-286-1683 E-Mail: `Dennis.Chornay@gsfc.nasa.gov` Web: `http://ipb.gsfc.nasa.gov`
Reference	

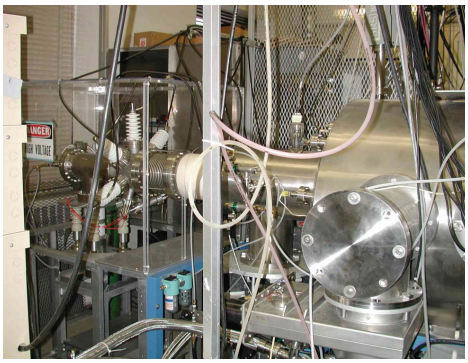

Figure A.12: Ion beam HV section.

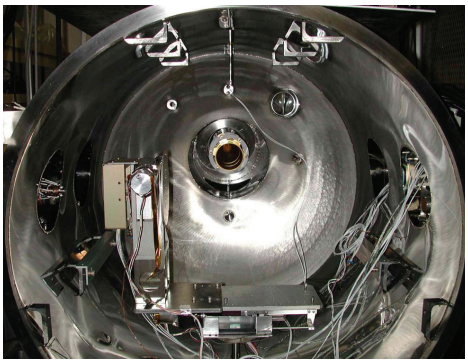

Figure A.13: Vacuum chamber 1.

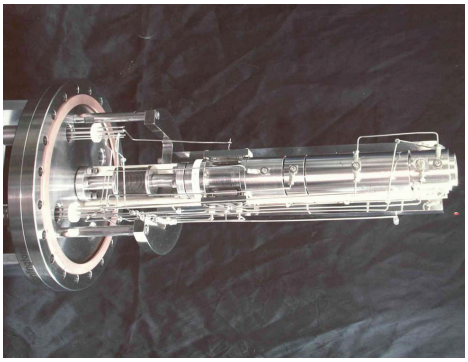

Figure A.14: Ion gun.

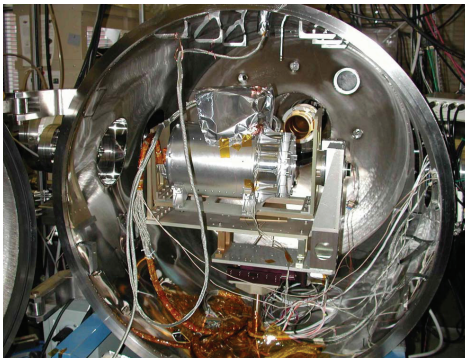

Figure A.15: Vacuum chamber 1, with instrument prototype.

Table A.13: NASA Goddard Space Flight Center Facility: GSFC-IPB-2

Category	Ion and Electron Beam.
Description	Versatile, high vacuum calibration facility for ion and electron beam characterization of space plasma physics detectors/instruments.
Vacuum system	Chamber 2 is a cylindrical chamber, 91.4 cm diameter by 96.5 cm in length. Totally dry pumping system with a pressure of $\sim 1 \times 10^{-7}$ mbar using one 25.4 cm cryogenic pump.
Ion Beam	A Multi-Charge State Source (MCSS) with mass selection using a Wien filter and resolution $\sim$10. The MCSS and Chamber 1 ionization source are interchangeable.
Electron Beam	A commercial electron gun (Comstock) with an energy range of 20–5000 eV, an energy width $<$0.7 eV and a beam diameter of $\sim$5–15 mm. The electron beam is orthogonal to the ion beam.
Monitors, Gauges	Beam monitors consist of a 25 mm diameter 2-D imaging system (Quantar) and a Faraday cup with a Keithley 6517A electrometer.
Instrument Mounting	Stages are configured to accommodate instrument under test (maximum weight $\sim$25 kg). Multiple SHV, BNC, Triaxial and SMA feedthroughs.
Rotation, Translation	Two rotation and two translation stages are computer controlled. Two additional translation stages are used for mounting beam monitors.
GSE	Computer control of all stages, power supplies, digital and analog I/O. Readout and recording of stage position, chamber pressure, beam monitor etc, together with sensor data. CAMAC system for fast A/D and TOF data acquisition using Sparrow KMAX software.
Miscellaneous	Automatic chamber pump down from atmosphere, overpressure protection circuit for failsafe shutdown. Other components include Helmholtz coil system, SRS 200 Residual Gas Analyzer and a solar intensity UV source (Opthos).
Contact	Dennis Chornay NASA Goddard Space Flight Center Code 692, Interplanetary Physics Branch Greenbelt, MD 20771, USA Tel: +1-301-286-7307 Fax: +1-301-286-1683 E-Mail: `Dennis.Chornay@gsfc.nasa.gov` Web: `http://ipb.gsfc.nasa.gov`
Reference	

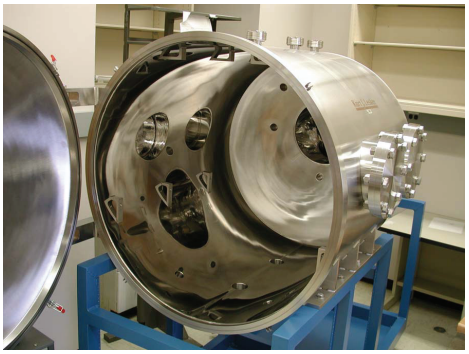

Figure A.16: Vacuum chamber 2.

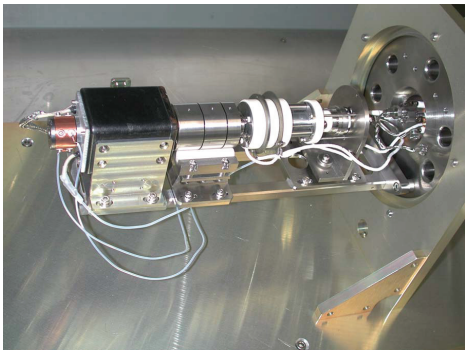

Figure A.17: Multi-Charge State Source (MCSS).

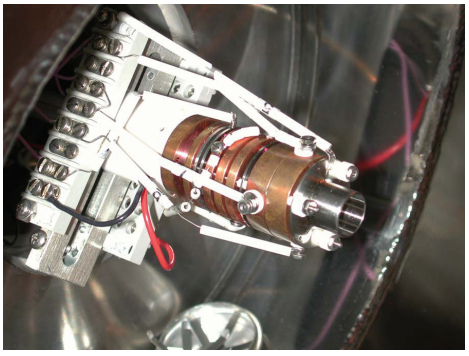

Figure A.18: Electron gun.

Figure A.19: UV source.

Table A.14: NASA Goddard Space Flight Center Facility: GSFC-REF

Category	Ion and Electron Accelerators.
Description	2 MeV and 150 keV instrument calibration accelerators.
Test Chambers	Three test chambers are available for housing the detector/instrument for calibration: 49.5 cm L × 49.5 cm W × 58.4 cm H; 43.2 cm D × 76.2 cm H; 76.2 cm D × 96.5 cm H (can be borrowed from APL). All the test chambers operate over a pressure range of $\sim 5\times10^{-8}$ mbar to $\sim 5\times10^{-7}$ mbar using cryogenic pumps.
2 MeV Accelerator	Accelerator provides electron, and ion beams with energies from 35 keV to 1.7 MeV with a beam intensity in the range of 10^{-9} to 1 μA cm^{-2}.
150 keV Accelerator	Accelerator provides electron and ion beams with energies from 1 keV to 130 keV with a beam intensity in the range of 10^{-9} to 1 μA cm^{-2}.
Common	Both accelerators provide beams of H, He, C, N, O, Ne, Ar, Kr, and Xe ions. The beam diameter is defined by an aperture ranging in size from 0.05 to 1.27 cm in 9 steps or 5.1 cm without an aperture.
Monitors, Gauges	The beam monitor, usually solid-state, is mounted just inside the entrance port on a remotely movable arm, and is positioned directly in the beam or completely out.
Instrument Mounting	50.8 cm × 50.8 cm chamber: Instruments sit on a 0.64 cm thick, 15.2 cm diameter turntable, mounted on a 1.91 cm vertical shaft coming up through the base plate. Max. weight is ∼11.3 kg. The shaft/turntable can be raised up and down manually, and can be manually or computer scanned in steps repeatable to $0.2^\circ \pm 0.1^\circ$. 43.2 cm D by 76.2 cm H chamber: Instruments sit on the 43.2 cm diameter turntable and must be spaced up and down with shims or slotted feet. Maximum weight is ∼22.7–34.0 kg. The turntable is remotely or manually adjustable to $360^\circ \pm 0.1^\circ$.
GSE	Solid-state detectors, pulse counters and pulse height analyzers are used for measuring particle rates and energies. Several HP 6201L scaler timers, two Nuclear Data Model 62 and two Canberra 35+ multi-channel analyzers are available.
Miscellaneous	Fine control of beam energies and low beam intensities.
Contact	Stephen K. Brown NASA Goddard Space Flight Center Code 561, Radiation Effects Facility Greenbelt, MD 20771, USA Tel: +1-301-286-5795, Fax: +1-301-286-4699 E-Mail: `Stephen.K.Brown@nasa.gov` Web: `http://radhome.gsfc.nasa.gov/radhome/ref/GSFC_REF.html`
Reference	

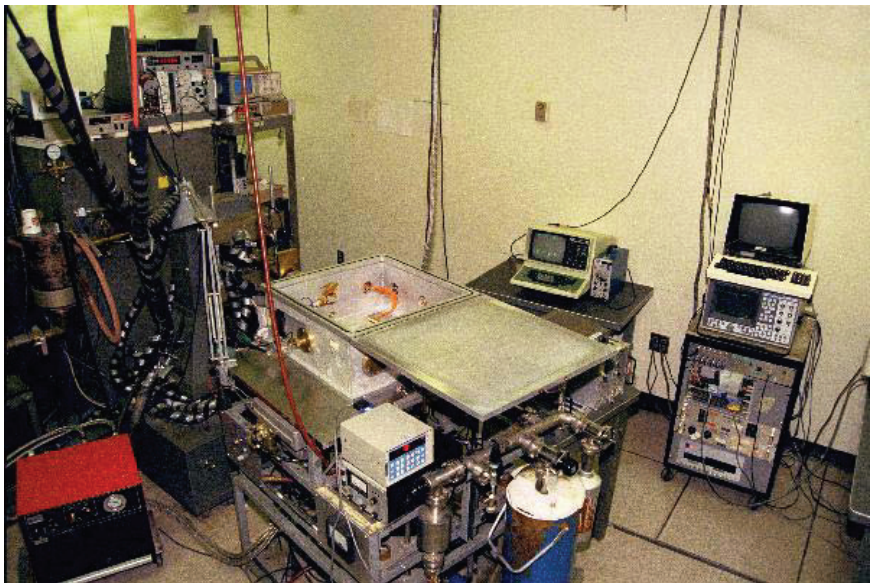

Figure A.20: Radiation Effects Facility (GSFC REF) 150 keV accelerator, steering magnet, 49.5 cm L × 49.5 cm W × 58.4 cm H test chamber, pumping station and turntable controls.

Figure A.21: Radiation Effects Facility (GSFC REF) steering magnet, electrostatic focus and 76.2 cm D × 96.5 cm H test chamber for the instrument Van de Graaff.

Table A.15: Hanscom Air Force Base Facility: HAFB

Category	Ion and electron beam.
Description	High vacuum facility for ion and electron beam characterization of space plasma physics instruments.
Vacuum system	Chamber 2.4 m long × 1.2 m diameter. Cyropumped to pressures in 10^{-7} mbar range.
Ion beam	20 eV – 30 keV ion source. Ions produced by electron impact.
Electron beam	10 eV – 30 keV electron source. Electrons produced by UV photoemission from gold. Flux $\sim 2 \times 10^{-10}$ mA/m^2, energy half-width 0.4 eV, angular half-width 1.2° at 1 keV.
Instrument mounting	Computer controlled 2-axis rotation system (0.02° resolution).
Monitors, Gauges	Beam diagnostics using Amptektron channel electron multiplier mounted in fixture with X and Y translation; can be mounted on gimbal table for angular beam characterization. 10 cm diameter Faraday cup.
Miscellaneous	External Helmholtz coils to reduce ambient magnetic field.
Contact	David Cooke Battlespace Environment Div - Space Hazards Branch Air Force Research Laboratory, VSBX 29 Randolph Road Hanscom Air Force Base, MA 01731, USA Tel: +1 781 377 2931 Fax: E-mail: david.cooke@hanscom.af.mil
Reference	*Biddle and Reynolds* [1986]; *Marshall et al.* [1986]

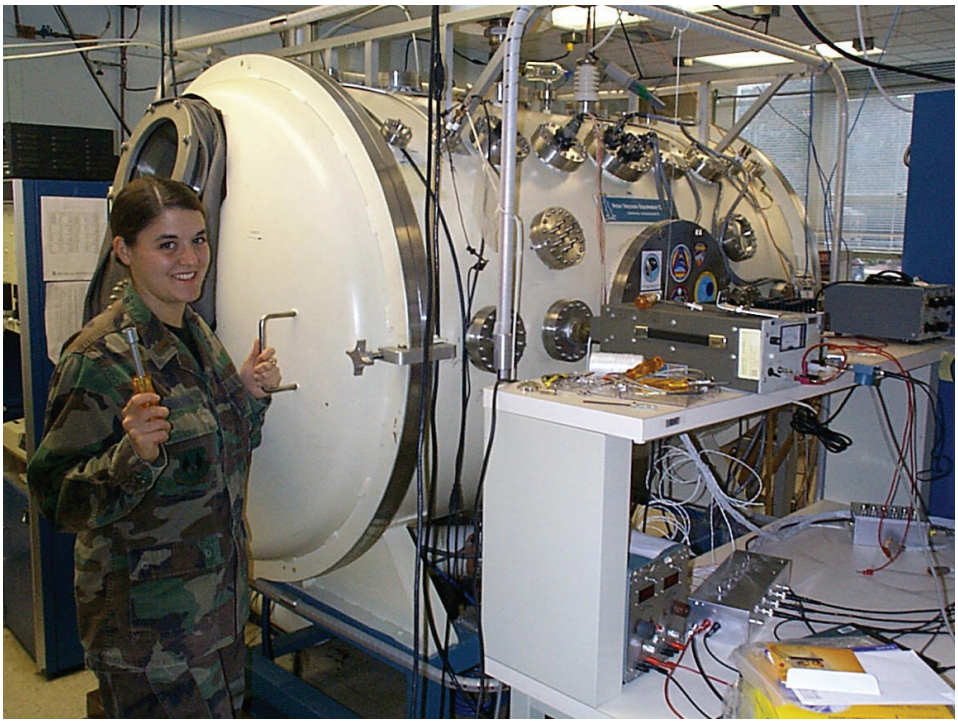

Figure A.22: HAFB calibration facility.

Table A.16: Institutet för Rymdfysik: IRF

Category	Ion and electron beam.
Description	High vacuum, ion and electron facilities for characterization and calibration of plasma spectrometers and energetic neutral atom imagers used for direct in situ measurements in planetary magnetospheres.
Vacuum system	Oil free forepumps, turbopumps and cryopumps. Main chambers: 1500 mm diameter and 1600 mm length, and 600 mm diameter and 700 mm length. Operational pressure $< 5 \times 10^{-7}$ mbar.
Ion beam	Peabody Scientific Duoplasmatron ion source. IRF-1 facility energy range: 30 eV – 50 keV. IRF-2 facility energy range 100 eV – 30 keV. Energy bandwidth < 1 %. Nominal beam is parallel, 8 cm diameter; focused beam is 3 – 4 mm diameter. Using charge exchange on the residual gas over the distance between the focusing lens and the instrument inlet (approximately 2 m) neutral beams are produced with an efficiency of 2 – 3 %.
Electron beam	IRF-1 facility energy range: 100 eV – 100 keV. IRF - 2 facility energy range: 100 eV – 60 keV. In both facilities the vacuum tank is shared between electron and ion beams. Electron and ion beam characteristics are similar.
Beam monitor	Faraday cup.
Instrument mounting	Turn table. The mounting plate is 365 mm diameter. The ion beam is horizontal (IRF-1) or vertical (IRF-2), electron beam is vertical on both facilities.
Rotation, Translation	IRF-1 facility: 4-axis positioning system; 2 rotations $\pm 180°$ and $360°$ about two orthogonal axes normal to ion beam line; horizontal translation 350 mm and vertical translation 310 mm. All stages are computer controlled. IRF-2 facility: 2-rotation system, rotations about two orthogonal axes normal to ion beam line.
GSE	Computer control of the turn table.
Miscellaneous	Vacuum pumps and valves controlled through interlock system using relay logic. Logic set up to prevent actions that may be harmful to the vacuum system.
Contact	Stas Barabash Swedish Institute of Space Physics 981 28, Kiruna, Sweden phone: +46-980-79122 E-Mail: `stas@irf.se`
Reference	

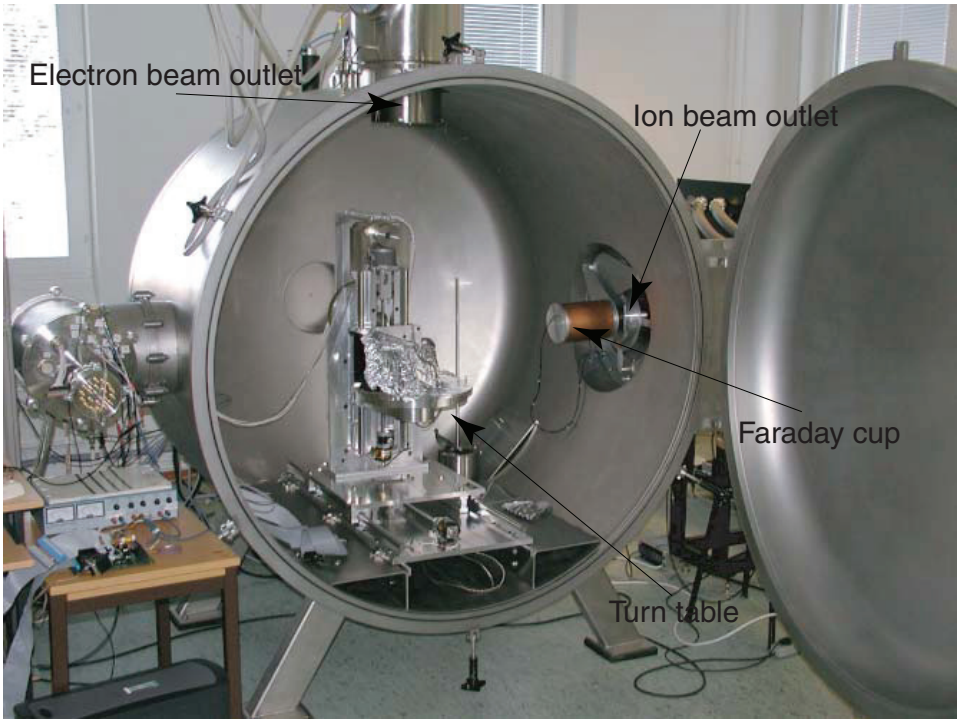

Figure A.23: IRF-1 ion and electron calibration facility. Open tank.

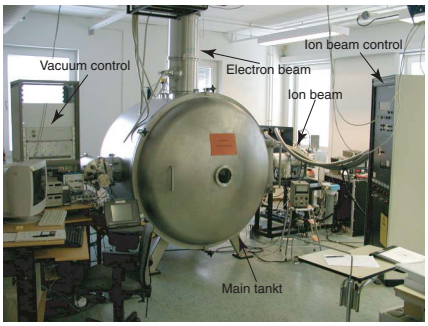

Figure A.24: IRF-1 ion and electron calibration facility. General view.

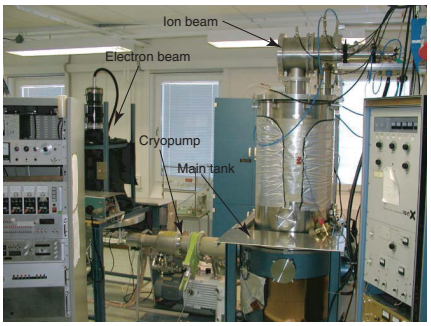

Figure A.25: IRF-2 ion and electron calibration facility. General view.

Table A.17: Institute of Space and Astronautical Science Facility: ISAS-Ion-1

Category	Ion calibration.
Description	High vacuum, ion calibration system for electron energy spectrometers, ion energy spectrometers, and ion mass spectrometers for measurements in the magnetosphere. The calibration ions are created from gases.
Vacuum system	The main chamber is 900 mm diameter $\times$ 1050 mm long, has a Daikin 2200 l s^{-1} cryopump, an Osaka Vacuum 1500 l s^{-1} turbopump, and an Alcatel 610 l min^{-1} rotary pump. The ion gun chamber has an Osaka Vacuum 150 l s^{-1} turbopump and Alcatel 75 l min^{-1} rotary pump.
Ion Beam	Beam energy range is 1–30 keV and is less than 5.0 cm diameter with an angular divergence less than 0.1°. The beam can be rastered.
Monitors, Gauges	Thermo-couple gauge, Bayard-Alpert hot filament ion gauges for pressure measurement. Ion beam diagnostics by an MCP with position sensing anode mounted on movable arm.
Instrument Mounting	Instruments are mounted on rotation table (50 cm $\times$ 50 cm) by a screw (M5). The interval between tapped holes on the table is 25 mm.
Rotation, Translation	$\pm$180° and $\pm$15° about two orthogonal axes normal to ion beam line. Movable arm rotates $\pm$180° about a vertical axis normal to ion beam line with $\pm$1.0 cm vertical translation.
GSE	Computer control of ion gun and optimization of controlled ion source lenses. Computer control of rotation table, movable arm, readout of their position, and computer control of high voltage power supply for sensors under calibration.
Contact	Yoshifumi Saito Institute of Space and Astronautical Science 3-1-1 Yoshinodai Sagamihara, Kanagawa 229-8510 Japan Tel: +81-42-759-8171 Fax: +81-42-759-8456 E-Mail: `saito@stp.isas.jaxa.jp`
Reference	*Hirahara and Mukai* [1992]

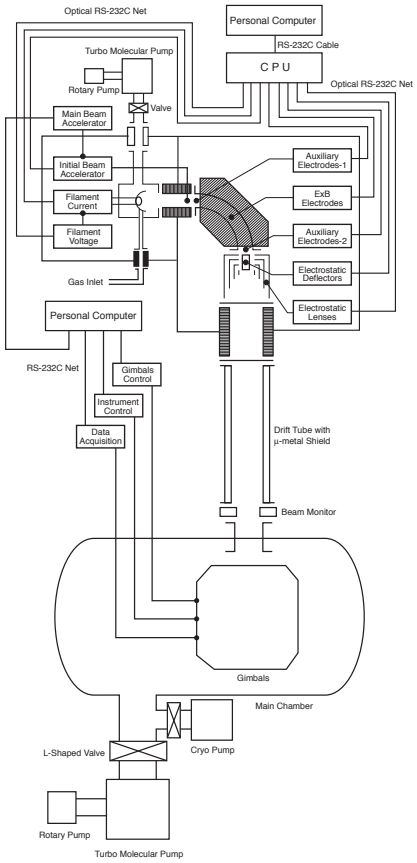

Figure A.26: Schematic block diagram of ISAS calibration facility.

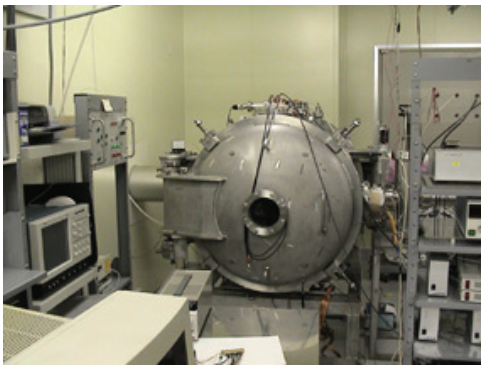

Figure A.28: Main chamber.

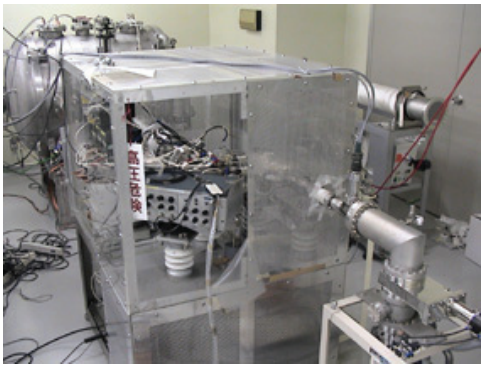

Figure A.29: Ion source.

Figure A.27: ISAS calibration facility.

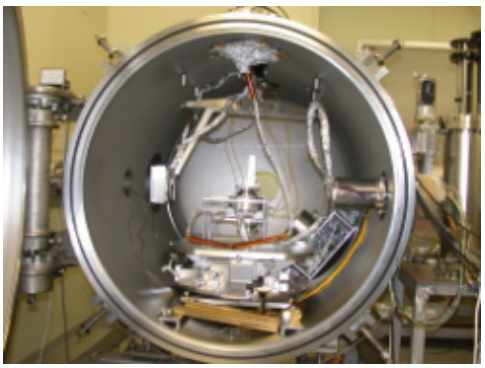

Figure A.30: Inside main chamber.

Table A.18: Institute of Space and Astronautical Science Facility: ISAS-Ion-2

Category	Ion calibration.
Description	High vacuum, ion calibration system for electron energy spectrometers, ion energy spectrometers, and ion mass spectrometers for measurements in the planetary magnetosphere. Calibration ions are created from gaseous and non-gaseous materials.
Vacuum system	The main chamber is 1200 mm diameter $\times$ 2100 mm with an ULVAC 2300 l s^{-1} cryopump, an Osaka Vacuum 1500 l s^{-1} turbopump and an Alcatel 635 l min^{-1} rotary pump. The ion gun chamber has a Varian 500 l s^{-1} turbopump and an Alcatel 250 l min^{-1} rotary pump. The external magnetic field is shielded to less than 4.5 mG.
Ion Beam	The commercial Colutron G-2-D ion source with an energy range 500 eV–10 keV (1 eV–10 keV with decelerator) has a beam $\sim$1.0 mm diameter. Ions are created from both nongaseous and gaseous materials.
Monitors, Gauges	Thermo-couple gauge and Bayard-Alpert hot filament ion gauges for pressure measurement. Ion beam diagnostics by a CEM mounted on rotation table.
Instrument Mounting	Instruments can be mounted on a rotation table (30 cm $\times$ 30 cm) by screw (M5). The interval between tapped holes on the mounting plated is 25 mm.
Rotation Table	$\pm$180° and $\pm$60° about two orthogonal axes normal to ion beam line, $\pm$15° about an axis parallel to the ion beam line.
GSE	Computer control of rotation table and readout of its position.
Contact	Yoshifumi Saito Institute of Space and Astronautical Science 3-1-1 Yoshinodai Sagamihara, Kanagawa 229-8510 Japan Tel: +81-42-759-8171 Fax: +81-42-759-8456 E-Mail: `saito@stp.isas.jaxa.jp`
Reference	

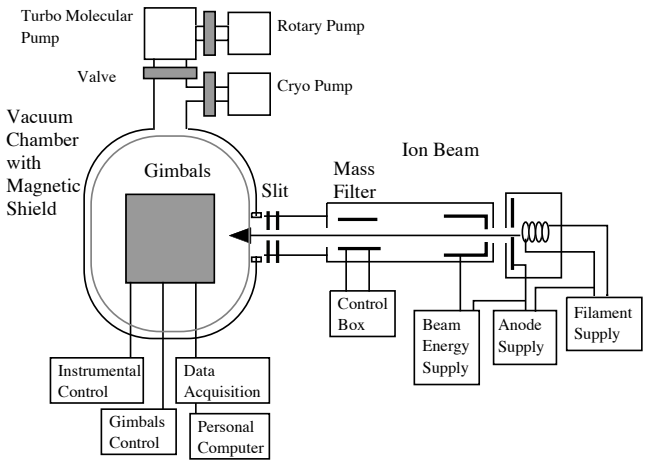

Figure A.31: Schematic block diagram of ISAS calibration facility.

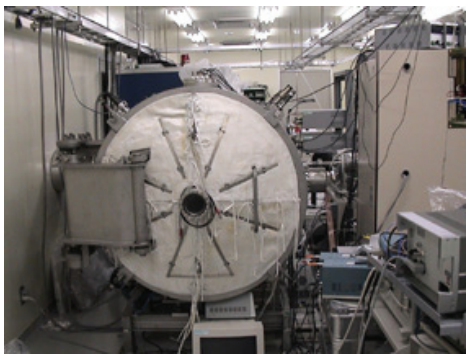

Figure A.32: Main chamber with magnetic shield.

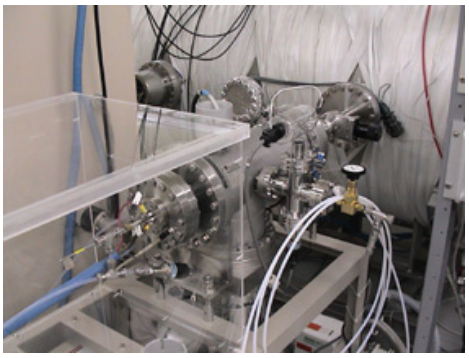

Figure A.33: Ion source.

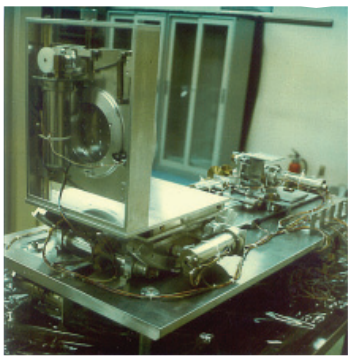

Figure A.34: Rotation table.

Table A.19: Ionenstrahllabor, Berlin Facility: ISL

Category	High Energy Ion beam.
Description	High vacuum characterization and calibration facility for testing space plasma instruments with high energy ions.
Vacuum System	Large vacuum chamber for samples.
Ion Source	Electron cyclotron resonance. Injector 1: 5.5 MeV van de Graaff accelerator. Injector 2: 200 kV platform followed by a radio frequency quadrupole. Also k=130 cyclotron.
Mass-to-charge analyzer	90° magnet.
Instrument Mounting	Sample holder can be moved in all directions.
Contact	Andrea Denker Hahn-Meitner Institut Abteilung SF4 Glienicker Str. 100 D-14109 Berlin, Germany Tel: +49 30 8062-2498 Fax: +49 30 8062-2293 E-mail: denker@hmi.de
Reference	http://www.hmi.de/isl/index_en.html

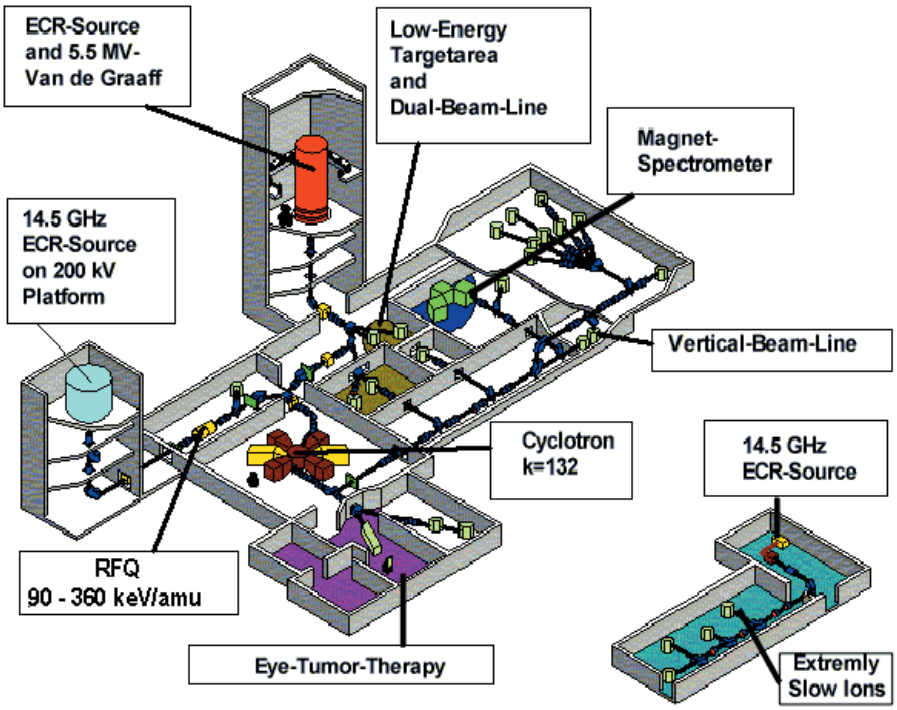

Figure A.35: ISL facility for high energy ion irradiation.

Table A.20: Los Alamos National Laboratory Facility: LANL-1

Category	Neutral Atomic Beam.
Description	Neutral atomic beams of oxygen, nitrogen, and other species are generated using a laser sustained plasma discharge. The collimated atomic beam is propagated into a UHV vacuum system for experiments involving exposure of materials to the atomic species, thin film growth, etching studies, and other investigations.
Vacuum system	Turbopumps.
Neutral Beam	Laser sustained discharge source of strictly neutral atom beam species having kinetic energies from 1 to 5 eV and an extremely high flux of $\sim 10^{17}$ atoms cm^{-2} s^{-1} over a 5.1 cm diameter area.
Monitors, Gauges	Mass spectrometer, ion gauges, capacitance manometer, spinning rotor gauges, torsion balance for beam flux measurements.
Instrument Mounting	Internal size volume is ~ 0.5 m^3. External size <1.3 m height from ground to beam axis.
Rotation, Translation	5-axis sample manipulator (x, y, z, azimuth, tilt) for internal samples.
GSE	Modern laboratory data acquisition and analysis.
Miscellaneous	
Contact	Mark Hoffbauer Los Alamos National Lab Chemistry Division C-ADI, MS J 565 Los Alamos, NM 87545, USA Tel: +1-505-667-0511 Fax: +1-505-665-4631 E-Mail: mhoffbauer@lanl.gov
Reference	*Cross and Blais* [1989]

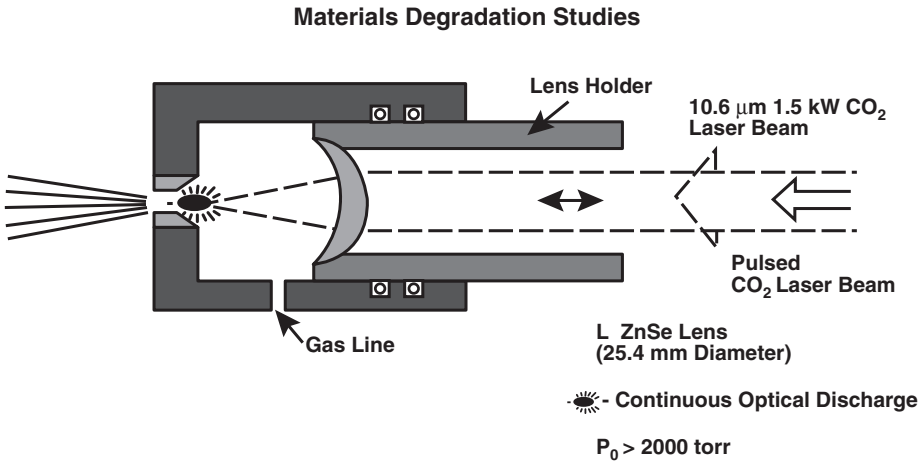

Figure A.36: Continuous-wave laser-sustained plasma neutral O-atom source [*Cross and Blais*, 1989].

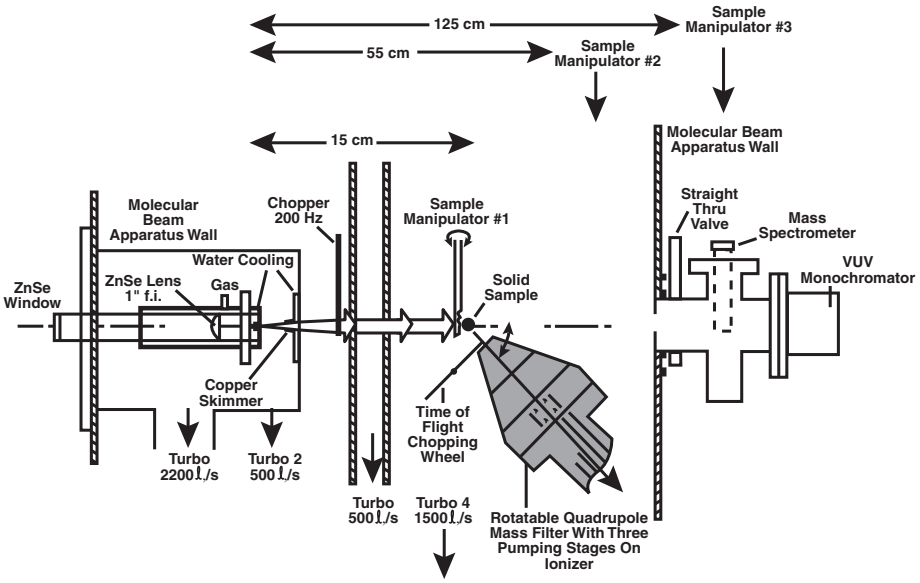

Figure A.37: Atom oxygen exposure facility [*Cross and Blais*, 1989].

Table A.21: Los Alamos National Laboratory Facility: LANL-2

Category	Neutral Atomic Beam.
Description	Neutral beam scattering system used with a specialized torsion balance for making very precise measurements of momentum accommodation coefficients, absolute flux density measurements, and for determining scattered gas velocity and angular distributions from engineering surfaces. Virtually all gases and combinations of gases can be used with this system, including oxygen, nitrogen, carbon monoxide, carbon dioxide, water, rare gases, sulfur dioxide, and many others.
Vacuum system	Diffusion pumps and turbopumps.
Neutral Beam	Molecular beam flux is $\leq 10^{17}$ cm^{-2} s^{-1} over <1 cm^2 and the beam speed is 0.5 – 5.0 km s^{-1}.
Gauging	Mass spectrometer, ion gauges, capacitance manometer, spinning rotor gauges and a torsion balance for beam flux measurements.
Instrument Mounting	Internal size volume is $\sim$0.2 m^3. External size $<$1.3 m height to beam axis.
Rotation, Translation	4-axis sample manipulator (x, y, z, incident angle) for internal samples.
GSE	Modern laboratory data acquisition and analysis.
Contact	Mark Hoffbauer Los Alamos National Lab Chemistry Division C-ADI, MS J 565 Los Alamos, NM 87545, USA Tel: +1-505-667-0511 Fax: +1-505-665-4631 E-Mail: mhoffbauer@lanl.gov
Reference	*Cook et al.* [1996]; *Cook and Hoffbauer* [1997, 1998]

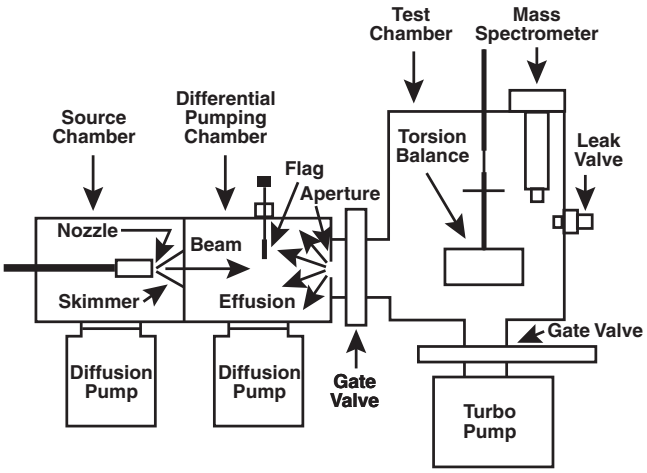

Figure A.38: Schematic diagram of system with torsion balance to measure absolute molecular beam flux. The molecular beam produced by a nozzle at high pressure and temperature passes through a skimmer into a differential pumping chamber and then through an aperture before entering the test chamber with the torsion balance and mass spectrometer [*Cook et al.*, 1996].

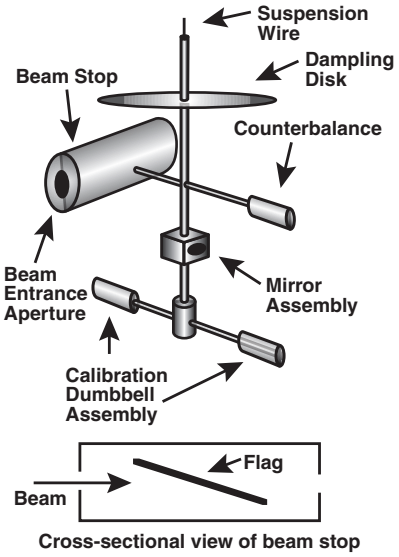

Figure A.39: Schematic diagram of torsion balance to measure absolute molecular beam flux [*Cook et al.*, 1996].

Table A.22: Los Alamos National Laboratory Facility: LANL-ISR1

Category	Testing and calibration facility with ion source.
Description	Facility for (a) the test and calibration of ion and electron energy-per-charge spectrometers and ion mass spectrometers over a broad range of energy, mass, flux, and incident angle and (b) development of new detection and instrument technologies.
Vacuum System	Primary chamber: Cylindrical, 94 cm long by 135 cm diameter, oil-free roughing and cryo high-vacuum pumps, capable of 10^{-7} mbar overnight or 3×10^{-8} mbar after a few days. Secondary chamber: 6-way cross made of 14 cm pipe, turbo-pumped.
Ion Source	0.2–50 keV energy, 1–20 mm diameter (rastered), 1 pA – 1 nA intensity beams of positive ions of common gases, energy resolution $<$1 eV. Magnetic momentum-per-charge analyzer. Turbo-pumped.
Thermal Gas	The desired gas is admitted into the ionization region by a feedback-controlled leak valve.
Instrument Mounting	A mounting plate can be drilled, or a new one made in a nearby shop, as needed to accept any instrument.
Rotation, Translation	2 orthogonal 360° rotations, and one 20 cm translation in a direction along one rotation axis, orthogonal to the other.
GSE	A National Instruments PXI-1042 with Labview is the basis for data acquisition. The positioners can be computer-driven and analog data can be digitized, at the desired settings, automatically. Keithley 617 electrometers and Bertan 225 High Voltage supplies can also be Labview-driven.
Miscellaneous	Quantar imaging MCP system is available, along with a variety of Faraday Cups, MCPs, Channel Electron Multipliers, and Photomultipliers. A variety of NIM electronics is available, and Multichannel pulse height, and Time-of-Flight analyzes can be performed. A UV lamp and 121 nm notch filter is available. A second, small chamber with a variety of actuators, flanges, and electrical feedthroughs occupies a dedicated beam line. A Class 100 clean room is nearby. Access is available to a nearby 1 – 10 MeV/q tandem Van de Graaff accelerator.
Contact	Ron Harper Los Alamos National Laboratory Los Alamos, NM 87545, USA Mail Stop D466 Tel: +1-505-667-1747 Fax: +1-505-665-7395 E-Mail: `rharper@lanl.gov`
Reference	

Figure A.40: Photograph of LANL-ISR1 facility.

Table A.23: Lockheed Martin ATC Ion Calibration Facility: LMATC-ICF

Category	Medium-energy ion calibration facility.
Description	Ion calibration facility for space-flight plasma spectrometers in the energy range 1 keV to ∼100 keV, species H^+ to ∼Xe^+.
Vacuum System	8000 liter high-vacuum target chamber with all-metal construction, a 1500 l s^{-1} turbo-pumped ion source, a 1000 l s^{-1} turbo-pumped target chamber and a 500 l s^{-1} cryopump alternate for high-vacuum and noise reduction. In-chamber flexible liquid nitrogen plumbing for thermal environment control. Target-chamber bake-out facility. Automated pumping monitor and control to protect high-value hardware.
Ion Beam	Dual-Plasmatron ion source with source-point lens and steering provides a 250 eV to ∼10 keV extraction energy. The inlet gas is selectable (H to ∼Xe) with a 10 kGauss 90° mass filter upstream of a maximum acceleration energy of ∼100 keV. The source projection lens has ∼7 meter drift tube (drift-tube beam translation and steering under development). The target beam diameter is ∼10 cm and the target flux is ∼10 nA cm^{-2} – ∼1 fA cm^{-2}.
Monitors, Gauges	Automated in-vacuum ion beam profile monitors: a horizontal scan cart with a 32-sector vertical micro-channel-plate sensor (under development), a fixed-height single channeltron, and fixed-height Faraday cup sensors. Gauges include thermal-couples and nude ion gauge pressure monitors plus a target-chamber residual gas analyzer.
Instrument Mounting	Two-axis instrument manipulation unit on target-chamber turntable. Maximum instrument mass is ∼10 kg, maximum rotational inertia is ∼3600 kg cm^2 and maximum instrument distance from beam-line rotation center is ∼30 cm. Turntable provides ∼11.5° s^{-1} slew with programmable speed and excursion limits, and provides ∼60 Nm maximum running torque.
Rotation, Translation	Two-axis 360° freedom (pitch and yaw) has 360°/1024 resolution or jitter (rotation freedom somewhat limited by instrumentation cabling). Computerized system for manual or programmable control. PC/DOS interface (Windows software under development).
Contact	Gordon Smith Advanced Technology Center (L924/201) Lockheed-Martin Space Systems Company 3251 Hanover Street Palo Alto, CA 94304, USA Tel: +1-650-424-2188 Fax: +1-650-424-3333 E-Mail: `Gordon.R.Smith@lmco.com` Web: `http://lmms.external.lmco.com/atc`
Reference	

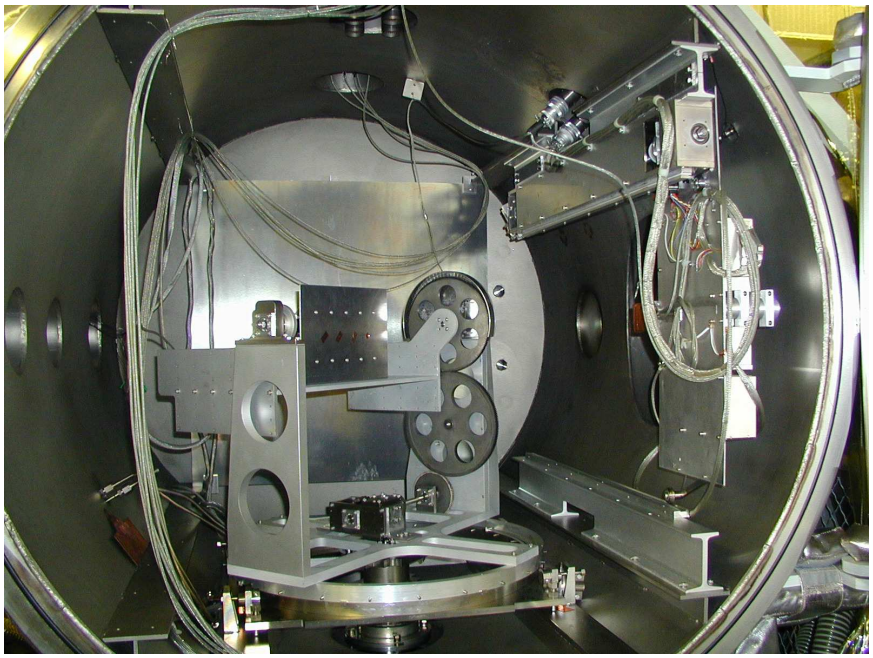

Figure A.41: Target chamber.

Figure A.42: Accelerator control station.

Figure A.43: Ion source.

Table A.24: NASA Marshall Space Flight Center Facility: MSFC-LEEIF

Category	Testing and calibration facility with electron and ion sources.
Description	High vacuum laboratory system for the calibration of single or multiple charged particle detectors over their range of particle energy, mass, flux, and angular acceptance.
Vacuum system	Cylindrical chamber 122 cm in diameter and 183 cm in length, dry pump/blower pump combination leading to (2) parallel 25.4 cm diameter cryogenic pumps. Reaches $\sim 1 \times 10^{-6}$ mbar in 1 hour.
Ion Source	Ion beam 8 cm in diameter, 1 – 3000 eV energy, current densities varying from 0.01 – 100 pA cm^{-2}. Each energy range has 12 bit resolution. ^{63}Ni electron source, average energy 17 keV, maximum energy 67 keV.
Thermal Gas	Various gases are leaked into gas inlet near the ion source for mass calibration. Leak rate is controlled.
Instrument Mounting	Instrument is mounted to a vertical plate which rotates in two orthogonal dimensions and accommodates large instruments.
Rotation, Translation	2-D rotation ($\pm 120°$ and $\pm 180°$ orthogonal) and 2-D translation. Computer control and readout of positions.
GSE	Computer control and readout of ion gun, Faraday cup, power supply voltages, and rotation and translation positions. Analog, digital, counter, and GPIB computer cards available for instrument control and acquisition of data. Software is available to write data acquisition and display routines for testing and calibration.
Miscellaneous	Quantar^{TM} two-dimensional particle-imaging system for beam diagnosics, UTI^{TM} residual gas analyzer, Amptektron^{TM} ion and electron detector, various UV sources and automatic chamber pressure alarm.
Contact	Victoria Coffey NASA Marshall Space Flight Center SD50, Space Science Department Huntsville, AL 35812, USA Tel: +1-256-961-7635 Fax: +1-256-961-7216 E-Mail: `Victoria.N.Coffey@nasa.gov`
Reference	*Biddle and Reynolds* [1986]

Figure A.44: Photograph of LEEIF chamber.

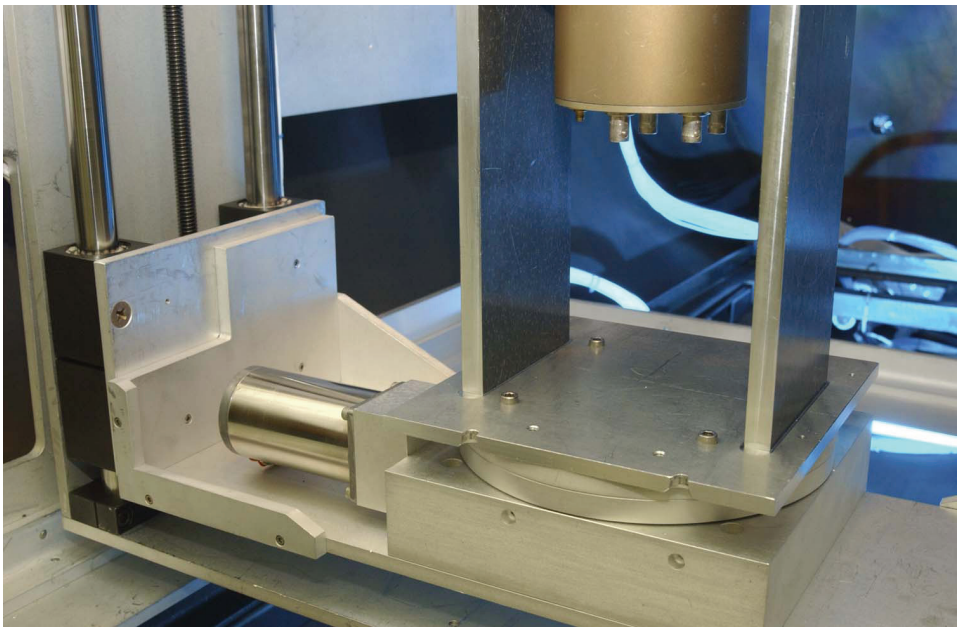

Figure A.45: Photograph of rotation system inside chamber.

Table A.25: Mullard Space Science Laboratory Facility: MSSL-ECF

Category	Electron calibration facility.
Description	Electron instrument calibration facility.
Vacuum system	The main chamber is 304 stainless steel, 3041.1 m long, 1.0 m diameter with a rotary pump, turbopump and helium cryopump. Base pressure 5×10^{-7} mbar. A grounded μ-metal shroud (0.7 m long, 0.6 m wide and 0.6 m in height) inside the chamber, ensures the residual magnetic field is $<$ 1/10 of Earth's magnetic field. The electron beam divergence $\leq1^\circ$ at 1 keV. The whole assembly is mounted on Teflon rails.
Electron Beam	Cathodeon HG2 mercury UV lamp transmits through a quartz window onto a gold-coated quartz disc inside the chamber (15 mW cm^{-2} at 253.7 nm with 150 mA anode current) with a noise fluctuation in the output $\leq$0.6 %. The quartz lamp envelope cuts off wavelengths below 230 nm to avoid ozone production. There is also a tritium source with an end-point energy of 18.6 keV and peak near 6 keV, a ^{63}Ni source with an end-point energy of 66.9 keV and a ^{151}Sm with an end-point energy of 76.7 keV.
Monitors, Gauges	Faraday cup and channeltron detectors. The Faraday cup is used at currents $>$1 pA and as low as 100 fA. At lower currents a channeltron detector placed very close to the instrument apertures is used. A cross-calibration of the channeltron with the Faraday cup is performed at around 1 pA current in order to get absolute current measurements.
Instrument Mounting	2-axis rotary table.
Rotation, Translation	Rotary table has azimuth and elevation variable. The center of the instrument aperture is at the center of rotation for both axes. The Newport Micro-Control UR100 rotates stages with position feedback and 0.01° resolution. Each motor has a travel limit of $\pm179^\circ$.
GSE	16-channel, fast, high-resolution data acquisition system for pulse height distribution studies. A 15-channel system with line drivers followed by counters for data acquisition and DAC's for instrument control. Computer control of all individual elements with software routines to allow monitored voltage settings to the different components, instrument position variation, and to acquire/display data from the instrument and beam.
Contact	David Linder Mullard Space Science Laboratory, Space Physics Group University College London Holmbury St. Mary, Dorking, Surrey RH5 6NT, UK Tel: +44-1483-204169 Fax: +44-1483-278312 E-Mail: `drl@mssl.ucl.ac.uk` Web: `http://www.mssl.ucl.ac.uk`
Reference	*Marshall et al.* [1986]

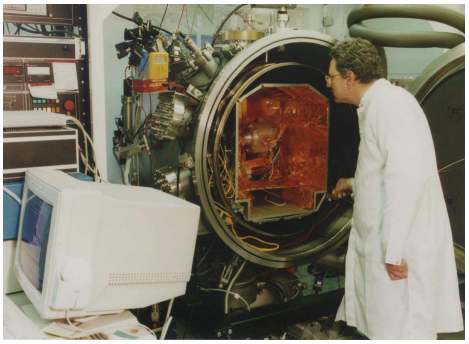

Figure A.46: The MSSL calibration chamber.

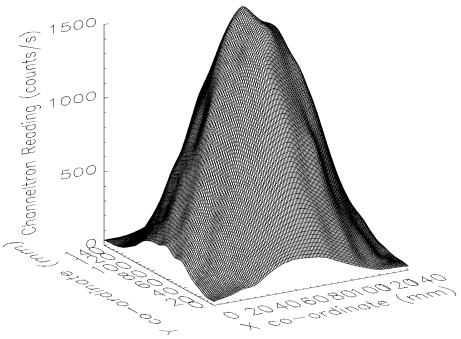

Figure A.47: Profile plot of typical electron beam profiles.

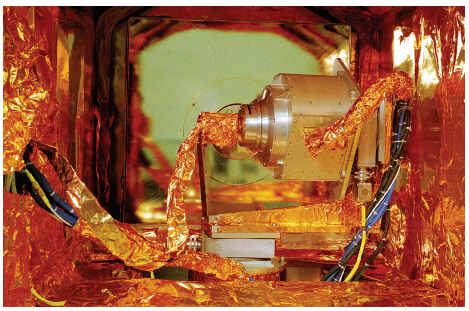

Figure A.48: The Cassini CAPS electron spectrometer mounted on the rotary stages inside the calibration chamber.

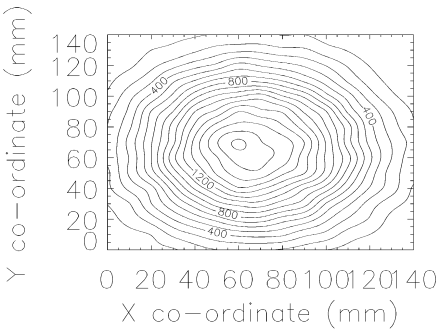

Figure A.49: Contour of typical electron beam profile.

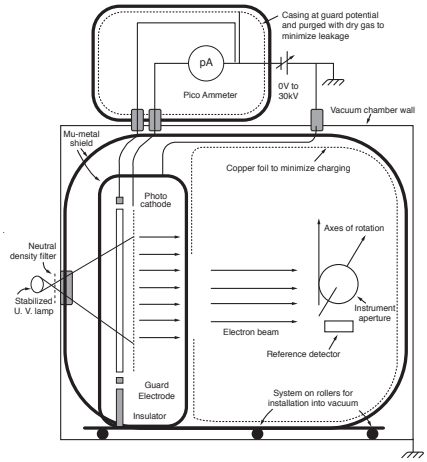

Figure A.50: Schematic of the calibration system.

Table A.26: Northeast Proton Therapy Center Facility: NPTC

Category	Ion Accelerator.
Description	230 MeV Proton Cyclotron.
Vacuum system	N/A (tests performed in air).
Proton Beam	Accelerator provides undegraded proton beams of between 100 MeV and 230 MeV. Lower energy beams (down to 20 MeV) can be produced by the introduction of energy degraders into the beam. The beam intensity is up to 80 nA cm^{-2} and the beam diameter is between 0.5 cm and 20 cm.
Monitors, Gauges	Beam current is monitored during irradiation by use of a transmission ion chamber (thin foil). The chamber is calibrated before irradiation using a Faraday cup, thimble ion chamber or a radiation sensitive diode.
Instrument Mounting	A variety of instrument mounting and aligning equipment are available. A laser alignment system used to define beam center.
Miscellaneous	The facility is used primarily for medical treatments but non-medical experimental time is available on weekends and nights.
Contact	Ethan Cascio The Northeast Proton Therapy Center at Massachusetts General Hospital 30 Fruit St., Boston, Ma. 02114, USA Tel: +1-617-724-9529 Fax: +1-617-724-9532 E-Mail: ecascio@partners.org
Reference	*Cascio et al.* [2003]

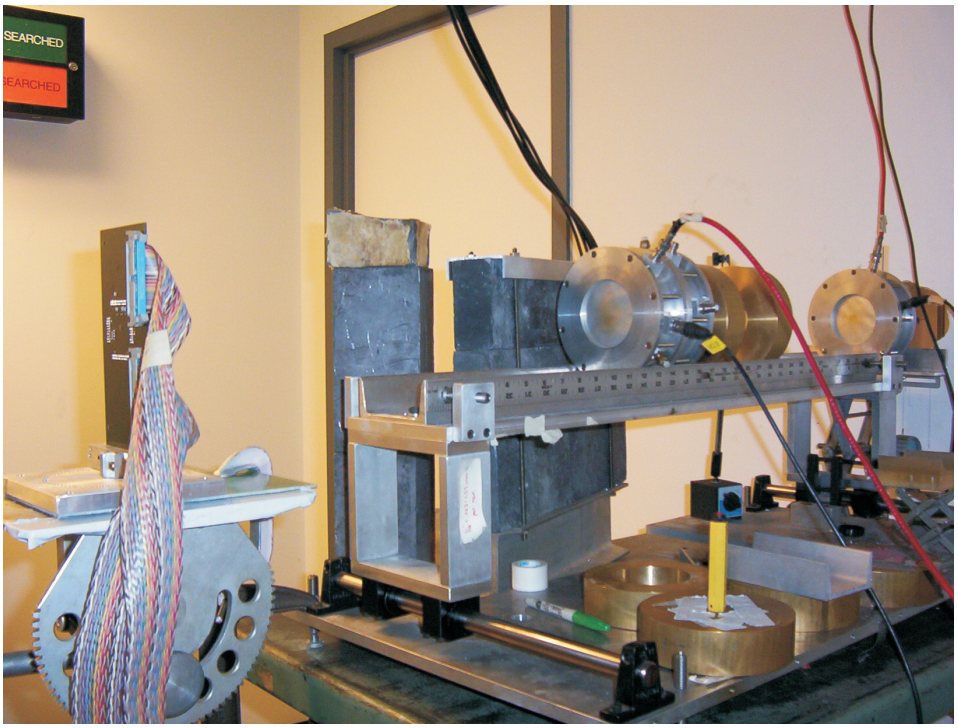

Figure A.51: NPTC beam line.

Table A.27: RPI Gaerttner Laboratory Electron Calibration Facility: RPI-LINAC

Category	Electron Accelerators.
Description	Electron calibration facility and radiation effects facility. A 8 MeV to 70 MeV electron traveling wave linear accelerator with a beam current of more than 100 μA and a beam diameter of 1 cm to 50 cm, produces intense bremsstrahlung and neutron radiation fields with pulsed dose rates above 10^{11} rads s^{-1} and integrated doses up to many gigarads.
Monitors, Gauges	Digital oscilloscopes. Dosimetry with thermoluminescent dosimeters (TLD) and radiochromic film.
Instrument Mounting	Remote controlled table for radiation testing of electronics.
Contact	Robert C. Block Gaerttner LINAC Laboratory Rensselaer Polytechnic Institute 110 8^{th} St., NES Bldg. Room I-7 Troy, NY 12180-3590, USA Tel: +1-518-276-6404 Fax: +1-518-276-4007 E-Mail: `blockr@rpi.edu` or Peter Brand Gaerttner LINAC Laboratory Rensselaer Polytechnic Institute 110 8^{th} St., LINAC Labratory Troy, NY 12180-3590, USA Tel: +1-518-276-6406 Fax: +1-518-276-4007 E-Mail: `brandp@rpi.edu` Web: `http://www.linac.rpi.edu`
Reference	

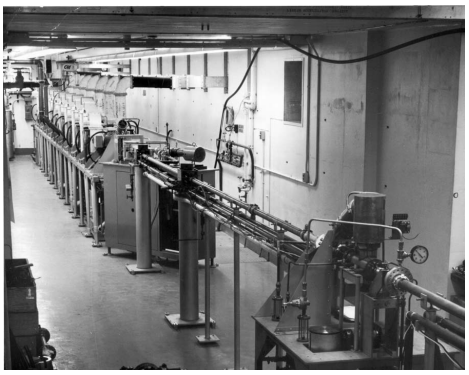

Figure A.52: LINAC beam line.

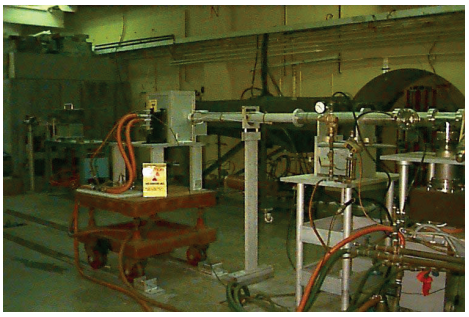

Figure A.53: High energy port, target station 1.

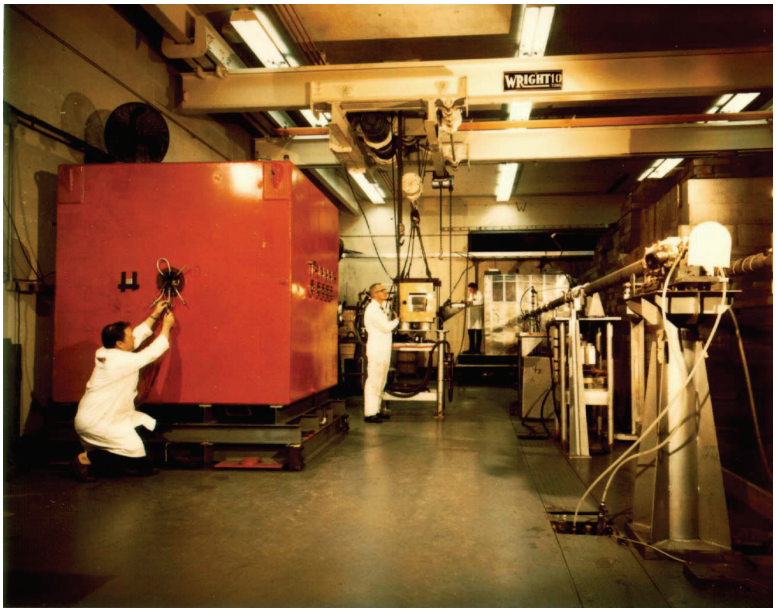

Figure A.54: Target station.

Table A.28: Southwest Research Institute Facility: SwRI-ECF

Category	Electron calibration facility.
Description	High vacuum, computer controlled calibration facility for testing space plasma instruments with electrons.
Vacuum system	All metal vacuum chamber with roughing pump, turbopump and cryopump combination produces pressures as low as $\sim 8 \times 10^{-7}$ mbar, reaching $\sim 5 \times 10^{-6}$ mbar in about 2 hours from atmosphere. The chamber is a cylinder with its axis parallel to the floor, 76.2 cm long and 61 cm diameter.
Electron Beam	Electron source uses 11 SC-2 Ultraviolet Products Pen Ray Mercury-Argon lamp with an Action Research neutral density filter array external to vacuum chamber. The UV penetrates a quartz window and contacts a 400 Angstrom gold layer inside vacuum chamber. Electrons are ejected by photon collisions. The electron acceleration uses a 205A-30N Bertan power supply with 0.8V resolution. The beam diameter less than 1.9 cm, the distance from electron beam exit to instrument inlet is adjustable by about 7.6 cm. The maximum energy is less than 30 keV.
Monitors, Gauges	Granville-Phillips^{TM} 307 ion gauge and Dycor^{TM} Ametek^{TM} HQ100 residual gas analyzer on main chamber.
Instrument Mounting	Internal to the vacuum system rotation mounting plate on a teardrop shaped goniometer, about 11.4 cm in diameter. The support weight about 500 g, depending on balance. Four 25-pin D connections provide external access to the vacuum system.
Rotation, Translation	Rotation $\pm 15° \times \pm 10°$ or $\pm 15° \times \pm 180°$ perpendicular to the vertical beam axis with $\pm 0.1°$ resolution. Two orthogonal axes normal to the electron beam line provide a translation 8.9 cm $\times$ 10.2 cm travel at 0.0025 cm resolution.
GSE	Computer control of electron gun power supply, high voltage Bertan supplies, goniometer positioning, counting system and a 16 channel serial port read-back system with joystick, manual, or computer control modes.
Miscellaneous	Power from four Bertan 205-05R (reversible) ± 5 kV power supplies with separate high voltage feedthroughs is available in the chamber and power from three Kepko ABC low voltage supplies. SR620 Stanford Research Systems counter.
Contact	Rudy Frahm Department of Space Science and Engineering Southwest Research Institute 6220 Culebra Road San Antonio, TX 78238, USA Tel: +1-210-522-3855 Fax: +1-210-647-4325 E-Mail: `rfrahm@swri.edu`
Reference	

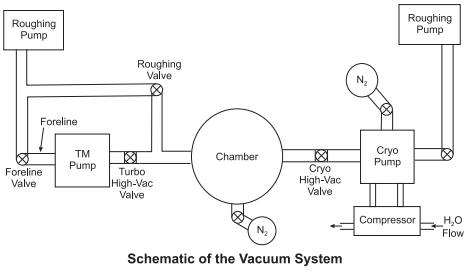

Figure A.55: Schematic of vacuum system.

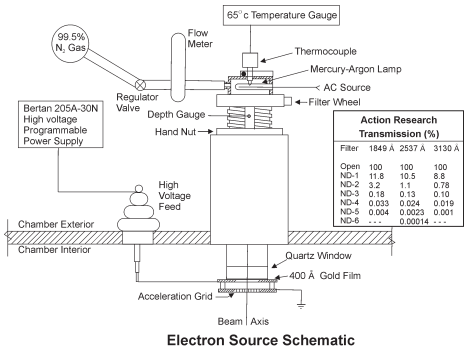

Figure A.56: Schematic of electron source.

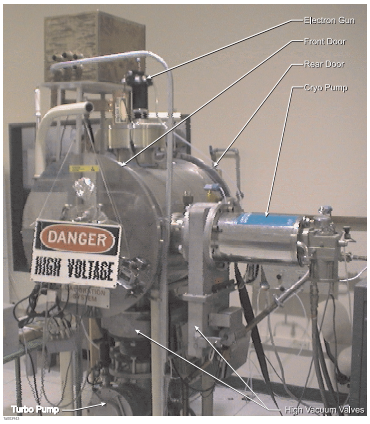

Figure A.57: Picture of the facility.

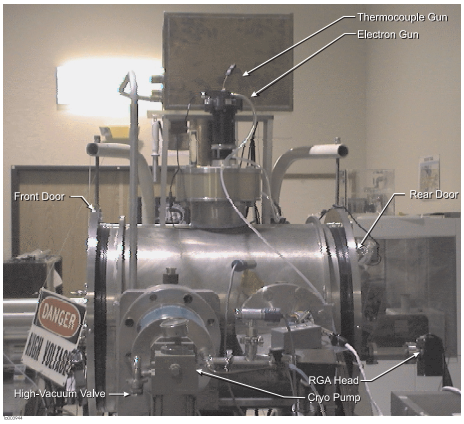

Figure A.58: Side view picture of the facility.

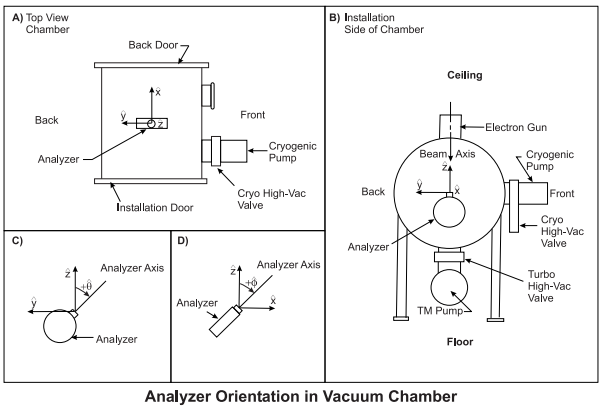

Figure A.59: Analyzer orientation in vacuum chamber.

Table A.29: Southwest Research Institute Facility: SwRI-IDCF

Category	Ion and neutral beam calibration facility.
Description	Ultra-high vacuum ion calibration system for characterization of plasma spectrometers and Energetic Neutral Atom imagers.
Vacuum system	Oil free pumping. The main chamber has two 3000 l s^{-1} Helix-CTI Cryogenics Cryo-Torr 10. The ion beam flight tube has a 1500 l s^{-1} Cryo and a 400 l $^{-1}$ Shimadzu 403LM turbomolecular pump.
Ion Beam	Peabody Scientific^{TM} Duoplasmatron ion source, energy range 500 eV to 51 keV, ΔE$\sim$10 eV at 10 keV. The beam can be rastered up to 10 cm diameter (unrastered 1.3 cm), the ion beam exit to the instrument inlet distance is 5 m. Ion species can range from protons up to large molecules and can be in either a positive or negative charge state.
Neutral Beam	Charge exchange with the residual background gas converts $\sim$2 % of ion beam flux into a neutral beam.
Monitors, Gauges	Pfeiffer^{TM} Vacuum Compact Full Range^{TM} Bayard-Alpert hot filament ion gauges and Dycor^{TM} 200 u residual gas analyzer on the main chamber. Ion beam diagnostics consist of a Faraday cup and Amptektron detector to measure beam flux, and 2-D imaging MCP detector to measure beam uniformity.
Instrument Mounting	The main vacuum chamber is a 122 cm diameter cylinder with axis normal to beam line. Access to the instrument is through ConFlat flanges with sizes up to 33.7 cm. Internal mounting cradle allows mounting an instrument of length 70 cm and 30 kg mass.
Rotation, Translation	4-axis positioning system (Newport Corporation) with 2 rotational, $\pm$170° about two orthogonal axes normal to the ion beam line each with 0.01° accuracy, $\pm$15 cm horizontal translation with 5 micron accuracy and $\pm$7 cm vertical translation.
GSE	Computer control of the positioning system and recording of pressures, temperatures and valve states. Software has scripting capability. The computer interface allows for limited control of the facility by the test object.
Miscellaneous	Vacuum pumps and valves are controlled through an interlock system using relay logic set up to prevent actions that may be harmful to either vacuum system or test object. Vacuum control system is continuously monitored by a facility computer.
Contact	Philip Valek Space Science and Engineering Division, Space Science Department Southwest Research Institute P.O. Box 28510 San Antonio, TX 78228-0510, USA Tel: +1-210-522-3385, Fax: +1-210-522-9935 E-Mail: `pvalek@swri.edu` Web: `http://www.swri.edu/9what/releases/callab.htm`
Reference	

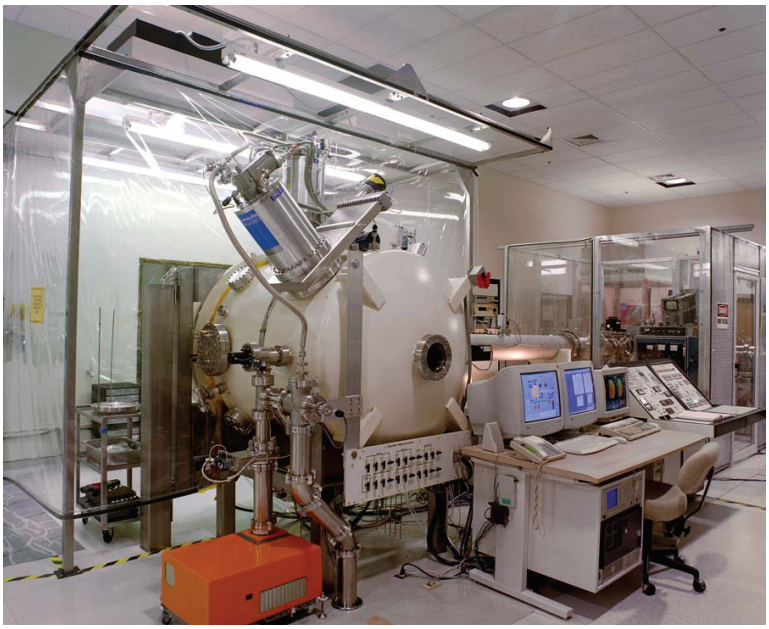

Figure A.60: Overall view of ion calibration system.

Figure A.61: Closer view of instrument chamber.

Table A.30: University of Bern Facility: UBern-CASYMIR

Category	Neutral thermal gas and neutral gas beam.
Description	High vacuum, gas calibration system for thermal gas and neutral gas beam characterization of mass spectrometers and other sensors used for direct in situ sampling of cometary and other low density atmospheres.
Vacuum System	All metal, bakeable to 300°C. Main chamber 1000 l s^{-1} Pfeiffer TMU 1000 turbomolecular pump, chevron baffle with P-75 Polycold cryocooler. Base pressure $\geq 5\times10^{-10}$ mbar.
Gas Manifold	Gas mixing unit with 4 flow controllers for permanent gases, 2 flow controllers/meters for solid and liquid vapors.
Thermal Gas	Variable inlet leak, free molecular flow pressure reduction by 0.5 mm diameter orifice prior to gas entering main chamber.
Neutral Beam	Hypersonic high pressure vacuum expansion of gas mixture. Beam speed 0.3–4 km s^{-1}.
Monitors, Gauges	Granville-Phillips Stabil-Ion ionization gauge, Balzers QMS 200 residual gas analyzer. Neutral beam diagnostics consist of mechanical chopper and molecular beam detector with ABB Extrel detector and fast ion gauge.
Instrument Mounting	Mounted on platform with 5 degrees of freedom, external to the vacuum system, connected by a bellows.
Rotation, Translation	Two degrees of freedom for rotation and 3 degrees of freedom for translation.
GSE	Computer control and readout of system sensors.
Miscellaneous	
Contact	Kathrin Altwegg Physics Institute University of Bern Sidlerstrasse 5, CH-3012 Bern Switzerland Tel: +41 31 631 4420 Fax: +41 31 631 4405 E-Mail: `kathrin.altwegg@phim.unibe.ch`
Reference	*Graf et al.* [2004]; *Westermann et al.* [2001]; *Westermann* [2000] `http://www.phim.unibe.ch/rosina/casymir/index.html`

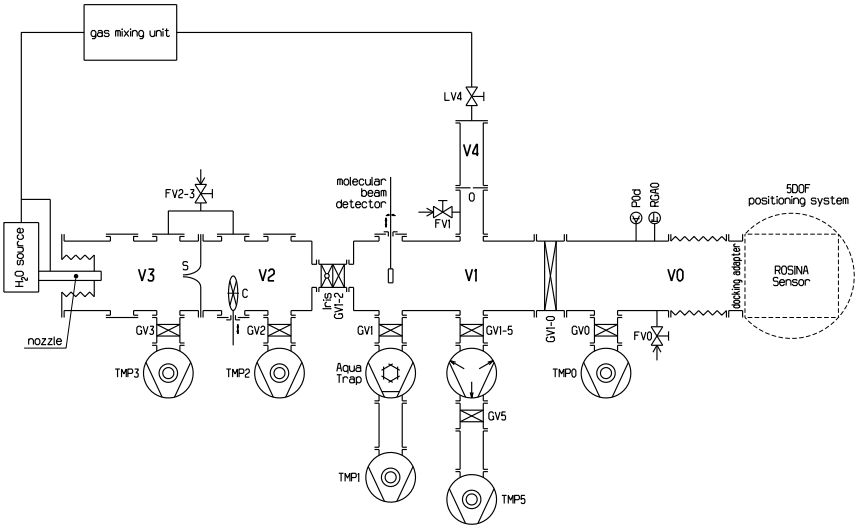

Figure A.62: CASYMIR system with components: bellows chamber with docking adapter V0, main vacuum chamber V1, collimator chamber V2, expansion chamber V3, reference chamber V4, gate valve GV, Stabil-Ion gauge P0d, residual gas analyzer RGA0; chambers V0-V3 pumped by turbomolecular pumps, TMP0-TMP5; skimmer S, chopper disk C, orifice O, venting valves FV0-FV3.

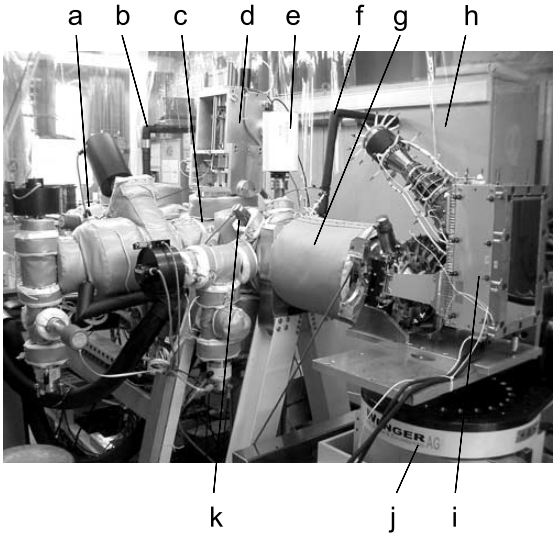

Figure A.63: Picture of CASYMIR system with DFMS instrument: (a) vacuum chambers V3 and V2, (b) gas supply tube to the nozzle, (c) main chamber V1, (d) support for beam detector system, (e) residual gas analyzer RGA0, (f) gas supply tube for leak valve, (g) docking section , (h) gas mixing unit, (i) DFMS, (j) 5-axis table instrument platform, and (k) Stabil-Ion reference gauge.

Table A.31: University of Bern Facility: UBern-CASYMS

Category	Ion beam.
Description	Versatile ion beam calibration facility for characterization of space plasma instrumentation, in particular solar wind and suprathermal particle instruments.
Vacuum system	All metal system, fully automatic control; main chamber cryo pump 3000 l s^{-1}, pressure $<1\times10^{-7}$ mbar; pump-down with turbo-molecular pump (Pfeiffer 2100 l s^{-1}).
Ion Beam	Electron impact ion source, 3 keV/e beam energy, post-acceleration up to 100 keV/e and post-deceleration down to 5 eV/e. Wien-filter for m/q selection.
Monitors, Gauges	Ion beam diagnostics: fixed CEM detector (0.1 cm^2), movable CEM beam (0.1 cm^2) scanner and movable Faraday cup (5.0 cm^2).
Instrument Mounting	Internal in vacuum system on an articulated table.
Rotation, Translation	Rotation of $\pm44°$ in vertical plane, $\pm44°$ in horizontal plane, 20-260 mm vertical translation, $\pm$ 179° rotation on turntable.
GSE	Computer control of table position, ion source, ion beam and beam diagnostics.
Contact	Kathrin Altwegg Physics Institute University of Bern Sidlerstrasse 5, CH-3012 Bern Switzerland Tel: +41 31 631 4420 Fax: +41 31 631 4405 E-Mail: `kathrin.altwegg@phim.unibe.ch`
Reference	*Steinacher et al.* [1995]; *Ghielmetti et al.* [1983]

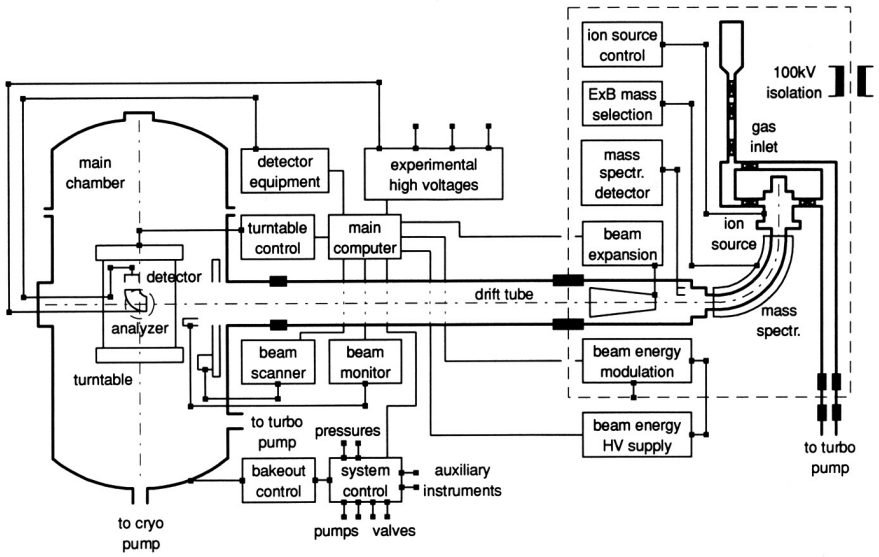

Figure A.64: Schematic diagram of the CASYMS ion calibration system showing ion source, mass spectrometer, beam expander, drift tube and main chamber with beam diagnostics.

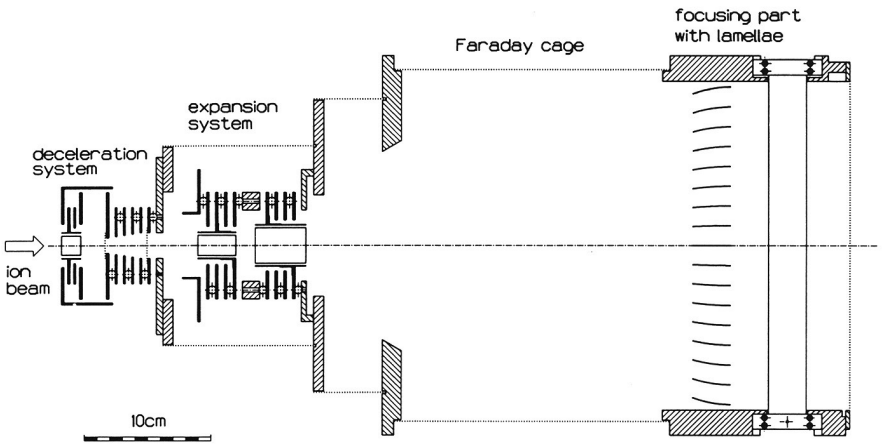

Figure A.65: Schematic of beam expansion system.

Table A.32: University of Bern Facility: UBern-MEFISTO

Category	Ion and neutral beam.
Description	Versatile ion beam calibration facility for characterization of space plasma instrumentation, in particular solar wind and supra-thermal particle instruments. Energetic neutral atoms can be produced as well.
Vacuum system	All metal system, fully automatic control; main chamber cryo pump 4000 $l\,s^{-1}$, 1×10^{-8} mbar; pump-down with turbo-molecular pump (Pfeiffer 500 $l\,s^{-1}$) and fore pump (Alcatel 80 $m^3\,h^{-1}$); ion source chamber turbo-molecular pump Pfeiffer 250 $l\,s^{-1}$ and fore pump Alcatel 12 $m^3\,h^{-1}$.
Ion Beam	Electron-cyclotron resonance ion source, home made, 3 keV/e beam energy, post-acceleration up to 100 keV/e. Wien-filter for m/q selection; Beam can be rastered; beam size adjustable, from 0.1 to 8 mm diameter; distance from ion beam exit to instrument inlet is about 1 m; ion beam diagnostics can be moved into beam line with Faraday cup and Channeltron detectors (current measurement and pulse-counting mode).
Thermal Environment	Vacuum system is bakeable up to 300 °C, liquid nitrogen shroud inside vacuum chamber, instrument table is temperature controlled from −80 °C to +150 °C.
Neutral Beam	Neutral beam down to 15 eV is realized by neutralizing a decelerated ion beam.
Gauging	Bayard-Alpert hot filament ion gauge (Stabil Ion Gauge, Granville Philips), Penning ion gauge, Hiden^{TM} residual gas analyzer on main chamber.
Instrument Mounting	Internal in vacuum system on an articulated table. Two rotations and two translations are available. Table is temperature controlled. Many ports for high-voltage, low-voltage, digital signals, and high-frequency feedthroughs; 8 temperature sensors for the instrument.
Rotation, Translation	Rotation of ±25° in vertical plane, ±90° in horizontal plane, about two orthogonal axes normal to ion beam line; ±5.0 cm horizontal translation; presently manually set, computer interface in progress.
GSE	Computer control of vacuum system, bake-out system, liquid nitrogen system, and table temperature with recording. Computer control of table position and ion source is in progress.
Miscellaneous	Automatic overpressure protection system and protection if there is a high voltage discharge; clean-room environment (Class 100) around chamber and laminar flow box; deuterium lamp for UV calibrations.
Contact	Peter Wurz Physics Institute University of Bern Sidlerstrasse 5, CH-3012 Bern, Switzerland Tel: +41 31 631 44 26, Fax: +41 31 631 44 05 E-Mail: `peter.wurz@phim.unibe.ch`
Reference	*Marti et al.* [2001], `http://www.phim.unibe.ch/mefisto/`

Figure A.66: Front view of the Mefisto calibration facility. *Left:* instrument chamber, residual gas analyzer (black box). *Middle:* roughing pump, beam monitor, and gate valve. *Right:* ion source cabinet and electronics rack.

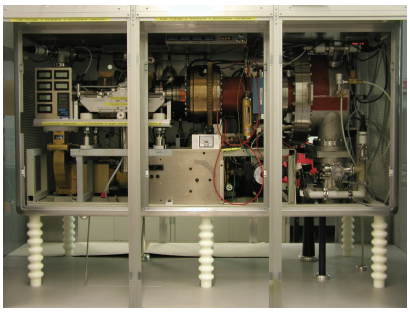

Figure A.67: Front view of ECR ion source. *Left:* 2.45 GHz ECR ion source. Middle: Wien filter. *Right:* 180° energy analyzer. The whole cabinet can be floated up to 100 kV.

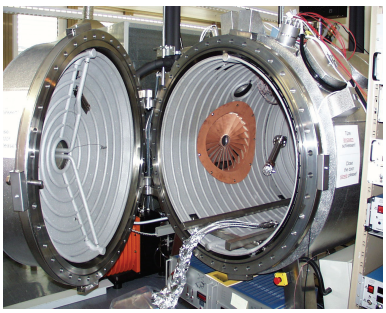

Figure A.68: View of inside of the instrument chamber, showing the cryo shrouds of the chamber and the chamber door. The ion beam enters the chamber through the center hole of the fan-like structure.

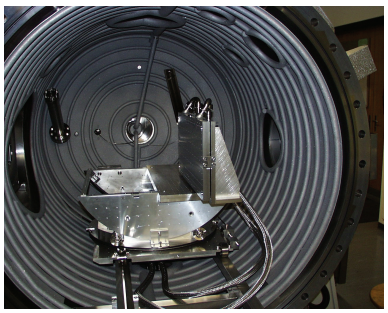

Figure A.69: Instrument table with horizontal and vertical rotation. Instrument cooling plate is mounted vertically in this case. X-Y table motion is not installed.

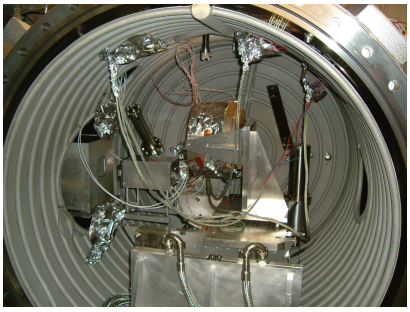

Figure A.70: IBEX-Lo instrument (the cylindrical structure) mounted on the table for calibration with energetic neutral atoms. The small rectangular box in front of IBEX-Lo is the beam neutralizer.

Table A.33: University of Calgary Facility: UCalgary

Category	Ion and electron beam.
Description	High vacuum facility for ion and electron beam characterization of space plasma physics instruments.
Vacuum system	Chamber 1 m diameter.
Ion beam	Two ion gun sources: 1 eV–10 keV, 200 eV–150 keV.
Electron beam	5 eV–1 keV.
Instrument mounting	Instruments mount on high resolution positioning table.
Miscellaneous	Helmholtz coil to reduce ambient magnetic field to 10^{-3} Earth's intrinsic field. Chamber enclosed inside a class 100K cleanroom.
Contact	Dr. Dave Knudsen Department of Physics and Astronomy The University of Calgary Calgary, Alberta CANADA T2N 1N4 Tel: +1 (403) 220-8651 E-mail: Knudsen@phys.ucalgary.ca Dr. Peter Amerl Tel: +1 (403) 220-8769 E-Mail: Amerl@phys.ucalgary.ca Dr. Andrew Yau Tel: +1 (403) 220-8825 E-Mail: Yau@phys.ucalgary.ca Fax: +1 (403) 282-5016
Reference	www.phys.ucalgary.ca/isr_labs/html/sail.html

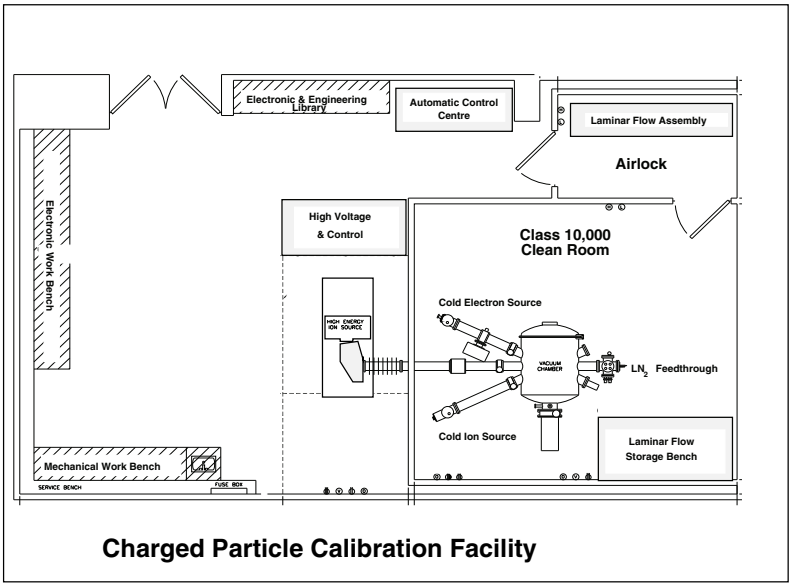

Figure A.71: Schematic of charged particle calibration facility.

Figure A.72: View of vacuum tank from inside of cleanroom.

Table A.34: University of California Berkeley Facility: UCB-SSL

Category	Ion and electron beam.
Description	High vacuum characterization and calibration facility for testing space plasma instruments with electrons and ions.
Vacuum System	Stainless steel target chamber (D = 0.6 m, L = 0.7 m) with base pressure capability of $<1\times10^{-6}$ mbar. CTI Cryotorr pump with oil free scroll pump comprises the target chamber pumping system. Secondary pumping system for ion source is a V-301 turbomolecular pump with oil free backing pump.
Ion Source	Peabody Scientific^{TM} DP ion source with 25 kV extraction gap and 25 kV accelerator gap. Species mass/energy selected via Wien filter. Neutral beam deflector minimizes background. Energy range 2 to 50 keV, energy width 0.5 % over full range over 50 eV, particle flux 10^3 to 10^5 cm^{-2}s^{-1}, species H^+, He^+, Ne^+, O^+, N^+, Ar^+, beam cross-section 4 cm.
Electron Source	Electron energy range 100 eV to 30 keV. Electron production via UV photoemission from Chromium.
Instrument Mounting	Two manipulator systems, built in-house, are used to control the position of instruments within a vacuum chamber during calibration and testing activities.
Rotation, Translation	Each manipulator moves with three degrees of freedom: there is one linear axis for translational motion of the payload; one yaw axis allowing about $\pm20°$ degrees of movement in the XY plane; and a rotation axis for rotating the payload about an axis parallel to the yaw direction.
GSE	The manipulator drive current is supplied by a National Instruments 4-axis motor drive box (leaving one axis available for possible future expansion). Servo control is accomplished with a National Instruments PCI motion control card installed in the PC which drives the manipulator. NI provides a simple user interface in its Measurement and Automation Explorer software.
Miscellaneous	The target chamber is fully enclosed within a class 10,000 clean room. A laminar flow bench allows work to be performed in a class 100 environment.
Contact	Dr. James McFadden UC Berkeley Space Sciences Laboratory 7 Gauss Way Berkeley, CA 94720, USA Tel: +1-510-642-9918 Fax: +1-510-643-8302 E-Mail: `mcfadden@ssl.berkeley.edu`
Reference	

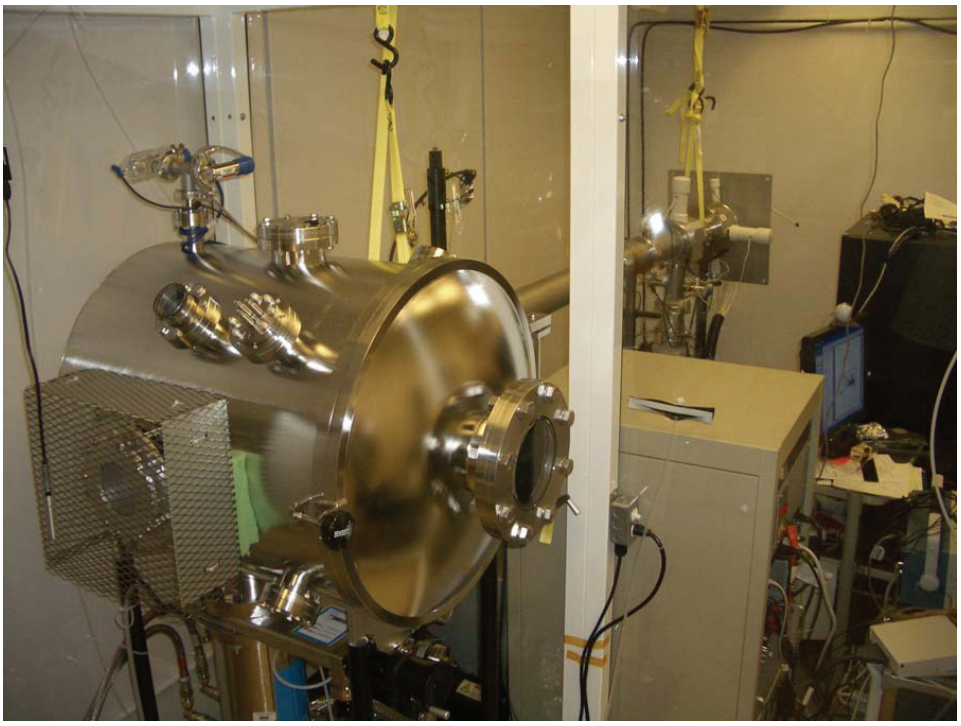

Figure A.73: One of the University of California, Berkeley vacuum calibration chambers. The near side of the 30 inch chamber has an UV photocathode gun [*Lessard et al.*, 1998] that provides a 10 cm electron beam at energies up to 30 keV. On the opposite side of the chamber is a Peabody Scientific mass selectable ion source, with drift tube to reduce background, and an energy range of 2 to 50 keV. Having both guns on the same chamber facilitates testing of instruments that contain both ion and electron detectors. The vacuum chamber and electron gun reside inside the clean room while the ion gun extends into the outer room for easy access.

Table A.35: University of Denver Facility: UDenver-1

Category	Ion and Neutral Beam.
Description	High vacuum, field free, calibration facility for neutral and ion beam characterization of upper atmosphere sensors.
Vacuum system	All metal, bakeable to 300°C, differentially pumped ion source, liquid nitrogen trapped diffusion pump.
Ion Beam	Modified Duoplasmatron source, energy range 20-3000 eV, energy resolution <3 eV, beam size <2 mm with beam currents calibrated to 5 %.
Neutral Beam	H atoms produced by laser photodetachment of electrons from H^- resulting in a ground state H atom beam with flux calibrated to 5 %.
Monitors, Gauges	Bayard-Alpert hot filament ionization gauge and SRS residual gas analyzer (RGA) on target chamber.
Instrument Mounting	Internal mounting for instruments up to 15.2 cm in depth along the beam line 20.3 cm width and 25.4 cm height, instrument is mounted to baseplate with 15 kg maximum mass.
Rotation, Translation	Not available.
GSE	Computer readout of instrument operating parameters, beam currents (fluxes), temperatures, RGA and pressure gauges is available.
Miscellaneous	Automatic overpressure protection for vacuum system and all instrument electronics with failsafe shutdown.
Contact	Bert van Zyl Department of Physics and Astronomy 2112 E. Wesley Ave. University of Denver Denver, CO 80208, USA Tel: +1-303-871-2116 Fax: E-Mail: `bvanzyl@du.edu`
Reference	*van Zyl et al.* [1976]

Figures: See system UDenver-2

Table A.36: University of Denver Facility: UDenver-2

Category	Ion and Neutral Beam.
Description	High vacuum, field free, calibration facility for neutral and ion beam characterization of upper atmospheric detectors.
Vacuum system	All metal, bakeable to 300°C, differentially pumped ion source and cyro-pumped.
Ion Beam	Modified Colutron^{TM} source, energy range 3-1000 eV, energy resolution <2 eV, beam size <2 mm with beam currents calibrated to 5 %.
Neutral Beam	H and O atoms produced by laser photodetachment of electrons from H^- and O^-, respectively, resulting in ground state H or O atom beam with flux calibrated to 5 %.
Monitors, Gauges	Bayard-Alpert hot filament ionization gauge and SRS residual gas analyzer (RGA) on target chamber.
Instrument Mounting	Internal mounting for instruments up to 50.8 cm in depth along the beam line with 50.8 cm width and 50.8 cm in height. Instrument is mounted to baseplate or dual axis gimbal. Maximum mass 50 kg balanced. External mounting possible.
Rotation, Translation	Complete elevation and azimuth.
GSE	Computer readout of instrument operating parameters, beam currents (fluxes), temperatures, RGA and pressure gauges is available.
Miscellaneous	Automatic overpressure protection for vacuum system and all instrument electronics with failsafe shutdown.
Contact	Bert van Zyl Department of Physics and Astronomy 2112 Wesley Ave. University of Denver Denver, CO 80208, USA Tel: +1-303-871-2116 Fax: E-Mail: `bvanzyl@du.edu`
Reference	*Stephen et al.* [1996]

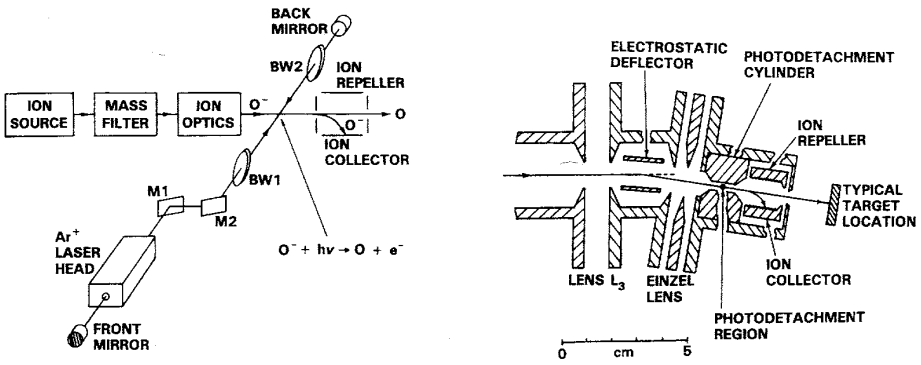

Figure A.74: Left: Schematic of University of Denver O^- photo-detachment system for producing neutral O atoms. Right: Schematic of lens system and window for laser beam source. [*Stephen et al.*, 1996].

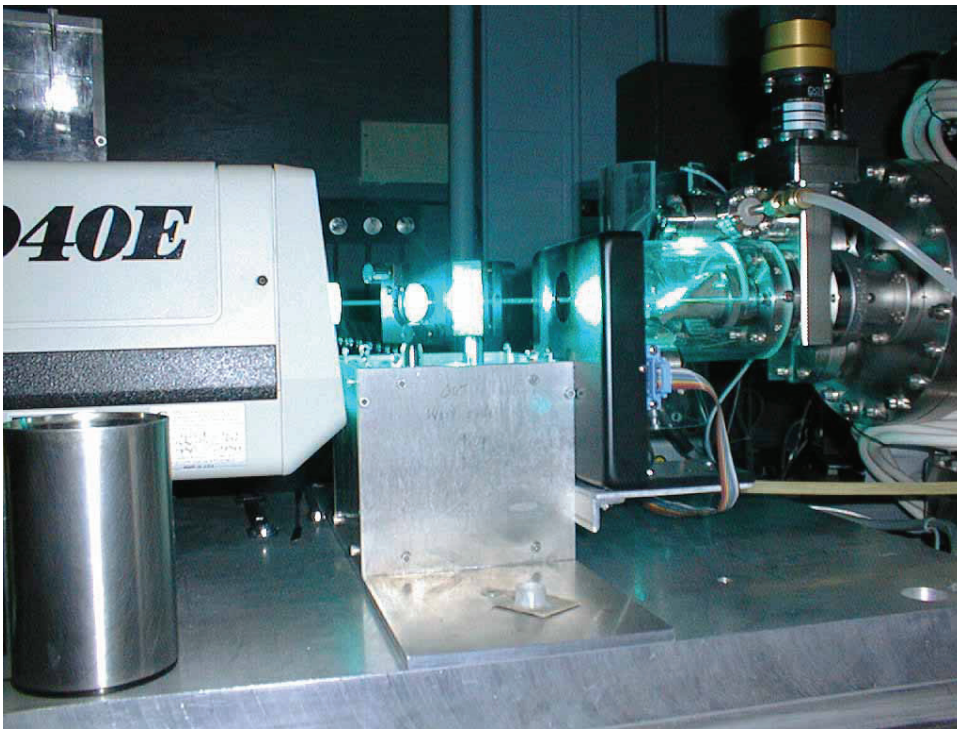

Figure A.75: Picture of University of Denver O^- photo-detachment system for producing neutral O atoms. [*Stephen et al.*, 1996].

Table A.37: University of Michigan Laboratory: UMichigan-MASS-SPEC

Category	Ion Accelerator.
Description	Ion beam accelerator system for small- to medium-sized instrument calibration and characterization.
Vacuum system	Chamber 1: Upright cylindrical chamber, 61 cm in diameter, with a volume of 200 l. Base pressure of $\sim 10^{-7}$ mbar maintained by 20.3 cm cryogenic pump. 1 m drift tube for beam cooling. Chamber 2: Upright cylindrical chamber, 81 cm diameter, with 200 l volume. Base pressure of $\sim 10^{-8}$ mbar maintained by scroll pump-backed turbopump and 20.3 cm diameter cryopump. 1 m drift tube for beam cooling.
Ion Beam	Electron impact ionization source with an energy range of 500 eV to 10 keV, typically used with acceleration system to increase maximum energy to 30 keV. Energy width <1 eV. Beam size 2 cm diameter after 1 m drift tube. Mass selection (H-Ar) by Wien filter with a resolution of $\sim$400. Beam current $\leq$1.5 nA. Additional 500 eV to 10 keV electron impact ionization source is available.
Monitors, Gauges	Convectron gauge, Bayard-Alpert hot filament ion gauge.
Instrument Mounting	Two rotational and two translational stages (computer-controlled) are available.
Rotation, Translation	$\pm 25^\circ$ about two orthogonal axes normal to ion beam line with $\pm$5.0 cm horizontal translation manually set.
GSE	Multiple SHV, HV ceramic (20 kV), BNC and 9-pin D-shell feedthroughs available at various locations on main cylinder. 10, 20 and 30 kV power supplies are available.
Miscellaneous	Vacuum failure interlock protects HV instruments in case of vacuum loss. 10 solar Ly-α sources (Opthos). 4-axis motion control system.
Contact	Patrick Koehn University of Michigan Space Research Building 2455 Hayward St Ann Arbor, MI 48109-2143, USA Tel: +1-734-647-6834 Fax: +1-734-615-9723 E-Mail: `koehn@umich.edu`
Reference	

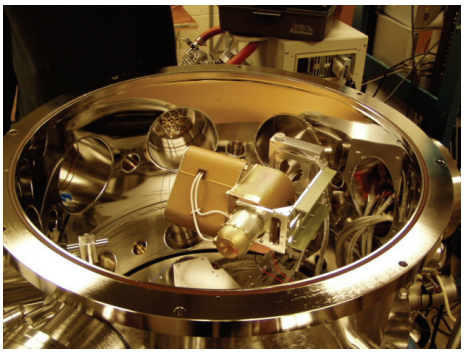

Figure A.76: Chamber 1 was utilized during the final calibration of the Fast Imaging Plasma Spectrometer, one of the instruments aboard NASA's MESSENGER mission, a Mercury orbiter.

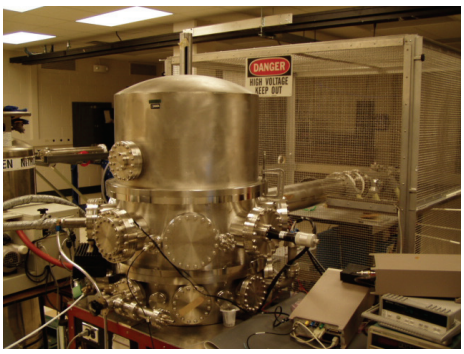

Figure A.77: Chamber 1 attached to the ion accelerator. This chamber can accommodate small- to medium-sized spaceflight instruments.

Figure A.78: Ion accelerator system for the University of Michigan's MASS SPEC Laboratory. The system provides an ion beam with an energy of up to 30 keV.

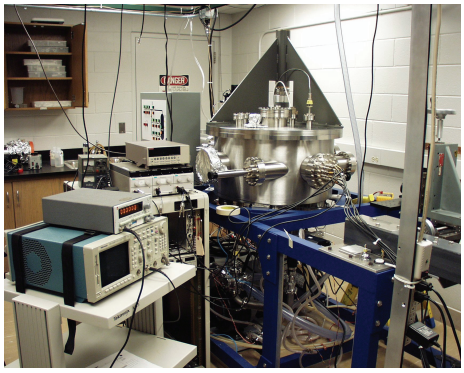

Figure A.79: Chamber 2 of the MASS-SPEC Laboratory is ideal for subsystem testing or the characterization of small spaceflight instruments.

Table A.38: University of New Hampshire Facility: UNH

Category	Ion beam.
Description	High vacuum facility for ion beam characterization of space plasma physics detectors/instruments.
Vacuum system	Chamber 91.4 cm diameter, 122 cm length. Oil-free scroll pump for roughing out, 35.6 cm CTI cryohead pump for 1×10^{-6} mbar high vacuum operation.
Ion Beam 1a,1b	Two ion gun sources (1a-SIG: $\leq$2 keV, 1b-BIG: $\leq$50 keV), separately mounted.
Instrument mounting	Instruments mount on a 60 cm rotary table, supported by a FerroFluidic feedthrough capable of 360° rotation. Supports 20 kg test item.
Beam Motion	1b-BIG ion gun is mounted on a rotating table capable of $\pm$20° off axis.
Monitors, Gauges	Granville-Phillips Series 307 Vacuum Gauge Controller.
GSE	Varies with programs.
Miscellaneous	Instruments currently mount to a cold plate capable of -20°C operation. Automatic overpressure relay to be installed 9/2004. Equipped with SRS 100 RGA. Entire chamber enclosed inside a class 10K cleanroom tent.
Contact	Mark Popecki UNH Space Science Center 39 College Rd. Morse Hall Rm. Durham, NH 03824, USA Tel: +1 603-862-2957 Fax: +1 603-862-3584 E-mail: `mark.popecki@unh.edu`
Reference	

Figure A.80: University of New Hampshire Space Plasma Experiment Testing Facility: Vacuum chamber in class 10K clean tent.

Figure A.81: Internal view of vacuum chamber, showing instrument turn table.

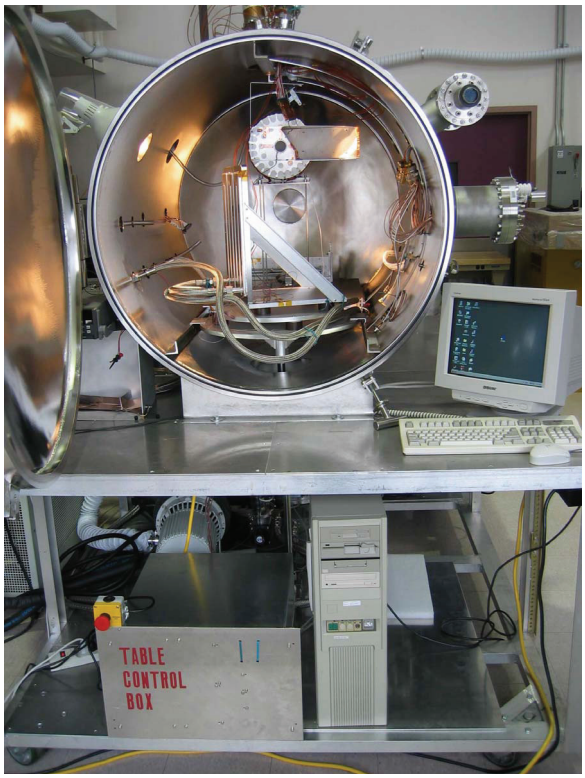

Figure A.82: Table rotation control and cold plate on table (front), 1b-BIG (50 keV) ion gun (rear).

Bibliography

Biddle, A.P. and J.M. Reynolds, Integrated development facility for the calibration of low-energy charged particle flight instrumentation, *Rev. Sci. Instrum.*, **57 (4)**, 572–582, 1986.

Cascio, E.W., J.M. Sisterson, J.B. Flanz, and M.S. Wagner, The proton irradiation program at the Northeast Proton Therapy Center, in *Proc. IEEE Radiation Effects Data Workshop*, 141–144, 2003.

Cook, S.R., M.A. Hoffbauer, J.B. Cross, H. Wellenstein, and M. Fink, A specialized torsion balance designed to measure the absolute flux density of hyperthermal molecular beams containing reactive species, *Rev. Sci. Instrum.*, **67**, 1781–1789, 1996.

Cook, S.R. and M.A. Hoffbauer, Absolute momentum transfer in gas-surface scattering, *Phys. Rev. E*, **55**, R3828–R3831, 1997.

Cook, S.R. and M.A. Hoffbauer, Analyzing gas-surface interactions using the reduced force coefficients, *Phys. Rev. E*, **58**, 504–511, 1998.

Cross, J.B. and N.C. Blais, High-energy/intensity CW atomic oxygen beam source, in *Rarified Gas Dynamics: Space-Related Studies*, E.P. Muntz, D.P. Weaver, and D.H. Campbell, Eds., Progress in Astronautics and Aeronautics, AIAA, Washington, D.C., **116**, 143–155, 1989.

Ghielmetti, A.G., H. Balsiger, R. Banninger, P. Eberhardt, J. Geiss and D.T. Young, Calibration system for satellite and rocket-borne ion mass spectrometers in the energy range from 5 eV/charge to 100 keV/charge, *Rev. Sci. Instrum.*, **54 (4)**, 425–436, 1983.

Graf, S., K. Altwegg, H. Balsiger, A. Jackel, E. Kopp, U. Langer, and W. Luithardt, A cometary neutral gas simulator for gas dynamic sensor and mass spectrometer calibration, *J. Geophys. Res.*, **109**, E07S08, doi:10.1029/2003JE002188, 2004.

Hirahara M. and T. Mukai, Fast ion energy mass spectrometer with wide acceptance angle for space research 2: Experimental results, *ISAS Research Note*, **501**, 1992.

Lessard, M., G.P. Garbe, and R.L. Arnoldy, , A calibration source for low energy electron detectors, in *Measurement Techniques in Space Plasmas: Particles*, R. Pfaff, J. Borovsky, and D.T. Young, Eds., Geophys. Monogr. Ser., American Geophysical Union, Washington, D.C., **102**, 301–306, 1998.

Marshall, F.J., D.A. Hardy, A. Huber, J. Pantazis, and J. McGarity, Calibration system for electron detectors in the range from 10 eV to 50 keV, *Rev. Sci. Instrum.*, **57**, 229–235, 1986.

Marti, A., R. Schletti, P. Wurz, and P. Bochsler, Calibration facility for solar wind plasma instruments, *Rev. Sci. Instrum.*, **72(2)**, 1354–1360, 2001.

Steinacher, M., F. Jost, U. Schwab, A modern and fully automated calibration system for space ion mass spectrometers, *Rev. Sci. Instrum.*, **66 (8)**, 4180–4187, 1995.

Stephen, T.M., B. van Zyl, and R.C. Amme, Generation of a fast atomic-oxygen beam from O^- ions by resonant cavity radiation, *Rev. Sci. Instrum.*, **67**, 1478–1482, 1996.

Van Zyl, B., N.G. Utterback, and R.C. Amme, Generation of a fast atomic hydrogen beam, *Rev. Sci. Instrum.*, **47**, 814–819, 1976.

Westermann, C., W. Luithardt, E. Kopp, T. Koch, R. Liniger, H. Hofstetter, J. Fischer, K. Altwegg, and H. Balsiger, A high precision calibration system for the simulation of cometary gas environments, *Meas. Sci. Technol.*, **12**, 1594–1603, 2001.

Westermann, C., A Novel Calibration System for the Simulation of Cometary Gas Environments, Ph.D. thesis, University of Bern, 2000.

A.5 Glossary of Metrology

This section is intended to provide the readers with the definitions of certain terms often used in the calibration of instruments. The definitions were taken from the Swedish National Testing and Research Institute (`http://www.sp.se/metrology/eng/terminology.htm`), the Guide to the Measurement of Pressure and Vacuum, National Physics Laboratory and Institute of Measurement & Control, London, 1998 and VIM, International Vocabulary of Basic and General Terms in Metrology, 2^{nd} Ed., ISO, Geneva, 1993.

Accuracy The closeness of the agreement between a test result and the accepted reference value [ISO 5725]. See also precision and trueness.

Adjustment Operation of bringing a measuring instrument into a state of performance suitable for its use.

Bias The difference between the expectation of the test results and an accepted reference value [ISO 5725].

Calibration A set of operations that establish, under specified conditions, the relationship between values of quantities indicated by a measuring instrument (or values represented by a material measure) and the corresponding values realized by standards.
The result of a calibration may be recorded in a document, e.g. a calibration certificate. The result can be expressed as corrections with respect to the indications of the instrument.
Calibration in itself does not necessarily mean that an instrument is performing in accordance with its specification.

Certification A process performed by a third party that confirms that a defined product, process or service conforms with, for example, a standard.

Confirmation Metrological confirmation is a set of operations required to ensure that an item of measuring equipment is in a state of compliance with requirements for its intended use. Metrological confirmation normally includes, for example, calibration, any necessary adjustment or repair and subsequent recalibration, as well as any required sealing and labeling.

Corrected result Result of a measurement after correction for systematic error.

Correction The value which, added algebraically to the uncorrected result of a measurement, compensates for an assumed systematic error. The correction is equal to the assumed systematic error, but of the opposite sign. Since the systematic error can not be known exactly, the correction is subject to uncertainty.

Dead band Maximum interval through which a stimulus may be changed in both directions without producing a change in response of a measuring instrument [VIM 5.13].

Detector Device or substance that indicates the presence of a phenomenon, body, or substance when a threshold value of an associated quantity is exceeded. NOTES: 1) In some fields the term ”detector” is used for the concept of sensor. 2) In chemistry the term ”indicator” is frequently used for this concept.

Device Any artifactual object designed to perform an action or process, with or without an operator in attendance.

Drift A slow change of a metrological characteristic of a measuring instrument.

Error ((of indication) of a measuring instrument) The indication of a measuring instrument minus a 'true' value of the corresponding input quantity, i.e. it has a sign.

Expectation (of the measurable quantity) The mean of a specified population of measurements.

Fiducial error (of a measuring instrument) Error of a measuring instrument divided by a (fiducial) value specified for the instrument [VIM 5.28].

Fiducial value Can be the span or upper limit of nominal range of measuring instrument.

Group standard A set of standards of chosen values that, individually or in combination, provides a series of values of quantities of the same kind.

Inspection Involves measurement, investigation or testing of one or more characteristics of a product, and includes a comparison of the results with specified requirements in order to determine whether the requirements have been fulfilled.

Instrument constant Coefficient by which the direct indication of a measuring instrument must be multiplied to give the indicated value of the measurand or of a quantity to be used to calculate the value of the measurand [VIM 5.8].

Kind, quantities of the same Quantities that can be placed in order of magnitude relative to one another [VIM 1.1].

Laboratory bias The difference between the expectation of the test results from a particular laboratory and an accepted reference value [ISO 5725].

Limiting conditions Extreme conditions that a measuring instrument is required to withstand without damage, and without degradation of specified metrological characteristics when it is subsequently operated under its rated operating conditions [VIM 5.6].

(Measurable) quantity Attribute of a phenomenon, body or substance that may be distinguished qualitatively and determined quantitatively [VIM 1.1].

Measurand Particular quantity subject to measurement [VIM 2.6].

Measurement Set of operations having the object of determining a value of a quantity [VIM 2.1].

Measurement procedure Set of operations, described specifically, used in the performance of particular measurements according to a given method [VIM 2.5].

Measurement signal Quantity that represents the measurand and which is functionally related to it [VIM 2.8].

Measurement standard, Etalon Material measure, measuring instrument, reference material or measuring system intended to define, realize, conserve or reproduce a unit or one or more values of a quantity to serve as a reference [VIM 6.1].

Measuring chain Series of elements of a measuring instrument or system that constitutes the path of the measurement signal from the input to the output [VIM 4.4].

Measuring range Set of values of measurands for which the error of a measuring instrument in intended to lie within specified limits [VIM 5.4].

Measuring system Set of measuring instruments and other devices or substances assembled and adapted to the measurement of quantities of specified kinds within specified intervals of values.

Measuring instrument A device or combination of devices designed for measurement of quantities.

Measuring transducer Device that provides at its output a quantity having a determined relation to the quantity at its input.

Metrology The science of measurement.

National (measurement) standard Standard recognized by a national decision to serve, in a country, as the basis for assigning values to other standards of the quantity concerned.

Nominal range Range of indications obtainable with a particular setting of the controls of a measuring instrument [VIM 5.1].

Nominal value Rounded or approximate value of a characteristic of a measuring instrument that provides a guide to its use [VIM 5.3].

Precision The closeness of agreement between independent test results obtained under stipulated conditions [ISO 5725].

Quality Relates to all the characteristics that meet an expressed or implied need.

Reference Accepted value that serves as an agreed-on reference for comparison, and which is derived from a theoretical or established value, based upon scientific principles, or from an assigned or certified value, based upon experimental work of some national or international organization, or from a consensus or certified value based upon collaborative experimental work under the auspices of a scientific or engineering group. When these are not available, the reference value is taken to be the expectation of the measurable quantity.

Reference conditions Conditions of use prescribed for testing the performance of a measuring instrument or for intercomparison of results of measurements [VIM 5.6].

Relative error Error of measurement divided by a true value of the measurand [VIM 3.12].

Repeatability Precision under repeatability conditions.

Repeatability conditions Conditions where independent test results are obtained with the same method on identical test items in the same laboratory by the same operator using the same equipment within short intervals of time [ISO 5725].

Reproducibility Precision under reproducibility conditions.

Reproducibility conditions Conditions where test results are obtained with the same method on identical test items in different laboratories with different operators using different equipment.

Resolution Smallest change of measured quantity which changes the indication of an measuring instrument.

Result of a measurement Value attributed to a measurand, obtained by measurement [VIM 3.1].

Response characteristic Relationship between a stimulus and the corresponding response, for defined conditions [VIM 5.9].

Response time Time interval between the instant when a stimulus is subjected to a specified abrupt change and the instant when the response reaches and remains within specified limits around its final steady value [VIM 5.17].

Sensitivity Change in the response of a measuring instrument divided by the corresponding change in the stimulus.

Sensor Element of a measuring system that is directly affected by the phenomenon, body, or substance carrying the quantity to be measured. Note in some fields the term 'detector is used for this concept.

Span Modulus of the difference between the two limits of a nominal range [VIM 5.2].

Stability Refers to the ability of a measuring instrument to maintain constant its metrological characteristics with time.

Standard, national Standard recognized by a national decision to serve, in a country, as the basis for assigning values to other standards of the quantity concerned (see National standard).

Standard, primary Standard that is designated or widely acknowledged as having the highest metrological qualities and whose value is accepted without reference to other standards of the same quantity.

Standard, reference Standard, generally having the highest metrological quality available at a given location or in a given organization, from which measurements made there are derived. The reference standard itself must be periodically calibrated against a higher standard or in the case of national measurements institute in key comparisons.

Standard, secondary Standard whose value is assigned by comparison with a primary standard of the same quantity.

Standard, transfer Standard used as an intermediary to compare standards.

Standard, working Standard that is used routinely to calibrate or check material measures, measuring instruments or reference materials.

Systematic error Mean that would result from an infinite number of measurements of the same measurand carried out under repeatability conditions minus a true value of the measurand [VIM 3.14].

Transformed value Value of measurement signal representing a given measurand [VIM 2.9].

Testing A technical investigation, e.g. as to whether a product fulfills its specified performance.

Threshold Largest change in a stimulus that produces no detectable change in the response of a measuring instrument, the change in the stimulus taking place slowly and monotonically [VIM 5.11].

Traceability Means that a measured result can be related to stated references, usually national or international standards, through an unbroken chain of comparisons, all having stated uncertainties.

Trueness The closeness of agreement between the average value obtained from a large series of test results and an accepted reference value [ISO 5725]. The measure of trueness is usually expressed in terms of bias.

Uncertainty of measurement A parameter, associated with the result of a measurement, that characterizes the dispersion of the values that could reasonably be attributed to the measurand. It can also be expressed as an estimate characterizing the range of values within which the true value of a measurand lies.
When specifying the uncertainty of a measurement, it is necessary to indicate the principle on which the calculation has been made.

Uncorrected result Result of a measurement before correction for systematic error [VIM 3.3].

Unit (of measurement) Particular quantity, defined and adopted by convention, with which other quantities of the same kind are compared in order to express their magnitudes relative to that quantity [VIM 1.7].

Verification An investigation that shows that specified requirements are fulfilled.

The precise definitions of the terms listed here can also be found in a number of international standards documents, including:

IEC 60050 International Electrotechnical Vocabulary
ISO 3534-1 Statistics - Vocabulary and symbols -
Part 1. Probability and general statistical terms
ISO 5725 Accuracy (trueness and precision) of measurement methods and results.
ISO 8402 Quality management and quality assurance - Vocabulary

ISO 10 012 Quality assurance requirements for measuring equipment:
Part 1: Metrological confirmation system for measuring equipment.
EN 45 020 General terms and their definitions concerning standardization
and related activities.
Webster's Dictionary

A.6 Acronyms

Institutions

AEB	Atmospheric Experiment Branch (NASA GSFC) (USA)
AFRL	Air Force Research Laboratory (USA)
BIPM	Bureau International des Poids et Mesures (France)
CETP	Centre d'étude des Environnements Terrestre et Planétaires (France)
ESA	European Space Agency
GSFC	NASA Goddard Space Flight Center (USA)
HAFB	Hanscom Air Force Base (USA)
IEC	International Electrotechnical Commission
IPB	Interplanetary Physics Branch (NASA GSFC) (USA)
IKI	Russian Space Research Institute (Russia)
IPSL	Institut Pierre Simon Laplace (France)
IRFK	Institutet for Rymdfysik (Institute of Space Physics), Kiruna (Sweden)
ISAS	Institute of Space and Astronautical Science (Japan)
ISO	International Organization for Standardization
ISSI	International Space Science Institute (Switzerland)
KRISS	Korean Research Institute of Standards and Science
LANL	Los Alamos National Laboratory (USA)
LMATC	Lockheed-Martin Advanced Technology Center (USA)
JPL	Jet Propulsion Laboratory (USA)
MPAe	Max-Planck-Institut fur Aeronomie (Germany)
MSFC	NASA Marshall Space Flight Center (NASA) (USA)
MSSL	Mullard Space Science Laboratory (UK)
NASA	National Air and Space Administration (USA)
NIST	National Institute of Standards and Technology (USA)
NOAA	National Oceanic and Atmospheric Administration (USA)
NPL	National Physics Laboratory (UK)
NPTC	Northeast Proton Therapy Center at Massachusetts General Hospital (USA)
NRL	Naval Research Laboratory (USA)
PTB	Physikalisch-Technische Bundesanstalt (Germany)
RPI	Rensselaer Polytechnic Institute (USA)
SEC	Space Environment Center (NOAA) (USA)
SwRI	Southwest Research Institute (USA)
SLAC	Stanford Linear Accelerator Center (USA)
UoB	University of Bern (Switzerland)
UCSD	University of California, San Diego (USA)
UCB	University of California, Berkeley (USA)

UD	University of Denver (USA)
UNH	University of New Hampshire (USA)
UM	University of Michigan (USA)
UTD	University of Texas, Dallas (USA)
VSSE	AFRL Space Vehicles Directorate/Space Electronics and Protection Branch (USA)

Spacecraft

ACE	Advanced Composition Explorer, measures solar wind at L1
AE	Atmosphere Explorer, a series of low altitude NASA science missions
Aeros-A, -B	Two German-US collaboration satellites in low altitude, polar orbit for atmospheric studies
Akebono	Japanese science mission in an elliptical, high inclination orbit also known as EXOS-D
AMPTE	Active Magnetospheric Particle Tracer Explorers; international science mission using chemical releases to actively determine magnetospheric transport processes; consisted of the 3 spacecraft CCE, IRM, and UKS
ATS	Applications Technology Satellite, a series of NASA technology development satellites in geostationary orbit
Alouette	Polar orbit, low altitude science mission
BepiColombo	ESA planetary exploration mission to Mercury currently in development
Cassini	Mission to Planet Saturn
CCE	Charge Composition Explorer, part of the AMPTE mission
Chandra	NASA X-ray astronomy mission
Cluster	Magnetospheric four spacecraft mission
CONTOUR	COmet Nucleus TOUR, comet encounter mission
CRAF	Comet Rendezvous Asteroid Flyby, originally a component of the Cassini interplanetary mission but ultimately canceled
CRRES	Combined Release and Radiation Effects Satellite, geostationary transfer orbit
DE	Dynamics Explorer, a dual satellite, polar orbit science mission
Deep Space 1	The first of NASA's New Millennium Program series of technology development spacecraft
DMSP	Defense Meteorological Satellite Program, a series of polar orbit operational satellites
DSP	Defense Satellite Program, a series of DoD operational missions
DSX	Demonstration and Science Experiment, a DoD mission
ESRO	European Space Research Organization, also a series of scientific satellite missions sponsored by ESRO
Equator-S	Near geostationary orbit for magnetospheric studies
FAST	Fast Auroral SnapshoT, polar orbit auroral mission
Galileo	International mission to Jupiter including a planetary orbiter
GEOS	GEOstationary Scientific satellite, a two satellite program by ESA for the study of fields and particles at geostationary altitude
Geotail	Low inclination, highly elliptical orbit for magnetospheric studies
Giotto	ESA space mission to comet Halley

GOES	Geostationary Operational Environmental Satellite, operated by NOAA
Helios-1,-2	Two ESA interplanetary science missions
HST	Hubble Space Telescope, a NASA astronomy mission
Huygens	The Titan probe/lander, a component of the Cassini mission to Saturn
IBEX	Interstellar Boundary Explorer, a NASA science mission in development
IMAGE	Imager for Magnetopause-to-Aurora Global Exploration, polar orbit
IMP	Interplanetary Monitoring Probe, a series of NASA interplanetary science missions
Injun	A series of low altitude high inclination science missions implemented by the University of Iowa
IRM	Ion Release Module, a subsatellite deployed on the AMPTE mission
ISEE	International Sun Earth Explorer, a three satellite mission in various orbits
ISIS	International Satellites for Ionospheric Study, two polar orbit science satellites
LANL	Los Alamos National Laboratory spacecraft series
Mariner	A series of NASA planetary science missions
Mars Express	ESA mission to Mars
Mars Surveyor	NASA planetary mission orbiting a spacecraft around Mars
MMS	Magnetospheric Multiscale Mission
MSX	Midcourse Space experiment, a DoD mission to study optical background from the atmosphere and space
NOAA	National Oceanic and Atmospheric Administration satellites a series of polar orbit operational satellites, also called POES
Nozomi	Japanese Institute of Space and Aeronautical Science planetary exploration mission to Mars. Also known as Planet-B
NPOESS	National Polar Orbiting Environmental Satellite System
OGO	Orbiting Geophysical Observatory, a series of NASA science missions in both polar and low inclination orbits
Pioneer	A series of NASA planetary and interplanetary science missions
POES	Polar Operational Environmental Satellite a series of polar orbit operational satellites operated by NOAA
Polar	high inclination polar orbit
PVO	Pioneer Venus Orbiter, planetary mission
Rosetta	ESA comet encounter mission
San Marco	A series of Italian-NASA low altitude, low inclination satellite missions for atmospheric research
SCATHA	Spacecraft Charging AT High Altitude, a low inclination, highly elliptical orbit DoD science mission
SOHO	Solar and Heliospheric Observatory, measures Sun and solar wind at L1
STEREO	Solar-Terrestrial Relations Observatory, two spacecraft in solar orbit at 1 Astronomical Unit for solar wind and solar physics science
S85-1	High inclination, low altitude Defense Department Space Test Program mission
THEMIS	Time History of Events and Macroscale Interactions during Substorms, a multi-satellite NASA Explorer mission

TIROS	Television and InfraRed Observing Satellite
Triana	A proposed mission to monitor the solar wind at L1
TSX	Tri Service experiment, a series of DoD missions with science and operational goals
UARS	Upper Atmosphere Research Satellite, 600 km altitude orbit, high inclination
UKS	United Kingdom Satellite, part of the AMPTE mission
Ulysses	A spacecraft in polar heliocentric orbit for heliospheric science studies
Viking	Swedish spacecraft mission for auroral studies also an early NASA planetary mission to Mars
Wind	upstream solar wind mission
Voyager	mission to the outer planets

Instruments

ALSEP	Apollo Lunar Science Experiment Package, a science instrument package left on the moon during the Apollo missions
ASPERA	Analyzer of Space Plasma and Energetic Atoms, an instrument on the Mars Express and Venus Express missions
AXIS	Atmospheric X-ray Imaging Spectrometer, a component of the PEM instrument on the UARS satellite
BNMS	Bus Neutral Gas Mass Spectrometer, an instrument on the PVO mission
BUGATTI	Bonn University Gas Analyzer for Turbulence and Turbopause Investigation, an instrument flown on sounding rockets
CAPS	Cassini Plasma Spectrometer
CASYMIR	Calibration System for the Mass Spectrometer Instrument ROSINA
CASYMS	Calibration System for Mass Spectrometers
CEASE	Compact Environmental Anomaly SEnsor, flown on several spacecraft (i.e. DSX)
CELIAS	Charge, Element and Isotope Analysis System, an instrument suite onboard the ESA SOHO spacecraft
CIS	Cluster Ion Spectrometer, an instrument on the Cluster spacecraft
CODIF	COmposition DIstribution Function, part of the CIS instrument on the Cluster satellites
COLLISA	Collection of InterStellar Atoms
COPS	COmet Pressure Sensor, a component of the ROSINA instrument onboard the Rosetta spacecraft
COS	Cosmic Origins Spectrograph, an instrument on the NASA HST spacecraft
COSPIN	Comic ray and Solar Particle Investigations, an instrument suite on the Ulysses spacecraft
CRIS	Cosmic-Ray Isotope Spectrometer, instrument onboard theACE satellite
CTOF	Charge Time-Of-Flight, a component of the CELIAS instrument suite on the SOHO Spacecraft

DFMS	Double Focusing Mass Spectrometer
EAe, EAp	Electron and Proton Energy Analyzers, part of the Geotail LEP instrument
EESA-H, EESA-L	Electron ElectroStatic Analyzer-High and Low geometric factor, components of the Wind 3D instrument on Wind
ELENA	Emitted Low-Energy Neutral Atoms, a component of the SERENA instrument under development of the BepiColombo mission
ELS	Electron Spectrometer, a component of the ASPERA instrument
EPACT	Energetic Particle Acceleration Composition and Transport an instrument suite onboard the Wind spacecraft
EPIC	Energetic Particles and Ion Composition, an instrument on the Geotail spacecraft
GCMS	Gas Chromatograph Mass Spectrometer, an instrument onboard the Huygens Titan reentry probe component of the Cassini mission
GPMS	Galileo Probe Mass Spectrometer, an instrument onboard the atmospheric entry probe component of the Galileo mission
LOLET	An instrument to measure radiation dose from low energy particles
HEEA	High Energy Electron Analyzer, a component of the PEACE instrument
HENA	High Energy Neutral Atom detector, an instrument onboard the IMAGE satellite
HEPAD	High Energy Proton And Alpha detector, an instrument on the GOES spacecraft
HEPS	High Energy Proton Spectrometer, an instrument on the Air Force Demonstration and Science Experiment (DSX)
HIA	Hot Ion Analyzer, part of the CIS instrument on Cluster
HILET	An instrument to measure radiation dose from high energy particles
Hydra	A plasma instrument onboard the NASA Polar spacecraft, named for the many-headed monster of mythology
IE	Ion Emitter, an spacecraft potential control device on the Geotail satellite
ILENA	Imager for Low Energy Neutral Atoms
IMS	Ion Mass Spectrometer, an instrument on the Cassini spacecraft also Ion Mass Spectrometer instrument on the MSX spacecraft
IMS-HI	Ion Mass Spectrometer-High energy, instrument on the CRRES satellite
INMS	Ion and Neutral Mass Spectrometer, an instrument on the Cassini Spacecraft
LECP	Low Energy Charged Particle, an instrument on the NASA Voyager planetary science mission
LEEA	Low Energy Electron Analyzer, a component of the PEACE instrument
LEMMS	Low Energy Magnetospheric Measuring System, a component of the MIMI (Magnetospheric IMaging Instrument) suite on the Cassini planetary science mission
LENA	Low Energy Neutral Atom detector, an instrument onboard the

	IMAGE satellite
LEP	Low Energy Particle, an experiment on Geotail
LEPA	Low Energy Plasma Analyzer, instrument on the AMPTE mission
LET	Low Energy Telescope, an instrument on the Ulysses spacecraft also acronym for Linear Energy Transfer
LOLET	An instrument to measure radiation dose from low energy particles
MEA	Medium Electron A spectrometer, instrument onboard the CRESS satellite
MACSIMS	Measurements of Atmospheric Constituents by Selective Ion Mass Spectrometry
MASS	High MASS Resolution Spectrometer, a component of the SMS instrument suite onboard the NASA Wind spacecraft for solar wind research
MENA	Medium Energy Neutral Atom detector, an instrument onboard the IMAGE satellite
MEPA	Medium Energy Particle Analyzer, an instrument on the AMPTE/CCE satellite
MEPED	Medium Energy Proton and Electron Detector, a component of the SEM on the POES spacecraft
MEFISTO	Messinstrument für Flugzeitinstrumente
MFI	Magnetic Field Instrument, an instrument on the NASA Wind satellite
MTOF	Mass Time-Of-Flight spectrometer, a component of the CELIAS instrument suite on the SOHO spacecraft
NACE	Neutral Atmospheric Composition Experiment, an instrument onboard the San Marcos 3 spacecraft
NATE	Neutral Atmosphere Temperature Experiment on the San Marco, Aeros and Atmosphere Explorer spacecraft
NMS	Neutral Mass Spectrometer onboard the Nozomi spacecraft also Neutral Mass Spectrometer onboard the Giotto spacecraft
NGIMS	Neutral Gas and Ion Mass Spectrometer, an instrument on the CONTOUR spacecraft
ONMS	Orbiter Neutral Mass Spectrometer, an instrument on Pioneer Venus Orbiter
OSS	Open-Source neutral mass Spectrometer, an instrument onboard the AE series of science missions
PEACE	Plasma Electron And Current Experiment, an instrument on the Cluster spacecraft
PEM	Particle Environment Monitor, an instrument onboard the UARS satellite
PEPE	Plasma Experiment for Planetary Exploration, an instrument on the NASA Deep Space 1 mission
PESA-H, PESA-L	Proton Electrostatic Analyzer, High and Low geometric factor, components of the Wind 3D instrument on Wind
PLASTIC	PLasma And SupraThermal Ion Composition onboard the two spacecraft STEREO mission
PLS	PLasma Science instrument on the NASA Voyager planetary

	science mission
PM	Proton Monitor, a component of the CELIAS instrument suite on the SOHO satellite
PSI	Plasma Source Instrument, a component of the TIDE instrument on the Polar spacecraft used to control the spacecraft potential
RAPID	Research with Adaptive Particle Imaging Detectors, an instrument suite onboard the Cluster spacecraft
REFLEX	Return Flux Experiment, an instrument onboard a shuttle mission
ROSINA	Rosetta Orbiter Spectrometer for Ion and Neutral Analysis
RPA-1	Réme Plasma Analyzer, an instrument on the Giotto spacecraft
RTOF	Reflectron Time-Of-Flight spectrometer
SCENIC	Spectroscopic Camera for Electrons, Neutral, and Ion Composition a component of the RAPID instrument suite onboard Cluster spacecraft
SEM	Space Environment Monitor, a suite of particle detectors flown on the POES spacecraft
SERENA	Search for Exospheric Refilling and Emitted Natural Abundances an instrument under development for the BepiColombo mission
SIMS	Secondary Ion Mass Spectrometry
SIS	Solar Isotope Spectrometer, onboard the ACEE spacecraft
SMS	Suprathermal Mass Spectrometer on board the Akebono spacecraft also an instrument suite (Solar Wind and Suprathermal Ion Composition) composed of SWICS, MASS and STICS onboard the Wind spacecraft
SSJ/4	Special Sensor J-4, an auroral energy particle instrument on the DMSP spacecraft
STEP	Supra Thermal Energetic Particle telescope, a component of the EPACT instrument suite onboard the Wind spacecraft
STICS	SupraThermal Ion Composition Spectrometer Spectrometer, a component of the SMS suite onboard the NASA Wind spacecraft for solar wind research
STOF	Suprathermal Time-Of-Flight, a component of the CELIAS instrument suite on the SOHO spacecraft
SWE	Solar Wind Experiment, an instrument suite onboard the NASA Wind satellite
SWEA	Solar Wind Electron Analyzer onboard the two spacecraft STEREO mission
SWICS	Solar Wind Ion Composition Spectrometer , a component of the SMS instrument suite onboard the NASA Wind spacecraft for solar wind research also Solar Wind Ion Composition Spectrometer onboard the ESA spacecraft Ulysses exploring the solar poles
SWIMS	Solar Wind Ion Composition/Mass Spectrometer onboard the NASA spacecraft ACE (Advanced Composition Explorer)
SWOOPS	Solar Wind Observations Over the Poles of the Sun, solar wind instrument onboard the Ulysses spacecraft
TED	Total Energy Detector, a component of the SEM on the POES

	spacecraft
TIDE	Thermal Ion Dynamics Experiment on board the NASA Polar spacecraft
TIMAS	Toroidal Imaging Mass-Angle Spectrograph onboard the NASA Polar spacecraft
TNR	Thermal Noise Receiver, a component of the WAVES instrument suite on the Wind satellite
UACS	Upper Atmosphere Composition Spectrometer onboard the Space
URAP	Unified RAdio and Plasma wave, an instrument onboard the Ulysses spacecraft
UVI	Ultra Violet Imager, an instrument onboard the NASA Polar satellite
VEIS	Vector Electron Ion Spectrometer, a component of the SWE instrument suite on the Wind spacecraft
WATS	Wind And Temperature Spectrometer, an instrument onboard the DE low altitude spacecraft
WAVES	An instrument suite for the detection of electromagnetic radiation on the NASA Wind satellite
Wind 3D	A plasma and energetic particle instrument on the Wind spacecraft
WHISPER	Wave of HIgh frequency and Sounder for Probing of Electron, a wave instrument on the Cluster spacecraft

Other Acronyms

ADC	Analog-to-Digital Converter, also A/D
amu	Atomic mass unit
APD	Avalanche Photo Diode
AVF	Azimuthally Varying Field cyclotron design
CASYMIR	Calibration System for the Mass Spectrometer Instrument ROSINA
CASYMS	Calibration System for Mass
CCD	Charge Coupled Device
CDG	Capacitance Diaphragm Gauge, a form of gas pressure gauge
CEM	Continuous Electron Multiplier, Channel Electron Multiplier
CFT	Constant Fraction Trigger
CME	Coronal Mass Ejection
cps	Counts per second
CSDA	Continuous Slowing Down Approximation
DAC	Digital-to-Analog Converter, also D/A
DC	Direct Current
DoD	United States Department of Defense
DVU	Design Verification Unit
ECF	Electron Calibration Facility
EM	ElectroMagnetic
EMC	ElectroMagnetic Contamination
EMI	ElectroMagnetic Interference
EMIC	Electromagnetic Ion Cyclotron waves

ENA	Energetic Neutral Atom
EPROM	Erasable Programmable Read Only Memory
EQM	Engineering Qualification Model
ESA	Electrostatic Analyzer
ESD	Electron Stimulated Desorption, also Electrostatic Discharge
EU	Engineering Unit
EUV	Extreme UltraViolet
eV	Electron Volt
FC	Faraday cup
FEC	Fast Event Count
FOV	Field of View
FPGA	Field-Programmable Gate Array
FS	Flight Spare
FU	Flight Unit
FUV	Far Ultra Violet
FWHM	Full Width Half Maximum
G	Geometric factor
GCU	Gas Calibration Unit
GeV	Giga electron Volt
GF	Geometric factor
GPL	General Public License
GSE	Ground support equipment
GPIB	General Purpose Interface Bus
HV	High Voltage
IDCF	Instrument Development and Calibration Facility
IFC	In Flight Calibration
IPS	Ion Propulsion System
KAFKA	Karbonfolienkollisionsanalysator
keV	kilo electron Volt
Kn	Knudsen number
LED	Light Emitting Diode
LEEIF	Low Electron Energy and Ion Facility
LEF	Linear Electric Field
LP	Langmuir Probe
L/D	Length to Diameter ratio
MALDI	Matrix-Assisted Laser Desorption Ionization
MCA	Multi Channel Analyzer
MCP	Microchannel Plate, Multi-Channel Plate
MDG	Molecular Drag Gauge, a form of gas pressure gauge
MeV	Mega electron Volt
NMI	National Measurement Institute
PCT	Parametric Current Transducer
PEC	Processed Event Count
PHD	Pulse Height Distribution, also Pulse Height Discriminator
PMT	PhotoMultiplier Tube
PSBL	Plasma Sheet Boundary Layer
PSD	Position Sensitive Detector

REF	Radiation Effects Facility
RF	Radio Frequency
RGA	Residue Gas Analyzer
RPA	Retarding Potential Analyzer
SAA	South Atlantic Anomaly
SC, S/C	SpaceCraft
SRG	Spinning Rotor Gauge, a form of gas pressure gauge
SSD	Solid-State Detector
SSL	Surface Science Laboratory detector
SW	Solar Wind
TAC	Time-to-Amplitude Converter
TDC	Time-to-Digital Converter
TOF	Time-Of-Flight
TOF-E	Time-Of-Flight with energy detection in an SSD
UHV	Ultra High Vacuum
UV	UltraViolet
V-A	Voltage-Ampere, also I-V for Current-Voltage
VICKSI	Van de Graaff Isochronous Cyclotron Kombination für Schwere Ionen

Radiation Effects on Electronics

LET	Linear Energy Transfer (in MeV mg^{-1} cm^{-2}): the average energy deposited by incident ions along their track, and a useful parameter to describe heavy ion properties (whereas energy (in MeV) is enough for protons).
MOS	Metal Oxide Semiconductor
RADFET	RADiation sensitive metal oxide Field Effect Transistor
SEB	Single Event Burnout affecting power MOSFETs.
SEDR	Single Event Dielectric Rupture, mainly affecting power MOSFETs and occasionally other devices (e.g. EEPROMs, FPGAs, some analog devices.)
SEFI	Single Event Functional Interrupt, i.e. the device turns to an undefined mode; a power reset is usually necessary to recover.
SEGR	Single Event Gate Rupture, mainly affecting power MOSFETs and occasionally other devices (e.g. EEPROMs, FPGAs, some analog devices.)
SEL	Single Event Latch-up
SET	Single Event Transient, i.e. transient signals mainly generated by analogue devices, that propagate in the circuit if not filtered.
SEU	Single Event Upset (or soft error), i.e. the logic state of a memory cell is changed.
SHE	Single Hard Error (stuck bit) i.e. memory cells stuck in a given logic state.

A.7 Space Physics Basics

A.7.1 Distribution Functions

Gaussian or Normal distribution

$$P(x) = \frac{1}{\sigma\sqrt{2\pi}} \exp\left[-\frac{(x-\mu)^2}{2\sigma^2}\right] \tag{A.34}$$

Maxwell-Boltzmann distribution

$$f(\boldsymbol{r}, \boldsymbol{v}) = n\left(\frac{m}{2\pi kT}\right)^{3/2} \exp\left[-\frac{m(\boldsymbol{v}-\boldsymbol{u})^2}{2kT}\right] \tag{A.35}$$

Bi-Maxwellian distribution

$$f(\boldsymbol{r}, \boldsymbol{v}, t) = \left(\frac{m}{2\pi k}\right)^{3/2} \frac{n}{T_\perp\sqrt{T_\parallel}} \exp\left[-\frac{m(v_\parallel - u_\parallel)^2}{2kT_\parallel}\right] \exp\left[-\frac{m(v_\perp - u_\perp)^2}{kT_\perp}\right] \tag{A.36}$$

Kappa distribution

$$f(\boldsymbol{v}) = \frac{n}{\omega_0^3(\pi\kappa)^{3/2}} \frac{\Gamma(\kappa+1)}{\Gamma(\kappa-\frac{1}{2})} \left[1 + \frac{|\,\boldsymbol{v}-\boldsymbol{u}\,|^2}{\kappa\omega_0^2}\right]^{-(\kappa+1)} \tag{A.37}$$

Power law

$$f(E) = f_0 E^{-\kappa} \tag{A.38}$$

Poisson distribution

$$P(x) = \frac{\mu^x}{x!} \exp[-\mu] \tag{A.39}$$

In the Gaussian and Poisson distribution the parameters μ and σ^2 correspond to the mean and the variance of the distribution. In Equations A.35 to A.38 n is the number density, m is the particle mass, k the Boltzmann constant, T the plasma temperature, u the average plasma flow speed, v the speed of the individual particle, ω_0 the most probable speed, κ the exponent, $\parallel$ the direction parallel to the magnetic field line, and $\perp$ the direction perpendicular to the magnetic field line.

A.7.2 Space Physics Terms

The following Tables A.39 and A.40 list definitions and non-relativistic formulae of commonly used terms in space physics.

Table A.39 illustrates the chain required to go from the number of counts in a single accumulation period, for a detector element in an electrostatic analyzer detector system that was at a fixed analyzer center pass-band energy E_i during that interval, to a numerical value for the velocity distribution at that energy E_i and look direction. It is assumed that the particle flux is constant over the energy range given by ΔE_i. If the particle flux is not constant over ΔE_i, a more complex conversion is required.

Table A.39: Conversion of raw counts to distribution function for one sensor accumulation period.

Uncorrected raw counts per acc. period	$r_{j,i}$	#/acc. time
Corrected counts per accumulation period	$R_{j,i} = r_{j,i}/\epsilon_i$	#/acc. time
Counts per unit time	$C_{j,i} = R_{j,i}/\Delta t$	#/s
Modified number flux	$J^*_{j,i} = C_{j,i}/G_{j,i}$	#/(cm^2 sr s)
Differential-directional number flux	$j_{j,i} = J^*_{j,i}/\Delta E_i$	#/(cm^2 sr s eV)
Directional number flux	$J_{j,i} = J^*_{j,i}/(\Delta E_i/E_i)$	#/(cm^2 sr s)
Distribution function	$f_j = J_{j,i} E_i^{-2} m^2/2$	s^3/(cm^6 sr)

j : spin step
i : energy step
ϵ_i : efficiency at a particular energy
$G_{i,j}$: geometric factor in (cm^2 sr)
E_i : center energy of step i
ΔE_i : energy passband of analyzer at energy E_i
m : ion mass

Table A.40: Space physics terms

Term	Definition	Formula	Unit
Velocity (also called phase space) distribution function	Number of particles N within differential volume $\mathrm{d}^3 r$ having vector velocities within $\mathrm{d}^3 v$ of $\boldsymbol{v}$	$f(\boldsymbol{r}, \boldsymbol{v}) = N/(\mathrm{d}^3 r\, \mathrm{d}^3 v)$	$\mathrm{s}^3\ \mathrm{m}^{-6}$
Number density	Total number of particles N in a volume $\mathrm{d}^3 r$	$n(\boldsymbol{r}) = \iiint f(\boldsymbol{r}, \boldsymbol{v})\, \mathrm{d}^3 v = \iiint f(\boldsymbol{r}, \boldsymbol{v}) v^2\, \mathrm{d}v \sin\theta\, \mathrm{d}\theta\, \mathrm{d}\phi = N/\mathrm{d}^3 r$	m^{-3}
Differential directional number flux	Number of particles N of energy within $\mathrm{d}E$ of E, crossing a unit area per unit time within a differential solid angle, the unit area conventionally oriented normal to the particle velocity vector	$j(E, \Omega) = v^2 m^{-1} f(\boldsymbol{r}, \boldsymbol{v}) = 2Em^{-2} f(\boldsymbol{r}, \boldsymbol{v}) = N(E, \Omega)/(\mathrm{d}A\, \mathrm{d}E\, \mathrm{d}\Omega\, \mathrm{d}t)$	$\mathrm{m}^{-2}\ \mathrm{s}^{-1}\ \mathrm{sr}^{-1}\ \mathrm{J}^{-1}$
Directional number flux	Number of particles N integrated over all energies crossing a unit area per unit time originating from a unit solid angle	$J = \int j(E, \Omega)\, \mathrm{d}E = \mathrm{d}F/\mathrm{d}\Omega = N(\Omega)/(\mathrm{d}A\, \mathrm{d}\Omega\, \mathrm{d}t)$	$\mathrm{m}^{-2}\ \mathrm{s}^{-1}\ \mathrm{sr}^{-1}$
Number flux, sometimes termed number flux density	Number of particles N from all directions crossing a unit area per unit time	$F = \iint j(E, \Omega)\, \mathrm{d}E\, \mathrm{d}\Omega = N/(\mathrm{d}A\, \mathrm{d}t)$	$\mathrm{m}^{-2}\ \mathrm{s}^{-1}$
Fluence	Total number of particles N crossing a unit area integrated over a time interval	$I = \int F\, \mathrm{d}t = N/\mathrm{d}A$	m^{-2}
Omnidirectional number flux	Total number of particles entering the surface of a sphere of unit cross-sectional area	$J_{\mathrm{omni}} = \int F\, \mathrm{d}A_{\mathrm{sphere}}$	s^{-1}

Table A.40: Space physics terms (continued)

Term	Definition	Formula	Unit
Differential directional energy flux	Energy carried by N particles of energy $\mathrm{d}E$ of E, crossing a unit area per unit time within a unit solid angle, the unit area conventionally oriented normal to the particle velocity vector	$EJ = E\,j(E,\Omega) = E\,N(E,\Omega)/(\mathrm{d}A\,\mathrm{d}E\,\mathrm{d}\Omega\,\mathrm{d}t)$	$\mathrm{J\,m^{-2}\,s^{-1}\,sr^{-1}\,J^{-1}}$
Directional energy flux	Energy carried by N particles crossing a unit area per unit time within a unit solid angle	$\mathrm{d}(EF)/\mathrm{d}\Omega = \int E\,j(E,\Omega)\,\mathrm{d}E = E\,N(\Omega)/(\mathrm{d}A\,\mathrm{d}t\,\mathrm{d}\Omega)$	$\mathrm{J\,m^{-2}\,s^{-1}\,sr^{-1}}$
Total energy flux	Total energy carried by N particles crossing a unit area per unit time	$EF = \iint E\,j(E,\Omega)\,\mathrm{d}E\,\mathrm{d}\Omega = E\,N/(\mathrm{d}A\,\mathrm{d}t)$	$\mathrm{J\,m^{-2}\,s^{-1}}$
Geometric factor, GF, for an instrument without energy selectivity	The ratio between a sensor count-rate, assumed 100 % efficient, and an incident directional number flux that is isotropic over the instruments field of view	$GF = \mathrm{countrate}/(\mathrm{d}F\,\mathrm{d}\Omega)$	$\mathrm{m^2\,sr}$
Energy dependent geometric factor for an instrument with energy selectivity	The ratio between a sensor count-rate, assumed 100 % efficient, and an incident differential-directional number flux that is isotropic over the instruments field of view and assumed constant over the energy passband of the instrument	$GF(E) = \mathrm{countrate}/J$	$\mathrm{m^2\,sr\,J}$
Efficiency	The probability that a particle detector will register a count when impacted by an incident particle	Sensor-count-rate/incident-particle-rate	unitless number, 0.0 to 1.0

A.7.3 Moments Calculation

The velocity moments are calculated from the particle counts C_{ijk} at energy step E_i ($i = 1, 2, \ldots, I$), azimuthal sector ϕ_j ($j = 1, 2, \ldots, J$; ϕ also depends on i) and elevation angle θ_k ($k = 1, 2, \ldots, K$):

$$C_{ijk} = C_{ijk}\alpha_k \tag{A.40}$$

where α_k is a correction factor which includes the geometrical factor, the detection efficiency and the energy width.

Number density:

$$n = \sum_{i,j} \frac{1}{v_i} \sum_{k=1}^{K} C_{ijk} \tag{A.41}$$

with $v_i = \sqrt{2E_i/m}$ and m the particle mass.

Bulk velocity:

$$nV_x = \sum_{i,j} \cos\phi_{ij} \sum_{k=1}^{K} C_{ijk} \cos\theta_k \tag{A.42}$$

$$nV_y = \sum_{i,j} \sin\phi_{ij} \sum_{k=1}^{K} C_{ijk} \cos\theta_k \tag{A.43}$$

$$nV_z = \sum_{i,j} \sum_{k=1}^{K} C_{ijk} \sin\theta_k \tag{A.44}$$

Pressure tensor:

$$P_{xx} = \sum_{i,j} v_i \cos^2\phi_{ij} \sum_{k=1}^{K} C_{ijk} \cos^2\theta_k \tag{A.45}$$

$$P_{yy} = \sum_{i,j} v_i \sin^2\phi_{ij} \sum_{k=1}^{K} C_{ijk} \cos^2\theta_k \tag{A.46}$$

$$P_{zz} = \sum_{i,j} v_i \sum_{k=1}^{K} C_{ijk} \sin^2\theta_k \tag{A.47}$$

$$P_{xy} = \sum_{i,j} v_i \cos\phi_{ij} \sin\phi_{ij} \sum_{k=1}^{K} C_{ijk} \cos^2\theta_k \tag{A.48}$$

$$P_{yz} = \sum_{i,j} v_i \sin\phi_{ij} \sum_{k=1}^{K} C_{ijk} \cos\theta_k \sin\theta_k \tag{A.49}$$

$$P_{zx} = \sum_{i,j} v_i \cos\phi_{ij} \sum_{k=1}^{K} C_{ijk} \cos\theta_k \sin\theta_k \tag{A.50}$$

Heat flux tensor:

$$H_{xxx} = \sum_{i,j} v_i^2 \cos^3 \phi_{ij} \sum_{k=1}^{K} C_{ijk} \cos^3 \theta_k \tag{A.51}$$

$$H_{xyy} = \sum_{i,j} v_i^2 \cos \phi_{ij} \sin^2 \phi_{ij} \sum_{k=1}^{K} C_{ijk} \cos^3 \theta_k \tag{A.52}$$

$$H_{xzz} = \sum_{i,j} v_i^2 \cos \phi_{ij} \sum_{k=1}^{K} C_{ijk} \cos \theta_k \sin^2 \theta_k \tag{A.53}$$

$$H_{yyy} = \sum_{i,j} v_i^2 \sin^3 \phi_{ij} \sum_{k=1}^{K} C_{ijk} \cos^3 \theta_k \tag{A.54}$$

$$H_{yxx} = \sum_{i,j} v_i^2 \sin \phi_{ij} \cos^2 \phi_{ij} \sum_{k=1}^{K} C_{ijk} \cos^3 \theta_k \tag{A.55}$$

$$H_{yzz} = \sum_{i,j} v_i^2 \sin \phi_{ij} \sum_{k=1}^{K} C_{ijk} \cos \theta_k \sin^2 \theta_k \tag{A.56}$$

$$H_{zzz} = \sum_{i,j} v_i^2 \sum_{k=1}^{K} C_{ijk} \sin^3 \theta_k \tag{A.57}$$

$$H_{zxx} = \sum_{i,j} v_i^2 \cos^2 \phi_{ij} \sum_{k=1}^{K} C_{ijk} \sin \theta_k \cos^2 \theta_k \tag{A.58}$$

$$H_{zyy} = \sum_{i,j} v_i^2 \sin^2 \phi_{ij} \sum_{k=1}^{K} C_{ijk} \sin \theta_k \cos^2 \theta_k \tag{A.59}$$

$$H_{xyz} = \sum_{i,j} v_i^2 \cos \phi_{ij} \sin \phi_{ij} \sum_{k=1}^{K} C_{ijk} \sin \theta_k \cos^2 \theta_k \tag{A.60}$$

A.7.4 Typical Parameters of Space Plasma

Table A.41 lists typical space plasma parameters in different regions in space.

A.7.5 Comparative Characteristics of Different Mass Spectrometers

Table A.42 briefly summarize advantages and disadvantages of different mass spectrometer designs.

Table A.41: Typical parameters of space plasma

Measure	Radiation belt	Ring current	Plasmasphere	Plasmasheet	Tail lobe	Magnetosheath boundary layer	Solar wind	VLISM
Ion energy	1- 100 MeV	1-200 keV	$<$ 1 eV	5 keV	1-5 keV	1-6 keV	1.1 keV	
Electron energy	50 keV - 10 MeV	$<$ 10 keV	$<$ 1 eV	1 keV	0.2-1 keV	0.1-0.2 keV	13 eV	
Location	$1.2 < L < 2.5$	$3 < L < 6$	$1.2 < L < 5$	30 R_E	30 R_E	30 R_E	1 AU	
Density/Particle flux	$< 10^8$ m^{-2}s^{-1} H^+ (at 50 MeV)	$\lesssim 10^6$ m^{-3}	$> 10^8$ m^{-3}	3×10^5 m^{-3}	$\lesssim 10^4$ m^{-3}	1-20 $\times 10^6$ m^{-3}	10^7 - 10^{10} m^{-3}	$\sim 10^6$-10^7 m^{-3}
Composition	H^+, e^-	H^+, O^+, He^+, e^-	H^+, e^-	H^+, e^-	H^+, e^-	H^+, e^-	$\simeq$ 96 % H^+, (0-20 %) He^{2+}, e^-	H ($\simeq$ 90 %), He ($\simeq$ 10 %)
Magnetic field strength	2-20 μT	0.1-1 μT	0.2-18 μT	2-10 nT	20 nT	25-40 nT	$\sim$1-30 nT	0.1-0.5 nT

VLISM: very local interstellar medium

Table A.42: Comparison of instrument technology

Mass Spectrometer Type	Advantages	Disadvantages
Magnetic - Single focusing mass spectrometer	Low energy simple operation, no RF voltages very good mass resolution with proper ion sources simultaneous collection of two - three mass peaks very high sensitivity	High mass
Magnetic - Double focusing mass spectrograph	excellent mass resolution very high mass rejection ratio simultaneous detection of a wide range of mass peaks	more complex operation High mass
RF		
Quadrupole - linear	Compact instrument good mass range accepts positive or negative ions in same instrument no magnetic field high efficient ion transmission, ion energy independent high pressure tolerant	Complex electronics RF needed (power) but at a fairly low mass resolution
Quadrupole ion trap	very compact very high mass resolution high mass accuracy very high sensitivity large mass range very rapid analysis can be operated at relatively high pressure	low energy ions needed needs RF higher power higher RF drive frequencies
Ion cyclotron resonance	simple construction very compact very high mass resolution very high mass accuracy very high sensitivity large mass range very rapid analysis can be operated at relatively high pressure	low energy ions needed needs magnet (mass) needs RF higher power Fourier Transform variant needs corresponding computing power
TOF	High mass resolution, large mass range light-weight wide acceptance angle very rapid analysis high sensitivity low cost simple design	 Complex electronics needs relatively low operating pressure
Wien filter	simultaneous collection of range of mass peaks No RF voltage	

A.8 SI Units

The following text on the International System of Units (SI units) is taken from the NIST web page `http://physics.nist.gov/cuu/Units/index.html`

A.8.1 SI Base Units

The SI is founded on seven SI base units for seven base quantities assumed to be mutually independent, as given in Table A.43.

Table A.43: SI base units

Base quantity	**Name**	**Symbol**
length	meter	m
mass	kilogram	kg
time	second	s
electric current	ampere	A
thermodynamic temperature	kelvin	K
amount of substance	mole	mol
luminous intensity	candela	cd

A.8.2 SI Derived Units

Other quantities, called derived quantities, are defined in terms of the seven base quantities via a system of quantity equations. The SI derived units for these derived quantities are obtained from these equations and the seven SI base units. Examples of such SI derived units are given in Table A.44, where it should be noted that the symbol 1 for quantities of dimension 1 such as mass fraction is generally omitted. For convenience, 22 SI derived units have been given special names and symbols, as shown in Table A.45.

The derived unit in Table A.45 with the special name degree Celsius and special symbol °C deserves comment. Because of the way temperature scales used to be defined, it remains common practice to express a thermodynamic temperature, symbol T, in terms of its difference from the reference temperature $T_0 = 273.15$ K, the ice point. This temperature difference is called a Celsius temperature, symbol t, and is defined by the quantity equation

$$t = T - T_0$$

The unit of Celsius temperature is the degree Celsius, symbol °C. The numerical value of a Celsius temperature t expressed in degrees Celsius is given by

$$t/^\circ\mathrm{C} = T/\mathrm{K} - 273.15$$

It follows from the definition of t that the degree Celsius is equal in magnitude to the kelvin, which in turn implies that the numerical value of a given temperature difference or temperature interval whose value is expressed in the unit degree Celsius (°C) is equal to the numerical value of the same difference or interval when its value is expressed in

Table A.44: Examples of SI derived units

Derived quantity	**Name**	**Symbol**
area	square meter	m^2
volume	cubic meter	m^3
speed, velocity	meter per second	m/s
acceleration	meter per second squared	m/s^2
wave number	reciprocal meter	m^{-1}
mass density	kilogram per cubic meter	kg/m^3
specific volume	cubic meter per kilogram	m^3/kg
current density	ampere per square meter	A/m^2
magnetic field strength	ampere per meter	A/m
amount-of-substance concentration	mole per cubic meter	mol/m^3
luminance	candela per square meter	cd/m^2
mass fraction	kilogram per kilogram, which may be represented by the number 1	kg/kg = 1

the unit kelvin (K). Thus, temperature differences or temperature intervals may be expressed in either the degree Celsius or the Kelvin using the same numerical value. For example, the Celsius temperature difference t and the thermodynamic temperature difference T between the melting point of gallium and the triple point of water may be written as $\Delta t = 29.7546°\text{C} = \Delta T = 29.7546\ \text{K}$.

The special names and symbols of the 22 SI derived units with special names and symbols given in Table A.45 may themselves be included in the names and symbols of other SI derived units, as shown in Table A.46.

Table A.45: SI derived units with special names and symbols

Derived quantity	**Name**	**Symbol**	**Expression in terms of other SI units**	**Expression in terms of SI base units**
plane angle	radian[a]	rad	-	$\mathrm{m\,m^{-1}} = 1^b$
solid angle	steradian[a]	sr[c]	-	$\mathrm{m^2\,m^{-2}} = 1^b$
frequency	hertz	Hz	-	$\mathrm{s^{-1}}$
force	newton	N	-	$\mathrm{m\,kg\,s^{-2}}$
pressure, stress	pascal	Pa	$\mathrm{N/m^2}$	$\mathrm{m^{-1}\,kg\,s^{-2}}$
energy, work, quantity of heat	joule	J	N m	$\mathrm{m^2\,kg\,s^{-2}}$
power, radiant flux	watt	W	J/s	$\mathrm{m^2\,kg\,s^{-3}}$
electric charge, quantity of electricity	coulomb	C	-	s A
electric potential difference, electromotive force	volt	V	W/A	$\mathrm{m^2\,kg{,}s^{-3}{,}A^{-1}}$
capacitance	farad	F	C/V	$\mathrm{m^{-2}\,kg^{-1}\,s^4\,A^2}$
electric resistance	ohm	Ω	V/A	$\mathrm{m^2\,kg\,s^{-3}\,A^{-2}}$
electric conductance	siemens	S	A/V	$\mathrm{m^{-2}\,kg^{-1}\,s^3\,A^2}$
magnetic flux	weber	Wb	V s	$\mathrm{m^2\,kg\,s^{-2}\,A^{-1}}$
magnetic flux density	tesla	T	Wb/m2	$\mathrm{kg\,s^{-2}}\,A^{-1}$
inductance	henry	H	Wb/A	$\mathrm{m^2\,kg\,s^{-2}\,A^{-2}}$
Celsius temperature	degree Celsius	°C	-	K
luminous flux	lumen	lm	cd sr[c]	$\mathrm{m^2\,m^{-2}\,cd} = \mathrm{cd}$
illuminance	lux	lx	$\mathrm{lm/m^2}$	$\mathrm{m^2\,m^{-4}\,cd} = \mathrm{m^{-2}\,cd}$
activity (of a radionuclide)	becquerel	Bq	-	$\mathrm{s^{-1}}$
absorbed dose, specific energy (imparted), kerma	gray	Gy	J/kg	$\mathrm{m^2\,s^{-2}}$
dose equivalent[d]	sievert	Sv	J/kg	$\mathrm{m^2\,s^{-2}}$
catalytic activity	katal	kat		$\mathrm{s^{-1}\,mol}$

[a] The radian and steradian may be used advantageously in expressions for derived units to distinguish between quantities of a different nature but of the same dimension; some examples are given in Table A.46.

[b] In practice, the symbols rad and sr are used where appropriate, but the derived unit "1" is generally omitted.

[c] In photometry, the unit name steradian and the unit symbol sr are usually retained in expressions for derived units.

[d] Other quantities expressed in sievert are ambient dose equivalent, directional dose equivalent, personal dose equivalent, and organ equivalent dose.

Table A.46: Examples of SI derived units whose names and symbols include SI derived units with special names and symbols

Derived quantity	**Name**	**Symbol**
dynamic viscosity	pascal second	Pa s
moment of force	newton meter	N m
surface tension	newton per meter	N/m
angular velocity	radian per second	rad/s
angular acceleration	radian per second squared	rad/s^2
heat flux density, irradiance	watt per square meter	W/m^2
heat capacity, entropy	joule per kelvin	J/K
specific heat capacity, specific entropy	joule per kilogram kelvin	J/(kg K)
specific energy	joule per kilogram	J/kg
thermal conductivity	watt per meter kelvin	W/(m K)
energy density	joule per cubic meter	J/m^3
electric field strength	volt per meter	V/m
electric charge density	coulomb per cubic meter	C/m^3
electric flux density	coulomb per square meter	C/m^2
permittivity	farad per meter	F/m
permeability	henry per meter	H/m
molar energy	joule per mole	J/mol
molar entropy, molar heat capacity	joule per mole kelvin	J/(mol K)
exposure (X- and γ-rays)	coulomb per kilogram	C/kg
absorbed dose rate	gray per second	Gy/s
radiant intensity	watt per steradian	W/sr
radiance	watt per square meter steradian	W/(m^{2}sr)
catalytic (activity) concentration	katal per cubic meter	kat/m^3

A.8.3 SI Prefixes

Table A.47: SI prefixes

Factor	Name	Symbol	Factor	Name	Symbol
10^{1}	deka	da	10^{-1}	deci	d
10^{2}	hecto	h	10^{-2}	centi	c
10^{3}	kilo	k	10^{-3}	milli	m
10^{6}	mega	M	10^{-6}	micro	μ
10^{9}	giga	G	10^{-9}	nano	n
10^{12}	tera	T	10^{-12}	pico	p
10^{15}	peta	P	10^{-15}	femto	f
10^{18}	exa	E	10^{-18}	atto	a
10^{21}	zetta	Z	10^{-21}	zepto	z
10^{24}	yotta	Y	10^{-24}	yocto	y

It is important to note that the kilogram is the only SI unit with a prefix as part of its name and symbol. Because multiple prefixes may not be used, in the case of the kilogram the prefix names of Table A.47 are used with the unit name "gram" and the prefix symbols are used with the unit symbol "g." With this exception, any SI prefix may be used with any SI unit, including the degree Celsius and its symbol °C.

Example 1: 10^{-6} kg = 1 mg (one milligram), but not 10^{-6} kg = 1 μkg (one microkilogram).

Example 2: Consider the earlier example of the height of the Washington Monument. We may write $h_W = 169000$ mm = 16 900 cm = 169 m = 0.169 km using the millimeter (SI prefix milli, symbol m), centimeter (SI prefix centi, symbol c), or kilometer (SI prefix kilo, symbol k).

Because the SI prefixes strictly represent powers of 10, they should not be used to represent powers of 2. Thus, one kilobit, or 1 kbit, is 1000 bit and not 2^{10} bit = 1024 bit. To alleviate this ambiguity, prefixes for binary multiples have been adopted by the International Electrotechnical Commission (IEC) for use in information technology.

A.8.4 Units Outside the SI

Certain units are not part of the International System of Units, that is, they are outside the SI, but are important and widely used. Consistent with the recommendations of the International Committee for Weights and Measures (CIPM, Comité International des Poids et Mesures), the units in this category that are accepted for use with the SI are given in Table A.48.

The liter in Table A.48 deserves comment. This unit and its symbol l were adopted by the CIPM in 1879. The alternative symbol for the liter, L, was adopted by the CGPM in 1979 in order to avoid the risk of confusion between the letter l and the number 1. Thus, although both l and L are internationally accepted symbols for the liter, to avoid this risk the preferred symbol for use in the United States is L. Neither a lowercase script letter ℓ nor an uppercase script letter $\mathcal{L}$ are approved symbols for the liter.

Table A.48: Units outside the SI that are accepted for use with the SI

Name	Symbol	Value in SI units
minute (time)	min	1 min = 60 s
hour	h	1 h = 60 min = 3600 s
day	d	1 d = 24 h = 86400 s
degree (angle)	°	$1° = (\pi\ /180)$ rad
minute (angle)	′	$1' = (1/60)° = (\pi/10\ 800)$ rad
second (angle)	″	$1'' = (1/60)' = (\pi/648\ 000)$ rad
liter	L	1 L = 1 $dm^3 = 10^{-3}$ m^3
metric ton [a]	t	1 t = 10^3 kg
neper [b]	Np	1 Np = 1
bel [c]	B	1 B= $(1/2)$ ln 10 Np
electronvolt [d]	eV	1 eV= 1.60218×10^{-19} J, approx.
unified atomic mass unit [e]	u	1 u= 1.66054×10^{-27} kg, approx.
astronomical unit [f]	ua	1 ua= 1.49598×10^{11} m, approx.

[a] In many countries, this unit is called "tonne"

[b] Although the neper is coherent with SI units and is accepted by the CIPM, it has not been adopted by the General Conference on Weights and Measures (CGPM, Conférence Générale des Poids et Mesures) and is thus not an SI unit.

[c] The bel is most commonly used with the SI prefix deci: 1 dB = 0.1 B.

[d] The electronvolt is the kinetic energy acquired by an electron passing through a potential difference of 1 V in vacuum. The value must be obtained by experiment, and is therefore not known exactly.

[e] The unified atomic mass unit is equal to 1/12 of the mass of an unbound atom of the nuclide ^{12}C, at rest and in its ground state. The value must be obtained by experiment, and is therefore not known exactly.

[f] The astronomical unit is a unit of length. Its value is such that, when used to describe the motion of bodies in the solar system, the heliocentric gravitation constant is $(0.01720209895)^2$ ua^3d^{-2}. The value must be obtained by experiment, and is therefore not known exactly.

Other units outside the SI that are currently accepted for use with the SI by NIST are given in Table A.49. These units, which are subject to future review, should be defined in relation to the SI in every document in which they are used; their continued use is not encouraged. The CIPM currently accepts the use of all of the units given in Table A.49 with the SI except for the curie, roentgen, rad, and rem. Because of the continued wide use of these units in the United States, NIST still accepts their use with the SI.

Table A.49: Other units outside the SI that are currently accepted for use with the SI, subject to further review.

Name	Symbol	Value in SI units
nautical mile		1 nautical mile = 1852 m
knot		1 nautical mile per hour = (1852/3600) m/s
are	a	1 a = 1 dam^2 = 10^2 m^2
hectare	ha	1 ha = 1 hm^2 = 10^4 m^2
bar	bar	1 bar = 0.1 MPa = 100 kPa = 1000 hPa = 10^5 Pa
Ångstrøm	Å	1 Å = 0.1 nm = 10^{-10} m
barn	b	1 b = 100 fm^2 = 10^{-28} m^2
curie	Ci	1 Ci = 3.7 x 10^{10} Bq
roentgen	R	1 R = 2.58 x 10^{-4} C/kg
rad	rad	1 rad = 1 cGy = 10^{-2} Gy
rem	rem	1 rem = 1 cSv = 10^{-2} Sv

A.9 Constants

Table A.50: Fundamental Constants. The number in parenthesis is the one-standard-deviation uncertainty in the last two digits of the given value (2006 CODATA recommended values).

Atomic mass unit	u	=	$1.660538728(83) \times 10^{-27}$ kg
Avogadro constant	N_A	=	$6.02214179(30) \times 10^{23}$ mol^{-1}
Boltzmann constant	k	=	$1.3806504(24) \times 10^{-23}$ J K^{-1}
Elementary charge	e	=	$1.602176487(40) \times 10^{-19}$ C
Mass ratio proton/electron	m_p/m_e	=	1836.15267247(80)
Permeability of vacuum	μ_0	=	$4\pi\ 10^{-7}$ N A^{-2}
		=	$12.566370614\ldots \times 10^{-7}$ N A^{-2}
Permittivity of vacuum	ϵ_0	=	$1/\mu_0 c^2 = 8.854187817\ldots \times 10^{-12}$ F m^{-1}
Planck constant	$\hbar$	=	$6.62606896(33) \times 10^{-34}$ Js
Rest mass electron	m_e	=	$9.10938215(45) \times 10^{-31}$ kg
Rest mass proton	m_p	=	$1.672621637(83) \times 10^{-27}$ kg
Rest mass neutron	m_n	=	$1.674927211(84) \times 10^{-27}$ kg
Rest mass hydrogen atom	m_H	=	1.00794(7) u
Rest mass helium atom	m_{He}	=	4.002602(2) u
Rest mass alpha particle	m_α	=	$6.64465620(33) \times 10^{-27}$ kg
Rest energy electron	$m_e c^2$	=	$8.18710438(41) \times 10^{-14}$ J
Rest energy proton	$m_p c^2$	=	$1.503277359(75) \times 10^{-10}$ J
Speed of light	c	=	2.99792458×10^8 m/s
Universal gas constant	R	=	kN_A = 8.314472(15) J $K^{-1}mol^{-1}$

A.10 Units and Unit Conversion

Table A.51: Conversion of energy units

	u	kg	MeV	K	J
1 u	1	1.6606×10^{-27}	9.3150×10^{2}	1.0810×10^{13}	1.4924×10^{-10}
1 kg	6.0220×10^{26}	1	5.6095×10^{29}	6.5096×10^{39}	8.9876×10^{16}
1 MeV	1.0735×10^{-3}	1.7827×10^{-30}	1	1.1605×10^{10}	1.6022×10^{-13}
1 K	9.2507×10^{-14}	1.5362×10^{-40}	8.6173×10^{-11}	1	1.3807×10^{-23}
1 J	6.7004×10^{9}	1.1126×10^{-17}	6.2415×10^{12}	7.2429×10^{22}	1

Different vacuum pressure units are used throughout the world. In the United States the non SI unit Torr is still commonly used to measure vacuum pressure, even in scientific circles. Europe uses the SI acceptable unit mbar, while in Japan pressure must be measured in pascal. In order to facilitate the convergence to SI units, the following table on pressure units conversion is given.

Table A.52: Conversion of pressure units

1 ↓ = ... →	mbar	Pa (N/m^2)	dyn cm^{-2} (μbar)	atm (phys.)	Torr (mm Hg)	inch Hg	Micron (μ)	cm H_2O	kp cm^{-2} (at tech.)	lb in^{-2} (psi)	lb ft^{-2}
mbar	1	10^2	10^3	9.87×10^{-4}	0.75	2.953×10^{-2}	7.5×10^2	1.02	1.02×10^{-3}	1.45×10^{-2}	2.089
Pa	10^{-2}	1	10	9.87×10^{-6}	7.5×10^{-3}	2.953×10^{-4}	7.5	1.02×10^{-2}	1.02×10^{-5}	1.45×10^{-4}	2.089×10^{-2}
μbar	10^{-3}	0.1	1	9.87×10^{-7}	7.510^{-4}	2.953×10^{-5}	7.5×10^{-1}	1.02×10^{-3}	1.02×10^{-6}	1.45×10^{-5}	2.089×10^{-3}
atm	1013	1.01×10^5	1.01×10^6	1	760	29.92	7.6×10^5	1.03×10^3	1.033	14.697	2116.4
Torr	1.33	1.33×10^2	1.33×10^3	1.316×10^{-3}	1	3.937×10^{-2}	10^3	1.3595	1.36×10^{-3}	1.934×10^{-2}	2.7847
in Hg	33.86	33.9×10^2	33.9×10^3	3.342×10^{-2}	25.4	1	2.54×10^4	34.53	3.453×10^{-2}	0.48115	70.731
μ	1.33×10^{-3}	1.33×10^{-1}	1.333	1.316×10^{-6}	10^{-3}	3.937×10^{-5}	1	1.36×10^{-3}	1.36×10^{-6}	1.934×10^{-5}	2.785×10^{-3}
cm H_2O	0.9807	98.07	980.7	9.678×10^{-4}	0.7356	2.896×10^{-2}	7.36×10^2	1	10^{-3}	1.422×10^{-2}	2.0483
at	9.81×10^2	9.81×10^4	9.81×10^5	0.968	7.36×10^2	28.96	7.36×10^5	103	1	14.22	2048.3
psi	68.95	68.95×10^2	68.95×10^3	6.804×10^{-2}	51.71	2.036	51.71×10^3	70.31	7.03×10^{-2}	1	1.44×10^2
lb ft^{-2}	0.4788	47.88	478.8	4.725×10^{-4}	0. 3591	1.414×10^{-2}	359.1	0.488	4.88×10^{-4}	6.94×10^{-3}	1

Normal conditions: 0 °C and sea level, i.e. $p = 1013$ mbar = 760 mm Hg = 760 torr = 1 atm

in Hg = inches of mercury; 1 mtorr (millitorr) = 10^{-3} torr = 1 μ (micron) = 1 μm Hg column

Pound-force per square inch = lbf in^{-2} = lbf / sqin = psi (psig = psi gauge = pressure above atmospheric pressure, pressure gauge reading; psia = psi absolute = absolute pressure)

Pound-force per square foot = lbf / sqft = lbf / ft^2; kgf/sqcm^2 = kg force per square cm = kp / cm^2 = at

1 dyn cm^{-2} (cgs) = 1 μbar (microbar) = 1 barye; 1 bar = 0.1 Mpa; 1 cm water column (cm water column = g / cm^2 at 4 °C) = 1 Ger (Geryk)

atm = physical atmosphere; at = technical atmosphere; 100 - (× mbar / 10.13) = y % vacuum

A.11 Relative Isotopic Standard

Table A.53: Atomic weights and isotopic compositions for all elements. The uncertainties are listed in parenthesis. Brackets [ ] indicate the mass number of the most stable isotope.

Z		*A*	Rel. Atomic Mass	Isotopic Composition	Standard Atomic Weight	Notes
1	H	1	1.0078250321(4)	99.9885(70)	1.00794(7)	g,m,r,c,w
	D	2	2.0141017780(4)	0.0115(70)		
	T	3	3.0160492675(11)			
2	He	3	3.0160293097(9)	0.000137(3)	4.002602(2)7	g,r,a
		4	4.0026032497(10)	99.999863(3)		
3	Li	6	6.0151223(5)	7.59(4)	6.941(2)	g,m,r,b,d
		7	7.0160040(5)	92.41(4)		
4	Be	9	9.0121821(4)	100	9.012182(3)	
5	B	10	10.0129370(4)	19.9(7)	10.811(7)	g,m,r
		11	11.0093055(5)	80.1(7)		
6	C	12	12.0000000(0)	98.93(8)	12.0107(8)	g,r
		13	13.0033548378(10)	1.07(8)		
		14	14.003241988(4)			
7	N	14	14.0030740052(9)	99.632(7)	14.0067(2)	g,r,e
		15	15.0001088984(9)	0.368(7)		
8	O	16	15.9949146221(15)	99.757(16)	15.9994(3)	g,r
		17	16.99913150(22)	0.038(1)		
		18	17.9991604(9)	0.205(14)		
9	F	19	18.99840320(7)	100	18.9984032(5)	
10	Ne	20	19.9924401759(20)	90.48(3)	20.1797(6)	g,m,r,a
		21	20.99384674(4)	0.27(1)		
		22	21.99138551(23)	9.25(3)		
11	Na	23	22.98976967(23)	100	22.989770(2)	
12	Mg	24	23.98504190(20)	78.99(4)	24.3050(6)	
		25	24.98583702(20)	10.00(1)		
		26	25.98259304(21)	11.01(3)		
13	Al	27	26.98153844(14)	100	26.981538(2)	
14	Si	28	27.9769265327(20)	92.2297(7)	28.0855(3)	r
		29	28.97649472(3)	4.6832(5)		
		30	29.97377022(5)	3.0872(5)		
15	P	31	30.97376151(20)	100	30.973761(2)	
16	S	32	31.97207069(12)	94.93(31)	32.065(5)	g,r
		33	32.97145850(12)	0.76(2)		
		34	33.96786683(11)	4.29(28)		
		36	35.96708088(25)	0.02(1)		
17	Cl	35	34.96885271(4)	75.78(4)	35.453(2)	m
		37	36.96590260(5)	24.22(4)		
18	Ar	36	35.96754628(27)	0.3365(30)	39.948(1)	g,r,a
		38	37.9627322(5)	0.0632(5)		

Z		*A*	Rel. Atomic Mass	Isotopic Composition	Standard Atomic Weight	Notes
		40	39.962383123(3)	99.6003(30)		
19	K	39	38.9637069(3)	93.2581(44)	39.0983(1)	
		40	39.96399867(29)	0.0117(1)		
		41	40.96182597(28)	6.7302(44)		
20	Ca	40	39.9625912(3)	96.941(156)	40.078(4)	g,r,f
		42	41.9586183(4)	0.647(23)		
		43	42.9587668(5)	0.135(10)		
		44	43.9554811(9)	2.086(110)		
		46	45.9536928(25)	0.004(3)		
		48	47.952534(4)	0.187(21)		
21	Sc	45	44.9559102(12)	100	44.955910(8)	
22	Ti	46	45.9526295(12)	8.25(3)	47.867(1)	
		47	46.9517638(10)	7.44(2)		
		48	47.9479471(10)	73.72(3)		
		49	48.9478708(10)	5.41(2)		
		50	49.9447921(11)	5.18(2)		
23	V	50	49.9471628(14)	0.250(4)	50.9415(1)	
		51	50.9439637(14)	99.750(4)		
24	Cr	50	49.9460496(14)	4.345(13)	51.9961(6)	
		52	51.9405119(15)	83.789(18)		
		53	52.9406538(15)	9.501(17)		
		54	53.9388849(15)	2.365(7)		
25	Mn	55	54.9380496(14)	100	54.938049(9)	
26	Fe	54	53.9396148(14)	5.845(35)	55.845(2)	
		56	55.9349421(15)	91.754(36)		
		57	56.9353987(15)	2.119(10)		
		58	57.9332805(15)	0.282(4)		
27	Co	59	58.9332002(15)	100	58.933200(9)	
28	Ni	58	57.9353479(15)	68.0769(89)	58.6934(2)	
		60	59.9307906(15)	26.2231(77)		
		61	60.9310604(15)	1.1399(6)		
		62	61.9283488(15)	3.6345(17)		
		64	63.9279696(16)	0.9256(9)		
29	Cu	63	62.9296011(15)	69.17(3)	63.546(3)	r
		65	64.9277937(19)	30.83(3)		
30	Zn	64	63.9291466(18)	48.63(60)	65.409(4)	
		66	65.9260368(16)	27.90(27)		
		67	66.9271309(17)	4.10(13)		
		68	67.9248476(17)	18.75(51)		
		70	69.925325(4)	0.62(3)		
31	Ga	69	68.925581(3)	60.108(9)	69.723(1)	m
		71	70.9247050(19)	39.892(9)		
32	Ge	70	69.9242504(19)	20.84(87)	72.64(1)	h
		72	71.9220762(16)	27.54(34)		

Z		*A*	Rel. Atomic Mass	Isotopic Composition	Standard Atomic Weight	Notes
		73	72.9234594(16)	7.73(5)		
		74	73.9211782(16)	36.28(73)		
		76	75.9214027(16)	7.61(38)		
33	As	75	74.9215964(18)	100	74.92160(2)	
34	Se	74	73.9224766(16)	0.89(4)	78.96(3)	r
		76	75.9192141(16)	9.37(29)		
		77	76.9199146(16)	7.63(16)		
		78	77.9173095(16)	23.77(28)		
		80	79.9165218(20)	49.61(41)		
		82	81.9167000(22)	8.73(22)		
35	Br	79	78.9183376(20)	50.69(7)	79.904(1)	
		81	80.916291(3)	49.31(7)		
36	Kr	78	77.920386(7)	0.35(1)	83.798(2)	g,m,a
		80	79.916378(4)	2.28(6)		
		82	81.9134846(28)	11.58(14)		
		83	82.914136(3)	11.49(6)		
		84	83.911507(3)	57.00(4)		
		86	85.9106103(12)	17.30(22)		
37	Rb	85	84.9117893(25)	72.17(2)	85.4678(3)	g
		87	86.9091835(27)	27.83(2)		
38	Sr	84	83.913425(4)	0.56(1)	87.62(1)	g,r,f
		86	85.9092624(24)	9.86(1)		
		87	86.9088793(24)	7.00(1)		
		88	87.9056143(24)	82.58(1)		
39	Y	89	88.9058479(25)	100	88.90585(2)	
40	Zr	90	89.9047037(23)	51.45(40)	91.224(2)	g
		91	90.9056450(23)	11.22(5)		
		92	91.9050401(23)	17.15(8)		
		94	93.9063158(25)	17.38(28)		
		96	95.908276(3)	2.80(9)		
41	Nb	93	92.9063775(24)	100	92.90638(2)	
42	Mo	92	91.906810(4)	14.84(35)	95.94(2)	g
		94	93.9050876(20)	9.25(12)		
		95	94.9058415(20)	15.92(13)		
		96	95.9046789(20)	16.68(2)		
		97	96.9060210(20)	9.55(8)		
		98	97.9054078(20)	24.13(31)		
		100	99.907477(6)	9.63(23)		
43	Tc	97	96.906365(5)		[98]	
		98	97.907216(4)			
		99	98.9062546(21)			
44	Ru	96	95.907598(8)	5.54(14)	101.07(2)	g
		98	97.905287(7)	1.87(3)		
		99	98.9059393(21)	12.76(14)		

Z		*A*	Rel. Atomic Mass	Isotopic Composition	Standard Atomic Weight	Notes
		100	99.9042197(22)	12.60(7)		
		101	100.9055822(22)	17.06(2)		
		102	101.9043495(22)	31.55(14)		
		104	103.905430(4)	18.62(27)		
45	Rh	103	102.905504(3)	100	102.90550(2)	
46	Pd	102	101.905608(3)	1.02(1)	106.42(1)	g,r
		104	103.904035(5)	11.14(8)		
		105	104.905084(5)	22.33(8)		
		106	105.903483(5)	27.33(3)		
		108	107.903894(4)	26.46(9)		
		110	109.905152(12)	11.72(9)		
47	Ag	107	106.905093(6)	51.839(8)	107.8682(2)	g
		109	108.904756(3)	48.161(8)		
48	Cd	106	105.906458(6)	1.25(6)	112.411(8)	g
		108	107.904183(6)	0.89(3)		
		110	109.903006(3)	12.49(18)		
		111	110.904182(3)	12.80(12)		
		112	111.9027572(30)	24.13(21)		
		113	112.9044009(30)	12.22(12)		
		114	113.9033581(30)	28.73(42)		
		116	115.904755(3)	7.49(18)		
49	In	113	112.904061(4)	4.29(5)	114.818(3)	
		115	114.903878(5)	95.71(5)		
50	Sn	112	111.904821(5)	0.97(1)	118.710(7)	g
		114	113.902782(3)	0.66(1)		
		115	114.903346(3)	0.34(1)		
		116	115.901744(3)	14.54(9)		
		117	116.902954(3)	7.68(7)		
		118	117.901606(3)	24.22(9)		
		119	118.903309(3)	8.59(4)		
		120	119.9021966(27)	32.58(9)		
		122	121.9034401(29)	4.63(3)		
		124	123.9052746(15)	5.79(5)		
51	Sb	121	120.9038180(24)	57.21(5)	121.760(1)	g
		123	122.9042157(22)	42.79(5)		
52	Te	120	119.904020(11)	0.09(1)	127.60(3)	g,h
		122	121.9030471(20)	2.55(12)		
		123	122.9042730(19)	0.89(3)		
		124	123.9028195(16)	4.74(14)		
		125	124.9044247(20)	7.07(15)		
		126	125.9033055(20)	18.84(25)		
		128	127.9044614(19)	31.74(8)		
		130	129.9062228(21)	34.08(62)		
53	I	127	126.904468(4)	100	126.90447(3)	

Z		*A*	Rel. Atomic Mass	Isotopic Composition	Standard Atomic Weight	Notes
54	Xe	124	123.9058958(21)	0.09(1)	131.293(6)	g,m
		126	125.904269(7)	0.09(1)		
		128	127.9035304(15)	1.92(3)		
		129	128.9047795(9)	26.44(24)		
		130	129.9035079(10)	4.08(2)		
		131	130.9050819(10)	21.18(3)		
		132	131.9041545(12)	26.89(6)		
		134	133.9053945(9)	10.44(10)		
		136	135.907220(8)	8.87(16)		
55	Cs	133	132.905447(3)	100	132.90545(2)	
56	Ba	130	129.906310(7)	0.106(1)	137.327(7)	
		132	131.905056(3)	0.101(1)		
		134	133.904503(3)	2.417(18)		
		135	134.905683(3)	6.592(12)		
		136	135.904570(3)	7.854(24)		
		137	136.905821(3)	11.232(24)		
		138	137.905241(3)	71.698(42)		
57	La	138	137.907107(4)	0.090(1)	138.9055(2)	g
		139	138.906348(3)	99.910(1)		
58	Ce	136	135.907140(50)	0.185(2)	140.116(1)	g,f
		138	137.905986(11)	0.251(2)		
		140	139.905434(3)	88.450(51)		
		142	141.909240(4)	11.114(51)		
59	Pr	141	140.907648(3)	100	140.90765(2)	
60	Nd	142	141.907719(3)	27.2(5)	144.24(3)	g,f
		143	142.909810(3)	12.2(2)		
		144	143.910083(3)	23.8(3)		
		145	144.912569(3)	8.3(1)		
		146	145.913112(3)	17.2(3)		
		148	147.916889(3)	5.7(1)		
		150	149.920887(4)	5.6(2)		
61	Pm	145	144.912744(4)		[145]	
		147	146.915134(3)			
62	Sm	144	143.911995(4)	3.07(7)	150.36(3)	g
		147	146.914893(3)	14.99(18)		
		148	147.914818(3)	11.24(10)		
		149	148.917180(3)	13.82(7)		
		150	149.917271(3)	7.38(1)		
		152	151.919728(3)	26.75(16)		
		154	153.922205(3)	22.75(29)		
63	Eu	151	150.919846(3)	47.81(3)	151.964(1)	g
		153	152.921226(3)	52.19(3)		
64	Gd	152	151.919788(3)	0.20(1)	157.25(3)	g
		154	153.920862(3)	2.18(3)		

Z		*A*	Rel. Atomic Mass	Isotopic Composition	Standard Atomic Weight	Notes
		155	154.922619(3)	14.80(12)		
		156	155.922120(3)	20.47(9)		
		157	156.923957(3)	15.65(2)		
		158	157.924101(3)	24.84(7)		
		160	159.927051(3)	21.86(19)		
65	Tb	159	158.925343(3)	100	158.92534(2)	
66	Dy	156	155.924278(7)	0.06(1)	162.500(1)	g
		158	157.924405(4)	0.10(1)		
		160	159.925194(3)	2.34(8)		
		161	160.926930(3)	18.91(24)		
		162	161.926795(3)	25.51(26)		
		163	162.928728(3)	24.90(16)		
		164	163.929171(3)	28.18(37)		
67	Ho	165	164.930319(3)	100	164.93032(2)	
68	Er	162	161.928775(4)	0.14(1)	167.259(3)	g
		164	163.929197(4)	1.61(3)		
		166	165.930290(3)	33.61(35)		
		167	166.932045(3)	22.93(17)		
		168	167.932368(3)	26.78(26)		
		170	169.935460(3)	14.93(27)		
69	Tm	169	168.934211(3)	100	168.93421(2)	
70	Yb	168	167.933894(5)	0.13(1)	173.04(3)	g
		170	169.934759(3)	3.04(15)		
		171	170.936322(3)	14.28(57)		
		172	171.9363777(30)	21.83(67)		
		173	172.9382068(30)	16.13(27)		
		174	173.9388581(30)	31.83(92)		
		176	175.942568(3)	12.76(41)		
71	Lu	175	174.9407679(28)	97.41(2)	174.967(1)	g
		176	175.9426824(28)	2.59(2)		
72	Hf	174	173.940040(3)	0.16(1)	178.49(2)	f
		176	175.9414018(29)	5.26(7)		
		177	176.9432200(27)	18.60(9)		
		178	177.9436977(27)	27.28(7)		
		179	178.9458151(27)	13.62(2)		
		180	179.9465488(27)	35.08(16)		
73	Ta	180	179.947466(3)	0.012(2)	180.9479(1)	
		181	180.947996(3)	99.988(2)		
74	W	180	179.946706(5)	0.12(1)	183.84(1)	
		182	181.948206(3)	26.50(16)		
		183	182.9502245(29)	14.31(4)		
		184	183.9509326(29)	30.64(2)		
		186	185.954362(3)	28.43(19)		
75	Re	185	184.9529557(30)	37.40(2)	186.207(1)	

Z		*A*	Rel. Atomic Mass	Isotopic Composition	Standard Atomic Weight	Notes
		187	186.9557508(30)	62.60(2)		
76	Os	184	183.952491(3)	0.02(1)	190.23(3)	g,r,f
		186	185.953838(3)	1.59(3)		
		187	186.9557479(30)	1.96(2)		
		188	187.9558360(30)	13.24(8)		
		189	188.9581449(30)	16.15(5)		
		190	189.958445(3)	26.26(2)		
		192	191.961479(4)	40.78(19)		
77	Ir	191	190.960591(3)	37.3(2)	192.217(3)	
		193	192.962924(3)	62.7(2)		
78	Pt	190	189.959930(7)	0.014(1)	195.078(2)	
		192	191.961035(4)	0.782(7)		
		194	193.962664(3)	32.967(99)		
		195	194.964774(3)	33.832(10)		
		196	195.964935(3)	25.242(41)		
		198	197.967876(4)	7.163(55)		
79	Au	197	196.966552(3)	100	196.96655(2)	
80	Hg	196	195.965815(4)	0.15(1)	200.59(2)	
		198	197.966752(3)	9.97(20)		
		199	198.968262(3)	16.87(22)		
		200	199.968309(3)	23.10(19)		
		201	200.970285(3)	13.18(9)		
		202	201.970626(3)	29.86(26)		
		204	203.973476(3)	6.87(15)		
81	Tl	203	202.972329(3)	29.524(14)	204.3833(2)	
		205	204.974412(3)	70.476(14)		
82	Pb	204	203.973029(3)	1.4(1)	207.2(1)	g,r,f
		206	205.974449(3)	24.1(1)		
		207	206.975881(3)	22.1(1)		
		208	207.976636(3)	52.4(1)		
83	Bi	209	208.980383(3)	100	208.98038(2)	
84	Po	209	208.982416(3)		[209]	
		210	209.982857(3)			
85	At	210	209.987131(9)		[210]	
		211	210.987481(4)			
86	Rn	211	210.990585(8)		[222]	
		220	220.0113841(29)			
		222	222.0175705(27)			
87	Fr	223	223.0197307(29)		[223]	
88	Ra	223	223.018497(3)		[226]	
		224	224.0202020(29)			
		226	226.0254026(27)			
		228	228.0310641(27)			
89	Ac	227	227.0277470(29)		[227]	

Z		*A*	Rel. Atomic Mass	Isotopic Composition	Standard Atomic Weight	Notes
90	Th	230	230.0331266(22)		232.0381(1)	g
		232	232.0380504(22)	100		
91	Pa	231	231.0358789(28)	100	231.03588(2)	
92	U	233	233.039628(3)		238.02891(3)	g,m,r,d,f
		234	234.0409456(21)	0.0055(2)		
		235	235.0439231(21)	0.7200(51)		
		236	236.0455619(21)			
		238	238.0507826(21)	99.2745(106)		
93	Np	237	237.0481673(21)		[237]	
		239	239.0529314(23)			
94	Pu	238	238.0495534(21)		[244]	
		239	239.0521565(21)			
		240	240.0538075(21)			
		241	241.0568453(21)			
		242	242.0587368(21)			
		244	244.064198(5)			
95	Am	241	241.0568229(21)		[243]	
		243	243.0613727(23)			
96	Cm	243	243.0613822(24)		[247]	
		244	244.0627463(21)			
		245	245.0654856(29)			
		246	246.0672176(24)			
		247	247.070347(5)			
		248	248.072342(5)			
97	Bk	247	247.070299(6)		[247]	
		249	249.074980(3)			
98	Cf	249	249.074847(3)		[251]	
		250	250.0764000(24)			
		251	251.079580(5)			
		252	252.081620(5)			
99	Es	252	252.082970(50)		[252]	
100	Fm	257	257.095099(7)		[257]	
101	Md	256	256.094050(60)		[258]	
		258	258.098425(5)			
102	No	259	259.10102(11)		[259]	
103	Lr	262	262.10969(32)		[262]	
104	Rf	261	261.10875(11)		[261]	
105	Db	262	262.11415(20)		[262]	
106	Sg	266	266.12193(31)		[266]	
107	Bh	264	264.12473(30)		[264]	
108	Hs	277	269.13411(46)		[277]	
109	Mt	268	268.13882(34)		[268]	
110	Uun	281	271.14608(20)		[281]	
111	Uuu	272	272.15348(36)		[272]	

Z		*A*	Rel. Atomic Mass	Isotopic Composition	Standard Atomic Weight	Notes
112	Uub	285			[285]	
113						
114	Uuq	289			[289]	
115						
116	Uuh	292			[292]	

Notes:

a Air reference material used for the best measurement.

b Commercially available Li materials have atomic weights that range between 6.939 and 6.996; if a more accurate value is required, it must be determined for the specific material. Note: The range given in Atomic Weights of the Elements 1995 was 6.94 to 6.99.

c The range of ^{2}H in tank hydrogen is 0.0032 - 0.0184 atom %.

d Materials depleted in ^{6}Li and ^{235}U are commercial sources of laboratory shelf reagents. In the case of Li such samples are known to have ^{6}Li abundances in the range 2.007 – 7.672 atom %, with natural materials at the higher end of this range.

e The Commission on Atomic Weights and Isotopic Abundances recommends that the value of 272 be employed for ^{14}N/^{15}N of N_2 in air for the calculation of atom % 15N from measured δ^{15}N values.

f Evaluated isotopic composition is for most but not all commercial samples. Some isotopes are altered because of the contribution of a daughter product from the radioactive decay of another element. These isotopes are: ^{40}Ca, ^{87}Sr, ^{138}Ce, ^{143}Nd, ^{176}Hf, ^{187}Os, ^{206}Pb, ^{207}Pb, ^{208}Pb, and ^{235}U. Because the abundances must add up to 100 percent the abundances of all isotopes of an element are affected.

g Geological specimens are known in which the element has an isotopic composition outside the limits for normal material. The difference between the atomic weight of the element in such specimens and that given in the table may exceed the stated uncertainty.

h An electron multiplier was used for these measurements and the measured abundances were adjusted using a square root of the masses.

m Modified isotopic compositions may be found in commercially available material because it has been subjected to an undisclosed or inadvertent isotopic fractionation. Substantial deviations in the atomic weight and isotopic composition of the element from that given in the table can occur.

r Range in isotopic composition of normal terrestrial material limits the precision of isotopic composition and atomic weight. The tabulated values should be applicable to any normal material.

w Fresh water reference material used for the best measurement.

From: Coursey, J.S., D.J. Schwab, and R.A. Dragoset, (2003), Atomic Weights and Isotopic Compositions (version 2.4). [Online] Available: `http://physics.nist.gov/Comp` [2004, July 21]. National Institute of Standards and Technology, Gaithersburg, MD. Originally published as T.B. Coplen, Atomic weights of the elements 1999, *Pure Appl. Chem.*, **73**, 667–683, 2001; K.J.R. Rosman and P.D.P. Taylor, Isotopic compositions of the elements 1997, *J. Phys. Chem. Ref. Data*, **27**, 1275–1287, 1998; and G. Audi and A.H. Wapstra, The 1995 update to the atomic mass evaluation, *Nucl. Phys. A*, **595**, 409–480, 1995.

A.12 Fragmentation Patterns and Total Ionization Cross-Sections

There are several gases of aeronomic interest for measurement by a mass spectrometers, as stable, radical or disequilibrium species (see Table A.54).

Table A.54: Atmospheric gases of interest

Planet or Body	**Atmospheric Gases of Aeronomic Interest**
Earth, Venus, Mars	H_2, He, H_2O, N_2, CO, O_2, NO, Ar, CO_2, Xe
Titan	C_2H_2 (acteylene), Ar, CO_2, CO, C_2H_6 (ethane), C_2H_4 (ethylene), He, H_2, Kr, CH_4 (methane), C_3H_4 (allyene, propadiene), Ne, Xe, N_2, O_2, C_3H_8 (propane), HCN (hydrogen cyanide), C_4H_2 (diacetylene), C_2N_2 (cyanogen), HC_3N (methylacthylene), CH_3CN (acetonitrile)
Jupiter, Saturn	H_2, He, H_2O, CH_4 (methane), C_2H_6 (ethane), C_2H_2 (acteylene), C_2H_4 (ethylene), C_3H_4 (allyene, propadiene), C_3H_8 (propane), C_4H_2 (1,3-butadiyne), C_6H_6 (benzene), H_3N (ammonia), H_2S (hydrogen sulfide), PH_3 (phosphine), CO, CO_2, GeH_4, AsH_3, HCl, $(H_2)_2$, Ne, Ar, Kr, Xe
Comets	Ar, CO_2, CH_4 (methane), H_2, Ne, O_2, Kr, Xe, N_2, C_2H_6 (ethane), C_3H_8 (propane), C_2H_2 (acteylene), C_2H_4 (ethylene), He, Xe, H_2O, CH_4O (methyl alcohol), H_3N (ammonia), CO, CH_2O (formaldehyde), HCN (hydrogen cyanide), C_2N_2 (cyanogen), HC_3N (methylacthylene), and CH_3CN (acetonitrile)
Radicals	H, C, N, O, OH, CS, CH_3, Cl, ...

The response of a generic mass spectrometer ion source has been given in Chapter 3.1.2. For electron impact, the number of ions produced per second is proportional to the ionizing electron current, the total ionization cross section of the gas species at a given electron energy, the time spent in the ionizing region and the efficiency of extraction. The variety of ions produced from a single gas species can be simple or complex depending on how the electron impact process fragments and ionizes the species. Included in this section are the branching ratios and total ionization cross sections of some of the more common species encountered in planetary atmospheric gas measurements. The ratio of the total ionization cross section of a given gas to that of molecular nitrogen is useful when applying the results to a specific mass spectrometer response since the molecular nitrogen sensitivity is easily measured in the laboratory. Examples of the branching ratios (mass fragmentation patterns) and total ionization cross sections are given below. In the case of the noble gases Ar, Kr, and Xe the branching ratios include significant isotopic contributions at both the single and double ionized mass-to-charge (M/Z in units of Daltons per charge) ratios. Fragmentation patterns are also useful for identification of gas species. In conjunction with

the total ionization cross section, they can be used for first order spectral deconvolution when laboratory data for that particular gas species and instrument are not available.

In the work of Srivastava and colleagues on the total ionization cross-section and branching ratio (fragmentation pattern) of many species, special care was taken to collect all of the ions produced in the ionization process. In this sense, they represent the "best" measurements of the ionization cross-section and fragmentation pattern for a given species. However, theses measurements may not apply to most mass spectrometers because these instruments typically do not detect all of the ions produced in the ion source (i.e. there is an instrument discrimination function). The NIST mass spectral fragmentation database and the measurements of *Duric et al.* [1991] and *Harrision et al.* [1966] are probably closer to the performance of most typical spaceflight mass spectrometers.

A.12.1 Neutral Gas Electron Impact Mass Fragmentation Patterns

The NIST neutral gas fragmentation data were taken from the NIST/EPA/NIH Mass Spectra Library, V2.0 a, build Jul 1, 2002 (`http://www.nist.gov/srd/nist1a.htm`) distributed by the Standard Reference Data Program of the National Institute of Standards and Technology. Copyright by the U.S. Secretary of Commerce. The electron impact mass spectrometer data are obtained at the traditional value of 70 eV, however there is little change over the range 40–200 eV according to Stephen E. Stein. Note that the NIST ratios have a maximum value of 999 and a minimum value of 1. Some spectra list Tr for trace amounts (less than 1). In the following table, the values have been normalized such that 999 is equal to 1.000. Tr is translated as 0.000. The reference for the library is `http://www.nist.gov/srd/nist1a.htm` (purchase Windows version) or `http://www.nist.gov/srd/nist1.htm` (purchase ASCII version), `http://webbook.nist.gov/` (on line reference for mass spectra; view image of digitized spectrum; download (or view) spectrum image in SVG format; download spectrum in JCAMP-DX format).

Contact:
Stephen E. Stein
Mass Spectrometry Data Center
National Institute of Standards and Technology
Gaithersburg, MD 20899-8380, USA
Tel: +1 301 975-2505
E-mail: `sstein@nist.gov`

Table A.55: NIST neutral gas fragmentation patterns for gases of aeronomic interest

M/Z	$\mathbf{H_2}$ Hydrogen	**He** Helium	$\mathbf{CH_4}$ Methane	$\mathbf{H_3N}$ Ammonia	$\mathbf{H_2O}$ Water	$\mathbf{C_2H_2}$ Acetylene	**CHN** Hydrogen cyanide	**CO** Carbon monoxide
1	0.021							
2	1.000							
3								
4		1.000						
5								
6								
7								
8								
9								
10								
11								
12			0.038			0.007	0.042	0.047
13			0.106			0.032	0.017	
14			0.204	0.022		0.001	0.017	
15			0.888	0.075			0.001	
16			1.000	0.801	0.009			0.017
17			0.016	1.000	0.212			
18				0.004	1.000			
19					0.005			
20					0.003			
21								
22								
23								
24						0.050		
25						0.191		
26						1.000	0.168	
27						0.022	1.000	
28						0.001	0.017	1.000
29							0.001	0.012
30								

Table A.55: NIST neutral gas fragmentation patterns (continued)

M/Z	$\mathbf{C_2H_4}$ Ethylene	$\mathbf{N_2}$ Nitrogen	$\mathbf{CH_2O}$ Formaldehyde	**NO** Nitric oxide	$\mathbf{C_2H_6}$ Ethane	$\mathbf{O_2}$ Oxygen	$\mathbf{CH_4O}$ Methyl Alcohol	$\mathbf{C_3H_4}$ Propyne, Allene
1								
2	0.001				0.002		0.003	
3								
4								
5								
6								
7								
8								
9								
10								
11								
12	0.005		0.010		0.004		0.002	0.017, 0.041
13	0.009		0.010		0.010		0.006	0.017, 0.034
14	0.021	0.137	0.010	0.075	0.030		0.016	0.012, 0.040
15	0.003		0.020	0.024	0.044		0.123	0.011, 0.003
16				0.015	0.001	0.218	0.001	
17							0.003	
18							0.007	
19							0.001	—— , 0.031
20								—— , 0.038
21								
22								
23								
24	0.023				0.005			0.011, 0.027
25	0.078				0.035			0.025, 0.046
26	0.529				0.232			0.025, 0.048
27	0.624				0.332			—— , 0.007
28	1.000	1.000	0.240		1.000		0.045	
29	0.023	0.007	1.000		0.215		0.445	
30	0.001		0.581	1.000	0.262		0.064	
31			0.005	0.004	0.005		1.000	
32				0.002		1.000	0.744	
33							0.011	
34							0.001	
35								
36								0.053, 0.094
37								0.198, 0.326
38								0.285, 0.405
39								0.793, 0.963
40								1.000, 1.000
41								0.035, 0.033
42								0.002, 0.001

Table A.55: NIST neutral gas fragmentation patterns (continued)

M/Z	$\mathbf{C_2H_3N}$ Acetonitrile	$\mathbf{C_3H_8}$ Propane	$\mathbf{CO_2}$ Carbon dioxide	$\mathbf{C_4H_2}$ 1,3-Butadiyne Diacetylene	$\mathbf{C_3HN}$ Propiolonitrile	$\mathbf{C_2N_2}$ Ethanedinitrile
12	0.014	0.003	0.087	0.038	0.041	0.010
13	0.009	0.006		0.024	0.008	
14	0.054	0.022			0.006	
15	0.010	0.072				
16		0.004	0.096		0.000	
17					0.000	
18					0.000	
19		0.007				
20		0.008				
21						
22			0.019			
23						
24	0.007			0.026	0.065	
25	0.012	0.005		0.095	0.079	
26	0.015	0.091		0.006	0.034	0.070
27	0.009	0.419			0.006	
28	0.021	0.588	0.098		0.001	
29		1.000	0.001			
30		0.022				
31						
32					0.000	
33						
34						
35						
36		0.003		0.029	0.034	
37		0.030		0.054	0.031	
38	0.092	0.053		0.010	0.066	0.030
39	0.176	0.189			0.008	
40	0.504	0.028			0.000	
41	1.000	0.134				
42	0.026	0.060				
43		0.231				
44		0.274	1.000			
45		0.009	0.012			
46			0.004		0.000	
47					0.000	
48				0.084		
49				0.360		
50				1.000	0.264	
51				0.042	1.000	
52				0.002	0.034	1.000
53					0.000	0.020

Table A.55: NIST neutral gas fragmentation patterns (continued)

M/Z	**Ar** Argon	**Kr** Krypton	**Xe** Xenon
20	0.146		
36	0.003		
38	0.000		
40	1.000		
41		0.034	
42		0.159	
43		0.049	
62			0.000
64			0.013
65			0.029
66			0.177
67			0.069
68			0.060
78		0.006	
80		0.042	
82		0.206	
83		0.205	
84		1.000	
86		0.306	
124			0.003
126			0.003
128			0.070
129			0.985
130			0.152
131			0.794
132			1.000
134			0.378
136			0.319

A.12.2 Neutral Gas Electron Impact Total Ionization Cross Sections

The following table is short listing of total ionization cross sections. A list of experimental data on electron impact ionization for atoms and ions ranging from H to U is given in *Tawara and Kato* [1987]. An early compilation of cross-sections for atoms, atomic ions and diatomic molecules is given in *Rapp and Englander-Golden* [1965]; *Keiffer and Dunn* [1966]; *Keiffer* [1969]. Statistical methods have been used to calculate the total ionization cross-sections for organic molecules by *Fitch and Sauter* [1983] who predicted the average cross section for 179 organic compounds with an average error of about 4.7%.

NIST has an Electron-Impact Ionization Cross Section Database. The total ionization cross-section of a number of atoms and molecules are calculated over an energy range from threshold to several keV. The theory (the Binary-Encounter-Bethe (BEB) model) used in this ionization cross section database is designed for electron-impact ionization and combines the Mott cross section with the high-T behavior of the Bethe cross section. It does not use any fitting parameters, and provides a simple analytic formula for the ionization cross section per atomic/molecular orbital. The total ionization cross section for a target is obtained by summing the orbital cross sections. For many molecules, a comparison is made with experimental data where they exist. The BEB data web site reference is:
`http://physics.nist.gov/PhysRefData/Ionization/intro.html`

Contact:
Dr. Yong-Ki Kim
Atomic Physics Division
National Institute of Standards and Technology
Gaithersburg, MD 20899-8423, USA
phone 301-975-3203
fax 301-990-1350
email `yong-ki.kim@nist.gov`

Table A.56: NIST BEB total ionization cross sections for 70 eV and 25 eV

Species	**70 eV** 10^{-16} **cm**^{2}	**XS/XSN2**	**25 eV** 10^{-16} **cm**^{2}	**XS/XSN2**
Hydrogen atom (H)	0.593		0.428	
Helium (He)	0.326	0.13	0	0.0
Carbon (C)	2.32		1.44	
Nitrogen (N)	1.55		0.675	
Oxygen (O)	1.36		0.519	
Hydrogen molecule (H_2)	1.021	0.41	0.521	0.63
Water (H_2O)	2.275	0.91	0.930	1.13
Nitrogen molecule (N_2)	2.508	1.00	0.825	1.00
Ammonia (NH_3)	3.036	1.20	1.494	1.81
Nitric oxide (NO)	2.807	1.12	1.102	1.34
Oxygen molecule (O_2)	2.441	0.97	0.775	0.94
Carbon monoxide (CO)	2.516	1.00	0.891	1.08
Carbon dioxide (CO_2)	3.521	1.40	1.144	1.39
Hydrogen sulfide (H_2S)	4.145	1.65	2.773	3.36
Nitrous oxide (N_2O)	3.710	1.48	1.315	1.59
Nitrogen dioxide (NO_2)	3.532	1.42	1.132	1.37
Ozone (O_3)	3.520	1.40	1.144	1.39
Carbon monosulfide (CS)	4.548	1.81	2.588	3.14
Carbonyl sulfide (COS)	4.925	1.96	2.254	2.73
Disulfur (S_2)	7.927	3.15	5.816	7.05
Sulfur dioxide (SO_2)	4.992	1.98	2.194	2.66
Carbon disulfide (CS_2)	7.970	3.17	5.527	6.70
Formaldehyde (CH_2O)	4.140	1.64	1.834	2.23
Methane (CH_4)	3.524	1.41	1.748	2.12
Acetylene (C_2H_2)	4.374	1.72	2.399	2.91
Ethylene (C_2H_4)	5.115	2.04	2.653	3.22
Ethane (C_2H_6)	6.422	2.56	3.435	4.16
Allene (C_3H_4)	8.080	3.22	4.385	5.32
Propyne (C_3H_4)	7.662	3.06	4.192	5.08
Propene (C_3H_6)	8.736	3.48	4.688	5.66
Propane (C_3H_8)	8.619	3.44	4.338	5.26
Diacetylene (C_4H_2)	8.895	3.55	4.980	6.04
Vinylacetylene (C_4H_4)	9.868	3.93	5.475	6.64
Trans-butadiene (C_4H_6)	10.897	4.34	5.985	7.25
1-Butene (C_4H_8)	11.755	4.61	6.212	7.52
Trans-2-butane (C_4H_8)	11.829	4.72	6.306	7.64
Isobutane (C_4H_8)	11.902	4.75	6.274	7.61
Benzene (C_6H_6)	15.025	5.99	8.354	10.13

Table A.57: Total ionization cross sections

Gas	**XS Ref. 1 75 eV**	**XS/2.75 Ref. 1**	**XS/XSN2 Ref. 2 75 eV**	**SN/SNN2 Ref. 2 IG**	**SN/SNN2 Ref. 19,21 IG**	**Ref. 70 eV**	**XS**	**XS/XSN2**
He	0.38	0.14	0.13	0.19	0.164–0.190	3	0.32	0.12**
					0.221	18	0.365	0.138
						23	0.39	0.15**
						24	0.318	0.12**
Ne	0.62	0.23	0.25	0.33	0.305–0.320	3	0.52	0.20**
					0.358	11	0.56	0.20
						18	0.584	0.220
						23	0.62	0.23**
						24	0.488	0.18**
Ar	3.52	1.28	1.23	1.37	1.37–1.46	3	2.82	1.06**
					1.34	11	3.53	1.26
						18	3.15	1.189
						23	2.81	1.06**
						24	2.78	1.05**
Kr	5.29	1.92	1.84	1.91	1.89–2.00	3	4.32	1.64**
					1.88	11	5.18	1.84
						18	4.79	1.808
						23	3.5	1.32**
						24	3.94	1.49**
Xe	7.31	2.66	2.62	2.79	2.78–2.83	18	5.82	2.196
					2.5	11	7.49	2.67
						3	5.42	2.05**
						23	5.10	1.92**
						24	5.35	2.02**

Table A.57: Total ionization cross sections (continued)

Gas	**XS Ref. 1 75 eV**	**XS/2.75 Ref. 1**	**XS/XSN2 Ref. 2 75 eV**	**SN/SNN2 Ref. 2 IG**	**SN/SNN2 Ref. 19,21 IG**	**Ref. 70 eV**	**XS**	**XS/XSN2**
H_2	1.01	0.37	0.38	0.44	0.41	4	0.980	0.37**
					0.491	11	1.29	0.46
						18	1.104	0.417
D_2			0.40	0.40		18	1.115	0.421
N_2	**2.75**	1.00	1.00	1.00	1.00	6	2.587	0.98**
						11	2.81	1.00
						18	2.65	1.00
O_2	2.55	0.93	0.96	0.87	0.67–0.92	5,8	2.46	0.93**
					0.879	11	3.04	1.08
						18	2.71	1.023
O						20	1.28	
Air			0.75	0.97	0.89–0.93			
NO	3.06	1.11	1.24	1.17*		16	3.20	1.21**
						18	3.31	1.249
CO	2.99	1.09	1.06	1.02	0.97–1.04	7	2.36	0.89**
					0.950	5	2.50	0.94**
						11	3.03	1.08
						18	2.84	1.072
CO_2	4.31	1.57	1.39	1.36	1.36–1.47	7	3.10	1.17**
					1.35	11	4.05	1.44
						18	3.61	1.362
H_2O	2.96	1.08	1.03	1.25		12	3.029	1.14**
N_2O	6.45	2.35	1.30	1.66*		16	3.35	1.26**
						18	3.91	1.475
NO_2						16	3.20	1.20**

Table A.57: Total ionization cross sections (continued)

Gas	**XS Ref. 1 75 eV**	**XS/2.75 Ref. 1**	**XS/XSN2 Ref. 2 75 eV**	**SN/SNN2 Ref. 2,21 IG**	**Ref. 70 eV**	**XS**	**XS/XSN2**
CH_4	4.30	1.56	1.63	1.49	5,7	3.60	1.39
				1.58	7	4.04	1.52**
					5	3.66	1.38**
					10	3.64	1.37**
					11	4.67	1.66
					18	4.16	1.570
					22	3.93	1.48
					23	4.24	1.6**
C_2H_2	4.98	1.81	2.06	1.66	9	5.04	1.90**
				0.614	11	4.61	1.64
C_2H_4	6.66	2.42	2.27	2.14	11	6.12	2.18
				1.29	18	6.47	2.442
					22	5.76	2.17
C_2H_6	8.35	3.04	2.74	2.53	10	6.13	2.31**
				2.58	11	8.39	2.99
					22	6.93	2.62
C_3H_4 (propyne)						7.40	2.86
				1.41			
C_3H_4 (allene)						7.20	2.78
				1.31			
C_3H_6	9.73	3.54	3.25	3.16			
				1.77	11	8.97	3.19
					22	8.82	3.33

Table A.57: Total ionization cross sections (continued)

Gas	**XS**	**XS/2.75**	**XS/XSN2**	**SN/SNN2**		**XS**	**XS/XSN2**
	Ref. 1	**Ref. 1**	**Ref. 2**	**Ref. 2,21**	**Ref.**		
	75 eV		**75 eV**	**IG**	**70 eV**		
cyclo-C_3H_6	10.80	3.93	3.75				
					11	10.4	3.70
					22	8.48	3.2
C_3H_8	11.10	4.04	3.64	3.80	10	8.62	2.12**
				3.44	11	11.6	4.13
					22	10.09	3.81
C_4H_8			3.82	3.60			
				2.07			
i-C_4H_8	12.90	4.69					
C_4H_{10}			4.57	4.37			
i-C_4H_{10}	14.40	5.24					
				4.02			
n-C_4H_{10}	14.10	5.13			11	14.4	5.12
				4.04			
C_5H_{10}			4.81				
i-C_5H_{10}	17.50	6.36					
cyclo-C_5H_{10}	17.30	6.29	6.01		11	16.9	6.01
C_5H_{12}			5.60				
n-C_5H_{12}	18.60	6.76			11	17.7	6.09
i-C_5H_{12}	18.00	6.55					
neo-C_5H_{12}	16.90	6.15					
					11	17.0	6.05
C_6H_6	16.90	6.15	5.19	5.18	11	13.4	4.77
cyclo-C_6H_8	17.90	6.51					
cyclo-C_6H_{10}	19.10	6.95			11	15.5	5.52
1,5-C_6H_{10}	15.80	5.75					
cyclo-C_6H_{12}	23.60	8.58	6.60	6.40*	11	17.9	6.37
n-C_6H_{14}					11	17.9	6.37

Table A.57: Total ionization cross sections (continued)

Gas	**XS Ref. 1 75 eV**	**XS/2.75 Ref. 1**	**XS/XSN2 Ref. 2 75 eV**	**SN/SNN2 Ref. 2,21 IG**	**Ref. 70 eV**	**XS**	**XS/XSN2**
1-C_6H_{12}	20.00	7.27					
C_6H_{12}			6.49	6.73*			
C_6H_{14}			6.77	6.60*			
n-C_6H_{14}	22.30	8.11			11	20.8	7.4
$C_6H_5CH_3$				6.81			
C_7H_{16}	30.00	10.91	7.72	7.60*	11	22.5	8.01
C_8H_{16}			7.22				
C_8H_{18}			8.18				
C_9H_{18}			8.72				
C_9H_{20}			8.86				
$C_{10}H_{20}$			10.37				
CH_3Cl	9.46	3.44					
C_2H_5Cl	12.30	4.47			11	10.8	3.84
CH_3Br	11.20	4.07					
CH_3I	12.90	4.69					
CH_2CH_2O	7.55	2.75					
CH_3OH					17	4.69	1.77**
CH_3CHO	7.95	2.89			11	6.93	2.47
C_3H_6O	11.70	4.25					
$(CH_3)_2O$	12.80	4.65			11	9.33	3.32
$(CH_3)_2CO$	12.10	4.40			11	10.2	3.63
NH_3	3.54	1.29	1.23	1.11*	15	3.0113	1.14**
				0.645			
PH_3	11.30	4.11					
H_2S	5.42	1.97	2.03	2.20*	14	3.928	1.48**
					11	6.92	2.46
HCl	4.30	1.56	1.61	1.65*			
HCN	6.80	2.47					
$(CN)_2$	10.80	3.93					
CS_2	14.00	5.09			15	8.4078	3.17**
SO_2	14.00	5.09			13	6.93	2.61**

Table A.58: Abbreviations

Abbr.	Name
*	Cold-cathode gauge
**	Normalize to N_2 cross section value of 2.65×10^{-16} cm^2
1	*Kiser* [1965]
2	*Nakao* [1975]
3	*Krishnakumar and Srivastava* [1988]
4	*Krishnakumar and Srivastava* [1994]
5	*Kanik et al.* [1993]
6	*Krishnakumar and Srivastava* [1990]
7	*Orient and Srivastava* [1987]
8	*Krishnakumar and Srivastava* [1992]
9	*Zheng and Srivastava* [1996]
10	*Duric et al.* [1991]
11	*Harrision et al.* [1966] Note data taken at 75 eV electron energy.
12	*Rao et al.* [1995]
13	*Orient and Srivastava* [1984]
14	*Rao and Srivastava* [1993]
15	*Rao and Srivastava* [1991]
16	*Lopez et al.* [2003]
17	*Srivastava et al.* [1996]
18	*Rapp and Englander-Golden* [1965]
19	*Holanda* [1972]
20	*Zipf* [1996]
21	*Nakayama and Hojo* [1974]
22	*Nishimura and Tawara* [1994]
23	*Vallance et al.* [1997]
24	*Wetzel et al.* [1987]
IG	Ion gauge sensitivity at ∼110 eV average electron energy with grid potential at 150 V
Ref.	Reference
SNN2	Ion gauge sensitivity for a gas relative to that for N_2
XS	Cross section of gas in units of 10^{-16} cm^2
XSN2	Cross section of gas relative to that of molecular nitrogen, N_2, in the same column for Ref. 1 and 2; in the general reference column in Ref. 18 and 11 are divided by the N_2 cross-section in that reference

Bibliography

The following abbreviations are used to indicate the methods used to determine the ionization cross-section in the papers listed in the bibliography:

TIC	Measured total ionization cross-section.
CTIC	Calculated total ionization cross-section.
PIC	Measured partial ionization cross-section.
IGTIC	Ion gauge total ionization cross-section.

Bartlett, P.L. and A.T. Stelbovics, Calculations of electron-impact total-ionization cross sections, *Phys. Rev. A*, **66**, 012707-1 – 012707-10, 2002. CTIC

Duric, N., I. Cadez, and M. Kurpea, Electron impact total ionization cross-sections for methane, ethane and propane, *Int. J. Mass Spectrom. and Ion Processes*, **108**, R1–R10, 1991. TIC

Fitch, W.L. and A.D. Sauter, Calculation of relative electron impact total ionization cross sections for organic molecules, *Anal. Chem.*, **55**, 832–835, 1983. CTIC

Grill, V., G. Walder, P. Scheier, M. Kurdel, and T.D. Mark, Absolute partial and total electron impact ionization cross sections for C_2H_6 from threshold up to 950 eV, *Intl. J. Mass Spectrom. and Ion Processes*, **129**, 31–42, 1993. PIC

Harrison, A.G., E.G. Jones, S.K. Gupta, and G.P. Nagy, Total cross sections for ionization by electron impact, *Can. J. Chem.*, **44**, 1967–1973, 1966. TIC

Holanda, R., Sensitivity of hot-cathode ionization vacuum gauges in several gases, *NASA Technical Note*, **TN D-6815**, 1972. IGTIC

Kanik, I., S. Trajhmar and J.C. Nickel, Total electron scattering and electronic state excitations cross sections for O_2, CO and CH_4, *J. Geophys. Res.*, **98**, 7447–7460, 1993. TIC

Keiffer, L.J., Low-energy electron-collision cross-section data. Part I:Ionization, dissociation, vibrational excitation, *Atomic Data*, **1 (1)**, 19–89, 1969. Erratum *Atomic Data*, **1 (19)**, 359, 1969. TIC

Keiffer, L.J. and G.H. Dunn, Electron impact ionization cross-section data for atoms, atomic ions and diatomic molecules: I. Experimental data, *Rev. Mod. Phys.*, **38 (1)**, 1–35, 1966. TIC

Kiser, R.W., *Introduction to Mass Spectrometry and Its Applications*, Appendix III, Total Ionization Cross Sections, 300, Prentice-Hall, Inc., Englewood Cliffs, N.J., 1965. TIC

Krishnakumar, E. and S.K. Srivastava, Ionisation cross sections of rare-gas atoms by electron impact, *J. Phys. B*, **21**, 1055–1082, 1988. PIC

Krishnakumar, E. and S.K. Srivastava, Cross sections for the production of N_2^+, N^++N_2^{2+} and N^{2+} by electron impact on N_2, *J. Phys. B:*, **23**, 1893–1903, 1990. PIC

Krishnakumar, E. and S.K. Srivastava, Cross-sections for electron impact ionization of O_2, *Int. J. Mass Spectrom. and Ion Processes*, **113**, 1–12, 1992. PIC

Krishnakumar, E. and S.K. Srivastava, Electron correlation effects in the dissociative ionization of H_2, *J. Phys. B*, **27**, L251–L258, 1994. TIC

Lopez, J., V. Tarnovsky, M. Gutkin, and K. Becker, Electron-impact ionization of NO, NO_2, and N_2O, *Int. J. Mass Spectrom.*, **225**, 25–37, 2003. PIC

Nakao, F., Determination of the ionization gauge sensitivity using the relative ionization cross-section, in *Proc. 6th Int. Vacuum Congress 1974 Japan, J. Appl. Phys.*, **Suppl. 2, Pt. 1**, 113–4116, 1974. IGTIC

Nakayama, K. and H. Hojo, Relative ion gauge sensitivities to various hydrocarbon gases, *Vacuum*, **25 (9/10)**, 431–435, 1955. IGTIC

Nishimura, H. and H. Tawara, Total electron impact ionization cross sections for simple hydrocarbon molecules, *J. Phys. B*, **27**, 2063–2074, 1994. TIC

Orient, O.J. and S.K. Srivastava, Electron impact ionisation of H_2O, CO, CO_2 and CH_4, *J. Phys. B*, **20**, 3923–3936, 1987. PIC

Orient, O.J. and S.K. Srivastava, Mass spectrometric determination of partial and total electron impact ionization cross sections of SO_2 from threshold up to 200 eV, *J. Chem. Phys.*, **80 (1)**, 140–143, 1984. PIC

Rao, M.V.V.S., I. Iga, and S.K. Srivastava, Ionization cross-sections for the production of positive ions from H_2O by electron impact, *J. Geophys. Res.*, **100**, 26421–26425, 1995. PIC

Rao, M.V.V.S. and S.K. Srivastava, Electron impact ionization and attachment cross-sections for H_2S, *J. Geophys. Res.*, **98**, 13137–13145, 1993. PIC

Rao, M.V.V.S. and S.K. Srivastava, Cross-sections for direct and dissociative ionization of NH_3 and CS_2, *J. Geophys. Res.*, **96**, 17563–17567, 1991. PIC

Rapp, D. and P.E. Englander-Golden, Total cross sections for ionization and attachment in gases by electron impact. I. Positive ionization, *J. Chem. Phys.*, **43**, 1464–1479, 1965. TIC

Smith, O.J., Cross-sections for formation of parent and fragment ions by electron impact from C2N2, *Int. J. Mass Spect.*, **54**, 55–59, 1983. PIC

Srivastava, S.K. and E. Krishnakumar, Cross-sections for the production of cations by electron impact on methanol, *J. Geophys. Res.*, **101**, 26155–26160, 1996. PIC

Tawara, H. and T. Kato, Total and partial ionization cross sections of atoms and ions by electron impact, *Atomic and Nuclear Data Tables*, **36**, 167–353, 1987. PIC

Tarnovsky, V. and K. Becker, The electron-impact ionization of Ar and Kr revisted: A critical analysis of double-to-single ionization cross section ratio measurements using the fast atom-beam technique, *Z. Phys. D*, **22**, 167–353, 1987. PIC

Tian, C. and C.R. Vidal, Cross sections of the electron impact dissociative ionization of CO, CH_4 and C_2H_2, *J. Phys. B*, **22**, 603–610, 1992. PIC

Vallance, C., S.A. Harris, J.E. Hudson, and P.W. Harland, Absolute electron impact ionization cross sections for CH_3X, where X=H, F, Cl, Br, and I, *J. Phys. B*, **30**, 2465–2475, 1997. TIC

Wetzel, R.C., F.A. Baiocchi, T.R. Hayes and R.S. Freund, Absolute cross sections for electron-impact ionization of rare-gas atoms by the fast-neutral-beam method, *Phys. Rev. A*, **35**, 559–577, 1987. TIC

Zheng, S.-H. and S.K. Srivastava, Electron-impact ionization and dissociative ionization of acetylene, *J. Phys. B*, **29**, 3235–3244, 1996. PIC

Zipf, E.C., The ionization of atomic oxygen by electron impact, *Planet. Space Sci.*, **33**, 1303–1307, 1985. PIC

A.13 Authors' Addresses

Andre Balogh
International Space Science Institute, Hallerstrasse 6, 3012 Bern, Switzerland
andre.balogh@issibern.ch

Larry H. Brace †

Dennis J. Chornay
Interplanetary Physics Branch, Mail Code 692, NASA Goddard Space Flight Center, Greenbelt, MD 20771, USA
dennis.j.chornay@gsfc.nasa.gov

Andrew J. Coates
Mullard Space Science Laboratory, University College London, Holmbury St. Mary, Dorking, Surrey RH5 6NT, United Kingdom
ajc@mssl.ucl.ac.uk

Victoria Coffey
Space Plasma Physics Branch, Space Science Laboratory, Mail Code ES83, NASA Marshall Space Flight Center, Huntsville, AL 35812, USA
victoria.coffey@msfc.nasa.gov

Dennis DeCoste
Jet Propulsion Laboratory, MS 126-347, 4800 Oak Grove Drive, Pasadena, CA 91109, USA
decoste@aig.jpl.nasa.gov

Bronislaw K. Dichter
Assurance Technology Corporation, 84 South Street, Carlisle, MA 01741, USA
dichter@assurtech.com

David S. Evans
Space Environment Center, NOAA, 325 Broadway, Boulder, CO 80305, USA
david.s.evans@noaa.gov

Michael J. Golightly
Air Force Research Laboratory, 29 Randolph Road, Hanscom Air Force Base, MA 01731, USA
michael.golightly@hanscom.af.mil

Walter R. Hoegy
Leelanau Research, 13601 S Beaver Pond Rd., Empire, MI 49630-9622, USA
wrhoegy@gmail.com

Ernest Holeman
Institute for Scientific Research, Boston College, St Clement's Hall 402, 140 Commonwealth Avenue, Chestnut Hill, MA 02467, USA
ernest.holeman@Hanscom.af.mil

Katherine Kadinsky-Cade
Air Force Research Laboratory, 29 Randolph Road, Hanscom Air Force Base, MA 01731, USA
katharine.kadinsky-cade@hanscom.af.mil

Justin Kasper
Kavli Institute for Astrophysics and Space Research, Massachusetts Institute of Technology, Building 37-673, 77 Massachusetts Ave., Cambridge, MA 02139-4307, USA
jck@space.mit.edu

Wayne T. Kasprzak
Atmospheric Experiments Laboratory, NASA Goddard Space Flight Center, Mail Code 699, Greenbelt, MD 20771, USA
wayne.t.kasprzak@nasa.gov

Dhiren Kataria
Mullard Space Science Laboratory, University College London, Holmbury St. Mary, Dorking, Surrey RH5 6NT, United Kingdom
dok@mssl.ucl.ac.uk

Lynn Kistler
Space Science Center, University of New Hampshire, Morse Hall, Durham, NH 03824-3525, USA
lynn.kistler@unh.edu

Davin E. Larson
Space Sciences Laboratory, University of California, Berkeley, CA 94720, USA
davin@ssl.berkeley.edu

Alan J. Lazarus
MIT/CSR, Room 37-687, 77 Massachusetts Ave., Cambridge, MA 02139-4307, USA
aji@space.mit.edu

Walter Lennartsson
Lockheed Martin ATC, Palo Alto Research Lab., 3251 Hanover Street, Palo Alto, CA 94307-1191, USA
lenn@mail.spasci.com

Arnaud Masson
ESA/ESTEC, Research and Scientific Support Department, Keplerlaan 1, 2201 AZ, Noordwijk, The Netherlands
amasson@rssd.esa.int

James McFadden
Space Sciences Laboratory, University of California, Berkeley, CA 94720, USA
mcfadden@ssl.berkeley.edu

Forrest S. Mozer
Space Sciences Laboratory, University of California, Berkeley, CA 94720, USA
mozer@ssl.berkeley.edu

Toshifumi Mukai
Institute of Space and Astronautical Science, 3-1-1 Yoshinodai, Sagamihara, Kanagawa 229-8510, Japan
mukai@stp.isas.jaxa.jp

Keith Ogilvie
Laboratory for Extraterrestrial Physics, NASA Goddard Space Flight Center, Mail Code 692, Greenbelt, MD 20771, USA
keith.w.ogilvie@nasa.gov

Götz Paschmann
Max-Planck-Institut für extraterrestrische Physik, Postfach 1312, D-85741 Garching, Germany
goetz.paschmann@mpe.mpg.de

Fred Rich
Air Force Research Laboratory, 29 Randolph Road, Hanscom Air Force Base, MA 01731, USA
frederick.rich@hanscom.af.mil

David W. Robinson
National Physics Laboratory, Teddington, Middlesex, TW11 0LW, United Kingdom
david.robinson@npl.co.uk

Yoshifumi Saito
Institute of Space and Astronautical Science, 3-1-1 Yoshinodai, Sagamihara, Kanagawa 229-8510, Japan
saito@stp.isas.jaxa.jp

Jack Scudder
Dept. of Physics and Astronomy, University of Iowa, Van Allen Hall, Iowa City, IA 52240, USA
jds@hydra.physics.uiowa.edu

John Steinberg
Los Alamos National Laboratory, P.O. Box 1663, MS D466, Los Alamos, NM 87545, USA
jsteinberg@lanl.gov

Oleg Vaisberg
Space Research Institute, Russian Academy of Sciences, Profsoyuznaya 84/32, Moscow, GSP-7, 117997, Russia
olegv@iki.rssi.ru

Rudolf von Steiger
International Space Science Institute, Hallerstrasse 6, 3012 Bern, Switzerland
vsteiger@issibern.ch

Martin Wüest
Vacuum Control, INFICON Aktiengesellschaft, Alte Landstrasse 6, 9496 Balzers, Liechtenstein
martin.wuest@inficon.com

Peter Wurz
Physikalisches Institut der Universität Bern, Sidlerstrasse 5, 3012 Bern, Switzerland
peter.wurz@phim.unibe.ch

Index